

DISSERTATION

A TRIPLE-MOMENT BULK HAIL MICROPHYSICS SCHEME TO INVESTIGATE
THE SENSITIVITIES OF HAIL TO AEROSOLS

Submitted by

Adrian Matthew Loftus

Department of Atmospheric Science

In partial fulfillment of the requirements

For the Degree of Doctor of Philosophy

Colorado State University

Fort Collins, Colorado

Spring 2012

Doctoral Committee:

Advisor: William R. Cotton

Steven A. Rutledge

Susan C. van den Heever

Viswanathan N. Bringi

ABSTRACT

A TRIPLE-MOMENT BULK HAIL MICROPHYSICS SCHEME TO INVESTIGATE THE SENSITIVITIES OF HAIL TO AEROSOLS

Hail is a frequent occurrence in warm season deep convection in many mid-latitude regions and causes significant damage to property and agricultural interests every year. Hail can also have a substantial impact on the precipitation characteristics of deep convection as well as on the dynamic and thermodynamic properties of convective downdrafts and cold-pools, which in turn can affect storm evolution and propagation. In addition, large and often destructive hail commonly occurs in severe convection, yet most one- (1M) and two-moment (2M) bulk microphysics schemes in cloud-resolving numerical models are incapable of producing large hail (diameter $D \geq 2$ cm). The limits imposed by fixing one or two of the distribution parameters in these schemes often lead to particularly poor representations of particles within the tails of size distribution spectra; an especially important consideration for hail, which covers a broad range of sizes in nature. In order to improve the representation of hail distributions in simulations of deep moist convection in a cloud-resolving numerical model, a new triple-moment bulk hail microphysics scheme (3MHAIL) is presented and evaluated. The 3MHAIL scheme predicts the relative dispersion parameter for a gamma distribution function via the prediction of the sixth moment (related to the reflectivity factor) of the distribution in addition to the mass mixing ratio and number concentration (third and zeroth moments, respectively) thereby allowing for a fully prognostic distribution function. Initial testing of this scheme reveals significant improvement in

the representation of sedimentation, melting, and formation processes of hail compared to lower-order moment schemes.

The 3MHAIL scheme is verified in simulations of a well-observed supercell storm that occurred over northwest Kansas on 29 June 2000 during the Severe Thunderstorm and Electrification and Precipitation Study (STEPS). Comparisons of the simulation results with the observations for this case, as well as with results of simulations using two different 2M microphysics schemes, suggest a significant improvement of the simulated storm structure and evolution is achieved with the 3MHAIL scheme. The generation of large hail and subsequent fallout in the simulation using 3MHAIL microphysics show particularly good agreement with surface hail reports for this storm as well as with previous studies of hail in supercell storms. On the other hand, the simulation with 2M microphysics produces only small hail aloft and virtually no hail at the surface, whereas a two-moment version of the 3MHAIL scheme (with a fixed relative dispersion parameter) produces unrealistically high amounts of large hail at low levels as a result of artificial shifts in the hail size spectra towards larger diameter hail during the melting process.

The 3MHAIL scheme is also used to investigate the impact of changing the concentrations of aerosols that act as cloud condensation nuclei (CCN) on hail for the 29 June 2000 supercell case. For the simulated supercells in the particular environment examined, an increase in CCN from 100 to 3000 cm^{-3} leads to an increase in the numbers and a decrease in the sizes of cloud droplets, as expected, yet the overall storm dynamics and evolution are largely unaffected. Increases in CCN lead to non-monotonic responses in the bulk characteristics of nearly all hydrometeor fields, surface precipitation, and cold-pool strength. However, higher concentrations of CCN also result in larger hail sizes and greater amounts of large diameter (≥ 2

cm) hail both aloft as well as at the surface. Analyses of the hail formation and growth mechanisms for these simulations suggest that the combination of increased sizes of new hail particles and localized reductions in numbers of new hailstones forming near maximum growth regions with increasing CCN tends to promote conditions that lead to increased hail sizes and amounts of large hail.

ACKNOWLEDGEMENTS

I would like to my advisor Bill Cotton for giving me the opportunity to carry out this research under his guidance and for his valuable insight. I have significantly benefited from his profound knowledge in cloud microphysics and dynamics. I would also like to thank my committee members Steve Rutledge, Sue van den Heever, and Viswanathan Bringi, as well as former committee member Wayne Schubert, for providing helpful suggestions on conducting this research project. Sue van den Heever provided both encouragement and theoretical insight in working out some of the numerous modeling issues faced during this research.

Gustavo Carrió is thanked for his input and assistance in developing the microphysics code, as well as his constant encouragement. Steve Saleeby also provided valuable advice and help regarding the microphysics formulations in the RAMS model. Bob Walko is acknowledged for answering numerous questions about the details of the RAMS model. George Bryan is thanked for his advice on dealing with instabilities associated with the use of observational data to initialize the model.

I thank Louie Grasso for his support and the many conversations we had regarding modeling severe storms and working through unexpected obstacles during this research. I also thank David Lerach and Fang Wang for their moral support and encouragement.

I am grateful to my junior college teacher Paul Sirvatka who stimulated my interest in the science underlying severe storms, weather, and the atmosphere. I also extend thanks to my Masters advisors, Chuck Doswell III and Dan Weber, who continued to mentor me well after I had completed my Masters work at the University of Oklahoma.

I thank my family for all of their love, support, and encouragement. The values of hard work, the desire to learn, and determination instilled upon me by my parents have greatly aided me throughout my journey in academics and in life. I thank my beautiful daughter Sarah for bringing a smile to my face at the ends of many long days and for constantly inspiring me. Lastly, this dissertation would not have been possible without the constant amor, support, patience, understanding, and motivation from my beautiful and loving wife Andrea, with whom I share my success in completing my PhD.

Financial support for this research was provided by the National Science Foundation under grants ATM-0324324, ATM-0638910, and AGS-1005041.

TABLE OF CONTENTS

ABSTRACT.....	ii
ACKNOWLEDGEMENTS.....	v
1. Introduction.....	1
2. Background	4
2.1 Observed characteristics and variability of hail and hail distributions.....	5
2.2 Factors affecting hail growth and hail distributions within deep moist convection.....	10
2.2.1 Updraft characteristics and temperature dependencies.....	10
2.2.2 Liquid water content.....	11
2.2.3 Hailstone embryos.....	13
2.2.4 Hail attributes affecting growth.....	16
2.2.5 Melting of hail.....	19
2.2.6 Aerosol effects.....	20
2.2.6.1 General aerosol impacts on deep convection.....	20
2.2.6.2 Aerosol impacts on hail.....	24
2.3 Dynamical and thermodynamical effects of hail on convection.....	28
2.4 Hail in supercells.....	29
2.5 Radar observations of hail.....	38
2.6 Overview of microphysical schemes.....	40
2.6.1 Bulk microphysical schemes.....	42
2.6.2 Bin microphysical schemes.....	45
3. Model Description.....	48
3.1 Overview of hydrometeors in the RAMS model.....	48
3.2 Derivation of reflectivity factor and hail reflectivity equations.....	56
3.3 Collection.....	60
3.3.1 Bulk collection.....	60
3.3.2 Binned riming of hail.....	70
3.3.3 Alternative methods for the formation of hail.....	72
3.3.3.1 MY05b three-component freezing.....	73
3.3.3.2 F94 hail formation from rain colliding with pristine ice particles.....	75
3.3.3.3 Adjustment to newly formed hail number concentrations.....	78
3.4 Vapor and sensible heat transfer.....	82
3.5 Melting and shedding.....	85
3.5.1 Shedding.....	86
3.5.2 Melting of smallest hailstones.....	90
3.6 Sedimentation.....	96
3.7 Other routines and modifications.....	99
3.7.1 Updating the hail distribution shape parameter v_h	99
3.7.2 Modification to diameter threshold for collisional breakup of rain.....	102
4. Testing of the 3MHAIL microphysics scheme	103
4.1 1M, 2M, and 3MHAIL sedimentation vs. bin sedimentation scheme.....	103
4.2 Combined sedimentation and melting tests.....	123
4.2.1 Hail shaft A simulations.....	126

4.2.2 Hail shaft B simulations.....	146
4.3 Hail formation tests.....	166
4.3.1 Rain-ice collisions in the absence of hail.....	168
4.3.2 Formation of new hail via rain-ice collisions in the presence of pre-existing hail.....	171
4.4 Summary.....	179
5. Verification of 3MHAIL scheme	182
5.1 Introduction.....	182
5.2 Overview of the 29 June 2000 supercell storm.....	183
5.3 General model description and experimental setup.....	187
5.4 Results.....	192
5.4.1 General characteristics of simulated storms and comparisons with observations.....	194
5.4.2 Detailed comparisons with observations.....	209
5.4.3 Microphysical and thermodynamic characteristics of simulated storms.....	232
5.4.3.1 Hail formation and growth processes.....	240
5.4.3.2 Surface precipitation and cold-pool evolution.....	264
5.5 Summary.....	281
6. Sensitivity of hail size distributions to CCN experiments.....	286
6.1 Introduction.....	286
6.2 CCN sensitivity experiments.....	287
6.2.1 General storm evolution and dynamics.....	289
6.2.2 General CCN effects on hydrometeor fields.....	294
6.2.3 CCN effects on hail.....	304
6.2.4 Effects of CCN on surface precipitation and low-level thermodynamics.....	331
6.3 Summary.....	350
7. General summary and suggestions for future work.....	354
7.1 Summary.....	354
7.2 Future work.....	358
REFERENCES.....	363
APPENDIX A.....	382
A.1 Construction of melting and shedding look-up tables for 3MHAIL scheme.....	382
A.2 Original 3MHAIL method for melting of smallest hailstones.....	386
APPENDIX B.....	391
B.1 Bulk sedimentation table construction for 3HAIL.....	391
B.2 Bin sedimentation model (for 1D sedimentation tests; Section 4.1).....	393
B.3 1D sedimentation tests for 3MHAIL vs original RAMS 1M and 2M sedimentation.....	394
APPENDIX C Computation of radar reflectivity from model hydrometeor fields using T-matrix/Mueller matrix method.....	405
C.1 Construction of T-matrix look-up tables.....	405
C.2 Mueller matrix calculations.....	408

1. Introduction

Microphysical processes occurring in deep moist convection are small-scale phenomena that can have a significant impact on the evolution of deep moist convection (Farley and Orville 1986; Srivastava 1987; Ziegler 1988; Jewett et al. 1990; Johnson et al. 1993). While the effects of these processes on convection are capable of being explicitly represented in numerical cloud models today, the processes themselves occur on the sub-grid scale and are thus routinely parameterized using bulk microphysics schemes. These parameterizations typically involve the prognosis of one or two of the moments of the hydrometeor distribution functions and allow for dynamical feedbacks between the convection and the hydrometeor distributions. Previous studies have shown, however, that the storm structure, evolution, and surface precipitation characteristics are sensitive to the parameter values that govern the evolution of the hydrometeor distributions (Meyers et al. 1997, hereafter M97; Ziegler 1988; Gilmore et al. 2004, hereafter GSR04; Cohen and McCaul 2006, Dawson et al. 2010). The characteristics of hail distributions in particular can have a marked influence on the raindrop distributions (Heymsfield and Hjelmfelt 1984; Ziegler 1988) as well as on the dynamic and thermodynamic properties of convective downdrafts and cold pools (Wisner et al. 1972; Rasmussen et al. 1984; Srivastava 1987; Hjelmfelt et al. 1989; Orville et al. 1989; Proctor 1989; Straka and Anderson 1993; GSR04; van den Heever and Cotton 2004, hereafter VC04), which in turn can affect storm evolution and propagation (GSR04, VC04).

It is therefore proposed that improvements in the representation of hail distributions would minimize the sensitivities associated with hail in numerical simulations and ultimately lead to better model solutions of deep moist convection. In addition, large and often destructive hail

commonly occurs in severe convection, yet most single- and double-moment bulk microphysics schemes are incapable of producing large hail (diameter $D \geq 2$ cm). The current study aims to provide a more realistic and detailed representation of hail distributions in the Regional Atmospheric Modeling System (RAMS) through the prognosis of the 6th moment of the distribution, which is related to the radar reflectivity factor for hail (Z_h), in addition to the mass mixing ratio and number concentration, which are already predicted in RAMS. This new triple-moment bulk microphysics scheme for hail (referred to herein as 3MHAIL) is verified in simulations of the 29 June 2000 supercell case (Tessendorf et al. 2005) from the Severe Thunderstorm Electrification and Precipitation Study (STEPS) (Lang et al. 2004) field campaign. This storm produced hail with diameters in excess of 5 cm and a brief tornado. In addition, the 3MHAIL scheme is used to investigate the sensitivities of hail size distributions to changes in CCN concentrations, a topic that has recently gained attention due to the growing interest in aerosol-cloud interactions. The triple-moment scheme is only applied to the hail distribution at this time due to complicating factors such as uncertain (or unknown) collection efficiencies, drop breakup for rain and highly irregular shapes and varying densities for graupel and snow that greatly hinder the computations of the 6th moment for these other hydrometeor categories.

The outline of the paper is as follows. Chapter 2 provides a literature survey detailing the characteristics of hail, hail production processes, feedbacks between hail and deep convection, radar observations of hail, and an overview of microphysical schemes. A description of the 3MHAIL scheme is presented in Chapter 3, and initial testing of the various components of this scheme is covered in Chapter 4. In Chapter 5, results from simulations of the 29 June 2000 supercell using the 3MHAIL as well as two different 2M microphysics schemes are analyzed and compared with observations of this storm, and differences among the simulations are discussed.

The effects of CCN on the simulated hail distributions for the 29 June 2000 supercell case are investigated in Chapter 6. A summary of the conclusions drawn from this study and suggestions for future work are presented in Chapter 7.

2. Background

The majority of the precipitation produced within mid-latitude deep convection during the warm season is from frozen particles that often melt to rain prior to reaching the surface (Braham 1964; Mason 1971; Wisner et al. 1972; Dye et al. 1974; Knight et al. 1974; Farley and Orville 1986; Knight and Knight 2001; Khain and Pokrovsky 2004). The dominant mechanism of precipitation formation in deep convective high-based clouds (such as those occurring over the High Plains of US) is diffusional growth of ice crystals and subsequent riming to larger particle sizes (Knight 1982). Even in deep convection over the tropics and sub-tropics, in which precipitation initially develops from warm rain processes, ice processes, once begun, can dominate the precipitation formation mechanism (Smith et al. 1999; Atlas et al. 2004). The importance of hail in rainfall production was noted by Rasmussen and Heymsfield (1987c), who cited strong evidence that a majority of surface rainfall from an intensely observed Montana hailstorm originated as shed water drops from both growing and melting hailstones. Similarly, List (2010) asserts that collection and subsequent shedding of accreted liquid water from growing hailstones is one of the primary mechanisms for transforming cloud droplets to raindrops in deep convection.

Cotton and Anthes (1989) state that clouds dominated by warm-rain processes are more efficient rain producers than clouds dominated by ice processes. However, ice processes can have significant impacts on the dynamics, thermodynamics, precipitation distributions, and longevity of deep convective clouds, particularly for severe convective storms (Johnson et al. 1993; van den Heever 2001). Studies by Jewett et al. (1990) and Johnson et al. (1993) revealed increases in total surface precipitation, maximum vertical velocities, and perturbation potential

temperatures aloft for supercell simulations in which ice processes were included compared to similar simulations that did not include ice microphysics. Comparisons between the 'no-ice' and 'ice' simulations of Johnson et al. (1993) also revealed that the inclusion of ice processes led to increased storm longevity owing to decreased downdraft strength, greater spatial separation of the downdraft from the updraft, and a 'warmer' low-level cold pool, factors which allowed the storm's gust front to propagate with the storm rather than propagating away from the storm as in the no-ice case. Results from supercell simulations incorporating fixed large mean hail diameters by van den Heever (2001) were similar to those from the ice case of Johnson et al. (1993). It is clear from these studies that correct representation of microphysical processes associated with ice hydrometeors, particularly hail, in numerical simulations of deep convection is crucial for accurate prediction of precipitation and overall convective evolution.

2.1) *Observed characteristics and variability of hail and hail distributions*

Hail generated by deep moist convection in nature varies over a wide range of sizes, with 'equivalent' diameters ranging from approximately 0.5 mm (Huschke 1959) up to 13-17 cm and larger in extreme cases (Klimowski et al. 1998; Scharfenberg et al. 2005). The largest hailstones observed in the US include the 3 September 1970 Coffeyville, KS hailstone (Figure 2.1), which had a mass of 766 g and a maximum circumference of 44 cm (Roos 1972), the 22 June 2003 Aurora, NE hailstone with a record maximum circumference of 47.6 cm and a diameter of 17.78 cm (Guyer and Ewald 2004), and the recent 23 July 2010 Vivian, SD hailstone (Figure 2.2) that measured 20.3 cm in diameter, 47.3 cm in circumference, and weighed about 880 g (report from NWS Aberdeen, SD).

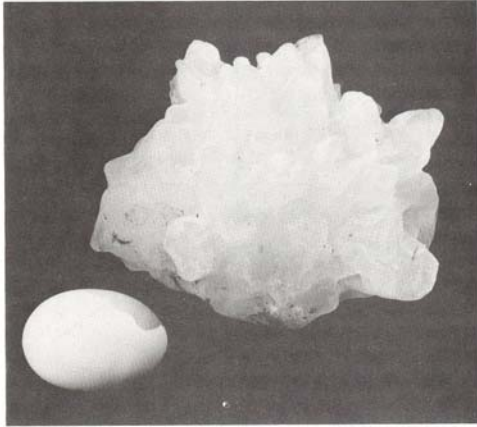


Figure 2.1: Hailstone from Coffeyville, KS storm [from Knight and Knight 1971]



Figure 2.2: Picture of the most massive hailstone ever recorded in the US, which fell from a severe hailstorm in Vivian, SD on 23 July 2010 [photo courtesy of NWS Aberdeen, SD].

There is also a great deal of variability in hail distributions within and among hail-producing storms (Marwitz 1972a, b; Changnon 1973; English 1973; Federer and Waldvogel 1975; Nelson and Young 1979; Ziegler et al. 1983; Miller et al. 1988, 1990; Musil et al. 1991, Knight et al. 2008). Marwitz (1972b) and Changnon (1973) noted the existence of small-scale 'hailstreaks' within surface hailswaths associated with individual thunderstorms and observed considerable variability of hail sizes and numbers within the hailstreaks themselves. Federer and Waldvogel (1975) examined hail distributions of a multicell hailstorm in Switzerland and reported that large hail preceded small hail at the surface as well as maxima in number concentrations and median diameters that were offset from the center of the hailswath. From observations of hailstorms in South Africa, Carte and Kidder (1966) found that large diameter hailstones at the surface tended to occur in conjunction with smaller diameter stones (i.e., broad size spectra), whereas hailfalls comprising only small stones tended to have nearly monodisperse size spectra. Based on near-simultaneous aircraft and ground observations, Auer and Marwitz (1972) described hail size distributions as being very narrow (essentially monodisperse) and consisting of relatively few but large stones near organized updrafts as well as on the ground below the updrafts. Cheng and

English (1983) and Cheng et al. (1985) investigated relationships between the parameters of fitted hail size distributions and storm characteristics, such as cloud base height and maximum water mass flux, and found significant differences in the distribution parameters for individual storms.

Dennis et al. (1971) examined hail size distributions at the ground for six hailstorms in South Dakota and found differences in the concentrations and size ranges of hail among the storms, even though the hail median diameter was similar for all storms. Hail number concentrations at the surface ranging from 0.001 m^{-3} to just over 4 m^{-3} were reported by English (1973) and Cheng and English (1983) for several severe Alberta hailstorms; the ranges of hail concentrations aloft were estimated to be about an order of magnitude larger than at the surface (English 1973). A summary of direct and derived measurements of hail distributions presented by Auer (1972) show that hailstones with diameters between 0.5 and 2.5 cm typically exist in concentrations ranging from 1 to 10^{-2} m^{-3} , whereas larger diameter hail ($> 2.5 \text{ cm}$ to about 8 cm) exhibit concentrations between 10^{-2} to 10^{-6} m^{-3} .

Measurements of hail sizes and concentrations within deep convective clouds are few owing to the inherent danger to aircraft; most in-cloud observations of hail were made by an armored T-28 aircraft during various field campaigns such as the National Hail Research Experiment (NHRE) in the 1970s over the High Plains of the US (Sand et al. 1972; Musil et al. 1973) and the Cooperative Convective Precipitation Experiment (CCOPE) in the early 1980s over southeastern Montana (Knight 1982). Musil et al. (1976) reported on in-storm observations for a hailstorm over northeast Colorado on 9 July 1973 for which the greatest number concentrations of particles larger than 5 mm in diameter, presumably graupel and hail, had values between roughly 3 and 11.6 m^{-3} and were located along the edges of updrafts at temperature levels ranging from -2 to

-12 °C. During the CCOPE field project, aircraft measurements of hail mass and number concentrations aloft (at temperatures near -15 °C) were found to have maximum values that ranged from roughly 0.1 to 12 g m⁻³ and from 1 m⁻³ to around 35 m⁻³, respectively, with maximum sizes ranging from a few mm to greater than 5 cm (Musil et al. 1991). In addition, large spatial and temporal variations in maximum number concentration values and hail sizes were observed aloft (Musil et al. 1991) as well as at the surface (Miller et al 1988) for individual storms. Maxima in hail concentrations and sizes for the CCOPE storms were better correlated with larger reflectivity values rather than with strong reflectivity gradients (Musil et al. 1991), which is in contrast to findings by Musil et al. (1973) and Musil et al. (1976).

The shapes of hailstones also vary widely in nature, with the most common shape resembling an ellipsoid. Browning and Beimers (1967) analyzed hailstones from Oklahoma storms and found that large hailstones almost always exhibit some degree of oblateness, which tends to increase with continued growth of the hailstone. A study by Knight (1986) also found increasing oblateness with increasing sizes for hailstones obtained from different geographical regions. English (1973) observed hailstone shapes ranging from conical to oblate spheroids, with conical shapes exhibited only by the smaller stones, and Carte and Kidder (1966) reported on apple-shaped hailstones that fell in South Africa. Other examples of the high degree of variability of hailstone shapes come from Knight and Knight (1970c) who observed two distinctly different symmetries (oblate spheroids and flattened, prolate stones) for comparably-sized large hailstones that fell from the same storm in a single location, as well as Knight et al. (2008) who reported on an unusual case in which large disk-shaped hailstones from a hailstorm over Boulder, CO were observed. Large hailstones often exhibit lobed structures (Figures 2.1 and 2.2) that initially arise from surface irregularities during the early growth stages (Browning 1966; Knight and Knight

1970a). These initial surface protrusions grow faster than the surrounding hailstone surface and become more marked with continued hail growth due to increased collection efficiency and heat transfer of the projections themselves (Browning 1966; Bailey and Macklin 1968). Browning (1967) also points out that the lobed structure of large hailstones indicates that the hail grew by primarily accreting small cloud droplets as opposed to large cloud droplets or raindrops. In addition, lobes that nearly cover the entire surface indicate the hailstone tumbled while growing, whereas lobes situated on only a portion of the surface reveal the hailstone fell with a preferred orientation while growing (Browning 1966; Knight and Knight 1970a).

The density of hailstones is often less than that of pure ice (0.917 g cm^{-3}) and tends to vary radially from core to surface as a result of trapped air bubbles within the concentric ice layers, although most measurements indicate bulk density values between 0.8 to 0.9 g cm^{-3} (Mossop and Kidder 1961; Prodi 1970; Pruppacher and Klett 1980). Hail particles can have rather low densities during their initial growth from embryos (Farley 1987b; Knight et al. 2008), and density typically increases rapidly as the hailstones grow through accretion of liquid water, though there are rare cases of low-density hail observed at the ground. For example, Knight and Heymsfield (1983) examined hailstones with unusually low densities (0.31 to 0.61 g cm^{-3} at sizes ranging from 0.63 to 1.54cm) from a hailstorm that occurred over Boulder, CO on 4 March 1982. Farley (1987b) argues that low-density hail embryos experience increased rates of accretion and diffusional growth in addition to reduced terminal velocities, which can maintain the particle in favorable growth regions, and these combined factors can lead to larger hail.

2.2) *Factors affecting hail growth and hail distributions within deep moist convection*

2.2.1) *Updraft characteristics and temperature dependence*

Convective updrafts must be strong enough to support hailstones, with larger hail typically associated with stronger updrafts (Ludlam 1958; English 1973; Browning and Foote 1976; Musil et al. 1991). Nelson (1983) and Foote (1984) demonstrated that broad moderate updrafts (20 to 40 m s⁻¹) are more likely to produce large hail ($D > 2$ cm) than narrower moderate or even strong ($> \sim 35$ m s⁻¹) updrafts owing to the longer residence time of growing hailstones in favorable growth regions. An updraft that tilts with height is another factor that can affect hail growth both directly and indirectly. The horizontal component of velocity within a tilted updraft allows for hail particles to be carried across the updraft and places a limit on the amount of time in which these particles can reside in favored growth regions as well as size sorting of hailstones such that the largest particles fall close to the updraft edge while smaller particles fall further away from the updraft (Browning 1977). The degree of tilt may also govern whether or not particles falling out of an updraft at upper levels re-enter the updraft at lower levels and experience further growth (Browning 1977). A tilted updraft also prevents much of the precipitation from accumulating within the updraft (e.g., precipitation loading, which would decrease the buoyancy of the updraft and cause it to decay) and allows for spatial separation between the updraft and the precipitation-induced downdraft thereby leading to a longer-lived storm in general (Browning and Ludlam 1962; Browning 1977). Hail growth occurs only at temperatures between 0 and -40 °C, with the majority of growth favored at temperatures between -10 and -25 °C (Nelson 1983; Foote 1984).

2.2.2) Liquid water content

Because hailstones grow primarily by accreting liquid water which subsequently freezes (Schumann 1938; Ludlam 1958), the distribution of liquid water content (LWC) impacts accretion rates, and thus growth rates of hail, and can determine whether hailstones with surface temperatures near 0 °C undergo wet or dry growth (Browning 1963; Bailey and Macklin 1968; Lesins and List 1986; Rasmussen and Heymsfield 1987c; Cotton and Anthes 1989). Of course, air temperature is another controlling factor for whether or not hailstones may experience wet growth, and as air temperatures decrease, higher values of LWC are required in order for wet growth to commence for a hailstone of a given size (Bailey and Macklin 1968; Rasmussen and Heymsfield 1987c) as shown in Figure 2.3. Dry growth typically occurs in environments characterized by low LWC values and/or relatively cold temperatures (with respect to the hailstone surface temperature) such that heat transfer to the environment via conduction and evaporation is efficient. This efficient cooling of the hailstone surface allows all collected supercooled water to freeze, often trapping air bubbles within the ice structure that give the hail particle an opaque appearance. In environments with high LWC and/or relatively warm

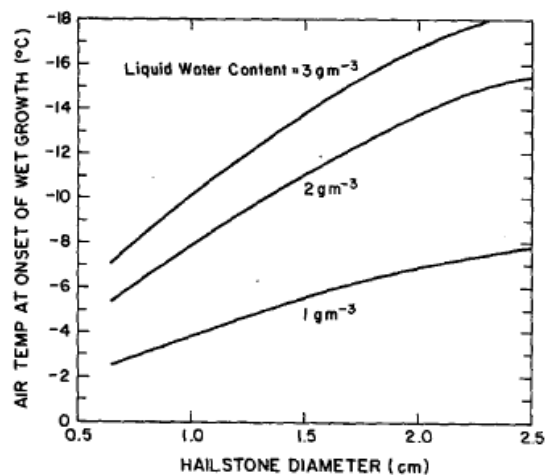


Figure 2.3: Liquid water content required to produce wet growth on various hailstone sizes as a function of air temperature. Hailstones are assumed to have a density of 0.91 g cm⁻³, and to collect cloud droplets with unit collection efficiency. [from Rasmussen and Heymsfield 1987c].

temperatures, wet growth of hail can occur in which all of the collected water by a hailstone is not immediately frozen; the hailstone surface becomes wet with a temperature very near 0 °C and the ice structure assumes a clear appearance. Some of the unfrozen collected water during wet growth is shed from the hailstone surface (Ludlam 1958) and can be a significant source of surface rainfall (Rasmussen and Heymsfield 1987c; List 2010).

English (1973) noted that hailstones within time-varying updrafts tend to alternate between wet and dry growth regimes more frequently than those in steady-state updrafts and could help explain the alternating layers of clear and opaque ice commonly observed in hailstones. LWC has also been shown to affect shedding rates of liquid drops from large hail below the melting level, with increasing LWC generally leading to increased amounts of shedding (Rasmussen and Heymsfield 1987b, hereafter RH87b). Miller et al. (1988) computed hail trajectories in a supercell and reported that variability in LWC primarily affected the number rather than the sizes of hailstones, though a similar study by Miller et al. (1990) showed that substantial increases (decreases) in LWC led to an increase (decrease) in maximum hail size. List (1963) and Lesins and List (1986) describe an additional growth regime for hail, termed 'spongy growth', in which some of the collected unfrozen water is trapped in an ice matrix on the hailstone surface rather than being shed thereby allowing for greater hailstone growth rates than suggested by the theoretical Schumann-Ludlam Limit (SLL). This growth regime is essentially a subcategory of the wet growth regime and therefore has similar dependencies on LWC and air temperature. Spongy growth was also investigated in wind tunnel experiments of icing by Macklin (1961) who found that spongy growth of ice occurred owing to the simultaneous collection of liquid droplets and ice crystals. Mason (1971) stated that spongy growth rates could increase by the additional collection of ice crystals and snowflakes. Analyses of the internal structures of freshly

fallen hailstones by Browning et al. (1968) determined that many of the hail embryos grew spongy initially. However, based on examinations of numerous hailstones over several decades, Knight and Knight (2005) believe that spongy growth beyond the initial growth stages of natural hailstones is rather rare and typically only accounts for a minor fraction of hail wet growth, a conclusion also reached by Carte (1966) nearly 40 years prior.

2.2.3) *Hailstone embryos*

The sizes, numbers, and regions of millimeter-sized particles serving as 'hail embryos' can impact hail size distributions throughout deep convection. The term hail embryo is referred to here as a small diameter (~0.1 to ~5mm) ice particle that serves as a precursor to the formation of a hailstone. The characteristics of hailstone embryos vary depending on geographical region and are largely dependent on cloud base temperature, with colder (warmer) cloud base temperatures tending to favor graupel (frozen raindrops) as the dominant hail embryo type (Knight 1981). Additionally, Foote (1985) pointed out that collision-coalescence processes are typically too slow in continental thunderstorms to account for large raindrops that could subsequently freeze and serve as hail embryos. Detailed observations of hailstones from High Plains thunderstorms by Knight and Knight (1970b, 1979) and Knight et al. (1974) found that hail embryos are typically graupel particles, and to a lesser extent frozen supercooled raindrops.

Mossop and Kidder (1961) and Knight and Knight (1970b) initially suggested that a necessary step for the formation of large hail is the formation of hail embryos in one set of conditions followed by the 'injection' of these embryos into another set of conditions. Larger embryos in an updraft typically experience faster growth rates than smaller ones owing to their larger surface areas, though larger embryos don't necessarily lead to larger hail (Musil 1970;

Foote 1984; Brimelow et al. 2002). In fact, Charlton and List (1968) suggested that growth of embryos to large hail sizes was more probable when the number of hail embryos is small owing to reduced competition for the liquid water available for growth. Paluch (1978) showed that more numerous embryos leads to increased competition for available water, which in supercells could limit hail sizes in one part of the storm while promoting hail growth in another region, depending on the initial locations of the embryos in relation to the updraft. Studies by Dye et al. (1983), Nelson (1983), Xu (1983), and Miller et al. (1983, 1988, 1990) demonstrated that the source regions of hail embryos dictate, to a degree, the trajectories that hail particles follow in a storm, and thus the ensuing growth rates encountered along those trajectories, ultimately affecting the evolution of hail size spectra.

A concept relevant to the transformation of hail embryos to hailstones is that of unfair competition (Browning 1977; Knight and Knight 2001), which suggests that natural mechanisms such as size sorting will cause a few favored embryos to be the first to encounter regions of undepleted cloud water, and these particles will have the greatest chance of eventually growing to large hail. Given a region of updraft containing embryos of varying sizes overlying a region of supercooled cloud water, the larger embryos fall faster than the smaller ones and will thus have unfair access to the undepleted cloud water. These particles will then begin to deplete the cloud water through accretion and grow larger still before their smaller counterparts gain access to it. Browning (1977) postulated that the strength and steadiness of updrafts in many supercells renders them inefficient at converting cloud droplets to rain such that favored embryos will continually encounter a large reservoir of supercooled cloud droplets.

Studies of a multicell thunderstorm over northeast Colorado by Heymsfield et al. (1980) and Heymsfield (1983) found that hail embryos first formed in developing 'feeder' cells (also referred

to as flanking towers) adjacent to main updraft from aggregates and graupel. These embryos were then advected by the environmental flow (as they sedimentated) into the primary updraft (Figure 2.4) where they grew rapidly into hail particles. Similar findings were described in studies of multicellular hailstorms in Oklahoma by Ziegler et al. (1983), in Alberta by Cheng and Rogers (1988), and in Colorado by Brandes et al. (1995). Frozen drop embryos were also noted to originate from melted ice particles that were transported into the main updraft via low-level inflow (Heymsfield et al. 1980). In contrast, Kennedy and Detwiler (2003) examined hail origins in a NE CO multicell storm using in situ aircraft and polarimetric radar data and found that hail embryos were generated primarily via a recycling process of graupel particles from the forward portions of the storm rather than from feeder cells. Browning (1977) suggested an additional concept for hail origination in multicell storms in which hail embryos first develop in the cumulus stage of flanking towers, termed 'daughter clouds', adjacent to a mature stage cell. The mature cell eventually begins to dissipate while the daughter cell continues growing and reaches the mature stage, at which point the hail embryos experience a water-rich environment and grow rapidly to hail size. Thus, unlike the feeder cell concept in which hail embryos are physically

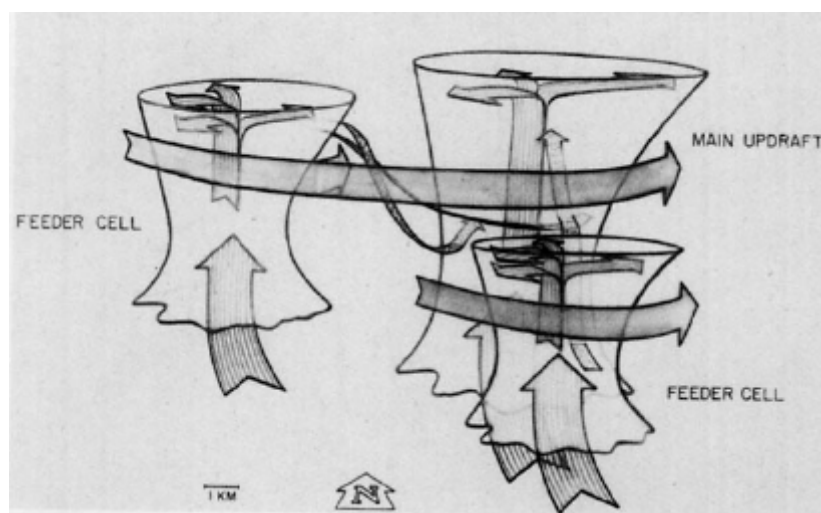


Figure 2.4: Schematic representation of the hail formation process via feeder cells for a multicellular hailstorm. Arrows: no shading, environmental winds relative to the storm; vertical shading: updraft air; stippled shading: dominant hail-producing trajectories. [from Heymsfield et al. 1980]

transported from developing cells to an adjacent mature cell where they encounter pre-existing favorable growth conditions, hail embryos in a daughter cloud remain within the cell and find themselves in an increasingly favorable environment for hail growth as the cloud develops into a mature cell. Both of these concepts are based on the idea that hail embryos are most favored to grow into hailstones when they are incorporated into a developing updraft since their larger fall velocities will allow them to remain within the updraft core and take advantage of high LWCs (Heymsfield 1983).

Numerous ideas exist regarding the sources of hail embryos in supercells, some of which include re-circulation of particles into the updraft from the 'embryo curtain' (see Figure 2.12) [also referred to in the literature as the forward overhang region] encompassing the primary updraft periphery (Browning and Foote 1976; Farley and Orville 1986; Miller et al. 1988), and growing cells along the supercell flanks (Miller and Fankhauser 1983; Krauss and Marwitz 1984). Miller et al. (1990) showed a variety of embryo regions for a single supercell storm that included growing graupel particles in addition to drops from melted graupel along the updraft edges, shedding of drops from hail undergoing wet growth above the freezing level, shedding from melting hail below the freezing level, and even graupel ingested from cumulus congestus that merged with the supercell.

2.2.4) Hailstone attributes affecting growth

The shapes and sizes of hailstones largely dictate the terminal velocities and thus the accretion rates of hailstones. Browning (1963) claimed that oblate hailstones have lower critical LWC values than similar spherical hailstones and thus grow at a slower rate. However, calculations on hailstone growth rates by English (1973) showed that 'flatter' hailstones grow

faster via accretion than do more spherical hailstones of similar size due to the increased sweep-out volume. The terminal velocity (V_{th}) of a hailstone (Eqn. 2.1) is a function of its density ρ_h , its diameter D_h (equivalent spherical diameter), the drag coefficient C_D , and air density ρ_a (Charlton and List 1972b; Knight and Knight 2001),

$$V_{th} = \left(\frac{4g\rho_h D_h}{3C_D\rho_a} \right)^{0.5} \quad (2.1)$$

Observational and experimental measurements of hail terminal velocities have shown that C_D varies as a function of hail shape and to a lesser extent hail surface characteristics (Macklin and Ludlam 1961; Charlton and List 1972b; Roos and Carte 1973; Matson and Huggins 1980; Knight and Heymsfield 1983). The value of C_D for a smooth sphere is roughly 0.45, and increasing oblateness tends to increase the value of C_D (Macklin and Ludlam 1961; Matson and Huggins 1980) and thus lead to slower fall speeds. Based on measurements of free falling artificial hailstones of various sizes and shapes, Macklin and Ludlam (1961) found values of C_D ranging from about 0.45 to about 0.8 and suggested a value of $C_D = 0.6$ for diameters greater than 1 cm, whereas a value of $C_D = 0.8$ was implied in the empirically-derived hailstone terminal velocity

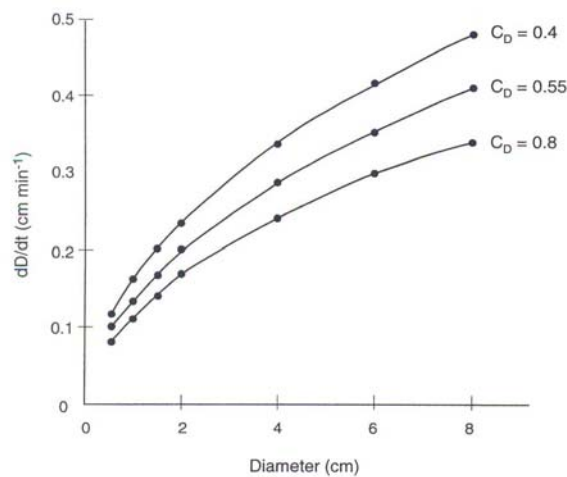


Figure 2.5: Growth rates of hail for different drag coefficient values assuming air density at 500 mb and -20 °C. [from Knight and Knight 2001].

formula of Roos and Carte (1973) for large ($3 > D > 12$ cm) hailstones. Matson and Huggins (1980) measured terminal velocities of primarily small (D of about 5 to 25 mm), naturally-falling hailstones and reported C_D values ranging from 0.65 to 1.3 with mean values around 0.87 to 0.92. Thus, it is apparent that drag coefficients for natural hail are larger than that for smooth spheres having the same mass. The effect of C_D on hail growth rates is clearly evident in Figure 2.5, which shows that, all else being equal, increasing values of C_D (increasing oblateness) generally correspond to slower growth rates.

Rough surfaces and protuberances (lobes) lead to increased heat transfer away from hailstones and more rapid freezing of collected water (Browning 1966; Bailey and Macklin 1968; Knight and Knight 1970c). Browning (1966) also noted that surface lobes lead to increased drag (slower fall speeds) as well as increase the critical water content value at which hailstones transition to wet growth regime. Surface lobes may also increase collision efficiencies between hailstones and cloud droplets, particularly for hail undergoing wet growth (Bailey and Macklin 1968; Knight and Knight 1970a), although Macklin and Bailey (1966, 1968) found that hail-cloud collision efficiencies depend more on hail size and tend to decrease with increasing hailstone diameter. This latter result is somewhat compensated by the fact that larger hailstones have greater terminal velocities and cross-sectional areas than smaller particles and can therefore collect more droplets per unit time, which ultimately leads to increasing growth rates for increasing hailstone size (Xu 1983; Johnson 1987). The ventilation factor, defined as the ratio of water mass flux to or from a moving versus a motionless hydrometeor (Pruppacher and Klett 1980) depends on the size and surface roughness of the hailstone, with larger ventilation factors, and hence enhanced heat transfers between a hailstone and its environment, for increasing size and surface roughness (Bailey and Macklin 1968). In spite of the fact that hailstone attributes

affect growth rates of hail, the inherent difficulty and excessive computational cost of attempting to encompass the wide variety and complexity of hailstone features in microphysical models for use in three-dimensional simulations has forced many modelers to simply assume hailstones can be represented as smooth spheres. This approach is taken in the 3MHAIL model as well.

2.2.5) Melting of hail

Melting rates of hail depend on hail size, air temperature, relative humidity (RH), and the melting level height. Melting is faster at warmer air temperatures, higher RH values and for smaller hailstone sizes, which have a lower mass-to-area ratio, all of which lead to increased heat transfer from the environment to the hailstone surface (Pruppacher and Klett 1980; Rasmussen and Heymsfield 1984). Lower RH values tend to slow melting rates due to reduced heat transfer resulting from competition between evaporative cooling and convective heating at the hailstone surface (Foote 1984; RH87b; Srivastava 1987). In addition, RH87b found that shedding commences at a higher altitude for larger environmental RH values. The height of the melting level (ML) also governs both the amount and size of hail arriving at the ground as it determines the amount of time a falling hailstone spends in air with temperatures greater than 0° C, and thus the amount of melting that can occur prior to reaching the surface (Foote 1984; RH87b). Melting seems to increase oblateness of hailstones as well (Macklin 1964; Browning and Beimers 1967). Browning and Beimers (1967) attribute increased oblateness during melting to previous spongy ice growth at the top and bottom of the hailstone, with the less dense spongy ice melting faster than the denser ice on the sides of the stone. Macklin (1964) argued that differences in heat transfer rates to the melting hailstone over its surface accounted for the increases in oblateness,

with greater transfer rates existing at the upstream and downstream of the stone and lower rates along the hailstone's sides.

2.2.6) Aerosol effects

2.2.6.1) General aerosol impacts on deep convection

The distributions of aerosols in deep convection serving as cloud condensation nuclei (CCN; particles having radius r between 0.1 and 1 μm), giant cloud condensation nuclei (GCCN; $r \geq 1\mu\text{m}$), and ice nuclei (IN) affect liquid cloud droplet and ice crystal distributions, which in turn, impact the hydrometeor distributions that develop out of the cloud and ice particle distributions (Rosinski and Kerrigan 1969). For deep convection developing in a given thermodynamic environment, the primary effect of increasing the numbers of CCN is to produce many small cloud droplets (Squires 1956, 1958; Squires and Twomey 1961; Warner and Twomey 1967; Twomey 1977; Rosenfeld 1999, 2000; Khain and Pokrovsky 2004; Khain et al. 2005; Wang 2005; van den Heever et al. 2006). These droplets are not efficient in producing rain via the collision-coalescence process, but rather they continue growing slowly by vapor deposition as they are carried upwards in the updraft and studies have found that an increase in CCN numbers can severely delay or even prohibit the onset of rainfall (Warner 1968; Albrecht 1989; Rosenfeld and Lensky 1998; Rosenfeld 2000; Andreae et al. 2004; Khain et al. 2005; Lee et al. 2008b). The reduced efficiency of the numerous small cloud droplets in producing rain can lead to significant increases in supercooled water aloft, which is then available for riming by ice particles (van den Heever et al 2006; Carrió et al. 2010; Khain et al. 2011). At the same time, decreases in cloud droplet sizes with increasing CCN can also result in decreased riming growth

owing to reduced collection efficiencies of smaller droplets (Levin and Cotton 2009; Carrió et al. 2010).

Secondary effects of increased numbers of CCN on the dynamics and precipitation processes of deep convection can be quite different depending on the environmental conditions as well as the initial strength and type of deep convection occurring (Khain et al. 2004, 2005; Lynn et al. 2005; Seifert and Beheng 2006; Tao et al. 2007; Lee et al. 2008a; Khain and Lynn 2009, van den Heever et al. 2011). Seifert and Beheng (2006) and Lee et al. (2008a) found that increased CCN concentrations in single-cell convection occurring in low CAPE and low shear environments tended to reduce total surface precipitation and maximum updraft velocities. A reduction in surface precipitation from simulated ordinary single-cell storms over Texas under conditions of enhanced CCN was also reported by Khain and Pokrovsky (2004) and Khain et al. (2005), although greater maximum updraft speeds with increasing CCN were noted by Khain and Pokrovsky (2004) as a result of increased latent heating from both condensation and freezing. Some studies have shown that for multi-cell type storms in environments characterized by large values of convective available potential energy [CAPE] and moderate to strong wind shear, increased aerosol contents led to increased surface precipitation due to greater evaporation and convergence at low levels, increased updraft and downdraft strengths, invigoration of new convective cells, and better overall organization of convection (Khain et al. 2005; Lynn et al. 2005; Seifert and Beheng 2006; Lee et al. 2008a,b; Ntelekos et al. 2009). Interestingly, Khain et al. (2005) and Tao et al. (2007) simulated the same Oklahoma squall line using 2D models with bin microphysics, yet the impacts of increasing CCN on precipitation led to contrasting results, with enhancement in the Khain et al. study and suppression in the Tao et al. study. The opposing aerosol impacts on precipitation in these latter two studies were attributed to differences in the

configurations of the model dynamics and setup (Tao et al. 2007). Increases in CCN have also been shown to result in non-monotonic responses in hydrometeor fields and surface precipitation in simulations of continental isolated multicellular deep convection (Fan et al. 2007; Li et al. 2008; Carrió et al. 2010) as well as tropical deep convection (Wang 2005). Simulations of supercell storms have found that increases in CCN generally have little impact on updraft strength given the strong dynamical forcing in supercells (Seifert and Beheng 2006; Lerach et al. 2008; Khain and Lynn 2009; Storer et al. 2010; Lim et al. 2011). However, different responses in the precipitation characteristics of supercells to increasing CCN have been noted, with reduced precipitation reported in the studies of Lerach et al. (2008), Khain and Lynn (2009), Storer et al. (2010), and Lim et al. (2011), whereas Seifert and Beheng (2006) found changes in CCN had very little impact on precipitation.

Dust lofted into the atmosphere and transported away from its source region can serve as rather effective IN, as well as GCCN if the dust particles become coated with sulfates (Levin et al. 1996), in addition to serving as CNN (Rosinski et al. 1973; van den Heever et al. 2006). Desert dust serving as IN can allow ice nucleation to occur at warmer subfreezing temperatures such that ice particles can initially form lower in the cloud (Demott et al. 2003; Sassen et al. 2003). A preliminary study of hailfalls in southwestern France in the presence of Saharan dust found a deficit in the numbers of small hailstones ($D < 1.4$ cm) at the surface compared to cases in which this dust was absent (Dessens et al. 2004), thus suggesting that dust aerosols in deep convection could potentially impact hail distributions. The actual effects of the dust on hail distributions in the study by Dessens et al. (2004) was not considered, although the authors mentioned that the height of the 0 °C isotherm was higher in dust cases and therefore more melting of the smallest hailstones could have accounted for the deficit of these sizes at the

surface. Numerical simulations of deep convection over Florida in the presence of Saharan dust by van den Heever et al. (2006) showed that the increased CCN, GCCN and IN concentrations attributed to the dust led to more numerous intense and broader updrafts, similar to what was observed, than in the case where aerosol concentrations were suppressed (denoted as the clean case). The increase in initial updraft strength was attributed to increases in the latent heat release owing to the formation of more numerous liquid and ice particles as a result of the increased aerosol concentrations. The study also found that simulations enhancing either the IN or GCCN concentrations alone had a greater impact on updraft strength during the mature phase of convection than increases in CCN concentrations alone. Graupel and hail mixing ratios were shown to be larger and extend over a deeper layer in the enhanced aerosol case versus the clean case. The higher hail mixing ratios resulted from increased riming of graupel in the presence of increases in the liquid water mixing ratios in the mid-levels of the storm due to the more numerous small cloud drops, although in general, enhancements in aerosol concentrations led to a reduction in total surface precipitation relative to the clean case. Similar simulations of multi-cell convection over Florida carried out by Tao et al. (2007) showed only a minimal impact on updraft strength and total surface precipitation at higher CCN values in contrast to the results of van den Heever et al. (2006). The different findings of these two studies could certainly be due to differences in the dimensionality of the models as well as in microphysical schemes (2D with bin microphysics in Tao et al. 2007; 3D with two-moment bulk microphysics in van den Heever et al. 2006).

2.2.6.2) *Aerosol impacts on hail*

Aerosol populations acting as CCN and IN could play an important role in initiating hail embryos as these affect both the cloud droplet spectra and the probabilities of ice nucleation (Rosinski and Kerrigan 1969; Danielson 1977; Young 1977). Studies by Khain and Pokrovsky (2004), Khain et al. (2005), Seifert and Beheng (2006), and van den Heever et al. (2006) have shown that low values of CCN tend to favor warm-rain processes over ice processes in continental clouds, and therefore would likely tend to inhibit growth of hail to large sizes. This argument is somewhat supported by the observational study of Andreae et al. (2004) in which the rare occurrence of large hail at the surface was reported in deep convection over the Amazon in the presence of enhanced aerosol concentrations from forest fires. However, few studies have systematically investigated the direct impact aerosols could potentially have on hail distributions with the exceptions of Noppel et al. (2010) and Khain et al. (2011). Many of the ideas regarding how aerosols may affect hail distributions and hail growth are rooted in various hail suppression concepts. The most common theory of the majority of hail suppression techniques is that the introduction of sufficient amounts of IN to initiate freezing in supercooled clouds will reduce the supply of supercooled liquid available for hailstone growth and produce additional hail embryos to compete for the available supercooled water (Iribarne and De Pena 1962; Dennis 1977; Young 1977). The most common models regarding suppression of hail via seeding of aerosols include:

- *Beneficial competition* (Iribarne and De Pena 1962; Young 1977): Seeding with IN material in the embryo source regions of hailstorms in order to produce many more embryos than would occur naturally. The large numbers of embryos then compete for the available liquid water in the updraft such that the result is many small hailstones that would lose a larger fraction of their mass to melting prior to reaching the surface. Danielson

(1977) suggested that, in the presence of large values of supercooled LWC, great numbers of hail embryos would be required to effectively suppress hail growth via this concept.

- *Premature rainout* (English 1986): The idea behind this concept is to inject IN into feeder and daughter clouds prior to the natural development of significant numbers of ice crystals such that the precipitation process is accelerated. Some of the precipitation particles would then fall out of the embryo source region before reaching the main updraft (or before the updraft of the daughter cloud intensifies significantly) thereby reducing the embryo supply to the storm.
- *Trajectory lowering* (Young 1977): Similar to premature rainout, except hygroscopic aerosols (i.e. salts, presumably acting as GCCN) are injected into the lower portions of the embryo source regions in order to produce larger precipitation particles. These additional larger precipitation particles then deplete the LWC such that less supercooled liquid is available in regions of hail growth, provided large numbers of these larger particles exist (on the order of 100 m^{-3}). In addition, the larger particles follow lower trajectories in hail growth regions such that the amount of time spent in these regions is reduced and ultimately only smaller hailstones are produced.
- *Glaciation concept* (Young 1977): IN are released in regions containing supercooled liquid such that much of this liquid is converted to ice particles, thereby reducing the amount of supercooled liquid available for hail growth. This concept has largely been abandoned owing to the infeasibility of incorporating enormous amounts of IN over a large region of the storm.

Based on these hail suppression concepts, one might argue that increases in aerosols acting as IN could lead to a decrease in maximum hail size and a greater number of small hailstones.

However, these models were developed on the premise that local changes in aerosol concentrations within select regions of hailstorms affect hail growth whereas in reality, deep convection developing within or moving into a region of enhanced aerosol populations would likely not possess a natural mechanism to focus aerosols into the preferred locations mentioned in the suppression techniques. In addition, the majority of hail suppression projects on real hailstorms have produced inconclusive results (Dennis 1977; Federer et al. 1986; Knight and Knight 2001) such that the extent of aerosol effects on hail in nature remains largely unknown.

Several numerical modeling studies have revealed sensitivities of hail distributions to the artificial introduction of IN or to changes in the cloud droplet size distribution (CDS). Farley (1987b) attempted to simulate the effects of seeding feeder cells with IN (silver iodide and dry ice) on hail production within a multicell hailstorm and found that only a slight reduction in surface hailfall resulted in the seeded case versus the non-seeded case. Using a 1D cloud model with mixed-phase microphysics, Danielson et al. (1972) showed that a cloud/rain drop size distribution with an extended tail to include larger sizes led to more rapid hail growth compared to those distributions which were skewed toward smaller sizes. This was due to exhaustion of the smaller particles to the anvil, whereas the few larger particles in the tail of the distribution had terminal velocities that allowed them to remain in favorable growth regions. Though this study did not explicitly simulate aerosol effects on hail, the conclusions drawn regarding the impacts of the characteristics of the CDS on hail growth suggest that, because aerosols affect the CDS (section 2.2.6.1), they should therefore affect hail growth.

More recently, Noppel et al. (2010) and Khain et al. (2011) investigated the impacts of CCN on hail distributions in simulations of a severe hailstorm over SW Germany. Using a 3D model with two-moment bulk microphysics, Noppel et al. (2010) found that as concentrations of cloud

droplets increased from values of 100 to 2000 cm^{-3} (as a proxy for increased values of CCN), an increase in the number of graupel particles converted to hail was observed. The more numerous hailstones generated in the high CCN cases were also generally smaller than those for cases with lower values of CCN, and thus typically resulted in only small amounts of hail reaching the surface. However, the authors also found that hail production remained favorable for this particular storm as both the cloud droplet number concentrations increased and the shape of the CDS D narrowed. In addition, this study found that for a narrow CDS D containing larger droplets, increases in cloud droplet concentrations from 100 to 350 cm^{-3} led to an increase in the number of large hailstones produced, whereas virtually no large hail was produced as cloud droplet concentrations increased further. While the results of this study showed sensitivity of hail distributions to CCN concentrations, the authors noted that a clear relationship between CCN populations and hail distributions could not be established. The investigation of Khain et al. (2011) used a 2D model with bin (spectral) microphysics and reported increases in the amounts of hail mass and hailstone sizes as a result of increasing CCN concentrations. The authors attributed the larger hail mass and sizes to increased riming growth of hail as a result of greater amounts of supercooled liquid water content arising under conditions of enhanced CCN concentrations. At lower values of CCN, efficient coalescence of larger cloud droplets to raindrops at low levels led to smaller amounts of supercooled water aloft. This resulted in increased competition of snow and small graupel particles for the available supercooled water, and therefore, slower growth of these particles to larger sizes. The contrasting results of these two studies regarding the effects of CCN on hail certainly suggest that further work on this topic is warranted.

2.3) *Dynamical and thermodynamical effects of hail on convection*

List et al. (1968) and Ziegler (1988) showed that latent heating due to freezing of accreted liquid water on growing hailstone surfaces could increase updraft temperatures locally. The magnitude of this increase was dependent on the sizes and numbers of hailstones present and led to an increase in positive buoyancy if the magnitude of the net drag force of the hail on the updraft was relatively small. GSR04 and Cohen and McCaul (2006) also showed an increase in updraft temperatures aloft due to freezing, but this added heat was minor relative to the heat added from condensation of cloud drops at lower levels. The accretion process can also cause local decreases in LWC and lessen available water for growth of future hailstones (List et al. 1968; Young 1977; Heymsfield and Hjelmfelt 1984), though this effect is thought to be significant primarily for large number concentrations of hail (English 1973) and hail size distributions that are approximately mono-disperse (Charlton and List 1972).

Numerical simulations by Srivastava (1987), GSR04, and VC04 demonstrated that, in general, larger concentrations of small hail sizes led to more intense low-level convective downdrafts owing to increased cooling associated with greater melting and evaporation rates. VC04 also reported that shifting the hailstone distributions towards smaller sizes in supercells led to deeper and more intense (colder) low-level cold pools that propagated faster, which in turn impacted storm movement and lifetime. Knupp (1988) showed that melting graupel particles can make significant contributions to the cooling of downdraft air, especially for storms with low cloud bases and/or relatively moist sub-cloud layers for which evaporative cooling is lessened, and these results could certainly be extended to hail given that the melting processes of graupel and hail are somewhat similar (RH87b). Evidence to support this claim is provided by Wakimoto and Bringi (1988) who, based on radar and visual observations of a severe thunderstorm over

Alabama on 20 July 1986, revealed that melting hail had a significant role in the development of a microburst. In addition, Atlas et al. (2004) found that narrow hail (and graupel) distributions of small sizes melt and subsequently cool the air over a shallower layer than if the distributions are broader and/or are comprised of larger particles, and thus the former distribution types are more conducive to microbursts.

Hail has also been shown to affect raindrop size distributions and ultimately surface precipitation characteristics via complete melting of hail (Ziegler 1988) and shedding of liquid drops during wet growth and melting (Joe et al. 1976; Rasmussen and Heymsfield 1987c; List 2010), processes which depend strongly on the hail size spectra (Rasmussen et al. 1984). Both GSR04 and VC04 found that hail distributions weighted towards small hailstones resulted in surface rainfall over a larger area with little or no hail reaching the ground, whereas distributions weighted towards larger hail resulted in increased surface rainfall and hailfall over smaller areas. Shedding of liquid water from hailstones could also be a potential source of hail embryos (Browning 1963; Heymsfield and Hjelmfelt 1984; Rasmussen and Heymsfield 1987b, c; Miller et al. 1988, 1990), as well as a source of liquid drops within and above hail growth regions (Joe et al. 1980), both of which would affect future hail growth as discussed in section 2.2.3.

2.4) *Hail in supercells*

As the current work is concerned with simulating hail in a supercell storm, a brief overview of these storm types as well as a conceptual model of hail growth in supercells is presented. These storms often produce the largest hail observed at the surface (Nelson and Young 1979) and account for a disproportionate amount of hail damage (Moller et al. 1994; Changnon 2001). Supercell storms are characterized by a quasi-steady updraft (Browning 1977), a deep and

persistent mesocyclone (rotating updraft) (Johns and Doswell 1992), and an organized airflow pattern that allows the storm to unload its precipitation in a manner that doesn't disrupt the inflow of warm moist air to the updraft (Browning 1964). These storms are favored to form in environments characterized by moderate to high instability and strong vertical wind shear over a deep layer (Marwitz 1972a; Weisman and Klemp 1982, 1984; Weisman and Rotunno 2000).

The conceptual supercell model put forth by Browning (1964) and later modified by Lemon and Doswell (1979) contains an intense updraft and two downdrafts, the forward flank downdraft (FFD) and the rear flank downdraft (RFD), as the primary structural features (Figures 2.6 and 2.7). The strong updraft acts as an obstacle in the environmental flow, diverting this flow around

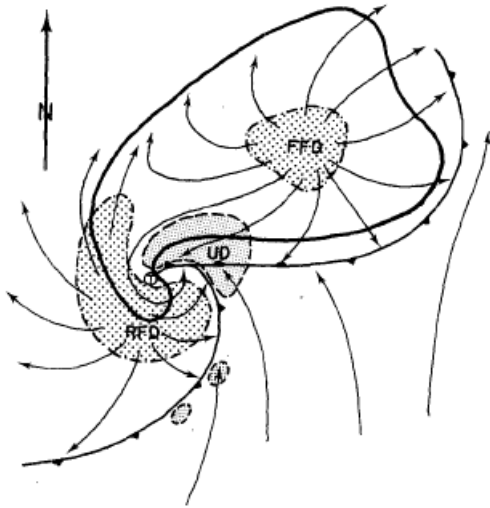


Figure 2.6: Schematic plan view of a tornadic supercell at the surface. The thick line encompasses the radar echo, gust fronts are depicted using convective frontal symbols, the relative position of the updraft (UD) is finely stippled, and the FFD and RFD are coarsely stippled. Ground-relative streamlines are also shown. Storm motion is to the northeast. [from Lemon and Doswell 1979].

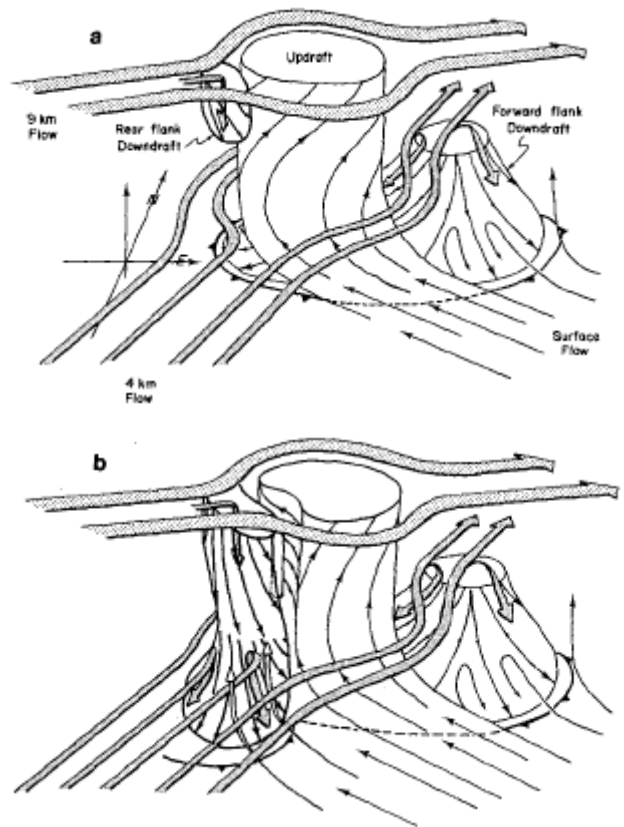


Figure 2.7: Schematic three-dimensional depiction of the updraft, FFD, and the initiation of the RFD in an evolving supercell storm (frame **b** follows frame **a** in time). Gust fronts are denoted as in Figure 2.6. Conceptual storm-relative flow lines are also shown. Salient features are labeled in frame **a**. [from Lemon and Doswell 1979].

the updraft and creating a stagnation zone on the upwind side of the updraft (Figure 2.7). The FFD is located in the precipitation region downwind (relative to the mid-level flow) of the updraft, whereas the RFD is located immediately upwind (relative to the upper level flow) of the updraft. Both downdrafts are heavily influenced by cooling associated with evaporation and melting of precipitation, although the RFD is also affected by the environmental flow around the updraft and the flow associated with the mesocyclone, as depicted in Figure 2.7b. Upon reaching the surface, the air within the downdrafts diverges, creating the forward flank gust front (Figures 2.6 and 2.7a) and the rear flank gust front (Figures 2.6 and 2.7b) along the leading edges of the cold outflow. The resulting convergence along these fronts enhances the influx of warm, moist environmental air into the storm, thereby maintaining or even strengthening the storm. New cells, referred to as flanking line towers (Figure 2.8), can also develop along the rear flank gust front and merge with the primary updraft. As mentioned in the previous section, the characteristics of the convectively-generated outflow and resultant low-level cold pool have a major impact on the storm propagation and longevity, and precipitation physics play an essential role in developing and maintaining the outflow and cold pool structure.

The general distributions of precipitation at the surface as well as within a typical supercell are shown in Figures 2.8 and 2.9, respectively, though departures from these structures are to be expected for individual storms. The observed variations in hail sizes in supercells are generally distributed in a systematic manner with respect to the updraft location, with the largest hailstones falling closest to the updraft (Browning and Ludlam 1962; Browning and Donaldson 1963) and the smallest particles falling further away from the updraft owing to their greater susceptibility to advection by horizontal flow within the storm. Aircraft observations of moderately intense supercells over northeast CO also found that hail was most often observed near the edges of

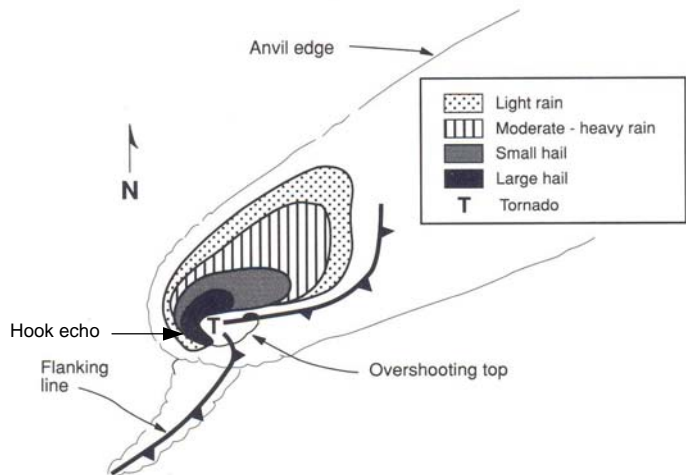


Figure 2.8: Plan view schematic of supercell features showing typical surface precipitation patterns, surface gust fronts (frontal symbols), updraft (collocated with tornado and overshooting top), hook echo location, and cloud boundaries (thin lines). Storm motion is to the east. [adapted from Houze 1993].

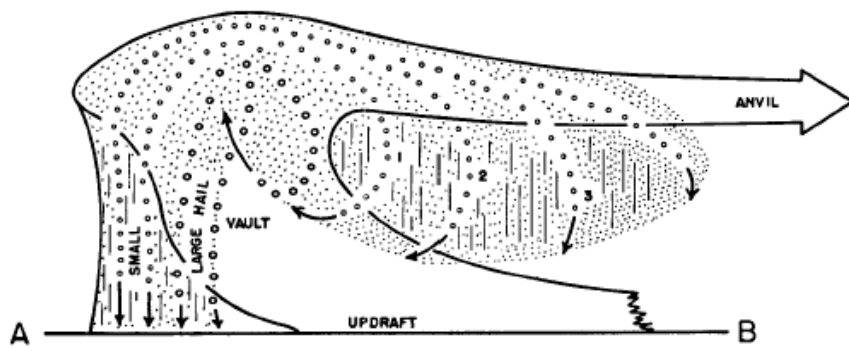


Figure 2.9: Schematic of vertical cross section oriented along direction of mean shear vector through supercell vault region illustrating precipitation regions (stippling) and associated downdrafts (vertical hatching) along with possible precipitation trajectories (dotted curves). [from Browning 1964].

updrafts and accompanied with high LWC values (Musil et al. 1973). Owing to their unique airflow structure, supercell storms typically exhibit distinct radar reflectivity patterns associated with the precipitation such as low-level hook echoes (Figures 2.8 and 2.10a), weak echo regions (WERs), bounded weak echo regions (BWERS) (Figures 2.10b,c) and forward overhang regions (Figure 2.10c). Hook echoes result from precipitation particles that are carried around the updraft by the mesocyclonic flow and then enter the rear flank downdraft as illustrated by the storm-

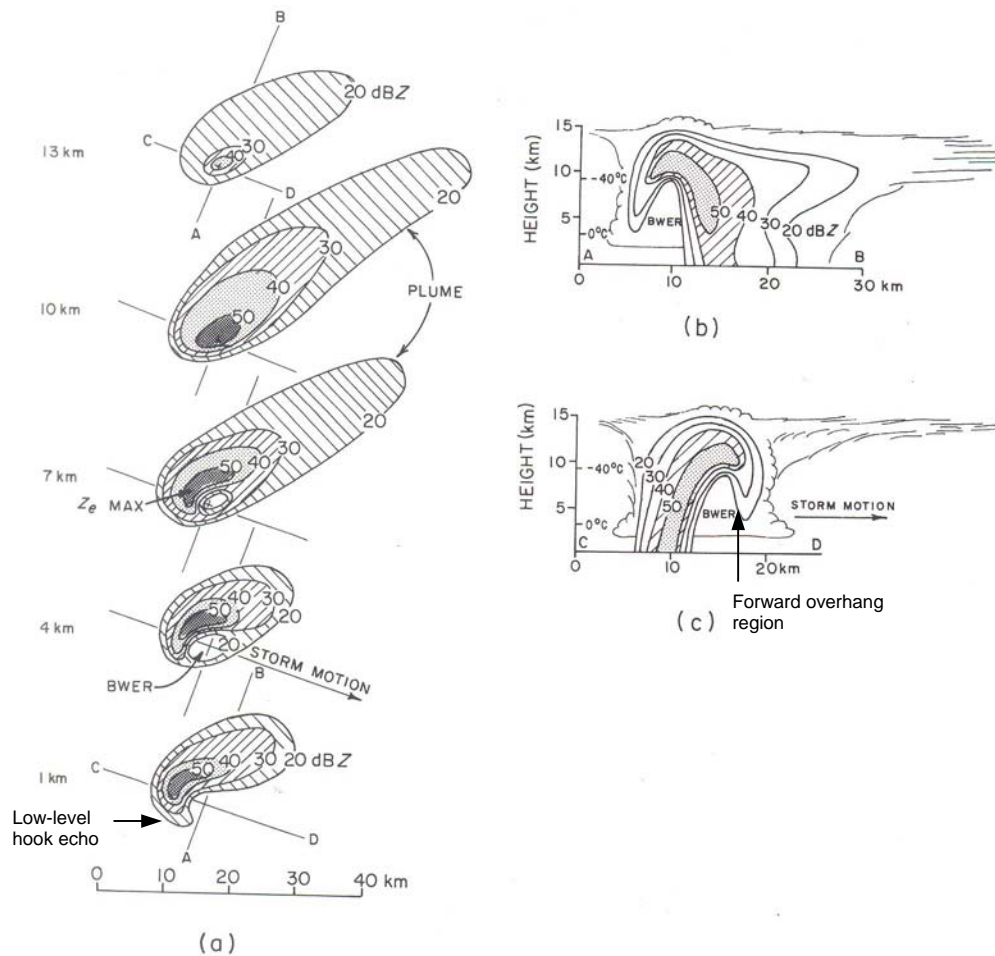


Figure 2.10: Schematic illustrating the variation of radar reflectivity patterns with height in supercell thunderstorms observed in Alberta, Canada. Horizontal sections of reflectivity (dBZ) at various altitudes are shown in (a). Vertical sections are shown in (b) and (c). Salient features are labeled and cloud boundaries are sketched. [adapted from Chisholm and Renick 1972].

relative flow pattern in Figure 2.7b. WERs and BWERs are localized minima in the reflectivity fields and are caused by intense updrafts that rapidly carry developing precipitation particles upwards into the upper regions of the storm. The forward overhang region, or embryo curtain as described by Browning and Foote (1976), is often located immediately adjacent to and above the WER or BWER region (e.g., Figures 2.10c and 2.12) and results from precipitation particles that are suspended within weaker updrafts or falling slowly relative to the updraft velocities. The identification of these reflectivity features in early studies of supercells provided key information

regarding the growth of hail and particularly large hail in severe convection (Browning et al. 1963; Marwitz 1972a,b,c; Browning and Foote 1976).

It was originally believed that large hail generated within many supercells formed via the multiple incursion theory (Huschke 1959), in which hailstone growth occurred over numerous up- and down-cycles within the updraft and downdrafts. This theory helped explain to a degree the amount of time required for growth to large sizes as well as provided an explanation for the alternating layers of clear and opaque ice often comprising the hailstone structure (Browning and Ludlam 1962). However, other studies found that repeated incursions of growing hailstones into the updraft often required too much time compared to observations, some of which reported hail at the surface within roughly 15 to 20 minutes of the formation of radar detectable precipitation particles (Hitschfeld and Douglas 1963; Chisholm 1973).

The inconsistencies of the multiple incursion theory for hail growth led Browning and Foote (1976) to formulate a three stage conceptual model of hail growth in supercells (Figure 2.11). Their model was based on analysis of a supercell that occurred over northeast Colorado on 21 June 1972 and produced a hailswath about 300 km long and 15-20 km wide. The stages of hail growth they envisioned are as follows:

- 1) Embryos initially develop in a relatively narrow region of the updraft periphery where upward vertical velocities are of the order of 10 m s^{-1} , where they grow to millimeter size (trajectory 1). Particles that develop closer to the updraft core experience much larger updraft speeds and do not have sufficient time to grow to embryo sizes as they are rapidly transported to the anvil region of the storm (trajectory 0).

- 2) Embryos forming on the western edge of the updraft are then transported southward by the divergent flow around the updraft (trajectory 2), and the embryos that are large enough can fall

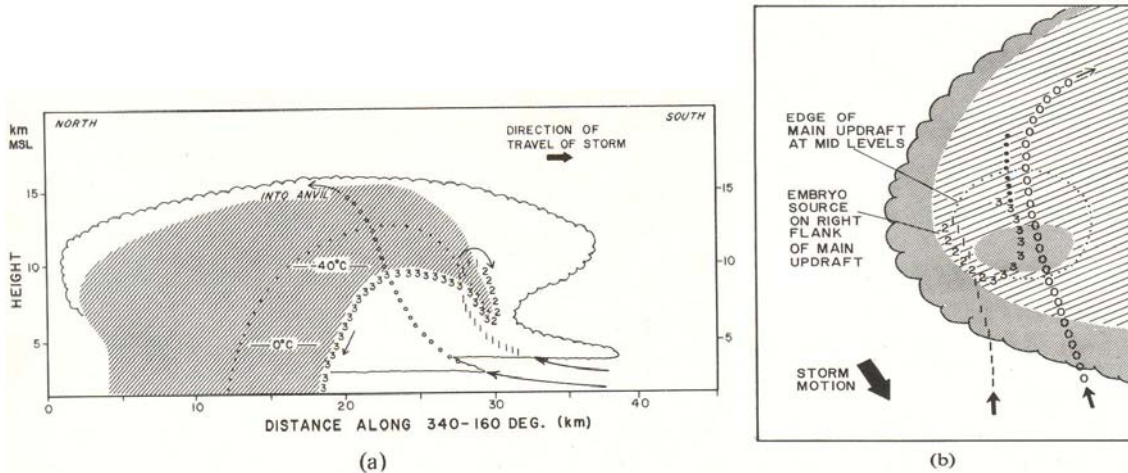


Figure 2.11: Schematic model of hailstone trajectories within a supercell storm based on the airflow model (Figure 2.12) of Browning and Foote (1976). Frame (a) shows hail trajectories in a vertical section along the direction of travel of the storm and frame (b) shows these same trajectories in plan view. Trajectories 1, 2, and 3 represent the three stages of growth of large hail discussed in the text. The transition from stage 2 to 3 corresponds to the re-entry of a hailstone embryo into the main updraft prior to the final up-and-down trajectory during which the hailstone may grow large, especially if it grows close to the boundary of the vault. Other, slightly less favored hailstones will grow a little further away from the edge of the vault and will follow trajectories resembling the dotted trajectory. Cloud particles growing 'from scratch' within the updraft core are carried rapidly up and out into the anvil along trajectory 0 before they can attain precipitation size. [from Browning and Foote 1976].

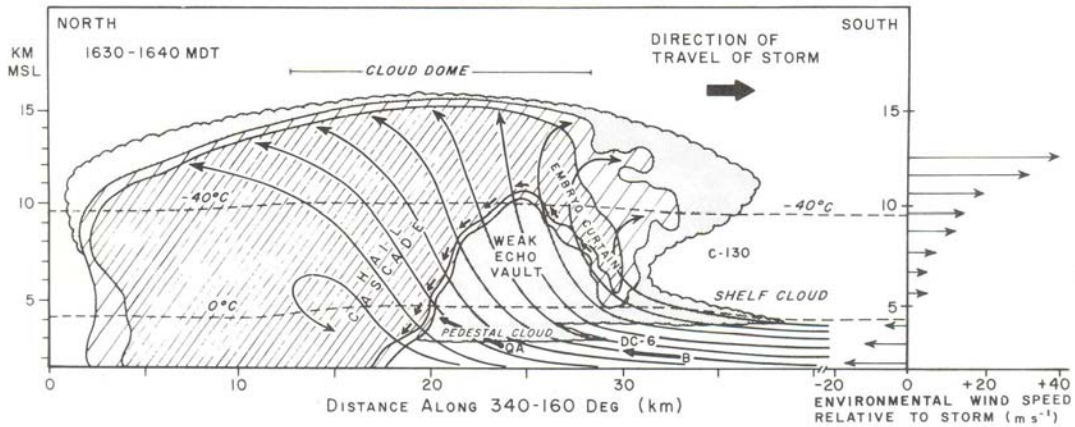


Figure 2.12: Vertical section showing features of the visual cloud boundaries of the 21 June 1972 Fleming, CO supercell storm superimposed on the radar echo pattern for the times indicated in the figure. The section is oriented in the direction of travel of the storm. Two levels of radar reflectivity are represented by different densities of hatched shading, and areas of cloud devoid of detectable echo are shown stippled. Bold arrows denote wind vectors in the plane of the diagram as measured by aircraft. Short thin arrows skirting the boundary of the vault represent a hailstone trajectory. The thin lines are streamlines of airflow relative to the storm drawn to be consistent with the other observations. A profile of the wind components along the storm's direction of travel, derived from a Sterling, CO sounding 50 km to the south of the storm is shown to the right of the diagram. [from Browning and Foote 1976].

into the region of weak updrafts that characterizes the 'embryo curtain', which is depicted in Figure 2.12. Some particles can also enter the embryo curtain from the main updraft as elements of the main updraft are eroded due to environmental flow impinging on the western flank of the updraft prior to circulating southward around the updraft. As the embryos descend in the embryo curtain, further growth is likely, though this growth could be slow as the liquid water content within this region is probably rather low. The larger particles then fall to the lower tip of the embryo curtain where they may re-enter the foot of the main updraft (Figures 2.11a and 2.12).

3) The growing particles increase rapidly in size as they encounter near-adiabatic LWCs during their ascent in the main updraft, and this rapid growth occurs in a single up-and-down cycle along the periphery of the weak echo region (trajectory 3; see also Figure 2.12). Embryos that enter the updraft at lower levels are more likely to have fallspeeds that nearly match the updraft speed such that the particles have sufficient time to accrete copious amounts of liquid water as they slowly ascend within the updraft, and these particles have the greatest probability of attaining the largest sizes. Eventually, the hailstones reach a level of balance near the top of the vault, a region in which a large amount of growth is inferred to occur (Atlas 1966; English 1973; Nelson 1983) as the hailstones continue to traverse the updraft. Once the fallspeeds of the hailstones become too great to be maintained by the updraft, they descend into the downdraft region (depicted as the 'hail cascade' in Figure 2.12), with the largest particles falling closest to the boundary of the vault where continued exposure to near-adiabatic water contents allows for further growth. Both Browning et al. (1963) and Browning and Foote (1976) emphasized that the stringent requirement of the growing embryos to maintain terminal velocities that approximately match the updraft speed while ascending accounts for the infrequency of large hail, not the scarcity of hail embryos entering the updraft.

The hail growth model proposed by Browning and Foote (1976) is not without its deficiencies however. One issue with this model is that it assumes steady-state flow conditions within a supercell, whereas more recent analyses of supercells suggest an underlying cellular or pulsating nature superimposed on the main updraft region (Knight and Knight 2001). Goyer (1977) noted that multicell hailstorms and supercells can exhibit quasi-steady state surface hailfalls of low concentrations along with embedded pulsations of high concentrations, suggesting that hail formation mechanisms in both storm types are largely similar, and Nelson (1987) stressed the importance of cellularity within an overall supercell-like organization for intense hail formation. Studies by Krauss and Marwitz (1984), and Cheng and Rogers (1988) further emphasized the role of the flanking line towers acting as feeder cells in supplying pulses of embryos that accounted for pulses in hail formation. Similarly, Miller and Fankhauser (1983) reported that hail embryos first formed in developing feeder cells near the main updraft of a supercell-like storm and were then moved into the main updraft. Miller et al. (1988) also found that the recycling trajectory of Browning and Foote was absent in the supercell they examined. Instead, hail embryos re-entering the main updraft most likely emanated from shedding processes within the lower portion of the forward overhang or the upwind stagnation zone. Another deviation from the Browning and Foote model was noted by Miller et al. (1990), who examined hail within a supercell and found growth trajectories of large hail through the updraft core as well as along the updraft peripheries. While the Browning and Foote model may be applicable in some cases, it seems more likely that hail formation and growth mechanisms in supercells include elements consistent with those found in multicell hailstorms as well.

2.5) *Radar observations of hail*

Doppler radar reflectivity values exceeding roughly 50 to 55 dBZ are usually an indicator of hail (Chisholm 1968; Mason 1971; Foote and Wade 1982), and values exceeding 65 dBZ have been observed in storms with large hail (Miller et al. 1988, 1990; Zrnić et al. 1993; Scharfenberg et al. 2005). Previous studies have also noted strong correlations between the regions of greatest reflectivity values and large hail observed at the ground (Browning et al. 1968; Mason 1971; Foote and Wade 1982; Aydin et al. 1986; Miller et al. 1988, 1990). Spatial reflectivity patterns such as WERs, BWERs and vaulted structures (e.g., Figures 2.9, 2.10 and 2.12) resulting from local minima in precipitation-sized particle concentrations have been found to be associated with particularly intense updrafts and are typical features of many hail-producing supercell and multicell storms (Browning and Ludlam 1962; Marwitz 1972a,b,c; Chisholm 1973; Browning and Foote 1976; Chalon et al. 1976; Foote and Wade 1982; Heymsfield and Musil 1982; Knight 1984; Musil et al. 1986; Nelson 1987; Musil et al. 1991). Auer and Marwitz (1972) reported on several hail encounters in aircraft within regions of strong horizontal reflectivity gradients in the vicinity of updrafts near cloud bases of High Plains thunderstorms. They noted that the largest hail was located in these reflectivity gradients that border the WERs with almost no liquid precipitation present. Analyses of in-cloud observations of a hailstorm over northeastern Colorado by Musil et al. (1973) also found hail to be present in strong reflectivity gradients near the edge of the WER. Similar reports of hail along the periphery of the WER in regions of weaker updrafts/ downdrafts and high reflectivity were presented in Musil et al. (1986) for a Montana hailstorm in addition to an increase in particle size as the aircraft approached the WER. This latter finding implied that size sorting of hail was occurring with larger hail existing in regions of stronger updraft.

Polarimetric radars, which can emit and receive linearly polarized horizontal (Z_H) and vertical (Z_V) waves, are able to provide information on types of hydrometeors as well as estimates of particle sizes in different regions of deep moist convection (Bringi et al. 1986; Höller et al. 1994; Hubbert et al. 1998; Tessendorf et al. 2005). There are several polarimetric variables that are typically used in conjunction with the standard reflectivity factor to identify hail in convection. Differential reflectivity (ZDR), computed from the ratio of received powers Z_H and Z_V , is related to the axis ratio and size of hydrometeors and can be used to distinguish regions of large oblate drops ($ZDR \geq +1$) as well as regions of wet, large, and/or tumbling hail ($-2 \leq ZDR \leq +1$) (Bringi et al. 1986; Höller et al. 1994, Straka et al. 2000). The linear depolarization ratio (LDR) is a function of the ratio of the cross-polar to the copolar powers received and is sensitive to hydrometeor shape, thermodynamic phase and canting (Straka et al. 2000). LDR has been shown to be a good indicator of hail above the melting level (Bringi et al. 1986; Holler et al. 1994) as well as large wet hail below the melting level (Carey and Rutledge 1998; Hubbert et al. 1998), with increasing LDR values typically corresponding to larger hail sizes. The correlation coefficient (ρ_{HV}) between Z_H and Z_V is also useful to determine regions of rain, hail and rain mixed with hail (Zrnić et al. 1993; Hubbert et al. 1998; Straka et al. 2000). ρ_{HV} decreases from a value of unity due to increasing hail size, broadening of the hail size spectra, wetting of hail, and mixing of hail with liquid drops of various sizes (Balakrishnan and Zrnić 1990). The diagnostic hail differential reflectivity (HDR) parameter (Aydin et al. 1986), originally formulated to distinguish hail from rain, can also be used to infer hail size (Kennedy and Detwiler 2003; Depue et al. 2007). HDR is computed by subtracting a prescribed function of ZDR from the horizontally polarized reflectivity (Z_H), and values equal to or greater than 21 dB often signifies the presence of large diameter ($D \geq 19$ mm) hail (Depue et al. 2007).

2.6) *Overview of microphysical schemes*

Representation of cloud and precipitation processes through the use of microphysical models are an integral part of all numerical cloud models, and there are a plethora of schemes of varying degrees of sophistication in use today. Microphysical schemes vary in the number of predicted hydrometeor species and types of microphysical processes represented and are divided into two classes: bulk microphysics and bin (spectral) microphysics, which are described in more detail in the following sections. The simplest microphysical schemes used in cloud models represent only warm rain processes following Kessler (1969), who developed parameterizations for condensation, evaporation, coalescence of cloud droplets into raindrops, collection of cloud particles by rain, and sedimentation in order to predict the mass mixing ratios of cloud and rain hydrometeors. Simple Kessler-type schemes have been used in many three-dimensional simulations of supercells that were able to successfully reproduce many of the features and dynamical processes characteristic of supercells (e.g., Klemp and Wilhelmson 1978, Johnson et al. 1993). However, as mentioned in the beginning of this chapter, ice processes in deep convection have been shown to have increasingly important roles in many aspects of storm evolution, and thus these processes should be accounted for in microphysical schemes.

Many of the schemes following the Kessler paradigm have strived to include ice processes as well as more complete representation of the interactions between microphysics and cloud dynamics. Early microphysical models that incorporated simple ice processes include single-class ice schemes that predicted mass mixing ratios of cloud ice (Ogura and Takahashi 1971) or hail (Wisner et al. 1972), and the two-class ice [cloud ice and hail] scheme of Bennets and Rawlins (1981), all of which parameterized the additional processes of sublimation, accretion of liquid water by ice particles, freezing and melting. Other more complex two-class ice models are

those of Orville and Kopp (1977), which included wet and dry growth of hail as well as shedding of liquid from hail, Cotton et al. (1982), which modeled primary nucleation of ice crystals and allowed for large ice particles to be classified as either graupel or hail, and Koenig and Murray (1976), the latter being unique among these schemes at the time in that it predicted number concentrations of ice particles in addition to ice hydrometeor mass. Lin et al. (1983) developed a complex three-class ice scheme (commonly referred to as the LFO scheme) that predicted the mixing ratios of cloud ice, snow, and hail. A variation of the LFO scheme by Rutledge and Hobbs (1984) assigned graupel as the large ice category rather than hail. Cotton et al. (1986) also expanded their two-class ice scheme to three classes with an additional aggregate species and predicted on the number concentrations of pristine ice crystals, including a parameterization for secondary ice crystal production via the Hallet-Mossop (1974) rime-splintering process.

A greater understanding of microphysical processes and advancements in computing power have led to the development of sophisticated schemes that include even more categories of ice hydrometeors and parameterizations of the numerous processes involved among the hydrometeors and the convection. Some of these advanced schemes include the four-class ice scheme [ice crystals, snow, graupel, and hail] of Ferrier (1994), the five-class ice scheme [pristine ice crystals, snow, aggregates, graupel, and hail] presented in Cotton et al. (2003), and even a ten-class ice scheme [two ice crystal habits, rimed cloud ice, snow, three graupel categories of differing densities, frozen drops, small hail, and large hail] developed by Straka and Mansell (2005). Both the number and type of predicted hydrometeor categories or species has an enormous impact on the microphysical and dynamical evolution of simulated deep moist convection. For example, Ferrier et al. (1995) found that predicting graupel and hail as separate categories produced more realistic storm characteristics for both tropical and mid-latitude

convection. van den Heever and Cotton (2004) noted that excluding hail as a species in their supercell simulations gave results that were similar in magnitude to those from variations in fixed mean hail diameter. Lastly, Straka and Mansell (2005) state that the added flexibility associated with more categories in the 10-ice scheme allows for smoother transitions in particle densities and terminal velocities. The authors compared their scheme with the simpler LFO scheme (specifying either graupel or hail, but not both) in simulations of idealized continental multicellular convection and found that the 3-ice had high reflectivity values (> 50 dBZ) throughout the simulation whereas the 10-ice scheme produced pulses of very high reflectivity (55-65 dBZ). In addition, the 3-ice graupel case produced more mass in graupel/hail field than 3-ice hail case, which had more mass in the snow field. These findings point out that tuning a microphysical scheme to include or exclude certain hydrometeor characteristics can undoubtedly impact the results and substantiate the use of more categories in microphysical schemes.

2.6.1) *Bulk microphysical schemes*

Bulk microphysical schemes employ analytical distribution functions to represent the hydrometeor distributions and usually predict one or two characteristics of the distribution such as mass mixing ratio (related to the 3rd moment) and/or particle concentration (related to the 0th moment). The two most commonly used distribution functions are the exponential distribution (e.g., Marshall and Palmer 1948; GSR04) and the gamma distribution (e.g., Walko et al. 1995, hereafter W95), although lognormal distribution functions may work as well (Feingold and Levin 1986). Observations of hail from thunderstorms at various locations suggest that exponential-type distributions adequately describe hail size spectra for some situations (Federer and Waldvogel 1975; Musil et al. 1976; Cheng et al. 1985), although gamma distributions work

better for others (Ziegler et al. 1983; Wang et al. 1987; Wong et al. 1988). The gamma distribution is advantageous for hail as it is capable of representing peaks often observed in the size spectra (Ziegler et al. 1983; Wong et al. 1988), whereas the exponential distribution inherently assumes that the smallest particles are most numerous and has been noted to poorly represent distributions at smaller diameters (GSR04; Straka and Mansell 2005). In addition, Dessens and Fraile (1994) provide theoretical evidence that a collection of hailstones observed to conform to an exponential-type at the ground more correctly correspond to a gamma-type distribution while in free fall.

The RAMS cloud-resolving model uses gamma distributions for all hydrometeors (cloud, large cloud, rain, pristine ice, snow, aggregates, graupel, and hail; hereafter referred to as c , $c2$, r , p , s , a , g , and h) and currently has the option of utilizing either a single-moment (W95) or a double-moment (M97) bulk microphysics scheme. The large cloud droplet mode ($c2$) is akin to drizzle drops and complements the initial cloud mode (c) in representing the dual modes of cloud droplets that are often observed in nature (Saleeby and Cotton 2004). The benefits of a double-moment (referred to here as 2M) over a single-moment (referred to here as 1M) scheme include improvements in predicted surface precipitation and overall storm evolution, along with better representations of microphysical processes (Ferrier 1994, hereafter F94; M97; Reisner et al. 1998; Milbrandt and Yau 2006b; Mansell 2008; Morrison et al. 2009). Using results from two-dimensional simulations, M97 showed that for a highly idealized convective environment, the amount of surface precipitation was more than 50% greater and dominated by (small) hail in a 1M scheme case versus a 2M scheme case in which the dominant precipitation at the surface was in the form of rain. It should be noted, however, that the results in M97 are presented for the very early stages of convective development (15 to 30 minutes) and are thus subject to skepticism as

they are more representative of the initial warm bubble rather than fully developed deep convection. Dawson et al. (2010) noted that simulated supercell thunderstorms using 1M microphysics schemes tend to produce colder and more expansive cold pools than simulations that use 2M microphysics owing to stronger evaporative cooling of raindrops associated with larger numbers of small drops that are directly related to a large fixed intercept parameter. In their simulations of polarimetric radar signatures of a supercell storm, Jung et al. (2010) found that a 2M scheme produced signatures that matched observations much more closely than for the case of a 1M scheme. One issue with both the 1M and 2M schemes is that one or more of the distribution parameters must remain fixed, and thus, the values assigned to the fixed parameter(s) are often tuned according to the particular environment and storm type being investigated (GSR04; Straka and Mansell 2005).

The prediction of multiple moments of a hydrometeor distribution lessens the constraints imposed by the parameterization and allows for more variability in the distribution. Milbrandt and Yau (2005a, b) (hereafter MY05a and MY05b) implemented a triple-moment bulk microphysics scheme (referred to as MY3M in this paper) that predicts the radar reflectivity factor Z for hydrometeors into a three-dimensional cloud model. The new scheme was tested for a real case of a severe Alberta hailstorm, and the simulated convection using the 3M scheme produced reflectivity and precipitation patterns that resembled observations much more closely than convection simulated with the 1M and 2M schemes (Milbrandt and Yau 2006a, b; hereafter MY06a and MY06b). Additionally, the maximum sizes of hail reaching the surface in the simulation with the MY3M scheme were comparable to what was actually observed (MY06a), whereas the maximum hail sizes reaching the surface using a 1M (2M) scheme were generally much larger (smaller) than for the MY3M scheme (MY06b). Dawson et al. (2010) examined

sensitivities of simulated tornadic supercells to the number of predicted moments of hydrometeor distributions in simulations using the Advanced Regional Prediction System (ARPS; Xue et al. 2000, 2003), into which the MY3M scheme was recently implemented. The authors found that the results using the higher order moment microphysical schemes, particularly with the MY3M scheme, compared much more favorably to the observed storms in agreement with the findings by MY06a,b.

2.6.2) Bin microphysical schemes

Bin or spectral microphysical schemes are formulated to predict the evolution of hydrometeors of discrete sizes. These schemes typically involve representation of the particle spectra with several tens of size (or mass) bins, and the evolution of the size distribution is explicitly calculated. Bin microphysical models are advantageous over bulk models in representing processes such as nucleation, collision-coalescence, and sedimentation of particles, though these advantages are offset by the considerable computing cost involved with predicting the evolution of individual size (mass) bins. Thus, bin schemes typically prevent simulations of clouds and convection in three-dimensions and are particularly ill-suited for sensitivity studies in which numerous simulations are performed. Of course, these schemes are useful to evaluate the components of the more efficient bulk microphysical schemes, particularly sedimentation processes (MY05a, Mansell 2010).

As with bulk schemes, bin microphysical models vary in complexity from treating only warm rain processes (e.g., Clark 1973; Kogan 1991) to inclusion of multiple ice species (e.g., Takahashi 1976; Reisin et al. 1996; Khain et al. 2004). Simple bin models typically incorporate only one size distribution function to describe both cloud ice and frozen precipitation (e.g., Hall

1980; Ovtchinnikov and Kogan 2000), for which the smallest particles are interpreted as ice crystals and the larger particles are considered to be graupel and/or hail, whereas more complex schemes contain several size distribution functions for different types of ice particles (e.g., Takahashi 1976; Reisin et al. 1996; Khain et al. 2004; Lynn et al. 2005). Size-dependent particle characteristics such as particle density, crystal habits and shape factors for ice species that affect collection rates and fall speeds are also capable of being represented in bin microphysical schemes (Takahashi 1976; Hall 1980; Farley and Orville 1986; Chen and Lamb 1994; Khain et al. 2004). For example, Farley (1987a) was able to simulate the initial low-density growth stages of hail through the incorporation of bin microphysics and found that enhanced hail growth and increased number concentrations of large hail resulted when allowing for variable hail density compared to using a fixed density. In addition, some spectral models (Farley and Orville 1986; Chen and Lamb 1994; Khain et al. 2004) include heat budget considerations to predict basic thermodynamic properties of ice particle bins, such as surface temperature and liquid water mass, which are especially important for hail growth processes. Explicit predictions of aerosol populations and activation of these aerosols can also be handled by bin schemes, as in the models presented by Yin et al. (2000) and Khain et al. (2004), though of course, the inclusion of additional species further increases the already high cost of these schemes. Another limitation of bin models is the problem of artificial spectrum broadening of the liquid categories due to diffusion as well as coarse model grid resolution as discussed in Khain et al. (2004), which could affect the evolution of hail distributions via the accretion process. Multimoment methods that predict two or more moments for each bin significantly reduce this artificial broadening and have the added benefit of conserving more than one moment of the distribution (Tzviou et al. 1987; Chen and Lamb 1994; Reisin et al. 1996). In addition, a fewer total number of bins are required

for these multimoment methods to achieve an accuracy comparable to that attained with the single-moment bin approaches.

Although bin schemes often represent hydrometeor distributions and many microphysical processes more realistically than bulk schemes, their use in three-dimensional cloud resolving and mesoscale models is often not feasible owing to their enormous computational cost. That being the case, methods have been designed for bulk schemes to emulate a bin model for certain microphysical processes such as droplet nucleation, stochastic collection, melting and sedimentation (Feingold et al. 1988; Feingold and Heymsfield 1992; Cotton et al. 2003; Saleeby and Cotton 2004). For example, explicit activation of CCN and GCCN in RAMS is accomplished by building look-up tables from an ensemble of Lagrangian-bin parcel model calculations that consider ambient cloud conditions for the activation of cloud droplets from aerosol particles (Feingold and Heymsfield 1992; Saleeby and Cotton 2004). The *bin-emulating* methods for collection, melting and sedimentation in RAMS used in the current work involve the use of separate bin models to create look-up tables spanning a wide range of possible distributions and are detailed in the model description section. Another option is to employ a hybrid bin/bulk model such as Farley and Orville (1986), Johnson et al. (1993), and Guo and Huang (2002) in which the graupel/hail species is predicted using a bin approach and the remaining species are predicted using bulk microphysics. This latter method supports the approach of the current work, namely using a more sophisticated 3M bulk model for the hail species while maintaining a 2M bulk prediction for the remaining species.

3. Model description

3.1) Overview of hydrometeor distributions in the RAMS model

Hydrometeors in RAMS are assumed to conform to a three-parameter gamma type distribution (Eqn. 3.1) (W95), where D is the particle diameter, D_n is the characteristic diameter ($D_n = 1/\lambda$, where λ is called the slope parameter in different mathematical expressions for gamma distributions [e.g., F94; MY05a]), and Γ is the complete gamma function. From W95, the number density distribution for any hydrometeor of diameter D is given by Eqn. (3.2), and in general, any moment P of the distribution can be computed using Eqn (3.3). For each hydrometeor category (denoted by subscript x [$x = c, c2, r, p, s, a, g, h$]), the two-moment microphysics scheme (2M) in RAMS predicts the mass mixing ratio (r_x), related to the 3rd moment of the distribution, and total number concentration (N_{tx}), related to the 0th moment of the distribution (M97). The shape parameter (ν_x) is the only remaining free parameter and controls the relative amounts of smaller versus larger hydrometeors. A value of $\nu = 1$ corresponds to the commonly used exponential or Marshall-Palmer distribution, and larger ν values correspond to increasingly more narrow size distributions with the peak of the distribution curve approaching the mean diameter (i.e., the 1st moment) of the distribution (Figs. 3.1 and 3.2).

$$f_{gam}(D_x) = \frac{1}{\Gamma(\nu_x)} \left(\frac{D_x}{D_{nx}} \right)^{\nu_x-1} \frac{1}{D_{nx}} \exp\left(-\frac{D_x}{D_{nx}} \right) \quad (3.1)$$

$$n_x(D_x) = N_{tx} f_{gam}(D_x) \quad (3.2)$$

$$M(P) = \int_0^{\infty} D^P f_{gam}(D) dD = D_n^P \frac{\Gamma(\nu + P)}{\Gamma(\nu)} \quad (3.3)$$

A fixed value for ν is assigned for each hydrometeor species for both the 1M and 2M microphysics versions of RAMS, and the choice of this value can impact various aspects of the microphysical processes during model runtime. Initial testing of the 1M and 2M schemes in RAMS in a two-dimensional framework found that increasing ν from 1 to 3 for all hydrometeor species led to decreased surface precipitation amounts in the 1M case (W95), and a nearly threefold increase of surface precipitation in the 2M case (M97). The reduced precipitation

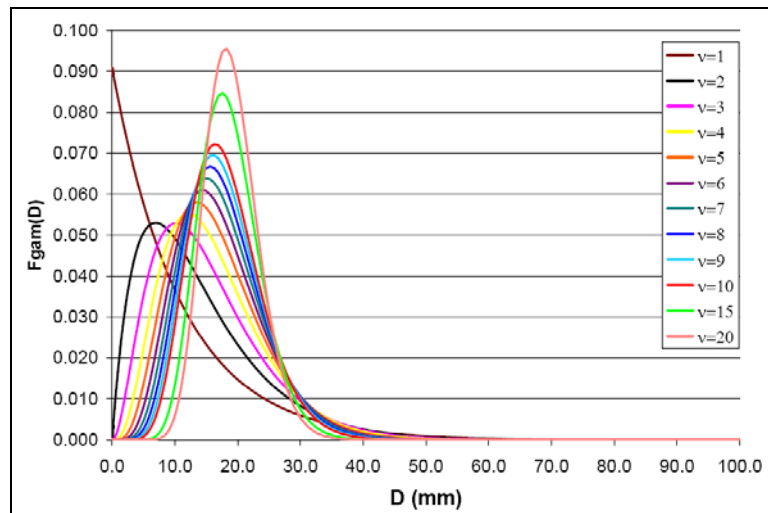


Figure 3.1: Gamma distribution curves for hail mean diameter of 20mm for ν ranging from 1 to 20.

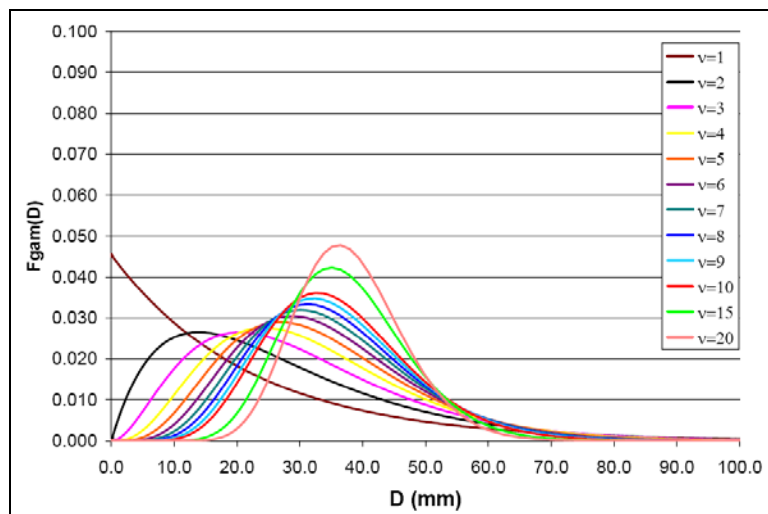


Figure 3.2: Gamma distribution curves for hail mean diameter of 40mm for ν ranging from 1 to 20.

associated with the larger ν values in the 1M case was presumably due to narrower spectral widths for pristine ice that resulted in reduced aggregation rates and more ice mass remaining aloft. W95 also reported that for larger ν values in the 1M scheme, cloud mean diameters increased which led to enhanced rain mass production via increased cloud self-collection (autoconversion) rates, and ultimately to increased hail mass production via rain-ice collisions. M97 also noted increased rain and hail mixing ratios with larger ν values for the 2M scheme, as well as significant increases in rain and graupel number concentrations and decreases in hail number concentrations. M97 give no explanation regarding their observed changes in number concentrations as a result of changing ν , thus one can only speculate as to the physical causes of their results.

Sensitivity studies by Cohen and McCaul (2006) using a 1M microphysics version of RAMS found that changing the value of ν_h from 1.5 to 5 while holding the hail mean mass diameter fixed led to an increase in collection rates owing to an increase in the mean surface area of hailstones in the distribution. However, this was for hail collecting a monodisperse cloud droplet distribution, and thus the effects of stochastic collection were not considered. The authors further reported that increasing the value of ν for all hydrometeor species resulted in greater production of precipitation and increased low-level evaporative cooling. van den Heever (2001) also employed a 1M version of RAMS to study the effects of different hail parameter values on supercells. In contrast to results reported by Cohen and McCaul (2006), van den Heever (2001) noted that increasing ν_h led to lower collection rates due to increasingly uniform fall velocities of hail associated with narrower size spectra when stochastic collection was considered. van den Heever (2001) also showed that varying ν_h from 1 to 5 resulted in decreases in melting and evaporation rates leading to smaller and warmer cold pools. These reduced cooling rates in turn

resulted in a general decreases in downdraft strengths, slower rates of occlusion, increases in low-level mesocyclone intensities, and ultimately longer-lived storms.

The author of the current work briefly expanded upon the work of van den Heever (2001) with an examination of the effects of varying only ν_h from 1 to 7 in idealized three-dimensional simulations of splitting supercell convection with RAMS using the 2M microphysics scheme. As found by W95 and M97, increases in rain mass mixing ratios along with corresponding increases in surface rainfall rates and accumulated precipitation values were observed for increasing ν_h values. Similar to results from van den Heever (2001), increases in ν_h resulted in earlier storm splitting along with reductions in the horizontal coverage of accumulated rainfall, in the spatial extent and intensity of low-level cold pools, and in hail mixing ratios. The latter finding here is in contrast to results from W95 and M97 with respect to the effects of changing ν_h on hail mixing ratios. The varying conclusions from these limited studies of the effects of ν_h on microphysical and convective-scale processes further justify the need for improved representation of time-dependent hail distributions and microphysical processes involving hail.

The mass of a hydrometeor in RAMS is expressed as a function of D using a power law relationship (Eqn. 3.4), where α_{mx} is the mass coefficient and β_{mx} is a dimensionless exponent, both of which are specific to each category. For spherical particles such as hail, $\beta_{mx} = 3$ and $\alpha_{mx} = \rho_x(\pi/6)$, where ρ_x is the hydrometeor density. The expression for hydrometeor terminal velocity [m s^{-1}] (Eqn. 3.5) also follows a power law relationship, where $\alpha_{V_{tx}}$ and $\beta_{V_{tx}}$ are the category-specific coefficient and exponent, respectively. Air density effects on fall speeds are not included in Eqn. (3.5), but are accounted for in the various RAMS look-up tables.

$$m = \alpha_{mx} D^{\beta_{mx}} \quad (3.4)$$

$$V_{tx} = \alpha_{V_{tx}} D^{\beta_{V_{tx}}} . \quad (3.5)$$

Table 3.1: RAMS default values of hydrometeor category coefficients for mass and terminal velocity power law relationships. Minimum and maximum mean mass diameters for each category are also given. It should be noted that the maximum mean mass diameter for the 2M microphysics scheme is set to 10 mm.

Category	α_m	β_m	ρ [kg m ⁻³]	α_{vt}	β_{vt}	$D_{\bar{m},\min}$	$D_{\bar{m},\max}$
cloud	524 [kg m ⁻³]	3	1000	3173	2	2 μm	40 μm
cloud2 (drizzle)	524 [kg m ⁻³]	3	1000	3173	2	65 μm	100 μm
rain	524 [kg m ⁻³]	3	1000	149	0.5	0.1 mm	5 mm
pristine ice	110.8	2.91	variable	5.769x10 ⁵	1.88	15 μm	125 μm
snow	2.739x10 ⁻³	1.74	variable	188.146	0.933	0.1 mm	10 mm
aggregates	0.496	2.4	variable	3.084	0.2	0.1 mm	10 mm
graupel	161 [kg m ⁻³]	3	300	93.3	0.5	0.1 mm	10 mm
hail	471 [kg m ⁻³]	3	900	161	0.5	0.8 mm	40 mm

Values α_{mx} , β_{mx} , α_{vtx} and β_{vtx} are listed in Table 3.1. Note that the velocity coefficient for hail (α_{vth}) in Table 3.1 corresponds to $C_D = 0.4537$, which is the drag coefficient value for spherically shaped hailstones. As hail particles typically possess fall speeds ranging from 10 to nearly 50 m s⁻¹, their trajectories deviate substantially from the airflow trajectories (Knight and Knight 2001), and thus an accurate representation of the sedimentation of hail is crucial to modeling hail growth. Details of sedimentation for the 3MHAIL scheme are presented in Section 3.6 and Appendix B. The mass mixing ratio for category x is given by Eqn. 3.6 (W95)

$$r_x = \frac{N_{tx}}{\rho_a} \alpha_{mx} D_{nx}^{\beta_{mx}} \frac{\Gamma(v_x + \beta_{mx})}{\Gamma(v_x)} \quad (3.6)$$

In Eqn. (3.6), ρ_a is the density of air. An expression for the characteristic diameter can be obtained by solving for D_{nx} in (3.6)

$$D_{nx} = \left[\frac{r_x \rho_a}{N_{tx} \alpha_{mx}} \frac{\Gamma(v_x)}{\Gamma(v_x + \beta_{mx})} \right]^{1/\beta_{mx}} \quad (3.7)$$

A quantity used throughout the RAMS microphysical model for all hydrometeors is the mean mass diameter ($D_{\bar{m}}$), which is the diameter of a particle having the mean mass of the distribution

and is *not equivalent* to the mean diameter (\bar{D}) of the distribution. The mean mass of the distribution is simply given by

$$\bar{m}_x = r_x / N_{tx}, \quad (3.8)$$

and the mean mass diameter can be obtained from Eqn 3.4 by replacing D with $D_{\bar{m}}$ and m with \bar{m} ,

$$D_{\bar{m}x} = (\bar{m}_x / \alpha_{mx})^{1/\beta_{mx}} = [r_x / (\alpha_{mx} N_{tx})]^{1/\beta_{mx}}. \quad (3.9)$$

Minimum and maximum mean mass diameters are specified for each hydrometeor species (Table 3.1) to ensure the hydrometeor distributions remain within physically reasonable limits. The default value for the maximum mean mass diameter for hail, $D_{\bar{m}h,max}$, in the 2M RAMS microphysics scheme is 10 mm, whereas this value is increased to 40 mm in the 3MHAIL scheme in order to better represent large hail. The addition of a large cloud droplet mode (cloud2 or drizzle drops) in combination with the traditional cloud droplet mode (cloud1, referred to herein simply as cloud) allows the representation of the bimodal distribution of droplets often seen in clouds (Hobbs et al. 1980). The cloud2 mode slows down the formation of rain from the collision-coalescence process of droplets by requiring self-collection of cloud droplets to first enter the cloud2 category rather than being transferred directly to the rain category (Saleeby and Cotton 2004). Note that the $D_{\bar{m}}$ range for cloud2 reported in Saleeby and Cotton (2004) has since changed from 40-80 μm to 65-100 μm in order to eliminate problems due to overlap between the cloud and cloud2 size distributions. The range of $D_{\bar{m}}$ is also used in formulating representative hail distributions during the construction of the various look-up tables for collection, melting, shedding, and sedimentation, the details of which are provided in later sections. The range of hail diameters for the 3MHAIL scheme look-up tables is 0.2 to 150mm so

that the integration of the gamma pdfs will not be truncated at the smallest hail sizes. Even though ice particles with diameters less than about 5 mm technically aren't considered to be hail, the amount of mass and reflectivity associated within these smaller sizes is insignificant when integrating over the entire hail size distribution. The hail distribution shape parameter ν_h can vary from 1.0 to 10.0. Tests incorporating an expanded range for ν_h (1.0 to 20.0) were performed for pure sedimentation in a 1D column, combined sedimentation and melting/shedding in a quiescent environment within a 3D model, and a full 3D simulation. Findings from these tests revealed that increasing the max value of ν_h from 10 to 20 did not have a significant effect on the results, though the expanded ν_h range is retained as an option in the model.

The temperature of a hydrometeor, particularly hail, can differ substantially from that of its immediate environment owing to latent heat release or absorption, melting effects and sensible heating due to collisions with other hydrometeors (Schumann 1938; Ludlam 1958; Macklin 1961; Srivastava 1987; Greenan and List 1995). Hydrometeor temperature, in turn, governs the rates of heat and vapor diffusion and sensible heat transfer of collisions (Drake and Mason 1966; Bailey and Macklin 1968; Pruppacher and Klett 1980; W95). In order to calculate hydrometeor category mean temperatures in RAMS, bulk internal energies (Q_x) of each hydrometeor category are predicted based on heat budget considerations according to the implicit method described by Walko et al. (2000). For reference, the equation for bulk internal energy for hydrometeor category x is given by Eqn 3.10, where i_x is the bulk ice fraction, c_i and c_l are the specific heats of ice and liquid, respectively, T_x is the hydrometeor mean temperature ($^{\circ}\text{C}$) of the distribution, and L_f is the latent heat of fusion. Q_x is defined to be zero for pure ice at 0°C . Heat storage is permitted for rain, graupel, and hail hydrometeors through the predicted Q_x values, which are

stored from one time step to the next such that the liquid water contents of graupel and hail can be diagnosed and rain may be out of equilibrium with its immediate environment,

$$Q_x = i_x c_i T_x + (1 - i_x)(c_l T_x + L_f). \quad (3.10)$$

The concentration of aerosols nucleated to form cloud droplets is obtained from a look-up table as a function of CCN concentration (N_{CCN}), CCN median radius, vertical velocity, and temperature. This look-up table is generated separate from the main model from an ensemble of Lagrangian-bin parcel model calculations (Feingold and Heymsfield 1992; Saleeby and Cotton 2004). The variable N_{CCN} is advected and diffused in the model, and has sinks and sources owing to nucleation and evaporation, respectively, of cloud droplets. Nucleation of GCCN to become cloud2 droplets is computed according to

$$N_{c2} = N_{GCCN}; \quad S_w > 0.0, \quad (3.11)$$

where N_{c2} is the concentration of cloud droplets [cm^{-3}] in the second cloud mode, N_{GCCN} is the GCCN concentration, and S_w represents supersaturation with respect to water. The variable N_{GCCN} is also advected and diffused, and nucleation of cloud2 droplets constitutes a sink for N_{GCCN} , whereas the sources of N_{GCCN} are evaporation of cloud2 droplets and/or raindrops. CCN and GCCN particles are considered to be composed of ammonium sulfate and NaCl, respectively. The number of pristine ice crystals formed via deposition-condensation freezing on IN is calculated as

$$N_{pris} = N_{IN} F_M, \quad (3.12)$$

where N_{IN} is the maximum concentration of IN available for activation, and F_M represents the fraction of available IN that are activated as a function of ice supersaturation (Meyers et al. 1992). F_M is maximized at ice supersaturations of 40%. N_{IN} is also a forecast variable in the model, thus it undergoes advection and diffusion, and has a sink owing to ice activation.

3.2) Derivation of reflectivity factor and hail reflectivity equations

The radar reflectivity factor Z_x is given by the sixth moment of the number density distribution (Dye et al 1974; Carbone and Nelson 1978), and the following derivation is for the hail radar reflectivity factor ($x = h$). (Strictly speaking, the 3MHAIL scheme predicts the sixth moment of the hail distribution, though the term hail reflectivity factor Z_h or simply hail reflectivity is used throughout this paper). Plugging in $P = 6$ to Eqn. 3.3 and multiplying by N_{th} gives

$$Z_h = M(6)N_{th} = D_{nh}^6 \frac{\Gamma(\nu_h + 6)}{\Gamma(\nu_h)} N_{th}, \quad (3.13)$$

and substituting Eqn. (3.7) into Eqn. (3.13) with $\beta_{mh} = 3$ yields

$$Z_h = N_{th} \frac{\Gamma(\nu_h + 6)}{\Gamma(\nu_h)} \left[\frac{r_h \rho_a}{N_{th} \alpha_{mh}} \frac{\Gamma(\nu_h)}{\Gamma(\nu_h + 3)} \right]^2. \quad (3.14)$$

The identity $\Gamma(x + n) = (x + n - 1)(x + n - 2) \cdots (x + 1)x\Gamma(x)$

(<http://mathworld.wolfram.com/GammaFunction.html>) is used to expand out gamma function expressions in (3.14)

$$\frac{\Gamma(\nu_h + 6)}{\Gamma(\nu_h)} = \frac{(5 + \nu_h)(4 + \nu_h)(3 + \nu_h)(2 + \nu_h)(1 + \nu_h)\nu_h \Gamma(\nu_h)}{\Gamma(\nu_h)}, \quad (3.15)$$

$$\left[\frac{\Gamma(\nu_h)}{\Gamma(\nu_h + 3)} \right]^2 = \left[\frac{\Gamma(\nu_h)}{(2 + \nu_h)(1 + \nu_h)\nu_h \Gamma(\nu_h)} \right]^2. \quad (3.16)$$

Substituting (3.15) and (3.16) into (3.14) and simplifying gives the final expression for Z_h

$$Z_h = \left(\frac{r_h \rho_a}{\alpha_{mh}} \right)^2 \frac{G(\nu_h)}{N_{th}}, \quad (3.17)$$

where the function G is given by

$$G(\nu_h) = \frac{(5 + \nu_h)(4 + \nu_h)(3 + \nu_h)}{(2 + \nu_h)(1 + \nu_h)\nu_h}, \quad (3.18)$$

similar to MY05a. The prediction of the sixth moment of the hail distribution, and thus Z_h , means the shape parameter ν_h becomes a predictive variable, and thus the hail distribution can be fully prognosed. It should be noted that Eqn 3.17 is valid only for spherical particles (i.e., $\beta_{mx} = 3$), a reasonable assumption for hailstones (Matson and Huggins 1980), which often tumble and gyrate while falling so as to appear spherical (Knight and Knight 1970c; Straka et al. 2000).

Following the methodology of MY05b, the reflectivity tendency equation for hail (Eqn. 3.19) consists of five terms for the advection, diffusion, and sources of Z_h , along with changes to Z_h by melting and sedimentation. The advection and diffusion terms are computed in the same manner as other scalars in RAMS. Unlike mass or air temperature, radar reflectivity is not a physical quantity, and thus advection and diffusion of reflectivity (or more appropriately the 6th moment) at first seems illogical. However, a gradient of a scalar field will necessarily be acted upon by these two processes in a numerical model (note that advection and diffusion of number concentrations are no more physical than advection and diffusion of reflectivity). The source term is comprised of the sum of the individual tendencies of Z_h for each possible microphysical process (except melting and sedimentation) and is classified into two types. The first type assumes that the changes in ν_h are negligible and includes collection of non-hail categories by hail, whereas the second type involves the formation of hailstones from rain-ice collisions (three-component freezing) and riming of graupel.

$$\frac{\partial Z_h}{\partial t} = -\vec{\nabla} \cdot (Z_h \vec{U}) + TURB(Z_h) + \left. \frac{dZ_h}{dt} \right|_{Source} + MELTING(Z_h) + SEDIM(Z_h) \quad (3.19)$$

Eqn. (3.19) is solved in several stages at each time step to obtain updated values of Z_h at each model scalar point. The advection and diffusion terms in Eqn (3.19) only depend on the grid point values of Z_h and are updated prior to application of the microphysics. The remaining three terms in Eqn. (3.19) are then computed in the microphysics module and an updated value of v_h is calculated based on the updated values of r_h , N_{th} and Z_h . Thus, all three parameters describing the hail size distribution at any grid point are free to change over time.

Following MY05b, three equations are used to compute the source and sink terms of the hail reflectivity tendency equation (3.19). These equations are not actually true tendency equations in that the incremental changes in r_h and N_{th} in one Δt due to the specified processes lead to a change in Z_h , as evident in the discrete forms of the equations (3.23-3.25), thus the term reflectivity adjustment is more appropriate. The first equation (3.20, 3.23) adjusts Z_h owing to collection and assumes the grid point v_h value is unaffected. The second equation (3.21, 3.24) adjusts Z_h owing to conversion of graupel to hail through riming, and the third equation (3.22, 3.25) deals with conversions to hail resulting from rain-ice interactions (i.e., 3-component freezing). For Eqn. (3.21), the reflectivity tendency of graupel (dZ_g / dt) is diagnosed via Eqn. (3.20) using the fixed distribution shape parameter value for graupel and subscripts changed to the graupel category (3.24), and dZ_g / dt is always negative since hail formation is a sink for graupel. The amount of cloud mass mixing ratio collected by graupel particles undergoing conversion is included in the Δr_g term in Eqn. (3.24). For rain-ice collisions leading to hail (3.22, 3.25), an assumed value of v_h^* must be assigned to the newly formed hail distribution (here it is set to 2.0). Tests reveal that the calculation of the reflectivity adjustment for hail formed in this manner is generally insensitive to the value of v_h^* owing to the relatively small diameters associated with the newly formed hail.

$$\left. \frac{dZ_h}{dt} \right|_{coll} = G(v_h) \left(\frac{\rho_a}{\alpha_{mh}} \right)^2 \left[2 \frac{r_h}{N_{th}} \left. \frac{dr_h}{dt} \right|_{coll} - \left(\frac{r_h}{N_{th}} \right)^2 \left. \frac{dN_{th}}{dt} \right|_{h-h \text{ coll}^*} \right] \quad (3.20)$$

$$\left. \frac{dZ_h}{dt} \right|_{g,rime \rightarrow h} = - \left(\frac{\alpha_{mg}}{\alpha_{mh}} \right)^2 \left. \frac{dZ_g}{dt} \right|_{g,rime \rightarrow h} \quad (3.21)$$

$$\left. \frac{dZ_h}{dt} \right|_{3comp} = G(v_h^*) \left(\frac{\rho_a}{\alpha_{mh}} \right)^2 \left[\left. \frac{dr_r + dr_p + dr_s + dr_a + dr_g}{dt} \right|_{3comp} \right]^2 \times \left(\left. \frac{dN_{th}}{dt} \right|_{3comp} \right)^{-1} \quad (3.22)$$

$$\Delta Z_h \Big|_{coll} = G(v_h) \left(\frac{\rho_a}{\alpha_{mh}} \right)^2 \left[2 \frac{r_h}{N_{th}} \Delta r_h \Big|_{coll} - \left(\frac{r_h}{N_{th}} \right)^2 \Delta N_{th} \Big|_{h-h \text{ coll}^*} \right] \quad (3.23)$$

$$\Delta Z_h \Big|_{g,rime \rightarrow h} = -G(v_g) \left(\frac{\rho_a}{\alpha_{mh}} \right)^2 \left[2 \frac{r_g}{N_{tg}} \Delta r_g \Big|_{g \rightarrow h} - \left(\frac{r_g}{N_{tg}} \right)^2 \Delta N_{tg} \Big|_{g \rightarrow h} \right] \quad (3.24)$$

$$\Delta Z_h \Big|_{3comp} = G(v_h^*) \left(\frac{\rho_a}{\alpha_{mh}} \right)^2 (\Delta r_r + \Delta r_p + \Delta r_s + \Delta r_a + \Delta r_g)^2 \Big|_{3comp} \times (\Delta N_{th} \Big|_{3comp})^{-1} \quad (3.25)$$

Initially, the effects of melting and shedding were included in (3.20) as in MY05b (who only modeled melting). However, it was determined that the adjustment methods, which adjust Z_h based on fractional changes to the 6th moment (M_6) of the hail distribution as described in sections 3.5.1 and 3.5.2, provided results that were more consistent with the mathematical formulations of these processes. Furthermore, complete melting of the smallest hail sizes could lead to a change in v_h , thereby violating the assumption that v_h remain constant in (3.20). The tendency of Z_h due to vapor deposition is neglected as the changes in hail mass due to this process are negligible compared to changes in mass owing to collection, melting, and shedding

(Iribarne and De Pena 1962; List 1963; Heymsfield and Pflaum 1985), thus changes in Z_h will also be negligible. The reflectivity adjustments (3.23-3.25) are applied immediately following collection within the microphysics module in RAMS using the pre-collection values of r_h and N_{th} (r_g and N_{tg}) for the r_h/N_{th} (r_g/N_{tg}) terms in Eqn. 3.23 (3.24).

The following sections detail the microphysical processes represented in the 3MHAIL scheme.

3.3) Collection

3.3.1) Bulk collection

Collision and coalescence of hydrometeors are computed primarily using a bulk approach to collection that is based on the stochastic collection equation (Verlinde et al. 1990). From W95 and M97, the rates of change of mixing ratio r_x and number concentration N_{tx} of category x coalesced into hydrometeors due to collisions with hydrometeors of category y are, respectively,

$$\frac{dr_x}{dt} = \frac{N_{tx}N_{ty}\pi F_\rho}{4\rho_a} \int_0^\infty \int_0^\infty m(D_x)(D_x + D_y)^2 |V_t(D_x) - V_t(D_y)| \times f_{gam}(D_x)f_{gam}(D_y)E_{x,y}dD_xdD_y \quad (3.26)$$

and

$$\frac{dN_{tx}}{dt} = \frac{N_{tx}N_{ty}\pi F_\rho}{4} \int_0^\infty \int_0^\infty (D_x + D_y)^2 |V_t(D_x) - V_t(D_y)| \times f_{gam}(D_x)f_{gam}(D_y)E_{x,y}dD_xdD_y \quad (3.27)$$

where V_t is the terminal velocity of a particle of diameter D , $E_{x,y}$ is the net collection efficiency for category x collection by category y , and $F_\rho = (1/\rho_a)^{0.5}$ is a density-weighting factor to account for increased terminal velocities at lower ambient densities. For the majority of hydrometeor interactions, it is assumed that $E_{x,y}$ is a constant and can thus be moved outside of the integral. In

actuality, $E_{x,y}$ varies widely for collection of cloud droplets by larger hydrometeors (F94; W95) and collection of ice crystals by rain drops (Lew et al. 1985), however, a constant value for $E_{x,y}$ is used to simplify the calculations as is often done in bulk schemes (e.g., F94; GSR04; MY05b, Straka and Mansell 2005). Laboratory studies of growing hailstones have generally found that hail growing wet has a collection efficiency near unity, with values less than unity attributed to shedding (Macklin and Bailey 1968; Lesins and List 1986; García-García and List 1992; Greenan and List 1995). Values of $E_{x,y}$ for hail in the bulk collection model are listed in Table 2. Cloud droplet autoconversion and collection of cloud drops by rain are solved using a method-of-moments (Tzivion et al. 1987) bin-emulating approach that accounts for variations in collection efficiencies over the cloud droplet spectrum, the details of which can be found in Cotton et al. (2003) and Saleeby and Cotton (2008). An optional bin-emulating riming scheme is available in RAMS that does account for varying efficiencies of ice hydrometeors collecting cloud droplets (see Section 3.3.2).

As detailed in W95 and M97, a large number of solutions to the double integrals in (3.26) and (3.27) are pre-computed for each possible category interaction spanning the ranges of $D_{\bar{m}_x}$ and $D_{\bar{m}_y}$ and stored logarithmically in three-dimensional look-up tables, the indices of which are $D_{\bar{m}_x}$, $D_{\bar{m}_y}$, and the pair (x,y) of the interacting categories. The construction of these tables for all collisions not involving hail entails solving the integral over D_y analytically while numerically computing the integral over discrete bins of D_x (Verlinde et al. 1990; W95). For the 3MHAIL scheme, the additional range of allowable v_h values is also considered (though only for collisions involving hail) when pre-computing the integrals in (3.26) and (3.27), and the solutions are stored in four-dimensional* look-up tables, the additional dimension being v_h . During model runtime, values for interacting pairs (x,y) are interpolated from the table bi-linearly over $D_{\bar{m}_x}$ and

Table 3.2: Collection efficiencies of hail for bulk collection in RAMS. T_h represents bulk hail distribution temperature, and Q_h represents bulk hail internal energy.

Collected hydrometeor x	Collection efficiency $E_{(x,h)}$
c , or $c2$	$\min[1.0, 1426 \times (\bar{m}_{c,c2} - 3.4 \times 10^{-14})^{0.28}]$ if $\bar{m}_{c,c2} > 3.4 \times 10^{-14} \text{ kg}$ 0.0 if $\bar{m}_{c,c2} \leq 3.4 \times 10^{-14} \text{ kg}$
r	1.0
p , s , a , or g	$\min[0.2, 10.0^{(0.035 \times T_h - 0.7)}]$ if $Q_h \leq 0.0$ (hail dry growth) 1.0 if $Q_h > 0.0$ (hail wet growth)
h	$\max[0.0, 0.1 + 0.05 \times T_h]$

$D_{\bar{m}_y}$ (and linearly interpolated over v_h also for the 3MHAIL scheme) to efficiently obtain values for the double integrals in (3.26) and (3.27). Thus, the amount of r_x coalescing with r_y over a time step is

$$\Delta r_x = \frac{N_{tx} N_{ty} \pi F_\rho E(x, y) \Delta t}{4 \rho_a} \times 10^{-J_r[(x,y), D_{\bar{m}_x}, D_{\bar{m}_y}, (v_h)^*]}, \quad (3.28)$$

and similarly, the change in N_{tx} collected into coalesced hydrometeors due to collisions with species y is

$$\Delta N_{tx} = \frac{N_{tx} N_{ty} \pi F_\rho E(x, y) \Delta t}{4} \times 10^{-J_N[(x,y), D_{\bar{m}_x}, D_{\bar{m}_y}, (v_h)^*]}, \quad (3.29)$$

where J_r and J_N are the interpolated tables values for mixing ratio and number concentration, respectively. When applicable, such as for collisions between liquid and frozen particles, the amount of r_y coalescing with r_x is also given by (3.28) except the x and y indices reversed.

The increased allowable size range for hail particles (0.2 to 150 mm) initially led to errors in the bulk collection rates, a problem attributed to the analytical/ numerical technique in W95 used to compute the double integral in the stochastic collection equations (3.26 and 3.27). This method is not valid for narrow size distributions (i.e., large shape parameter values) as stated in Verlinde et al. (1990). Differences in fall speeds between colliding categories are crucial factors in the collection process. However, the analytical portion of the integration only considers the

terminal velocity V_t of the characteristic diameter (D_n) of the distribution. This is analogous to using a mean-weighted fall speed that severely underestimates particle fall speeds when v_h is large, leading to much smaller values for collection rates. Size sorting associated with sedimentation, which generally causes distributions to narrow, compounded this problem. The solution was to implement a purely numerical integration scheme to compute the double integral in Eqns. 3.26 and 3.27 to account for the greater range of terminal velocity differences associated with the increased range of hail sizes while maintaining the assumption of constant collection efficiencies for collisions involving hail. This new numerical integration is now used to create the look-up tables for bulk collection involving hail for the 3MHAIL scheme; the old analytical/numerical method of solving Eqns 3.26 and 3.27 is still used for all other 2M hydrometeor categories.

Collisions between hydrometeors are classified into several groups according to interacting category types (liquid or frozen) and the resultant category of the coalesced particles (M97). The first group involves self-collection of hydrometeors, which results in a loss of N_{ix} and an increase in D_{mx} , except for cases where drop breakup for rain occurs. Based on photographic evidence of clumped hailstones from English (1973) and Knight et al. (2008), hail self-collection is permitted in the various RAMS microphysical schemes, though this is experimental and would likely only occur for smaller wetted hailstones in nature. The second type includes collisions between pristine ice and/or snow to form aggregates, which result in losses of mass and number of the colliding hydrometeors and a gain in mass and number for aggregates. Collisions between ice phase hydrometeors in which the resulting coalesced particles remain in the collector category (e.g., hail collecting pristine ice) comprise the third group of interactions. These interactions constitute a sink of mass and number for the collected particles and a mass source

for the collector hydrometeors. For the second and third collision types, a quantity of energy, $Q_x \Delta r_x$, accompanies the mixing ratio, Δr_x , transferred from the collected to the destination category.

A fourth type of interaction involves collection between liquid and frozen categories, the result of which may be a different category than the two colliding categories. This type of collection is crucial for the formation hail embryos and the growth of hail as detailed in Chapter 2. Three factors determine the destination category z in liquid-ice collection: 1) the category and amount of colliding ice (Δr_i), 2) the amount of rain or cloud water involved in collisions (Δr_l), and 3) the ice and liquid contents of the coalesced particles upon reaching thermal equilibrium. The first two factors are computed from Eqns (3.28) and (3.29) for the interacting categories, whereas the third is determined from the diagnosed liquid water fraction (LWF) based on the internal energy (Q^*) of the coalesced particles (Eqn 3.30). The LWF of the coalesced hydrometeors is calculated according to the quotient Q^*/L_f , where L_f is the latent heat of fusion. If the diagnosed LWF of the coalesced hydrometeors is greater than 0.99, then the destination category is rain. This can occur, for example, when large raindrops collide with small frozen particles within or below the melting level. For values of coalesced LWF less than 0.99, the coalesced mass (r_{coll}) is partitioned between the input ice category and the destination category based on the resulting liquid and ice contents of the coalesced hydrometeors according to Eqn 3.31 (M97). In Eqn 3.31, r_{liq} is the mass mixing ratio of the liquid portion of the coalesced hydrometeors upon reaching thermal equilibrium, Δr_z is the mass mixing ratio transferred to the destination category, and ζ and χ are empirically determined coefficients (M97) that depend on the type of ice hydrometeor as well as the collision type. If the destination category is the same as the input ice category (e.g., hail collecting cloud or rain), the amounts of mixing ratio and

internal energy transferred from the liquid category to the ice category are simply Δr_l and $Q_l \Delta r_l$, respectively. In cases where the destination and input ice categories are different, the partitioning of r_{colt} and Q^* between these two categories depends on the relative magnitudes of Δr_z and Δr_l . If $\Delta r_z > \Delta r_l$, r_{colt} and Q^* are sent to the destination category, and nothing is returned to the input ice category. If $\Delta r_z < \Delta r_l$, then Δr_z and $Q_l \Delta r_z$ are sent to the destination category, and $\Delta r_l - \Delta r_z$ and $Q_l (\Delta r_l - \Delta r_z)$ are returned to the input ice category,

$$Q^* = (Q_i \Delta r_i + Q_l \Delta r_l) / (\Delta r_i + \Delta r_l) \quad (3.30)$$

$$\Delta r_z = \min(r_{colt}, \zeta r_{liq} + \chi \Delta r_l) \quad (3.31)$$

$$\Delta N_{tz} = \max(0., (\Delta r_z / r_{colt}) \times n_{colt}). \quad (3.32)$$

Riming of snow and aggregates leads to a portion of the coalesced mass being transferred to the graupel category, and riming of graupel causes some of the coalesced mass to be transferred to the hail category. In addition, secondary production of ice crystals due to rime splintering (Hallet and Mossop 1974) is computed using the parameterization of Mossop (1978). The number concentrations of converted hydrometeors added to the destination category (ΔN_{tz}) is determined from a diagnostic equation (3.32) relating the fractional amount of mixing ratio transferred to the destination category to the number concentration of coalesced hydrometeors (n_{colt}) (M97). Hail collecting cloud (riming) or raindrops simply result in a gain of mass and internal energy for hail and a loss in mass, number, and internal energy for cloud or rain. As is the case for snow, aggregates, and graupel, riming of hail can also lead to ice splintering. Rain colliding with any frozen category except hail typically results in the coalesced mass and number being converted to the hail category (M97) and has been found to be the primary source of hail formation in simulations of deep convection using RAMS based on extensive tests of hail

formation performed as part of the current work. The sources and sinks for each hydrometeor category for liquid-frozen collisions and the associated destination categories are summarized in Table 3.3. Alternative methods to the existing logic of partitioning mass and number between the input ice categories and destination categories have recently been developed and implemented into the 3MHAIL scheme and are presented in section 3.3.3.

Examples of the 3MHAIL bulk collection tables as a function of $D_{\bar{m}h}$ and $D_{\bar{m}r}$ are shown in Figure 3.3 for rain-hail collisions, for which the distribution shape parameters of both categories are equal to 2.0. For comparison, the equivalent 2M bulk collection tables are shown as well. The bulk collection tables for hail collecting other hydrometeor species exhibit patterns and behaviors similar to the examples presented in Figures 3.3 and 3.4, and are thus not included here for brevity. The contours displayed in these plots are the collection table values multiplied by -1.0 so as to represent non-interpolated exponent values ($-J$) as in Eqns (3.28) and (3.29). In this manner, smaller contour magnitudes correspond to greater collection rates. These plots can similarly be

Table 3.3: Sources and sinks of hydrometeor mass mixing ratios (r), number concentrations (N_i), and internal energy (Q), and the resulting destination categories for liquid-frozen collisions. Variables in parentheses denote a possible conversion from the input ice category y to a different destination category as discussed in the text, and the notations 'F94' and 'MY05b' signify the use of alternative methods based on Ferrier (1994) and Milbrandt and Yau (2005b), respectively, to determine the destination categories.

x	y	Source	Sink	Destination
$c, c2$	s	$r_s, Q_s (r_g, N_{ig}, Q_g)$	$r_{c,c2}, N_{ic,c2}, Q_{c,c2} (r_s, N_{is}, Q_s)$	$s (g)$
$c, c2$	a	$r_a, Q_a (r_g, N_{ig}, Q_g)$	$r_{c,c2}, N_{ic,c2}, Q_{c,c2} (r_a, N_{ia}, Q_a)$	$a (g)$
$c, c2$	g	$r_g, Q_g (r_h, N_{ih}, Q_h)$	$r_{c,c2}, N_{ic,c2}, Q_{c,c2} (r_g, N_{ig}, Q_g)$	$g (h)$
$c, c2$	h	r_h, Q_h	$r_{c,c2}, N_{ic,c2}, Q_{c,c2}$	h
r	p	(r_h, N_{ih}, Q_h)	$r_r, N_{ir}, Q_r, r_p, N_{ip}, Q_p$	$h (h; F94)$
r	s	$r_h, N_{ih}, Q_h (r_s, Q_s \text{ or } r_g, N_{ig}, Q_g)$	$r_r, N_{ir}, Q_r, r_s, N_{is}, Q_s$	$h (s, g, \text{ or } h; \text{MY05b})$
r	a	$r_h, N_{ih}, Q_h (r_a, Q_a \text{ or } r_g, N_{ig}, Q_g)$	$r_r, N_{ir}, Q_r, r_a, N_{ia}, Q_a$	$h (a, g, \text{ or } h; \text{MY05b})$
r	g	$r_h, N_{ih}, Q_h (r_g, Q_g)$	$r_r, N_{ir}, Q_r, r_g, N_{ig}, Q_g$	$h (g \text{ or } h; \text{MY05b})$
r	h	r_h, Q_h	r_r, N_{ir}, Q_r	h

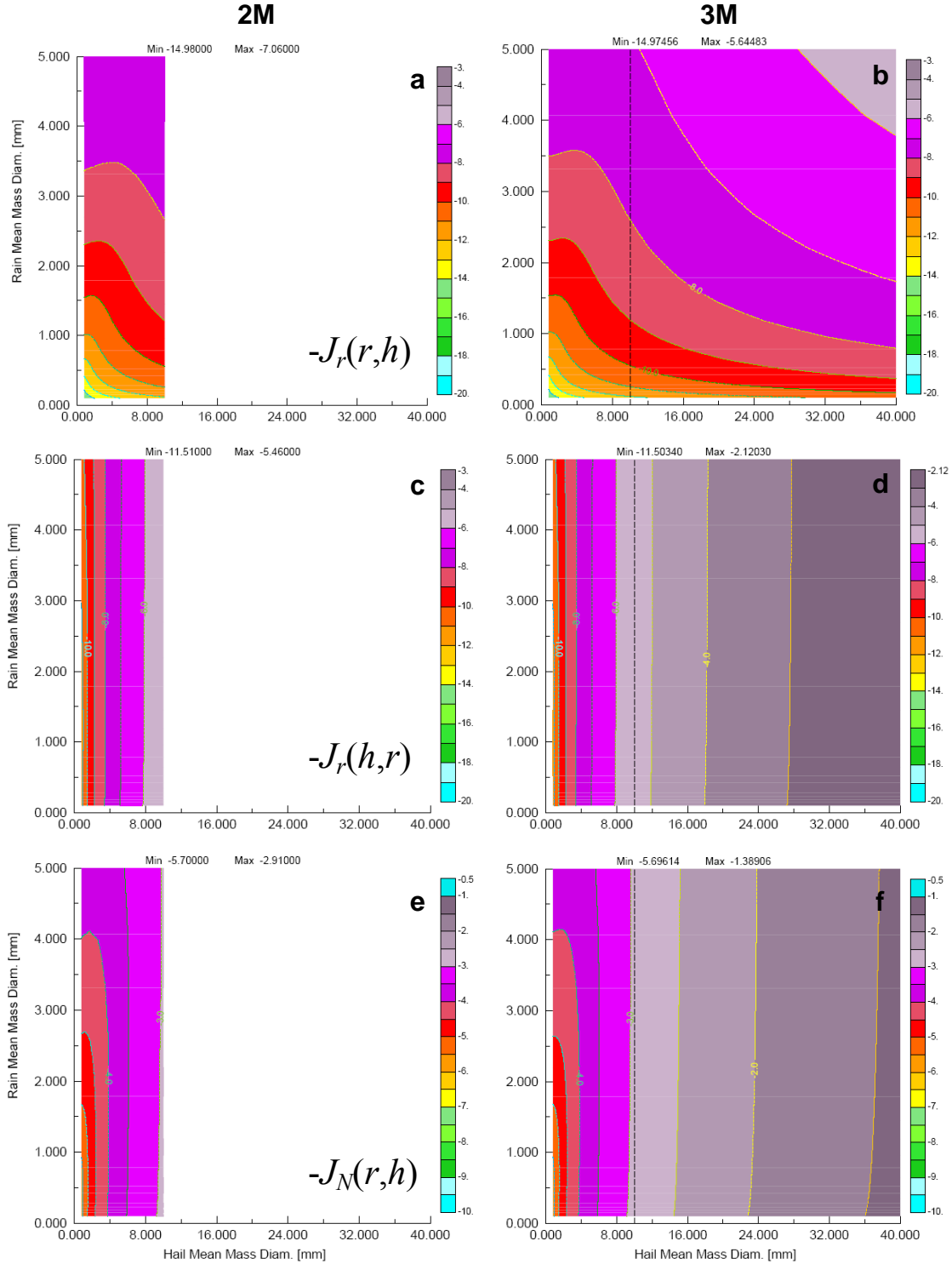


Figure 3.3: Contours of collection table values (negative exponents $[-J$ as in Eqns 3.28 and 3.29] for rain-hail interactions as function of D_{mr} and D_{mh} for the 2M collection (left column) and 3MHAIL collection (right column) schemes. Rain and hail distribution shape parameters are $v_r = v_h = 2.0$. Top row: mass table values for rain; middle row: mass table values for hail; bottom row: number table values for rain. Minimum and maximum table values are given at the top of each plot. Dashed vertical line in panels b, d, and f denotes upper limit of D_{mh} for the 2M scheme. Note the change in contour value range for number table.

interpreted as the relative amounts of r_r collected by r_h [$-J_r(r,h)$; panels a and b], the relative amounts of r_h involved in collection with r_r [$-J_r(h,r)$; panels c and d], and the relative amounts of N_{tr} collected by hail [$-J_N(r,h)$; panels e and f].

In comparing the values of the 3MHAIL collection tables (right column) with the 2M collection tables (left column) in Figure 3.3, it is evident that increasing the range of $D_{\bar{m}h}$ doesn't change the patterns of the table values, but simply extends the tables and allows for collection at larger $D_{\bar{m}h}$. In panels a and b, it is seen that increases in $D_{\bar{m}r}$ correspond to greater collection rates of r_r by r_h , whereas increases in $D_{\bar{m}h}$ generally correspond to increasing (decreasing) collection rates when $D_{\bar{m}h} > D_{\bar{m}r}$ ($D_{\bar{m}h} < D_{\bar{m}r}$). For $D_{\bar{m}r} < 0.5$ mm and $D_{\bar{m}h} >$ roughly 20 mm, collection rates of r_r by r_h are largely independent of $D_{\bar{m}h}$ (panel b). The relative amounts of r_h involved in collection with r_r depend only on $D_{\bar{m}h}$ (panels c and d), with larger relative amounts of hail mass collecting rain as $D_{\bar{m}h}$ increases owing to the increased fall speeds of the larger hail particles. The relative numbers of rain drops collected by hail particles is also primarily dependent on $D_{\bar{m}h}$ (panels e and f), with increasing values of $D_{\bar{m}h}$ leading to greater collection rates, again due to larger hail particles possessing greater fall speeds. At values of $D_{\bar{m}h}$ less than about 5 mm, the relative difference in fall speeds between raindrops and hail particles becomes small such that the relative amounts of N_{tr} collected by hail depend on $D_{\bar{m}r}$ in addition to $D_{\bar{m}h}$.

The dependence of the collection tables on v_h is illustrated in Figure 3.4, which shows the relative amounts of r_r collected by r_h for a fixed v_r value of 2.0 and v_h values of 1.0, 4.0, 7.0, and 10.0. Surprisingly, the collection table values exhibit similar patterns and magnitudes for the different values of v_h , and only a slight shift towards increasing table values is observed as v_h changes from 1.0 to 10.0, with the minimum $-J_r(r,h)$ value increasing less than 1% from

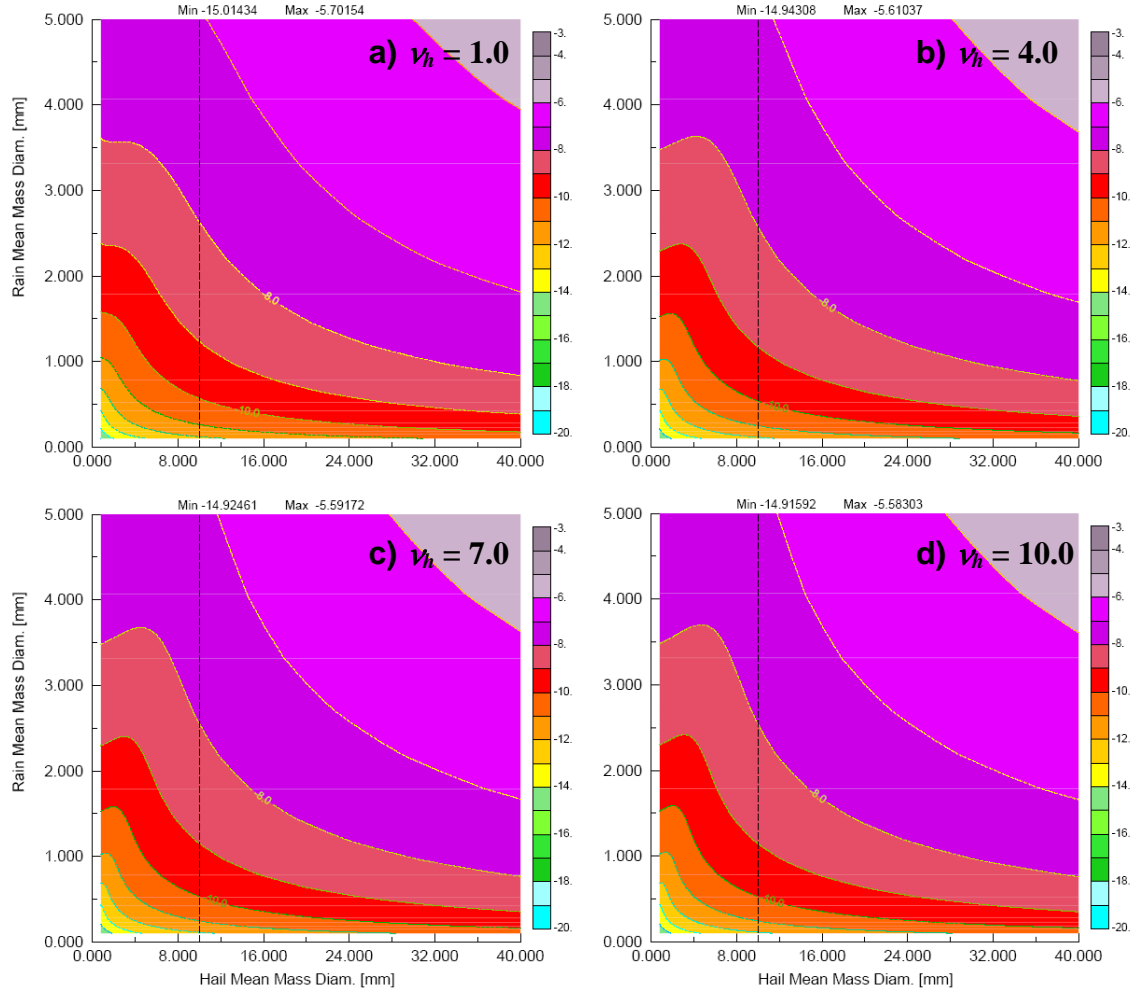


Figure 3.4: Contours of 3MHAIL collection table values expressed as $-J_r(r, h)$ as in panel b of Fig. 3.3 for various hail shape parameter values; a) $\nu_h = 1.0$, b) $\nu_h = 7.0$, c) $\nu_h = 7.0$, d) $\nu_h = 10.0$.

-15.01434 to -14.91592, and the maximum $-J_r(r, h)$ value increasing about 2% from -5.70154 to -5.58303. The most noticeable difference among the plots in Figure 3.4a occurs at small D_{mh} values ($< \sim 4$ mm). At these smaller diameters, a slight increase in collection rates is evident as ν_h increases from 1.0 to 4.0, and generally agrees with findings by Cohen and McCaul (2006) and M97 for the RAMS 1M and 2M versions of collection, respectively.

3.3.2) *Binned riming of hail*

The bin-emulating approach to riming of hail (and other precipitating ice hydrometeors, though this discussion will focus on hail) is detailed in Saleeby and Cotton (2008) and differs from traditional bin microphysics in that explicit riming computations for each size bin are not performed. Instead, this riming parameterization uses pre-computed look-up tables to determine the amount of cloud water collected by hail as a function of the mean diameters of cloud droplets and hail, the mixing ratio of hail, the number concentration of cloud droplets, and the time step length. To construct these tables, the gamma distribution curves covering a range of mass mixing ratios and mean diameters are first divided into a number of discrete bins, calculations are performed for all bin interactions using unique collection efficiencies for the particles involved, and the curves are then reconstructed to give the total riming that would occur.

The actual calculations for each interacting bin pair are carried out using the method of moments as described by Tzivion et al. (1987), which incorporates hydrometeor-dependent hydrodynamic collection kernels (Eqn 3.33). Collection efficiencies for hail (Eqn 3.34) collecting cloud droplets are determined from the Stokes parameter K_S (Eqn 3.35) based on the work of Greenan and List (1995) and have been extended to include the expanded range of hail diameters within the 3MHAIL scheme. It should be noted that the empirical formula (3.34) provided by Greenan and List (1995) was derived using 2 cm diameter hailstones,

$$K(x, y) = \left(\frac{9}{16} \pi \right)^{1/3} (x^{1/3} + y^{1/3})^2 E(x, y) |V_{tx} - V_{ty}| \quad (3.33)$$

$$E(x, y) = 0.59 K_S^{0.15} \quad (3.34)$$

$$K_S = (2\rho_d V a_d^2) / (9\eta a_h). \quad (3.35)$$

In equations 3.33 and 3.35, K is the collection kernel, x and y are the masses of the colliding particles, V_{tx} and V_{ty} are the terminal velocities of particles x and y , E is the collection efficiency for colliding particles x and y , ρ_d is the droplet density, V is the relative velocity between the cloud droplet and collector, a_d and a_h are the radii of the droplet and hail particle, respectively, and η is the dynamic viscosity. These equations are in cgs units. The method of moments previously used 36 mass-doubling bins to compute riming of hail, with bins 1-16 containing cloud droplet sizes (~ 3 to $< 100 \mu\text{m}$) and bins 17-36 comprising the hail sizes (~ 0.1 to 12 mm). For the 3MHAIL scheme, the number of bins is increased to 47 such that hail sizes range from roughly 0.1 to 134 mm .

An important point to address here is whether or not the collection efficiencies for riming hail can assume values larger than unity owing to the effects of wake capture. List (1977) defines net collection efficiencies for riming hail as '*the fraction of liquid water in the geometrically swept-out volume of air that is permanently accreted onto the hailstone.*' Ludlam (1958) and Macklin and Bailey (1966) show that collection efficiencies decrease with increasing hail size and decreasing cloud droplet diameter, and Greenan and List (1995) state that shedding reduces E_{net} such that values larger than 1.0 are generally not attainable. However, measurements of E_{net} values for riming hail from laboratory studies by Lesins and List (1986) and Garcia-Garcia and List (1992) do in fact show $E_{net} > 1.0$ at low liquid water contents corresponding to conditions of no shedding. E_{net} values greater than unity for riming of small, non-shedding graupel particles were measured by Heymsfield and Pflaum (1985) as well as computed by Khain et al. (2001) using theoretical considerations. Thus, it seems that for small riming hailstones that are incapable of shedding (Rasmussen and Heymsfield 1984), E_{net} could in fact be larger than 1.0 . This would allow for faster growth rates of smaller hailstones to larger sizes where shedding processes

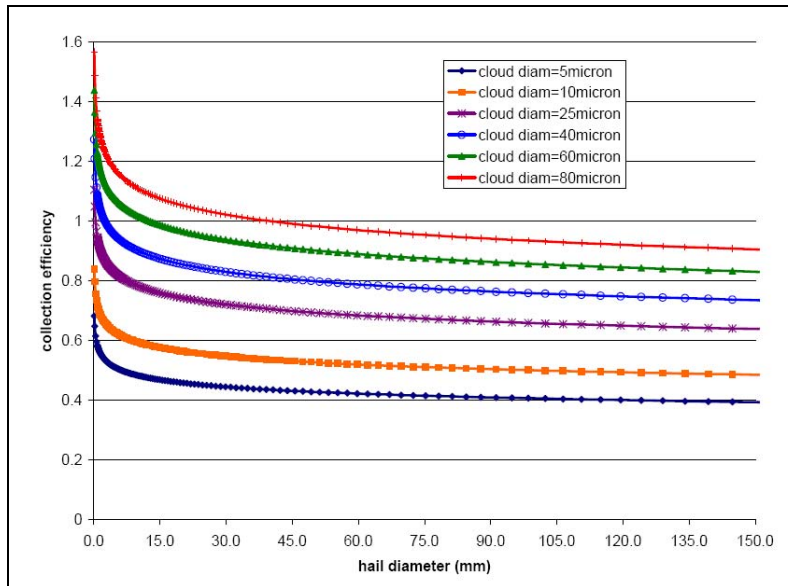


Figure 3.5: Calculated collection efficiencies from Eqn. 3.34 for hail collecting cloud droplets of specified diameter as a function of hailstone diameter.

would eventually become active and reduce E_{net} . As shedding processes in the RAMS microphysics are handled separately from collection processes, a choice was made to allow the computed E_{net} values from Eqn. (3.34) to exceed 1.0 rather than imposing a limiting value of unity. The resulting hail-cloud collection efficiencies are plotted in Figure 3.5, which shows that for cloud droplet diameters of about 40, 60, and 80 μm , efficiency values exceed 1.0 for hail diameters less than roughly 2.4, 12.3, and 39.1 mm, respectively. Note that hail particles with diameters greater than 9.0 mm may undergo shedding if the environmental conditions permit.

3.3.3) Alternative methods for the formation of new hail

The two microphysical pathways by which hail can form in RAMS are rain-ice collisions and riming of graupel, both of which rely solely on the 2M microphysics scheme collection algorithms to compute the mixing ratio and number concentration of the newly formed hailstones (e.g., Eqns 3.31 and 3.32). However, extensive testing of hail formation in simulated deep

convection within RAMS revealed that the current 2M collection schemes produced far too many new hailstones, on the order of 100s to 1000s per m^{-3} , within a single time step at a given grid point. Such large values do not agree with observations of hail number concentrations both in-cloud and at the surface as discussed in Section 2.1. In addition, the numbers of newly formed hailstones from rain-ice collisions were found to be about an order of magnitude larger than those produced via riming of graupel, which is the primary hail formation mechanism for High Plains storms (Knight and Knight 1970b, 1979; Knight et al. 1974). Furthermore, the addition of large numbers of newly created small hail particles to a pre-existing hail distribution caused a shift in the hail size distribution towards smaller sizes, thereby preventing the formation of large hail as intended by the 3MHAIL scheme. These issues were ultimately attributed to the logic of how mass and numbers are partitioned within the existing 2M collection algorithms, and thus, alternative collection algorithms were incorporated into the 3MHAIL scheme to better represent the formation of hail.

3.3.3.1) *MY05b three-component freezing*

As previously mentioned, hail is the *only* result from rain colliding with any frozen hydrometeor in the current RAMS 2M collection scheme. Even if small raindrops collide with larger frozen particles, the end result is hail formation. Cotton and Anthes (1989) note that freezing of supercooled raindrops via rain-ice interactions can result in either low-density graupel or high-density hail. Blahak (2008) introduced a spectral partitioning method by which rain-ice collisions could lead to cloud ice, graupel, or hail. Furthermore, large snow and aggregate particles collecting small raindrops could result in rimed snow and aggregates (Khain et al. 2004; MY05b). To change the way that mass and number are partitioned for rain-ice

interactions, the 3-component freezing algorithm of MY05b was implemented into the 3MHAIL microphysics for rain-snow, rain-aggregates, and rain-graupel collisions. This method determines the destination category based on the resulting density of the coalesced particles and allows for rain-ice interactions to result in 'rimed' snow or aggregates, graupel, or hail.

Rain colliding with snow, aggregates or graupel can produce a new frozen category z , the density (ρ_z) of which is computed from

$$\pi / 6(\rho_r D_{\bar{m}r}^3 + \rho_x D_{\bar{m}x}^3) = \pi / 6(\rho_z D_{\bar{m}z}^3), \quad (3.36)$$

where $x = [s, a, g]$, the destination category $z = [s, a, g, h]$, and $D_{\bar{m}z} = \max(D_{\bar{m}x}, D_{\bar{m}r})$ is the mean mass diameter of the coalesced particles. The destination category depends on which frozen category has the closest bulk density to ρ_z (Table 3.4). Snow and aggregates have variable density, with decreasing density values as particle sizes increase, and the densities of these hydrometeors are computed according to Eqn 3.37 (W95). Because Eqn 3.36 applies to the mean mass diameters of the colliding hydrometeor species, $D_{\bar{m}x}$ replaces D_x in (3.37) in order to compute the density of a snow or aggregate particle associated with the mean mass diameter of the distribution

$$\rho_x = (6 / \pi) \alpha_{mx} D_x^{\beta_{mx}-3}. \quad (3.37)$$

Table 3.4: Destination categories for rain-ice collisions as a function of the resulting density of the coalesced particles (after Milbrandt and Yau 2005b).

Ice category	$\rho_z \leq 0.5(\rho_{s,a} + \rho_g)$	$0.5(\rho_{s,a} + \rho_g) < \rho_z \leq 0.5(\rho_g + \rho_h)$	$\rho_z > 0.5(\rho_g + \rho_h)$
snow	snow	graupel	hail
aggregates	aggregates	graupel	hail
graupel	-	graupel	hail

Calculations of ρ_z using (3.36) and covering the ranges of $D_{\overline{mr}}$, $D_{\overline{ms}}$, and $D_{\overline{ma}}$ revealed that snow or aggregates colliding with raindrops always lead to hail formation whenever $D_{\overline{mx}} \leq D_{\overline{mr}}$, otherwise the destination category is the input ice category or graupel. Mass mixing ratio transfers from the rain (Δr_r) and ice (Δr_x) categories to the destination category are the same as currently formulated for the regular 2M collection scheme (Eqn 3.31), with the exception that the destination category is not restricted to hail only. Changes in number concentrations of the rain and input ice categories are computed according to Eqn 3.27, whereas the number concentration change (ΔN_{tz}) for the destination category, when applicable, is

$$\Delta N_{tz} = \frac{(\Delta r_r + \Delta r_x)}{(\pi/6)\rho_z D_{\overline{mz}}^3}, \quad (3.38)$$

where ρ_z is now the actual density of the destination category z , not the density computed from (3.36). In practice, the minimum of Eqns. 3.38 or 3.32 is used as the value for the number concentration of newly formed particles in the destination category as Eqn. 3.38 has been found to occasionally give values of ΔN_{tz} that are greater than the number concentrations of coalesced particles, n_{coll} . In cases where an entire population of rain or ice particles freezes in one time step, ΔN_{tz} is limited to N_{tr} or N_{ti} , whichever is smaller.

3.3.3.2) F94 hail formulation from rain colliding with pristine ice particles

When a supercooled drop comes into contact with ice crystals, the crystals act as freezing nuclei and the drop freezes. Based on numerous test simulations of deep convection using the RAMS model, it was found that the overwhelming majority of new hail number concentrations are generated via rain-pristine ice collisions, and the MY05b 3-component freezing formula still tended to produce large numbers of new hailstones for these collisions. F94 showed that for rain

colliding with ice crystals, the number of raindrops that freeze to form hailstones in one Δt can be severely overestimated in the presence of large numbers of ice crystals based on the stochastic collection equation, which assumes only one collision occurs per Δt between colliding particles. To alleviate this overestimation, F94 developed alternative collection equations for changes in rain mixing ratio and number concentrations due to collisions with ice crystals that allow for larger raindrops to collect more than one ice crystal in one Δt . Mansell et al. (2010) also use the F94 approach to limit raindrop freezing due to ice crystal collection in their two-moment bulk microphysics scheme in the Collaborative Model for Multiscale Atmospheric Simulation (COMMAS) model (Wicker and Wilhelmson 1995). A decision was made to implement the algorithm of F94 for rain-pristine ice collection, which is presented in terms of RAMS variables by equations 3.39-3.42,

$$\Delta r_r = N_{tr} \int_0^{\infty} m_r(D_r) P_{rp}(D_r) f_{gam}(D_r) dD_r \quad (3.39)$$

$$\Delta N_{tr} = N_{tr} \int_0^{\infty} P_{rp}(D_r) f_{gam}(D_r) dD_r, \quad (3.40)$$

where $P_{rp}(D_r)$ is the probability function for drop freezing,

$$P_{rp}(D_r) = \min[1, n_{rp}(N_{ip}, D_r)], \quad (3.41)$$

and

$$n_{rp}(N_{ip}, D_r) = (\pi / 4) E_{rp} N_{ip} D_r^2 F_{\rho} V_{tr}(D_r) \Delta t \quad (3.42)$$

is the number of pristine ice crystals collected by a drop in one Δt . The collection efficiency E_{rp} is zero for ice crystal diameters less than $40 \mu m$, and equal to unity for larger crystal diameters following Lew et al. (1985). As the lower limit on $D_{\bar{m}h}$ is $0.8 mm$, a limit of $D_{\bar{m}r} \geq 0.8 mm$ is also included for hail to form from rain-pristine ice collisions. When this condition is not met, collisions between rain and pristine ice are assumed not to occur. An example of raindrop sizes

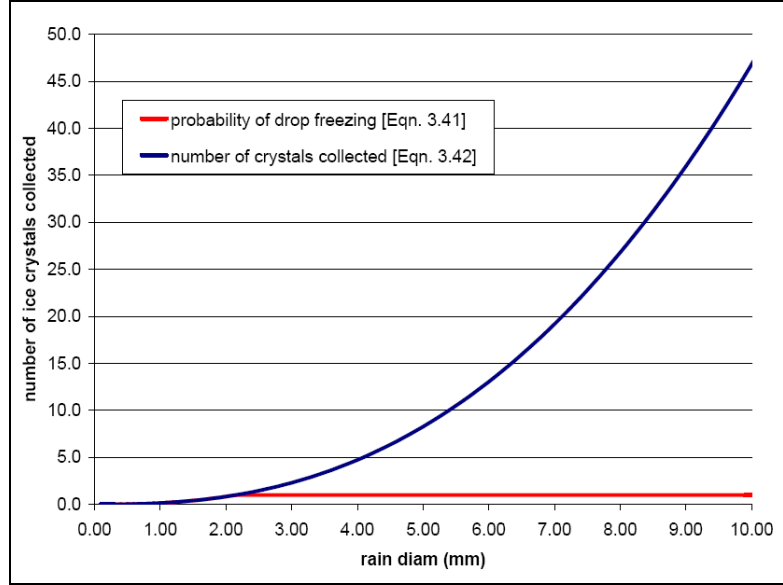


Figure 3.6: Number of ice crystals collected by raindrops (dark blue line) as function of raindrop diameter from Eqn 3.42, and number of drops frozen (red line) at each drop size based on Eqn 3.41. $N_{ip} = 10000 \text{ m}^{-3}$.

that can collect more than one ice crystal in one $\Delta t = 4 \text{ s}$ is shown by the dark blue line in Figure 3.6 for an ice crystal concentration N_{ip} of 10000 m^{-3} , and the number of drops frozen (m^{-3}) is shown by the red line (Figure 3.6). As seen from Figure 3.6, the diameter threshold for raindrops ($D_{r,thresh}$) that will collect more than one ice crystal in one Δt is about 2.2mm for this particular value of N_{ip} . Decreasing the value of N_{ip} will increase $D_{r,thresh}$, whereas increasing the value of N_{ip} will decrease $D_{r,thresh}$, thus this alternative method for computing hail formation from rain-pristine ice collisions is most effective at large values of pristine ice concentrations.

Equations 3.39 and 3.40 are solved at each grid point containing both rain and pristine ice by temporarily dividing the rain drop size distribution into 94 mass-doubling bins spanning the diameter range of $0.35\mu\text{m}$ to 1.73 cm and numerically integrating over the rain drop spectrum. Eqn 3.38 is also used to compute a temporary value for the number concentration of newly formed hailstones as for the MY05b 3-component freezing scheme. The lesser value of Δr_r as computed from (3.39) or Δr_r as computed from the regular RAMS 2M collection (Eqn. 3.31) is

then used as the amount of rain mixing ratio transferred to the hail category as newly formed hail. The minimum of (3.38), (3.40), or ΔN_{th} as computed from the regular 2M RAMS collection scheme (Eqn. 3.32) is taken as an intermediate value for the number concentration of newly formed hailstones prior to the application of the adjustment scheme presented in the next section.

3.3.3.3) *Adjustment to newly formed hail number concentrations*

F94 and Mansell (2010) argue that, because different hydrometeor categories often possess different distribution parameter values, it is advantageous to conserve higher order moments of hydrometeor distributions rather than to conserve number concentrations (M_0). This is particularly important when conversion of particles from one category to another occurs in 2M microphysics schemes that have different distribution shape parameters for the different categories, as is the case for the formation of hail in the present 3MHAIL scheme. F94 introduced a correction factor to conserve the radar reflectivity factor when the shape parameter ν changes from one particle distribution to another. The conservation of the reflectivity factor (in addition to conservation of mass) necessitates an adjustment to the number concentrations of newly converted particles for both three-component freezing and melting processes. Mansell et al. (2010) present a reflectivity-conserving formula similar to F94 in their two-moment microphysics scheme to adjust number concentrations of newly formed hail formed from riming of graupel. Based on these studies, a method is presented for the 3MHAIL scheme that adjusts only the number concentrations of newly formed hail particles in the presence of pre-existing hail distributions in order to preserve the 3rd and 6th moments of the hail distribution. As the 6th moments of the input categories are not considered in the 3MHAIL scheme, losses in number

concentrations from these categories are computed using the regular 2M collection equation (Eqn 3.27).

The change in hail reflectivity (ΔZ_h) associated with newly formed hail is computed assuming a non-monodisperse distribution for the new particles and using mixing ratio (Δr_h) and number concentration (ΔN_{th}) transferred to hail,

$$\Delta Z_{h,new} = \left(\frac{\Delta r_{h,new} \rho_a}{\alpha_{mh}} \right)^2 \frac{G(\nu_h^* = 2.0)}{\Delta N_{th,new}^*}, \quad (3.43)$$

where the function G is given by Eqn. (3.18), Δr_h has units of $[\text{kg kg}^{-1}]$, $\Delta N_{th,new}^*$ is the number concentration $[\text{m}^{-3}]$ of newly formed hail as computed from (3.32), (3.38), or (3.40) where appropriate, and an assumed ν_h^* value of 2.0 is used for the new hail particles. Further assuming ν_h doesn't change due to addition of newly formed *small* particles, the ratio of moments (3.44), which is a function of ν_h only, is constant. The assumption that ν_h doesn't change is justified by the fact that the amounts of mass and reflectivity associated with the newly formed hail particles are very small relative to the existing hail mass and reflectivity values. An expression equivalent to (3.44) in terms of N_{th} , r_h , and Z_h is given by Eqn. 3.45

$$\left. \frac{M6/M3}{M3/M0} \right|_{pre-newhail} = \left. \frac{M6/M3}{M3/M0} \right|_{post-newhail} = \frac{\Gamma(\nu + 6)/\Gamma(\nu + 3)}{\Gamma(\nu + 3)/\Gamma(\nu)}, \quad (3.44)$$

$$\left. Z_h N_{th} \left(\frac{\alpha_{mh}}{r_h} \right)^2 \right|_{pre-newhail} = (Z_h + \Delta Z_{h,new})(N_{th} + \Delta N_{th,new}) \left(\frac{\alpha_{mh}}{r_h + \Delta r_{h,new}} \right)^2, \quad (3.45)$$

where the variables with the subscripts *new* denote the quantities associated with the newly formed hail particles. Solving (3.45) for $\Delta N_{th,new}$ gives an expression (3.46) for the number concentration of newly formed hail particles added to an existing hail distribution that conserves both the 3rd and 6th moments of the distribution,

$$\Delta N_{th,new} = N_{th} \left[\frac{Z_h}{Z_h + \Delta Z_{h,new}} \left(\frac{r_h + \Delta r_{h,new}}{r_h} \right)^2 - 1 \right]. \quad (3.46)$$

An example of the normalized moments of resulting hail distributions due to the addition of a distribution comprised of small hail particles to an existing hail distribution comprised of larger particles is shown in Figure 3.7 for a non-adjustment method (panel c) and the current number adjustment method (panel d) using Eqn. (3.43) to compute $\Delta Z_{h,new}$. The normalized moments of the distribution to be added (panel a) and the existing distribution (panel b) are shown as well in Figure 3.7. The characteristics of each distribution are listed in Table 3.5, and the size distributions are plotted in Figure 3.8. A comparison of panels c and b in Fig. 3.7 reveals that the non-adjustment method shifts the moments of the resulting distribution such that the peaks in the moments occur at smaller hail sizes. Thus, although the numbers of small hailstones have increased, this occurs at the expense of shifting the relative amounts of mass and reflectivity from the larger to the smaller sizes. From Table 3.5, the amount of mass mixing ratio added to the existing hail distribution is minor, accounting for an increase of only about 2.5%, whereas the reflectivity of the resulting distribution has been severely reduced by about 95% for the non-adjustment case (c)! The primary factor responsible for such a large reduction in the reflectivity value is the ν_h value of 1.0 for the resulting distribution, which is associated with a reduction in the numbers of large particles (curve c, Fig 3.8). Also seen from Figure 3.8 is that the non-

Table 3.5: Distribution values associated with normalized integral moments of hail distributions displayed in Figure 3.7, and the hail size distributions shown in Figure 3.8.

Panel in Fig 3.7	N_{th} [kg ⁻¹]	r_h [kg kg ⁻¹]	Z_h [mm ⁶ m ⁻³]	$D_{\bar{m}h}$ [m]	ν_h
a	10.0	5.31×10^{-6}	111.21	0.001	2.0
b	0.05	2.12×10^{-4}	9.71×10^6	0.0208	8.0
c	10.05	2.1731×10^{-4}	4.23624×10^5	0.00358	1.0
d	0.0525	2.1731×10^{-4}	9.710111×10^6	0.0206	~7.94

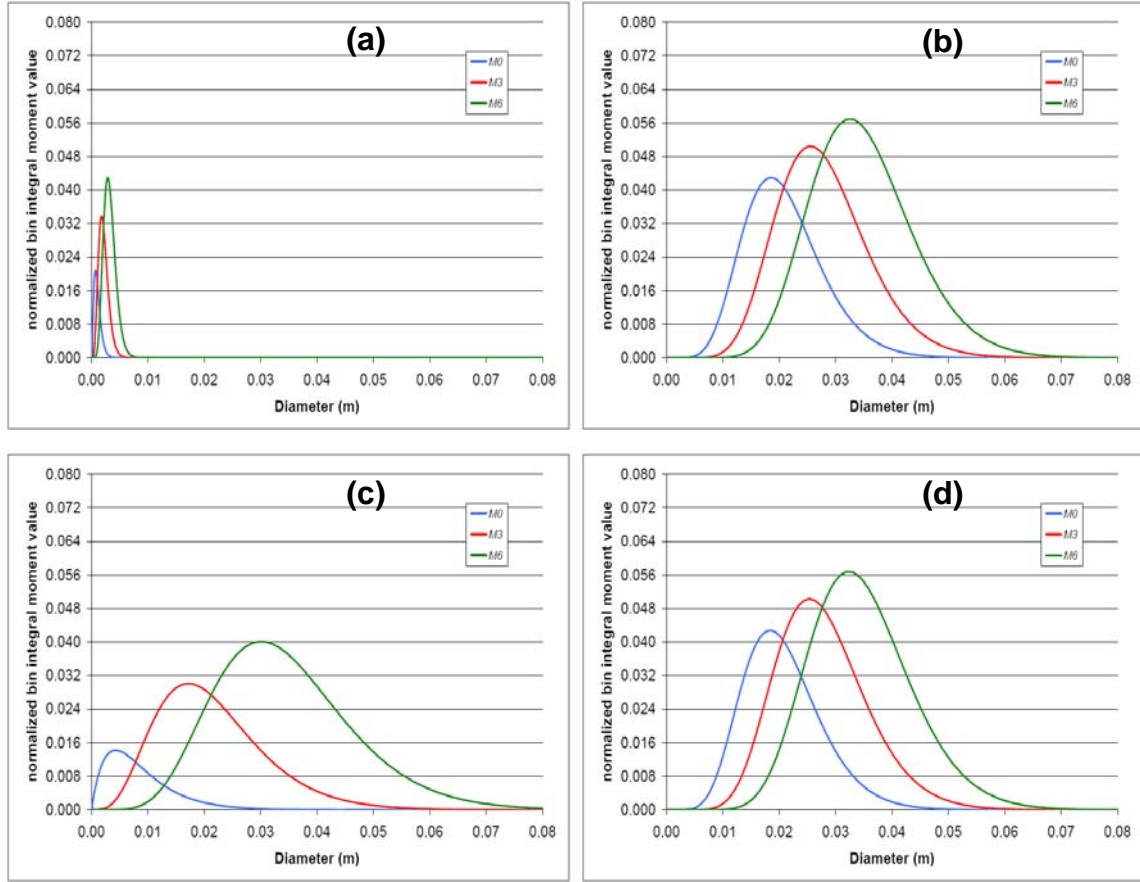


Figure 3.7: Normalized integral moments of hail distributions for: a) newly formed hail particles, b) existing hail distribution, c) resulting normalized moments for newly formed hail particles added to existing hail distribution via conservation of number and mass, and d) resulting normalized moments when number concentration of newly formed hail particles is adjusted such that mass and reflectivity are conserved. In all panels, the blue curve denotes $M0$, the red curve denotes $M3$, and the green curve denotes $M6$.

adjustment method (curve c) artificially 'fills the size gap' between the two initial hail size spectra (curves a and b). For the adjustment method, only a negligible shift in the moments of the resulting distribution occurs (panel d, Fig 3.7), and the resulting size distribution (curve d, Fig 3.8) is nearly identical to the pre-existing size distribution (curve b, Fig 3.8), though the numbers of newly added small hail particles are now reduced by 99.75% (Table 3.5). Note that although v_h of the existing distribution is assumed not to change owing to the addition of the small hail particles for Eqns (3.45) and (3.46), the final v_h of the resulting 'adjusted' distribution does in fact differ slightly from its initial value (7.94 versus 8.0).

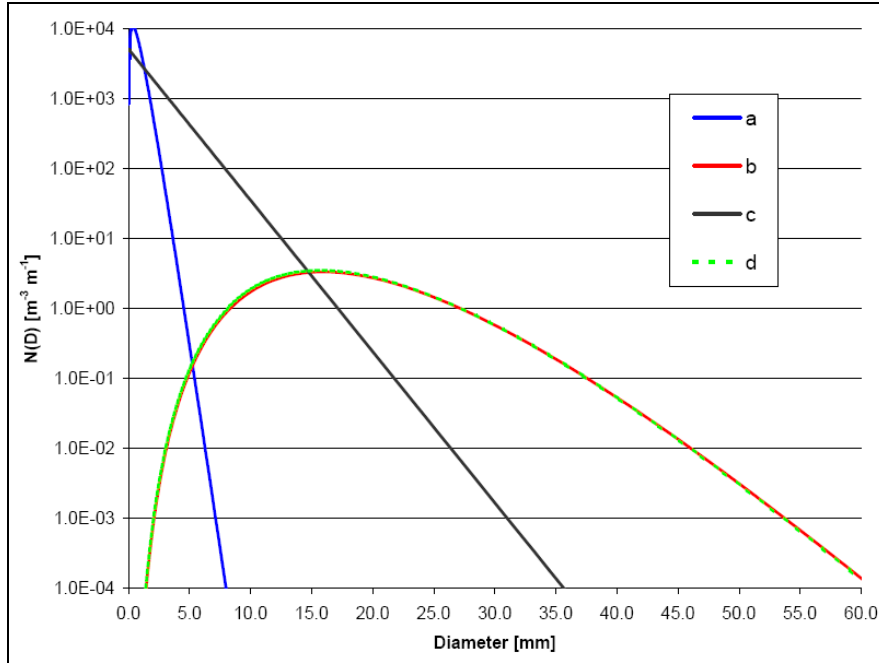


Figure 3.8: Resulting hail size distributions without adjustment to number concentration (c) and with adjustment to number concentration (d) from addition of newly formed particles (a) to an existing distribution (b). Size distributions are associated with parameters listed in Table 3.5.

This adjustment method is primarily aimed at preserving higher order moments for hail distributions weighted towards larger sizes. Additional results from the initial testing of this method indicate that, in the presence of an existing hail distribution comprised of small hailstones, the number concentrations of newly formed hailstones are largely unaffected by this adjustment algorithm.

3.4) Vapor and sensible heat transfers

Diffusion of vapor and sensible heat between hydrometeors and air are computed using the implicit method described in Walko et al. (2000), the full details of which are not included here for brevity. This method combines implicit forms of the energy and water conservation equations for all hydrometeors and air into a single predictive equation for future vapor mixing ratio of air ($r_v^{t+\Delta t}$) that takes into account the simultaneous fluxes of vapor and heat between air and all

hydrometeors. Updated values of r_x , hydrometeor temperature (T_x), and Q_x are obtained for each hydrometeor category following the calculation of $r_v^{t+\Delta t}$. With respect to the hail category, the primary variable of interest is Q_h as this will determine the growth mode (wet if $0 \leq Q_h < L_f$ or dry if $Q_h < 0$) and impact the melting and shedding processes as well as atmospheric cooling/heating. Below the melting level, T_h is required to remain at or below 0°C , and an increase in the value of Q_h due to vapor/heat diffusion signifies that melting processes are occurring.

From Walko et al. (2000), the equations for the updated values of r_h , T_h , and Q_h , assuming the hail distribution does not evaporate (sublimate) completely in one Δt , are given by (3.47), (3.48), and (3.49), respectively, with the variables listed in Table 3.6. The incremental change in air temperature owing to vapor/heat diffusion to/from the hail distribution is given by (3.50).

$$r_h|_{post-diff} = r_h^* + \psi N_{th}^* (F_{RE})_h 4\pi\Delta t \left[r_v^{t+\Delta t} - r_{sRh} - r'_{sRh} (T_h|_{post-diff} - T_{Rh}) \right] \quad (3.47)$$

$$T_h|_{post-diff} = \begin{cases} \frac{1}{C_i r_h^* + N_{th}^* (F_{RE})_h 4\pi\Delta t (\psi L_{iv} r'_{sRh} + \kappa)} \\ \times \left(N_{th}^* (F_{RE})_h 4\pi\Delta t \left[\psi L_{iv} (r_v^{t+\Delta t} + r'_{sRh} T_{Rh} - r_{sRh}) \right] + \kappa (T_{ac}^* + A(r_v^* - r_v^{t+\Delta t})) \right) + Q_h^* r_h^* & \text{if all ice} \\ 0^\circ\text{C} & \text{if mixed phase} \end{cases} \quad (3.48)$$

$$Q_h|_{post-diff} = \begin{cases} C_i T_h|_{post-diff} & \text{if all ice } (T_h|_{post-diff} < 0^\circ\text{C}) \\ \frac{1}{r_h^*} \left(N_{th}^* (F_{RE})_h 4\pi\Delta t \left[\psi L_{iv} (r_v^{t+\Delta t} + r'_{sRh} T_{Rh} - r_{sRh}) \right] + \kappa (T_{ac}^* + A(r_v^* - r_v^{t+\Delta t})) \right) + Q_h^* r_h^* & \text{if mixed phase} \end{cases} \quad (3.49)$$

$$\Delta T_{ac} = A(r_h|_{post-diff} - r_h^*). \quad (3.50)$$

Table 3.6: Descriptions for variables in Eqns (3.47-3.50).

Variable	Definition
A	$T_{il}\bar{L}/(C_p 253)$ for $T_{ac}^* < -20^\circ\text{C}$; $T_{il}\bar{L}/[C_p(2T_a^* - T_{il})]$ for $T_{ac}^* > -20^\circ\text{C}$
C_i	2093 J kg ⁻¹ K ⁻¹ Specific heat of ice
C_p	1004 J kg ⁻¹ K ⁻¹ Specific heat of air at constant pressure
L_{iv}	Latent heat of sublimation [2.834x10 ⁶ J/kg]
\bar{L}	Latent heat weighted between L_{iv} and L_{lv} according to the relative mixing ratios of ice and liquid contained in all hydrometeors
r_{sRh}	Saturation mixing ratio at T_{Rh} with respect to ice or liquid, whichever is appropriate for hailstone surface [kg kg ⁻¹]
r'_{sRh}	Rate of change of r_{sRh} with temperature T_{Rh}
r_{sl}	Saturation mixing ratio over water at air temperature T_{ac} [kg kg ⁻¹]
r_v	Water vapor mixing ratio [kg kg ⁻¹]
T_a, T_{ac}	Air temperature [K, °C]
T_{il}	Ice-liquid temperature [K]
T_{Rh}	max[0°C, $T_{ac}^* - \min(25, 700(r_{sl} - r_v))$] Reference temperature for hail [°C]
$()^*$	Value of variable prior to application of vapor/heat diffusion
κ	Thermal conductivity of air [J m ⁻¹ s ⁻¹ K ⁻¹]
ψ	Vapor diffusivity [m ² s ⁻¹]

All of the terms on the right hand sides of Eqns. (3.47, 3.48, and 3.49) are known prior to application of vapor/heat diffusion, with the exception of the *post-diff* subscript and $r_v^{t+\Delta t}$ terms. The F_{RE} term appearing in (3.47, 3.48, and 3.49) is the product of the ventilation coefficient f_{RE} and hail diameter integrated over the entire hail size distribution (3.51) and depends on both D_{nh} and v_h . The analytical solution for F_{RE} is given by (3.52), where $S = 0.5$ is the hail shape parameter (M97) and V_k is the dynamic viscosity, which is a function of the air temperature only. Two v_h -dependent factors ($f_{1,RE}$ and $f_{2,RE}$, Eqns. 3.53 and 3.54, respectively) of (3.52) are computed during model initialization for each incremental value of v_h , and the full F_{RE} term is then calculated during model runtime using Eqn. (3.55).

$$F_{RE} = \int_0^\infty D_h f_{RE}(D_h) f_{gam}(D_h) dD_h \quad (3.51)$$

$$F_{RE} = SD_{nh} \frac{\Gamma(v_h + 1)}{\Gamma(v_h)} + (0.229S\sqrt{\alpha_{vth}}) \sqrt{\frac{1}{V_k}} D_{nh}^{(1.5 + \frac{1}{2}\beta_{vth})} \frac{\Gamma(v_h + 1.5 + 0.5\beta_{vth})}{\Gamma(v_h)} \quad (3.52)$$

$$f_{1,RE}(\nu_h) = S \left(\frac{1}{\alpha_{mh}} \right)^{1/\beta_m} \left(\frac{\Gamma(\nu_h)}{\Gamma(\nu_h + \alpha_{mh})} \right)^{1/\beta_{mh}} \frac{\Gamma(\nu_h + 1)}{\Gamma(\nu_h)} \quad (3.53)$$

$$f_{2,RE}(\nu_h) = (0.229S\sqrt{\alpha_{vth}}) \left[\left(\frac{1}{\alpha_{mh}} \right)^{1/\beta_{mh}} \left(\frac{\Gamma(\nu_h)}{\Gamma(\nu_h + \alpha_{mh})} \right)^{1/\beta_{mh}} \right]^{(1.5 + \frac{1}{2}\beta_{vth})} \times \frac{\Gamma(\nu_h + 1.5 + 0.5\beta_{vth})}{\Gamma(\nu_h)} \quad (3.54)$$

$$F_{RE} = f_{1,RE}(\nu_h) \times \left(\frac{r_h^*}{N_{th}^*} \right)^{1/\beta_{mh}} + f_{2,RE}(\nu_h) \times \sqrt{\frac{1}{V_k}} \left(\frac{r_h^*}{N_{th}^*} \right)^{(1/\beta_{mh}) \times (1.5 + \frac{1}{2}\beta_{vth})} \quad (3.55)$$

In the regular 2M version of RAMS, a loss in N_{th} due to sublimation is diagnosed based on the fractional amount of hail mixing ratio lost. For the 3MHAIL scheme, the change in the value of Q_h is now used to determine changes in the amounts of N_{th} , r_h , and Z_h owing to completely melted hailstones as described in Section 3.5.2.

3.5) Melting and shedding

Melting alters the hail distribution through a narrowing of the distribution and a change in the value of D_{mh} . For example, Giaiotti et al. (2001) and Fraile et al. (2003) provide evidence of hail distributions that evolve from exponential-type ($\nu_h = 1$) aloft to gamma-type ($\nu_h > 1$) at lower levels as a result of melting. Shedding of liquid drops by hail occurs when hail is collecting liquid water (Ludlam 1958; Carras and Macklin 1973; Joe et al. 1976; Lesins and List 1986; Garcia-Garcia and List 1992), as well as when hail is undergoing melting (Rasmussen and Heymsfield 1984; RH87b). RAMS employs a bin-emulating approach to construct look-up tables for the melting and shedding processes that cover a wide range of representative hail distributions within the specified limits of D_{mh} and ν_h as well as the range of LWF values (0.0 to 1.0) The original 2M melt/shed scheme in RAMS accounts for shedding of liquid water from hail

as a result of vapor/heat diffusion and collection of liquid species, but does not explicitly deal with complete melting of the smallest hail sizes. Thus, major modifications were made to the original melt/shed scheme in order to make it compatible with the 3MHAIL scheme as well as to represent these processes in a more consistent manner.

A total of three look-up tables are computed for the 3MHAIL melt/shed scheme. The shedding table (S_{tab}) contains the fractional amount of hail mass mixing ratio lost due to shedding as a function of LWF , \bar{m}_h , and v_h . The melt table (M_{tab}) contains approximate bin integral values of the 0th moment as a function of bin index i , LWF , \bar{m}_h , and v_h for completely melted size bins only; bins that are not completely melted have table values of zero. A third melt table (Q_{tab}) contains the bin internal energy values q_i as a function of bin index i , LWF , \bar{m}_h , and v_h and is used in conjunction with a newly implemented complete melting scheme (Section 3.5.2). The details of the construction of the melt/shed tables can be found in Appendix A.

Both melting and shedding were initially calculated simultaneously following the applications of vapor/heat transfer and collection, however, testing of this algorithm led to the discovery that large numbers of hailstones were completely melting in one Δt , even at low LWF and large $D_{\bar{m}}$ values. Furthermore, as collection of liquid by hail has a negligible effect on the actual melting of the hail (Wisner et al. 1972; RH87b), a decision was made to compute melting of hail immediately following the vapor/heat transfer calculations, and then apply the shedding algorithm following vapor/heat transfer and collection.

3.5.1) *Shedding*

Once \bar{m}_h and Q_h have been updated following the application of vapor/heat transfer and collection, the bulk hail LWF is computed using Eqn. 3.56,

$$LWF = \begin{cases} 0 & Q_h \leq 0 \\ Q_h / L_f & 0 < Q_h < L_f \\ 1 & Q_h \geq L_f \end{cases} \quad (3.56)$$

If $LWF > 0.95$, the entire distribution is considered to be completely melted, and total r_h , N_{th} , and Q_h are transferred to the rain category and Z_h simply becomes zero. As is the case for the current 2M microphysics in RAMS, shedding is not applied if $LWF < 0.3$. Otherwise, using the updated grid point values of LWF , \bar{m}_h , and ν_h , the actual amount of hail mixing ratio shed (r_{shed}) is found by multiplying r_h by the appropriate S_{tab} value (3.57). r_{shed} is then subtracted from r_h and added to the rain category, and the number concentration of shed drops added to the rain category is determined by dividing r_{shed} by the mass of one shed droplet, which is assumed to have a diameter of 1mm. Hail number concentration is not affected by shedding.

$$r_{shed} = r_h \times S_{tab}(LWF, \bar{m}_h, \nu_h). \quad (3.57)$$

Shedding also reduces hail reflectivity values, and the following details the adjustment process. Assuming that ν_h doesn't change appreciably due to shedding (i.e., the spectral change in the hail size distribution is negligible), then the ratio of moments (Eqn. 3.58), which is a function only of ν_h , will also not change due to shedding. Rearranging Eqn. (3.58) gives the post-shed value of the 6th moment ($M6$) of the distribution as a function of the pre-shed $M6$ value and the relative change in the ratio of the squares of the 3rd moments ($M3$) after and prior to shedding (Eqn. 3.59),

$$\frac{M6/M3}{M3/M0} \Big|_{post-shed} = \frac{M6/M3}{M3/M0} \Big|_{pre-shed} = \frac{\Gamma(\nu+6)/\Gamma(\nu+3)}{\Gamma(\nu+3)/\Gamma(\nu)} \quad (3.58)$$

$$M6 \Big|_{post-shed} = M6 \Big|_{pre-shed} \frac{(M3)_{post-shed}^2}{(M3)_{pre-shed}^2}. \quad (3.59)$$

Substituting $M3 = D_n^3 \frac{\Gamma(\nu + 3)}{\Gamma(\nu)}$ into Eqn. (3.59) and noting that hail reflectivity is $Z_h = M6 \times N_t$,

gives an expression (3.60) equivalent to (3.59) in terms of Z_h and D_n ,

$$Z_h \Big|_{post-shed} = Z_h \Big|_{pre-shed} \frac{D_n^6 \Big|_{post-shed}}{D_n^6 \Big|_{pre-shed}}. \quad (3.60)$$

$D_{\bar{m}}$ can replace D_n using Eqns (3.7) and (3.9) to give the final expression for the post-shed hail reflectivity,

$$Z_h \Big|_{post-shed} = Z_h \Big|_{pre-shed} \frac{D_{\bar{m}h}^6 \Big|_{post-shed}}{D_{\bar{m}h}^6 \Big|_{pre-shed}}, \quad (3.61)$$

where

$$D_{\bar{m}h} \Big|_{post-shed} = \left(\frac{r_h - r_{shed}}{\alpha_{mh} N_{th}} \right)^{1/3}. \quad (3.62)$$

The validity of Eqn. (3.60) (or equivalently 3.61) was tested using a bin-shedding model with the assumptions that ν_h and the number concentrations in each shedding bin are constant. A value for N_{th} was specified, and for all possible incremental pairs of $(\nu_h, D_{\bar{m}h})$ representing unique gamma distributions, bin values for number concentration (N_{bin}), mixing ratio (r_{bin}), and reflectivity (Z_{bin}) were computed via multiplication of N_{th} with the bin integral values of the 0th, 3rd, and 6th moments (Eqn. A.5 in Appendix A). The pre-shed bulk values for mixing ratio and reflectivity (r_{pre} and Z_{pre}) were also computed by summing up the respective bin values. The bin-shedding model was then run for the applicable range of LWF values (0.3 to 0.95).

For each incremental LWF value, shedding was applied to each bin by multiplying the appropriate S_{tab} value with each bin mixing ratio value (3.63). A new mixing ratio for each bin ($r_{new,bin}$) was found by subtracting the amount of mixing ratio shed from the initial bin mixing

ratio (3.64), and a new bin diameter ($D_{new,bin}$) (3.65) was computed based on the new bin mixing ratio.

$$r_{shed,bin} = r_{bin} \times S_{tab}(LWF, \bar{m}_h, \nu_h) \quad (3.63)$$

$$r_{new,bin} = r_{bin} - r_{shed,bin} \quad (3.64)$$

$$D_{new,bin} = \left[\frac{r_{new,bin}}{\alpha_{mh} N_{bin}} \right]^{1/3}. \quad (3.65)$$

Based on $D_{new,bin}$, post-shed bin reflectivity values $Z_{new,bin}$ were calculated (3.66). The $r_{new,bin}$ and $Z_{new,bin}$ values were then summed to obtain the post-shed bulk mixing ratio (r_{post}) and reflectivity (Z_{post}) values. Next, the pre- and post-shed characteristic diameters were determined (3.67 and 3.68, respectively), and a ratio relating the relative change in Z ($M6$) to the relative change in $D_{\bar{m}h}^6$ (related to the square of $M3$) due to shedding was evaluated by rearranging Eqn (3.60) to obtain Eqn. (3.69).

$$Z_{new,bin} = N_{bin} * D_{new,bin}^6 * \rho_a * 10^{18} \quad (3.66)$$

$$D_{n,pre} = \left[\frac{r_{pre}}{N_t * \alpha} \right]^{1/3} / \left[\frac{\Gamma(\nu + 3)}{\Gamma(\nu)} \right]^{1/3} \quad (3.67)$$

$$D_{n,post} = \left[\frac{r_{post}}{N_t * \alpha} \right]^{1/3} / \left[\frac{\Gamma(\nu + 3)}{\Gamma(\nu)} \right]^{1/3} \quad (3.68)$$

$$\left[\frac{Z_{post}}{Z_{pre}} \right] / \left[\frac{D_{n,post}^6}{D_{n,pre}^6} \right] = 1.0. \quad (3.69)$$

The ratio expressed by (3.69) was found to be within 1% of 1.0 for all possible combinations of ν_h , $D_{\bar{m}h}$, and LWF , confirming that Eqn (3.60) is indeed valid over the specified ranges of ν_h ,

$D_{\overline{m}h}$, and LWF . The bin shedding model was also evaluated for several different values for N_{th} and ρ_a , and the ratio given by (3.69) consistently gave values equal to or very near 1.0.

3.5.2) *Melting of smallest hailstones*

The original method for adjusting N_{th} , r_h , and Z_h due to complete melting of the smallest hailstones in the 3MHAIL scheme is based on computing the maximum hail diameter that completely melts in one Δt ($D_{max,melt}$) and numerically integrating over discrete size bins to obtain the moment values associated with the completely melted portion of the size spectrum. As mentioned, the 2M scheme in RAMS does not explicitly adjust N_{th} due to complete melting of the smallest hail sizes. Instead, an implicit adjustment to N_{th} is performed based on the fractional amount of hail mixing ratio lost due to vapor and heat diffusion. As previously noted, the original 3MHAIL melting algorithm was eventually determined to be causing too large a reduction in N_{th} due to errors in the computation of the largest diameter to melt completely in one Δt and has since been replaced with a new algorithm based on the work of RH87b. The details and problems with the original method are presented in Appendix A for completeness.

Given the problems associated with the original 3MHAIL melting algorithm and the fact that the melting table (M_{tab}) does not consider environmental conditions or time, a more accurate method to compute changes in the distribution moments is presented. This new method is applicable only at environmental temperatures at or above freezing and involves determining $D_{max,melt}$ based on the Q_{tab} look-up table and the heat balance equation (3.70) presented in RH87b valid for N_{RE} values less than 3000 (i.e., hail particles having diameters less than 5 mm). Eqn. (3.70) represents the non-shedding melting stage in which an ice core is embedded within a spherical shell of circulating meltwater. This internal circulation leads to enhanced heat transfer

and eliminates any temperature gradients within the meltwater, such that the temperature of the liquid layer is 0 °C, the same as the surface of the melting ice core (Rasmussen et al. 1984). Heat storage on the hailstone is neglected in Eqn. (3.70) (including this would increase melting times) and collection of liquid species is omitted as this has a negligible effect on melting (Wisner et al. 1972; RH87b).

$$4\pi\rho_i L_f r^2 \frac{dr}{dt} = -4\pi a k_a [T_\infty - T_o] \bar{f}_h - 4\pi a L_v D_v [\phi \rho_{v,sat}(T_\infty) - \rho_{v,sat}(T_o)] \bar{f}_v \quad (3.70)$$

In (3.70), ρ_i is density of a hailstone [0.9 g cm⁻³], L_f is latent heat of fusion [~587 cal/g], r is the instantaneous ice core radius [cm], a is total particle radius (liquid layer + ice core) [cm], k_a is the thermal conductivity of air [cal cm⁻¹ sec⁻¹ °C⁻¹], T_∞ is the environmental temperature, T_o is melting temperature of ice [273.15K], L_v is the latent heat of vaporization [80 cal/g at 0 °C], D_v is vapor diffusivity [cm²/s], ϕ is the relative humidity, the $\rho_{v,sat}$ terms are the saturated vapor densities [g/cm³] over liquid at the specified temperatures, and \bar{f}_h and \bar{f}_v are the mean ventilation coefficients for heat and water vapor, respectively. The mean ventilation coefficients are

$$\bar{f}_v = 0.78 + 0.308(N_{SC})^{1/3} (N_{RE})^{1/2} \quad (3.71)$$

$$\bar{f}_h = 0.78 + 0.308(N_{PR})^{1/3} (N_{RE})^{1/2}, \quad (3.72)$$

where $N_{RE} = [2a\rho_\infty V_t(a) / \mu]$ is the Reynolds number (V_t is terminal velocity, μ is dynamic viscosity, ρ_∞ is the environmental density), $N_{SC} = \mu / (\rho_\infty D_v)$ is the Schmidt number, and

$N_{PR} = \mu / (c_p k_a)$ is the Prandtl number with c_p the specific heat of dry air. Solving Eqn. (3.70)

for dt gives

$$dt = \frac{4\pi\rho_i L_f}{-G1 - G2} r^2 dr, \quad (3.73)$$

where the $G1$ and $G2$ terms are

$$G1 = -4\pi a k_a [T_\infty - T_o] \bar{f}_h \quad (3.74)$$

$$G2 = -4\pi a L_v D_v [\phi \rho_{v,sat}(T_\infty) - \rho_{v,sat}(T_o)] \bar{f}_v \quad (3.75)$$

Eqn. (3.73) can now be integrated from $t = 0$ to $t = t_m$ and from $r = r$ to $r = 0$ to obtain the time for complete melting t_m (Eqn. 3.76). As the hailstone falls and melts, its environment changes and its terminal velocity decreases causing decreases in \bar{f}_h and \bar{f}_v as well. Thus in general, $G1$ and $G2$ must stay inside the integral. When considering a hailstone melting completely in a small time step ($\Delta t < 5$ s), changes in the hailstone's environment and in its terminal velocity can be neglected, and then the $G1$ and $G2$ terms are constants that can be moved outside the integral in Eqn. (3.76). These assumptions are made for all computations herein because melting of hail in one time step can only be computed at each scalar grid point rather than over a finite depth in RAMS. The assumptions also provide an analytical solution for t_m (3.77) that can be used to efficiently compute $D_{max,melt}$ at each grid point below the melting level given the environmental conditions.

$$\int_0^{t_m} dt = t_m = -4\pi \rho_i L_f \int_r^0 \frac{r'^2 dr'}{G1 + G2} \quad (3.76)$$

$$t_m = -\frac{4\pi \rho_i L_f}{G1 + G2} \frac{r^3}{3} \quad (3.77)$$

The method of solving $D_{max,melt}$ during model runtime is now presented. Prior to the application of heat/vapor transfer, the variables k_a , T_∞ , D_v , ϕ , $\rho_{v,sat}(T_\infty)$, and $\rho_{v,sat}(T_o)$ are computed for each grid point where $T_\infty \geq 0$ °C using the standard RAMS formulations. Using the same bin discretization as for the melting table construction (Appendix A), the ventilation coefficients \bar{f}_h and \bar{f}_v for individual size bins with diameters less than 5 mm are calculated

based on the environmental variables. The bulk hail LWF (Eqn. 3.56) is then used to obtain the liquid water fractions of hailstones in each size bin (LWF_i) from which the amount of liquid and ultimately, the ice core radii (r), can be ascertained. Because all hailstones in a given size bin are assumed to be of equal size, the LWF_i values will correspond to the liquid water fractions of individual hailstones. The LWF_i values of individual size bins of diameter D are computed from the pre-computed look-up tables of hail internal energy (Q_{tab}) for the current values of LWF , \bar{m} , and v_h via Eqn. (3.78), where $D = 2a$ is the total (liquid + ice) particle diameter.

$$LWF_i(D) = Q_{\text{tab}}(i, LWF, \bar{m}, v_h) / L_f \quad (3.78)$$

By definition, LWF_i gives the ratio of the liquid mass of the particle to the total (liquid + ice) particle mass (3.79), where the liquid mass is computed by (3.80) and the ice mass is found using (3.81).

$$LWF_i(D) = \frac{\text{liqmass}}{\text{totalmass}} = \frac{\text{liqmass}}{\text{icemass} + \text{liqmass}} \quad (3.79)$$

$$\text{liqmass} = \alpha_{mr}(D^3 - D_{ice}^3) \quad (3.80)$$

$$\text{icemass} = \alpha_{mh}D_{ice}^3. \quad (3.81)$$

In Eqns. (3.80) and (3.81), $D_{ice} = 2r$ is the diameter of the ice core, $\alpha_{mr}D^3$ is the mass of a spherical liquid particle with diameter D , and $\alpha_{mh}D_{ice}^3$ is the mass of an equivalent liquid particle of identical size to the ice core such that $\alpha_{mr}(D^3 - D_{ice}^3)$ is the mass of the liquid layer of the hailstone. Substitution of (3.80) and (3.81) into Eqn. (3.79) gives an expression for LWF_i in terms of total and ice core diameters (3.82), which is then solved for the ice core radius (r) (3.83).

$$LWF_i(D) = \frac{\alpha_{mr}(D^3 - D_{ice}^3)}{\alpha_{mh}D_{ice}^3 + \alpha_{mr}(D^3 - D_{ice}^3)} \quad (3.82)$$

$$r = \frac{D_{ice}}{2} = \frac{1}{2} \left[\frac{\alpha_{mr} D^3 (1 - LWF_i(D))}{\alpha_{mr} + LWF_i(D) \times (\alpha_{mh} - \alpha_{mr})} \right]^{1/3}. \quad (3.83)$$

The value of r computed from (3.83) is then used in Eqn. (3.77) to determine the complete melting time (t_m) of the hailstone based on the environmental conditions *as well as* the initial amount of liquid water coating the hailstone. The value for $D_{max,melt}$ is thus determined by using Eqn. (3.77) to find the largest hailstone size which satisfies the expression $t_m \leq \Delta t$, where Δt is the model time step length. Once $D_{max,melt}$ has been calculated and if the change in Q_h due to vapor/heat diffusion is positive, the fractional amounts of each moment P [$P = 0, 3, 6$] associated with the completely melted hailstones are then determined using Eqn. (3.84). Equation 3.84 gives the ratio of the moment integrated over the melted portion of the size distribution (D_{min} to $D_{max,melt}$) to the moment integrated over the entire size distribution, where the integrals in (3.84) are solved numerically (Eqn. A.5 in Appendix A). These fractional moment amounts are then multiplied by their respective physical quantities (N_{th} , r_h , and Z_h) to obtain the amounts lost ($N_{th, melt}$, $r_{h, melt}$, and $Z_{h, melt}$) due to complete melting of hail particles. $N_{th, melt}$ and $r_{h, melt}$ are subtracted from the hail category and added to the rain category, and $Z_{h, melt}$ is subtracted from Z_h .

$$\frac{M(P)|_{melted}}{M(P)} = \frac{\int_{D_{min}}^{D_{max,melt}} D^P f_{gam}(D) dD}{\int_{D_{min}}^{D_{max}} D^P f_{gam}(D) dD}. \quad (3.84)$$

Examples of the complete melting times for hailstones with different initial liquid water layer thickness values using Eqn. (3.77) are shown in Figures 3.9 and 3.10 for various environmental temperatures. Relative humidity is set to 100% for each temperature such these particular melting times are associated with the most rapid melting possible. It is clearly evident that as the initial liquid layer thickness increases (and the liquid water fraction of the individual hail sizes increases), the sizes of hailstones to melt completely in one Δt also increase for all ambient

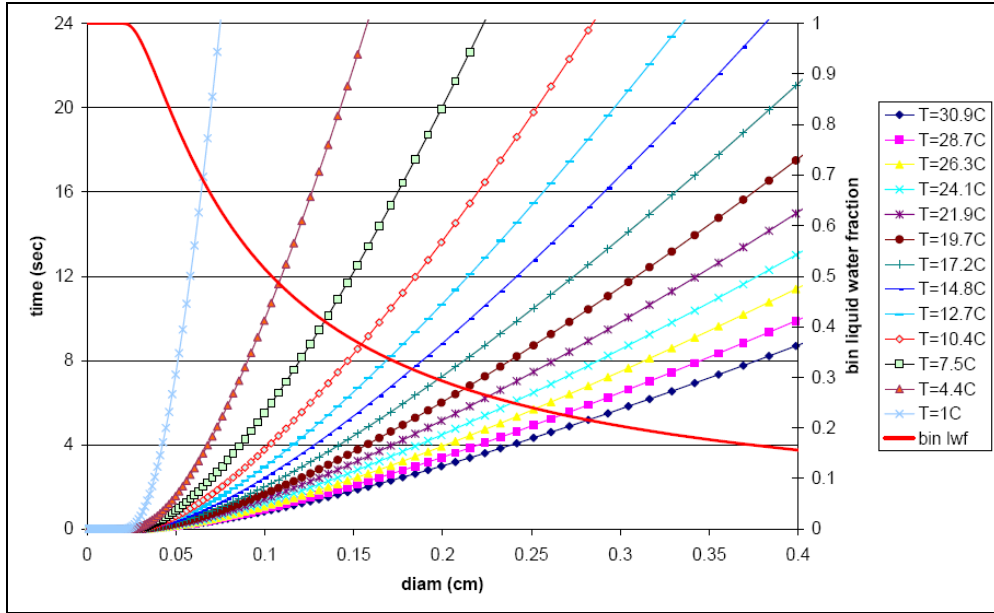


Figure 3.9: Times for complete melting of hailstones for various environmental temperatures [°C] for an initial liquid layer thickness of 0.01cm [0.1mm] computed using Eqn. (3.77). Liquid water fraction for individual hail sizes (LWF_i) is also shown (solid red line). RH is 100% for each temperature.

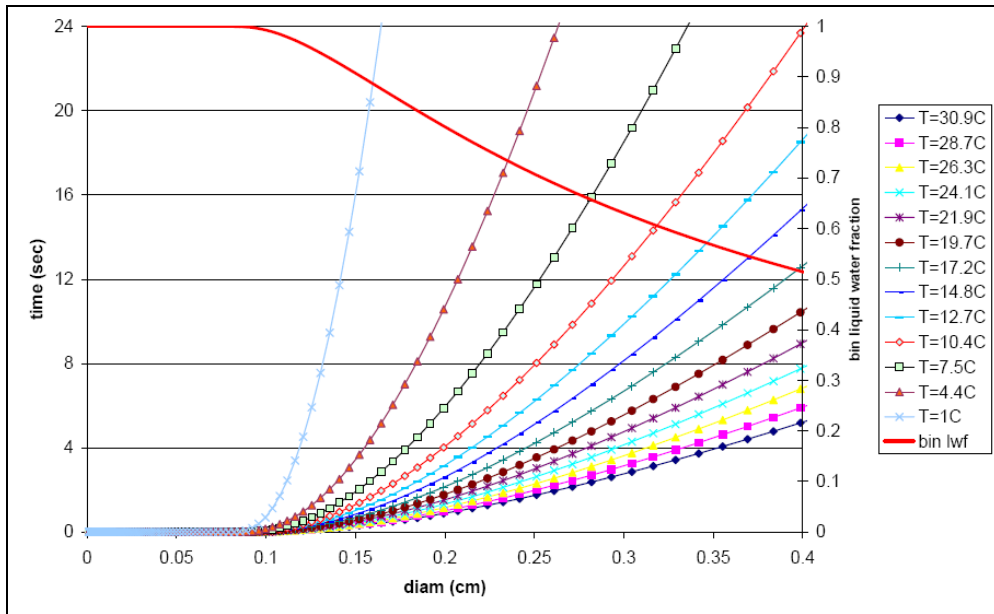


Figure 3.10: As in Fig 3.9, but for an initial liquid layer thickness of 0.04cm [0.4mm].

temperatures plotted. As expected, an increase in the environmental temperatures corresponds to an increase in the value of $D_{max,melt}$. Also seen is that a hailstone diameter of 4mm will not

completely melt in one $\Delta t = 4$ s for any ambient temperature even if its LWF_i value is around 52% (Fig 3.10).

3.6) Sedimentation

A major difference between the 3MHAIL scheme presented here and that of MY05a, b is that the sedimentation term for hail in the new scheme utilizes a '*bin-emulating*' approach rather than bulk moment-weighted fall speeds. The '*bin-emulating*' approach for hail sedimentation is designed to sedimentate the moments of the distribution in correct proportions and incorporates pre-computed look-tables that cover the range of possible distribution parameters over a wide range of distributions. These look-up tables are constructed by dividing the gamma distributions into discrete bins, computing the fractional amounts of the 0th, 3rd, and 6th moments for each bin, and determining the amount of each moment in a given grid cell that falls into each cell beneath in a given time step (Appendix B). During model runtime, the model level k of the hail distribution and the distribution properties $D_{\bar{m}h}$ and v_h determine which table values are used. The maximum number of levels ($k_{fall_{max}}$) over which the hail particles can be displaced in one Δt is determined by the displacement of the maximum hail diameter, $D_{h,max}$.

Sedimentation of the quantities N_{th} , r_h , $Q_h r_h$, and Z_h is carried out during model runtime using the following procedure beginning at the bottom of the hail layer and proceeding upwards to the top of the hail layer. For a given level $z(k)$, a loop over the levels ($kk = k, k-1, \dots, k - k_{fall_{max}} + 1$) into which the hail distribution can fall is then performed, and the amounts of each quantity placed into level $z(kk)$ are computed according to Eqn. 3.85

$$\Phi(kk) = \Phi(kk) + \Phi(k) \rho_a(k) / \rho_a(kk) \times SED_{\phi}[k, kk, \bar{m}_h(k), v_h(k)], \quad (3.85)$$

where $\Phi = N_{th}, r_h, Z_h,$ or $Q_h r_h$. Note that the $SEDr_h$ table is used for $Q_h r_h$. The factor $\rho_a(k)/\rho_a(kk)$ in Eqn. 3.85 accounts for density differences among the levels over which the distribution falls and ensures that all quantities are conserved during the sedimentation process. The current value of $\Phi(kk)$ is added to the previous $\Phi(kk)$ as quantities from higher levels (e.g., $z(k+1), z(k+2),$ etc.) may also fall into $z(kk)$. For levels $z(k \leq kfall_{max})$, the amount of hail precipitation arriving at the surface ($psfc_h$) for the current time step is computed using the SFC sedimentation table,

$$psfc_h = r_h(k)\rho_a(k) \times SFC[k, \bar{m}_h(k), v_h(k)]. \quad (3.86)$$

Size sorting of hail through sedimentation alone would tend to narrow the hail size spectra at all levels, and lower order moment schemes are generally not able to reproduce this effect in a realistic manner (MY05a; Wacker and Lüpkes 2009; Mansell 2010). The adjustment of the spectral shape parameter tends to limit excessive size sorting when moment-weighted bulk terminal velocities are used. On the other hand, bulk fall speeds, though computationally efficient, imply that the terminal velocities of each moment of a given distribution are largely independent of each other (MY05a), with greater terminal velocities assigned for larger moment values (GSR04, Wacker and Lüpkes 2009). For example, a distribution containing mainly numerous small particles may have similar Z_h values as one comprised of only a few large particles (Danielsen et al. 1972; Wakimoto and Bringi 1988), and thus both distributions could have similar bulk terminal velocities for the 6th moments. Particles in the first distribution would clearly fall more slowly, however, the bulk terminal velocity of the 6th moment (V_{Zh}),

$$V_{Zh} = \frac{\int_0^\infty D^6 V_{th}(D) n_h(D) dD}{\int_0^\infty D^6 n_h(D) dD} \quad (3.87)$$

for this distribution wouldn't reflect the slower fall speeds. An example of this is shown in Table 3.7 and Figure 3.11 for sample distributions labeled A, B, C, D, E, and F. Sample distributions A

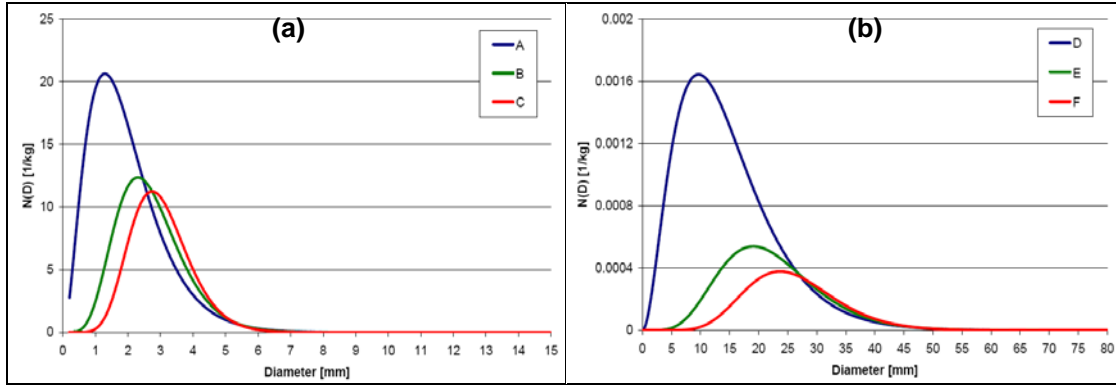


Figure 3.11: Number density distributions $N(D)$ for sample distributions (a) A, B, and C, and (b) D, E, and F given in Table 3.7. Note the different scales for the two panels.

and D are clearly weighted towards smaller hail sizes (Fig 3.11), yet as seen from Table 3.7, their reflectivity-weighted bulk terminal velocities are similar to the sample distributions that are weighted towards larger sizes (B, C, and E, F, respectively). For distributions A, B, and C, which have identical hail mixing ratio values, as v_h increases, a corresponding increase in $D_{\bar{m}}$ occurs yet the V_{Zh} values decrease slightly. This means that the reflectivity values associated with the smaller particles of distribution A 'fall' in a similar manner to or even more quickly than those associated with the larger particles of distributions B and C.

Table 3.7: Bulk terminal velocities (rightmost column) as computed from Eqn 3.87 for sample hail distributions A, B, and C, which have equal Z_h values of $358600 \text{ mm}^6 \text{ m}^{-3}$, and distributions D, E, and F, which have equal Z_h values of $5 \times 10^6 \text{ mm}^6 \text{ m}^{-3}$. Distribution parameters for each sample distribution are given as well.

Distribution	r_h [g/kg]	v_h	N_{th} [kg^{-1}]	$D_{\bar{m}}$ [mm]	Z_h [$\text{mm}^6 \text{ m}^{-3}$] (dBZ)	V_{Zh} [m/s]
A	3	2	990	1.86	358600 (55.55)	11.40
B	3	6	333	2.67	358600 (55.55)	10.84
C	3	10	234	3.008	358600 (55.55)	10.60
D	0.1	2	0.079	13.91	5000000 (67)	31.18
E	0.074	6	0.015	22.11	5000000 (67)	31.17
F	0.065	10	0.008	25.98	5000000 (67)	31.14

3.7) Other routines and modifications

3.7.1) Updating the hail distribution shape parameter ν_h

The distinguishing feature of the 3MHAIL scheme is the fact that ν_h is no longer constrained to remain fixed through the additional prediction of the 6th moment of the hail distribution. The hail shape parameter is updated twice within the RAMS 3MHAIL microphysics routine. The first update of ν_h occurs prior to application of any microphysical processes using the post-advection and diffusion, and the second update uses the updated intermediate values of N_{th} , r_h , and, Z_h following the application of vapor/heat diffusion, collection, and melting routines, but prior to the application of the sedimentation routine. The method to update ν_h entails the use of Eqn. 3.90; the ratio of predominant mass ($M6/M3$; Eqn. 3.88) (Mason 1971; Berry and Reinhardt 1974) to mean mass ($M3/M0$; Eqn. 3.89), which is unique to each ν_h value. These ratios are computed for the discrete ν_h values (Fig. 3.12) during model initialization and used during model runtime to determine the updated value of ν_h , denoted by ν_h^* , at each grid point. The predominant mass is defined as the mean mass of the mass density function, or the mass around which most of the mass is concentrated (Berry and Reinhardt 1974).

$$\frac{M6}{M3} = \frac{\int_0^{\infty} D^6 fgam(D)dD}{\int_0^{\infty} D^3 fgam(D)dD} = D_n^3 \frac{\Gamma(\nu + 6)}{\Gamma(\nu + 3)} \quad (3.88)$$

$$\frac{M3}{M0} = \frac{\int_0^{\infty} D^3 fgam(D)dD}{\int_0^{\infty} fgam(D)dD} = D_n^3 \frac{\Gamma(\nu + 3)}{\Gamma(\nu)} \quad (3.89)$$

$$\frac{M6/M3}{M3/M0} = \frac{\Gamma(\nu + 6)}{\Gamma(\nu + 3)} \frac{\Gamma(\nu)}{\Gamma(\nu + 3)} = F(\nu). \quad (3.90)$$

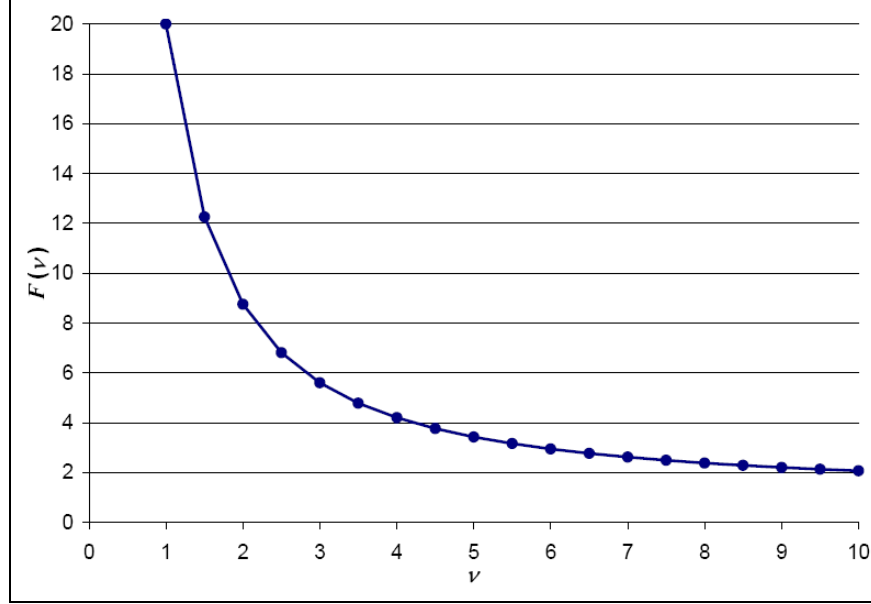


Figure 3.12: Plot of ratio of moments values $F(v)$ [Eqn. 3.90] for discrete v values ranging from 1.0 to 10.0.

The grid point values of v_h can vary continuously between 1.0 and 10.0 rather than forcing v_h to only take on discrete values, and a simple linear interpolation scheme is used to obtain interpolated values for the various look-up tables, which are computed only for discrete v_h values. Using the updated values of N_{th} , r_h , and, Z_h , a ratio (3.91) approximately equivalent to $F(v_h)$ is computed,

$$F(v_h) \approx Z_h N_{th} \left(\frac{\alpha_{mh}}{r_h} \right)^2 \times 10^{-18} = F^*(v_h^*), \quad (3.91)$$

where the 10^{-18} factor is needed to obtain a unitless value since $Z_h N_{th} \left(\frac{\alpha_{mh}}{r_h} \right)^2$ has units of

$[\text{mm}^6 \text{m}^{-6}]$. If $F^*(v_h^*)$ is less than $F(v_h = 10.0)$, then v_h^* is set to 10.0, and if $F^*(v_h^*)$ is greater than $F(v_h = 1.0)$, then v_h^* is set to 1.0. Otherwise, an iterative secant method (Eqn. 3.92) is used to compute the exact value of v_h^* based on the pre-computed $F(v)$ values (e.g., Fig. 3.12). The v and $v+0.5$ values corresponding to the pre-computed $F(v)$ and $F(v+0.5)$ values that straddle

$F^*(v_h^*)$ are used as the initial estimates v_h^{i-1} and v_h^i , respectively, in Eqn. (3.92). For example, if $F^*(v_h^*)=3.33$, then the straddling $F(v)$ values are $F(5.0)=3.4286$ and $F(5.5)=3.1622$, and the initial estimates are $v_h^{i-1}=5.0$ and $v_h^i=5.5$.

$$v_h^{i+1} = v_h^i - \frac{f(v_h^i) \times (v_h^{i-1} - v_h^i)}{f(v_h^{i-1}) - f(v_h^i)}. \quad (3.92)$$

The function f in Eqn. (3.92) is given by

$$f(v_h^i) = \frac{(5 + v_h^i)(4 + v_h^i)(3 + v_h^i)}{(2 + v_h^i)(1 + v_h^i)v_h^i} - F^*(v_h^i). \quad (3.93)$$

Equation 3.92 is computed iteratively until the error function (3.94) is less than 1×10^{-5} . Typically only several iterations are required until the solution for v_h^{i+1} converges to v_h^* .

$$\mathcal{E} = \left| \frac{v_h^{i+1} - v_h^i}{v_h^{i+1}} \right| \quad (3.94)$$

The interpolating factors for the various look-up tables and v_h -dependent factors are given by Eqns. (3.95) and (3.96), where v_h^{i-1} and v_h^i are the initial estimates used in Eqn. (3.92).

Interpolated table values are computed by multiplying the table values corresponding to v_h^{i-1} and v_h^i by g_1 and g_2 , respectively, and the same is done to compute interpolated values for the v_h -dependent factors.

$$g_1 = 2.0 \times (v_h^i - v_h^*) \quad (3.95)$$

$$g_2 = 2.0 \times (v_h^* - v_h^{i-1}). \quad (3.96)$$

3.7.2) Modification to diameter threshold for collisional breakup of rain

Investigations of the original 2M RAMS hail formation mechanism revealed that the erroneously large numbers of newly formed hail particles were partly attributed to the large numbers of raindrops, which, upon collisions with frozen particles, resulted in hail. A method to reduce the numbers of raindrops produced in the model by increasing the diameter threshold at which collisional breakup of raindrops occurred was tested and found to have a negligible impact on reducing both the number concentrations of rain and hail formation via rain-ice collisions with the original 2M collection algorithm. Nonetheless, this modification to the diameter threshold for raindrop breakup is retained as an option in the model. Collisional breakup of raindrops in RAMS is parameterized in the self-collection equation for rain through a modification of the coalescence efficiency E_c (Verlinde and Cotton 1993).

$$E_c(D_{\bar{m}r}) = \begin{cases} 1.0 & D_{\bar{m}r} < D_{cut} \\ 2.0 - \exp[A(D_{\bar{m}r} - D_{cut})] & D_{cut} \leq D_{\bar{m}r} \leq D_{spont} \\ -5.0 & D_{\bar{m}r} > D_{spont} \end{cases} \quad (3.97)$$

In the above equation, $A = 15182$ replaces the original value of $A = 0.1326 \times 10^7$, $D_{cut} = 1.5 \times 10^{-3}$ m is that cutoff mean mass rain diameter below which breakup does not occur and replaces the original value of $D_{cut} = 6 \times 10^{-4}$ m, and $D_{spont} = 3.0 \times 10^{-3}$ m is the spontaneous breakup diameter replacing the original value of $D_{spont} = 1.4 \times 10^{-3}$ m. Examinations of $D_{\bar{m}r}$ values for full 3D simulations of deep moist convection revealed that $D_{\bar{m}r}$ rarely exceeded 0.5 mm in hail formation regions, thus E_c almost always had a value of 1.0 and the number concentrations of raindrops were largely unaffected with respect to employing the original threshold diameters for breakup.

4. Testing of the 3MHAIL microphysics scheme

A number of tests were carried out on various parts of the RAMS microphysics that required major modification during implementation of the 3MHAIL scheme. These tests were necessary in order to ensure the 3MHAIL microphysics code worked properly as well as to showcase the improvements in the model solutions with the 3MHAIL scheme compared to the existing lower order moment microphysical schemes in RAMS. Specifically, the tests examined the sedimentation, melting, and collection routines as these routines were significantly altered from their original formulations in order to accommodate the 3MHAIL scheme. The following sections detail the procedures, analyses, and results for the different tests performed.

4.1) *1M, 2M, and 3MHAIL sedimentation schemes vs bin sedimentation scheme*

Extensive testing of the bin-emulating 3MHAIL sedimentation scheme was performed by applying the scheme to different initial hail distributions (Table 4.1) within a 1D column model separate from the main RAMS model. 1M and 2M versions of the 3MHAIL sedimentation scheme (using fixed ν_h values) were also modeled, and the results from all three sedimentation schemes were compared to those from a true bin sedimentation scheme (Appendix B).

[Comparisons between the 3MHAIL and the original RAMS 1M and 2M sedimentation schemes were also performed and these results are presented in Appendix B].

Pure sedimentation of hydrometeor distributions such as presented here have been previously examined by Wacker and Seifert (2001), MY05a, Wacker and Lüpkes (2009), Mansell (2010), and Milbrandt and McTaggart-Cowan (2010) (hereafter MMC10), but only for size distributions weighted toward small diameter particles, often initialized with an exponential size distribution,

Table 4.1: Names of 1D sedimentation test cases, time step lengths and initial hail distribution parameters (maximum values for N_{th} and r_h) for the time-height profiles displayed in Figures 4.1-4.3 and 4.5-4.7.

Figure	Case	Δt [s]	N_{th} [m^{-3}]	r_h [g m^{-3}]	v_h	$D_{\bar{m},\min}$ [cm]	$D_{\bar{m},\max}$ [cm]	$D_{\bar{m},\text{fixed}}$ [cm]
4.1	CON1	3	50.231	0.491	1	0.126	0.164	0.15
4.2	CON2	3	0.489	1.472	5	1.05	1.56	1.3
4.3	CON3	3	0.122	2.454	8	2.1	3.1	2.6
4.5	STR1	4	238.19	0.551	2	0.098	0.121	0.1
4.6	STR2	4	1.5	1.5	5	0.86	1.08	1.0
4.7	STR3	4	0.025	1.004	7	3.07	3.87	3.5

and using constant grid spacing. To date, this author is unaware of any studies that examine pure sedimentation of initially non-exponential size distributions (with the exception of Wacker and Lüpkes 2009) and/or sedimentation on vertical grids with variable grid spacing. As the full three-dimensional simulations of deep moist convection carried out as part of the present work (Chapter 5) use a vertically-stretched grid and allow for the development of large hail sizes, it is important to first understand how pure sedimentation affects the predicted hail distributions. To this end, sedimentation of various initial distributions was examined using constant vertical grid spacing as well as stretched vertical grid spacing.

The time-height profiles of the resulting N_{th} , r_h , Z_h and $D_{\bar{m}h}$ values using the different sedimentation schemes are displayed in Figures 4.1-4.3 and 4.5-4.7 for the initial hail distributions listed in Table 4.1. The initial values of r_h , N_{th} , and v_h were chosen such that distributions spanning the ranges of $D_{\bar{m}h}$ and v_h associated with the 3MHAIL scheme were represented. For the 1M scheme, r_h is predicted and N_{th} is diagnosed from the fixed $D_{\bar{m}h}$ value using Eqn. (3.9), whereas for the 2M scheme, both r_h and N_{th} are predicted. Z_h is diagnosed from r_h , N_{th} , and the fixed v_h value using Eqn. (3.17) for both the 1M and 2M sedimentation schemes. $D_{\bar{m}h}$ is diagnosed from the predicted r_h and N_{th} values using Eqn. (3.9) for the 2M and 3MHAIL schemes, and Eqn. (B.10) is used to compute $D_{\bar{m}h}$ for the bin scheme. All three bulk

sedimentation schemes conserve mass, the 2M and 3MHAIL schemes conserve number as well, and the 3MHAIL scheme also conserves reflectivity prior to hail reaching the surface. Constant vertical grid spacing of 153 m is employed for tests CON1, CON2 and CON3 (Figs. 4.1 to 4.3) as in MY05a, with the CON1 test comparable to the initial distribution presented in both MY05a and Mansell (2010). A vertically stretched grid is used for sedimentation tests STR1, STR2, and STR3 (Figs. 4.5 to 4.7), with spacing of 200 m at the lowest model level and a stretch ratio of 1.05 up through 6.1 km, above which the grid spacing is constant at 500 m. The initial hail distribution is defined by specifying r_h to vary sinusoidally over a layer between 8.1 to 9.3 km for constant grid spacing cases and 6.6 to 8.6 km for stretched grid cases, with a maximum value for r_h at 8.7 and 7.6 km for constant and stretched grid cases, respectively. N_{th} is specified as a constant multiplied by air density $\rho_a(z)$, v_h is initially constant over the layer, and Z_h is computed based on the values of r_h , N_{th} , and v_h . The initial hail distributions at the level of maximum r_h are also presented (panels d in Figs 4.1-4.3, 4.5-4.7), and the time-height profiles of $D_{\bar{m}h}$ for the 1M scheme are omitted as $D_{\bar{m}h}$ is fixed for this scheme. Different constant grid spacing values (50, 100, 200, and 250 m) as well as various combinations of minimum grid spacing values (25, 50, 100, and 250 m) and stretch ratios (1.01, 1.025 and 1.1) were also tested and generally gave results similar to those presented in Figures 4.1-4.3 and 4.5-4.7.

The time-height profiles displayed in Figures 4.1-4.3 and 4.5-4.7 show that the 3MHAIL sedimentation scheme (bottom rows) produces far superior results for N_{th} , r_h , and Z_h than either the 1M (top rows) or 2M (middle rows) schemes when compared to the true bin sedimentation scheme (solid curves in all panels) for the various initial distribution parameters shown. Gravitational size sorting is clearly evident in the bin sedimentation profiles as exhibited by the increase in mean mass diameter ($D_{\bar{m}}$) towards the surface as well as the progressive downward

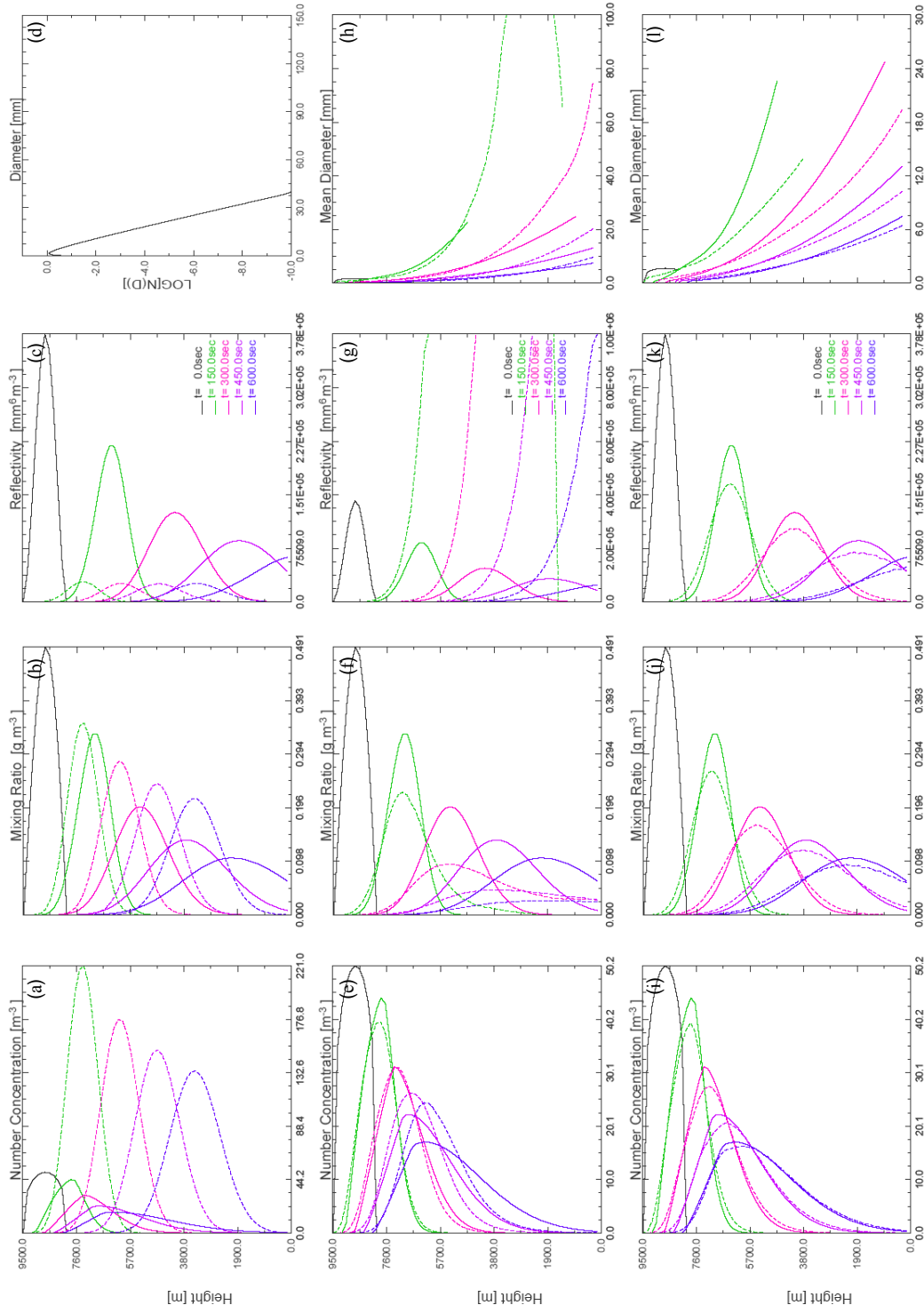


Figure 4.1: Time-height profiles of N_{th} (first column), r_h (second column), Z_{th} (third column), and mean mass diameter (fourth column) for a bin sedimentation scheme 1M (top row), 2M (middle row), and 3MHAIL (bottom row) sedimentation schemes for case CON1. Initial distribution (panel d) resembles an exponential distribution as in MY05a ($\nu_h = 1$) with maximum mean mass diameter values ranging from 1.26 to 1.64 mm. Note that in this and subsequent figures, the abscissa for the panel (a) has a different scale than panels (e) and (i). Also note the scale changes for panels (g) and (h) in this figure.

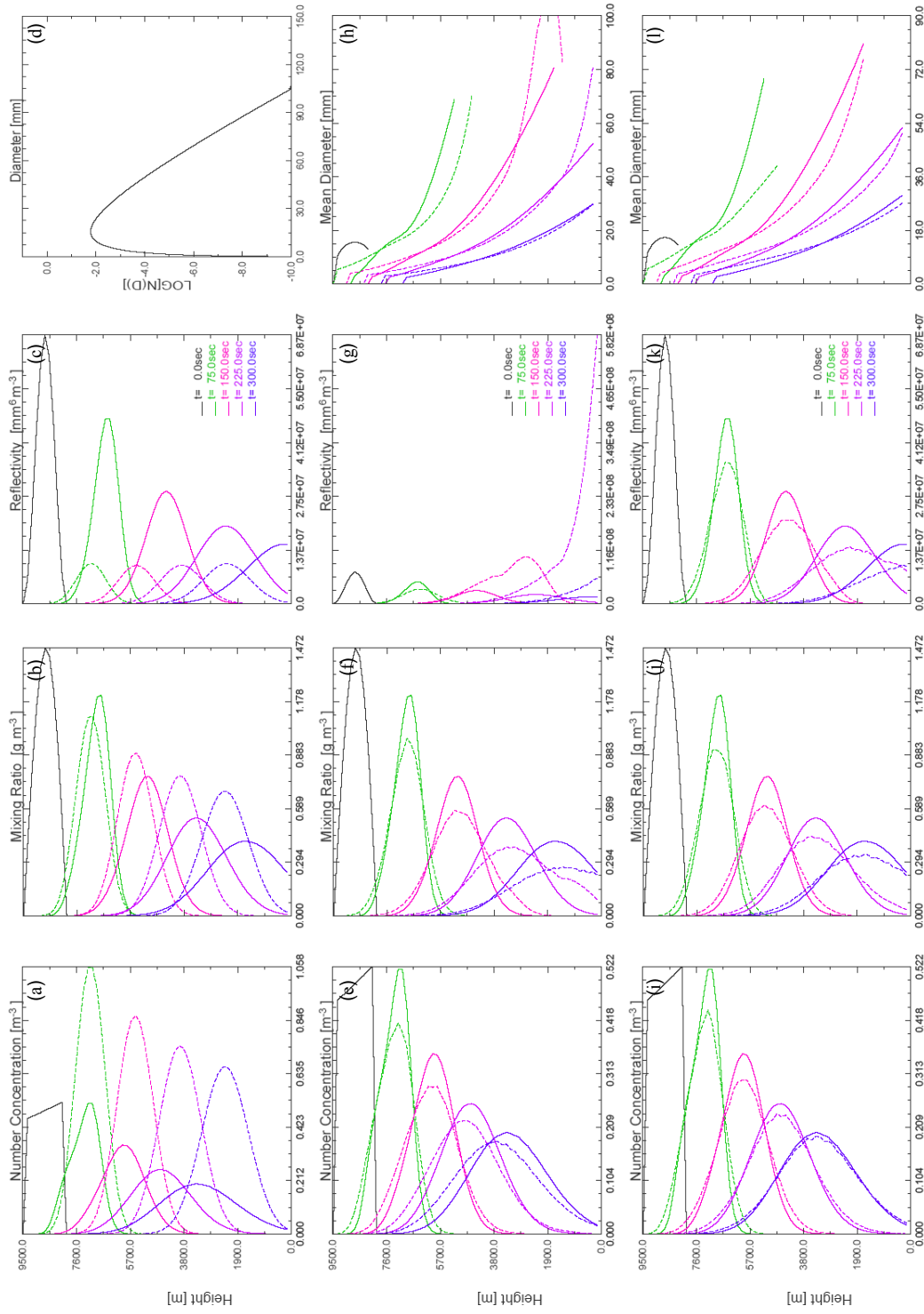


Figure 4.2: As in Figure 4.1, except for case CON2 in which distribution is initialized with parameters that resemble a narrow size distribution ($\nu_n = 5$) weighted towards moderate sizes (panel d), with maximum mean mass diameters ranging from 1.05 to 1.56 μm . Note the scale change for panel (g).

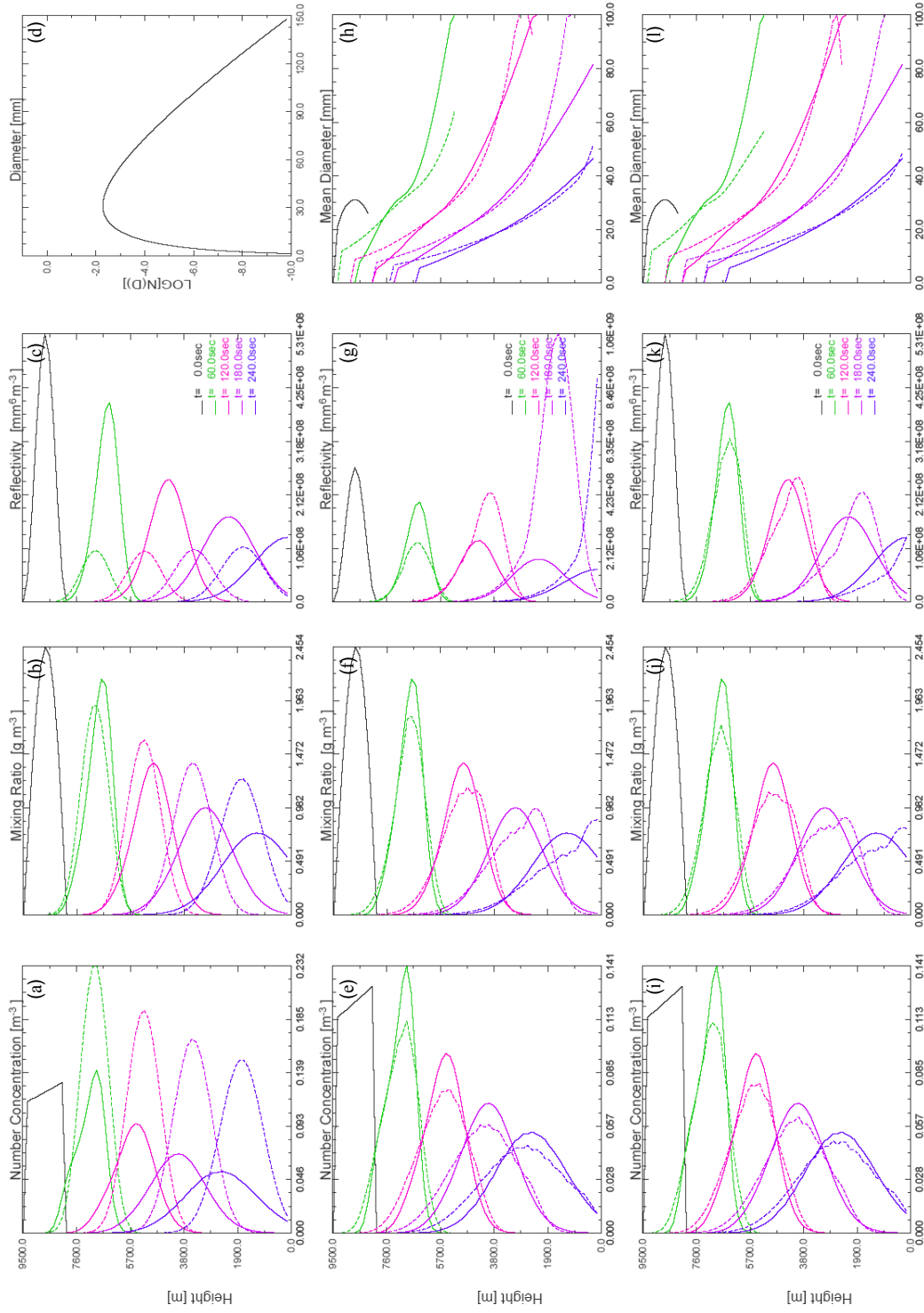


Figure 4.3: As in Figure 4.1, except for case CON3 in which distribution is initialized with parameters that resemble a narrow size distribution ($v_{\frac{1}{2}} = 8$) weighted towards large sizes (panel d), with maximum mean mass diameters ranging from 2.1 to 3.1 cm. Note the scale change for panel (g).

shift with time in the profiles for increasing moment order (N_{th} to r_h to Z_h). It should be noted that the $D_{\bar{m}h}$ values for 2M and 3MHAIL schemes shown in Figures 4.1-4.3 and 4.5-4.7 are instantaneous values; the maximum $D_{\bar{m}h}$ ($D_{\bar{m}h,max}$) value considered in the sedimentation tables is 40 mm. In cases where the instantaneous $D_{\bar{m}h}$ value may be greater than 40 mm (CON1, CON2, CON3, and STR3), the table values used to redistribute the predicted moments still correspond to a $D_{\bar{m}h}$ value of 40 mm. This is one shortcoming of this sedimentation algorithm, although in the full RAMS microphysics package, the hail distributions are limited by $D_{\bar{m}h,max}$ anyway such that this is not an issue. For the 1D sedimentation tests presented here, N_{th} is not adjusted when $D_{\bar{m}h}$ exceeds 40 mm in order to preserve number.

In all of the 1M sedimentation cases, N_{th} and Z_h are diagnosed directly from r_h , and thus the profiles of these diagnosed quantities are largely similar to those for r_h , with the maxima of N_{th} and Z_h following the maxima in r_h . These results demonstrate the inability of the 1M sedimentation scheme to represent size sorting and agree qualitatively with results from similar investigations of different 1D sedimentation models by MY05a, Wacker and Lüpkes (2009), and MMC10. Beyond $t = 0$, the 1M N_{th} profiles in all cases (Figs. 4.1a-4.3a and 4.5a-4.7a) exhibit values that are larger than those of the other schemes owing to the restriction that $D_{\bar{m}h}$ be constant, and the peak 1M N_{th} values tend to occur at lower heights compared to the other schemes, especially at later times. The diagnosed Z_h profiles for the 1M scheme in all cases (Figs. 4.1c-4.3c and 4.5c-4.7c) maintain their general vertical structures and maximum magnitudes with time, and the maxima in these profiles are generally less than those for all other schemes due to N_{th} values that are consistently greater in the 1M sedimentation cases. In addition, maxima in the 1M r_h profiles consistently lag the bin scheme r_h maxima (Figs. 4.1b-

4.3b and 4.5b-4.7b) suggesting sedimentation generally occurs too slowly in the 1M cases. For cases CON1, CON2, CON3, r_h values are consistently underpredicted at the leading edges (lower flanks) of the 1M profiles compared to the bin r_h profiles (Figs. 4.1b, 4.2b, and 4.3b), that is, the leading edges of the 1M r_h profiles lag behind bin solutions, and the maxima in the 1M r_h are generally overpredicted. These results are in agreement with similar analyses of 1M sedimentation on a vertical grid with constant spacing for exponential size distributions reported by MY05a, Wacker and Lüpkes (2009), and MMC10. By comparison, r_h values are initially overpredicted in the 1M scheme at the leading edges of the profiles for cases STR1, STR2, and STR3 (Figs. 4.5b, 4.6b, and 4.7b), but this overprediction of r_h at the leading profile edges decreases with time and increasing vertical resolution and actually changes to underprediction of r_h in the STR1 case (Fig. 4.5b). Unlike the constant grid spacing cases, the maxima in the 1M r_h profiles in the STR1, STR2, and STR3 cases are always less than those for the bin r_h profiles. The trailing edges (upper flanks) of the 1M r_h profiles are seen to lag the bin r_h profiles in all cases. In general, it appears that sedimentation of hail occurs too slowly for the 1M scheme with constant vertical grid spacing, whereas 1M sedimentation on a stretched vertical grid can proceed too quickly or too slowly depending on the characteristics of the hail distribution.

For case CON1, excessive size sorting is clearly evident in the 2M scheme as depicted by the r_h and D_{mh} profiles (Figs. 4.1f,h), with maximum D_{mh} values well exceeding those of the bin scheme at the leading (lower) edge of the sedimenting particles, similar to results presented by MY05a and Mansell (2010). Additionally, the 2M N_{th} values along the leading profile edge become increasingly underpredicted with time, whereas the maxima in the 2M N_{th} profiles become increasingly overpredicted with time (Fig. 4.1e). As a result of rapid differential sedimentation between r_h and N_{th} with the 2M scheme, the diagnosed Z_h profiles (Fig. 4.1g)

attain extremely large values ($> 10^{12} \text{ mm}^6 \text{ m}^{-3}$) early on and are consistently greater than the initial maximum Z_h values for the selected times shown. Wacker and Lüpkes (2009) and MMC10 also found that the diagnosis of the 6th moment (Z_h) from predicted lower order moments M_0 and M_3 (N_{th} and r_h) in their 2M sedimentation schemes could cause the maxima in Z_h to overshoot the initial maximum value. In comparison, the profiles of r_h , N_{th} , Z_h , and $D_{\bar{m}h}$ produced by the 3MHAIL scheme (Figs. 4.1i,j,k,l) show a much better match with the bin scheme profile, though the $D_{\bar{m}h}$ values are somewhat underpredicted by the 3MHAIL scheme prior to $t = 600 \text{ s}$ similar to the results for the 3M sedimentation scheme in MY05a.

MY05a and MMC10 attribute excessive size sorting in 2M sedimentation schemes to the fact that the ratio of the moment-weighted fall velocities (i.e., V_k/V_j , where k and j represent the moments and $k > j$) is always greater than 1, with the largest ratios for small values of ν and tending to 1 as ν increases (Fig. 4.4). Thus, for $k = 3$ and $j = 0$, the sedimentation rate of M_3 always exceeds that of M_0 , and since $D_{\bar{m}h}$ is proportional to M_3/M_0 , $D_{\bar{m}h}$ consistently increases along the leading edge of the sedimenting particles profile. Although the bulk sedimentation schemes herein do not use moment-weighted fall velocities and instead utilize look-up tables based on bin sedimentation, a similar analysis of the ratios of the look-up table values for the predicted moments yields a similar conclusion (Fig. 4.4). Also seen from the right panel in Figure 4.4 is that, for ν_h values less than about 5, the ratios of M_3/M_0 sedimentation table values depend on $D_{\bar{m}h}$ as well such that for a given ν_h value, the ratios increase as $D_{\bar{m}h}$ increases up to about 20 mm, and the ratios then decrease slightly as $D_{\bar{m}h}$ increases further. The decrease in the ratios for $D_{\bar{m}h} > 20 \text{ mm}$ is attributable to truncation of the size distribution at the largest diameters for small ν_h values which leads to an underestimation of M_3 . Physically, such wide

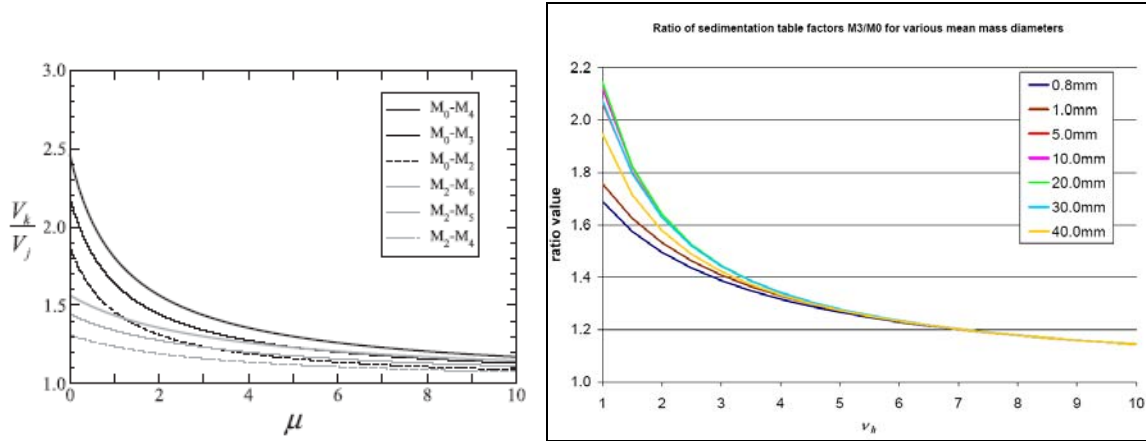


Figure 4.4: (Left) Ratio of bulk fall velocities V_k/V_j vs μ ($\mu = \nu - 1$) computed for various pairs of j and k [from Milbrandt and McTaggart-Cowan (2010)]. (Right) Ratios of $M3/M0$ sedimentation look-up table values as a function of ν_h for various values of $D_{\bar{m}h}$.

size distributions with large $D_{\bar{m}h}$ values are not realistic and are not permitted in the 3MHAIL scheme in practice, though these distributions are allowed in the modified 2M sedimentation scheme.

In cases CON2 and CON3, which are initialized with narrower size distributions and for which greater fixed ν_h values are used for the lower order moment schemes, the degree of excessive size sorting with the 2M scheme is reduced compared to the CON1 case as evident in the closer matching profiles between the 2M scheme and bin solutions for N_{th} , r_h , and $D_{\bar{m}h}$ (panels e, f, and h in Figs. 4.2 and 4.3). These results agree qualitatively with findings by MY05a and Mansell (2010) who reported that an increase in the fixed value of ν led to a decrease in the amount of excessive size sorting for 2M sedimentation. As in the CON1 case, the diagnosed Z_h values for the 2M scheme are once again overpredicted in the CON2 and CON3 cases and exceed the initial maximum Z_h values at later times (Figs. 4.2g and 4.3g). The resulting profiles for N_{th} , r_h , Z_h , and $D_{\bar{m}h}$ with the 3MHAIL scheme for cases CON2 and CON3 (panels i, j, k, and l in Figs. 4.2 and 4.3) generally match those for the bin scheme solutions much more closely than

the 2M and 1M scheme profiles, though the Z_h and $D_{\bar{m}h}$ values for the 3MHAIL scheme appear to be overpredicted in the CON3 case at times $t = 120$ and 180 s (Figs. 4.3k,l). [Increasing the maximum allowable ν_h value to 20.0 reduces the overprediction of Z_h and $D_{\bar{m}h}$ in the CON3 case (not shown).] The $D_{\bar{m}h}$ values are also too large for both the 2M and 3MHAIL schemes within the upper regions of these profiles beyond $t = 0$ in cases CON2 (Figs. 4.2h,l) and CON3 (Figs. 4.3h,l), though the amount of mass remaining at these levels for the times shown is negligible ($< 10^{-7}$ kg/kg).

Interestingly, the resulting r_h , N_{th} , and $D_{\bar{m}h}$ profiles for the 2M and 3MHAIL schemes in the CON3 case (Fig 4.3) are mostly similar, yet vast differences in the Z_h profiles exist between these two schemes. An analysis of the time-height profile of ν_h for the 3MHAIL scheme for the CON3 case (not shown) revealed these values rapidly reach the maximum allowable value of 10.0 at levels below the initial distribution height. From Eqn. (3.17) for Z_h and Fig. 3.12 for the ratios of moments $F(\nu)$ (which is equivalent to $G(\nu)$ in Eqn. 3.17), it is seen that Z_h is directly proportional to $G(\nu)$, which decreases as ν increases. Thus, since 2M sedimentation in the CON3 case has a fixed ν_h value of 8.0, whereas ν_h values of 10.0 are present in the 3MHAIL profiles at levels below the initial distribution height, the Z_h values would be expected to be greater for the 2M scheme. [This also helps explain the excessively large values in the 2M Z_h profiles for the CON1 and CON2 cases, which have fixed ν_h values of 1.0 and 5.0, respectively.] Time-height profiles of Z_h diagnosed from the predicted resulting r_h , N_{th} , and ν_h values for the 3MHAIL scheme for the CON3 case (not shown) reveal that Z_h values actually exceed the bin Z_h values at later times, though not nearly as much as in the 2M scheme. Increasing the maximum allowable ν_h value to 20.0 mitigates the large values of diagnosed Z_h in the 3MHAIL scheme as well as

reduces the overprediction of $D_{\bar{m}h}$, though the predicted Z_h values still show the best match to the bin Z_h profiles.

Due to the fact that the vertical resolution in the STR1, STR2, and STR3 cases is coarser than in the constant vertical grid spacing cases (200 to 500 m versus 153 m), the effects of numerical diffusion are greater in the former cases compared to the latter cases (Wacker and Seifert 2001). [Numerical diffusion in the vertical for the bulk sedimentation schemes herein results from the necessary assumption that hydrometeor distributions and their associated moments are evenly distributed over a layer (Appendix B). Within the profile's trailing flank, mass is exiting the layer from below at each time step, however, the mass remaining in the layer is implicitly redistributed over the entire layer. Likewise, within the leading profile flank, once mass enters a level from above, it is immediately redistributed over the entire layer leading to seemingly faster sedimentation rates.] This enhanced numerical diffusion in the stretched vertical grid cases results in reduced peak values and broader vertical profiles for the predicted quantities of the bulk sedimentation schemes compared to the bin solution profiles. Overprediction of the prognostic quantities is seen in the profile flanks for both the 2M and 3MHAIL schemes when a stretched vertical grid is employed (Figs. 4.5, 4.6, and 4.7), although the coarser vertical resolution appears to place a control on excessive size sorting with the 2M sedimentation scheme as evident in the 2M $D_{\bar{m}h}$ profiles (Figs. 4.5h, 4.6h, and 4.7h).

For the STR1 case, the 2M N_{th} profiles (Fig. 4.5e) show a slightly better match to the bin N_{th} profiles than do the 3MHAIL N_{th} profiles (Fig. 4.5i), particularly at later times. On the other hand, an examination of the r_h profiles reveals the 3MHAIL scheme (Fig. 4.5j) produces a closer match to the bin solutions than the 2M scheme (Fig. 4.5f). The predicted Z_h profiles for the 3MHAIL scheme (Fig. 4.5k) do not follow the bin Z_h profiles as closely as in the constant grid

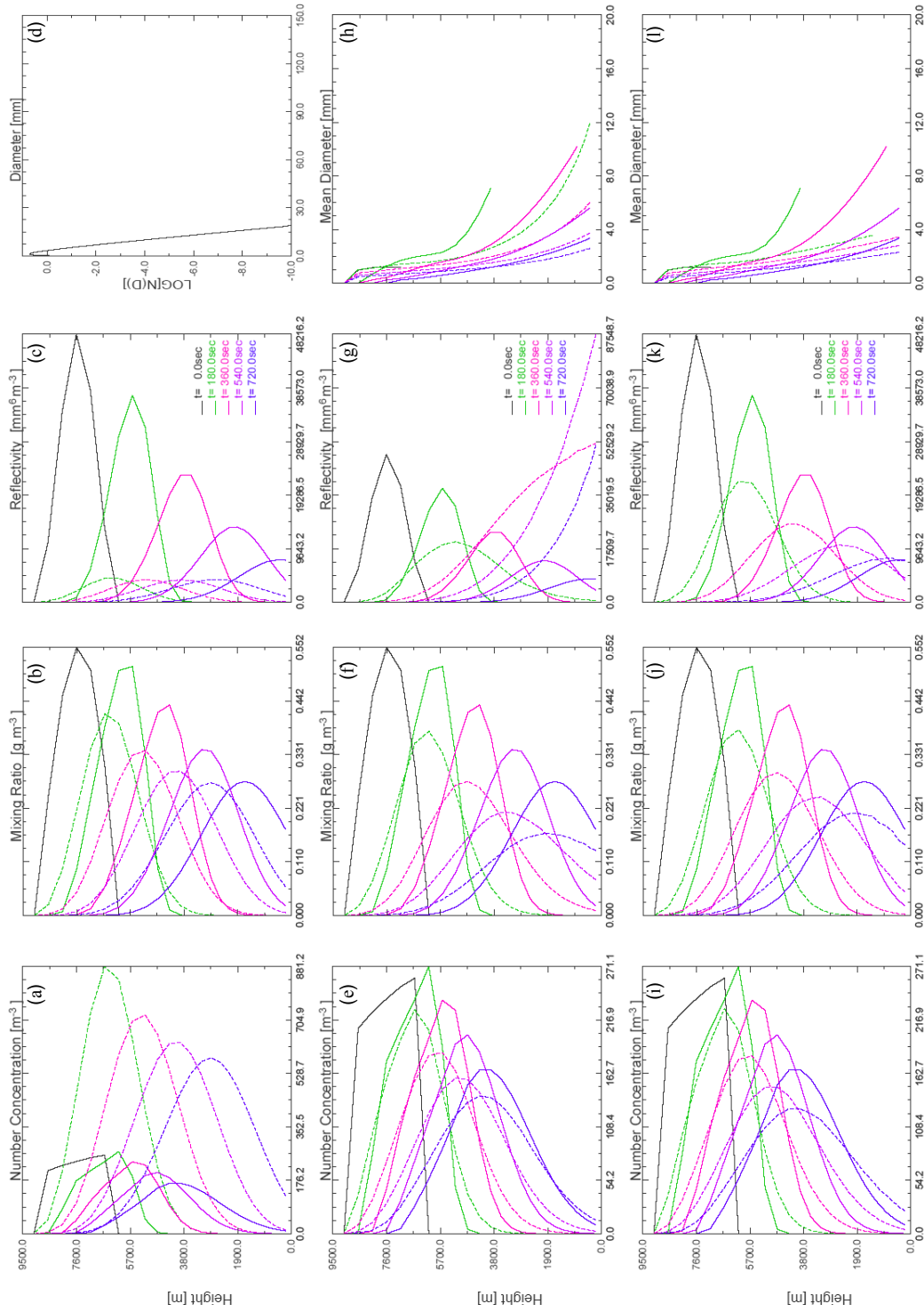


Figure 4.5: As in Figure 4.1, except for case STR1 in which distribution is initialized with parameters that resemble a wide size distribution ($V_{\text{r}} = 2$) weighted towards smaller hail sizes (panel d), with mean mass diameters ranging from 0.98 to 1.21 mm. Note the scale change for panel (g).

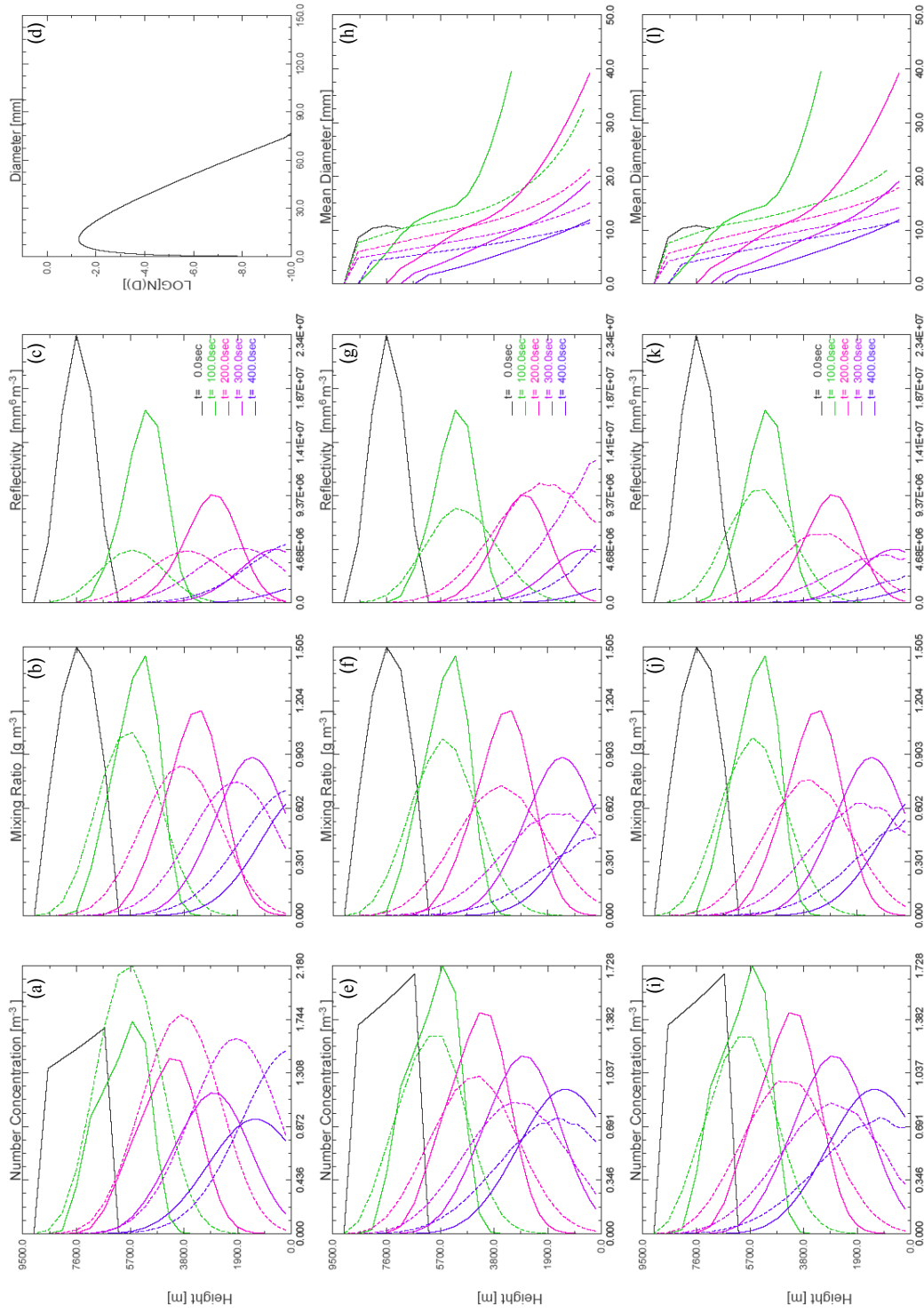


Figure 4.6: As in Figure 4.5, except for case STR2 in which distribution is initialized with parameters that resemble a narrower size distribution ($v_{1/2} = 5$) weighted towards moderate sizes (panel d), with mean mass diameters ranging from 0.86 to 1.08 cm.

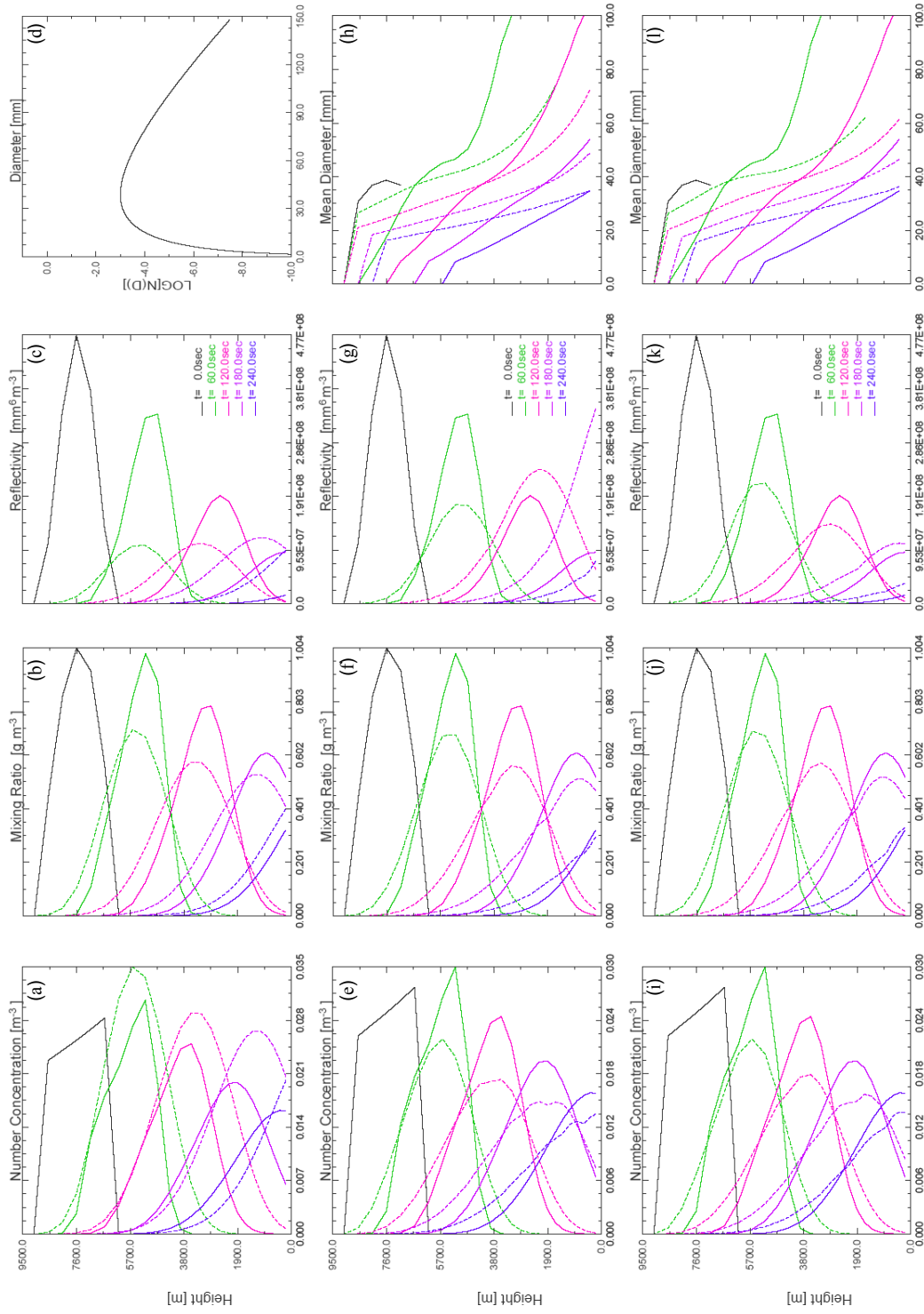


Figure 4.7: As in Figure 4.5, except for case STR3 in which distribution is initialized with parameters that resemble a narrow size distribution ($\psi_k = 7$) weighted towards large sizes (panel d), with mean mass diameters ranging from 3.07 to 3.87 cm.

spacing cases, with peak Z_h values lagging those for the bin scheme, though the 3MHAIL Z_h profiles tend towards the bin solutions at later times. The 3MHAIL Z_h profiles are much closer to the bin solution than the diagnosed 2M Z_h profiles (Fig. 4.5g), which are severely overpredicted and exceed the initial maximum Z_h values at times beyond $t = 180$ s. The excessively large Z_h values in the 2M scheme can generally be attributed to the small fixed value of $\nu_h = 2.0$ in the computation of Z_h (Eqn. 3.17) as well as the overpredicted amounts of r_h within the upper and lower flanks of the profiles (Fig. 4.5f). Neither the 2M or 3MHAIL schemes produce $D_{\bar{m}h}$ profiles that resemble the bin scheme $D_{\bar{m}h}$ profiles prior to $t = 720$ s, though surprisingly, the 2M $D_{\bar{m}h}$ profiles (Fig. 4.5h) show a better match with the bin scheme $D_{\bar{m}h}$ profiles than do the 3MHAIL $D_{\bar{m}h}$ profiles (Fig. 4.5i). This result may be misleading, however, as $D_{\bar{m}h}$ is directly related to the ratio r_h/N_{th} , and the greater (lesser) degree of overprediction of the r_h (N_{th}) values for the 2M versus 3MHAIL scheme within the leading profile edges causes these ratios to be larger in the 2M scheme.

In the STR2 case, the N_{th} and r_h profiles for the 2M (Figs. 4.6e,f) and 3MHAIL (Figs. 4.6i,j) schemes are largely similar at $t = 100$ s. Beyond this time, the maxima and the values within the leading (trailing) flanks of the N_{th} profiles in the 2M (3MHAIL) scheme show a slightly closer match with the bin solutions compared to the 3MHAIL (2M) scheme. A comparison of the 2M and 3MHAIL r_h profiles (Figs. 4.6f and 4.6j, respectively) at times $t = 200$ s and later reveals the opposite is true, with the maxima and the values within the leading (trailing) flanks of the r_h profiles in the 3MHAIL (2M) scheme exhibiting a better match with the bin solutions compared to the 2M (3MHAIL) scheme. For case STR3, as in STR2, the N_{th} and r_h profiles for the 2M (Figs. 4.7e,f) and 3MHAIL (Figs. 4.7i,j) schemes are mostly equivalent with similar patterns of overprediction of N_{th} and r_h within the leading and trailing profile flanks, and both schemes give

solutions that match fairly well with the bin scheme profiles of N_{th} and r_h . Similar to STR1, the predicted Z_h profiles for the 3MHAIL scheme in cases STR2 (Fig. 4.6k) and STR3 (Fig. 4.7k) exhibit an upward shift in the peak Z_h values relative to the bin scheme solutions and generally do not show a close match to the bin Z_h profiles early on, particularly in the STR2 case. The 2M Z_h values (Fig. 4.6g) in cases STR2 and STR3 become much larger than those for the bin scheme for the times shown, although the maxima in the 2M Z_h profiles do not exceed the initial maximum as in STR1 primarily due to the larger fixed v_h values in the STR2 and STR3 cases.

The $D_{\bar{m}h}$ profiles in cases STR2 and STR3 produced by both the 2M (Figs. 4.6h and 4.7h, respectively) and 3MHAIL (Figs. 4.6l and 4.7l, respectively) schemes are mostly dissimilar to those produced by the bin scheme. The 2M scheme gives slightly better results below ~ 3 km compared to the 3MHAIL scheme prior to $t = 300$ s in STR2 and $t = 240$ s in STR3 for the same reason as discussed for case STR1. The $D_{\bar{m}h}$ values for both the 2M and 3MHAIL schemes in cases STR2 and STR3 exceed the bin scheme values over an increasingly deeper portion of the vertical column with time, which suggests that too much mass remains in the trailing regions of the r_h profiles in these bulk schemes. It should be also noted that, although $D_{\bar{m}h}$ values greater than 5 mm (STR2) and 20 mm (STR3) remain near the levels of the initial distribution (between roughly 6.5 to 8 km) for both the 2M and 3MHAIL schemes even at $t = 400$ s (STR2) and $t = 240$ s (STR3), the amount of mass at these levels is very small ($< 10^{-7}$ kg/kg). The errors in the $D_{\bar{m}h}$ profiles for the bulk schemes simply point to the inherent difficulties in attempting to accurately represent sedimentation of hydrometeors on a vertically stretched grid using bulk distribution parameters. Nonetheless, the fact that the profiles of the *predicted* quantities for the 2M and 3MHAIL sedimentation schemes resemble those of the bin scheme in most aspects gives credence to these schemes.

Figure 4.8 shows the surface precipitation rates associated with each scheme for all cases. In general agreement with the results of MY05a, the arrival of surface precipitation is delayed for the 1M scheme compared to the other schemes in cases CON1, CON2, and CON3, the peak rates are overpredicted by about 50 to 55% relative to the bin solutions, and the precipitation episodes are of shorter duration with respect to the other schemes. The delays in the arrival of precipitation at the surface and the large precipitation rates for the 1M scheme reflect the slower sedimentation rates and the overprediction of the maxima in the profiles of r_h as seen in Figures 4.1b, 4.2b, and 4.3b. Precipitation arrives earliest at the surface for the 2M scheme compared to the other schemes in cases CON1 and CON2, which is consistent with findings from Wacker and Seifert (2001) and MY05a, and the peak precipitation rate for the 2M scheme is too large in case CON1 as in MY05a. In addition, the onset of surface precipitation is increasingly delayed and the peak precipitation rate decreases with the 2M scheme as the value v_h increases (from 1.0 in CON1 to 5.0 in CON2) similar to results reported by MY05a for a single distribution. The precipitation rates for the 3MHAIL scheme in cases CON1 and CON2 show the closest match to the bin scheme solutions with respect to timing and peak values, the latter of which are underpredicted by about 10 to 13%. In case CON3, the maximum precipitation rates of the 2M (108 mm hr^{-1}) and 3MHAIL (98 mm hr^{-1}) schemes are greater than for the bin scheme (77 mm hr^{-1}) and occur slightly earlier than in the bin scheme. The greater magnitudes and earlier occurrences of the peak rates in the 2M and 3MHAIL scheme can be attributed to the increasingly overpredicted peak profile values of r_h with time compared to those for the bin scheme (Figs. 4.3f, j).

The onset of surface precipitation is also delayed for the 1M scheme relative to the other schemes in case STR1, however, the maximum precipitation rates are now less than those for the

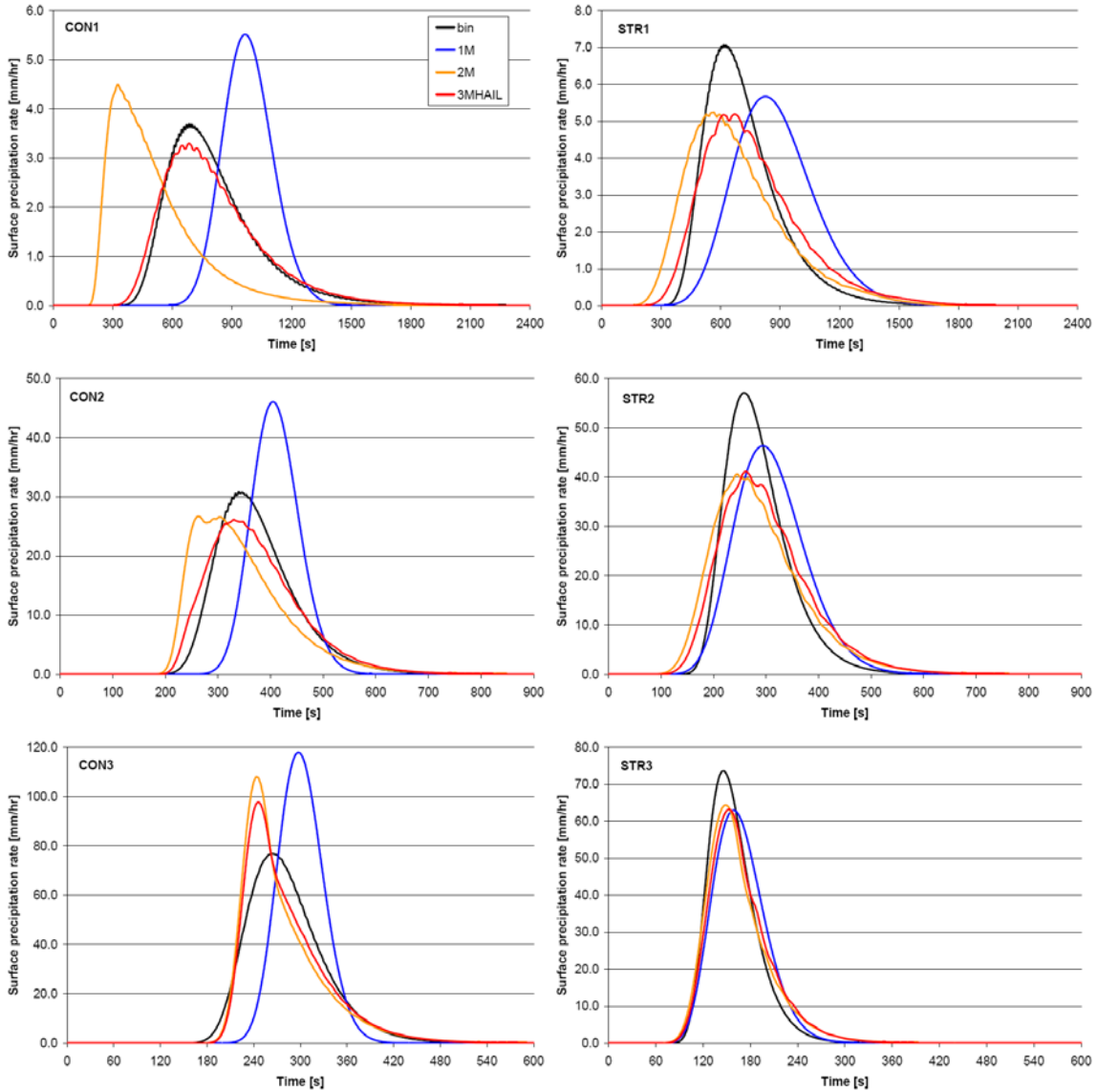


Figure 4.8: Surface precipitation rates [mm/hr (liquid equivalent)] for the 1D sedimentation tests using constant vertical grid spacing (left column) and stretched vertical grid spacing (right column). The colored lines in each panel depict the different schemes: 1M (blue), 2M (orange), 3MHAIL (red), and bin (black).

bin scheme but still exceed the peak rates of the 2M and 3MHAIL schemes. The latter result is also true for the 1M scheme in case STR2, though the timing of the peak in precipitation rate is still delayed compared the other schemes. Surface precipitation rates for the 2M and 3MHAIL schemes in cases STR1 and STR2 are mostly similar, with the main difference being that precipitation arrives at the surface and attains a peak rate earlier in the 2M scheme, though both

schemes produce peak rates about 30% less than the bin scheme in both cases. The time at which peak precipitation rates occur in the 3MHAIL scheme compares well with the occurrences in peak rates for the bin scheme in STR1 and STR2, and improvement in the timing of surface precipitation for the 2M scheme is seen as the value of v_h increases from 2.0 (STR1) to 5.0 (STR2). In case STR3, the overall timing and maximum precipitation rates in all three bulk schemes are comparable, with peak rates that are about 15% less than the bin solution, but otherwise match the bin solution quite well. The reduction in maximum surface precipitation rates for the bulk schemes relative to the bin scheme in cases STR1, STR2, and STR3 reflects the underprediction of the maximum r_h values as seen in the corresponding profiles in Figs. 4.5b,f,j, 4.6b,f,j, and 4.7b,f,j.

The results presented here for these simple 1D sedimentation tests covering a range of hail distribution types and vertical grid configurations demonstrate the superiority of the 3MHAIL scheme over both 1M and 2M sedimentation schemes. In addition, comparisons between the 1M and 2M profiles of N_{th} , r_h and Z_h in all cases concur with the general conclusions for similar 1D sedimentation tests reached by MY05a, Wacker and Lüpkes (2009), and Mansell (2010), namely that the prediction of two moments produces superior results versus the prediction of a single moment. An interesting finding from these tests is the apparent lack of excessive size sorting with the 2M sedimentation scheme when a stretched vertical grid is employed. Previous studies that showed excessive size sorting with two-moment ($M0-M3$) sedimentation were carried out on vertical grids with constant grid spacing (Wacker and Seifert 2001; MY05a; Mansell 2010; MMC10), and thus it is evident that the degree of differential sedimentation in two-moment schemes is also dependent on the vertical grid configuration.

The 3MHAIL sedimentation scheme generally tends to underpredict the maxima in the predicted quantities and overpredict values within the leading and trailing profile flanks, particularly in the stretched vertical grid cases, resulting in earlier onset of surface precipitation and reduced precipitation rates relative to the bin scheme. For the constant vertical grid spacing cases, the regions of underprediction and overprediction for the N_{ih} and Z_h profiles are in contrast to results from the 3M sedimentation (M_0 - M_3 - M_6) scheme of MMC10, who found that maxima in N_{ih} and Z_h were overpredicted, whereas underprediction of these quantities occurred within the leading and trailing profile regions. Additional tests of the 3MHAIL sedimentation scheme using constant vertical grid spacing of $\Delta z = 5$ m reveal that differences in the time-height profiles between the bulk and bin schemes are nearly eliminated (not shown), though the use of such high vertical resolution is typically not feasible in practice. For stretched vertical grids, sedimentation of individual moments using the 3MHAIL scheme match the bin solutions most closely for low ratios of vertical grid stretching and longer time step lengths. In addition, the amount of "implicit vertical diffusion" in the flanks of the N_{ih} , r_h , and Z_h profiles is reduced for decreasing stretch ratios as evident in comparisons between the 3MHAIL profiles on the stretched versus constant spacing vertical grids.

4.2) *Combined sedimentation and melting tests*

In order to examine the combined processes of sedimentation and melting, and to gauge the quality of the new melting algorithm, the three-dimensional (3D) RAMS cloud model is used to simulate the evolution of two different idealized hail shafts using the 3MHAIL and the modified 2M microphysics schemes. The modified 2M microphysics scheme used here is essentially the 3MHAIL scheme, except that the v_h values are fixed throughout the simulation and hail

reflectivity is diagnosed from the prognosed r_h and N_{th} values (as in Section 4.1). The background thermodynamic environment for these tests is that given by the temperature and dewpoint temperature profiles shown in Figure 4.9. (The sounding shown in Fig. 4.9 is that of the 29 June 2000 STEPS case and is used in Chapter 5 for verification of the 3MHAIL scheme as well as for aerosol sensitivity experiments in Chapter 6). As can be seen in Figure 4.9, the freezing level is around 3.5 km AGL (~ 590 mb), a relatively dry layer exists between roughly 2 and 3.5 km AGL, and a more moist layer lies beneath the dry layer. A stretched vertical grid identical to that for the pure sedimentation tests (Section 4.1) is employed, grid spacing of 500 m in the horizontal directions is used, and the time step length (Δt) is 4 sec.

During the first time step, hail distributions are assigned over a 'boxed' region consisting of 3 x 3 x 3 grid points in the vertical and horizontal directions, respectively, over the vertical layer from 3.73 to 4.52 km, just above the freezing level. Initial maxima of r_h , N_{th} , and D_m occur at 4.15 km within the central column of the 'box', and decrease to zero in the horizontal and vertical directions outside of the 'boxed' region. The hail distributions used here, denoted by A and B (Tables 4.2 and 4.3; Figure 4.10), are slightly modified versions of those used in the 1D sedimentation tests for cases STR3 and STR1 (Table 4.1). As in the 1 D sedimentation tests, Z_h is diagnosed from r_h , N_{th} , and the fixed v_h value using Eqn. (3.17) in the 2M cases. Because the abrupt insertion of a hydrometeor field at a single time step creates a buoyancy perturbation, the vertical winds are forced to zero every time step to omit the effects of advection, although diffusion is allowed to occur according to the model equations. Additional tests using a constant wind speed of $u = 10 \text{ m s}^{-1}$ were also performed and gave similar results (not shown).

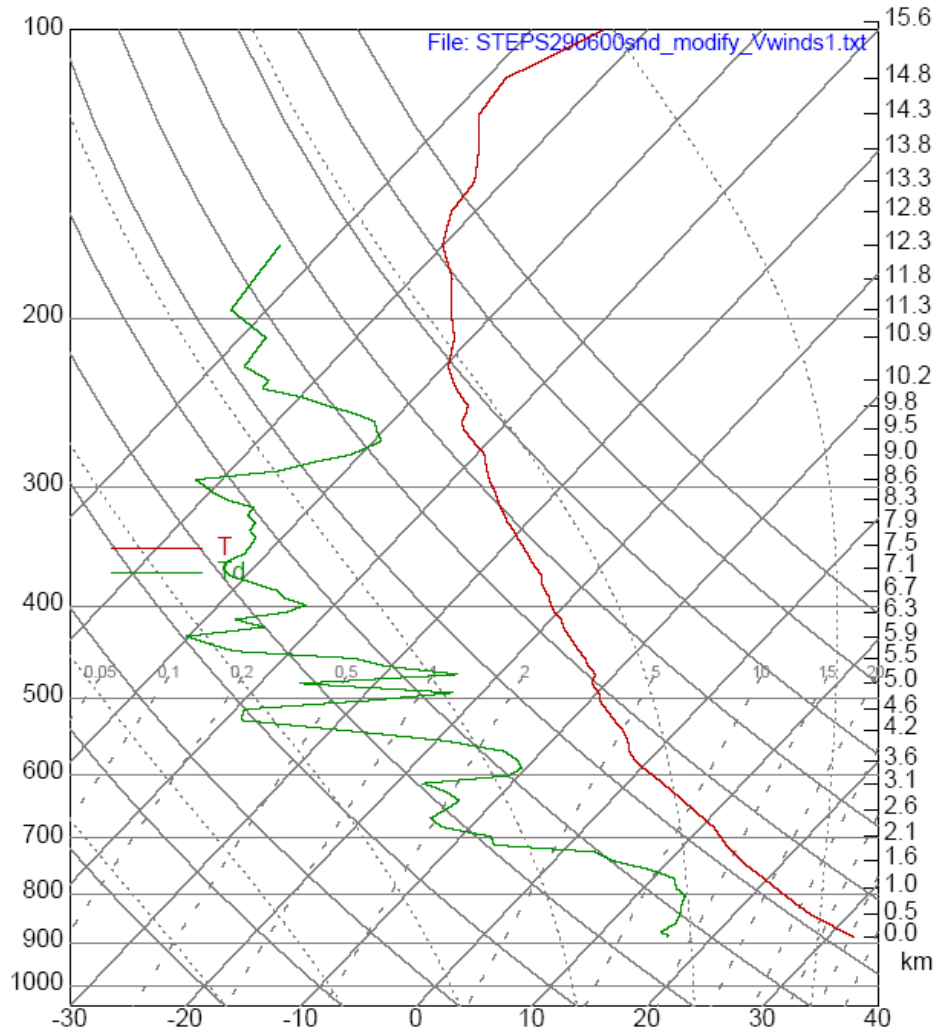


Figure 4.9: Environmental temperature and dewpoint temperature profiles used for combined sedimentation and melting tests. Sounding is for 29 June 2000 STEPS case and is derived from 2022 UTC MGLASS data near Goodland, KS up through about 14000 m, then interpolated data used above 14000m from Goodland, KS 18Z sounding. Skew- T plot made with 'skewpost' routine within the ARPS model v5.2.12.

Table 4.2: Initial distribution characteristics for combined sedimentation and melting test simulations.

Distribution	$N_{th,max}$ [m^{-3}]	$r_{h,max}$ [$g\ m^{-3}$]	v_h	$D_{\bar{m},min}$ [cm]	$D_{\bar{m},max}$ [cm]
A (STR3)	0.033	0.995	7.0	2.637	4.0
B (STR1)	174.48	0.404	2.0	0.086	0.17

Table 4.3: Combined sedimentation and melting test simulations for hail shafts A and B.

Experiment name	Description
NU2A, NU2B	modified 2M microphysics scheme, $v_h = 2.0$
NU4A, NU4B	modified 2M microphysics scheme, $v_h = 4.0$
NU7A, NU7B	modified 2M microphysics scheme, $v_h = 7.0$
3MNEWA, 3MNEWB	3MHAIL scheme with new melting algorithm (section 3.5.4)
3MOLDA, 3MOLDB	3MHAIL scheme with old melting algorithm

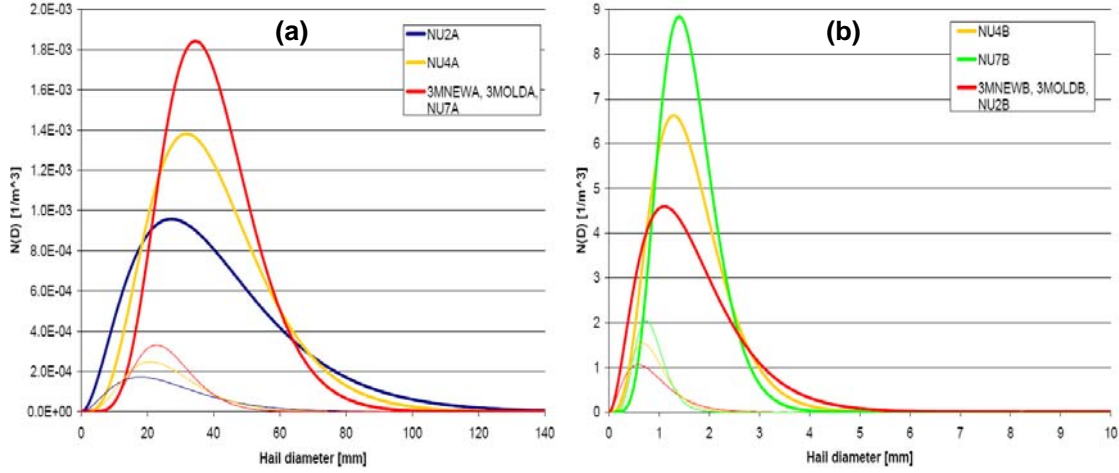


Figure 4.10: Initial hail size distributions for hail shaft A (panel a) and hail shaft B (panel b). Distributions for $D_{m,max}$ are represented by the bold lines, and distributions for $D_{m,min}$ are represented by the thin lines.

4.2.1) Hail shaft A simulations

Vertical cross-sections through the simulated hail shaft cores of the resulting hail equivalent reflectivity (Z_{he} ; Eqn. 4.1) and N_{th} fields for experiments NU2A, NU7A, and 3MNEWA are shown in Figure 4.11 for simulation times $t = 20, 60, 120, 180, 240,$ and 300 s. Similar plots for the resulting fields of r_h , rain mass mixing ratio (r_r), and number concentrations of hailstones with diameters greater than or equal to 1, 2, and 3 cm (N_{1cm} , N_{2cm} , and N_{3cm} , respectively; Eqn. 4.2) that meet or exceed a threshold of 10^{-4} m^{-3} are displayed in Figure 4.12. Vertical profiles of v_h through the central column of the hail shaft are also shown for the 3MNEWA case in Figures 4.11 and 4.12 at the selected times. In Eqn. 4.1, the ratio of the dielectric constants for ice and liquid water $|K|_i^2 / |K|_l^2 = 0.224$ (F94), and the values for the mass coefficients α_{mh} and α_{mr} for hail and rain, respectively, are given in Table 3.1 (Chapter 3.1).

$$Z_{he} = \frac{|K|_i^2}{|K|_l^2} \left(\frac{\alpha_{mh}}{\alpha_{mr}} \right)^2 Z_h \quad (4.1)$$

$$N_{D_{thresh}} = \int_{D_{thresh}}^{D_{max}} n(D) dD = \int_{D_{thresh}}^{D_{max}} N_{th}(D) f_{gam}(D) dD \quad (4.2)$$

At $t = 20$ s, the spatial distributions of N_{th} , Z_{he} (Fig. 4.11), r_h , N_{1cm} , N_{2cm} , and N_{3cm} (Fig. 4.12) are similar among the NU2A, NU7A, and 3MNEWA cases. The maximum Z_{he} magnitude at this time is found in NU2A (80.8 dBZ) compared with maximum Z_{he} values of 78.6 and 75.5 dBZ in cases 3MNEWA and NU7A, respectively, and larger values of Z_{he} are seen near the top of the hail shaft in 3MNEWA relative to NU2A and NU7A at $t = 20$ and 60 s (Fig. 4.11). Smaller Z_{he} magnitudes are expected in NU7A compared to NU2A due to the fact that $G(v_h)$ in Eqn. 3.17 decreases in value as v_h increases (see also Fig. 3.12), thus for given values of r_h and N_{th} , the computed Z_{he} value is less for larger v_h .

Between $t = 20$ and 120s, sedimentation of Z_{he} appears to occur most rapidly in NU2A (Fig. 4.11) owing to faster sedimentation of the largest r_h values in this case compared to NU7A and 3MNEWA (Fig. 4.12), similar to what was seen in the STR3 1D sedimentation case (Fig. 4.7). Sedimentation of Z_{he} in NU7A also seems to proceed more quickly than in 3MNEWA during this time period, though this can be attributed to faster sedimentation of N_{th} in NU7A relative to 3MNEWA (Fig. 4.11) as the evolution of the r_h fields for these two cases is largely similar (Fig. 4.12). Above roughly 3.5 km (below ~ 1 km), sedimentation of N_{th} generally proceeds slower (faster) in NU2A relative to NU7A (and to a lesser extent, 3MNEWA) owing to the more numerous small (large) hailstones associated with the initially broader size distributions within the NU2A hail shaft (Fig. 4.10a). Size sorting is clearly evident in all three cases through $t = 180$ s as seen in the increasing separation of the regions of N_{1cm} , N_{2cm} , and N_{3cm} with time (Fig. 4.12), though as expected, this process appears to occur more rapidly in NU2A compared to both NU7A and 3MNEWA. The increase in the fixed v_h value from 2 in NU2A to 7 in NU7A results in a reduction in the degree of size sorting, in general agreement with findings by MY05a and Mansell (2010). The evolution of the r_h fields and the N_{1cm} , N_{2cm} , and N_{3cm} regions are

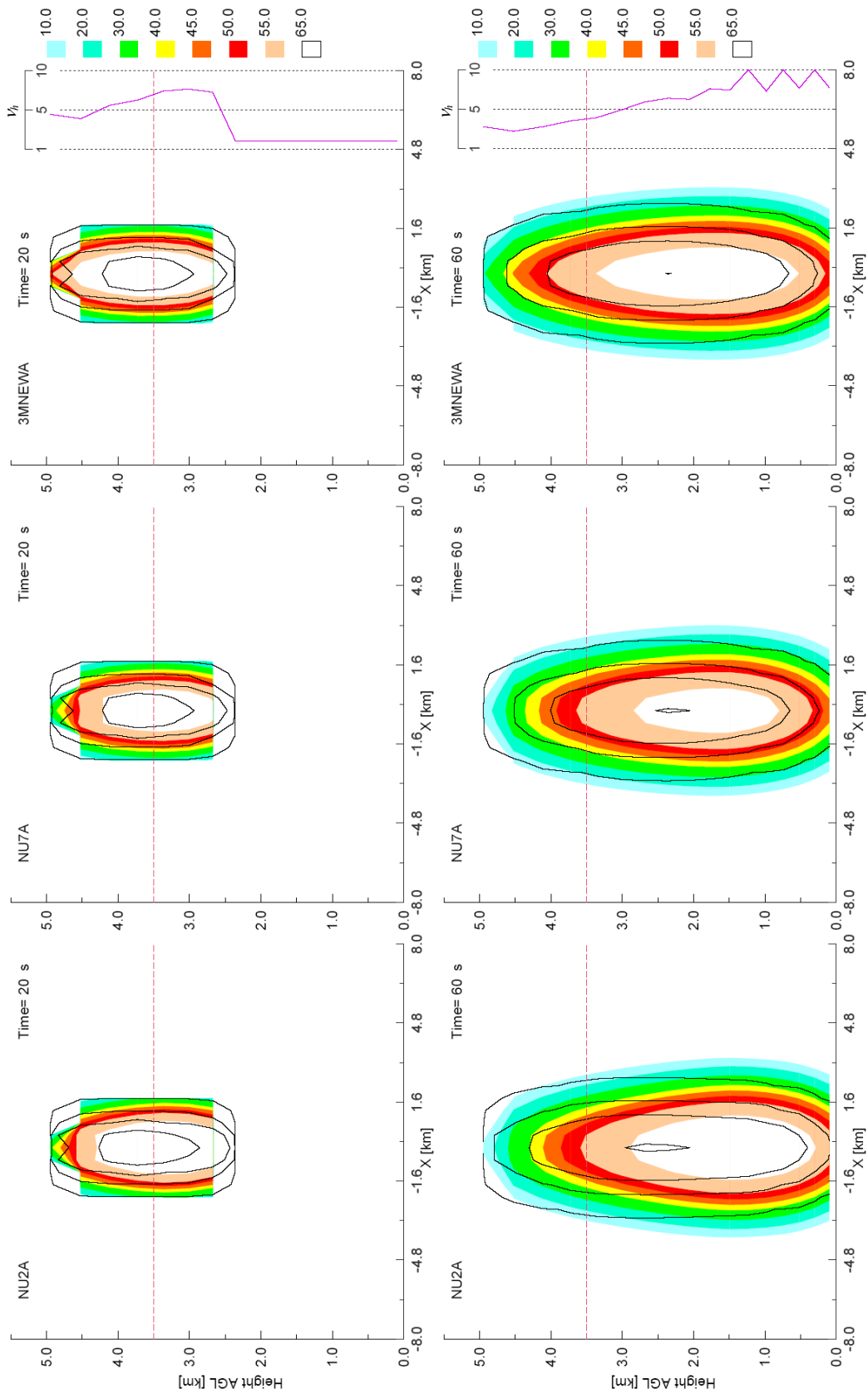


Figure 4.11: Vertical cross-sections through the hail core of hail shaft A showing equivalent hail reflectivity Z_{he} (shaded, dBZ) and hail number concentrations (black contours; values are $10^6, 10^4, 10^3, 10^2 \text{ m}^{-3}$) for the NU2A (left column), NU7A (middle column), and 3MNEWA (right column). Instantaneous vertical profiles of V_h through hail shaft axis are also plotted for 3MNEWA. Simulation times are labeled for each panel, and the red dashed line in each panel depicts approximate location of 0 °C isotherm.

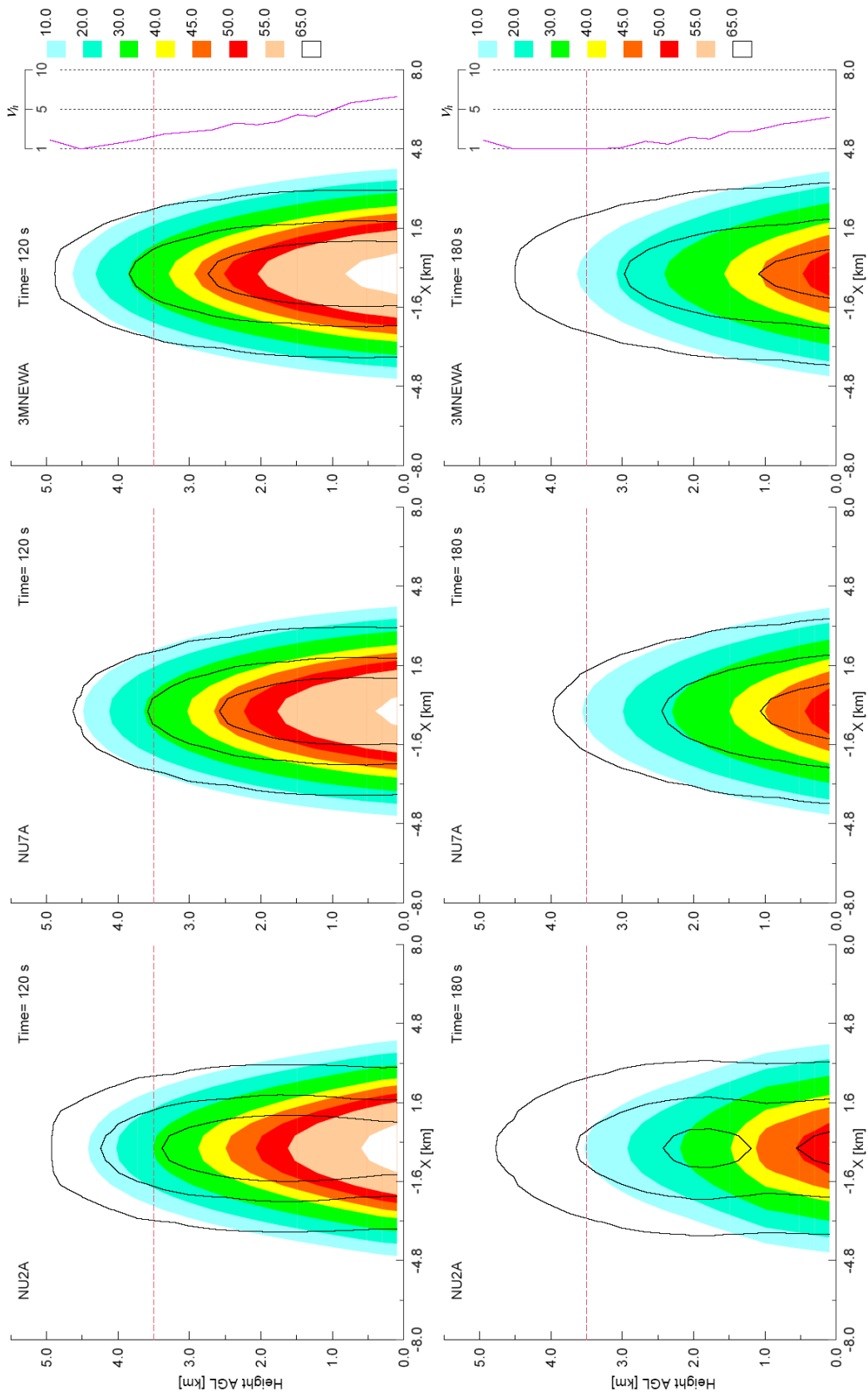


Figure 4.11: (continued)

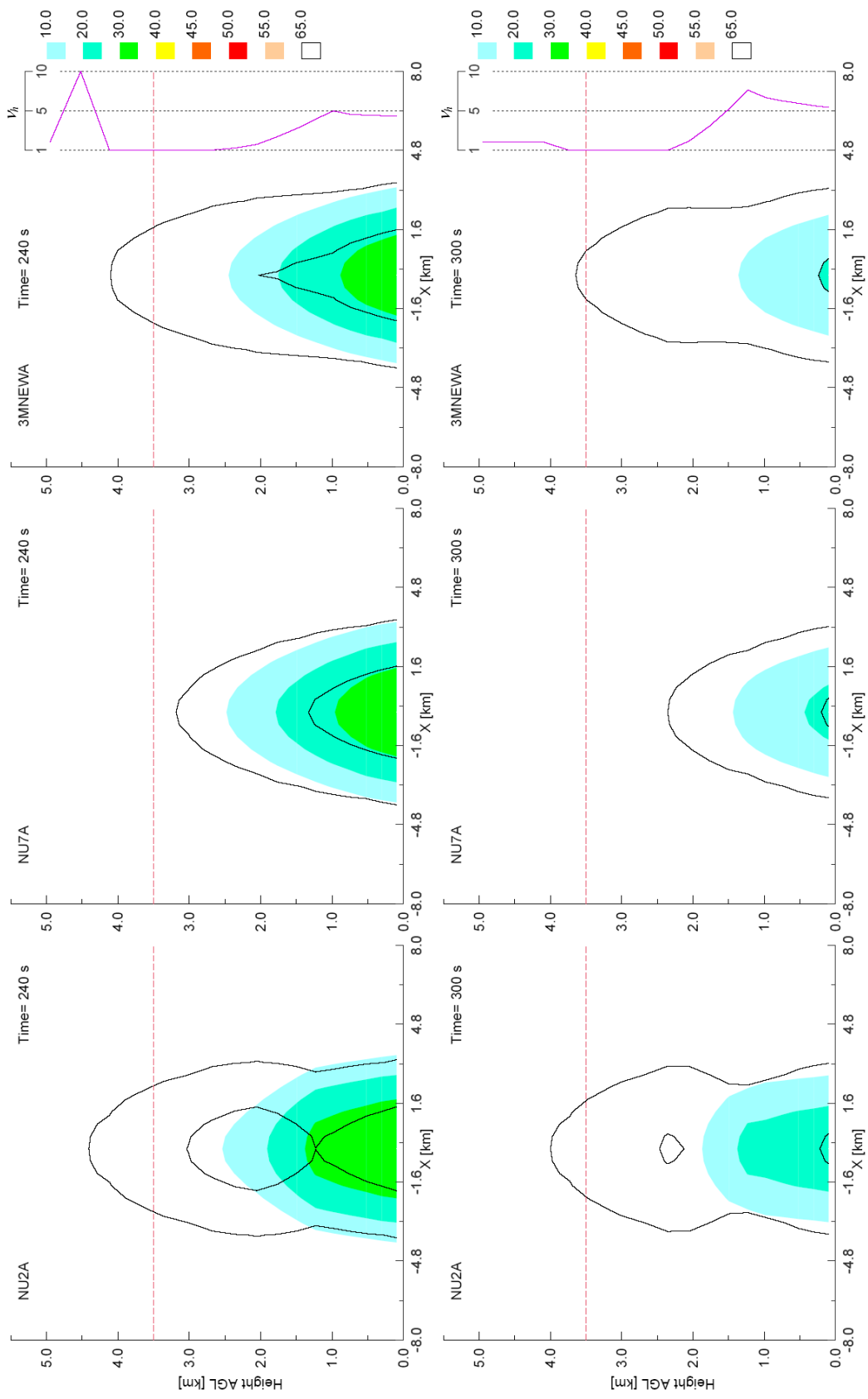


Figure 4.11: (continued)

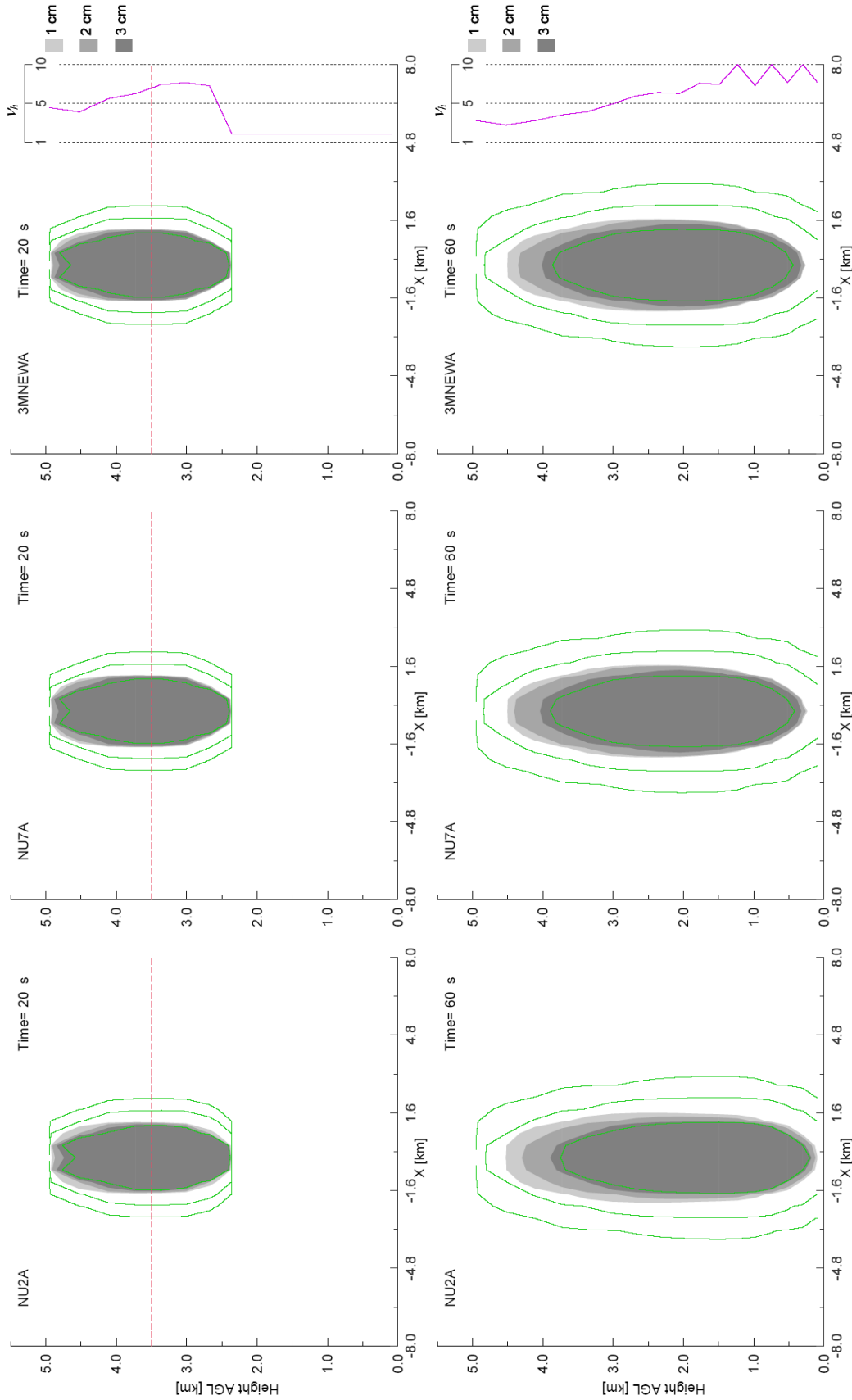


Figure 4.12: Vertical cross-sections through the hail core of hail shaft A showing hail (green contours) and rain (blue contours) mass mixing ratios [10^{-9} , 10^{-7} , 10^{-5} kg m^{-3}] and regions where the number concentrations of hailstones with diameters greater than 1, 2, and 3 cm exceed 10^4 m^{-3} (shaded) for the NU2A (left column), NU7A (middle column), and 3MNEWA (right column). Instantaneous vertical profiles of $v_{1/2}$ through hail shaft axis are also plotted for 3MNEWA. Simulation times are labeled for each panel, and the red dashed line in each panel depicts approximate location of 0°C isotherm.

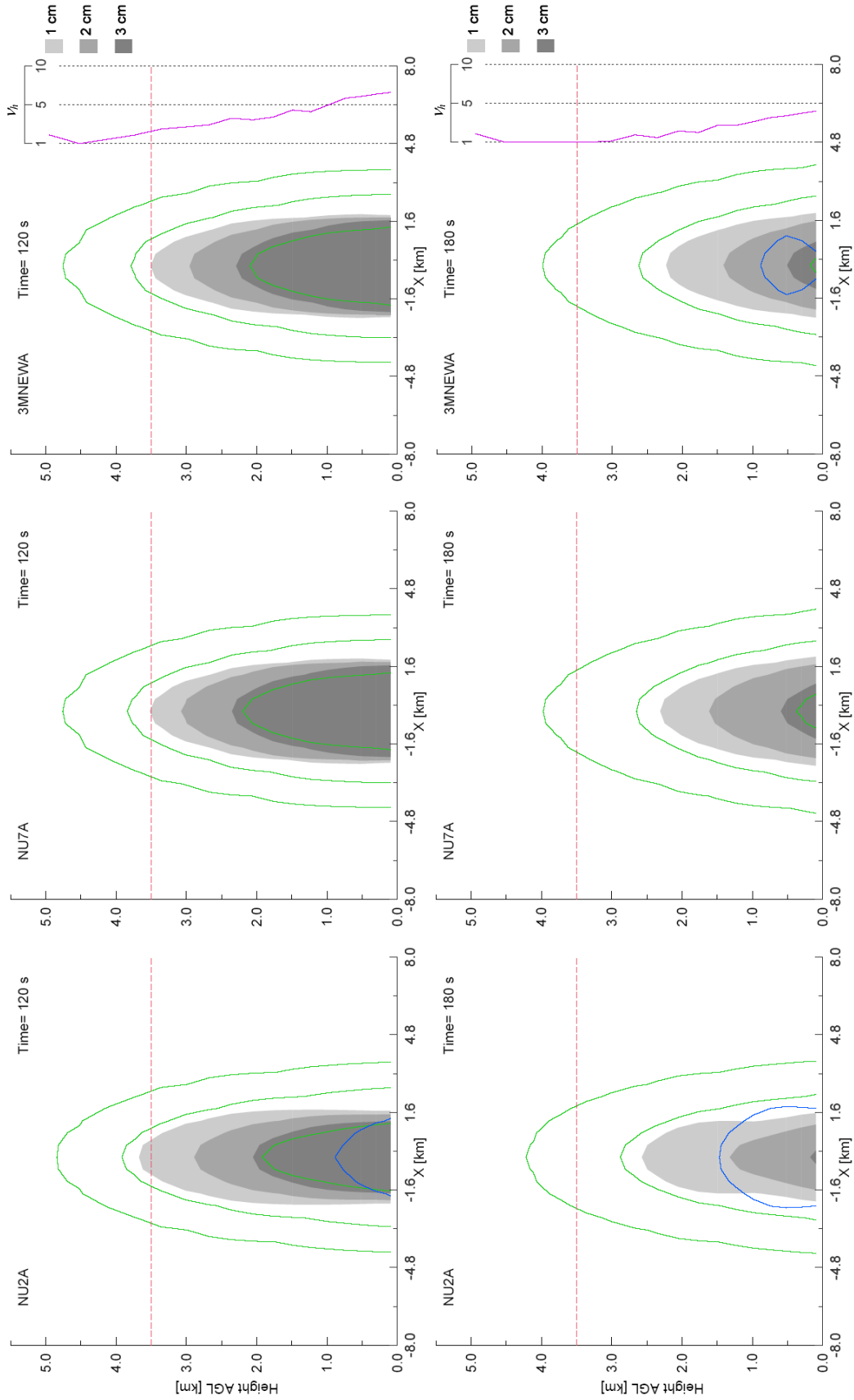


Figure 4.12: (continued)

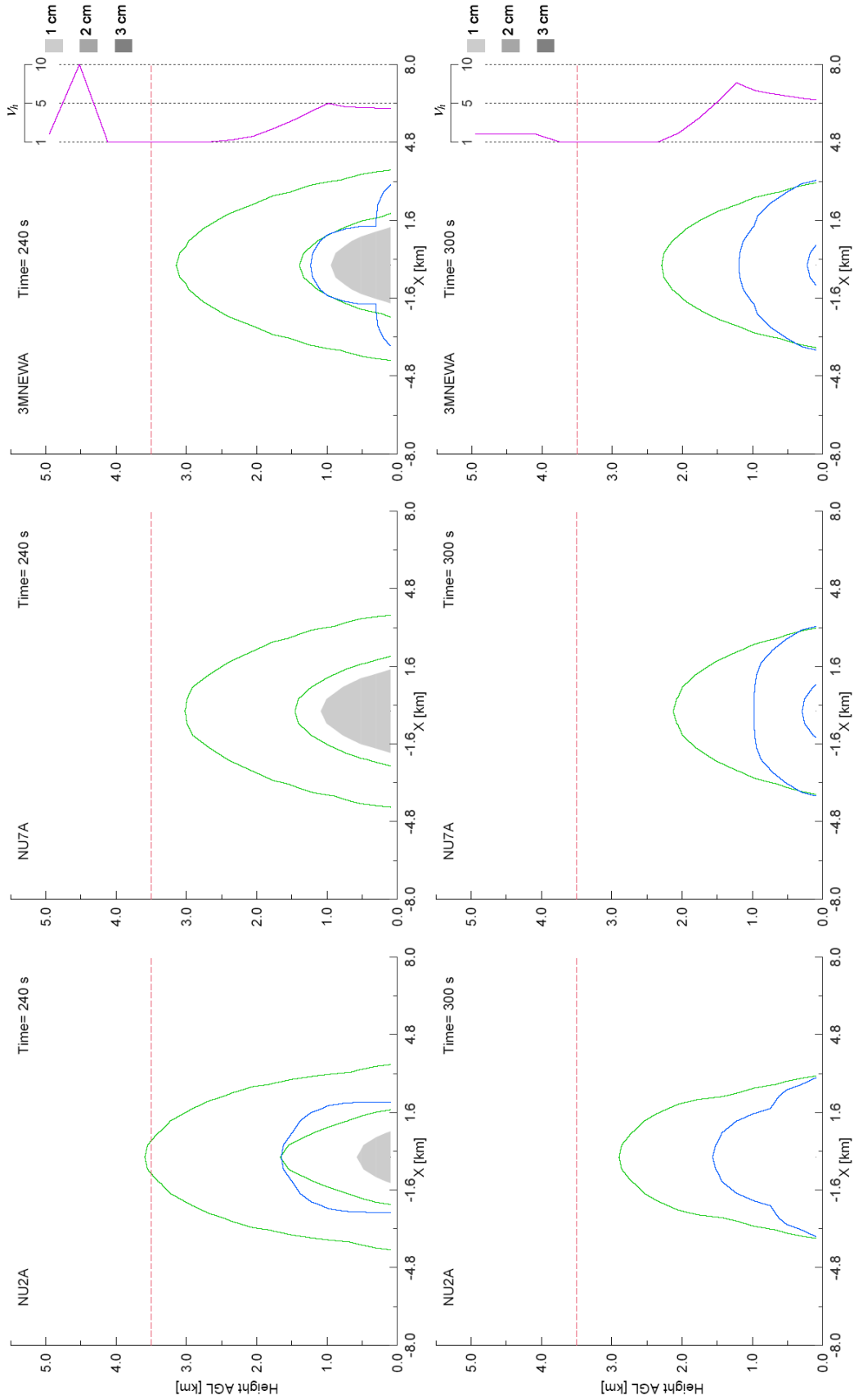


Figure 4.12: (continued)

approximately similar in NU7A and 3MNEWA (Fig. 4.12) which is somewhat unexpected given the general broadening (decreasing v_h values) of the hail size distributions in 3MNEWA, as well as the reduced amounts of melting in NU7A relative to 3MNEWA (Figs. 4.14 and 4.15) during this time period.

An examination of the vertical v_h profiles for 3MNEWA at the selected times (Figs. 4.11 and 4.12) reveals an initial narrowing of the hail size distributions (v_h values increase) at $t = 60$ s along the leading edge of the descending hail shaft (below ~ 2 km) associated with the fallout of the largest particles, and a broadening of the size distributions above about 2.5 km. Mansell (2010) noted a similar evolution in v for a descending graupel shaft in simulations of deep moist convection with three-moment microphysics. The size distributions then broaden (v_h values decrease) over the depth of the hail shaft through $t = 180$ s, though the general trend of broad size distributions aloft (above ~ 2 km) and increasing v_h values with decreasing height below roughly 2 km is maintained as the smallest hail particles begin to melt completely to rain between roughly $t = 60$ and 120 s (Figs. 4.14a, 4.15a). By $t = 180$ s, a significant amount of complete melting is occurring (Figs. 4.14a, 4.15a), and beyond this time, the hail size distributions narrow once again at lower levels due to losses of relatively large numbers of smaller particles, similar to findings by Giajotti et al. (2001) and Fraile et al. (2003). In general, the decrease in v_h values aloft results in slower sedimentation of N_{th} at these levels, such that the N_{th} contours in this case tend to be more similar to those in NU2A, whereas below ~ 2 km, the N_{th} contours in 3MNEWA evolve more closely to those in NU7A (Fig. 4.11). A similar trend becomes evident in the r_h fields at later times ($t = 240$ and 300 s) (Fig. 4.12), though not as clearly as in the N_{th} fields. The changes in the vertical v_h profile with time in 3MNEWA highlight the effects of sedimentation as

well as melting on v_h , and vice versa, which has a large impact on the production of rain from melting hail as discussed later.

Figure 4.13 shows time-height plots of $D_{\bar{m}h,\max}$ at each vertical level as well as regions where the fractional amounts of completely melted hailstones exceed 1% of the instantaneous N_{th} values for the hail shaft A simulations. In each panel, the largest $D_{\bar{m}h,\max}$ values are seen to reach the surface first in time, followed by increasingly smaller $D_{\bar{m}h,\max}$ values, and the magnitudes of $D_{\bar{m}h,\max}$ arriving at the surface are largely similar in time among all of the simulations up through roughly $t = 180$ s. On the other hand, differences are evident in the vertical distributions of $D_{\bar{m}h,\max}$ above ~ 2 km during this time period. For example, $D_{\bar{m}h,\max}$ decreases from 37 mm at $t = 20$ s to about 9 mm at 120 s at 3.5 km in NU2A (Fig. 4.13b), whereas decreases from 37 to 12.5 mm occur in both NEW3MA (Fig. 4.13a) and OLD3MA (Fig. 4.13e), and decreases from 37 to 13.5 mm and from 37 to about 18 mm occur in NU4A (Fig. 4.13c) and NU7A (Fig. 4.13d), respectively, during the same time period. Thus, it is apparent that for this particular set of simulations, the more rapid sedimentation of r_h (N_{th}) with smaller (larger) v_h values leads to $D_{\bar{m}h,\max}$ values that decrease faster (slower) with time at a given height prior to the onset of complete melting.

Interestingly, once complete melting of hail begins, the time-height contours of $D_{\bar{m}h,\max}$ begin to flatten indicating a reduction in the rates of decrease in $D_{\bar{m}h}$ at levels within the melting region. In NU2A (Fig. 4.13b) and OLD3MA (Fig. 4.13e), complete melting actually leads to instances in which the values of $D_{\bar{m}h,\max}$ (and $D_{\bar{m}h}$ in general) at certain heights remain constant or nearly constant in time even though hail mass is continuously decreasing at these heights via sedimentation (e.g., Fig. 4.12). An analysis of the ratios $\Delta r_h / \Delta N_{th}$ due to complete melting (not

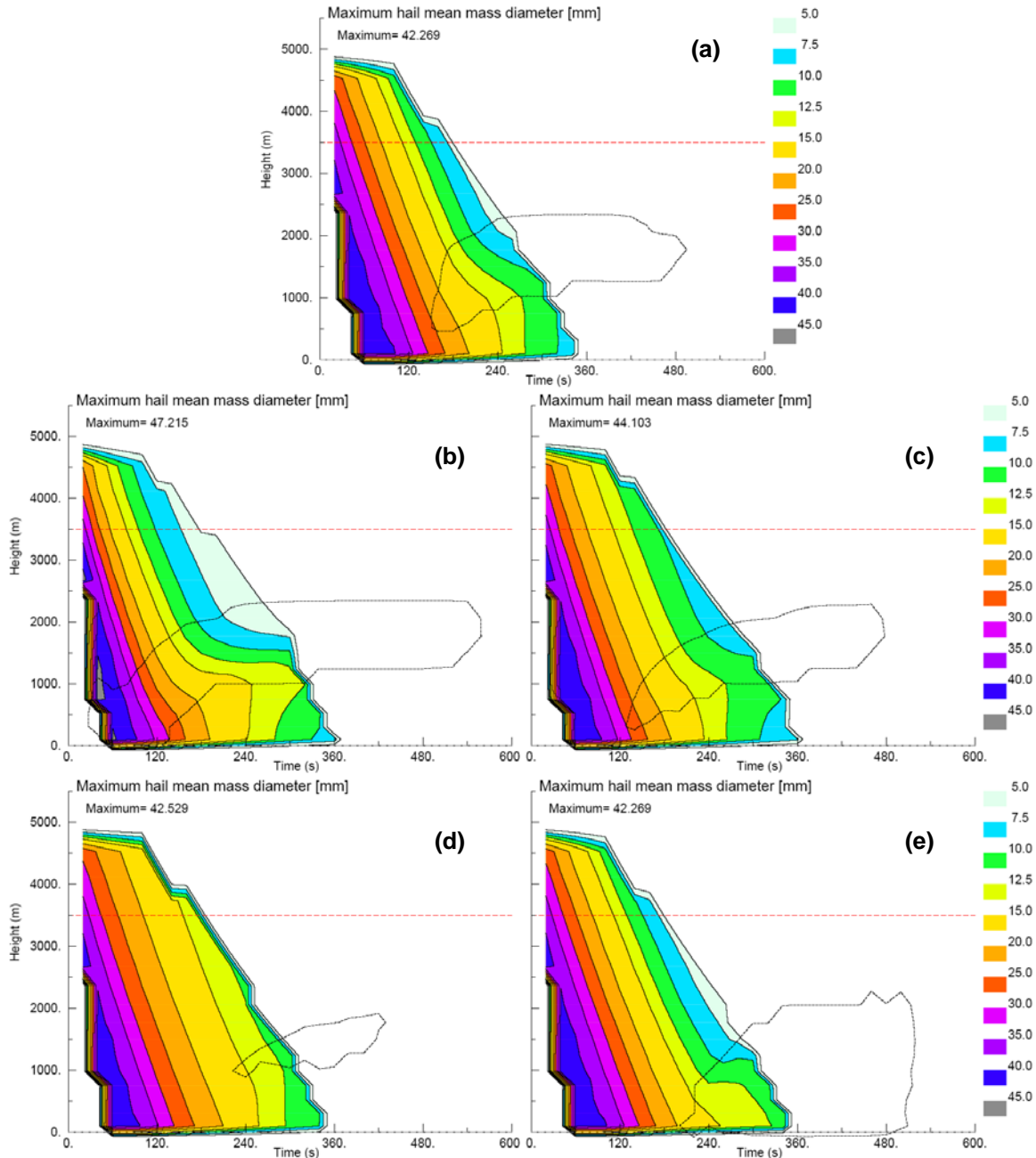


Figure 4.13: Time-height plots of maximum mean mass hail diameter D_{mh} (computed where $r_h \geq 10^{-8} \text{ kg kg}^{-1}$) at each vertical level for (a) 3MNEWA, (b) NU2A, (c) NU4A, (d) NU7A, and (e) OLD3MA. Dotted lines in each panel depict regions where the fractional amounts of completely melted hailstones exceed 1% of the instantaneous total hail number concentrations.

shown) reveals that these ratios are greater than 1.0 in all cases (i.e., losses of number occur faster than losses of mass), which can lead to D_{mh} values that increase with decreasing height as in NU2A and OLD3MA. This result is purely numerical as there is no growth mechanism for

hail in these simulations (the amount of rain mass collected by hail is negligible) and highlights the problem of using $D_{\bar{m}}$ as a direct measure of hydrometeor sizes as is often done in many studies. Additional runs in which complete melting was omitted revealed a steady and more rapid decrease in to $D_{\bar{m},\max}$ values with time for all cases (not shown) thereby proving that the reductions in the rates of decrease in $D_{\bar{m}h}$ at levels within the melting region are in fact due to complete melting.

Small amounts of rain (r_r of $O(10^{-9})$ kg m^{-3}) from completely melted hail first appear below 1 km around $t = 120$ s in NU2A and by $t = 180$ s in NEW3MA (Fig. 4.12). Rain does not appear in NU7A until after $t = 240$ s (Fig. 4.12), corresponding to the onset of shedding in this case (Fig. 4.16d). Owing to the rapid sedimentation of r_h in NU2A (Fig. 4.12), complete melting of hail commences shortly after initialization and is well under way by $t = 60$ s (Figs. 4.14b, 4.15b), whereas the onset of complete melting is increasingly delayed and total melting decreases in the 2M cases as v_h increases to 4 (Figs. 4.14c, 4.15c) and 7 (Figs. 4.14d, 4.15d). Complete melting in 3MNEWA (Figs. 4.14a, 4.15a) is also delayed relative to NU2A owing to the narrower size distributions comprised of mainly larger hailstones below ~ 2 km, and complete melting does not begin in 3MOLDA until around $t = 200$ s (Figs. 4.14e, 4.15e), concurrent with the onset of shedding in this case (Fig. 4.16e). The reason for such a long delay for the onset of melting in 3MOLDA relative to the other cases is due to the requirement that the bulk hail LWF values exceed 0.3 in the melting/shedding algorithm used in 3MOLDA (Section 3.5.1, Appendix A). In contrast, the new melting scheme (section 3.5.2) used in all of the other cases allows for complete melting of the smallest hailstones at bulk hail LWF values > 0.0 . By $t = 300$ s, the amounts of rain mass mixing ratio over the lowest km are larger in the NU7A and 3MNEWA

cases compared to NU2A (Fig. 4.12) owing to greater amounts of liquid shed from hail in the former cases (Figs. 4.16a and 4.16d, respectively) relative to the latter (Fig. 4.16b).

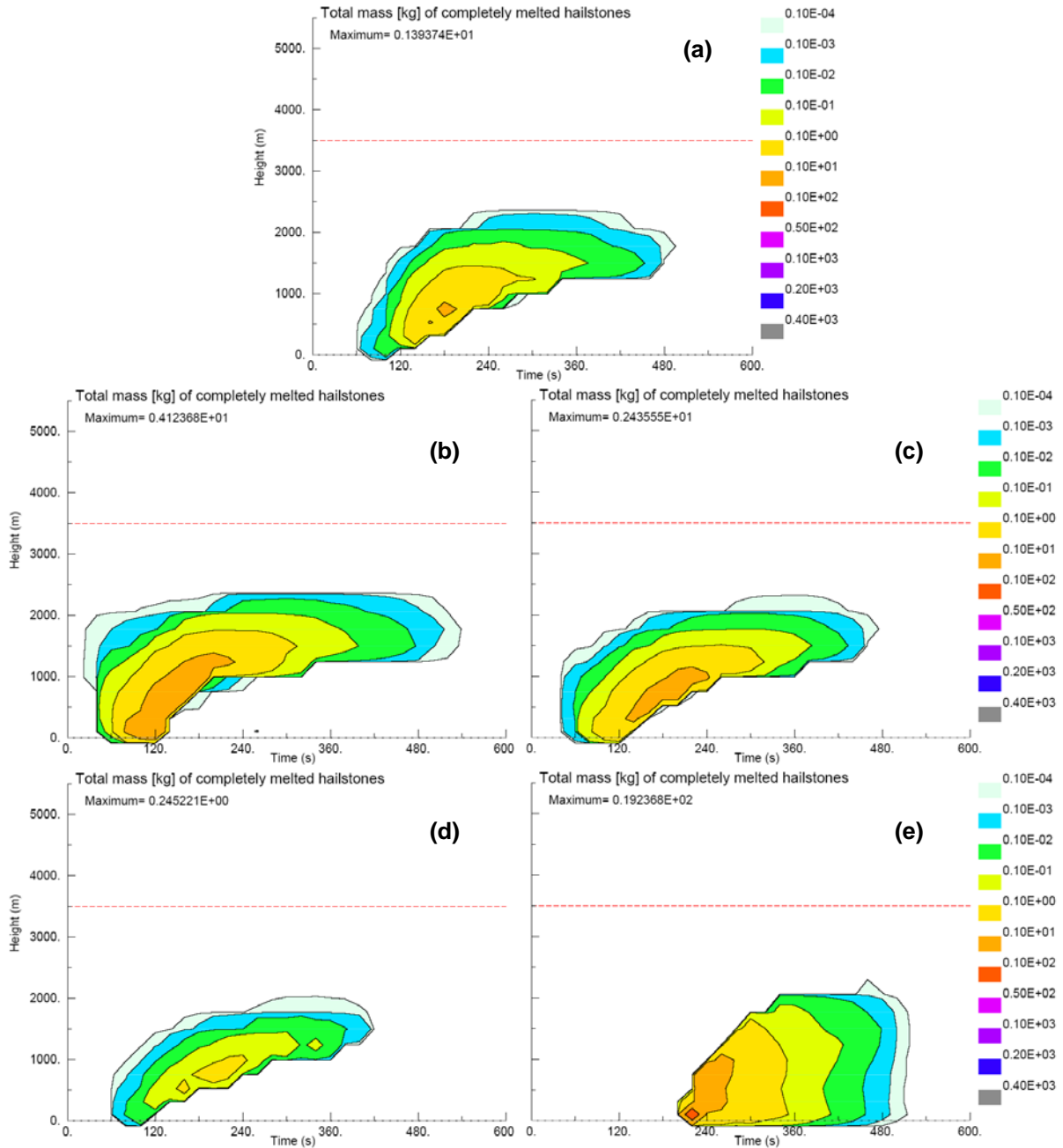


Figure 4.14: Time-height plots of total mass [kg] of completely melted hailstones at each vertical level for (a) 3MNEWA, (b) NU2A, (c) NU4A, (d) NU7A, and (e) OLD3MA.

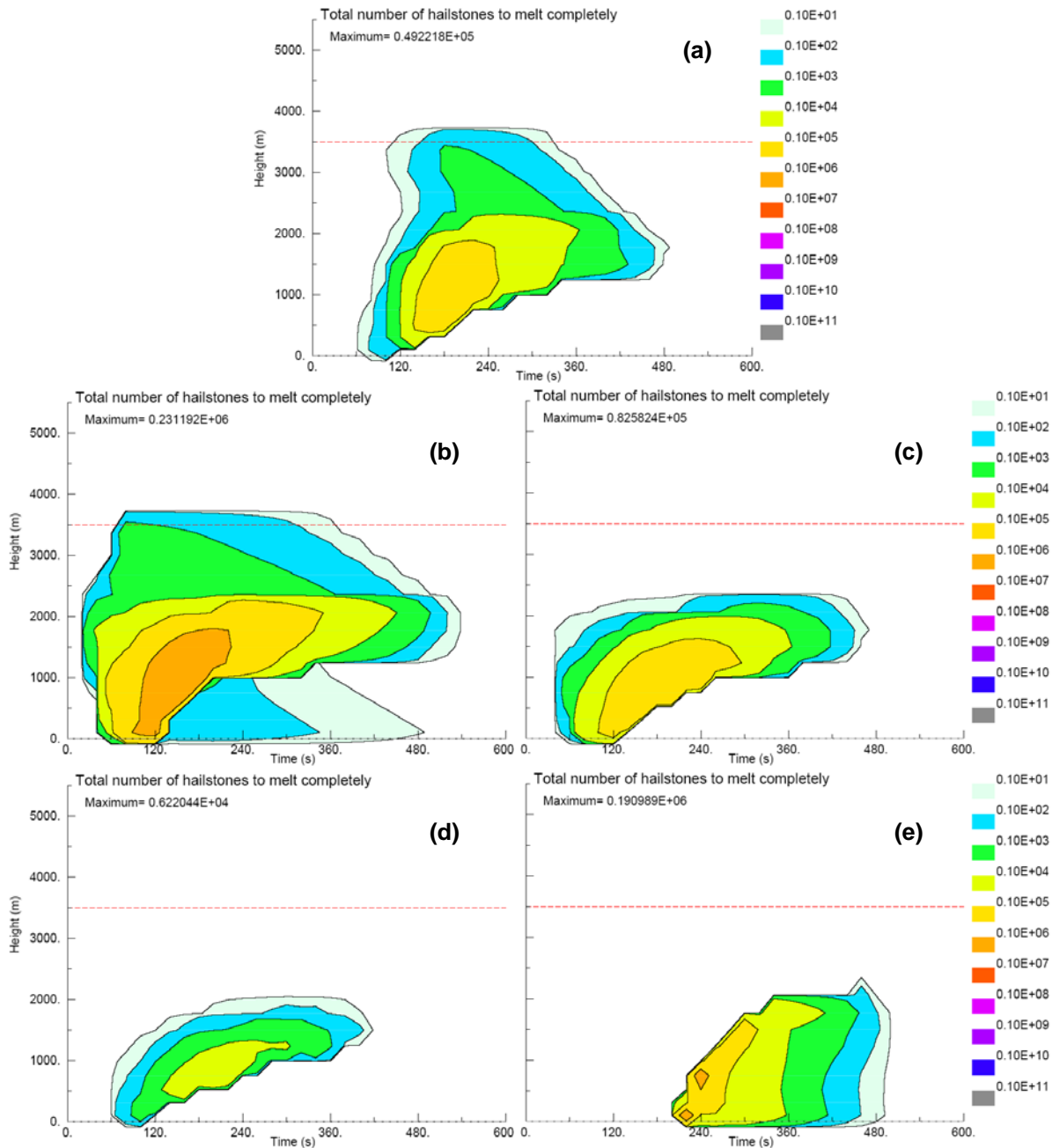


Figure 4.15: Time-height plots of total numbers of completely melted hailstones at each vertical level for (a) 3MNEWA, (b) NU2A, (c) NU4A, (d) NU7A, and (e) OLD3MA.

An examination of the time-height plots of total hail mass and numbers to completely melt (Figs. 4.14 and 4.15) for the hail shaft A cases reveals other interesting features. In general, the regions of complete melting in 3MNEWA and the 2M cases initiate near the surface, followed by increases in melting magnitudes and an upward shift of the melting regions, and finally the

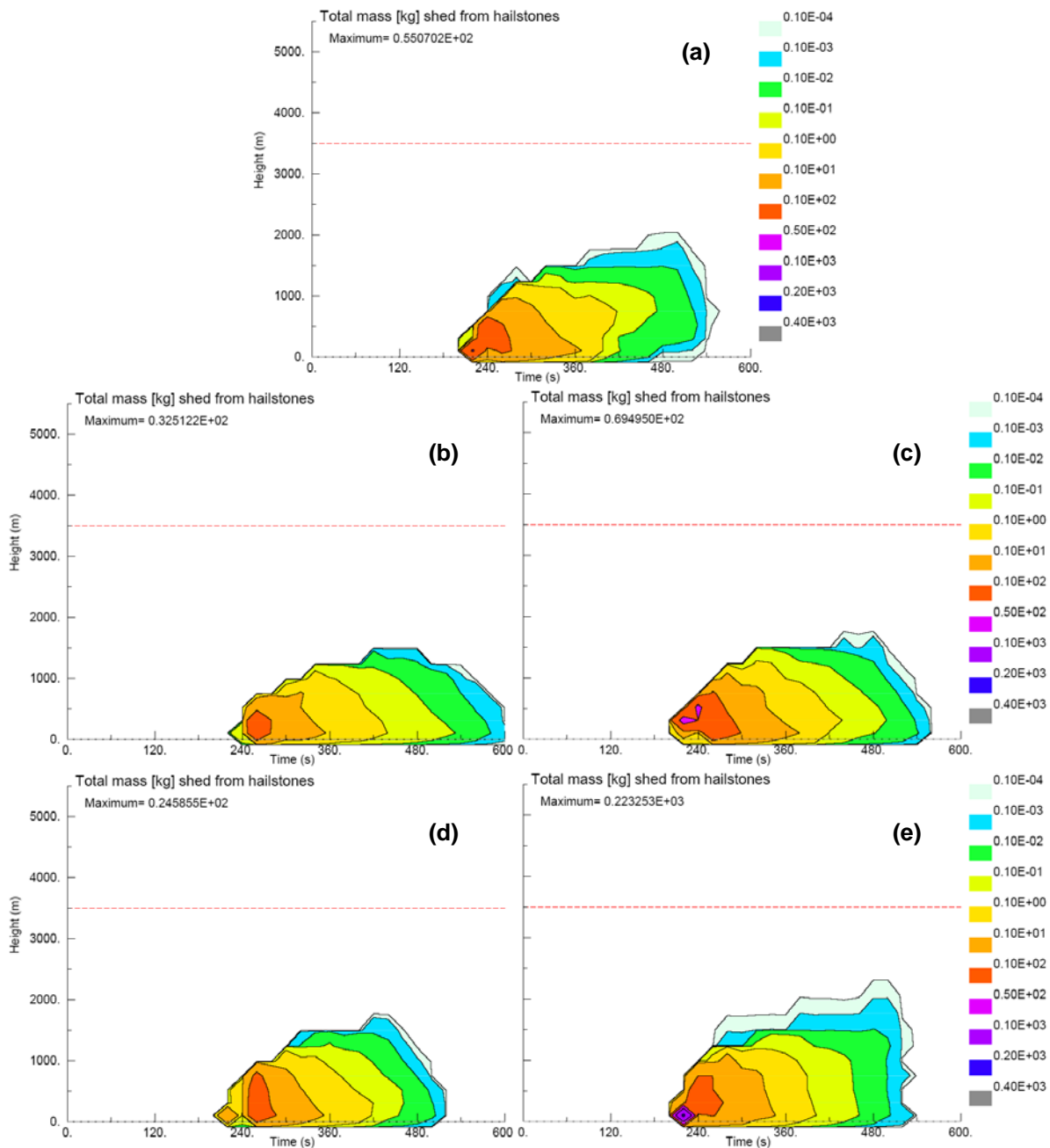


Figure 4.16: Time-height plots of total mass [kg] shed from hailstones at each vertical level for (a) 3MNEWA, (b) NU2A, (c) NU4A, (d) NU7A, and (e) OLD3MA.

magnitudes of melting decrease. The upwards shifts of the melting regions with time are associated with the more rapid melting of increasingly smaller hail particles, such that only the relatively larger hailstones remain below this region. In addition, the elevated melting regions are located within a layer containing higher relative humidity values (Fig. 4.9), which tend to hasten

the melting process (RH87b; Srivastava 1987). On the other hand, the evolution of melting in 3MOLDA is markedly different from the other cases, with the maximum losses of mass (Fig. 4.14e) and numbers (Fig. 4.15e) occurring at the onset of complete melting, followed by an expansion of the melting region upwards and a decrease in melting magnitudes. Due to the fact that hailstones larger than 5 mm in diameter can melt completely in one Δt in 3MOLDA (Fig. 4.17b), complete melting continues to occur all the way down to the surface in 3MOLDA, even at later times, rather than becoming confined to an elevated region as in the other cases. As seen in Figure 4.17b, $D_{max,melt}$ values in 3MOLDA are mostly between 6 and 8 mm, and values larger than 9 mm begin to appear after $t = 360$ s. While complete melting of 6 and 7 mm diameter hail particles in one Δt (4 s) is physically plausible provided these particles contain a significant amount of melted liquid, the increase in $D_{max,melt}$ values with time in 3MOLDA is unrealistic as sedimentation and melting processes continuously shift the hail size distributions towards smaller sizes. This clearly highlights the aforementioned problem of too much melting with the original melting algorithm (Appendix A). The evolution of the spatial pattern of total melted mass in 3MNEWA (Fig. 4.14a) resembles that of NU7A (Fig. 4.14d) early on ($t < 120$ s), but

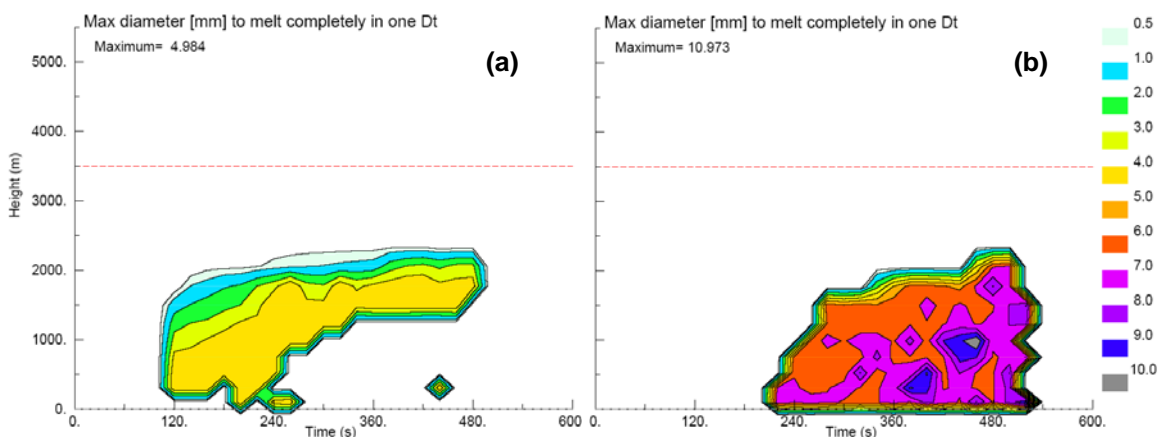


Figure 4.17: Time-height contours of maximum hail diameter [$D_{max,melt}$, mm] to melt completely in one time step in hail shaft A simulations for a) 3MNEWA and b) 3MOLDA.

becomes more similar to NU4A (Fig. 4.14c) and NU2A (Fig. 4.14b) as time progresses.

Likewise, the time-height pattern of total numbers of completely melted hailstones in 3MNEWA (Fig. 4.15a) shares similar features with each of the three 2M cases, such as losses in number above ~ 2 km in NU2A (Fig. 4.15b), and a melting pattern that resembles a combination of those displayed for NU4A (Fig. 4.15c) and NU7A (Fig. 4.15d) below ~ 2 km. Thus, it is evident that by allowing ν_h to vary as in 3MNEWA, the combined effects of sedimentation and melting are much better represented in these simulations versus the use of a fixed value for ν_h .

Time series of surface accumulated values and precipitation rates for hail and rain are displayed in Figure 4.18 for the hail shaft A cases. Hail first reaches the surface by 60 s in NU2A and by 80 s in all other cases (panels c and e), a peak in the surface hail precipitation rate is attained around 120 s (slightly earlier in NU2A) (panel e), and surface hailfall ends around 240 s (panel e). The maximum amount of accumulated hail at the surface (panel a) is largest in NU2A (0.3 kg m^{-2}), NU4A has the next highest amount (0.28 kg m^{-2}), and NU7A, 3MNEWA, and 3MOLDA have the smallest, though nearly identical amounts (0.27 kg m^{-2}). A similar trend is observed in the maximum hail precipitation rate (panel e) in which NU2A attains the greatest rate of nearly 20 mm hr^{-1} , whereas slightly smaller peak rates of 19 and 17.3 mm hr^{-1} are reached by NU4A and NU7A, respectively. Peak hail precipitation rates of 18 mm hr^{-1} are produced by both of the 3M cases (panel e). Total accumulated hail mass at the surface (panel c) is similar in all cases and ranges from about 823,500 kg in NU2A to 818,200 kg in 3MOLDA (Table 4.4). Thus, for the particular initial hail distributions in this set of simulations, it appears an increase in ν_h is associated with a decrease in accumulated hail mass at a given surface location as well as a decrease in peak hail precipitation rate, similar to findings of MY05a. Total hail mass reaching the surface seems to be only weakly dependent on the value of ν_h for these cases.

Table 4.4: Total accumulated masses at surface at $t = 600$ s for hail shaft A simulations.

Experiment name	Total accumulated hail mass at surface [kg]	Total accumulated rain mass at surface [kg]	Total precipitation mass at surface [kg]
NU2A	823493	760.2	824253.2
NU4A	819798	1911.2	821709.2
NU7A	818778	1376.3	820154.3
3MNEWA	818471	1187.8	819658.8
3MOLDA	818204	1424.9	819628.9

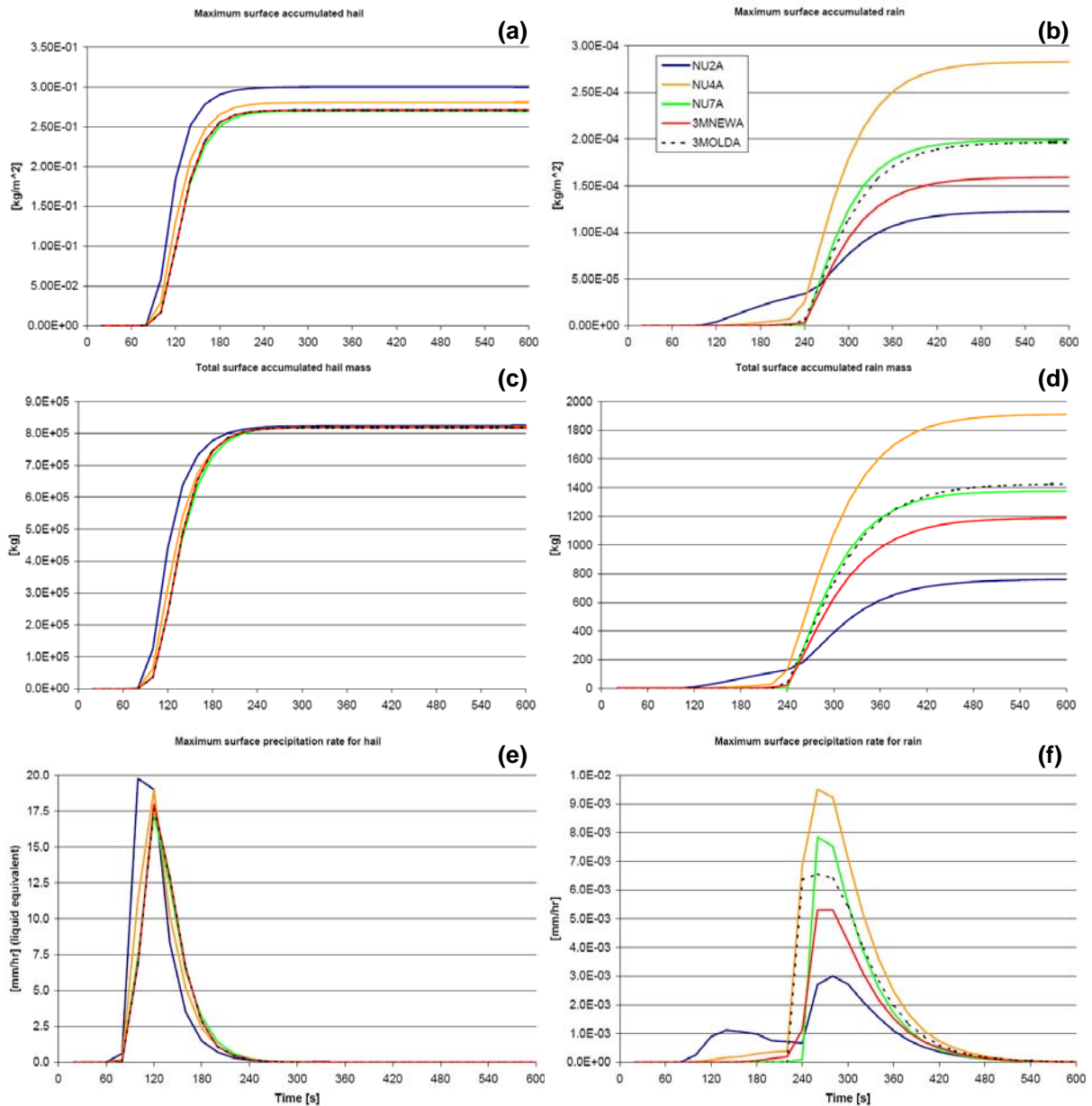


Figure 4.18: Time series of maximum accumulated amounts $[\text{kg m}^{-2}]$ at a single grid point at the surface (top row), total surface accumulated mass $[\text{kg}]$ (middle row), and maximum surface precipitation rates $[\text{mm hr}^{-1}]$ (bottom row) of hail (left column) and rain (right column) for the hail shaft A simulations.

Differences in the time series of the surface rain characteristics (panels b, d, and f in Fig. 4.18) are much more stark than those for hail. Rainfall reaches the surface first in NU2A around $t = 80$ s, around $t = 120$ s in NU4A, and by 240 s in NU7A (panels b and f). This delay in the onset of surface rainfall as the fixed v_h values increase from 2 to 4 to 7 corresponds to the increasing time lag for complete melting of hail to commence as well as the reduced melting magnitudes as v_h increases (Figs. 4.14b,c,d and 4.15b,c,d). However, it should be noted that the appearance of surface rainfall in NU7A is better correlated with the onset of shedding (around $t = 200$ s in Fig. 4.16d). Likewise, rainfall arrives at the surface earlier in 3MNEWA (by $t = 120$ s) than in 3MOLDA (by $t = 210$ s) (Fig. 4.18f) owing to the much earlier onset of complete melting in 3MNEWA (Figs. 4.14a, 4.15a), whereas complete melting and shedding commence simultaneously in 3MOLDA (Figs. 4.14e, 4.16e). The rapid increases in surface rain rates between $t = 200$ and 240 s in all cases (Fig. 4.18f) correspond to the onset of shedding, which is maximized shortly after commencing (Fig. 4.16) and generates rain mass values that are roughly an order of magnitude larger than those produced by complete melting in all cases (Fig. 4.14). The time periods during which both rapid increases in surface accumulated rain amounts (Figs. 4.18b,d) and peaks in maximum rain rates (Fig. 4.18f) occur are also consistent with shedding, as are the leveling off of accumulated amounts and steady decreases in maximum rain rates. This strongly implies that the surface rainfall characteristics in this set of simulations are primarily dependent on the shedding process, which makes physical sense as the majority of the hailstones have diameters greater than 9 mm (Fig. 4.10a), the threshold diameter for shedding (Rasmussen et al. 1984). The exception is NU2A, which, prior to the start of shedding ($\sim t = 240$ s), exhibits a slow increase in surface accumulated rain amounts (Fig. 4.18b,d) and an initial peak in

maximum rain rate around $t = 160$ s (Fig. 4.18f) due to enhanced melting that commences earlier compared to all other cases (Fig. 4.14).

The greatest values for maximum accumulated rain (Fig. 4.18b), total accumulated rain mass (Fig. 4.18d; Table 4.4), and maximum rain rate (Fig. 4.18f) are produced by NU4A. As surface rainfall is intimately linked with shedding in these simulations, an examination of Figure 4.16 reveals that NU4A produces the greatest amount of shed mass over time within the lowest 1 km as evident by the area encompassed by the 10 and 50 kg contours (Fig. 4.16c). These greater magnitudes of shedding are attributable to larger r_h values (i.e., more mass available for shedding) in addition to slightly higher bulk LWF values over the lowest kilometer compared to the other cases (not shown). On the other hand, cases NU7A (Fig. 4.16d), 3MOLDA (Fig. 4.16e) and 3MNEWA (Fig. 4.16a) exhibit smaller quantities of shed mass than in NU4A, and therefore have smaller values of accumulated rain (Fig. 4.18b,d) and peak rain rates (Fig.4.18f). (Note that while the maximum amount of shed mass (223.25 kg) occurs in 3MOLDA (Fig. 4.16e), this is limited to a single horizontal level at a single point in time, thus the maximum rain rate at a given surface location for this case is still not greater than for NU4A). The least amount of rain at the surface and the smallest rain rates occurs in NU2A due to a greater amount of precipitation arriving at the surface as hail (Fig. 4.18e) as well as this case having the lowest values of shed mass (Fig. 4.16b). Amounts of accumulated rain at the surface and peak rain rates are greater in 3MOLDA compared to 3MNEWA, though this is due to excessive melting and shedding in 3MOLDA as previously mentioned. In general, there does not appear to be a clear relationship between the value of ν_h and surface rainfall for the 2M cases, although the evolution of rainfall in these simulations is clearly sensitive to the value of ν_h . This undoubtedly lends support to the use of a variable ν_h as in the 3MHAIL scheme.

4.2.2) Hail shaft B simulations

The second set of test simulations (hail shaft B) examines the sedimentation and melting characteristics of hail distributions comprised of small hailstones (Fig. 4.10b). The same analysis method employed for the hail shaft A simulations is used here as well. Figure 4.19 shows vertical cross-sections through the simulated hail shaft cores of the resulting Z_{he} and N_{th} fields for experiments NU2B, NU7B, and 3MNEWB at simulation times $t = 20, 60, 120, 240, 360,$ and 540 s. The resulting fields of $r_h, r_r, N_{0.5cm}, N_{1cm},$ and N_{2cm} are displayed in Figure 4.20 for the same times, and vertical profiles of v_h through the central column of the hail shaft are shown for the 3MNEWB experiment in Figures 4.19 and 4.20.

As was the case in the hail shaft A simulations, the spatial distributions of N_{th} (Fig. 4.19) and r_h (Fig. 4.20) are similar among NU2B, NU7B, and 3MNEWB at $t = 20$ s. Cases NU2B and 3MNEWB exhibit similar patterns and maximum magnitudes of Z_{he} (Fig. 4.19), whereas the larger v_h values associated with the narrower initial hail size distributions for NU7B results in smaller Z_{he} values ($Z_{he,max} = 31.3$ dBZ) compared to NU2B ($Z_{he,max} = 36.4$ dBZ) and 3MNEWB ($Z_{he,max} = 37.6$ dBZ). Owing to initially identical hail size distributions, the regions of $N_{0.5cm}$ in NU2B and 3MNEWB are largely similar at $t = 20$ s (Fig. 4.20), and a small region of N_{1cm} is present between roughly 3 and 4 km in 3MNEWB due to slight broadening of the size distributions over this layer. On the other hand, the initial hail size distributions in NU7B contain fewer larger hailstones relative to NU2B and 3MNEWB (Fig. 4.10b), and thus a much smaller region of $N_{0.5cm}$ exists in the former case compared to the latter cases (Fig. 4.20).

As time progresses, sedimentation of Z_{he}, N_{th} (Fig. 4.19), and r_h (Fig. 4.20) is seen to occur most rapidly in NU2B within the leading edge of the hail shaft. From $t = 60$ s through 240 s, the diagnosed Z_{he} values in NU2B below roughly 2 km increase and eventually exceed the initial

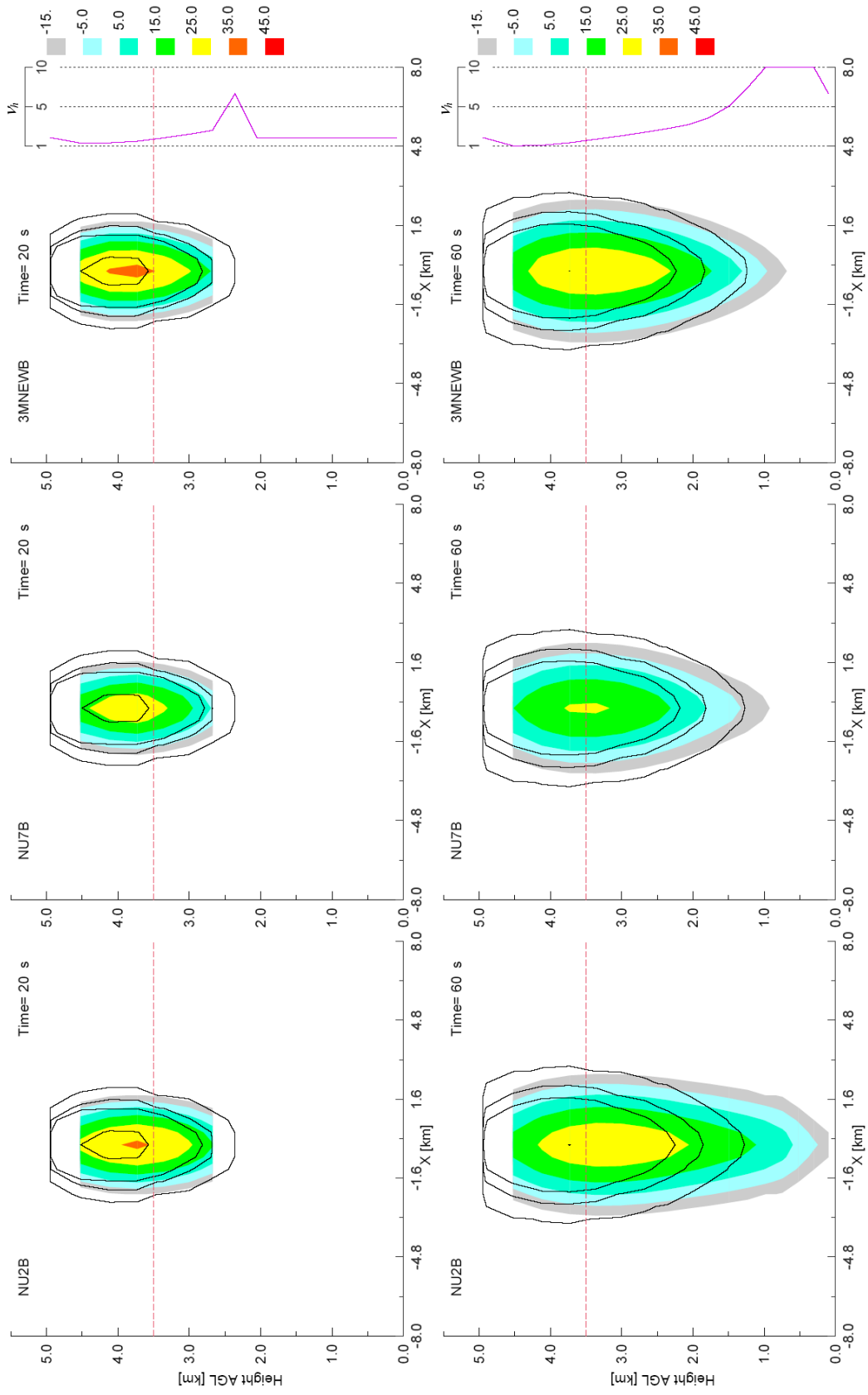


Figure 4.19: Vertical cross-sections through the hail core of hail shaft B showing equivalent hail reflectivity Z_{he} (shaded; dBZ) and hail number concentrations (black contours; values are 10^{-3} , 0.1, 1 and 100 m^{-3}) for the NU2B (left column), NU7B (middle column), and 3MNEWB (right column). Instantaneous vertical profiles of v_h through hail shaft axis are also plotted for 3MNEWB. Simulation times are labeled for each panel, and the red dashed line in each panel depicts approximate location of 0°C isotherm.

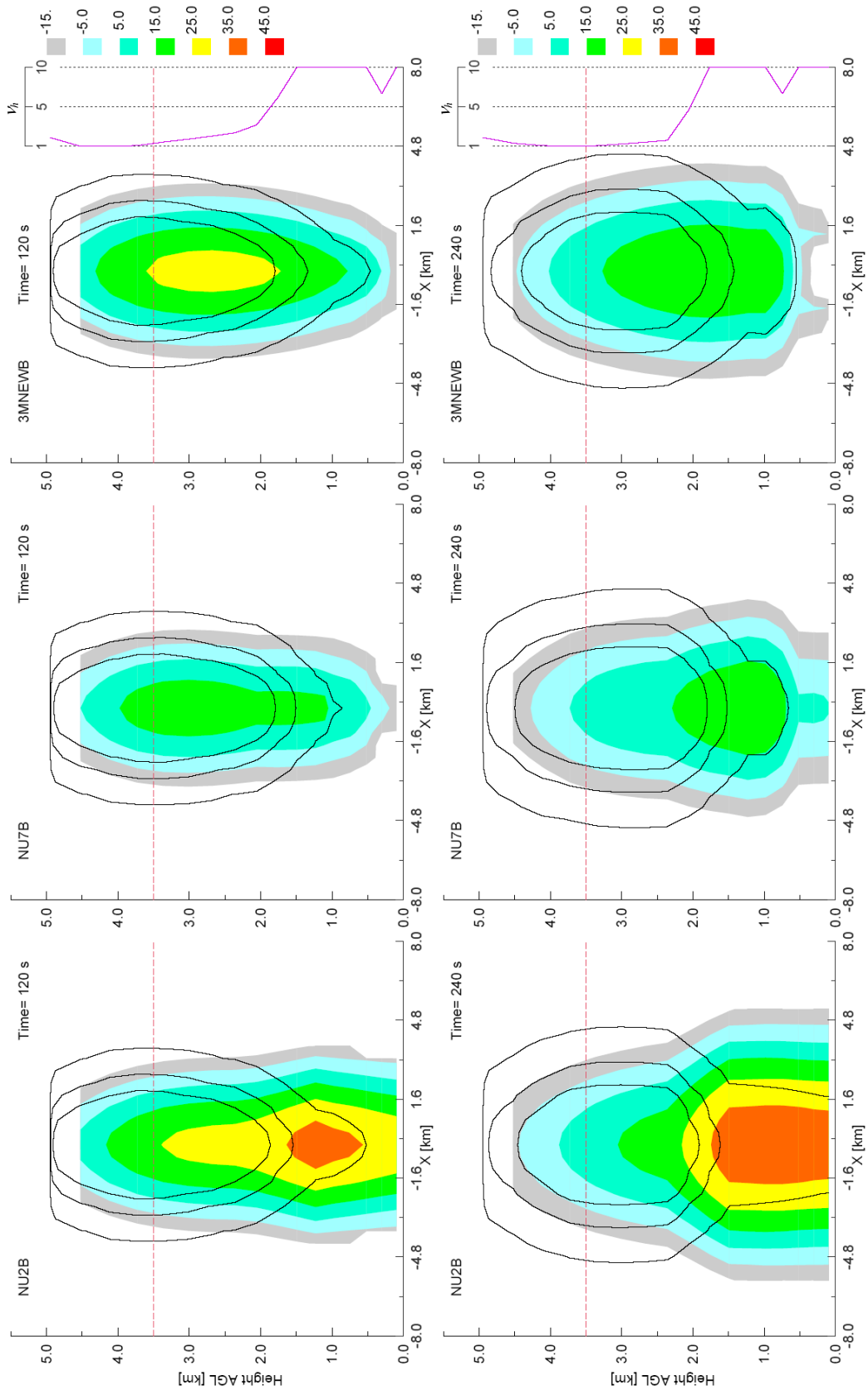


Figure 4.19: (continued)

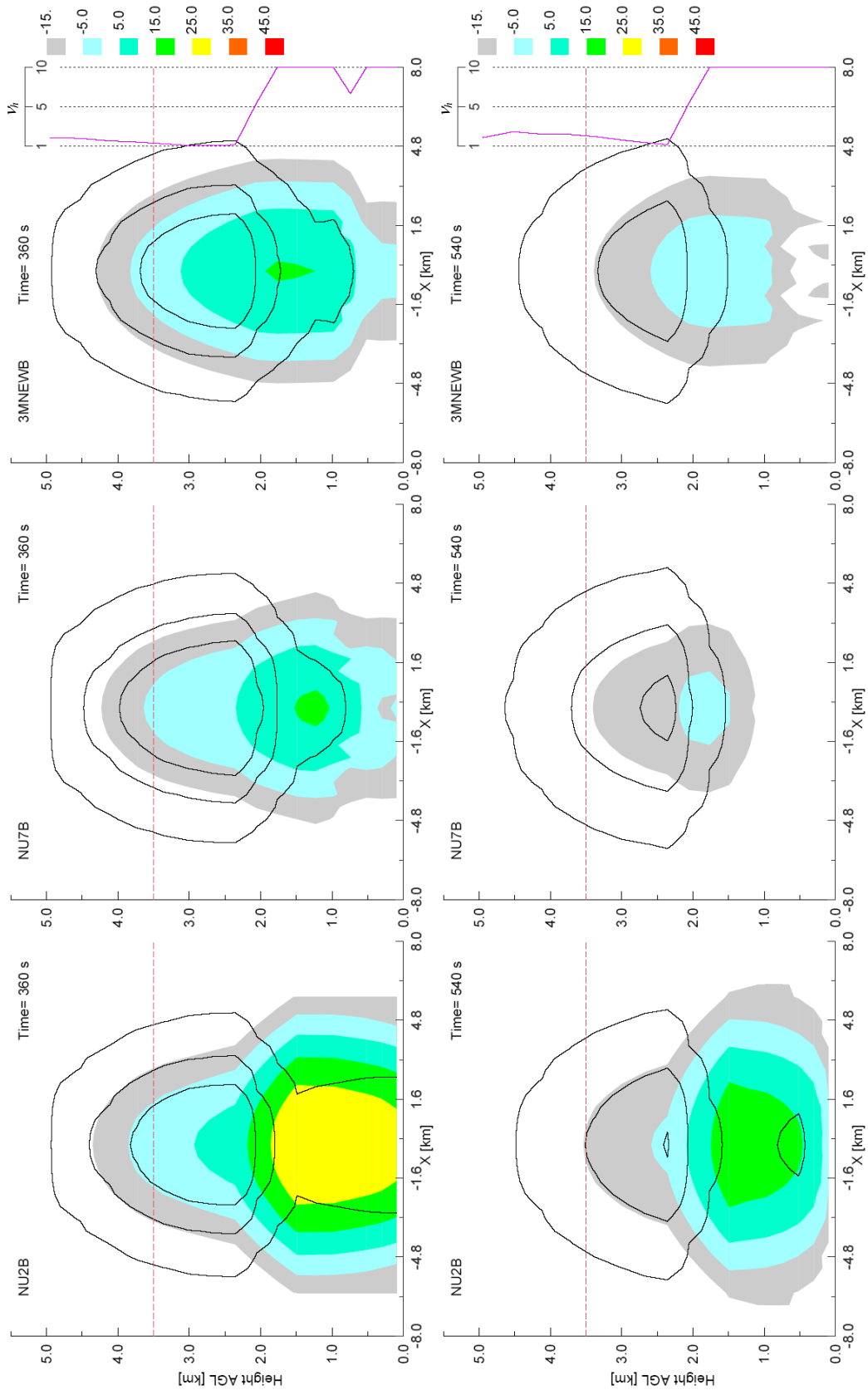


Figure 4.19: (continued)

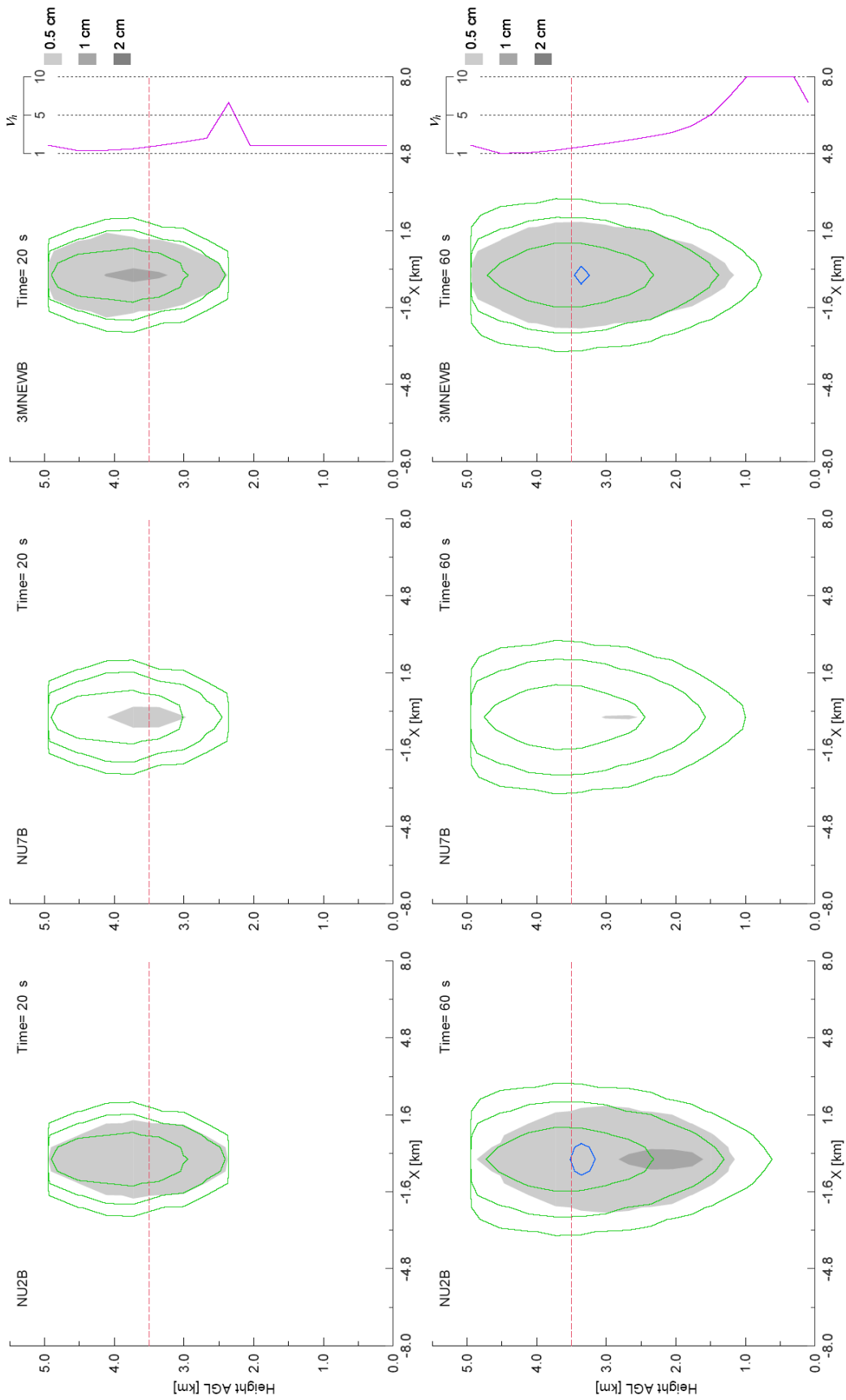


Figure 4.20: Vertical cross-sections through the hail shaft B showing hail mass mixing ratio (green contours; 10^{-9} , 10^{-7} , 10^{-5} kg m^{-3}), rain mass mixing ratio (blue contours; 10^{-9} , 10^{-7} , 10^{-6} , 5×10^{-6} kg m^{-3}), and regions where the number concentrations of hailstones with diameters greater than 0.5, 1, and 2 cm exceed 10^4 m^{-3} (shaded) for the NU2B (left column), NU7B (middle column), and 3MNEWB (right column). Instantaneous vertical profiles of v_h through hail shaft axis are also plotted for 3MNEWB. Simulation times are labeled for each panel, and the red dashed line in each panel depicts approximate location of 0°C isotherm.

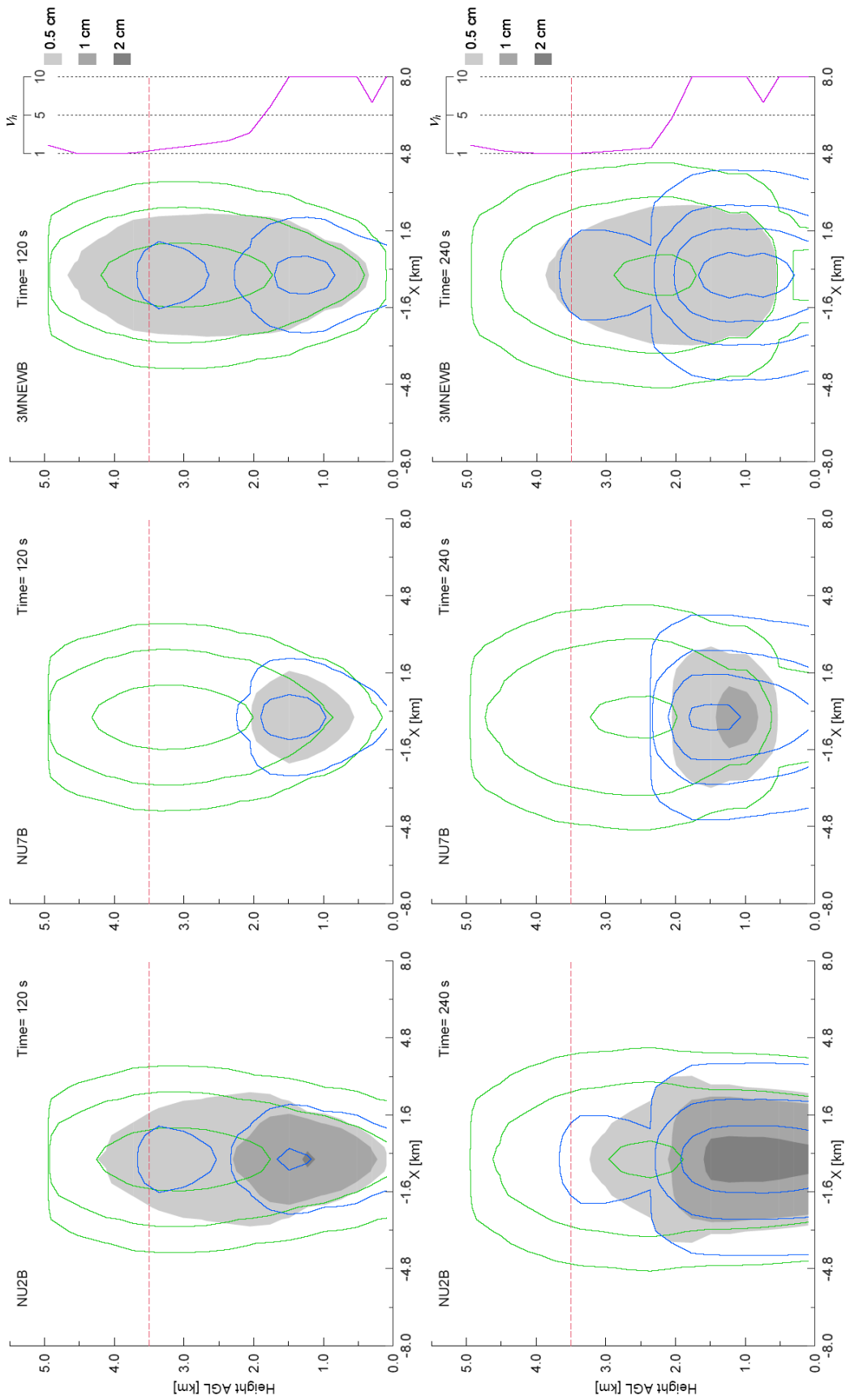


Figure 4.20: (continued)

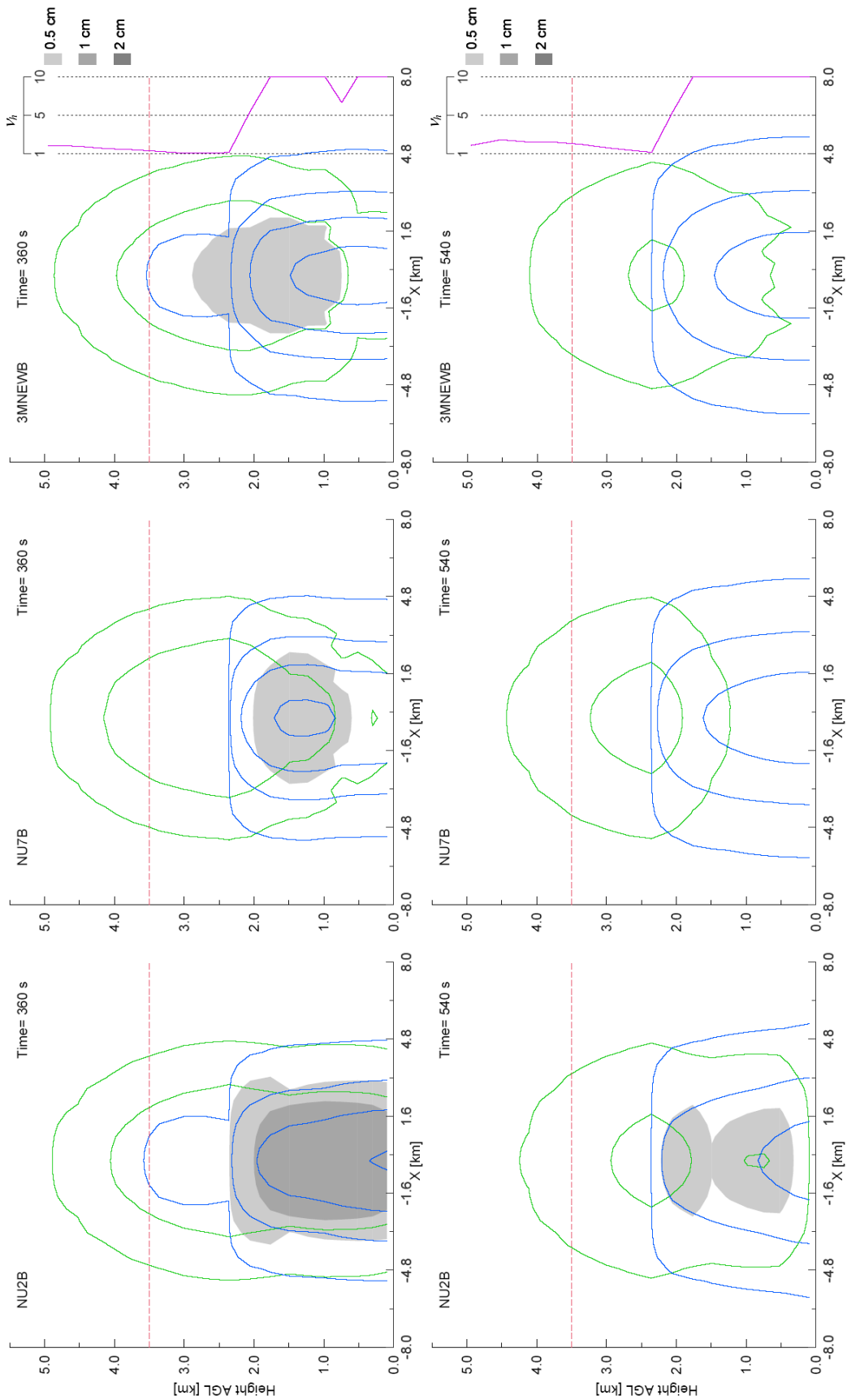


Figure 4.20: (continued)

$Z_{he,max}$ value by about 7 dBZ at $t = 240$ s (Fig. 4.19). In addition, regions of N_{1cm} and N_{2cm} appear within the lower portion of the NU2B hail shaft by $t = 60$ and 120 s, respectively, and grow in size with time (Fig. 4.20). These features are due primarily to erroneously large $D_{\bar{m}h,max}$ (and $D_{\bar{m}h}$) values over the lowest kilometer during this time period (Fig. 4.21b) as a result of excessive size sorting in NU2B, similar to what was observed in the STR1 case for 1D sedimentation (Fig. 4.4g,h). This excessive size sorting is exacerbated by losses in N_{th} due to complete melting of the smallest particles, which causes $D_{\bar{m}h}$ values to increase with decreasing height within the melting layer (Fig. 4.21b), leading to even more rapid sedimentation of r_h and N_{th} as well as increased values of Z_{he} , $N_{0.5cm}$, N_{1cm} and N_{2cm} at low levels (Figs. 4.19 and 4.20).

The NU7B case also exhibits increases in Z_{he} magnitudes from $t = 120$ through 240 s (Fig. 4.19) as well as the appearance and subsequent spatial increase in regions of $N_{0.5cm}$ and N_{1cm} from $t = 60$ through 240 s (Fig. 4.20) over the lowest 2 km. Even though these increases are not as great as in the NU2B case, the manifestation of regions of larger diameter hailstones (i.e., N_{1cm}) when the initial number concentrations of these particles were well below the specified threshold (10^{-4} m^{-3}) points to a significant deficiency in the 2M scheme. As in the hail shaft A simulations, complete melting of the smallest particles reduces N_{th} faster than r_h resulting in increases in $D_{\bar{m}h,max}$ with decreasing height in all hail shaft B cases (Fig. 4.21). However, without an accompanying narrowing of the size distribution, the numbers of larger particles in the 2M cases artificially increase. The numbers of larger hailstones do not increase in the 3MNEWB case (Fig. 4.20) owing to the shift from broad hail size distributions ($v_h \leq 2.0$) above the melting layer (~ 2.3 km) to narrow ones ($v_h \sim 10.0$) within and below the melting layer (Figs. 4.19 and 4.20).

A similar evolution in the vertical v_h profiles occurs in 3MOLDB (not shown), however, the maximum sizes of hailstones to melt completely in one time step are larger in this case compared to 3MNEWB (Fig. 4.22b) thereby resulting in excessive losses in N_{th} (Fig. 4.24e) and an unrealistic shift towards larger hail sizes at low levels (Fig. 4.21e). The time-height plot of $D_{max,melt}$ values for 3MOLDB (Fig. 4.22b) exhibits $D_{max,melt}$ magnitudes that are ≥ 6 mm within the lowest kilometer through about $t = 780$ s, with a band of $D_{max,melt}$ values greater than 7 mm seen around 650 m height during the same time span. Given the small hail sizes contained in the initial hail distributions for this case (Fig. 4.10b), such large magnitudes of $D_{max,melt}$ are totally unrealistic, particularly beyond $t = 360$ s as most of the hailstones with diameters 6 mm and larger would have reached the surface by this time from an initial height of 4.5 km. The pattern of $D_{max,melt}$ values is strikingly similar to that for $D_{\bar{m}h,max}$ over the lowest kilometer for this case (Fig. 4.21e) as the excessive losses of N_{th} due to overestimations of $D_{max,melt}$ lead to erroneously large $D_{\bar{m}h,max}$ values, which then feedback into the melting routine. When complete melting is omitted in the hail shaft B simulations, the observed increases in $D_{\bar{m}h}$ with decreasing height within the melting layer (Fig. 4.21) are removed. As complete melting of hail is clearly an integral part of the precipitation process (Foote 1984; Wakimoto and Bringi 1988; Hjelmfelt et al. 1989; Atlas et al. 2004) and cannot be omitted from the model, the overwhelming impact of complete melting on $D_{\bar{m}h}$ with the old 3MHAIL melting scheme is certainly an undesirable and unphysical result. Increases in $D_{\bar{m}h,max}$ with decreasing height due to complete melting are evident in 3MNEWB as well (Fig. 4.21a), however, the magnitudes of these increases are much less with new 3MHAIL melting scheme.

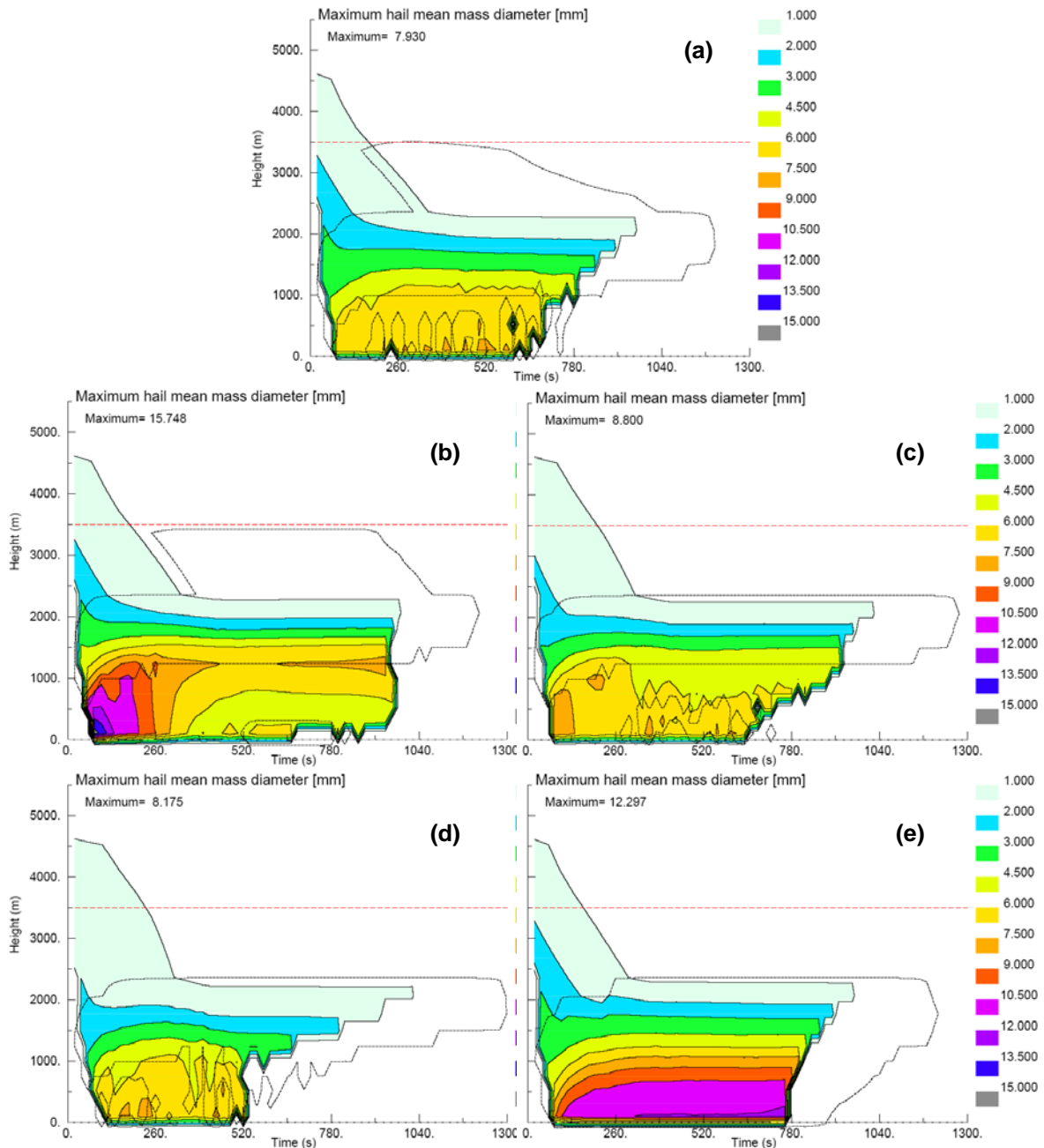


Figure 4.21: Time-height plots of maximum mean mass hail diameter D_{mh} (computed where $r_h \geq 10^{-8} \text{ kg kg}^{-1}$) at each vertical level for (a) 3MNEWB, (b) NU2B, (c) NU4B, (d) NU7B, and (e) OLD3MB. Dotted lines in each panel depict regions where the fractional amounts of completely melted hailstones exceed 1% of the instantaneous total hail number concentrations.

An examination of the spatial distributions of N_{th} (Fig. 4.19) and r_h (Fig. 4.20) reveals that these patterns are largely similar among the three cases above 2.3 km from $t = 20$ to 240 s. At times $t = 360$ and 540 s, the N_{th} and r_h distributions above 2.3 km for NU2B and 3MNEWB

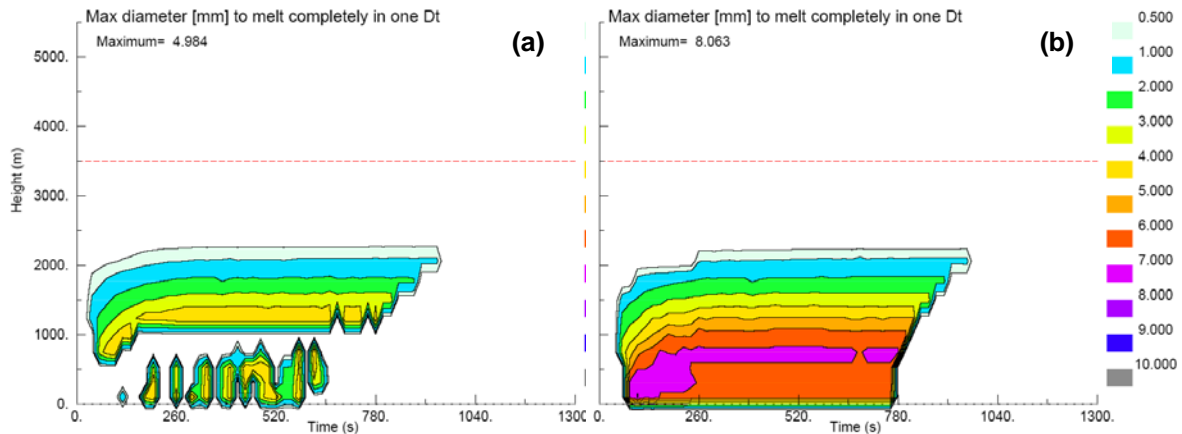


Figure 4.22: Time-height contours of maximum hail diameter [$D_{max,melt}$, mm] to melt completely in one time step in hail shaft B simulations for a) 3MNEWB and b) 3MOLDB.

remain mostly similar to each other, whereas the NU7B case exhibits larger N_{th} and r_h values relative to cases NU2B and 3MNEWB. The lower N_{th} and r_h values in NU2B and 3MNEWB at these heights and times are due to larger magnitudes of complete melting above 2.3 km in these cases compared to NU7B (Figs. 4.23 and 4.24). Below 2.3 km, the spatial patterns of N_{th} (Fig. 4.19), r_h (Fig. 4.20) and complete melting (Figs. 4.23 and 4.24) are most alike in NU7B and 3MNEWB for the selected times shown, and very little hail mass and number reach the surface in both cases. In contrast, excessive size sorting and overestimation of $D_{\bar{m}h}$ in NU2B leads to smaller magnitudes of complete melting below 2.3 km relative to NU7B and 3MNEWB (Figs. 4.23 and 4.24), and ultimately to a markedly different evolution of the N_{th} and r_h distributions below 2.3 km such that greater amounts of N_{th} and r_h are transported to the surface (Figs. 4.19 and 4.20). As was the case in the hail shaft A simulations, the use of a variable v_h results in a much improved representation of the evolution of the hail distributions in the current set of simulations.

Rain from complete melting first appears in the vicinity of the 0°C level at $t = 60$ s in the NU2B and 3MNEWB cases, and then at levels below 2.3 km by $t = 120$ s in all three cases (Fig. 4.20). A negligible amount of rain ($r_r < 10^{-10}$ kg m $^{-3}$) is produced via complete melting above 2.3

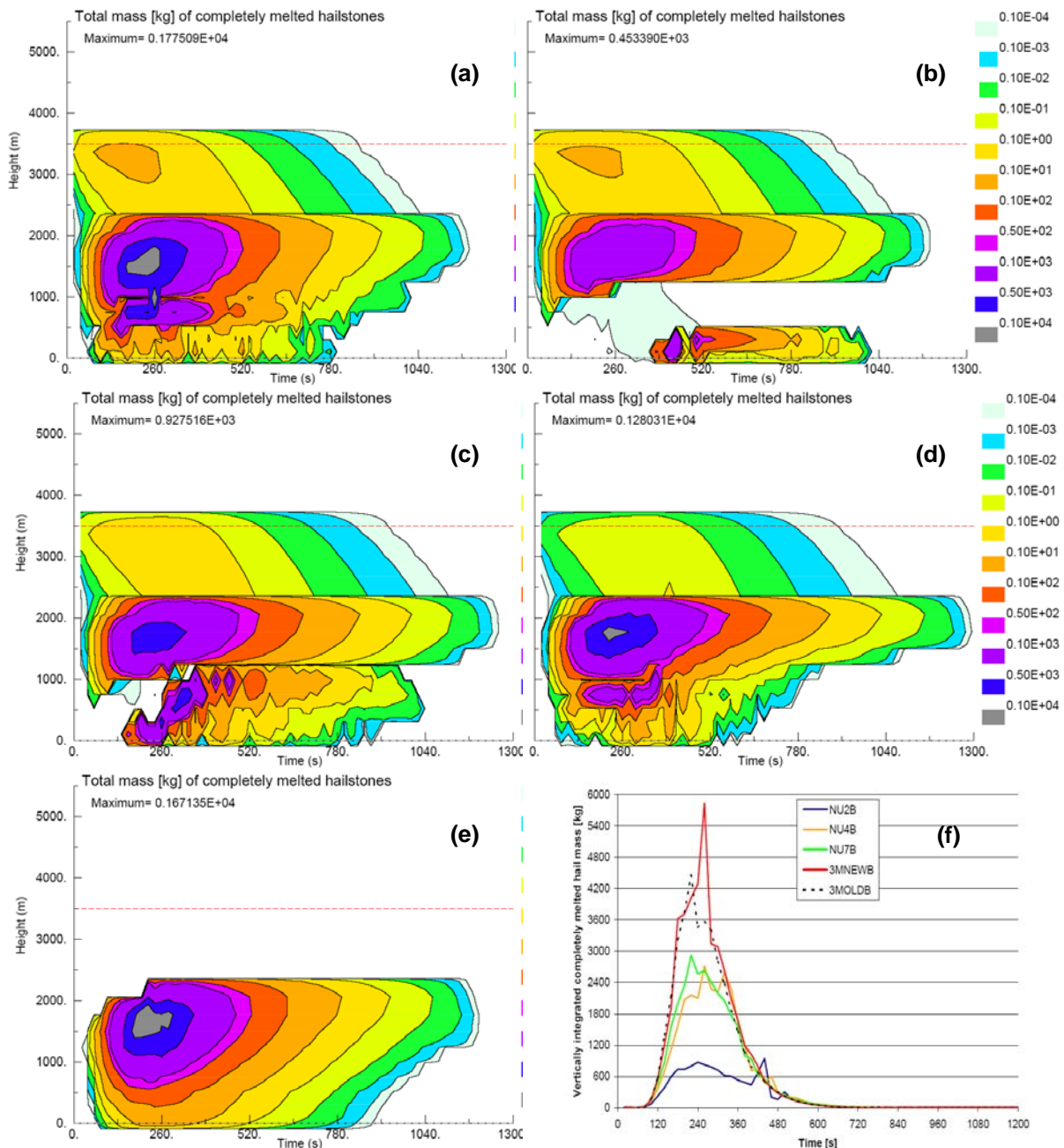


Figure 4.23: Time-height plots of total mass [kg] of completely melted hailstones at each vertical level for (a) 3MNEWB, (b) NU2B, (c) NU4B, (d) NU7B, and (e) OLD3MB. The vertically integrated mass [kg] of completely melted hail with time for panels a-e in shown in panel f.

km in NU7B (Fig. 4.20) owing to the fewer numbers of very small diameter hail particles in this case relative to NU2B and 3MNEWB (Fig. 4.10b). Unlike the hail shaft A simulations, the hail distributions for hail shaft B consist primarily of small diameter hailstones ($D < 1$ cm) that experience more rapid heat transfer from the environment to the hailstone surface owing to their

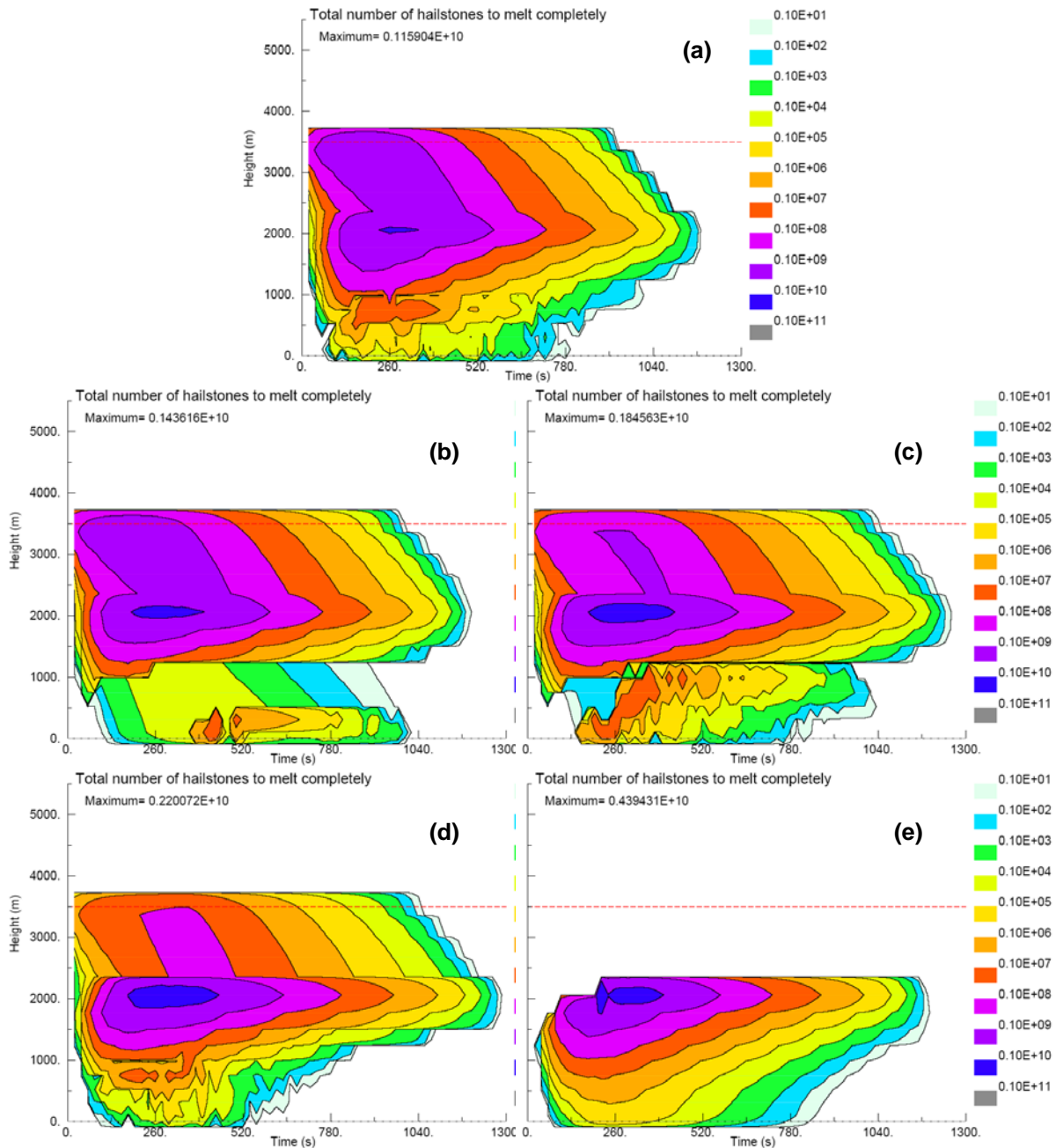


Figure 4.24: Time-height plots of total numbers of completely melted hailstones at each vertical level for (a) 3MNEWB, (b) NU2B, (c) NU4B, (d) NU7B, and (e) OLD3MB.

smaller mass-to-area ratio (Pruppacher and Klett 1980). Thus, the majority of rain in the hail shaft B cases is produced from complete melting of hail rather than shedding, with the exception of NU2B. This is evident from the greater magnitudes of total hail mass melted (Fig. 4.23) compared to total mass shed from hail (Fig. 4.25), again with the exception of NU2B for which

the vertically-integrated shed mass amounts are about twice those of completely melted hail. The greatest amount of complete melting is seen in 3MNEWB (Fig. 4.23a), NU7B exhibits smaller quantities of totally melted mass (Fig. 4.23d) than for 3MNEWB, and the least amount of complete melting occurs in NU2B (Fig. 4.23b). Not surprising, below 2.3 km, initial rain amounts generated by complete melting of hail in NU7B and 3MNEWB are greater than in NU2B (Fig. 4.20), and the spatial distributions of r_r beyond $t = 120$ s reveal that rain amounts are greatest (smallest) in 3MNEWB (NU2B).

The temporal and spatial patterns of complete melting for the hail shaft B simulations (Figs. 4.23 and 4.24) are more complex than those for the hail shaft A cases. For example, in 3MNEWB and the 2M cases, three distinct regions of complete melting are evident (Figs. 4.23 and 4.24). The first region extends from the vicinity of the 0 °C isotherm down to about 2.3 km and is associated with the melting of the smallest particles ($D < \sim 0.5$ mm) contained in the hail distributions. The second region spans from roughly 2.3 km downward to around 1 km and contains the maximum melting magnitudes, thus this is the primary melting layer in these simulations. Within this layer, the larger relative humidity values (Fig. 4.9) enhance the melting process (Foote 1984; RH87b; Srivastava 1987) as was seen for the hail shaft A simulations. The third region extends from approximately 1 to 1.2 km down to the surface and includes melting of all hail to rain at grid points with bulk hail LWF values greater than 0.95 as well as complete melting of smaller particles at grid points with bulk hail LWF values less than 0.95. The 3MOLDB case, on the other hand, exhibits a single contiguous region of complete melting below ~ 2.3 km (Figs. 4.23e, 4.24e), and no melting occurs above this height due to the requirement that bulk hail LWF values exceed 0.3 before melting (and shedding) can commence. A distinct separation between regions 2 and 3 exists in NU2B (Figs. 4.23b, 4.24b), and to a lesser extent in

NU4B (Figs. 4.23c, 4.24c), due to excessive size sorting and the associated large $D_{\bar{m}h}$ values, which shift the hail size distributions towards larger diameters and reduce the numbers of small particles. As a result, heat transfer from the environment to the hailstones is reduced, lower bulk hail LWF values are attained in these cases compared to NU7B and 3MNEWB (not shown), and less melting occurs. Similarly, excessively large $D_{\bar{m}h,\max}$ ($D_{\bar{m}h}$) values at low levels in 3MOLDB (Fig. 4.21e) lead to less total melting in this case compared to 3MNEWB (Fig. 4.23f). Also evident from Figures 4.23b,c,d and 4.24b,c,d is that an increase in the fixed value of ν_h for the 2M cases corresponds to an increase in the maximum magnitudes of hail mass and numbers to completely melt, in contrast to what was seen in the 2M cases of the hail shaft A simulations (Figs. 4.14 and 4.15). This result is related to a decrease in excessive size sorting as well as a reduction in the numbers of relatively larger hailstones as ν_h increases (Fig. 4.10b), similar to what was noted by MY05a.

The time-height plots of total mass shed from hail (Fig. 4.25) reveal a clear pattern of reduced total shedding amounts for increasing ν_h values, with the exception of 3MOLDB, for which the evolution of ν_h is similar to that in 3MNEWB although the amount of shedding is greater in the former than in the latter. The larger quantities of shed mass in NU2B, NU4B, and 3MOLDB result from the greater numbers of larger hailstones at low levels in these cases relative to NU7B and 3MNEWB due to the fact that bigger hailstones are capable of shedding more drops (and hence more mass) per unit time (RH87b). In all cases except 3MOLDB, maximum shedding occurs between the previously defined melting regions 2 and 3, in locations where the smallest hail particles of the initial distributions have completely melted to rain during their descent leaving only partially melted, relatively larger hailstones. In the 3MOLDB case, the descending hail distributions first experience complete melting of the smallest hail particles prior

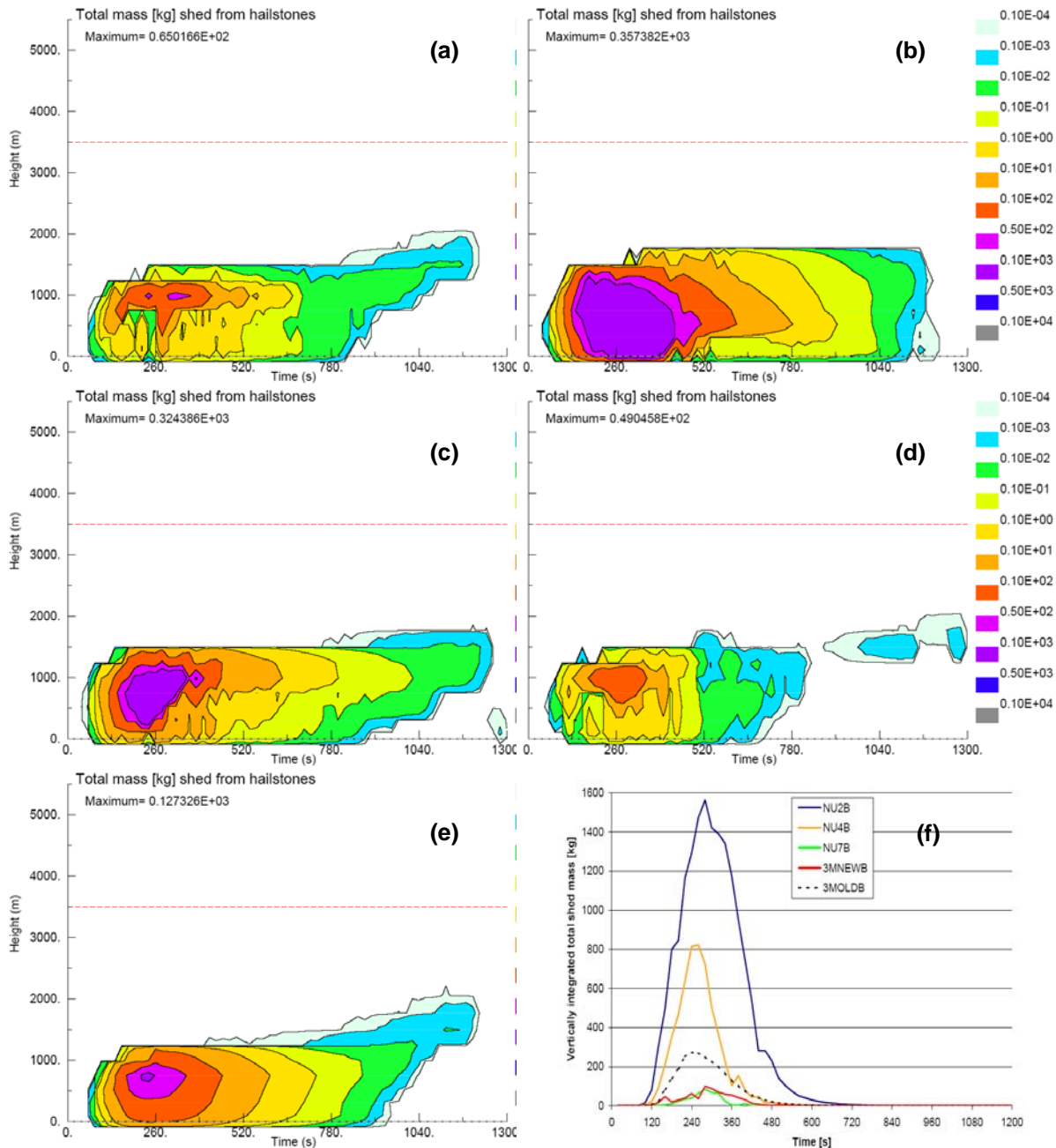


Figure 4.25: Time-height plots of total mass [kg] shed from hailstones at each vertical level for (a) 3MNEWB, (b) NU2B, (c) NU4B, (d) NU7B, and (e) OLD3MB. The vertically integrated shed mass [kg] from hail with time for panels a-e in shown in panel f.

to shedding as in the other cases, yet there appears to be very little correlation between decreases in the amounts of complete melting and maxima in shedding. One final important point regarding the sedimentation and shedding of hailstones in these simulations is that there should be very little if any shedding beyond $t = 300$ s. This time corresponds to the approximate time it

would take for a 9 mm hailstone to fall to the surface from an initial height of 4.5 km without any loss in mass. Larger hailstones capable of shedding would have already reached the surface prior to this time due to their faster fall speeds, thus only hailstones smaller than 9 mm in diameter would remain above the surface, and these hailstones should not shed any mass (Rasmussen et al. 1984, RH87a). In this respect, the NU7B case gives the most accurate results regarding the time at which shedding should cease, 3MNEWB gives less accurate results, whereas the duration of shedding in cases NU2B, NU4B, and 3MOLDB is much too long (Fig. 4.25). Due to the fact that the bulk microphysical schemes attempt to represent the hail distributions by means of a continuous size distribution function, errors of this sort are unavoidable. However, based on the foregoing analyses, the combined inaccuracies of sedimentation, melting, and shedding are minimized in the 3MNEWB case compared to the other cases.

Time series of surface hail and rain precipitation for the hail shaft B cases are shown in Figure 4.26. Hail reaches the surface by $t = 120$ s in all cases and accumulates through about $t = 480$ s, except in 3MOLDB, for which the duration of hailfall lasts until about $t = 600$ s (panel e). Surface hailfall is greatest in NU2B as evident by the nearly order of magnitude difference in maximum surface accumulated values between this case and 3MOLDB (panel a; Table 4.5), and in turn, surface hail accumulated amounts are nearly an order of magnitude larger in 3MOLDB compared to NU4A, NU7A, and 3MNEWB (panels a and c; Table 4.5). Due to the large magnitudes associated with the time series for NU2B (total surface accumulated hail mass of 57655 kg by $t = 1200$ s and peak hail precipitation rate of 0.24 mm hr^{-1} at $t = 260$ s), these are omitted from Figures 4.26c and 4.26e in order to highlight the features in the time series of the other cases. The amounts of hail and the hail precipitation rate at the surface are much larger in

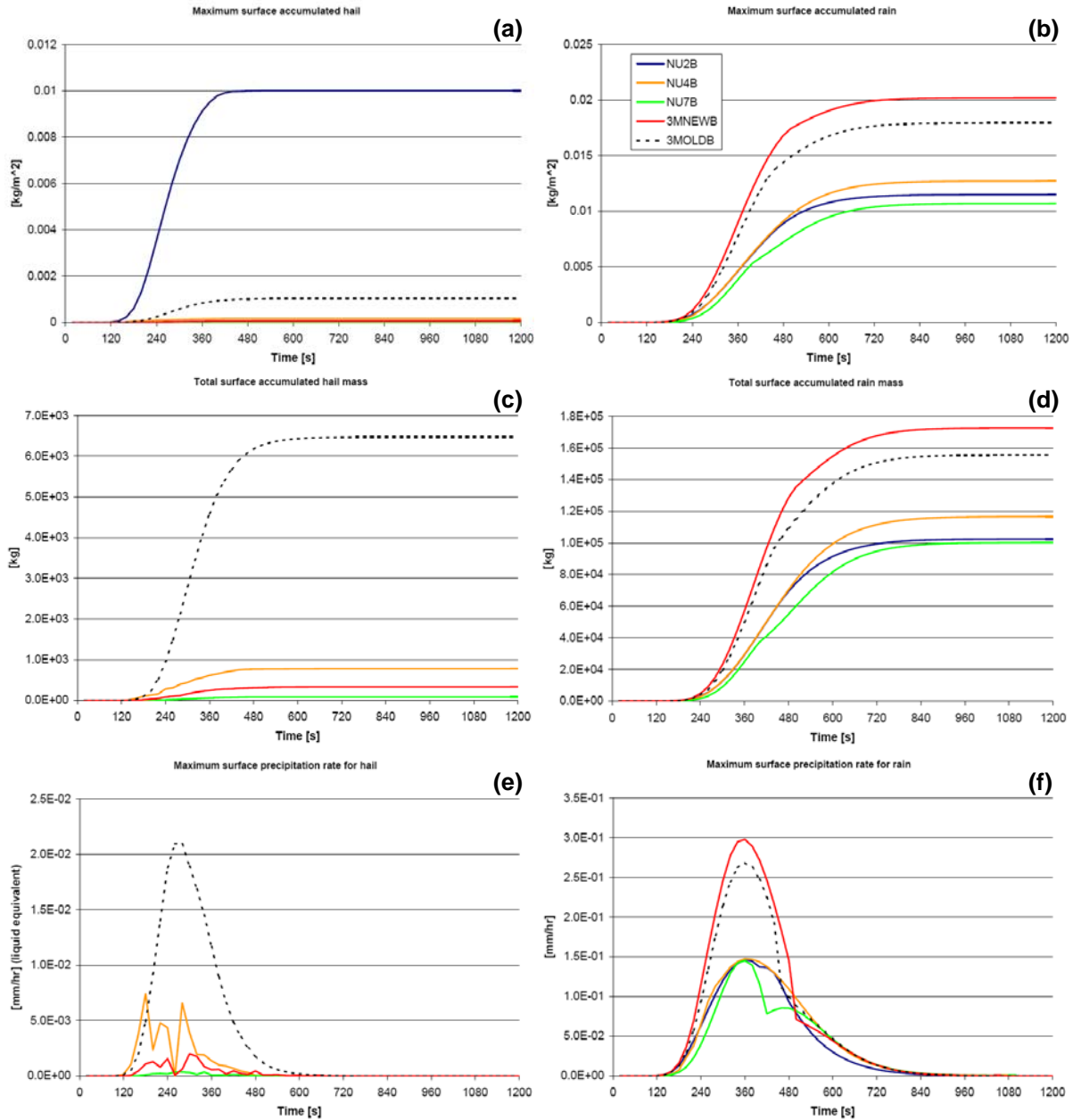


Figure 4.26: Time series of maximum accumulated amounts [kg m⁻²] at a single grid point at the surface (top row), total surface accumulated mass [kg] (middle row), and maximum surface precipitation rates [mm hr⁻¹] (bottom row) of hail (left column) and rain (right column) for the hail shaft B simulations.

NU2B owing to artificial increases in the numbers of larger hailstones as a result of more rapid sedimentation and decreased melting of hail mass relative to the other cases as previously discussed. Similar increases in larger diameter hail numbers due to excessive losses of N_{th} from complete melting in 3MOLDB account for the relatively large quantities of accumulated hail

Table 4.5: Total accumulated masses at surface at $t = 1200$ s for hail shaft B simulations.

Experiment name	Total accumulated hail mass at surface [kg]	Total accumulated rain mass at surface [kg]	Total precipitation mass at surface [kg]
NU2B	57655	102443	160098
NU4B	776.5	116624	117400.5
NU7B	81.5	100212	100293.5
3MNEWB	333.5	172668	173001.5
3MOLDB	6470.3	155634	162104.3

mass, greater peak hail precipitation rates, and longer duration of surface hailfall in this case compared to NU4A, NU7A, and 3MNEWB (Figs. 4.26c,e). In agreement with the findings of MY05a, an increase in the fixed v_h value in the 2M cases is associated with delay in the onset of hailfall at the surface as well as decreases in the amounts of accumulated hail and the maximum hail precipitation rates. This result is expected given the narrower initial hail size distributions (NU4B and NU7B) contain fewer relatively large hailstones compared to the broader size distribution for NU2B (Fig. 4.10b). A single peak at $t = 260$ s is observed in the maximum hail precipitation rates at the surface for the 3MOLDB case (also for case NU2B), whereas multiple peaks are evident in the time series of this quantity for cases NU4B, 3MNEWB, and NU7B (Fig. 4.26e). These multiple peaks in the latter cases are related to time-height variations in the magnitudes of complete melting and shedding over approximately the lowest kilometer as seen in Figures 4.23a,c,d and 4.25a,c,d. A relatively small secondary peak in the NU2B maximum hail precipitation rates around $t = 480$ s (not shown) corresponds to a relative minimum in complete melting within the lowest 500 m about the same time (Figs. 4.23b,f).

The time series of surface accumulated rainfall and rain rates (Figs. 4.26b,d,f) reveal these quantities are greatest in the 3M cases compared to the 2M cases due primarily to the greater magnitudes of complete melting in the 3M cases (Fig. 4.23). Case 3MNEWB exhibits the largest values of accumulated rain and highest peak rain rates as the amounts of completely melted hail

mass are greatest in this case (Figs. 4.23a,f). And although the quantities of completely melted hail in 3MOLDB are mostly similar to those in 3MNEWB (Fig. 4.23f), less rainfall reaches the surface in 3MOLDB due primarily to the fact that a greater quantity of hail falls to the surface in this case compared to 3MNEWB (Fig. 4.26c). For the 2M cases, accumulated rain amounts are largest in NU4B and smallest in NU7B (Figs. 4.26b,d) owing to greater amounts of shedding in the former versus the latter (Fig. 4.25f) as total melted mass between the two is similar (Fig. 4.23f). In all cases, surface rainfall commences at roughly $t = 120$ s, peak maximum rain rates are attained around $t = 360$ s, and rainfall generally ceases after $t = 900$ s (Fig. 4.26f). Maximum rain rates are similar in the 2M cases, with the exception of NU7B which exhibits a local minimum near $t = 420$ s due to local minima in both complete melting and shedding below 1 km at around the same time (Figs. 4.23d and 4.25d). In general, it is apparent that even though the individual processes of complete melting and shedding are sensitive to the fixed ν_h values in the 2M cases (Figs. 4.23b,c,d and 4.25b,c,d), the evolution of surface rainfall from these combined processes is similar. Thus, as was seen for the hail shaft A simulations, there does not seem to be a clear relationship between surface rainfall and ν_h for the 2M cases in this set of simulations. However, predicted amounts of surface rainfall and rain rates are likely too low in the 2M cases compared to 3MNEWB based on the better representation of the evolution of melting and shedding processes, and hence surface rainfall, in 3MNEWB.

These simulations of two very different hail shafts show that the 3MHAIL scheme with the new melting algorithm of RH87b seems to represent the combined sedimentation and melting processes much more accurately than the 2M or the 3MHAIL scheme that uses the old melting algorithm (3MOLD). The ability of the 3MHAIL scheme to predict changes in ν_h due to both sedimentation and melting allows for a much more realistic evolution of the hail spectra, such as

broadening aloft and narrowing at low levels as seen in simulations by MY06a and Mansell (2010). In addition, artificial shifts in the hail size distributions towards larger sizes evident in the cases with the 2M and 3MOLD schemes as a result of complete melting (particularly with hail shaft B) are mostly mitigated or are not seen with the 3MHAIL scheme. The new melting scheme allows complete melting of the smallest hailstones very close to the freezing level, though the bulk of the hail melts well below the 0 °C isotherm in both sets of simulations due to the subsaturated environment through which the hail falls (RH87b; Pruppacher and Klett 1997; Phillips et al. 2007). A well-defined melting layer is seen as well between roughly 1.0 and 2.3 km AGL in simulations with the new melting scheme, yet the 3MOLD scheme does not capture this feature well and instead predicts a continuous melting layer from about 2.3 km AGL all the way to the surface. Overall, the evolution of hail sedimentation, melting and shedding, and the characteristics of surface precipitation are seen to be sensitive to v_h in the 2M cases, whereas the prediction of v_h in the 3MHAIL scheme permits a more naturally varying evolution of these processes.

4.3) *Hail formation tests*

In this section, differences in hail formation via rain and ice hydrometeor collisions for the original RAMS bulk collection algorithm (Section 3.3.1) and the new bulk collection algorithms used in the 3MHAIL scheme (Section 3.3.3) are examined. Recall that in the original bulk collection algorithm, rain colliding with any frozen hydrometeor at sub-freezing temperatures results in the formation of hail, whereas the new algorithms allow for alternate outcomes for collisions between rain and frozen particles. The highly idealized tests presented herein involve simply 'inserting' rain and ice hydrometeor distributions into a sub-freezing, quiescent, cloud-free

environment and advancing the model microphysics forward one time step. In order to further simplify the analyses, all processes except vapor/heat diffusion and rain-ice collections are omitted (the inclusion of the vapor/heat diffusion process is necessary to obtain internal energies of the colliding particles prior to application of the collection routines). Using the same model setup as in Section 4.2, mixing ratios and number concentrations of rain and select ice species are prescribed at a single model grid point at a height of 5864.5 m, well above the freezing level (~ 3.5 km), at time $t = 0$. The air temperature at this height is roughly -15 °C (Fig. 4.9), and the relative humidity is set to 75% to ensure total evaporation of the 'injected' hydrometeors does not occur in the vapor/heat transfer routine.

Two series of tests using the different collection algorithms are performed: 1) collection between rain and ice hydrometeors in the absence of hail, and 2) collection between rain and ice hydrometeors in the presence of a pre-existing hail distribution. The second set of tests highlights differences in the resulting hail distributions owing to the adjustment of newly formed hail number concentrations (Section 3.3.3.3). Initial distribution parameters for rain (r), pristine ice (p), aggregates (a), and graupel (g) used in all hail formation tests are listed in Table 4.6. For each non-hail hydrometeor species, two different distributions (denoted by A and B in Table 4.6) are used such that four distribution combinations for each collision type are examined. The distribution shape parameter values are fixed at 2.0 for rain and non-hail ice hydrometeors, and

Table 4.6: Initial distribution values for mixing ratios r , number concentrations N_i , and mean mass diameters $D_{\bar{m}}$ of rain and ice species used in hail formation tests.

	r [kg kg ⁻¹]	A: N_i [kg ⁻¹]	B: N_i [kg ⁻¹]	A: $D_{\bar{m}}$	B: $D_{\bar{m}}$
rain (r)	0.001	1000.0	50.0	1.24 mm	3.67 mm
pristine ice (p)	0.001	2×10^8	2×10^7	25.9 μm	57.22 μm
aggregates (a)	0.001	10^5	500.0	0.622 mm	4.91 mm
graupel (g)	0.001	10^4	500.0	0.86 mm	2.34 mm

the ν_h values for newly formed hail distributions in test 1 are also set to 2.0. For the second series of tests, ν_h is updated based on the updated values of r_h , N_{th} , and Z_h following the collection process. The hail reflectivity tendency equation (3.25) is used to compute the resulting Z_h values following the collection process. The time step length (Δt) is 4 s for all tests.

4.3.1) Rain-ice collisions in the absence of hail

Table 4.7 lists the results for rain colliding with pristine ice particles. For this and subsequent tables in this section, the column headings denote the interaction type (lower case letters) and the specific combination of distributions (upper case letters), i.e., rA-pB corresponds to rain (r) distribution A colliding with pristine ice (p) distribution B. This naming convention is used in the discussion of the hail formation test results as well.

From Table 4.7, it is seen that collisions between rain and pristine ice always result in hail formation with the original RAMS 2M collection scheme (OR2M), whereas for 3MHAIL, hail is only formed when rain interacts with distribution pB. Rain colliding with distribution pA does

Table 4.7: Values after one Δt for newly formed hailstones resulting from rain-pristine ice (r-p) collisions for the original RAMS 2M (OR2M) and new 3M (3MHAIL) collection algorithms; hail mass mixing ratio r_h [kg kg^{-1}], hail number concentration N_{th} [kg^{-1}], hail reflectivity Z_h [$\text{mm}^6 \text{m}^{-3}$], and hail mean mass diameter D_{mh}^* [mm]. Column headings denote specific combination of initial distributions from Table 4.6.

	rA-pA	rA-pB	rB-pA	rB-pB
r_h : OR2M	1.0329×10^{-3}	1.0357×10^{-3}	1.0152×10^{-3}	1.01635×10^{-3}
r_h : 3MHAIL	0	1.0346×10^{-3}	0	1.01465×10^{-3}
N_{th} : OR2M	1000	1000	50	50
N_{th} : 3MHAIL	0	977.714	0	49.784
Z_h : OR2M	2.47625×10^4	2.4898×10^4	4.7849×10^5	4.7953×10^5
Z_h : 3MHAIL	0	2.541×10^4	0	4.8×10^5
D_{mh}^* : OR2M	1.299	1.3	3.506	3.508
D_{mh}^* : 3MHAIL	0	1.31	0	3.518

not result in hail formation with 3MHAIL because the mean mass diameter of distribution pA ($D_{\bar{m}p} = 25.9 \mu\text{m}$) is below the threshold of $40 \mu\text{m}$, and thus, the collection efficiency of these small ice crystals is zero (Lew et al. 1985). In the rA-pB and rB-pB tests, the r_h and N_{th} (Z_h and $D_{\bar{m}h}$) values of the newly formed hail particles are less (slightly greater) with 3MHAIL compared to those for OR2M as a result of allowing rain drops to collect more than one ice crystal per Δt (F94). Thus, for these particular initial distributions and environmental conditions, the 3MHAIL scheme generates fewer but slightly larger hailstones via rain-pristine ice collisions compared to those produced with OR2M, in which the entire raindrop distributions are converted to hail.

For the rain-aggregate set of tests, the OR2M and 3MHAIL schemes produce identical hail distributions for rain interacting with aggregate distribution A (Table 4.8), with both rain distributions converting entirely to hail in one Δt . In the rA-aA and rB-aA cases, larger raindrops collect smaller aggregate particles, which act as freezing nuclei for the raindrops, and since

Table 4.8: As in Table 4.7 for rain-aggregate (r-a) collisions. Changes in aggregate mixing ratio Δr_a [kg kg^{-1}] as well as values for newly formed graupel particles (r_g [kg kg^{-1}], N_{ig} [kg^{-1}]) resulting from r-a collisions are also listed when applicable.

	rA-aA	rA-aB	rB-aA	rB-aB
r_h : OR2M	1.0603×10^{-3}	7.8191×10^{-4}	1.02128×10^{-3}	1.1231×10^{-3}
r_h : 3MHAIL	1.0603×10^{-3}	0	1.02128×10^{-3}	0
N_{th} : OR2M	1000	86.141	50	21.31
N_{th} : 3MHAIL	1000	0	50	0
Z_h : OR2M	2.6095×10^4	1.6474×10^5	4.84196×10^5	1.3737×10^6
Z_h : 3MHAIL	2.6095×10^4	0	4.84196×10^5	0
$D_{\bar{m}h}^*$: OR2M	1.311	2.681	3.513	4.819
$D_{\bar{m}h}^*$: 3MHAIL	1.311	0	3.513	0
Δr_a : 3MHAIL	---	3.6869×10^{-4}	---	---
r_g : 3MHAIL	---	---	---	1.1231×10^{-3}
N_{ig} : 3MHAIL	---	---	---	21.31

$N_{ia} \gg N_r$, there are sufficient aggregate particles available to freeze all of the raindrops. Additionally, the larger sizes of raindrops in distribution rB relative to rA (Table 4.6) results in larger hailstone sizes (Table 4.8). Identical hail distributions are generated by OR2M and 3MHAIL in these two cases due to the fact that, for three-component freezing, the amounts of mass and numbers (when applicable) transferred from the colliding categories to the destination category with 3MHAIL are computed using the original RAMS 2M collection scheme as explained in Section 3.3.3.1. The 3MHAIL scheme simply employs an alternate classification algorithm for the destination category rain-ice collisions. Case in point, the resulting hydrometeor distributions for cases rA-aB and rB-aB are distinctly different between the OR2M and 3MHAIL schemes (Table 4.8). Hail is generated in both of these cases with OR2M, with greater amounts of hail mass and larger hailstones created in rB-aB compared to rA-aB due to the larger particle sizes in the former case versus the latter (Table 4.6). With the 3MHAIL scheme, the rain-aggregate collisions result in rain mass transferred to the aggregate category for case rA-aB, and the generation of graupel in case rB-aB, with the latter result noted by Cotton and Anthes (1989) as a possible outcome of rain-ice collisions. Because the density of aggregates decreases for increasing particle size, and $D_{\bar{m}_a}$ of distribution B is larger than $D_{\bar{m}_r}$ for both rain distributions A and B (Table 4.6), the resulting densities of the coalesced particles are less than the threshold for hail formation (Table 3.4, Section 3.3.3.1). Thus, for case rA-aB with the 3MHAIL scheme, the collection of small raindrops by relatively large aggregate particles is equivalent to aggregate riming, as suggested by Khain et al. 2004 and MY05b. In case rB-aB, the aggregate hydrometeors are only slightly larger than the raindrops with which they collide (Table 4.6) such that the density of the coalesced particles is greater than that for an aggregate of size $D_{\bar{m}_a}$ but less than $0.5(\rho_g + \rho_h)$, thus the coalesced particles are classified as graupel.

Table 4.9: As in Table 4.7 for rain-graupel (r-g) collisions. Changes in graupel mixing ratio Δr_g [kg kg⁻¹] resulting from r-g collisions are also listed when applicable.

	rA-gA	rA-gB	rB-gA	rB-gB
r_h : OR2M	1.0454×10^{-3}	7.5588×10^{-5}	1.0185×10^{-3}	7.803×10^{-4}
r_h : 3MHAIL	1.0454×10^{-3}	0	1.0185×10^{-3}	7.803×10^{-4}
N_{th} : OR2M	179.504	5.702	50	5.27
N_{th} : 3MHAIL	179.504	0	50	5.27
Z_h : OR2M	1.4131×10^5	2.3258×10^4	4.8156×10^5	2.68013×10^6
Z_h : 3MHAIL	1.4131×10^5	0	4.8156×10^5	2.68013×10^6
D_{mh}^* : OR2M	2.312	3.042	3.51	6.798
D_{mh}^* : 3MHAIL	2.312	0	3.51	6.798
Δr_g : 3MHAIL	---	6.372×10^{-5}	---	---

Table 4.9 lists the results for the rain-graupel collision tests. Due to the fact that $D_{mg} < D_{mr}$ in experiments rA-gA, rB-gA, and rB-gB, the computed densities of the coalesced particles are greater than the threshold for hail formation (Table 3.4, Section 3.3.3.1), and these particles are therefore classified as hail in the 3MHAIL scheme. This results in identical hail distributions generated by OR2M and 3MHAIL in each of these three cases, similar to the results for rain-aggregate experiments rA-aA and rB-aA (Table 4.8). It is also evident that, for cases rA-gA, rB-gA, and rB-gB, increases in the values of D_{mr} and D_{mg} result in increases in the sizes as well as the Z_h values of the newly formed hailstones (Table 4.9). For case rA-gB, $D_{mg} > D_{mr}$ such that the resulting coalesced particles are classified as graupel with 3MHAIL, thereby leading to an increase in r_g . In contrast, rain-graupel collisions with OR2M generate hail in this case, and a corresponding reduction in r_g occurs.

4.3.2) Formation of new hail via rain-ice collisions in the presence of pre-existing hail

The second series of experiments examines differences in resulting hail distributions with the OR2M and 3MHAIL collection schemes when newly formed hail is added to a pre-existing hail

distribution at a grid point. As explained by MY06a, the addition of newly formed small hailstones to an existing distribution in a three-moment microphysics scheme can result in a much broader hail distribution than either the existing or newly formed hail distributions. The scheme attempts to represent two distinctly different spectra with a single gamma distribution. In order to maintain most of the characteristics of the existing hail distribution, the 3MHAIL scheme employs an adjustment algorithm to the numbers of newly created hailstones by preserving the higher order moments ($M3$ and $M6$) of the resulting (existing + new) distribution (Section 3.3.3.3). The pre-existing hail distribution used in these experiments is prescribed at a single grid point at the same time ($t = 0$) as the rain and ice distributions and has values of $r_h = 0.001 \text{ kg kg}^{-1}$, $N_{th} = 0.26539 \text{ kg}^{-1}$, $Z_h = 4.19465 \times 10^7 \text{ mm}^6 \text{ m}^{-3}$, $\nu_h = 4.0$, and $D_{\bar{m}h} = 20 \text{ mm}$. Note that in this set of experiments, the existing hail distribution interacts with rain and ice distributions. The rain and ice distributions listed in Table 4.6 are used here as well.

The resulting changes in r_h , N_{th} , and Z_h , as well as the updated values of ν_h , and $D_{\bar{m}h}$ (denoted by $*$) following collection and computation of the hail reflectivity tendencies for rain-ice collisions in the presence of existing hail are displayed in Table 4.10. As in the previous set of experiments, new hail is formed in all cases with OR2M, whereas r-p collisions with 3MHAIL lead to hail only in cases rA-pB and rB-pB. The changes in r_h due to the addition of new hail as well as collection of rain and ice by the existing hail particles are identical for both OR2M and 3MHAIL in experiments rA-pB and rB-pB, although all other aspects of the resulting hail distributions are different. The resulting hail size distributions with OR2M become nearly exponential ($\nu_h^* = 1.01$) following the addition of newly created hailstones, and the $D_{\bar{m}h}^*$ magnitudes are significantly reduced from their original values of 20 mm. The adjustment of newly formed hail numbers with the 3MHAIL scheme results in considerably fewer numbers of

Table 4.10: Changes in r_h [kg kg^{-1}], N_{th} [kg^{-1}], and Z_h [$\text{mm}^6 \text{m}^{-3}$] in one Δt resulting from new hail formation via r-p collisions using the original RAMS 2M (OR2M) and new 3M (3MHAIL) collection algorithms in the presence of an existing hail distribution. Updated v_h^* and D_{mh}^* [mm] values following the addition of newly formed hailstones (when applicable) are listed as well.

	rA-pA	rA-pB	rB-pA	rB-pB
Δr_h : OR2M	1.0279×10^{-3}	1.0311×10^{-3}	1.0109×10^{-3}	1.01245×10^{-3}
Δr_h : 3MHAIL	0	1.0311×10^{-3}	0	1.01245×10^{-3}
ΔN_{th} : OR2M	995.424	995.424	49.779	49.779
ΔN_{th} : 3MHAIL	0	0.8321	0	0.8101
ΔZ_h : OR2M	2.4685×10^4	2.4839×10^4	4.7751×10^5	4.7895×10^5
ΔZ_h : 3MHAIL	0	2.9784×10^7	0	2.9463×10^7
v_h^* : OR2M	1.01	1.01	1.01	1.01
v_h^* : 3MHAIL	4.0	2.88	4.0	2.89
D_{mh}^* : OR2M	1.63	1.63	4.4	4.41
D_{mh}^* : 3MHAIL	20.02	15.79	20.02	15.85

new hailstones in cases rA-pB and rB-pB, however, the resulting hail size distributions are only slightly broader ($v_h^* \sim 2.88$) and the D_{mh}^* quantities are reduced to roughly 80% of their initial values. Changes in Z_h as computed with Eqn. 3.25 for these two cases are much larger with 3MHAIL than for OR2M due to the much smaller values of ΔN_{th} with 3MHAIL ($\Delta Z_h \propto 1 / \Delta N_{th}$).

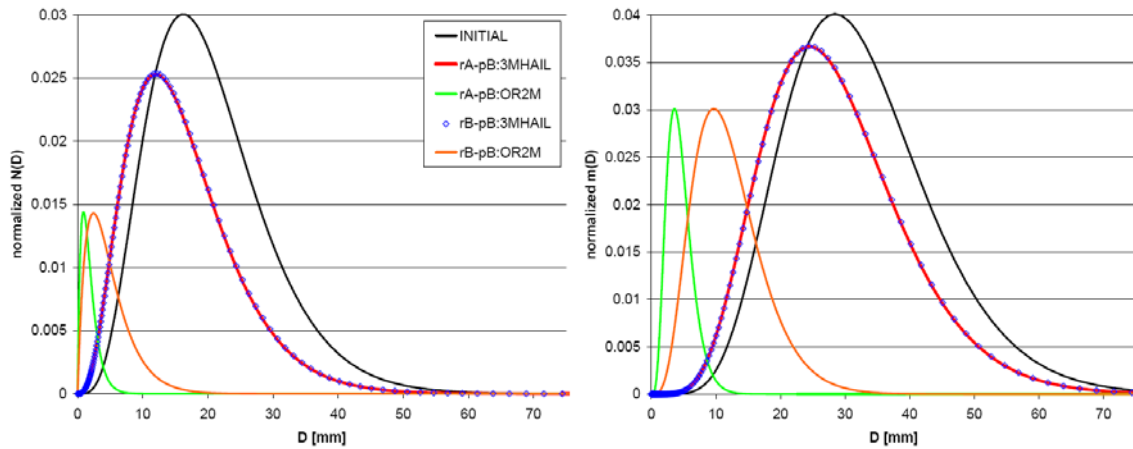


Figure 4.27: Normalized distributions for hail number (left panel) and hail mass (right panel) resulting from the addition of newly formed hail via rain-pristine ice collisions to an existing hail distribution (solid black line in each panel) for the OR2M and 3MHAIL collection schemes for cases rA-pB and rB-pB.

Plots of the normalized distributions of hail numbers and mass for the pre-existing and resulting hail distributions are displayed in Figure 4.27 for cases rA-pB and rB-pB. An examination of the normalized mass distribution for the pre-existing hail distribution reveals that the bulk of the mass is associated with hailstones having diameters between roughly 15 and 50 mm. It is also clearly evident from these plots that the OR2M collection scheme shifts the distributions towards smaller sizes such that virtually no mass remains associated with hail sizes greater than about 13 mm in case rA-pB and 33mm in case rB-pB. Furthermore, $D_{mh} = 20$ mm for the initial hail distribution, yet with OR2M, almost no hail particles with diameters greater than 20 mm exist in the resulting distributions for rA-pB and rB-pB. In contrast, the resulting shifts in the mass and number distributions with the 3MHAIL scheme are much less severe than with OR2M, such that the bulk of the mass for the resulting hail distributions with the 3MHAIL scheme is still associated with hailstones larger than about 12 mm. Of course, the newly formed small hail particles are under-represented in the resulting distributions with 3MHAIL, though at the same time, it is unrealistic for the mass of the larger hailstones in the initial distribution to be 'redistributed' over smaller diameter particles as in OR2M.

Results for rain-aggregate collisions occurring in the presence of an existing hail distribution are given in Table 4.11. As in the previous set of tests, no new hail is generated with 3MHAIL in cases rA-aB and rB-aB, and instead, rain is coalesced onto aggregates in rA-aB and graupel is formed in rB-aB. New hail is once again produced in all four cases with OR2M, and in cases rA-aA and rB-aA with 3MHAIL. Similar to the results for rain-pristine ice collisions, the resulting hail size distributions with OR2M become nearly exponential following the addition of newly created hailstones, and the D_{mh}^* magnitudes are reduced well below their original values of 20 mm. On the other hand, the resulting hail spectra for cases rA-aA and rB-aA with 3MHAIL are

Table 4.11: As in Table 4.10 for r-a collisions. Changes in aggregate mixing ratio (Δr_a) [kg kg^{-1}] as well as values for newly formed graupel particles (r_g [kg kg^{-1}], N_{ig} [kg^{-1}]) resulting from r-a collisions are also listed when applicable.

	rA-aA	rA-aB	rB-aA	rB-aB
Δr_h : OR2M	1.0558×10^{-3}	7.9087×10^{-4}	1.0177×10^{-3}	1.1195×10^{-3}
Δr_h : 3MHAIL	1.0558×10^{-3}	0	1.0177×10^{-3}	0
ΔN_{th} : OR2M	995.424	87.23	49.779	21.286
ΔN_{th} : 3MHAIL	0.856	0	0.814	0
ΔZ_h : OR2M	2.6042×10^4	1.6644×10^5	4.8395×10^5	1.37466×10^6
ΔZ_h : 3MHAIL	3.0271×10^7	0	2.9597×10^7	0
v_h^* : OR2M	1.01	1.01	1.01	1.01
v_h^* : 3MHAIL	2.87	4.0	2.89	4.0
D_{mh}^* : reg2M	1.64	3.52	4.41	5.94
D_{mh}^* : 3MHAIL	15.74	20.02	15.84	20.02
Δr_a : 3MHAIL	0	3.68×10^{-4}	0	0
Δr_g : 3MHAIL	0	0	0	1.1195×10^{-3}
ΔN_{ig} : 3MHAIL	0	0	0	21.286

only slightly broader than the initial size distribution and the D_{mh}^* values are about 80% of the initial D_{mh} magnitude, just as in cases rA-pB and rB-pB with 3MHAIL in the rain-pristine ice collision experiments (Table 4.10). The larger ΔN_{th} quantities for cases rA-aA and rB-aA with OR2M result in smaller ΔZ_h magnitudes compared to those with 3MHAIL (Table 4.11). The normalized distributions of hail numbers and mass for the pre-existing and resulting hail distributions in cases rA-aA and rB-aA are nearly identical to those shown in Figure 4.27 and are therefore not repeated here.

Table 4.12 lists the results for rain-graupel collisions in the presence of an existing hail distribution. Similar to the tests for which hail was absent initially, both OR2M and 3MHAIL generate new hail in cases rA-gA, rB-gA, and rB-gB, whereas for the rA-gB case, new hail is produced with OR2M and rain is coalesced onto graupel with 3MHAIL. The changes in r_h resulting from the addition of new hail as well as collection of rain and ice by existing hail are

Table 4.12: As in Table 4.10 for r-g collisions. Changes in graupel mixing ratio (Δr_g) [kg kg^{-1}] are also listed when applicable.

	rA-gA	rA-gB	rB-gA	rB-gB
Δr_h : OR2M	1.0416×10^{-3}	7.6951×10^{-5}	1.0152×10^{-3}	7.8024×10^{-4}
Δr_h : 3MHAIL	1.0416×10^{-3}	0	1.0152×10^{-3}	7.8024×10^{-4}
ΔN_{th} : OR2M	177.435	5.809	49.779	5.273
ΔN_{th} : 3MHAIL	.8445	0	0.811	0.57
ΔZ_h : OR2M	1.4286×10^5	2.3662×10^4	4.81499×10^5	2.6797×10^6
ΔZ_h : 3MHAIL	3.0017×10^7	0	2.9547×10^7	2.4796×10^7
ΔZ_h : adjust	1.6327×10^4	0	5.5028×10^4	3.0625×10^5
v_h^* : OR2M	1.01	1.01	1.01	1.01
v_h^* : 3MHAIL	2.87	4.0	2.89	2.56
D_{mh}^* : OR2M	2.9	7.23	4.41	8.81
D_{mh}^* : 3MHAIL	15.76	20.02	15.85	16.55
Δr_g : 3MHAIL	0	6.3673×10^{-5}	0	0

identical for both OR2M and 3MHAIL in experiments rA-gA, rB-gA and rB-gB. However, the adjustment of newly formed hail number concentration with 3MHAIL in each of these three cases results in many fewer new hail particles, greater changes in Z_h , and values of v_h^* and D_{mh}^* that are much more representative of the initial hail distribution compared to those for OR2M. As in the r-p and r-a hail formation experiments, the resulting hail distributions following the collection processes with OR2M are nearly exponential, and the D_{mh}^* magnitudes are significantly reduced relative to the initial D_{mh}^* (Table 4.12).

An examination of the normalized distributions of hail numbers and mass prior to and immediately following collection for experiments rA-gA, rB-gA, and rB-gB (Fig. 4.28) reveals a considerable shift towards smaller hail sizes for the resulting hail distributions with OR2M. Hailstones with $D \geq 20$ mm comprise a much greater percentage of the hail mass in the initial distribution than do smaller diameter particles, yet the amount of mass contained in the larger hail sizes following the addition of newly created hail is significantly reduced with OR2M in

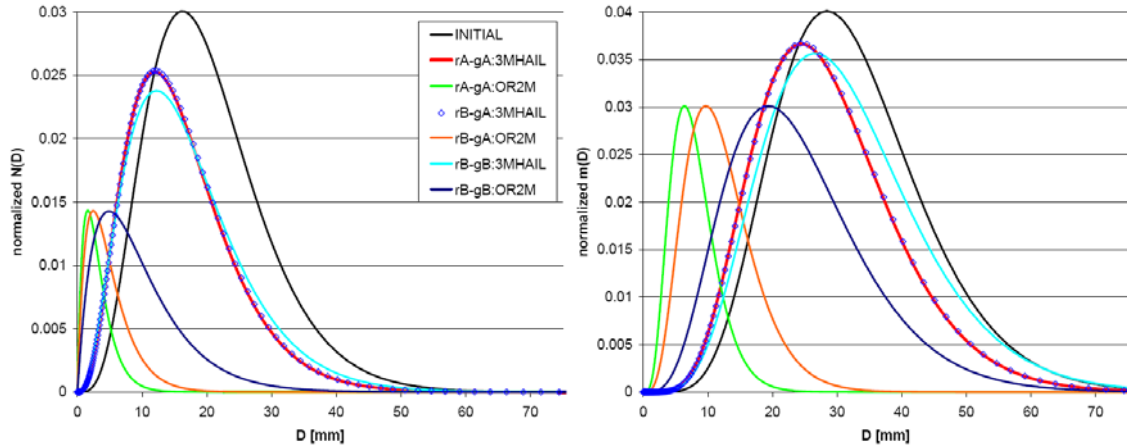


Figure 4.28: As in Figure 4.27, but for rain-graupel collision cases rA-gA, rB-gA, and rB-gB.

cases rA-gA and rB-gA. With the 3MHAIL collection scheme, the resulting number and mass distributions also experience shifts towards smaller diameters, though not nearly as drastic as with OR2M.

An examination of the normalized distributions of hail numbers and mass prior to and immediately following collection for experiments rA-gA, rB-gA, and rB-gB (Fig. 4.28) reveals a considerable shift towards smaller hail sizes for the resulting hail distributions with OR2M. Hailstones with $D \geq 20$ mm comprise a much greater percentage of the hail mass in the initial distribution than do smaller diameter particles, yet the amount of mass contained in the larger hail sizes following the addition of newly created hail is significantly reduced with OR2M in cases rA-gA and rB-gA. With the 3MHAIL collection scheme, the resulting number and mass distributions also experience shifts towards smaller diameters, though not nearly as drastic as with OR2M.

Additional tests for hail formation in the presence of pre-existing hail distributions were also performed using an initially broad hail distribution ($\nu_h = 2.0$) weighted towards small sizes ($D_{\bar{m}_h} = 1.62$ mm) as well as a narrow distribution ($\nu_h = 7.8$) weighted towards large hailstones ($D_{\bar{m}_h} =$

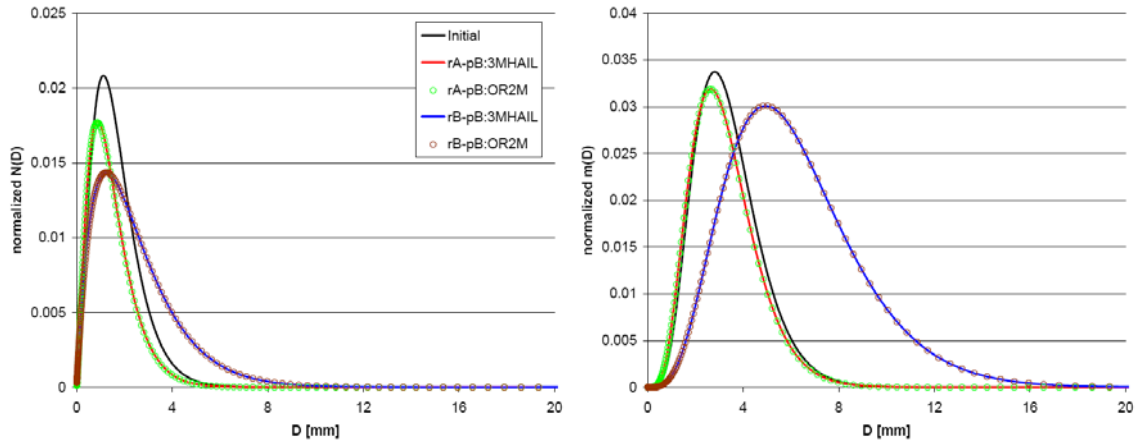


Figure 4.29: As in Figure 4.27 for additional rA-pB and rB-pB tests in which the initial (pre-existing) hail distribution is broad and weighted towards small hail sizes.

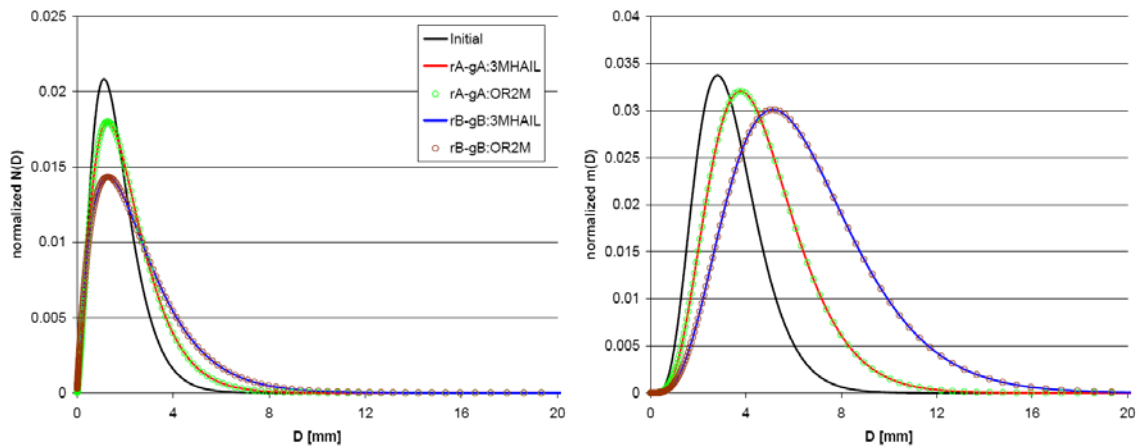


Figure 4.30: As in Figure 4.27 for additional rA-gA and rB-gB tests in which the initial (pre-existing) hail distribution is broad and weighted towards small hail sizes.

40 mm). In experiments with the broad distribution of small hailstones, the resulting hail distributions predicted by the OR2M and 3MHAIL schemes were nearly identical for cases in which new hail formation occurred for 3MHAIL (Figs. 4.29 and 4.30). The results for the pre-existing large hail case (not shown) followed a similar trend to the results presented in Tables 4.10-4.12, namely broadening of the final hail distributions towards exponential and unrealistic shifts in hail sizes towards much smaller diameters with OR2M (e.g., $D_{mh}^* = 1.73$ to 4.7 mm for r-p collisions, $D_{mh}^* = 1.74$ to 6.32 mm for r-a collisions, and $D_{mh}^* = 3.09$ to 9.57 mm for r-g

collisions). The use of the 3MHAIL scheme for the large hail case resulted in only slight broadening of the final hail distributions (v_h^* values of about 6.1) and $D_{\bar{m}h}^*$ magnitudes that ranged from 33.23 to 34.57 mm compared to the initial $D_{\bar{m}h}$ value of 40 mm.

In summary, the results from these hail formation tests clearly show the advantages of the 3MHAIL collection scheme for rain-ice collisions over the original RAMS 2M collection scheme. The 3MHAIL scheme allows for more realistic hydrometeor types resulting from interactions between rain and (non-hail) ice particles as opposed to the OR2M scheme, in which these interactions always result in the generation of new hail particles. In addition, adjusting the newly formed hail number concentrations with 3MHAIL when hail previously exists at a grid point provides an avenue for maintaining the general characteristics of the existing hail distribution, which is not possible in the approach taken in MY05a. For situations in which the characteristics of the newly formed hail distribution are similar to those of the existing distribution, the adjustment of newly created hail particles has much less of an impact on the resulting hail distribution such that the OR2M and 3MHAIL schemes tend to give comparable results (Figs. 4.29 and 4.30).

4.4) *Summary of 3MHAIL scheme tests*

The tests in the previous sections demonstrate that the various modifications made to the original (2M) RAMS microphysics sedimentation, melting, and hail formation algorithms in the 3MHAIL scheme result in much better representation of these processes compared to the lower-order moment schemes. The next step is to verify the full 3MHAIL scheme, and this is accomplished in the next chapter by simulating an actual supercell case that occurred over

northwest Kansas on 29 June 2000. The results of the tests carried out in the current chapter are summarized below.

- Sedimentation of hail using a one-dimensional column model for a variety of hail distributions on both constant and stretched vertical grids reveal the 3MHAIL scheme gives results that most closely resemble those of a true bin-sedimentation scheme compared to sedimentation using either the 1M or 2M versions (with fixed v_h) of the 3MHAIL sedimentation scheme. In the 1M version, the r_h profiles are generally underpredicted, surface precipitation is delayed, and the diagnosed N_{th} (Z_h) values tend to be much larger (smaller) relative to the solutions for the bin sedimentation scheme. With the 2M version, the predicted profiles of N_{th} are improved relative to those for the 1M case, although excessive size sorting of r_h occurs when a vertical grid with constant spacing is employed resulting in hail reaching the surface too early compared to the bin scheme. The use of a stretched vertical grid mitigates this excessive size sorting, however, on both grid types, the diagnosed values of Z_h tend to be severely overestimated with the 2M version. The 3MHAIL scheme tends to underpredict the maxima in r_h , N_{th} , and Z_h , and overpredict these values within the upper and lower regions of the individual profiles, particularly for cases in which a stretched vertical grid is used, yet the resulting profiles and surface precipitation rates still show the closest match to the bin scheme.
- Idealized simulations of the sedimentation and melting processes associated with two very different 'hailshafts' show that the 3MHAIL scheme with the melting algorithm of RH87b simulates these processes more accurately than either the modified 2M scheme or the 3MHAIL scheme with the old (RAMS) melting algorithm. Artificial shifts in the hail size distributions towards larger hail diameters as a result of complete melting of the smallest

particles occur in simulations with the modified 2M scheme as well as with the old melting algorithm in the 3MHAIL scheme whereas the new melting algorithm significantly reduces or eliminates this artificial shift. Broadening of the hail size spectra aloft due to faster sedimentation of the larger hailstones and narrowing of the size spectra below the melting level owing to complete melting of the smallest hail particles seem to be much more accurately represented with the 3MHAIL scheme compared to both the modified 2M scheme and the old melting algorithm. These tests also showed that the evolution of hail sedimentation, melting and shedding, and the surface precipitation characteristics are sensitive to the value of ν_h in the 2M scheme, whereas a naturally varying evolution of these processes via the prediction of ν_h is simulated with the 3MHAIL scheme.

- The implementation of the hail formation schemes of MY05b for three-component freezing and F94 for rain-pristine ice collisions allows for more realistic outcomes as a result of rain-ice collisions (i.e., rimed snow, aggregates, and graupel; graupel or hail formation) compared to the original RAMS 2M formulation in which hail *always* results from these collisions. With the 3MHAIL scheme, new hail particles formed in the presence of existing hail do not significantly alter the higher order moments of the existing hail distribution.

5. Verification of 3MHAIL scheme

5.1) *Introduction*

Idealized tests performed on the individual components of the 3MHAIL scheme in Chapter 4 revealed significant improvements to the representation of hail sedimentation, melting, and formation processes compared to the original lower-order moment formulations in the RAMS cloud model. In order to verify the 3MHAIL model and further gauge its quality, numerical simulations of a tornadic supercell that occurred in northwestern Kansas on 29 June 2000 during the Severe Thunderstorm Electrification and Precipitation Study (STEPS; Lang et al. 2004) field program are performed using the 3MHAIL as well as two other two-moment microphysics schemes. Simulations using single-moment bulk microphysics are not carried out as numerous studies have already focused on improvements in model solutions when using double-moment versus single-moment bulk schemes (F94; M97; Reisner et al. 1998; MY06b; Seifert and Beheng 2006; Mansell 2008; Morrison et al. 2009; Dawson et al. 2010; Jung et al. 2010; Bryan and Morrison 2012). Comparisons of the model results with analyses of observations from the actual event are made to assess how well the simulations with different microphysical approaches are able to reproduce observed storm features such as reflectivity structures, kinematic fields, and hail distributions. Additional analyses are also performed to examine differences in the microphysical characteristics of the modeled storms produced by the various microphysics schemes, with a particular focus on the processes of hail formation, growth, and melting as well as the role of hail in the morphology of low-level cold-pools. The results tend to show a significant improvement in the prediction of hail as well as in the overall storm evolution when the 3MHAIL scheme is applied versus the use of a two-moment scheme.

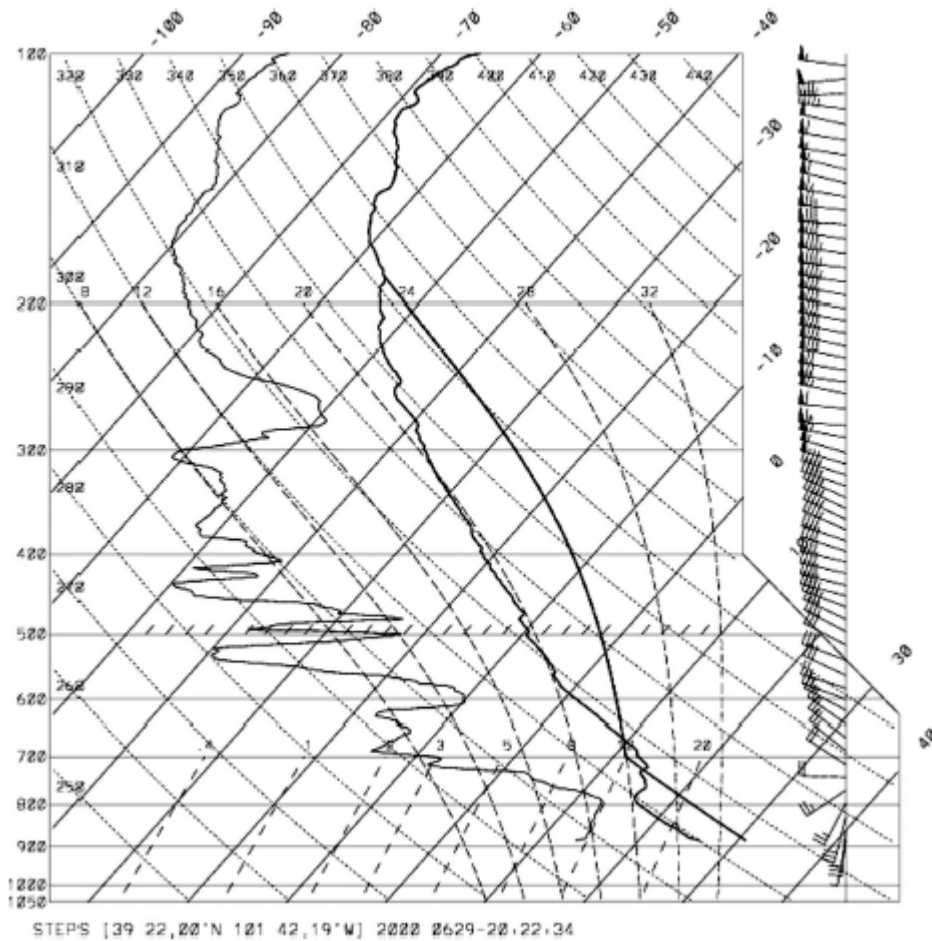


Figure 5.1: Skew-*T* plot of MGLASS sounding on 29 June 2000 at 2022 UTC near Goodland, KS [from TMWR05].

5.2) Overview of the 29 June 2000 supercell storm

The atmospheric environment in which the 29 June 2000 supercell occurred was supportive of supercell storm development (Johns and Doswell 1992; Moller et al. 1994). Environmental winds at low levels were southerly and veered to the west-northwest with height, as evident in the 2022 UTC sounding near Goodland, KS from the NCAR Mobile GPS/Loran Sounding Systems (MGLASS) (Fig. 5.1). This sounding was taken roughly 65 km to the southeast of where the storm initiated and about 1 hour prior to the first detection of the storm by radar (2130 UTC) (Kuhlman et al. 2006). A modestly high surface-based convective available potential energy (CAPE) value of 1254 J kg^{-1} and a strongly sheared, veering wind profile (0 to 3 km

storm relative helicity (SRH) values were around $330 \text{ m}^2\text{s}^2$) indicated the potential for supercell development (Moller et al. 1994; Rasmussen and Blanchard 1998).

The 29 June 2000 supercell storm initially formed over northeast Colorado during the afternoon along a southwest-northeast oriented dryline. The first radar echo associated with the storm was detected around 2130 UTC in the vicinity of the Colorado, Kansas, and Nebraska borders. During its early and maturing stages of development (approximately the first 2 hours), the observed storm was generally multicellular and moved to the east-southeast at a speed of about 10 m s^{-1} , with the updraft and reflectivity cores mostly collocated (Tessendorf et al. 2005, hereafter TMWR05). Based on analyses of polarimetric radar data by TMWR05, two periods of hail growth and fallout were evident during the time period from roughly 2215 to 2320 UTC,

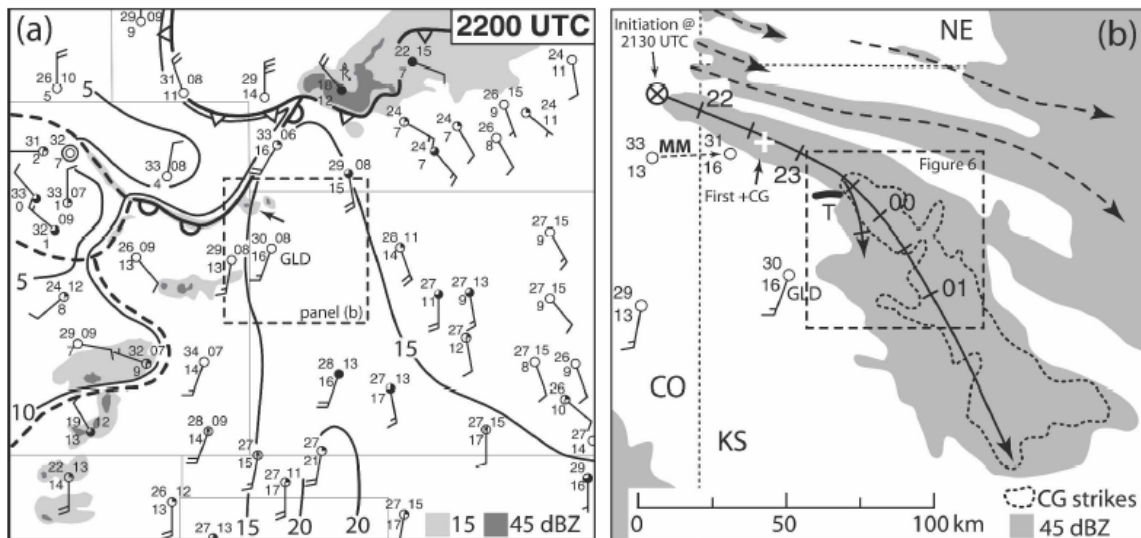


Figure 5.2: (a) Surface observations and reflectivity over the Central Plains at 2200 UTC. A southward-moving mesoscale cold front is indicated by the heavy curve with open triangles, a dryline is denoted by the scalloped curve, and other mesoscale boundaries are indicated by dashed lines. Isodrosotherms are analyzed every 5 °C (black curves). The first radar echoes of the storms are denoted by the arrow within the box for panel b. (b) Evolution of storm track, including 45-dBZ reflectivity swath and NLDN lightning during the period 2100-0300 UTC. Surface observations are from Goodland, KS (GLD) and mobile mesonet (MM) at approximately 2200 UTC. The storm path is indicated by the solid line through the gray dashed box; other storm paths are indicated by dashed lines. Station model includes temperature (°C) over dewpoint (°C) at left and mean sea level pressure (mb-1000) at upper right, with full wind barb equal to 5 m s^{-1} and half barb equal to 2.5 m s^{-1} . [From Kuhlman et al. 2006].

with confirmed surface reports of large hail ($D > 2\text{ cm}$) at 2235 UTC, and sizes up to 4.5 cm at 2305 UTC (*Storm Data*, <http://ww4.ncdc.noaa.gov/cgiwin/wwcgi.dll?wwEvent~Storms>) (Fig. 5.4). Concurrent with these two periods of hail growth, maximum radar reflectivity values increased to greater than 60 dBZ. By about 2320 UTC, a decline in hail growth and subsequent fallout had occurred, along with a reduction in maximum reflectivity values ($< 55\text{ dBZ}$) (Wiens et al. 2005), though the storm remained strong with maximum updraft speeds greater than 40 m s^{-1} (TMWR05).

Around 2330 UTC, the storm made a right turn (Fig. 5.2b), assumed more of a typical supercell structure with a strong mesocyclone at mid and low levels and a pronounced Bounded

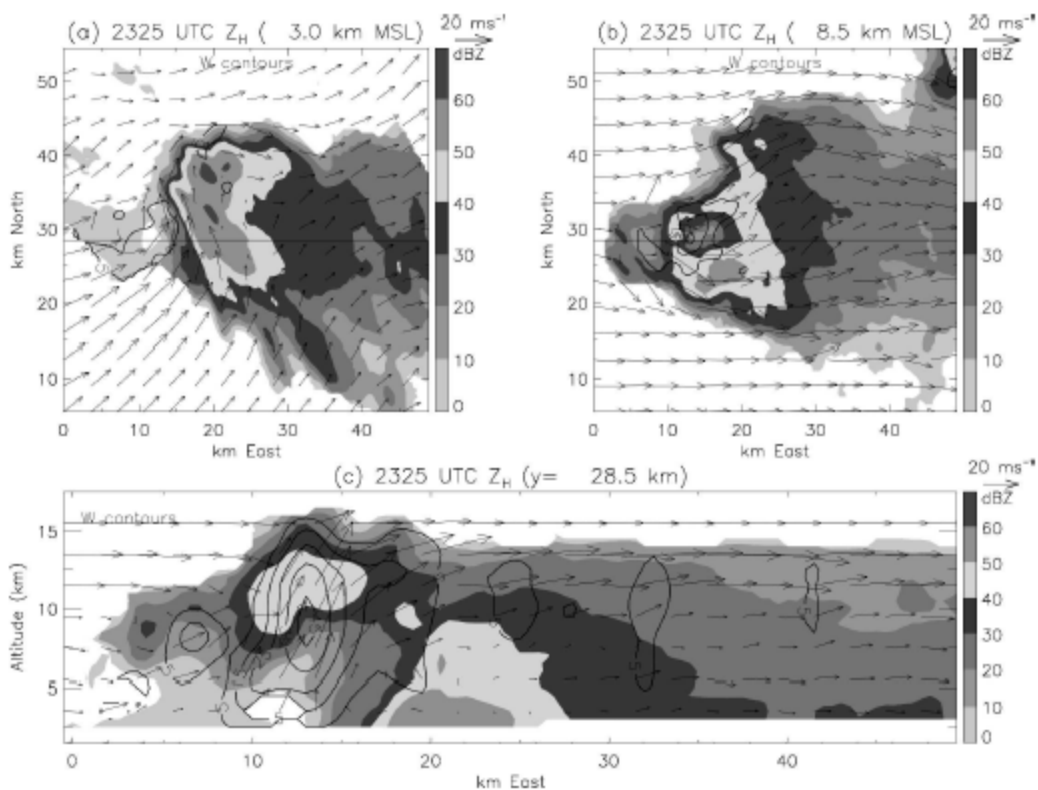


Figure 5.3: Synthesized winds and storm structure of the 29 June supercell representing the beginning of the tornadic period within the storm's severe right-moving mature phase at 2325 UTC: (a) horizontal cross section of grayscale reflectivity at $z = 3\text{ km}$ (MSL) and bold black updraft contours beginning at 5 m s^{-1} with a contour interval of 10 m s^{-1} , (b) horizontal cross section of grayscale reflectivity at $z = 8.5\text{ km}$ (MSL) with bold black updraft contours beginning at 15 m s^{-1} with a contour interval of 15 m s^{-1} , and (c) vertical cross section of grayscale reflectivity at $y = 28.5\text{ km}$ with bold black updraft contours beginning at 5 m s^{-1} with a contour interval of 10 m s^{-1} . All plots have storm-relative wind vectors overlaid. [From TMWR05].

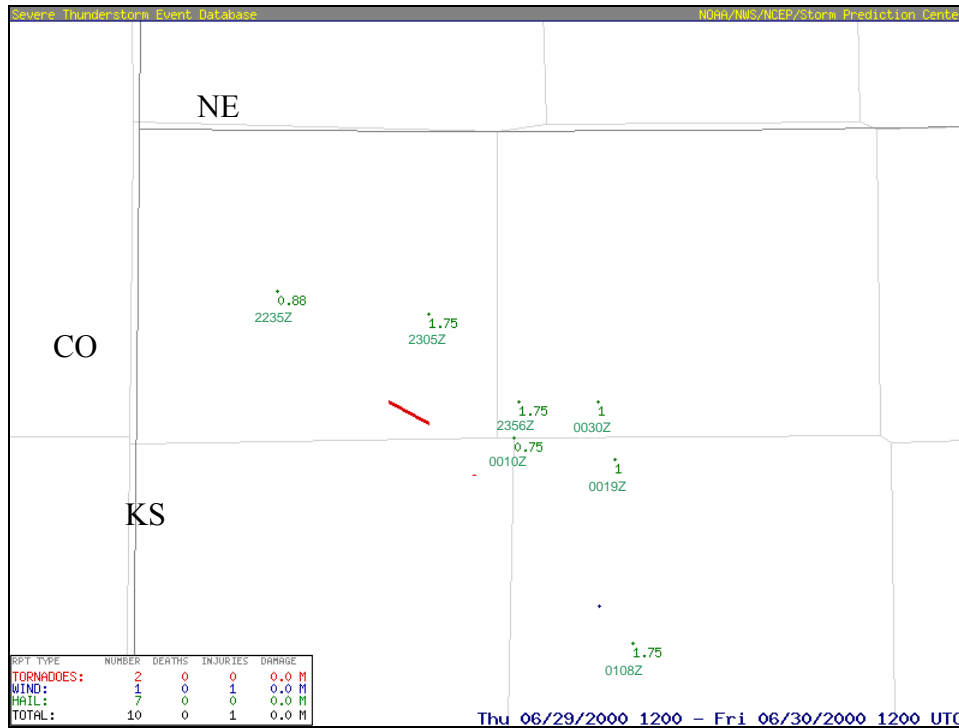


Figure 5.4: Hail location reports (green text) associated with 29 June 2000 supercell showing sizes (inches) and times of reports. Dark lines denote state boundaries and light lines denote county boundaries. Red diagonal line depicts path of tornado. Image made using SPC SeverePlot 3.0.

Weak Echo Region (BWER) in the reflectivity fields (Fig. 5.3), and traveled slightly slower (~ 9 m s^{-1}) towards the southeast (TMWR05). A tornado touchdown also occurred around this time (T in Fig. 5.2b). Once the storm made its right turn, the updraft core shifted to the southwest (right flank) of the reflectivity core, and strong cyclonic flow became established around the right flank of the updraft (Figs. 5.3a,b). A flanking line of weaker radar echoes extending to the west of the high reflectivity core (Fig. 5.3a), indicative of weaker updrafts along the outflow from the main storm, was also evident at lower levels (TMWR05). The storm was most intense between approximately 2330 and 0030 UTC, with maximum updraft speeds around 50 m s^{-1} and maximum reflectivity values greater than 65 dBZ aloft. Roughly 20 minutes after the right turn, the amount of hail above the melting level (as deduced from hail echo volume; see Fig. 5.11) significantly increased, reaching a peak value shortly thereafter, and a low level hook echo

appeared in the low-level reflectivity fields about 30 minutes after the right turn (TMWR05). Several reports of 2.5 to 4.5 cm diameter hail at the surface were made during this time (Fig. 5.4) (*Storm Data*; MacGorman et al. 2005). Shortly after 0030 UTC, the storm's intensity began to weaken and the hail echo volume declined somewhat (TMWR05; Wiens et al. 2005) as the storm continued moving southeast before merging with a mesoscale convective system in central Kansas (Kuhlman et al. 2006).

5.3) *General model description and experimental setup*

The Regional Atmospheric Modeling System (RAMS) is utilized for all simulations performed herein. RAMS uses the full set of non-hydrostatic compressible equations, which are advanced forward in time via a hybrid scheme of second-order accurate leapfrog and forward-in-time (Cotton et al. 2003). The model employs a time-splitting method in which the faster acoustic modes are integrated using a short time step and all other variables are integrated using a long time step (Klemp and Wilhelmson 1978). The model variables are solved on the Arakawa-C staggered grid (Mesinger and Arakawa 1976) with either a standard Cartesian coordinate system or a terrain-following coordinate scheme in the vertical (Cotton et al. 2003).

For the simulations carried out in this work, sub-grid turbulence is parameterized using the Smagorinsky (1963) deformation-K closure scheme with stability modifications of Lilly (1962) and Hill (1974). Radiative lateral boundary conditions for the normal velocity components (Klemp and Wilhelmson 1978) are applied with a phase speed of 30 m s^{-1} , and zero gradient conditions are applied to all variables. A rigid lid is used at the model top and a Rayleigh friction layer spans the top 8 model levels (4 km) to damp vertically-propagating gravity waves. A flat bottom boundary with a surface roughness height of 0.05 m is applied at the lower boundary to

account for surface friction effects (Louis et al. 1981), although the soil and vegetation schemes are not activated (i.e., no surface fluxes of heat or moisture into the model domain). Long- and short-wave radiation parameterization schemes are omitted in these simulations given the short duration of the simulations (3 hours) relative to the diurnal time scale (~ 12 hours).

As there are no data available for aerosols for this particular case, values typical of the High Plains region are assumed. Maximum values of aerosols acting as CCN are set to 600 cm^{-3} , 0.1 cm^{-3} for particles acting as GCCN, and $1 \times 10^5 \text{ kg}^{-1}$ ($\sim 100 \text{ L}^{-1}$) for IN particles. Horizontally homogeneous vertical profiles for CCN and GCCN aerosols are assigned at model initialization, with the maximum values occurring at the surface and decreasing linearly with height up to 4 km. Above 4 km, constant values of 100 cm^{-3} and $1 \times 10^{-5} \text{ cm}^{-3}$ are assigned for CCN and GCCN particles, respectively. IN particle concentrations are also initialized as horizontally homogeneous vertical profiles, with exponentially decreasing values with height. Sinks of CCN and GCCN via condensation of cloud particles are accounted for in the simulations, though the restoration of aerosol particles upon evaporation of cloud droplets is omitted. Allowing only sinks of CCN and no sources should have a minimal impact on model results. Saleeby and Cotton (2004) showed only small relative increases in CCN when restoration of CCN upon evaporation of cloud was included in idealized simulations of supercells. The impact of restoring CCN upon cloud evaporation is much greater for cloud systems evolving on longer time scales (e.g., orographic clouds) than the convective time scale (G. G. Carrió 2011 personal communication). The CCN aerosol profiles listed here are used in the verification of the 3MHAIL scheme as well as in simulations using two-moment microphysics. Sensitivity experiments that vary the maximum values of CCN aerosol profiles are also performed and will be covered in Chapter 6.

Table 5.1: Settings for the model options and parameterizations used in this work.

MODEL OPTION	SETTING/DESCRIPTION
Grid	Single grid; Arakawa C; standard Cartesian vertical coordinate $\Delta x = \Delta y = 500$ m, 288 x 264 points $\Delta z =$ variable (200 to 500 m; stretch ratio of 1.05), 58 vertical levels Model top: ~25 km
Timesteps	$\Delta t_{\text{long}} = 4$ sec; $\Delta t_{\text{accous}} = 0.4$ sec
Simulation duration	3.5 hours
Microphysics	reg2M : Two-moment bulk microphysics for all species (Meyers et al. 1997) [default RAMS two-moment scheme] 3MHAIL : Three-moment bulk microphysics for hail, reg2M for all other species mod2M : Two-moment version of 3MHAIL (fixed v_h) Bin-emulating self-collection for cloud and rain Bin-emulating riming for all ice species
Aerosols (CCN, GCCN, IN)	Explicit prediction of CCN, GCCN (Saleeby and Cotton 2004) and IN (Meyers et al. 1992) Initial horizontally homogeneous specified by vertical profile <ul style="list-style-type: none"> • CCN, GCCN: maximum value at surface with linear decrease to minimum value at 4 km; constant minimum value above 4 km • IN: Exponential decrease with height Aerosol sinks activated, aerosol restoration deactivated, no aerosol sources
Boundary conditions	Radiative lateral boundary (Klemp and Wilhelmson 1978) for normal velocity components; zero gradient for all other variables Rigid lid at model top with Rayleigh friction layer over top 4 km Flat lower boundary with surface roughness (Louis et al. 1981)
Turbulence parameterization	Smagorinsky (1963) deformation-K with stability modifications of Lilly (1962) and Hall (1974)
Radiation parameterization	Off
Surface parameterization	Off
Coriolis effect	On

All simulations are performed using a single model grid with dimensions of 144x132x25 km in the horizontal and vertical directions, respectively, centered at $x = 0$ km, $y = 0$ km. The horizontal grid spacing is 500 m, and variable grid spacing with a stretch ratio of 1.05 in the vertical is employed, ranging from 200 m at the lowest model level and increasing to a maximum of 500 m above about 6 km. The model long and short time steps are 4 and 0.4 seconds, respectively. These resolutions are adequate to resolve storm-scale features such as the structure and evolution of updrafts, downdrafts, mesocyclones, precipitation processes, and cold-pools,

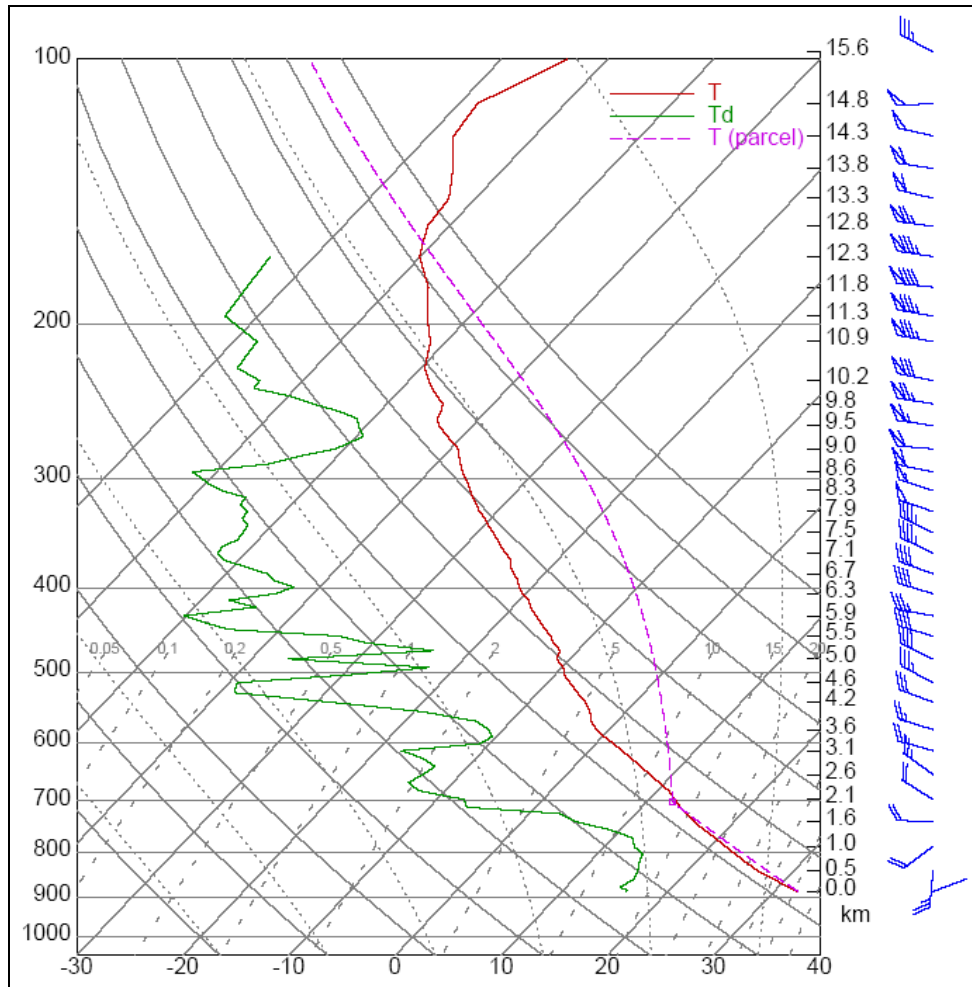


Figure 5.5: Modified input sounding used to initialize the simulations of the 29 June 2000 supercell. -- derived from MGLASS data up through about 14000 m, then interpolated data used above 14000m from Goodland, KS 18Z sounding. 'V' winds have been modified over lowest 2 km. Sounding made using 'skewtpost' routine within the ARPS model v5.2.12

but are insufficient to resolve tornadoes and other sub-storm scale features (Bryan et al. 2003). A summary of the model configuration used in this study is given in Table 5.1.

The horizontally homogeneous model environment is initialized using the atmospheric sounding shown in Fig. 5.5, which is a modified version of the MGLASS sounding presented in Fig. 5.1. The low-level temperature and moisture values are increased as in Kuhlman et al. (2006) to better reflect surface observations of the environment into which the storm propagated. In addition, the N-S components of the wind velocities are modified in the lowest 2 km of the

Table 5.2: Convective parameters and indices for sounding in Figure 5.5.

CAPE	3258 J/kg
LCL	701 mb; 2049m
LFC	687 mb; 2211m
Freezing level height (estimated)	590 mb; 3461m
LI, TT, KI, SWEAT	-9.1 °C, 62, 33, 673
BRN shear (0 to 6km)	16.3 m/s
SRH (0 to 3 km)	249 m ² s ⁻²
Mean storm motion	305° at 9 m/s

sounding (Fig. 5.6) in order to remove instabilities associated with small local Richardson numbers within this layer (Rosenthal and Lindzen 1983; G. Bryan 2011 personal communication). These modified winds result in a decrease of SRH from 327 m²s⁻² to 249 m²s⁻² (Table 5.2), however, this decreased SRH value is still well representative of tornadic supercell storms (Davies-Jones et al. 1990; Rasmussen and Blanchard 1998). The increased temperature and moisture within the convective boundary layer also result in an increase in CAPE from 1254 to 3258 J kg⁻¹ (Table 5.2), and a reduction in convective inhibition (CIN) from about 100 J kg⁻¹

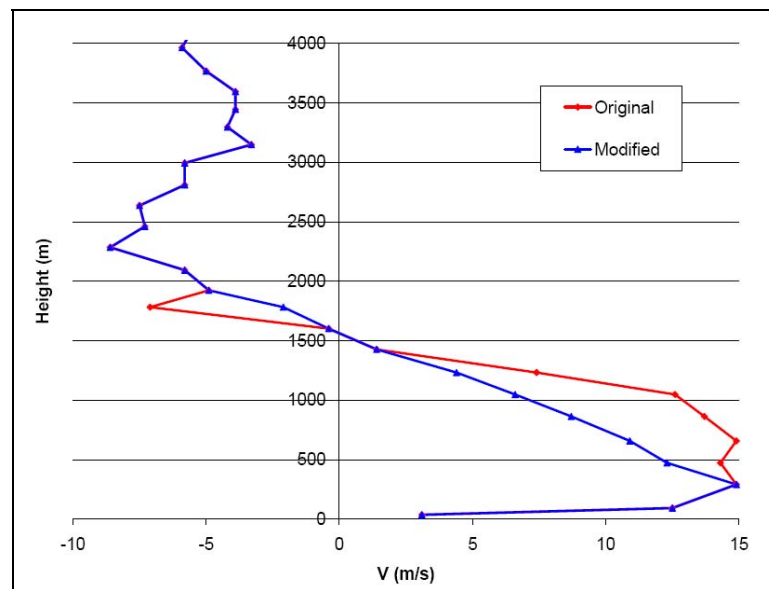


Figure 5.6: Vertical profile of model sounding (Fig. 5.5) N-S wind components modified over lowest 2 km compared to the original sounding (Fig. 5.1) N-S wind components.

Table 5.3: Names and descriptions of simulations performed for verification of 3MHAIL scheme

Experiment Name	Microphysics scheme
ccn600	3MHAIL (Chapter 3)
2Mccn600	modified 2M (3MHAIL with fixed v_h) (Chapter 4)
reg2Mccn600	two-moment bulk microphysics for all species (Meyers et al. 1997)

to less than 10 J kg^{-1} . An increase in the bulk Richardson number (BRN), defined as the ratio of CAPE to the lower tropospheric wind shear, from roughly 10 in the original sounding to 16.3 in the modified sounding (Table 5.2) also suggests an increased probability of supercell development ($15 < \text{BRN} < 35$ typical for supercells) (Weisman and Klemp 1984).

Three simulations are performed using different bulk microphysical schemes (Table 5.3); the 3MHAIL scheme (Chapter 3), the modified RAMS 2M scheme (Chapter 4, Section 4.2), and the regular RAMS 2M scheme (Meyers et al. 1997; Saleeby and Cotton 2004, 2008). In all three cases, convection is initialized at $t = 0$ using an ellipsoidal warm moist bubble with horizontal and vertical radii of 7 and 1.25 km, respectively, centered at $x = -50 \text{ km}$, $y = 30 \text{ km}$, and $z = 1.25 \text{ km}$. The potential temperature (θ') and moisture (r'_v) perturbations of the initiating bubble follow a cosine-squared distribution (Loftus et al. 2008), with $\theta'_{max} = 3\text{K}$ and $r'_v = 1.2r_v$ at the bubble center and decreasing to zero at the bubble edges. The simulations are run out to 210 minutes (3.5 hours).

5.4) Results

The results from the simulations are presented in two parts: comparisons of the simulated storms with the observed storm are shown first, followed by analyses and comparisons of the microphysical properties of the modeled storms using the different microphysics schemes. Analyses of the observations from TMWR05 are used as the primary basis for comparison with

the model results, thus every attempt is made to evaluate the model solutions using locations and times that coincide with the observations. For example, horizontal cross sections of model results are displayed at heights corresponding to 3 and 8.5 km MSL as in TMWR05. As the elevation of Goodland, KS is roughly 1.2 km MSL, model levels of 1.77 and 7.35 km AGL correspond to approximately 3 and 8.5 km MSL, respectively. Additionally, the model results are only evaluated for the portion of the domain containing the supercell storm whenever possible and generally do not include contributions from secondary cells that develop later in the simulations.

Quantitative evaluations of the model solutions include comparisons of the reflectivity structures of the observed and simulated storms. Following MY05a and MY06a, the total equivalent reflectivity (Z_e) is computed as the sum of the equivalent reflectivities for each hydrometeor category (except cloud and pristine ice),

$$Z_e = Z_{er} + Z_{es} + Z_{ea} + Z_{eg} + Z_{eh} . \quad (5.1)$$

Using Rayleigh theory, equivalent reflectivity is calculated as

$$Z_{ex} = \left(\frac{\alpha_{mx}}{\alpha_{mr}} \right) \frac{|K|_i^2}{|K|_w^2} Z_x , \quad (5.2)$$

where Z_x is the reflectivity factor [$\text{mm}^6 \text{m}^{-3}$] for species x ($x = r, s, a, g, h$) computed using Eqn. 3.13, and the ratio of dielectric constants for ice and water $|K|_i^2/|K|_w^2 = 0.224$ (F94). Equivalent reflectivity of rain is simply the reflectivity factor Z_r . The values for the mass coefficients α_x are listed in Table 3.1 of Chapter3, though a single mass coefficient ($\bar{\alpha}_{sa}$) is used for snow and aggregates assuming an average particle density of 100 kg m^{-3} (in practice, the particle densities of snow and aggregates vary with size). Z_{eh} in the 3MHAIL scheme is computed from the predicted reflectivity factor for hail (Z_h).

5.4.1) General characteristics of simulated storms and comparisons with observations

Convection develops rapidly in all three cases, with similar kinematic evolution through about the first 45 minutes, after which time the model solutions begin to diverge from one another (Fig. 5.7a). Two distinct updraft pulses are evident in the time series of maximum updraft speeds (w_{max}) for the three cases during this time period, the first being associated with the initiating bubbles and the second stronger pulse due to the regeneration of updrafts associated with low-level convergence brought about by outflows from the initial convection. The initial mode of convection in each case is multicellular (Figs. 5.8, 5.16-5.18), with new updrafts developing on the upshear side of the storm through about 75 minutes, and w_{max} values generally less than 40 m s^{-1} , in qualitative agreement with the observed storm during its developing and

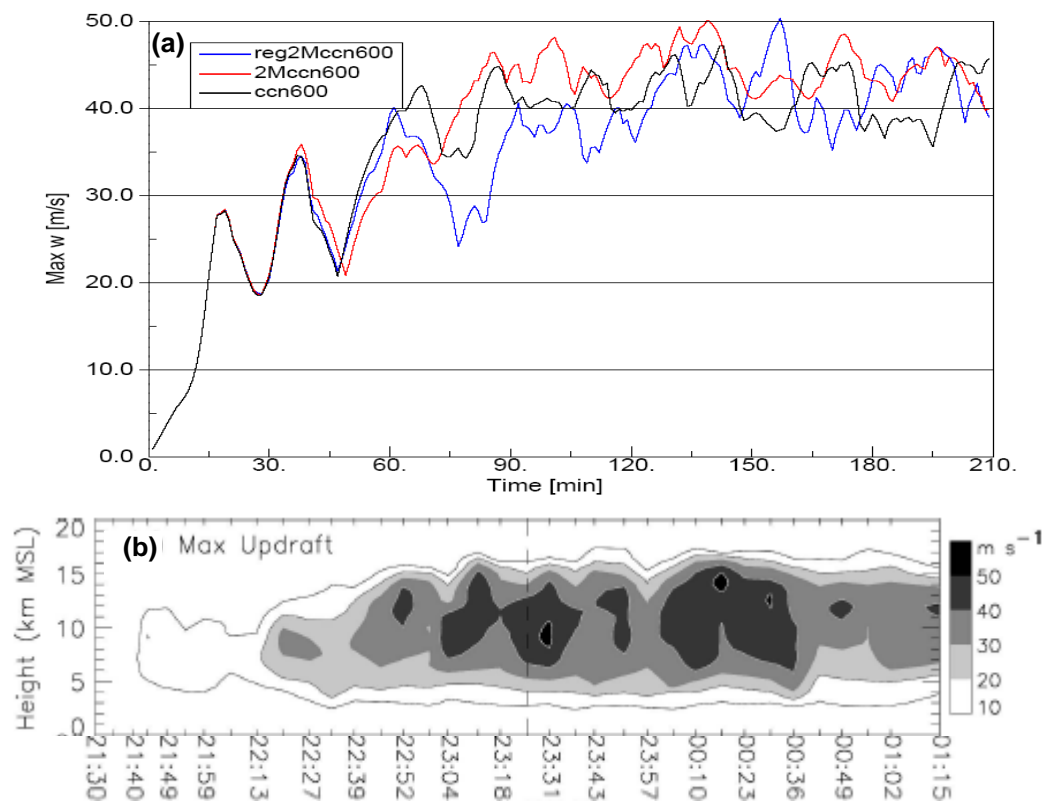


Figure 5.7: (a) Time series of domain maximum updrafts (m s^{-1}) for simulations reg2Mccn600 (blue), 2Mccn600 (red), and ccn600 (black). (b) Time-height contours of maximum updraft (m s^{-1}) for actual event as deduced from multi-Doppler analyses [From TMWR05]. Time scale for simulation results are aligned according to when the right turns of the simulated and observed storms occurred.

mature stages (TMWR05; Wiens et al. 2005). Storm motion for the first hour in all cases is generally to the east (95°) at about 10 m s^{-1} , similar to the speed and east-southeast movement of the observed storm prior to undergoing a right turn. Between approximately 60 and 90 minutes, the simulated storms transition from a multicell structure to more of a supercell structure with a single dominant updraft and a hook echo-like appendage in the low-level equivalent reflectivity (Z_e) fields (Fig 5.8a,b,c). In all three simulations, the storms make a right turn towards the southeast around 90 minutes (Figs. 5.8, 5.13), with the average storm speed in the ccn600 case ($\sim 9.5 \text{ m s}^{-1}$) similar to that of the observed storm (9 m s^{-1}) whereas the storms in the 2Mccn600 and reg2Mccn600 cases travel faster with average speeds of 11 m s^{-1} and 13 m s^{-1} , respectively.

The timing of the right turn is used as a basis for comparison between the observed and simulated storms. As the initiating mechanisms are distinctly different between the modeled and observed storms, the former initiated via a warm moist bubble and the latter forced via boundary layer convergence, the simulated storms develop into supercells much faster than the observed storm. Convection initiated with an initiating bubble (IB) develops and evolves much faster than convection initiated using a convergence method (Loftus et al. 2008), hence the right turns taken by the modeled storms after only 90 minutes are reasonable. Simulations of the same storm by Kuhlman et al. (2006) also utilized an IB to initiate convection and noted similar evolution and timing of the initial convection and subsequent right turn in their results. The overall morphologies of the simulated and observed storms agree quite well from the time of the right turn onward, particularly in the ccn600 case, as demonstrated in the following analyses.

The right turns taken by the modeled storms around 90 minutes are accompanied by increases in w_{max} (Fig. 5.7), positive vertical vorticity (ζ) at mid-levels (Fig. 5.9), and updraft volume (Fig. 5.10), with the exception of 2Mccn600 in which greater updraft volumes do not

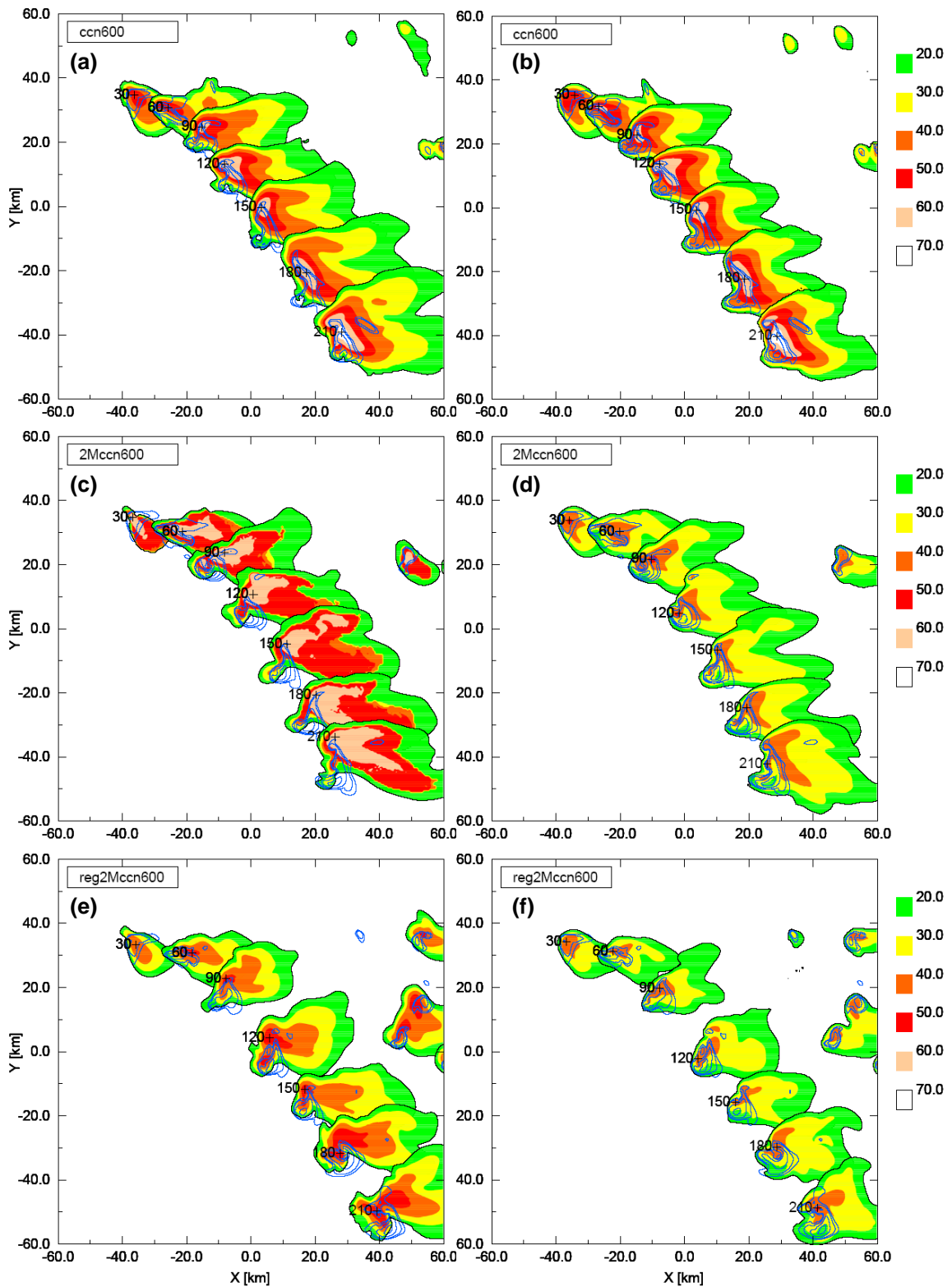


Figure 5.8: Evolution of simulated storm structures depicted every 30 min for (a,b) ccn600, (c,d) 2Mccn600, and (e,f) reg2Mccn600 at heights $z = 982$ m AGL (left column) and $z = 4.95$ km AGL (right column). Shaded fields are model equivalent reflectivity factor Z_e (dBZ) and blue contours are updraft at 4.95 km (values are 5, 10, 20, and 30 m s^{-1}). Black crosses next to times denote locations of maximum computed Z_e . In this and subsequent plan view plots, north is towards the top of the plots.

become established until after about 120 minutes. In agreement with the observed storm, the updraft cores have shifted to the right flank (south-southwest portion of the storm) of the reflectivity cores by this time, and the storms maintain these configurations for the remainder of the simulations (Fig. 5.8). Beyond 90 minutes, w_{max} values in cases ccn600 and 2Mccn600 generally remain above 40 m s^{-1} , with short-lived pulses of greater w_{max} values superimposed on the quasi-steady updrafts (Fig. 5.7a). In the reg2Mccn600 case, the simulated storm is initially somewhat weaker with w_{max} values fluctuating between 35 and 40 m s^{-1} from about 90 to 120 minutes, however, the magnitudes of w_{max} in all three cases beyond the initial bubble (i.e., $t > 30$ minutes) are certainly supportive of hail growth to large sizes (Ludlam 1958; Browning and Foote 1976; Nelson 1983). The simulations also exhibit a prolonged period of intense updraft between approximately 120 and 150 minutes at roughly the same time as a similar intense steady phase occurs in the observed storm (~ 2357 to ~ 0036 UTC) (Fig. 5.7b). Peak w_{max} values in cases 2Mccn600 and reg2Mccn600 are several m s^{-1} greater than in ccn600 (50 m s^{-1} compared to 46 m s^{-1}), though in general, the modeled storms exhibit similar maximum updraft intensities once they have reached a quasi-steady state and show good agreement with the observed storm.

The overall evolutions of the modeled storms match well with the observations as demonstrated by the progression of the Z_e fields for the three simulations (Figs. 5.8 and 5.13). It should be noted that the computed Z_e values for snow and aggregates are small owing to the generally small sizes of these particles predicted by the model, thus the Z_e fields in the mid- and upper-levels of the storms are not as extensive in the horizontal as in the observations. The distributions of Z_e magnitudes at approximately 1 km AGL for the times shown in Figure 5.8 for the ccn600 and reg2Mccn600 cases are generally comparable to the observed reflectivity values at 3 km (MSL) displayed in Figure 5.3a, whereas excessively high magnitudes of Z_e over a large

portion of the storm are evident at low levels in the 2Mccn600 case (Fig. 5.8c). As detailed in Chapter 4, the modified 2M microphysics scheme can lead to erroneously large reflectivity factors below the melting level owing to unphysical increases in hail mean mass diameters with the onset of melting. Because the hail distributions undergoing melting in the 2Mccn600 case do not become narrower, the hail mass is shifted towards larger diameter particles thereby leading to unreasonably large Z_{eh} magnitudes at low levels that dominate the computed Z_e values. At $z \sim 5$ km AGL, the Z_e magnitudes are greatest in the ccn600 case (Fig. 5.8b) due to the greater amounts of larger hail aloft in this case compared to the two-moment cases, which exhibit noticeably smaller Z_e values at this height (Figs. 5.8d,f). In addition, the reg2Mccn600 case exhibits lower Z_e values at 1 km due to the fact that this case produces primarily copious amounts of small hail that rapidly melts to form rain upon falling below the freezing level. Also of note is that a hook echo in the low-level Z_e fields appears at 90 minutes in the 2Mccn600 and reg2Mccn600 cases (Figs. 5.8c and 5.8e, respectively), whereas this feature is not evident until about 120 minutes in the ccn600 case (Fig. 5.8a). This latter observation compares well with the actual storm for which a low-level hook echo in the reflectivity fields appeared some 30 minutes after the storm turned right (TMWR05). Additional convection develops to the east-northeast of the primary storm after about 120 minutes in the 2Mccn600 and reg2Mccn600 cases, and after roughly 135 minutes in the ccn600 case. These weaker cells form along the outflow boundary of the main storm and do not interact with the supercell.

The elevated values of mid-level ζ_{max} that occur around 90 minutes and beyond (Fig. 5.9a,b,c) are associated with mid-level mesocyclones as apparent in the cyclonic flow patterns around the western and southern peripheries of the mid-level updrafts in each case (e.g., panels b in Figs. 5.16-5.18, 5.20-5.22, and 5.24-5.26). Although a direct match between the modeled and

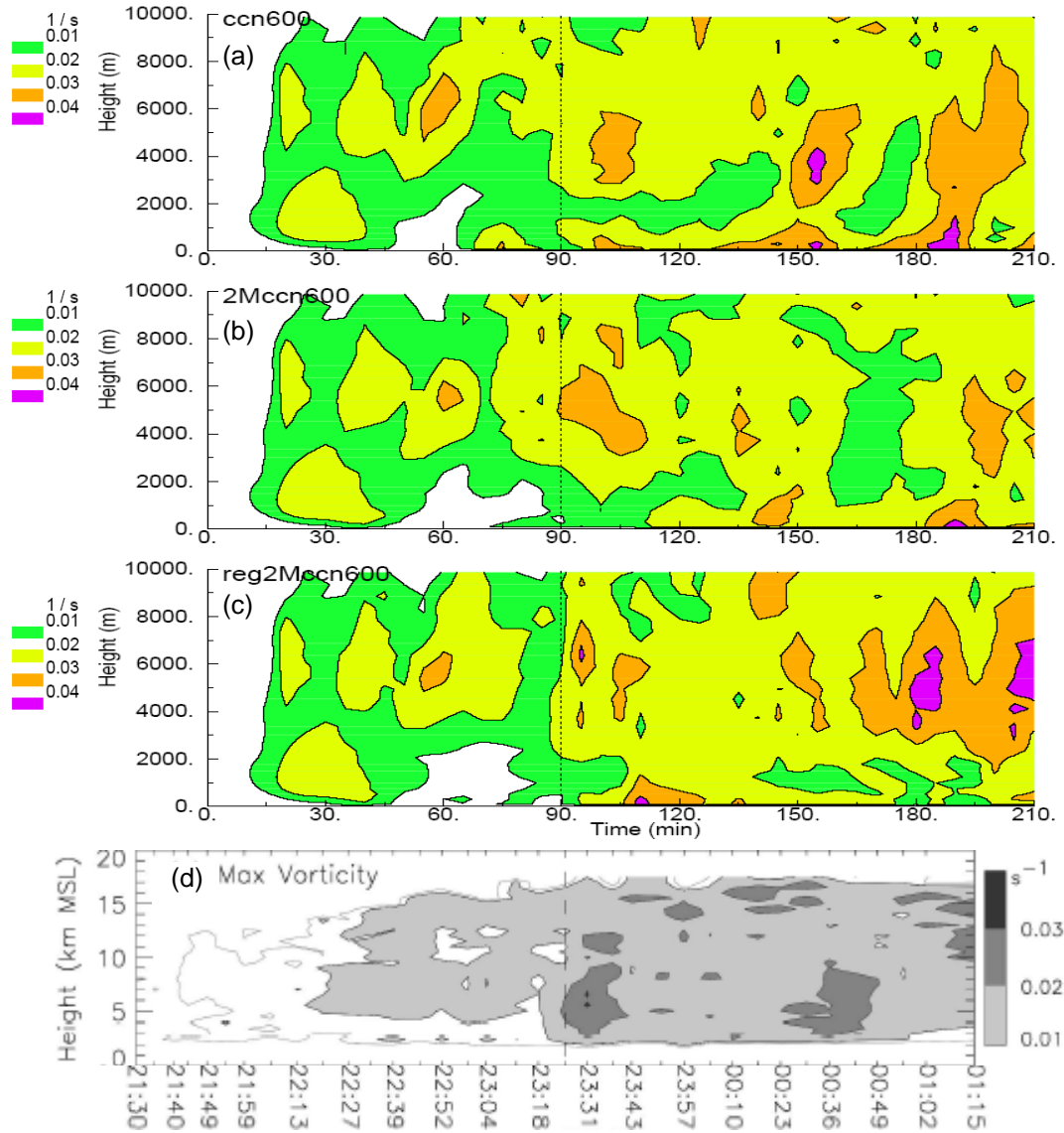


Figure 5.9: Time-height contours of maximum vertical vorticity (s^{-1}) for simulations (a) ccn600, (b) 2Mccn600, and (c) reg2Mccn600. (d) Time-height contours of maximum vertical vorticity (s^{-1}) synthesized from observations of 29 June 2000 supercell [From TMWR05]. Vertical dotted (dashed) lines in panels a-c (d) represent the time at which the storm made its right turn. Time scales for simulation results are aligned according to when the right turns of the simulated and observed storms occurred.

observed ζ_{max} is not expected, the time-height patterns of ζ_{max} between the simulated and the observed storms generally match quite well, with the exception of the 2Mccn600 case (Fig. 5.9). The observed time-height ζ_{max} fields exhibit two distinct peaks in ζ_{max} : the first occurs immediately following the right turn and a second peak is evident roughly one hour later (Fig.

5.9d). All three simulated cases display peak ζ_{max} values between about 90 and 115 minutes (Fig. 5.9a,b,c), similar to that seen in the observations. A secondary peak in ζ_{max} just after 150 minutes is clearly evident in the ccn600 case (Fig. 5.9a) and to a lesser extent in the reg2Mccn600 case (Fig. 5.9c), whereas the 2Mccn600 case actually shows a decrease in ζ_{max} after 150 minutes (Fig. 5.9b). Additional increases in ζ_{max} occur after 180 minutes in the simulations, however, the actual storm was beginning to exit the STEPS observational domain by this time (TMWR05) such that comparisons between the modeled and observed storms are subject to speculation. Overall, the time-height ζ_{max} fields for the ccn600 case appear to show the best match with the observations. Miller et al. (1988) and TMWR05 note the importance of low- and mid-level mesocyclone in the production of large hail; the horizontal flow within the mesocyclone permits growing hailstones to remain balanced or nearly balanced with the updraft speeds for an extended period of time.

An examination of the time-height contours of updraft volumes for the modeled storms (Fig. 5.10a,b,c) reveals patterns that share some similarities with those of the observed storm (Fig. 5.10d). Although the simulation updraft volumes are less than in the observations, there is generally good agreement between the modeled and observed storms with respect to the increase in updraft volume following the right turn, particularly for the ccn600 case. Subsequent maxima in updraft volume seen in the observations roughly 40 minutes after the right turn are also evident in the ccn600 and 2Mccn600 cases, though there appears to be a slight time lag in the simulation maxima compared to the observations. The decrease in updraft volume in the reg2Mccn600 case between roughly 125 and 160 minutes (Fig. 5.10c) is in contrast to the overall trend of increasing updraft volumes over greater depths that occurs during the same time period for the observed storm (Fig. 5.10d). In general, the patterns of updraft volume for the ccn600

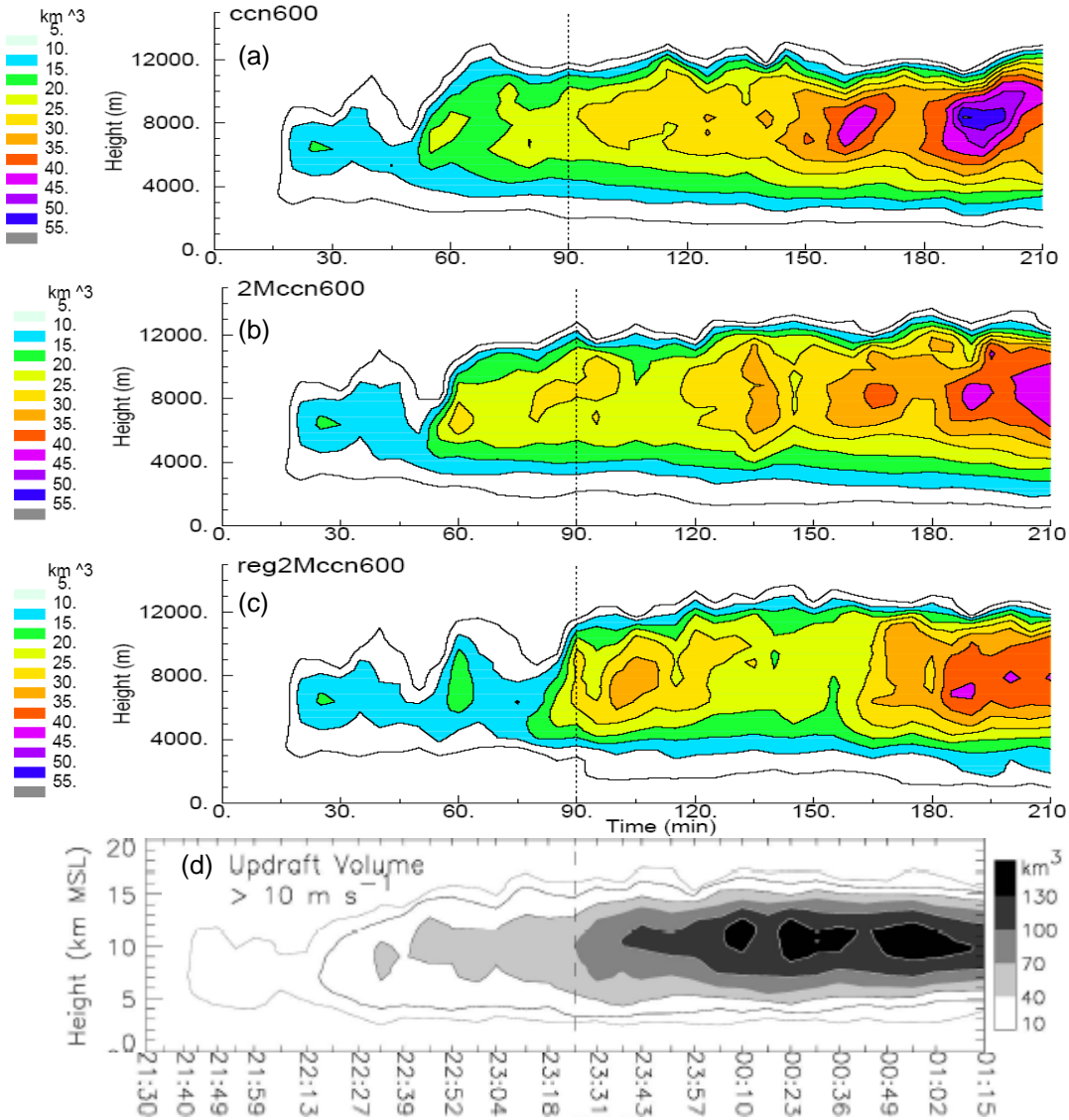


Figure 5.10: As in Fig. 5.9 except for storm updraft volume (km^3) greater than 10 m s^{-1} for simulations (a) ccn600, (b) 2Mccn600, and (c) reg2Mccn600. (d) Time-height contours of updraft volume (km^3) greater than 10 m s^{-1} synthesized from observations of 29 June 2000 supercell [From TMWR05]. Different scales are used in (a)-(c) compared to (d).

case show the closest match to the observed patterns, followed by those for the 2Mccn600 case.

This agreement is significant as detailed analyses performed by TMWR05 suggested updraft mass flux was one of the controlling factors for hail growth to large sizes for this storm.

Comparisons of the evolutions of hail and graupel volumes for the simulated storms with those deduced from the polarimetric radar measurements suggest the simulations are able to

reproduce the gross features of the bulk hail and graupel morphologies associated with the observed storm (Figs. 5.11 and 5.12). The exception here is the reg2Mccn600 case, which produced only minute amounts of graupel (less than the 0.1 g/kg threshold at any time throughout the duration of the simulation) and thus no plot is shown for this case in Figure 5.12. As previously mentioned, very little hail reaches the surface in the reg2Mccn600 case, and this is reflected in the sharp decrease hail volumes around 2km height. The distinct maxima in hail volume for the observed storm (Fig. 5.11d) both prior to and after its right turn were noted by TMWR05 and Weins et al. (2005) to occur roughly 10 to 15 minutes after a surge in updraft. These features are mostly reproduced in the simulations as well, albeit the magnitudes of hail volumes in the simulations are greater than in the observations owing to the propensity of the model to generate hail rather liberally, especially in the two-moment microphysics schemes. For example, beyond about 45 minutes, the hail volumes in cases 2Mccn600 (Fig. 5.11b) and reg2Mccn600 (Fig. 5.11c) are about 1.25 to 2 times larger than in ccn600 (Fig. 5.11a). Peak hail volumes evident between 135 and 165 minutes in the ccn600 and 2Mccn600 cases occur later relative to the timing of the right turn compared to the observations, yet these peaks are generally concurrent with local maxima seen between roughly 00:05 and 00:36 UTC in the observed hail volumes (Fig 5.11d). The later occurrence of these maxima in hail volume in the modeled storms is physically plausible given that large hail was reported at the surface well after the actual storm turned right (Fig. 5.4). In addition, the FHC algorithm used to deduce hydrometeor type only classifies the dominant species within a grid point whereas the computed hydrometeor volumes herein consider hail and graupel that may occupy the same grid point. In general, the magnitudes of hail volume in the ccn600 case compare more favorably to the observed values than do the two-moment cases.

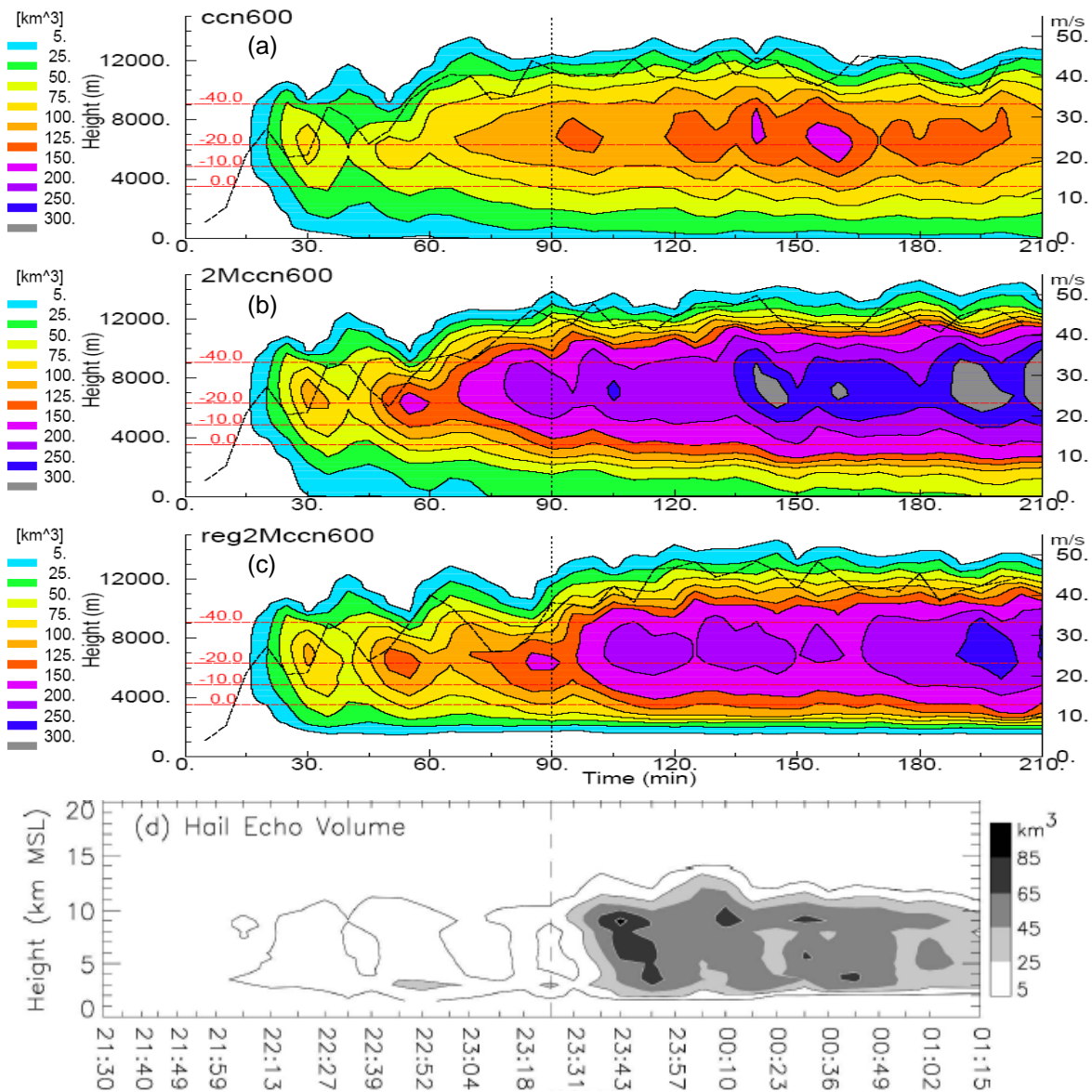


Figure 5.11: Time-height contours of storm hail volume [km^3] and time series of storm maximum updraft speeds (black dashed line; m s^{-1}) for simulations (a) ccn600, (b) 2Mccn600, and (c) reg2Mccn600. (d) FHC* total hail (small + large) echo volume (km^3), with contours beginning at 5 km^3 and a contour interval of 20 km^3 . [From TMWR05; *Fuzzy logic hydrometeor classification algorithm (FHC) used to deduce bulk hydrometeor types from polarimetric radar signals]. Horizontal red dashed lines in (a)-(c) depict approximate heights of 0, -10, -20, and -40 $^{\circ}\text{C}$ isotherms. Different scales are used in (a)-(c) compared to (d), and hail volumes for (a)-(c) taken as volume of grid points containing hail with mixing ratios of at least 0.1 g/kg .

The ccn600 case exhibits a mostly steady increase in graupel volumes with time (Fig. 5.12a), in qualitative agreement with the observed trend in graupel volumes (Fig. 5.12c), particularly around the time of the right turn and beyond. Graupel volumes for the 2Mccn600 case increase

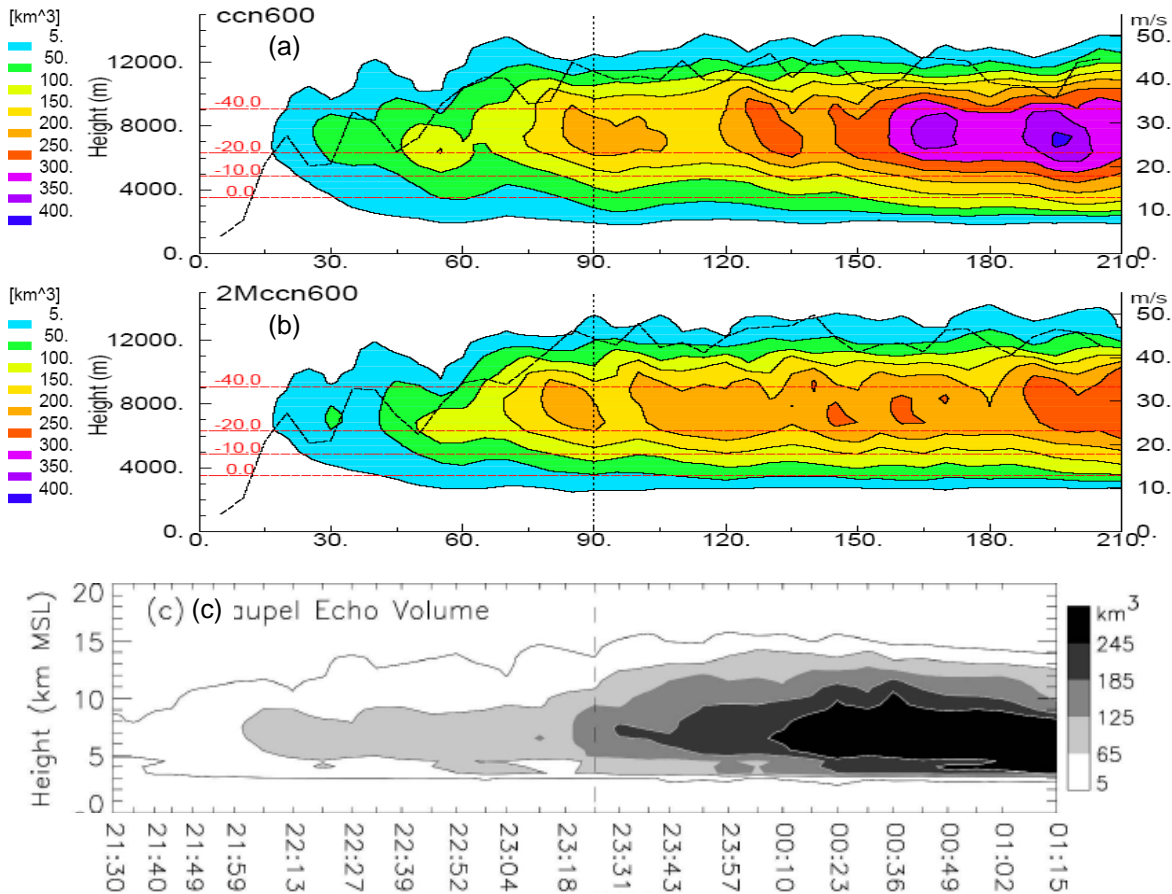


Figure 5.12: As in Fig. 5.11, except for storm graupel volume [km^3] for simulations (a) ccn600 and (b) 2Mccn600. (c) FHC* total graupel (low density + high density) echo volume (km^3), with contours beginning at 5 km^3 and a contour interval of 60 km^3 [From TMWR05]. Different scales are used in (a) and (b) compared to (c), and graupel volumes for (a) and (b) taken as volume of grid points containing graupel with mixing ratios of at least 0.1 g/kg .

steadily prior to the right turn, after which time these volumes remain nearly steady with only slight increases seen after 135 minutes. In fact, the ratios of graupel to hail volumes become less than 1.0 beyond 135 minutes in this case, whereas these ratios are consistently greater than 1.0 beyond 60 minutes in the ccn600 case which agrees with the analyses of Weins et al. (2005) for this storm. Furthermore, increases in graupel volumes to values greater than 300 km^3 after roughly 155 minutes in ccn600 (Fig. 5.12a) match very closely to similar increases seen beyond 00:15 UTC in the observations (i.e., Fig. 7a of Kuhlman et al. 2006). *The lack of graupel production in reg2Mccn600 highlights a deficiency in the binned riming scheme of Saleeby and*

Cotton (2008) as applied to snow and aggregates in generating graupel in deep convection.

Furthermore, most of the graupel that does form in the reg2Mccn600 case is rapidly transformed to hail via collisions with rain as will be shown in section 5.4.3.1. Cases ccn600 and 2Mccn600 employ the same binned riming scheme as in reg2Mccn600, yet graupel production in the former cases is primarily due to collection of relatively small raindrops by larger snow and aggregate particles as parameterized in the new three-component freezing algorithm (cf. Chapters 3.3 and 4.3). *The fact that this alternative method of graupel formation gives results that are similar to the observations (Fig. 5.12), especially in the ccn600 case, lends credence to the viability of the algorithm in generating graupel particles.*

A somewhat more quantitative assessment of the model results is made via comparisons of the fallout locations of hail from the hail growth model of TMWR05 applied to the observed storm with the surface accumulations (per 10 m^{-2}) of 1, 2, 3, and 4 cm diameter hail predicted in the simulations (Figs. 5.13 and 5.14). Diameter-dependent surface accumulated values are computed via multiplication of N_{1cm} , N_{2cm} , N_{3cm} , and N_{4cm} (Eqn 4.2) values at each grid point within the lowest model level above ground by the depth of the layer (98 m in this case) every two minutes and summing the resulting values for each grid point over time. The threshold value of 1 hailstone per 10 m^{-2} every 120 seconds follows MY06a, who used a threshold of 1 per 10 m^{-2} per 100 seconds to delineate physical observable quantities of large hail from negligible amounts. It is reasonably assumed that hailstones with diameters $\geq 1 \text{ cm}$ do not completely melt over the lowest 100 m. As the surface accumulated values are only updated every two minutes (the frequency output for selected hail model variables), the computed values underestimate the actual accumulation amounts predicted by the model. Nonetheless, the aim is simply to determine the general surface spatial distributions of hail sizes with respect to storm

features such as reflectivity and updraft cores as well as for comparison with actual reports of hail sizes at the surface (Fig. 5.4).

Hail diameters ≥ 2 cm in cases ccn600 (Fig. 5.13b) and 2Mccn600 (Fig. 5.13c) are distinctly associated with larger values of Z_e in close agreement with the observed storm (Fig. 5.13a) as well as with previous observations attributing large reflectivity values to large hail (Browning et al. 1968; Mason 1971; Foote and Wade 1982; Aydin et al. 1986; Miller et al. 1988, 1990). Large hail at the surface in cases ccn600 and 2Mccn600 is also seen to be located along the eastern and northern flanks of the updrafts (Fig. 5.14b,c) in agreement with the analyses of TMWR05 for this storm (Fig. 5.14a). Animations of large hail fallout locations with respect to updraft cores confirm this result (not shown). In addition, the largest hail sizes fall closest to the updraft in the ccn600 simulation owing to their greater fall speeds, whereas the smaller hailstones, which are more susceptible to advection by the horizontal flow, are seen to extend over a greater horizontal distance from the updraft (Fig. 5.14b). These spatial distributions of surface hailfall are consistent with previous studies of hailfalls in supercells (e.g. Browning and Ludlam 1962; Browning and Foote 1976; Houze 1993). In contrast, large hail reaching the surface extends some 25 to 40 km out from the updraft cores in the 2Mccn600 case (Fig. 5.14c) leading to a much wider hail swath of 2 cm and larger hailstones at the surface than is seen in the ccn600 case, for which the swath is typically less than 10 km wide (Fig. 5.13b). As previously noted, however, the large diameter hail at the surface in 2Mccn600 is primarily an artifact of unphysical increases in D_{mh} during melting. Only small amounts of hail with diameters ≥ 1 cm are evident at the surface in the reg2Mccn600 case after roughly 160 minutes (Fig. 5.14d), and no hail with diameters ≥ 2 cm reaches the surface in this case (Fig. 5.13d).

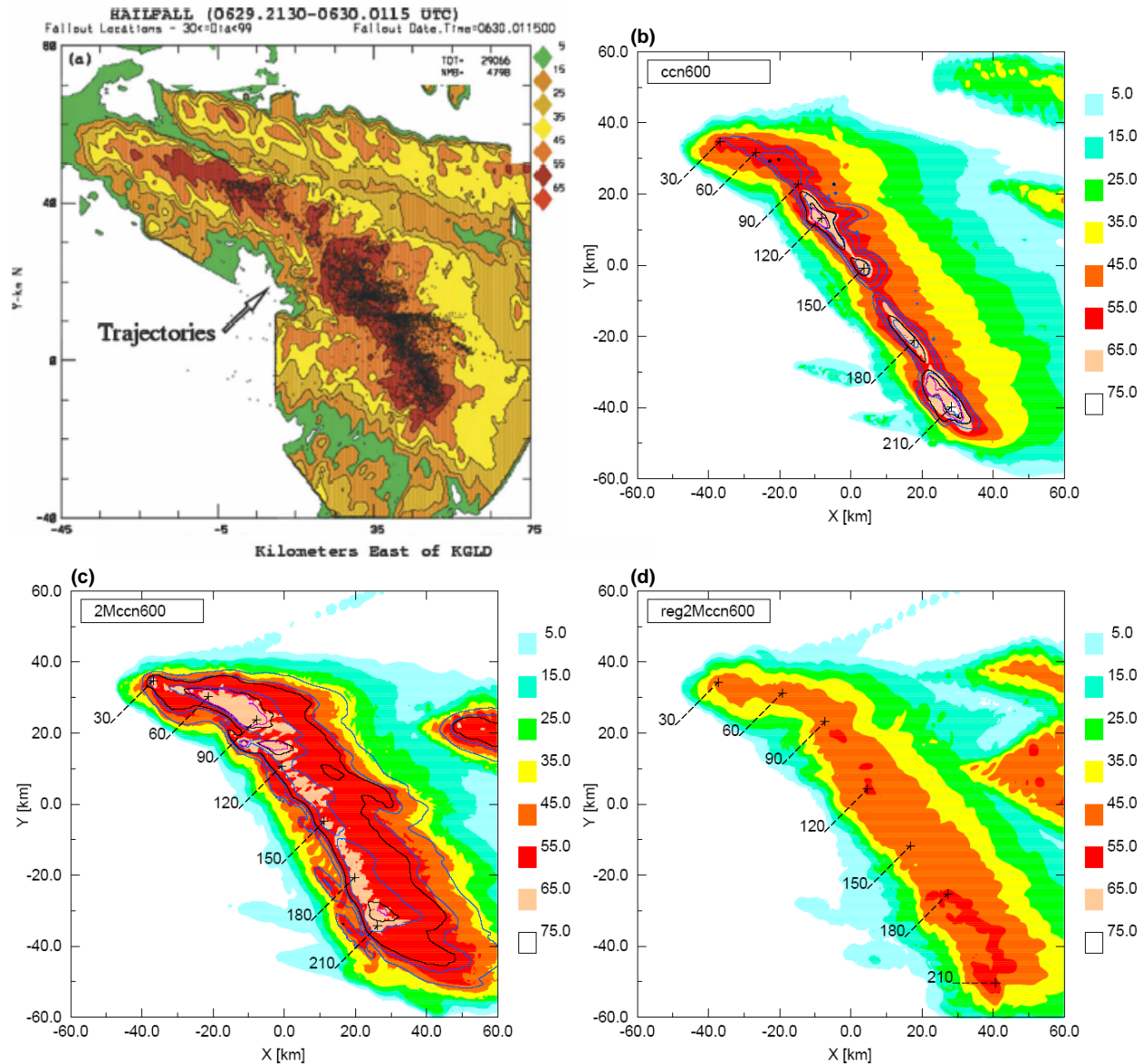


Figure 5.13: (a) Swath of maximum reflectivity (dBZ) from KLGD for the period 2130-0115 UTC and particle growth model hailfall with sizes greater than 30 mm overlaid as black dots [Fomr TMWR05]. (b-d) Swaths of maximum equivalent reflectivity Z_e factor (Z_e from hail, rain, graupel, snow, and aggregates) in vertical column (shaded; dBZ) and contours of 'accumulated' hail numbers per 10 m^2 at surface with diameters of at least 2 (blue), 3 (black), and 4 cm (purple) [contour values are 1, 10, and 100 per 10 m^2] for simulation time period from $t = 0$ to 210 min for (b) ccn600 (3MHAIL) simulation, (c) 2Mccn600 (mod2M) simulation, and (d) reg2M600 simulation. Locations of maximum Z_e at simulation times $t = 30, 60, 90, 120, 150, 180,$ and 210 minutes are denoted by the black crosses in b-d.

Five distinct periods of fallout consisting of hailstones with diameters ≥ 2 to 3 cm are evident in the ccn600 simulation (Fig. 5.13b); the first occurs between approximately 60 and 90 minutes, the second around 120 minutes, the third near 150 minutes, the fourth from roughly 170

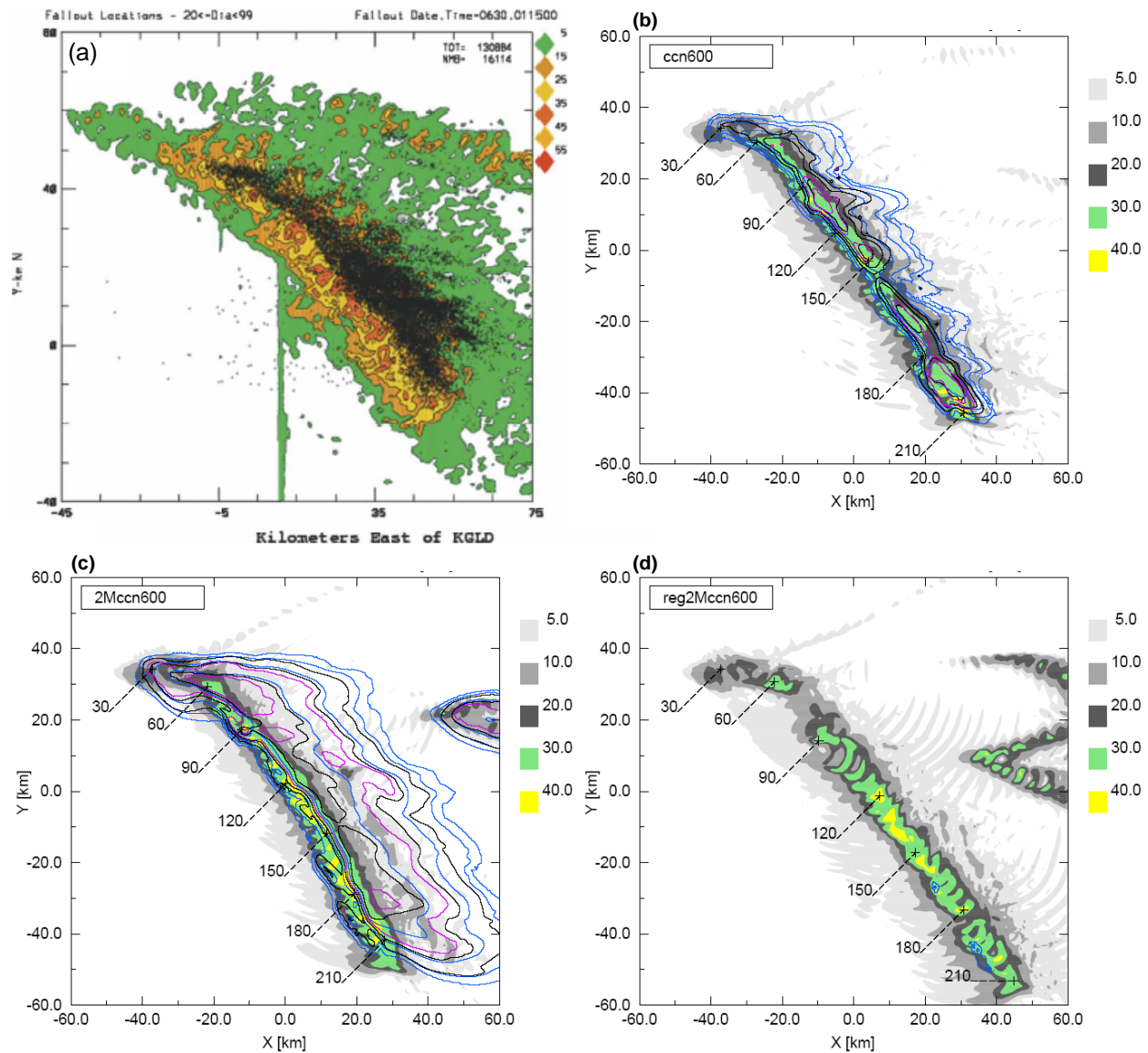


Figure 5.14: (a) Swaths of multi-Doppler-derived maximum updraft (m s^{-1}) in the vertical column for the period 2130-0115 UTC and particle growth model hailfall with sizes greater than 20 mm overlaid as black dots [From TMWR05]. (b-d) Swaths of maximum updraft in vertical column (shaded; m s^{-1}) and contours of 'accumulated' hail numbers per 10 m^2 at surface with diameters of at least 1 (blue), 2 (black), and 3 cm (purple) [contour values are 1, 10 and $100 \text{ per } 10 \text{ m}^2$] for simulation time period from $t = 0$ to 210 min for (b) ccn600 (3MHAIL) simulation, (c) 2Mccn600 (mod2M) simulation, and (d) reg2M600 simulation. Locations of maximum updraft at simulation times $t = 30, 60, 90, 120, 150, 180,$ and 210 minutes are denoted by the black crosses in b-d.

to 185 minutes, and the fifth from about 195 minutes onward. The most substantial of these hailfalls are the second and fifth, both of which contain significant amounts of very large hail ($D \geq 4 \text{ cm}$), though the validity of the final hailfall in this case is questionable as the storm nears the domain's lateral boundaries. Qualitative agreement between the evolution of these hailfalls and

the actual surface hail reports (Fig. 5.4) is generally quite good as the bulk of the reports of large hail occurred following the storm's right turn. In contrast, the 2Mccn600 case exhibits an unrealistic, nearly continuous fallout of hailstones of at least 2 and 3 cm diameters from about 30 minutes through the end of the simulation, with hail diameters ≥ 4 cm seen at surface mainly prior to right turn (Fig. 5.13c). These results clearly show that the ccn600 case is most successful in predicting the general locations and sizes of hail arriving at the surface for this particular storm.

5.4.2) *Detailed comparisons with observations*

Comparisons of the evolution of the modeled and observed storm structures are made by examining detailed horizontal and vertical cross-sections of reflectivity and wind fields during the storm's multicellular and supercell phases. The analysis times for the simulations are chosen to roughly correspond to those presented in TMWR05 for the different phases of the observed storm. Regions of hail are also shown for the model results in order to assess differences in the predicted sizes and spatial distributions among the three simulations.

The multicell stages of the simulated storms are depicted in Figures 5.16, 5.17, and 5.18 for the ccn600, 2Mccn600, and reg2Mccn600 cases, respectively. Two regions of enhanced Z_e representing two separate convective cells are evident in the horizontal and vertical cross-sections displayed for the ccn600 case (Fig. 5.16), similar to the reflectivity structure of the observed storm as it transitioned from multicellular to a more mature single cell stage (Fig 5.15). A two-cell signature in the Z_e fields is apparent only in the vertical cross-sections of the 2Mccn600 (Fig. 5.17c) and reg2Mccn600 (Fig. 5.18c) cases, and these two simulations also exhibit a lack of large hail and hence smaller Z_e values aloft ($z > 5$ km) (Figs. 5.17a,c; 5.18a,c)

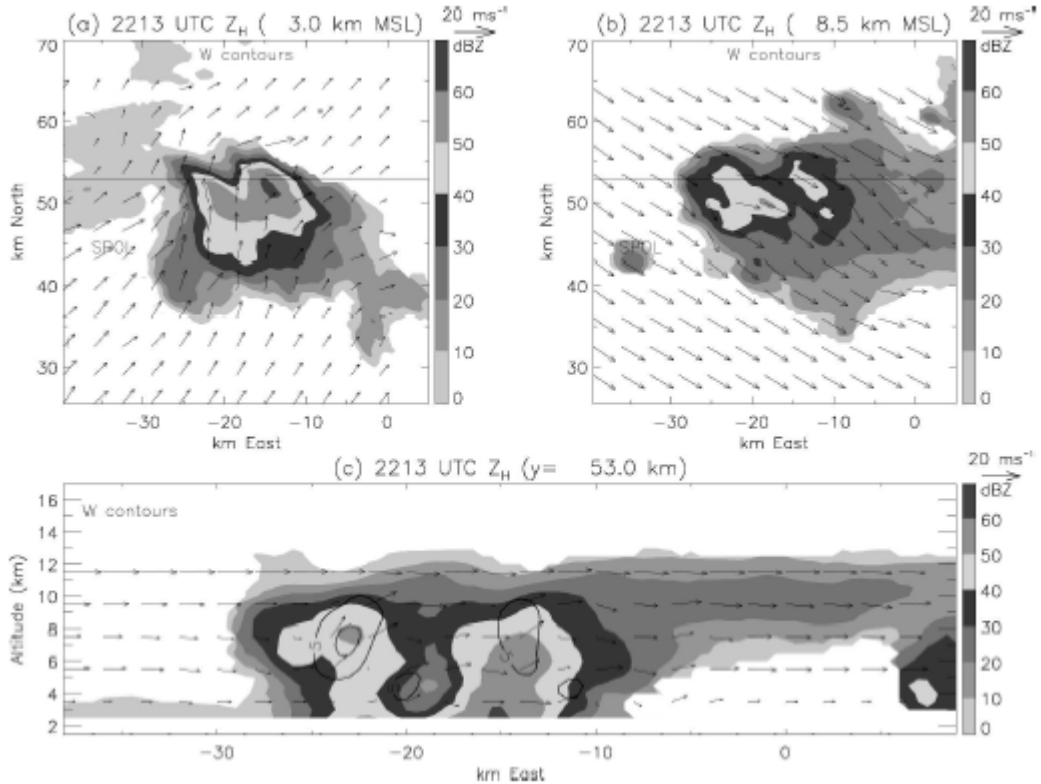


Figure 5.15: Synthesized winds and storm structure of the 29 June supercell at 2213 UTC during its early development stage just prior to reaching its mature phase: (a) horizontal cross section of grayscale reflectivity at $z = 3$ km (MSL) and bold black updraft contours beginning at 5 m s^{-1} with a contour interval of 10 m s^{-1} (due to the weak updrafts at this synthesis time no contours are evident in this frame), (b) horizontal cross section of grayscale reflectivity at $z = 8.5$ km (MSL) with bold black updraft contours beginning at 15 m s^{-1} with a contour interval of 15 m s^{-1} (again, no contours are evident in this frame due to the weak updraft at this time), and (c) vertical cross section of grayscale reflectivity at $y = 53$ km with bold black updraft contours beginning at 5 m s^{-1} with a contour interval of 10 m s^{-1} . All plots have storm-relative wind vectors overlaid. [From TMWR05].

compared to both the observed storm (Fig. 5.3b,c) and the ccn600 case (Fig. 5.11b,c). On the other hand, the exceedingly large Z_e values at low-levels in the 2Mccn600 case (Fig. 5.17a,c) can be directly attributed to the erroneous prediction of large and very large hail below the melting level. A westward-extending echo overhang between roughly 5 and 9 km seen in the reflectivity field of the observed storm (Fig. 5.15c) is also evident in the Z_e fields between approximately 2 and 7 km in the ccn600 case (Fig. 5.16c) and between 3 and 7 km in the 2Mccn600 case (Fig. 5.17c). A westward overhang region is also present between about 3 and 6 km in the reg2Mccn600 case (Fig. 5.18c), though it is less distinguished than in the other two simulations.

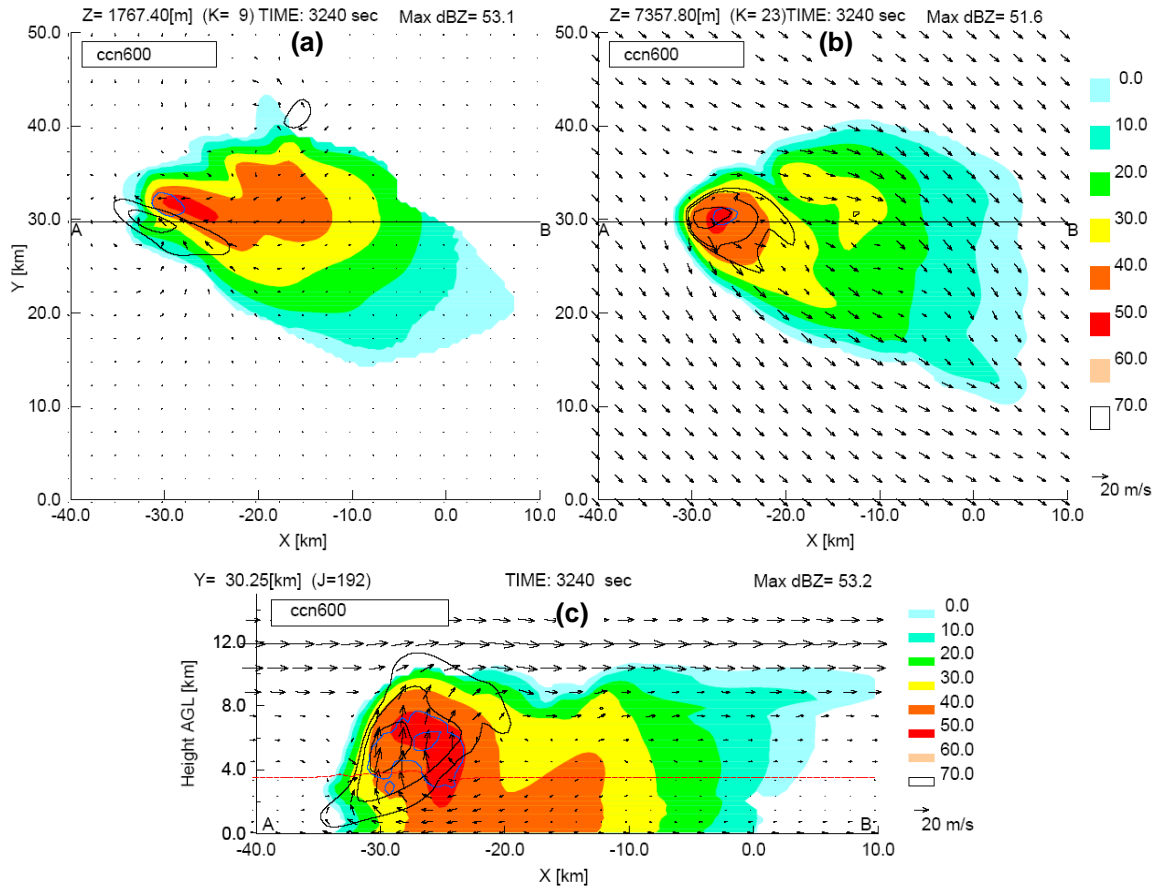


Figure 5.16: Horizontal cross sections for (a) $z = 1767$ m and (b) $z = 7358$ m, and (c) vertical cross section along line AB of model equivalent reflectivity factor Z_e [shaded, dBZ] (diagnosed for rain, graupel, snow, and aggregates; predicted for hail), storm-relative wind vectors, updraft contours [black; intervals are 5, 10, 20 m s^{-1} for horizontal plots and 5, 15, 25 m s^{-1} for vertical plot], and contours of N_{2cm} [blue; values are 1×10^{-4} , 0.01 m^{-3}] at time $t = 3240$ s (54 min) for simulation ccn600. Red dashed line represents 0°C isotherm.

In all three simulations, the eastern (rightmost) cell is decaying at the times shown, and the western cell is strengthening as evident by the dominant updraft on the western edge of the storm. This generally agrees with the analysis of the observed storm in Figure 5.15, though the updraft strengths in the simulations are greater than in the observations due to the fact that the simulated storms have progressed further into the mature stage relative to the actual storm for the analysis times shown. In addition, the establishment of low-level cyclonic flow along the southwest flanks of the simulated storms and divergent flow around the main updraft core at mid-levels is more representative of the observed storm during its mature phase (cf. Fig. 8 of TMWR05). Large hail in the ccn600 case is generally distributed over the width of the updraft at

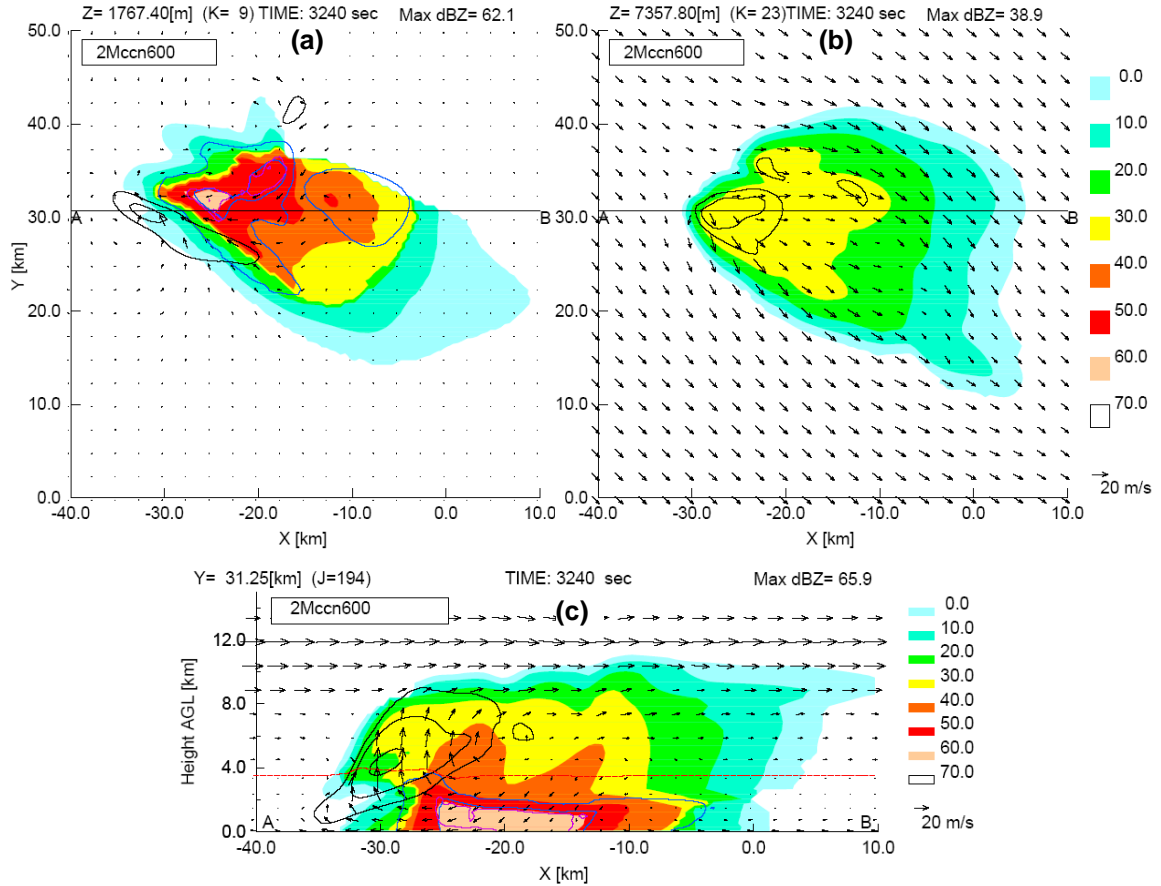


Figure 5.17: As in Fig. 5.16 for simulation 2Mccn600. Contours of N_{4cm} are also shown [purple; values are 1×10^{-4} , 0.01 m^{-3}].

mid-levels, with the greatest concentrations found just to the east of the updraft core around 6 km (Fig. 5.16c). This result is consistent with observations of Smith et al. (1976), who noted that hail concentrations aloft are typically maximized along the updraft edges, as well as with observational studies which found the growth of large hail often occurs near the updraft edges (e.g., Browning and Foote 1976; Orville 1977; Rasmussen and Heymsfield 1987c). As a 2 cm diameter hailstone has a fall speed of roughly 22 m s^{-1} , the location of maximum N_{2cm} appears to represent a balanced growth region as it coincides with a region of updraft with similar velocities (Nelson 1983). The mid-level cyclonic flow evident in the time-height plot of ζ_{max} (Fig. 5.9a) transports these hailstones northward away from the updraft core where the hailstones fall out

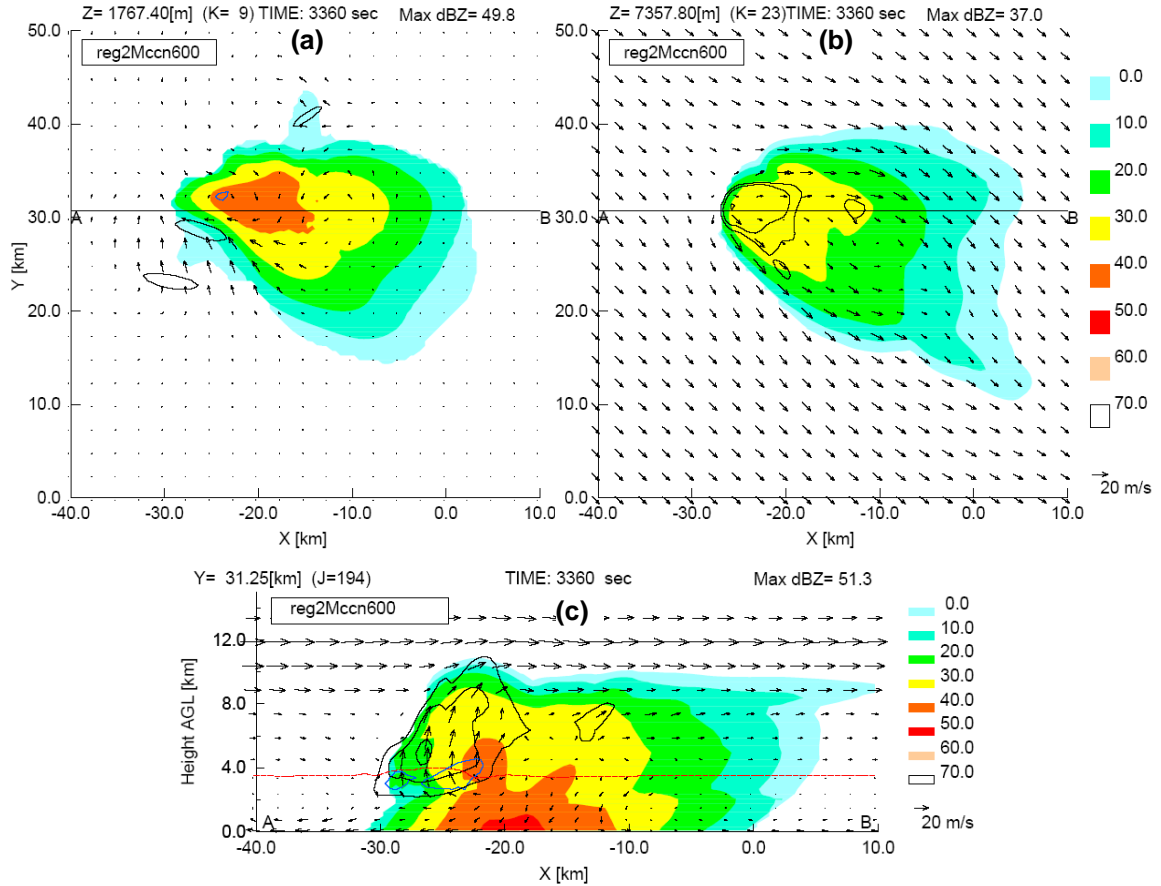


Figure 5.18: As in Fig. 5.16, except at time $t = 3360$ s (56 min) for simulation reg2Mccn600. Blue contours are now N_{ice} [values are $1 \times 10^{-4} \text{ m}^{-3}$].

and lead to the region of large hail located to the north of the updraft at low-levels (Fig. 5.16a). The bulk of the large hail in the 2Mccn600 case is also located to the north of the low-level updraft (Fig. 5.17a). However, as no large hail is evident above the freezing level in this case (Figs. 5.17b,c), this is more likely due to the transport of smaller hailstones northward around the mid-level cyclone before falling out and undergoing melting, which then leads to the erroneous shift to large hail sizes as previously discussed. In the reg2Mccn600 case, moderately-sized hail ($D \geq 1$ cm) is seen near the updraft base in the vicinity of the freezing level (Fig. 5.18c). Additional analyses (not shown) reveal that these hailstones grow along the northern flank of the updraft between 3.5 and 5 km height before falling out to lower levels where they are advected

southward towards the updraft base. However, their fall speeds are greater than the updraft speed at these levels and they continue towards the surface and melt instead of being carried aloft.

By 90 minutes, the modeled storms have evolved into right-turning supercells, and this is reflected in the Z_e and wind fields displayed in Figures 5.20-5.22. A comparison of the simulated storm structures at 90 minutes with that for the observed storm as it turned right (Fig. 5.19) reveals the ccn600 case (Fig. 5.20) resembles the observations quite well, although key features such as the BWER and the orientation of the low-level reflectivity field are obviously different between the observed and modeled storm. In all three simulated storms, maximum Z_e values at midlevels are to the east and northeast of updraft core (Figs. 5.20b, 5.21b, and 5.22b) whereas the mid-level reflectivity maximum is to southeast of updraft core in the observations (Fig. 5.4b). TMWR05 attribute this observed reflectivity maximum to strong divergence around the southern

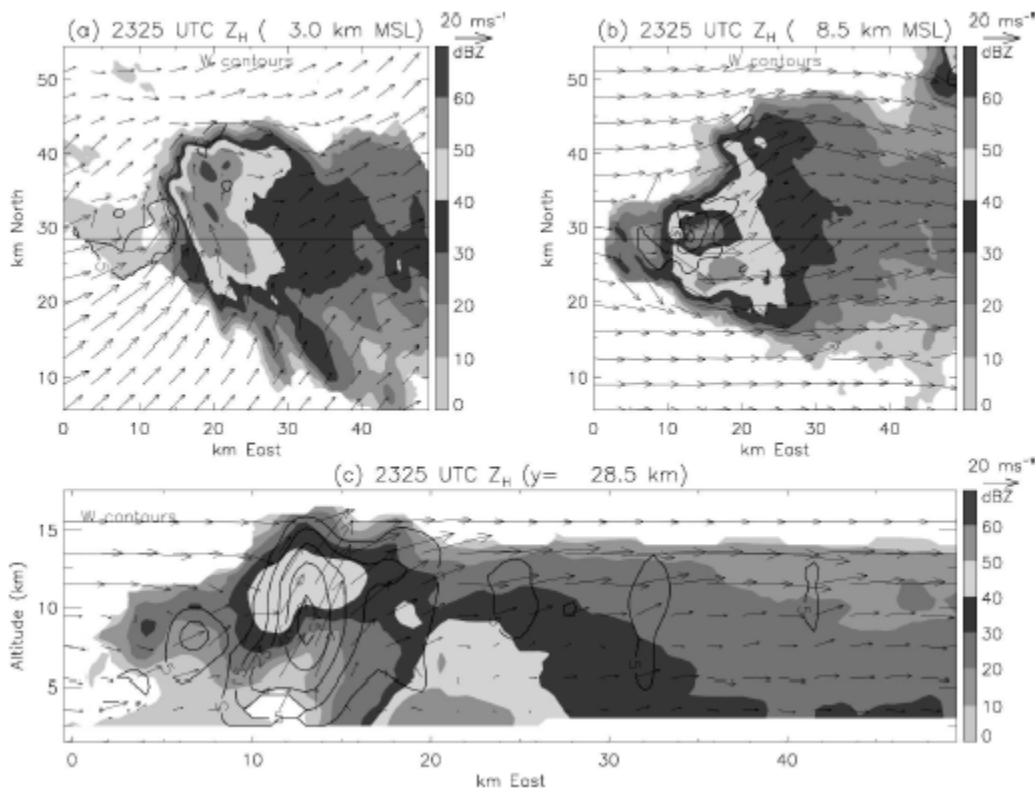


Figure 5.19: As in Fig. 5.15 except for synthesis time of 2325 UTC (beginning of right turn) and (c) $y = 28.5$ km. [From TMWR05].

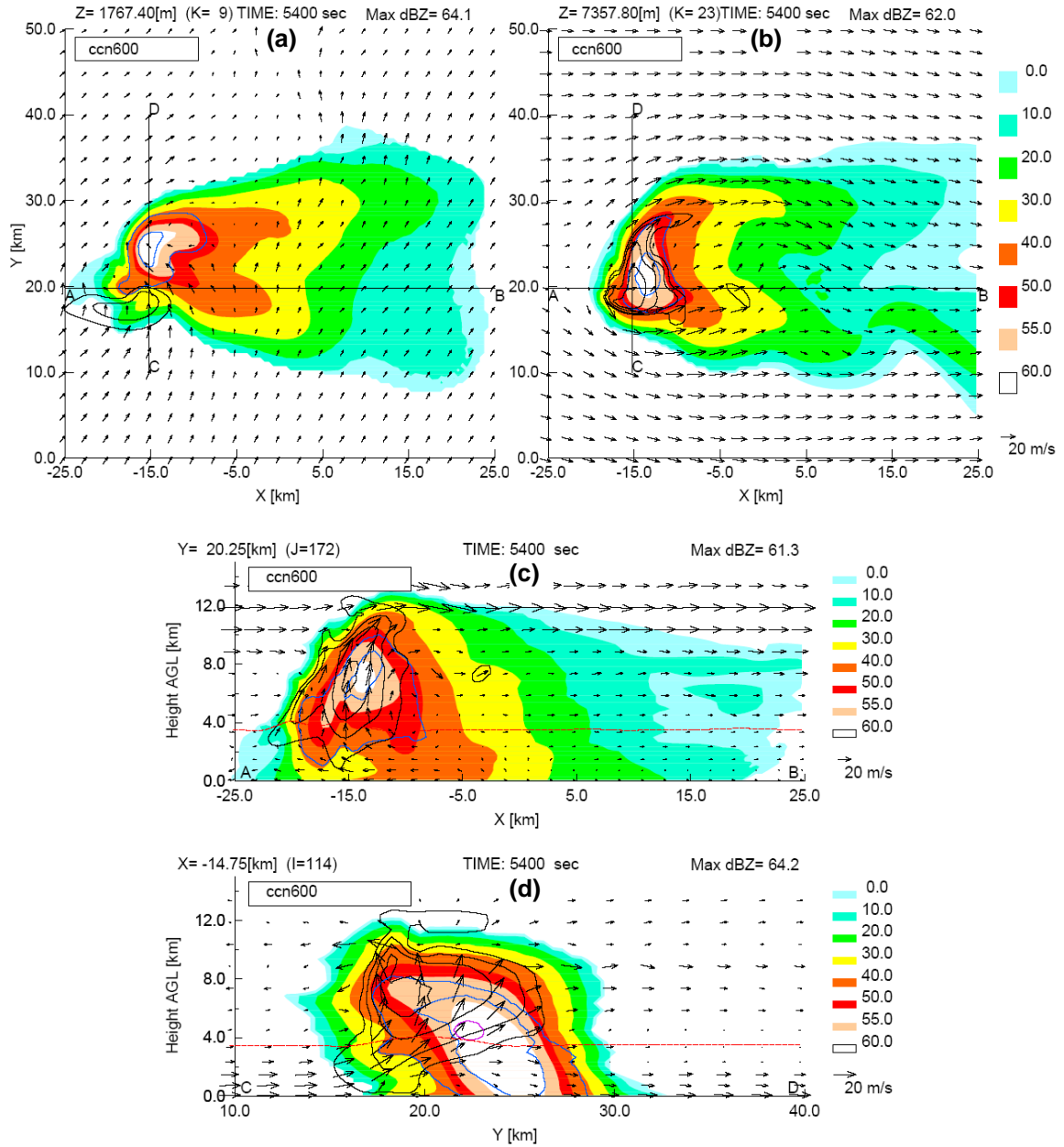


Figure 5.20: Horizontal cross sections for (a) $z = 1767$ m and (b) $z = 7358$ m, (c) east-west cross section along line AB, and (d) north-south cross section along line CD of model equivalent reflectivity factor Z_e [shaded, dBZ] (diagnosed for rain, graupel, snow, and aggregates; predicted for hail), storm-relative wind vectors, updraft contours [black; intervals are 5, 10, 20, 30, 40 m s^{-1} for horizontal plots and 5, 15, 25, 35, 45 m s^{-1} for vertical plot], and contours of N_{2cm} and N_{4cm} [blue and purple, respectively; values are 1×10^{-4} , 0.01 m^{-3}] at time $t = 5400$ s (90 min) for simulation ccn600. A 55 dBZ contour is included to highlight features in the Z_e field. Red dashed line represents 0°C isotherm.

flank of the mid-level updraft (Fig. 5.4b). Similar flow patterns exist at midlevels in the simulations (panel b in Figs. 5.20-5.22), though the model seems to predict stronger cyclonic

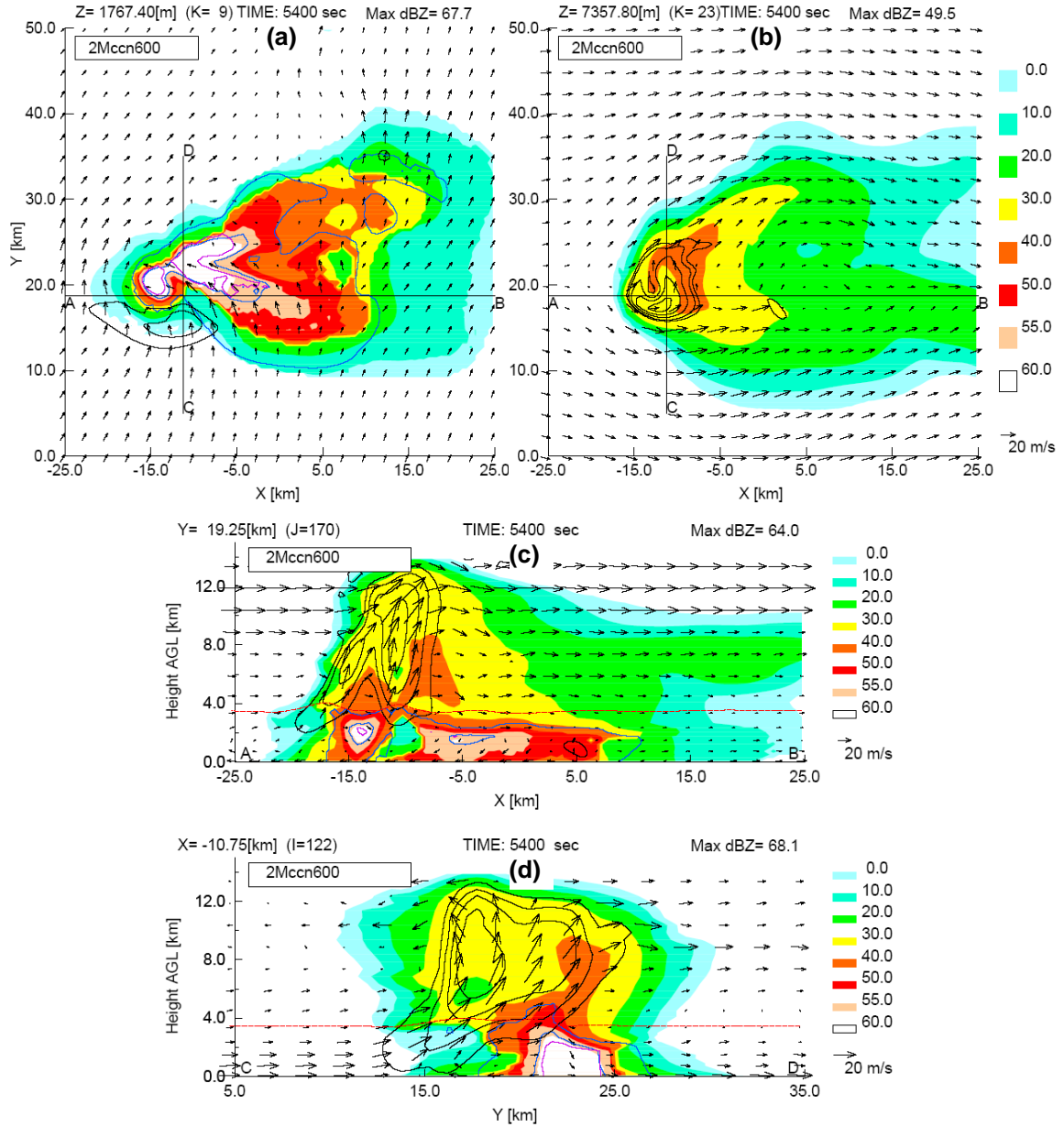


Figure 5.21: As in Fig. 5.20, except for simulation 2Mccn600 and model equivalent reflectivity factor Z_e is diagnosed for hail in addition to rain, graupel, snow, and aggregates.

flow at mid-levels compared to the observations (i.e., greater ζ_{max} values seen in Fig. 5.9) which likely results in greater transport of precipitation-sized particles northeastward. An overhang region of Z_e at mid and upper levels along the southern flank of the storm, similar to the embryo curtain region described by Browning and Foote (1976), is also evident in the simulations (panel

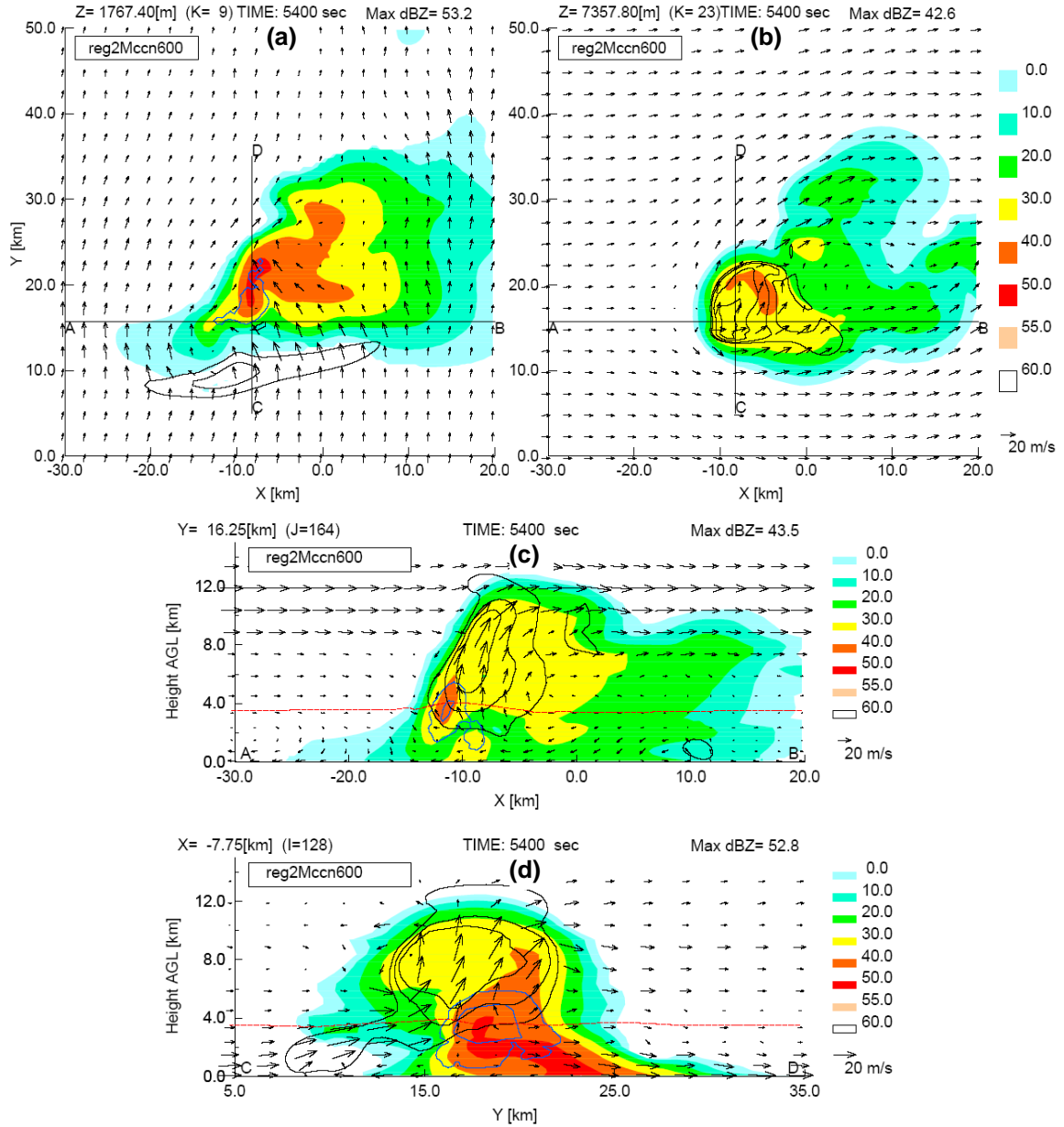


Figure 5.22: As in Fig. 5.20, except for simulation reg2Mccn600 and blue contours are $N_{lcm} [1 \times 10^{-4}, 0.01 \text{ m}^{-3}]$.

d in Figs. 5.20-5.22). TMWR05 also mentioned an overhang region on the southern flank of the observed storm following its right turn, though this is not explicitly shown in their analyses. A slight northeastward tilt of the updraft with height at this time (panels c and d in Figs. 5.20-5.22) results in the unloading of the bulk of the precipitation to the north and east of the updraft core (panel a in Figs. 5.20-5.22), which is consistent with observations of general precipitation

patterns associated with 'classic' supercells (Browning 1977; Lemon and Doswell 1979; Doswell and Burgess 1993). A cyclonic circulation is also evident at low levels near the cusp of the hook-echo-like appendage in the Z_e fields of the ccn600 (Fig. 5.20a) and 2Mccn600 (Fig. 5.21a) cases, in agreement with the observations (Fig. 5.4a), whereas this circulation is offset to the south of the hook-echo feature in reg2Mccn600 case (Fig. 5.22a). The low-level updraft is also located further south of the reflectivity core in the latter (Fig. 5.22a) as the storm-generated outflow has pushed well ahead of the mid-level updraft at this time as evident in Figure 5.22d.

The Z_e field in the east-west cross section for the ccn600 case at 90 minutes (Fig. 5.20c) displays what appears to be a BWER through the updraft axis at this time, though it is more compact in the horizontal and does not extend as high (only up to about $z = 5.5$ km) compared to the observed BWER (Fig. 5.19c), thus no BWER is evident in the horizontal cross section at midlevels (Fig. 5.20b). Nonetheless, the overall patterns of a reflectivity maximum above the BWER and a region of higher reflectivity at low levels to the east of the updraft in the observations (Fig. 5.4c) are generally predicted in the ccn600 case (Fig. 5.20a,c). A maximum in large hail concentrations directly above the BWER within the region of Z_e maximum (Fig. 5.20c), believed to be a favored region for rapid hail growth in quasi-steady supercells (English 1973; Browning and Foote 1976; Nelson 1983), is also seen in this case. The storm-relative flow pattern at this time is such that large hail above the BWER and to the northeast of the updraft core (Fig. 5.20b) is transported to the north and west by the cyclonic flow around the updraft as it falls, resulting in the region of large hail to the north of the updraft at low levels (Fig. 5.20a,d) in general agreement with the analyses of TMWR05.

The storms in the two-moment cases show some similarities to the observations at mid-levels, such as a divergent flow field around the updraft and weaker Z_e values within the updraft

core (Figs. 5.21b and 5.22b), albeit the Z_e magnitudes at this height are much smaller than the observed values (> 60 dBZ; Fig. 5.4b) as well as those in the ccn600 case (Fig. 5.20b). In general, however, the 2Mccn600 and reg2Mccn600 simulations at 90 minutes do not resemble the observed storm as it made its right turn, and this is particularly evident in the Z_e fields for these two cases. For example, the vertical cross sections for these cases (Figs. 5.21c,d and 5.22c,d) reveal that Z_e values of 50 dBZ and greater are mostly confined to heights below 4 km, and neither case exhibits a BWER. As hail tends to dominate the calculation of Z_e values above the freezing level, these results are attributed primarily to the absence of large hail aloft in these two simulations based on comparisons with the ccn600 case, which does produce large hail aloft. In addition, the melting-induced artificially large hail in the 2Mccn600 case leads to unrealistic patterns of $Z_e > 50$ dBZ below the freezing level (Fig. 5.21a,c,d). Interestingly, the north-south vertical cross sections for the 2Mccn600 (Fig. 5.21d) and reg2Mccn600 (Fig. 5.22d) cases reveal similar Z_e structures, with regions of greater Z_e values located below and to the north of the updraft core and sloping upward along the northern periphery of the updraft, and weaker Z_e values within the updraft core. This suggests that the mechanisms responsible for the formation, growth, and fall out of precipitation, particularly those for hail, are largely similar between these two cases at this time.

The final set of analyses compares the modeled storm structures at 116 minutes (Figs. 5.24-5.26) with the observations at 2343 UTC (Fig. 5.23), roughly 25 minutes following the right turn in the former compared to about 20 minutes for the latter. This time was selected as it corresponds to an intense precipitation episode of large hail at the surface in the ccn600 case (Fig. 5.13b; see also Figs. 5.46-5.48) as well as a local maximum of large hail aloft in the reg2Mccn600 case (see Fig. 5.31). Immediately prior to 116 minutes, the simulated storms

exhibit surges in updraft (Fig. 5.7a) and peaks in ζ_{max} values (Fig. 5.9a,b,c), similar to the observed storm behavior in updraft (Fig. 5.7b) and ζ_{max} values (Fig. 5.9d) just before 2343 UTC. Thus, it is surmised that the modeled storm kinematics at 116 minutes are mostly similar to those for the observed storm around 2343 UTC. As an additional measure of the accuracy of the simulation results, a transition (T) -matrix method (Waterman 1965; Barber and Yeh 1975) is employed to compute the complex scattering amplitudes of rain, graupel, snow, aggregates, and dry and liquid coated hail (Bringi and Seliga 1977; Depue et al. 2007) for a radar wavelength of 11 cm. The Mueller matrix method of Vivekanandan et al. (1991) is then used to compute the total reflectivity volume (Z_H) as well as the polarimetric radar quantities ZDR , LDR , and ρ_{hv} (Chapter 2.6) for each model grid point. The position of the 'radar' in the model domain is $x = -60$ km and $y = -40$ km, which corresponds to the general location of the CHILL radar relative to the actual storm track (cf. Fig. 5 of TMWR05). Further details of the T-matrix/Mueller matrix method used herein are provided in Appendix C.

An examination of the reflectivity structures of the simulated storms at 116 minutes reveals that the ccn600 case (Fig. 5.24) exhibits many of the general features apparent in the observed storm at 2343 UTC (Fig. 5.23), whereas the 2Mccn600 (Fig. 5.25) and reg2Mccn60 (Fig. 5.26) cases differ significantly from the observations. Both the observed storm (Fig. 5.23) and the ccn600 case (Fig. 5.24) display reflectivity values greater than 60 dBZ at low- and mid-levels, a region of weaker reflectivity values beneath a westward-extending echo overhang, a local reflectivity maximum (> 60 dBZ) within the updraft at mid-levels, and a broad region of reflectivity values exceeding 50 dBZ that extends downward and to the east of the updraft core. Reflectivity contours of 50 dBZ and greater generally mimic the distribution patterns of large hail in the ccn600 case in agreement with observations of large hail in supercell storms (Auer

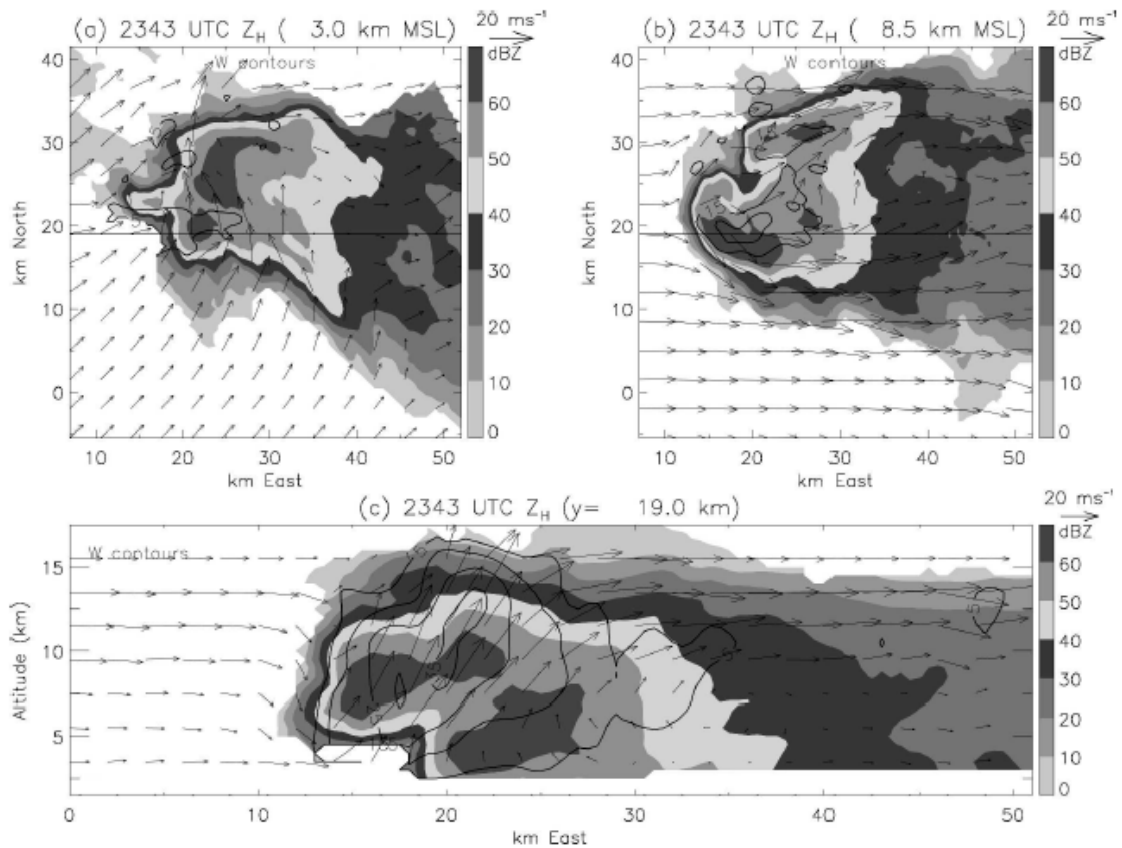


Figure 5.23: As in Fig. 5.15 except for synthesis time of 2343 UTC and (c) $y = 19$ km. [From TMWR05].

and Marwitz 1972; Marwitz 1972a; Browning and Foote 1976; Miller et al. 1988). In contrast, reflectivity values of 60 dBZ or greater and large hail are seen only below the freezing level in the 2Mccn600 case (Fig. 5.25a,c,d), though these values are erroneously large as previously discussed, and reflectivity values do not exceed 50 dBZ at any location for the reg2Mccn600 case owing to the relatively small hail sizes produced (Fig. 5.26). The two-moment cases also lack an overhang region on the western edge of the storm, and reflectivity values within the updraft generally decrease in magnitude with increasing height (Figs. 5.25c,d and 5.26c,d) owing to increasingly smaller hail sizes with height (Figs. 5.31 and 5.32). As previously noted, the reflectivity values associated with snow and aggregates in the simulated storms are much smaller than in the observations owing to the very small sizes of these particles predicted by the model,

hence the anvil regions of the simulated storms are noticeably absent in the computed reflectivity fields.

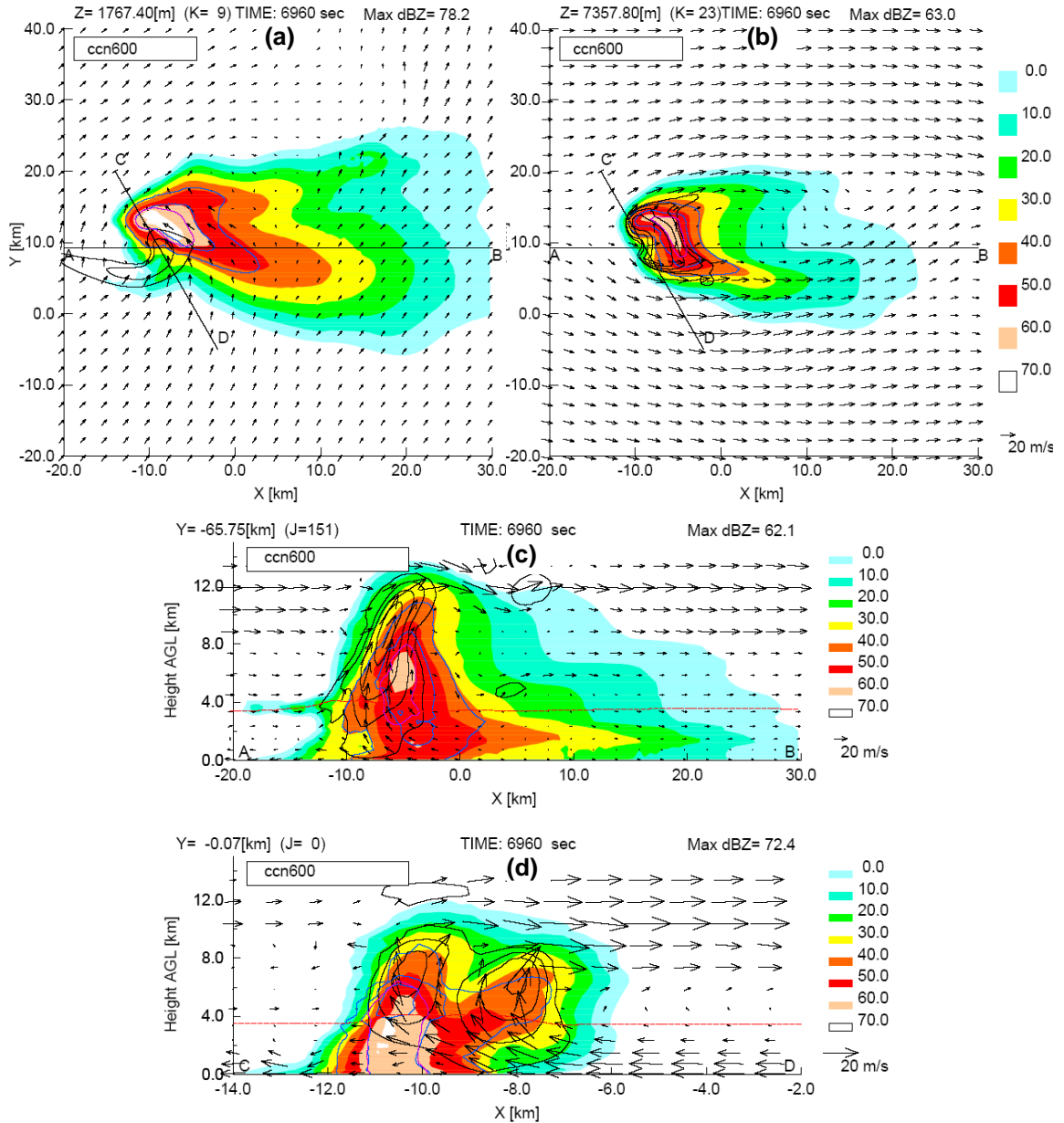


Figure 5.24: Horizontal cross sections for (a) $z = 1767$ m and (b) $z = 7358$ m, (c) east-west cross section along line AB, and (d) vertical cross section along line CD (approximate path of storm motion) at time $t = 6960$ s (116 min) for simulation ccn600. Fields shown are reflectivity [shaded, dBZ] computed using T-matrix scattering calculations for rain, hail, graupel, snow, and aggregates, storm-relative wind vectors, updraft contours [black; contour values are 5, 10, 20, 30, 40 m s^{-1} for horizontal plots and 5, 15, 25, 35, 45 m s^{-1} for vertical plot], and contours of N_{2cm} and N_{4cm} [blue and purple, respectively; contour values are 1×10^{-4} , 0.01 m^{-3}]. Reflectivity fields are computed assuming radar is located at $x = -60$ km, $y = -40$ km. Red dashed line represents 0°C isotherm.

Reflectivity maxima at low-levels are located to the north of the low-level updraft in the observed storm (Fig. 5.23a) as well as in the simulated storms (Figs. 5.24a, 5.25a, and 5.26a), with the maxima corresponding to hail fallout regions in the latter. At mid-levels, the observed storm exhibits a reflectivity maximum on the southwest flank of the updraft (Fig. 5.23b) whereas this maximum is seen on the northeast flanks of the updrafts in the ccn600 (Fig. 5.24b) and 2Mccn600 (Fig. 5.25b) cases. As the simulations and observations exhibit similar divergence patterns at mid-levels, the differences in reflectivity maxima locations are likely due to the transport of precipitation-sized particles further northward by the stronger mid-level cyclonic flow in the simulations at 116 minutes compared to the observed storm at 2343 UTC (Fig. 5.9), similar to what was seen in the previous set of analyses. No discernible reflectivity maximum is evident at mid-levels in the reg2Mccn600 case (Fig. 5.26b).

A pronounced forward overhang region is also displayed in the vertical cross section along the storm motion vector for the ccn600 case (Fig. 5.24d) at 116 minutes. This feature matches well with the embryo curtain shown in the radar synthesis of the 21 June 1972 Fleming, CO supercell analyzed by Browning and Foote (1976) (Fig. 2.12), a storm which occurred in the same region and exhibited similar evolution, motion, and hail fall patterns as in the 29 June 2000 supercell. Such distinct forward overhang regions are not seen in the storms at 116 minutes in the 2Mccn600 (Fig. 5.25d) and reg2Mccn600 (Fig. 5.26d) cases.

All three simulations display cyclonic flow within the low-level updraft core on the southwest flank of the storm at 116 minutes (Figs. 5.24a, 5.25a, and 5.26a) in agreement with the observed low-level flow pattern at 2343 UTC (Fig. 5.23a). In addition, the eastward tilting updrafts and maximum updraft speeds greater than 35 m s^{-1} evident in the simulated storms (Figs. 5.24c, 5.25c, and 5.26c) are largely similar to the updraft characteristics of the

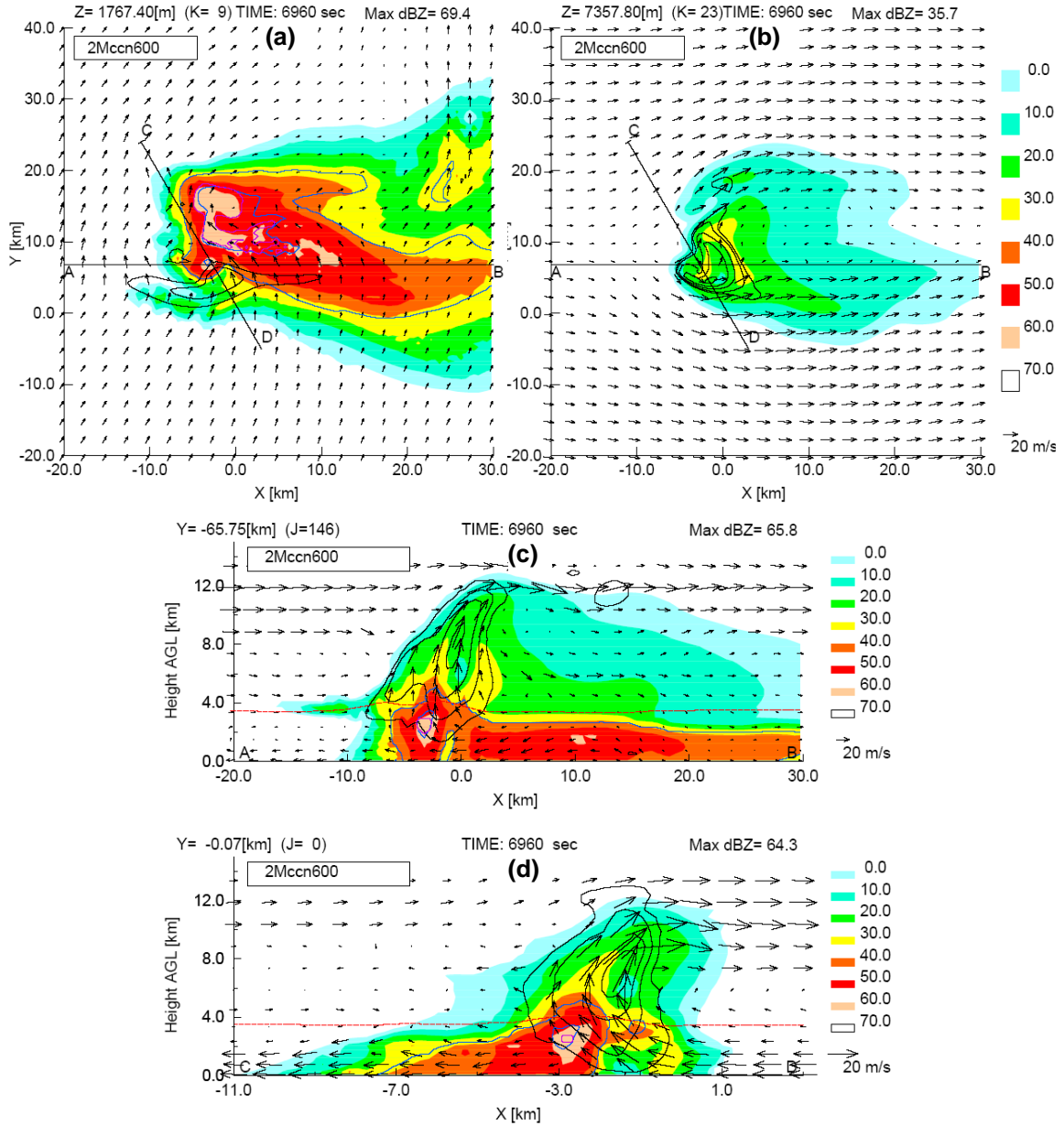


Figure 5.25: As in Fig. 5.24 for simulation 2Mccn600 at time $t = 6960$ s (116 min).

observations (Fig. 5.23c). Despite the similar kinematic structure between the modeled and observed storms, realistic spatial distributions of large ($D_h \geq 2$ cm) and very large ($D_h \geq 4$ cm) hail only exist in the ccn600 case (Fig. 5.24), as in the previous set of analyses. At this particular analysis time, large hail in the ccn600 case grows along the eastern and northern flanks of the updraft core as it is advected cyclonically around the periphery of the broad updraft (Fig.

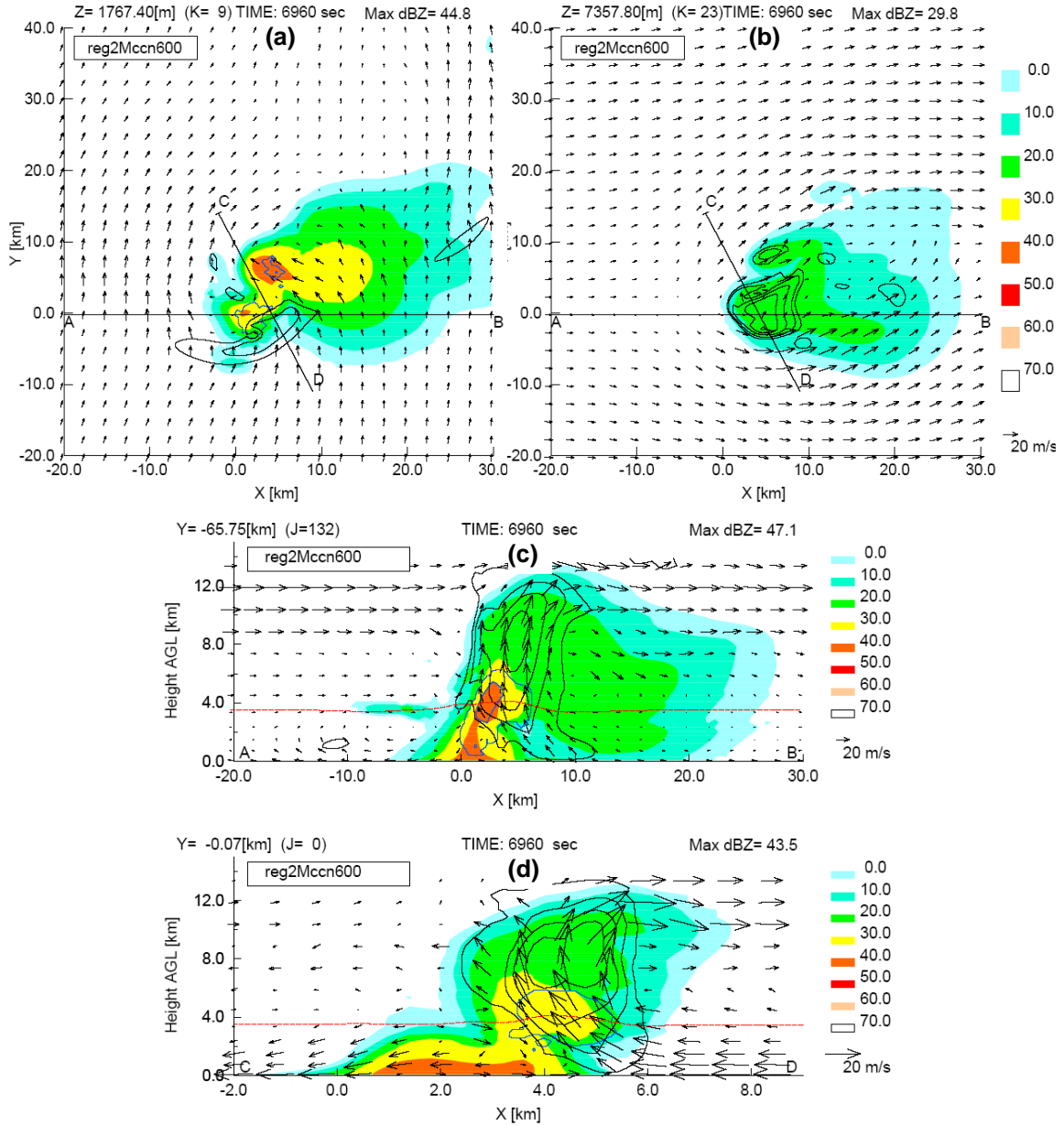


Figure 5.26: As in Fig. 5.24 for simulation reg2Mccn600 (N_{1cm}).

5.24b,c), eventually falling out to the surface on the northern and northwestern flanks of the updraft (Fig. 5.24a,d). Additional analyses of Z_e , N_{2cm} , N_{4cm} , and storm-relative flow fields at various heights between 1 and 10 km confirm the concurrent cyclonic movement of regions of high Z_e values and large hail around the updraft from the eastern flank at upper levels to the northern and northwestern flank at lower levels for the ccn600 case (not shown). This suggests

the large hail particles may have grown from particles initiated within the forward overhang region (Fig. 5.24d), as proposed by Browning and Foote (1976), as well as from particles within the mid-level mesocyclone in a manner similar to that described by Miller et al. (1988) given the relatively close proximity of very large hail to the mid-level circulation center (Fig. 5.24b).

Lastly, comparisons are made of the computed polarimetric variables ZDR , LDR , ρ_{hv} , and HDR for the simulations at 116 minutes (Figs. 5.27 and 5.28). The main purpose here is to gauge the ability of the modeled hydrometeor fields, particularly hail, to reproduce general features of polarimetric signals associated with supercells. In all three cases, regions of hail coincide with ZDR values between -0.5 and 0.5 dB throughout the storm (Fig 5.27a,c,e), which is fairly typical for hail based on observations as well as estimations from scattering models such as employed herein (Aydin et al. 1986; Bringi et al. 1986; Aydin and Zhao 1990; Depue et al. 2007). Noticeably absent from the simulated ZDR fields is a column of enhanced ZDR values extending above the freezing level (ZDR column; Illingworth et al. 1987), a characteristic of many hail-producing supercells (Bringi et al. 1986; Conway and Zrnić 1993; Hubbert et al. 1998) including the 29 June 2000 supercell (TMWR05). The positive ZDR values seen in Figure 5.27a,c,e are primarily associated with rain, though these values are lower than typical observed ZDR values owing to the generally small sizes of raindrops in all cases ($D_{\bar{m}} \leq 2$ mm). The reg2Mccn600 case (Fig. 5.27e) exhibits the most expansive region of enhanced ZDR values as well as the greatest maximum magnitude (1.87) compared to the other cases (1.38 for ccn600 and 0.75 for 2Mccn600). This is most likely due to larger raindrops at low levels in reg2Mccn600 as a result of greater amounts of complete melting of hail (Figs. 5.27e and 5.43e); rain formed from completely melted hail is typically larger than the 1 mm drops shed from hail as the hail particles are generally larger than 1 mm. Interestingly, a minimum in the ZDR field between $x = -10$ and 0

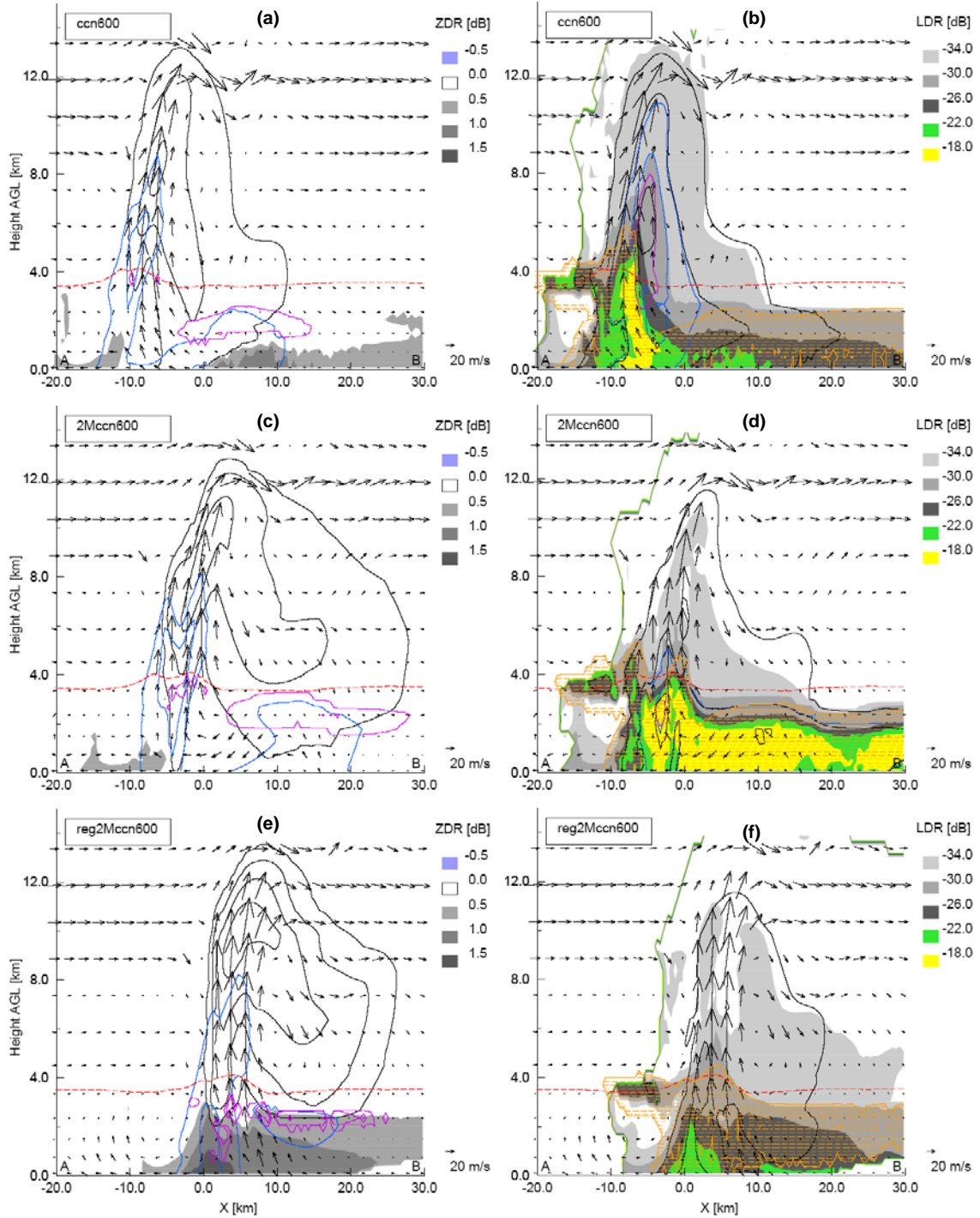


Figure 5.27: East-west cross sections along line AB in Figures 5.24-5.26 at 116 minutes. Left column shows shaded contours of ZDR [dB], mixing ratio contours [0.1, 1, 4 and 8 g kg^{-1}] of rain (blue) and hail (black), and complete melting rates of hail [purple; 0.001, 0.01, 0.1 $\text{g kg}^{-1} \Delta t^{-1}$] for (a) ccn600, (c) 2Mccn600, and (e) reg2Mccn600 cases. Right column shows shaded contours of LDR [dB], black contours of total reflectivity Z_H for hail, rain, graupel, snow, and aggregates [20, 40, and 60 dBZ], contours of N_{2cm} (blue) and N_{4cm} (purple) [10^4 , 0.01 m^{-3}], and regions of hail LWF > 0.25 (orange hatched area) for (b) ccn600, (d) 2Mccn600 and (f) reg2Mccn600 case. Radar variables computed using the T-matrix/Mueller matrix method described in the text, red dashed line denotes 0 °C isotherm, and storm-relative wind vectors are overlaid in each panel.

km in the ccn600 case (Fig. 5.27a) corresponds to the low-level hailshaft and is similar to that observed by Bringi et al. (1986) for a northeast CO hailstorm. No relative minima in ZDR are seen in the two-moment cases as erroneously large hail dominates the signal at low levels in 2Mccn600 (Fig. 5.27c) whereas virtually no hail reaches the surface in reg2Mccn600 (Fig. 5.27e).

LDR has been used by numerous investigators as an estimate of hail size, with greater LDR values in conjunction with large Z_H values typically associated with large wet hail within the vicinity of and below the freezing level (Carey and Rutledge 1998; Hubbert et al. 1998; Depue et al. 2007). The computed LDR fields for the simulations show that LDR values ≥ -18 dB are collocated with regions of large wet hail ($D_h \geq 2$ cm; hail bulk LWF ≥ 0.25) as evident for cases ccn600 (Fig. 5.27b) and 2Mccn600 (Fig. 5.27d), even though large hail in the latter is an artifact of the representation of melting. It is noted that the region of very large hail ($D_h \geq 4$ cm) below the freezing level in ccn600 is not associated with the highest LDR values owing to the lower bulk hail LWF values in this region (Fig. 5.27b). Case reg2Mccn600 has at most a negligible amount of large hail and thus LDR values are less than -18 dB (Fig. 5.27f) in agreement with findings by Carey and Rutledge (1998) and Depue et al. (2007). An LDR 'cap' (Bringi et al. 1997) atop a ZDR column as revealed in the radar syntheses of TMWR05 for this storm is not present in any of the simulations, though a column of higher LDR values (> -26 dB) within the updraft centered around $x = -6$ km is seen to extend several km above the freezing level in the ccn600 case (Fig. 5.27b). This ' LDR column' (for lack of a better term) indicates the likelihood of hail undergoing wet growth (Bringi et al. 1997; Carey and Rutledge 1998; Straka et al. 2000), and analyses of hail growth performed in the next section will show that this is indeed the case (cf. Fig. 5.40a).

Plots of the correlation coefficient ρ_{hv} for the simulations reveal that values of $\rho_{hv} < 0.98$ are generally collocated with regions of shedding by large hail in cases ccn600 (Fig. 5.28a) and 2Mccn600 (Fig. 5.28c). The small shed drops in the presence of the larger wet hail particles leads to a reduction in ρ_{hv} in agreement with observations and modeling studies of polarimetric variables for hail detection (Balakrishnan and Zrnić 1990; Aydin and Zhao 1990; Zrnić et al. 1993; Hubbert et al. 1998). On the other hand, ρ_{hv} values are much closer to unity in the reg2Mccn600 case due to the fact hail sizes are much smaller and negligible amounts of shedding are occurring (Fig. 5.28e). Decreases in ρ_{hv} also result from broadening of the hail size spectra (Balakrishnan and Zrnić 1990) as demonstrated by the expansive region of lower ρ_{hv} values in 2Mccn600 due to the broad hail spectra (v_h is fixed at 2.0) that contain (erroneously) large hail. In contrast, lower ρ_{hv} values are confined to a much more narrow zone with a region of large hail in ccn600 owing to the narrowing of the hail size distributions below the freezing level as discussed in Chapter 4.2. The region containing the largest hail in this case exhibits ρ_{hv} values > 0.98 owing to lower bulk hail LWF values (Fig. 5.27b) and the absence of significant shedding (Fig. 5.28a). This is similar to the results of Jung et al. (2010) who showed that ρ_{hv} values decrease slower for increasing hail sizes when hail is dry compared to when a water coating is present. It is noted that the computed ρ_{hv} values for the simulations are higher than the typically observed values for large hail, though this may be due to the fact that the simplified spheroid model for hail in the T-matrix code does not account for the irregular shapes and protuberances often associated with natural hail. Nonetheless, the relationships between the characteristics of the simulated hail distributions and the computed ρ_{hv} values generally agree with previous studies (Balakrishnan and Zrnić 1990; Aydin and Zhao 1990; Zrnić et al. 1993; Hubbert et al. 1998; Straka et al. 2000; Depue et al. 2007).

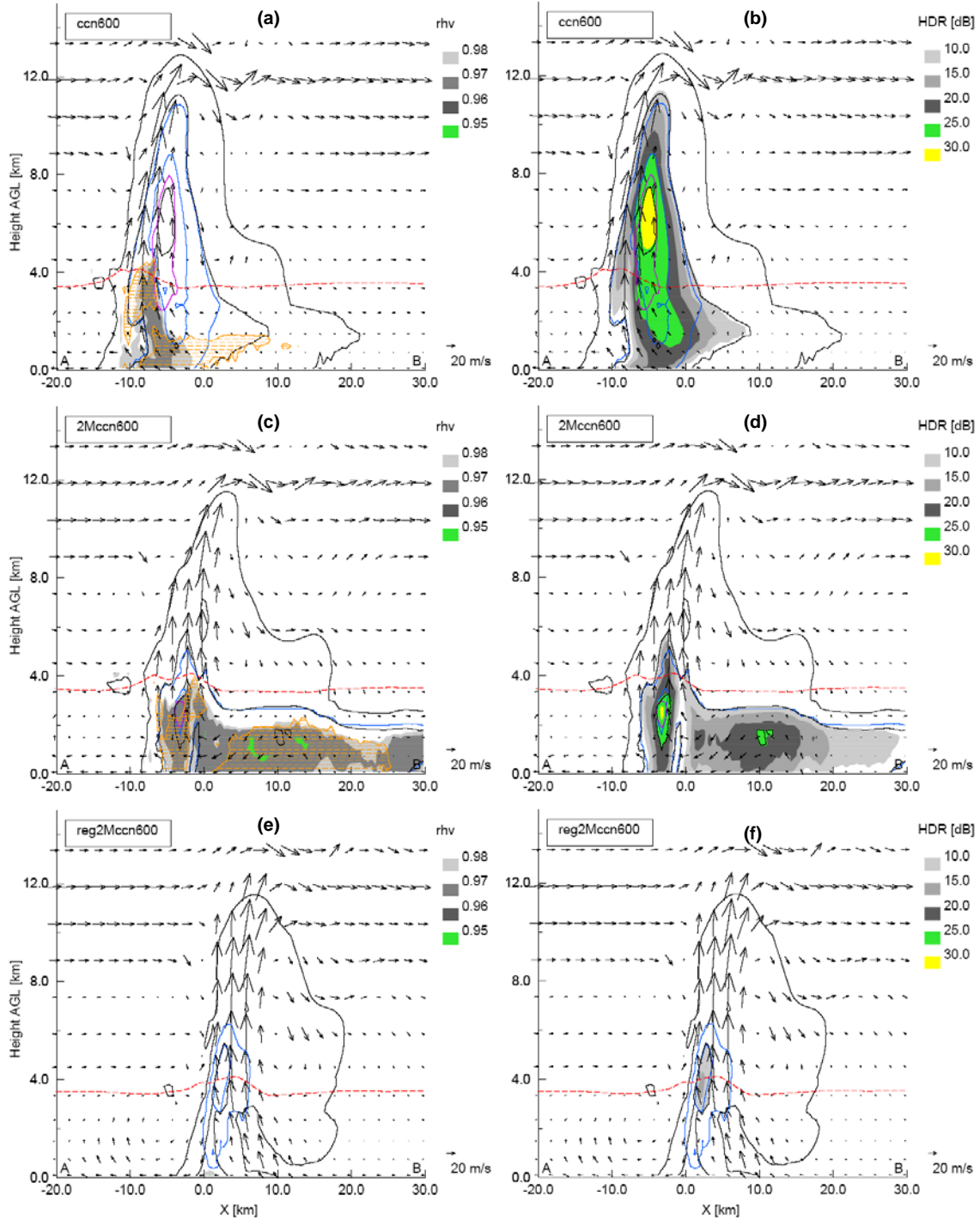


Figure 5.28: As in Figure 5.27, except shaded contours in left column are cross correlation coefficient ρ_{hv} , and shaded contours in right column are hail differential reflectivity HDR [dB]. Orange hatching in panels a, b, and c denotes regions of shedding from hail (shed rates $\geq 0.001 \text{ g kg}^{-1} \Delta t^{-1}$). In all panels, black contours are total reflectivity Z_H for hail, rain, graupel, snow and aggregates [20, 40, and 60 dBZ], contours of N_{2cm} (blue) and N_{4cm} (purple) [10^{-4} , 0.01 m^{-3}] are drawn for cases (a,b) ccn600 and (c,d) 2Mccn600, whereas blue contours are N_{1cm} [10^{-4} , 0.01 m^{-3}] for (e,f) reg2Mccn600 case.

Determination of hail sizes using the diagnostic hail differential reflectivity (*HDR*) parameter (Aydin et al. 1986) is compared with the model predicted hail sizes in Figure 5.28 for the three simulations. In general, computed *HDR* values ≥ 20 dB (30 dB) match closely with regions containing hail with diameters larger than 2 cm (4 cm) in the ccn600 case (Fig. 5.27b) in agreement with results from Depue et al. (2007) for both water-coated and dry hailstones. Larger *HDR* values are also generally associated with regions of large hail within the lower portions of the updraft in the 2Mccn600 case (Fig. 5.28d), although lower *HDR* values exist in the low-level downdraft region to the right of $x = 0$ km in an area containing (artificially) large hail. *HDR* values are typically less than 10 to 15 dB in reg2Mccn600 due to the smaller hail sizes and lower Z_H magnitudes in this case (Fig. 5.28f) in concurrence with findings by Depue et al. (2007).

Based on the analyses of the computed polarimetric variables for the three simulations, it is evident that the ccn600 case exhibits much more realistic polarimetric signatures associated with supercell precipitation processes, particularly with respect to hail, than do the two-moment cases. The lack of a well-defined *ZDR* column and *LDR* 'cap' in the computed radar fields is consistent among all three simulations, though the typical signatures for detection of large hail, namely larger values of Z_H and *LDR*, along with low *ZDR* and ρ_{hv} values (Bringi et al. 1986; Aydin et al. 1986; Balakrishnan and Zrnić 1990; Ryzhkov et al. 2005), are seen to correspond to regions of large hail in the ccn600 case (and the 2Mccn600 case as well), especially below the freezing level. In the reg2Mccn600 case, smaller Z_H magnitudes in combination with larger *ZDR* and r_{hv} values at lower levels are correctly associated with the smaller hail particles produced in this simulation. The *HDR* hail detection algorithm appears to give the best results with respect to locations of large hail in the ccn600 case and adequately depicts the region containing greater numbers of 1 cm hail particles in the reg2Mccn600 case.

The overall result from the preceding analyses is that the ccn600 simulation with triple-moment microphysics appears to represent the observed storm characteristics much more accurately than either of the simulations with two-moment microphysics. All three microphysical schemes tested are able to mostly capture the general evolution of the storm from an initial multi-cell state transitioning to a right-moving supercell, yet the simulations with 2M microphysics clearly diverge from the observed and inferred microphysical properties of the actual storm. Using the modified 2M microphysics scheme, the 2Mccn600 case artificially produces substantial amounts of large hail at low-levels, whereas the regular 2M microphysics scheme in reg2Mccn600 results in virtually no graupel production and very little hail reaching the surface. Similar flow fields are seen between the simulated and observed storms, yet the reflectivity fields are vastly different between the two-moment simulations and the observations, strongly suggesting the discrepancy lies in the inadequacies of the 2M microphysics scheme. Departures of the model solutions for the cases with 2M microphysics from the observations as well as from the ccn600 case are consistent throughout the duration of the simulations as revealed in additional similar analyses of the modeled storms at later times (not shown). A detailed examination of the microphysical evolution of the simulated storms presented in the next section aims to provide some insight into differences in hail production in the simulated storms as well as how these differences affect the general storm morphology and microphysical characteristics.

5.4.3) Microphysical and thermodynamic characteristics of simulated storms

The analyses of the previous two sections clearly demonstrate that differences in the complexity of the microphysical schemes lead to significant differences in the modeled storm hydrometeor fields, and ultimately, to differences in the storm evolution. This section examines

the impacts the different schemes have on the microphysical characteristics and hail processes of the simulated storms.

Vertical profiles of the time- and horizontally-averaged mass contents and number concentrations for each hydrometeor species are displayed in Figures 5.29 and 5.30, respectively. These profiles provide a generalized picture of the vertical distributions of hydrometeors in the simulated storms and highlight some of the major differences in storm microphysical structures as a result of differences in the model microphysics scheme. It should be mentioned that these profiles depend on the amounts of mass and number at each grid point as well as on the spatial coverage of the individual species at any given time. A hydrometeor category with large amounts of mass or number over a large spatial extent could have a similar domain total value as a category with lesser amounts of mass or number over a smaller spatial extent, although time-height profiles of total mass and numbers for each species (not shown) suggest that the profiles do in fact represent the average vertical structures of the simulated storms.

It is evident from Figure 5.30 that the majority of mass associated with precipitation-sized hydrometeors in all simulations is contained in the frozen categories, and this is in line with the fact that ice processes tend to dominate deep convection in mid-latitudes (Braham 1964; Mason 1971; Dye et al. 1974; Farley and Orville 1986; Knight and Knight 2001). In general, the 2Mccn600 and reg2Mccn600 simulations have smaller proportions of mass and number content contained in the pristine ice, snow, aggregates, and graupel categories compared to the ccn600 case, with the reg2Mccn600 case exhibiting the smallest values for these species overall (Figs. 5.29d,e,f,g and 5.30d,e,f,g; Table 5.4). On the other hand, the reg2Mccn600 simulation has the greatest amount of hail mass content aloft on average followed by 2Mccn600 and ccn600, and this trend is reversed below about 2 km (Fig. 5.30h) owing to the complete melting of nearly all

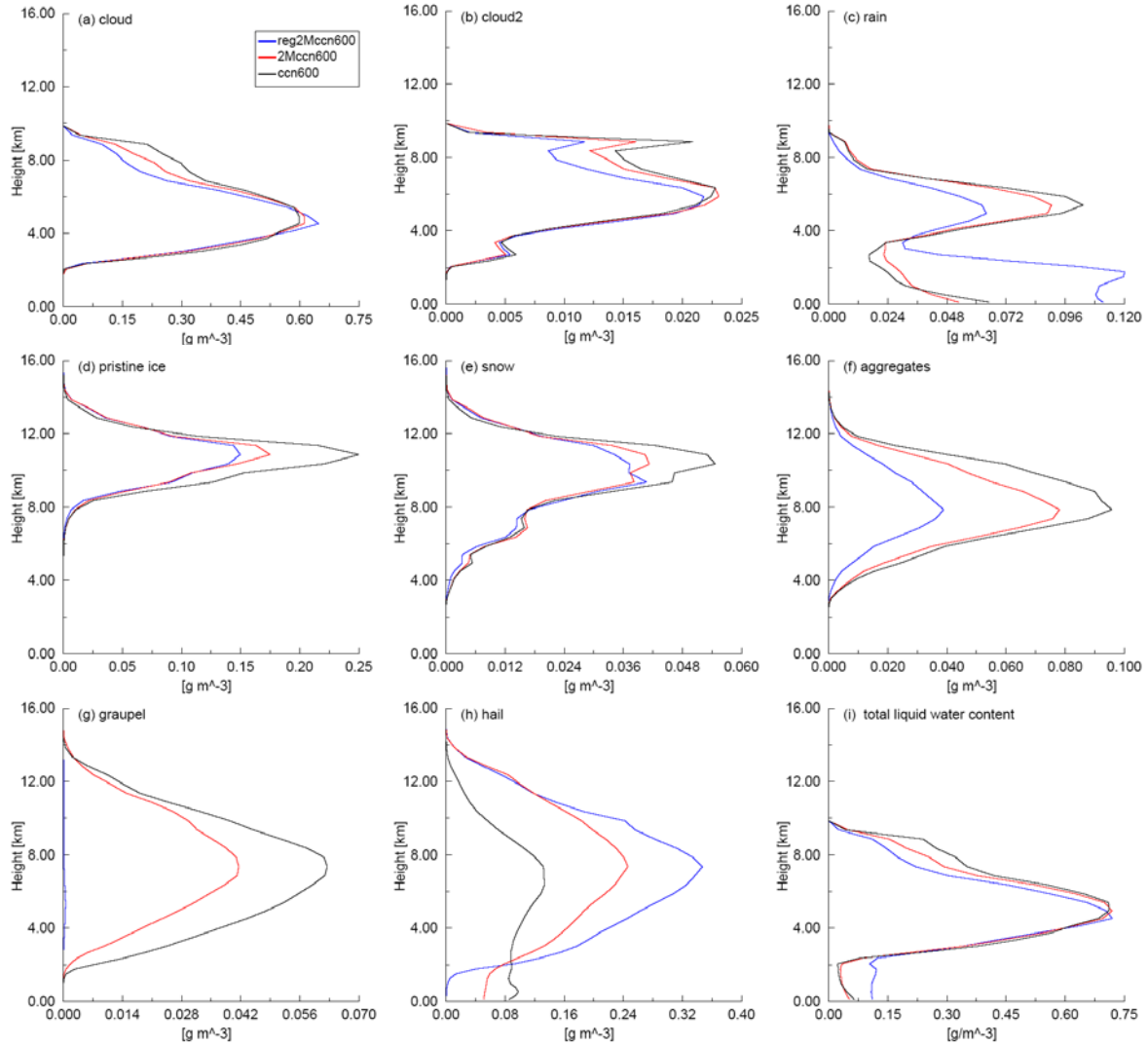


Figure 5.29: Temporally and spatially averaged water content [g m^{-3}] as a function of height over the entire domain for the 29 June 2000 STEPS simulations listed in Table 5.3. Temporal averaging has a 5 min frequency from $t = 5$ to 210 min and spatial averaging was performed horizontally for all grid points where species mixing ratios were greater than 0 g m^{-3} .

hail at low levels in the reg2Mccn600 case. In fact, hail mass accounts for the largest percentage of total hydrometeor mass in both of the two-moment cases throughout the duration of the simulations and is nearly twice as large as all the other ice species combined in the reg2Mccn600 case (Table 5.4). Average hail number concentrations in the two-moment simulations are about 5 to 6 times greater than in the ccn600 case (Fig. 5.30h). This is partly due to the non-adjustment of numbers of newly formed hail in the two-moment schemes as is done in the 3MHAIL scheme

Table 5.4: Species ranked according to average percentages of total hydrometeor mass (values in parentheses) for simulations prior to right turn ($t < 90$ min) and after right turn ($t \geq 90$ min).

ccn600		2Mccn600		reg2Mccn600	
$t < 90$ min	$t \geq 90$ min	$t < 90$ min	$t \geq 90$ min	$t < 90$ min	$t \geq 90$ min
hail (23.4)	pris (34.0)	hail (39.0)	hail (38.0)	hail (41.4)	hail (50.0)
cloud (22.3)	aggr (17.3)	cloud (21.5)	pris (23.5)	cloud (22.0)	pris (19.7)
pris (18.0)	hail (15.5)	pris (11.3)	aggr (12.0)	pris (13.7)	rain (9.0)
aggr (12.4)	grpl (13.8)	aggr (9.3)	grpl (8.2)	snow (7.6)	cloud (8.8)
grpl (9.0)	snow (9.2)	snow (7.1)	snow (7.2)	rain (7.3)	snow (6.7)
snow (8.3)	cloud (6.7)	grpl (5.9)	cloud (6.8)	aggr (6.5)	aggr (5.2)
rain (5.0)	rain (3.4)	rain (4.4)	rain (3.8)	cloud2 (1.6)	cloud2 (0.5)
cloud2 (1.6)	cloud2 (0.4)	cloud2 (1.5)	cloud2 (0.4)	grpl (0.05)	grpl (0.04)

(Chapter 3.3.3.3), and the result is more numerous hail particles with smaller sizes in the former than in the latter. Greater numbers of hail particles in the two-moment cases are also the result of much larger rates of hail formation associated with three-component freezing in these cases compared to the ccn600 case, particularly at temperatures colder than -20 °C (heights ≥ 6.3 km) (Fig 5.33a,c,e). This also helps explain the smaller average mass and number content values in the profiles of pristine ice, snow, aggregates, and to some extent graupel, in the two-moment cases relative to ccn600 (Figs. 5.29 and 5.30; Table 5.4). Greater collection rates of non-hail ice species by hail in 2Mccn600 and reg2Mccn600 relative to ccn600 (Fig. 5.39a,c,e) also play a role in reducing the mass and number contents of the non-hail ice categories in the former cases compared to the latter case. Greater average amounts of hail mass and numbers evident in the simulations with two-moment microphysics relative to the ccn600 case are qualitatively similar to findings by MY06b for hailstorm simulations using two- and three-moment bulk microphysics schemes.

The average cloud (small and large modes) mass content profiles are largely similar among the three simulations (Fig. 5.29a,b), with slightly greater mass contents between roughly 7 and 9

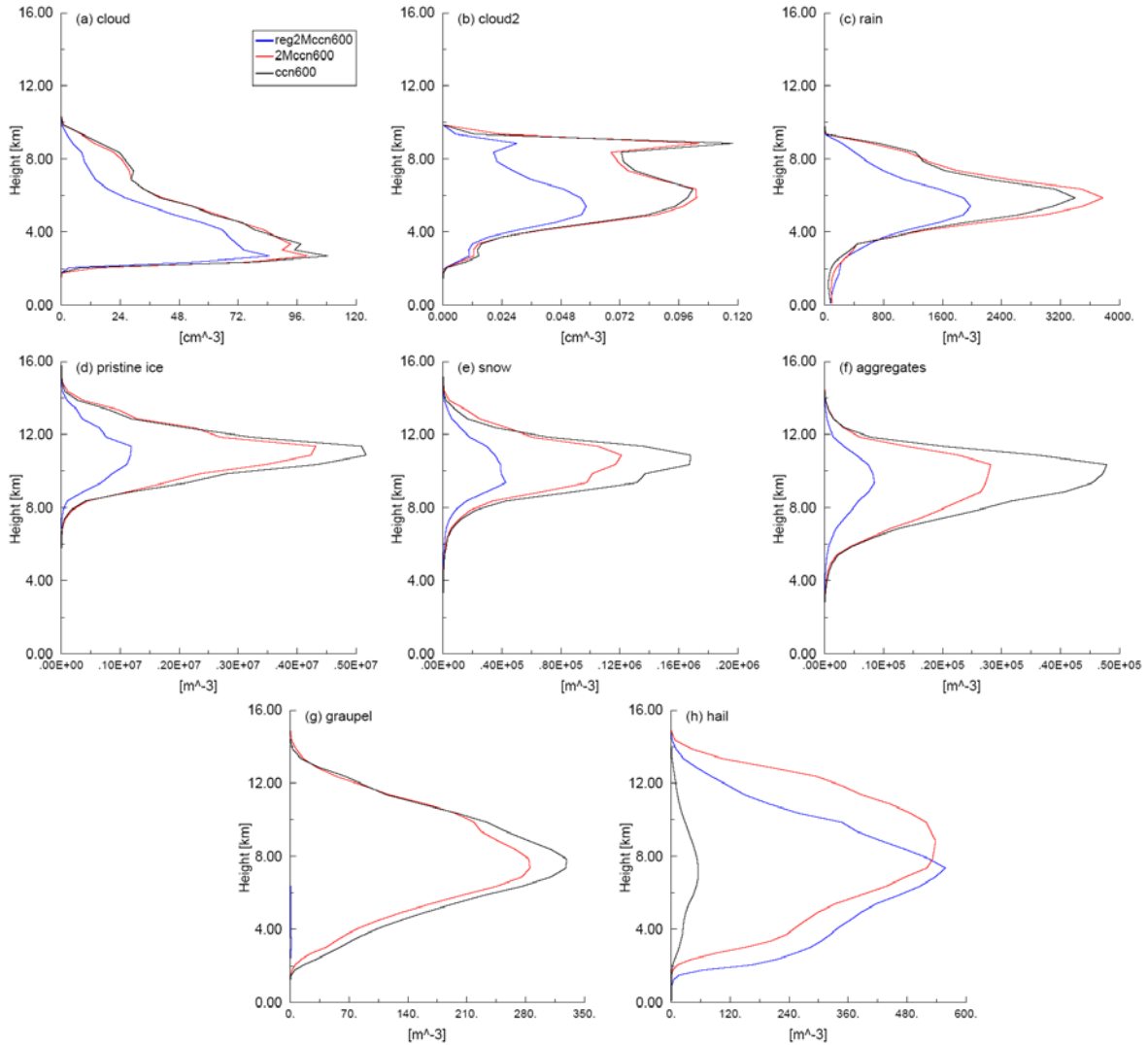


Figure 5.30: Temporally and spatially averaged number concentrations [cm^{-3} for cloud particles; m^{-3} all other species] as a function of height over the entire domain for the 29 June 2000 STEPS simulations listed in Table 5.3. Temporal averaging has a 5 min frequency from $t = 5$ to 210 min and spatial averaging was performed horizontally for all grid points where species number concentrations were greater than 0 m^{-3} .

km AGL in the ccn600 and 2Mccn600 cases compared to reg2Mccn600, whereas smaller average cloud number concentrations at mid-levels are seen in the latter case compared to the former cases (Fig. 5.30a,b). The reductions in cloud mass and number at these heights in the reg2Mccn600 are due in part to greater riming rates in this case relative to the ccn600 and 2Mccn600 simulations (Fig. 5.38a,c,e). Similarly, greater average rain mass and number contents above ~ 4 km in ccn600 and 2Mccn600 compared to reg2Mccn600 (Figs. 5.29c and 5.30c) are

the result of both decreased collection of rain by hail (Fig. 5.38b,d,f) and increased shedding by hail (Fig. 5.43b,d,f) in the former cases versus the latter. Below 4 km, average rain mass contents increase in all three cases (Fig. 5.29c) as a result of melting and shedding of hail, though complete melting of hail is much greater in reg2Mccn600 relative to ccn600 and 2Mccn600 (Fig. 5.43a,c,e) leading to a much greater increase in average rain mass content in the latter compared to the former cases. The resulting profiles of average liquid water content (both cloud modes plus rain, Fig. 5.29i) generally mimic the average cloud (rain) mass content profiles above (below) about 5 km (2km).

Even though the average amounts of hail number and mass contents are lowest in the ccn600 case compared to the two-moment cases, the numbers of hailstones with diameters $\geq 1, 2, 3,$ and 4 cm are significantly greater in the former compared to the latter cases as depicted in time-height contour plots of domain maximum $N_{1cm}, N_{2cm}, N_{3cm},$ and N_{4cm} (Figs. 5.31 and 5.32). (Note that time-height averages and total amounts of both numbers and mass of hailstones with diameters of at least 1, 2, 3, and 4 cm exhibit similar patterns to those shown in Figures 5.31 and 5.32 for all three simulations, though only the maximum concentrations are shown for brevity as well as to highlight differences in the maximum amounts of larger hailstones produced in the simulations.) As discussed in the previous analyses, artificial increases in hail sizes due to melting occur below the freezing level in the 2Mccn600 case and are clearly evident in the maximum $N_{1cm}, N_{2cm}, N_{3cm},$ and N_{4cm} fields for this case (Figs. 5.31c,d and 5.32c,d). The largest values of maximum $N_{2cm}, N_{3cm},$ and N_{4cm} in ccn600 (Figs. 5.31b and 5.32a,b) occur after the simulated storm's right turn ($t > 90$ min) and are seen as distinct maxima that generally succeed peaks in maximum updraft speeds (Fig. 5.7a). The greatest of these peaks arises just before 120 minutes and accounts for the intense episode of large hail at the surface around this time in

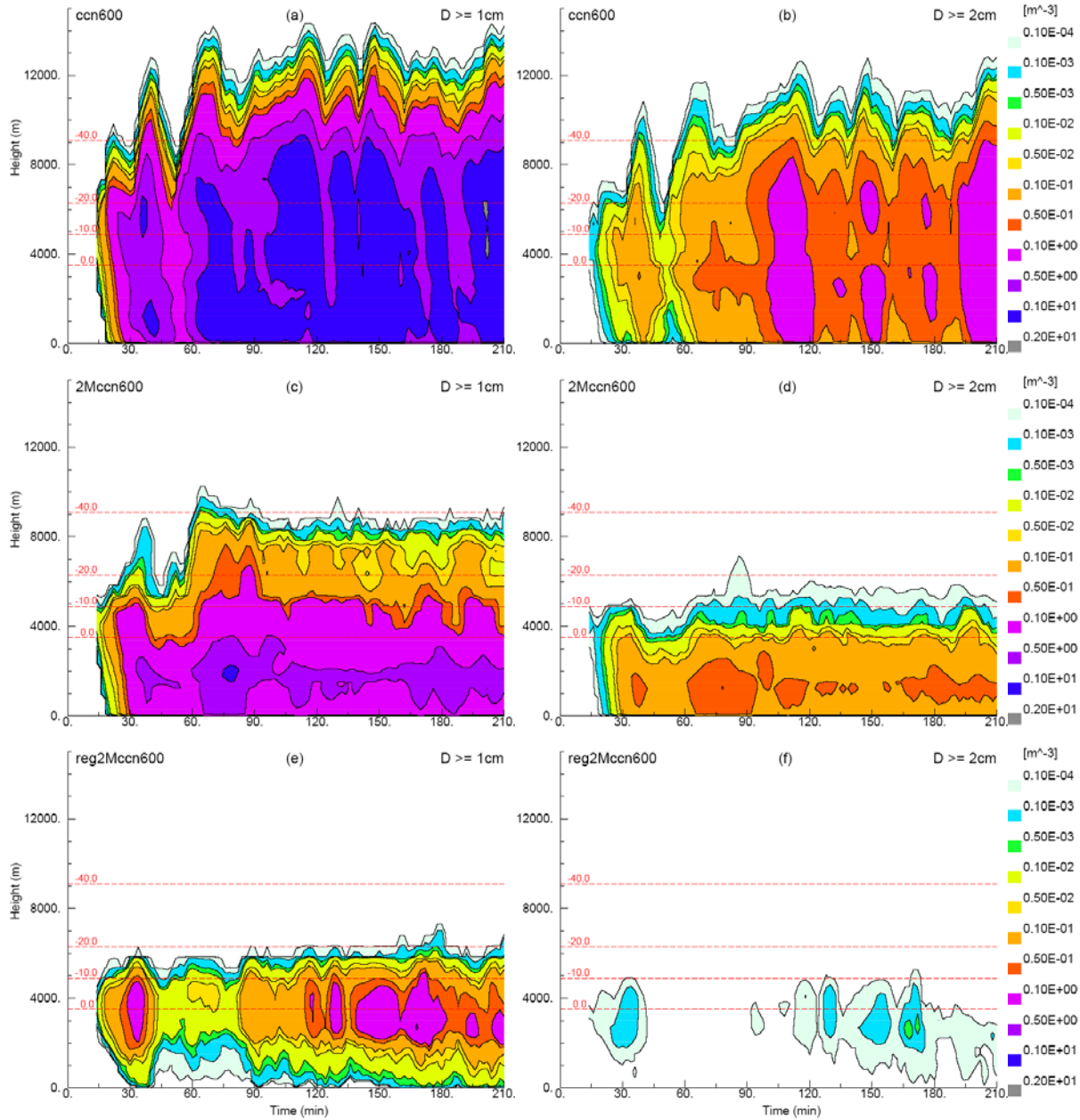


Figure 5.31: Time-height contours of domain maximum N_{1cm} (left column) and N_{2cm} (right column) [m^{-3}] for (a,b) ccn600, (c,d) 2Mccn600, and (e,f) reg2Mccn600 cases. Red dashed lines depict approximate heights of 0, -10, -20, and -40 °C isotherms.

ccn600 (Fig. 5.13b; see also Figs. 5.47 and 5.48). A similar pattern is evident in the reg2Mccn600 case beyond 90 minutes (Fig. 5.31e,f), with locally greater values of maximum N_{1cm} and N_{2cm} following peaks in maximum updraft speeds (Fig. 5.7a). In contrast, the largest

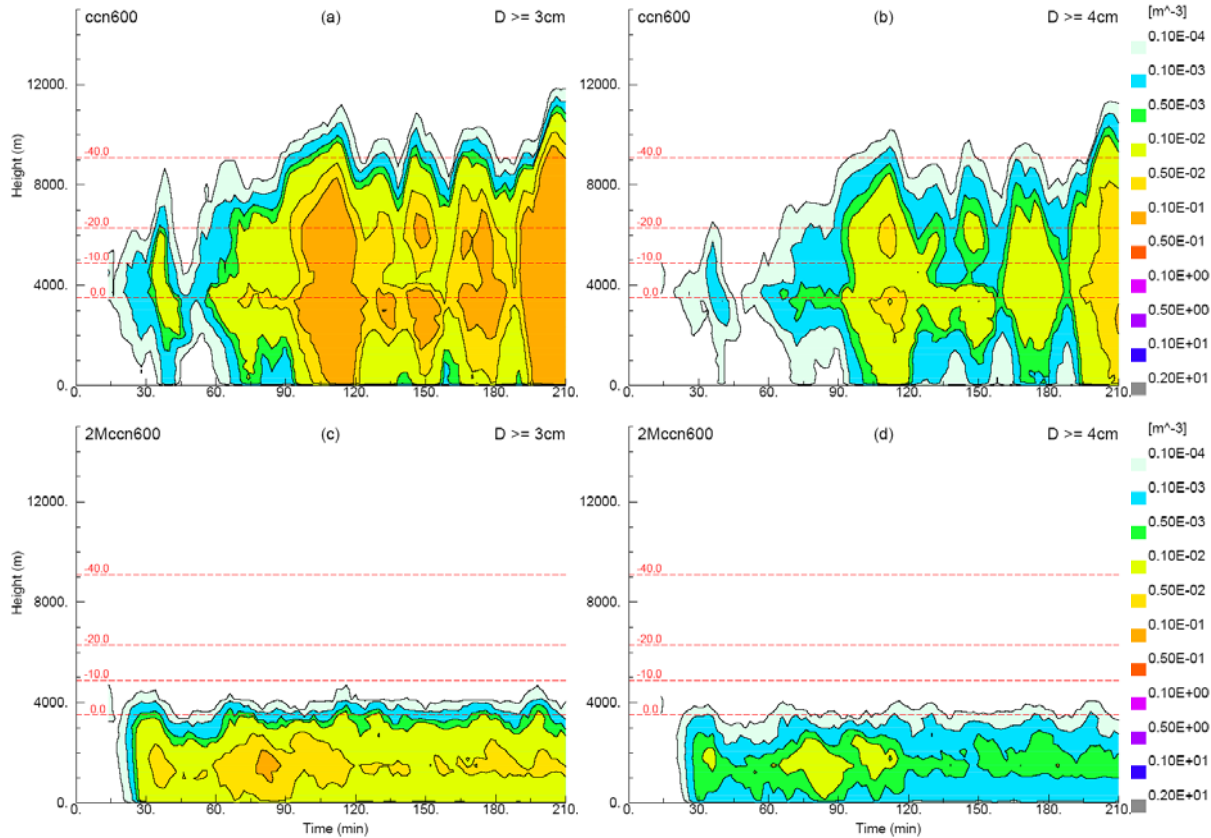


Figure 5.32: As in Figure 5.31 except for N_{3cm} (left column) and N_{4cm} (right column) [m^{-3}] for (a,b) ccn600 and (c,d) 2Mccn600. Domain maximum N_{3cm} and N_{4cm} for reg2Mccn600 are negligible and are thus omitted.

values of maximum N_{1cm} , N_{2cm} , N_{3cm} , and N_{4cm} occur prior to 90 minutes in 2Mccn600 (Figs. 5.31c,d and 5.32c,d), with relatively non-distinct patterns seen in these fields after 90 minutes.

Hailstones with sizes equal to or greater than 1, 2, 3, and 4 cm in concentrations of at least 1, 0.1, 0.01, and $0.001 m^{-3}$, respectively, are seen to extend well above the freezing level in ccn600 (Figs. 5.31a,b and 5.32a,b). These concentration values are reasonable based on previous observations of both moderately sized ($D \sim 1$ to 1.5 cm) and large hail aloft (Auer 1972; English 1973; Musil et al. 1976, 1991). Maximum N_{1cm} values in 2Mccn600 (Fig. 5.31c) and reg2Mccn600 (Fig. 5.31e) are smaller than in ccn600 though still physically reasonable, with values generally less than $0.5 m^{-3}$ between the freezing level and about 5 km. Above roughly 5 km, maximum N_{1cm} values rapidly decrease with height in reg2Mccn600, becoming negligible

above about 6km, whereas maximum N_{1cm} magnitudes exhibit a much slower decrease in 2Mccn600 with negligible values above approximately 9 km. Significantly smaller values of N_{2cm} , N_{3cm} , and N_{4cm} are evident above the freezing level in 2Mccn600 (Figs. 5.31d and 5.32c,d) compared to ccn600 (Figs. 5.31b and 5.32a,b), and virtually no large hail exists above roughly 6 km in the former case. Peak values of maximum N_{2cm} in the reg2Mccn600 case (Fig. 5.31f) are approximately 3 orders of magnitude less than in ccn600 and are primarily confined between about 2 and 5 km, with negligible amounts of N_{2cm} seen below roughly 2 km. The reg2Mccn600 case does not produce hail with sizes equal to or greater than 3 cm and thus plots of N_{3cm} and N_{4cm} are not shown for this case. MY06b also noted the failure of their various two-moment schemes to produce large hail in simulations of an Alberta hailstorm whereas their triple-moment scheme did so successfully. Although the maximum allowable hail mean mass diameter ($D_{\bar{m}h,max}$) is larger in 2Mccn600 (40 mm) than in reg2Mccn600 (10 mm; cf. Chapter 3.1), the lack of large hail aloft in both of these simulations clearly demonstrates that increasing the value of $D_{\bar{m}h,max}$ in the RAMS two-moment microphysics scheme does not result in the production of large hail.

5.4.3.1) *Hail formation and growth processes*

As the primary differences in the microphysical schemes used in the simulations pertain to the treatment of hail, analyses of the hail formation and growth mechanisms are performed to determine the underlying causes for the observed differences in the simulated hail fields among the simulations. These analyses also serve to further validate the improvements made to the RAMS microphysics with the implementation of the 3MHAIL scheme, similar to the highly idealized tests carried out in Chapter 4.

Time-height contour plots showing spatially averaged hail number and mass formation rates due to three-component freezing and riming of graupel for the three simulations are displayed in Figures 5.33 and 5.34. In these and subsequent time-height contour plots, values prior to $t = 30$ minutes are associated with the initiating bubble and are thus excluded from the analyses. It is clearly evident from these figures that three-component freezing dominates hail formation in all three cases, with riming of graupel playing a significantly smaller role in generating new hail, particularly with respect to the numbers of new hail particles (Fig. 5.33). As this is a High Plains storm with a modestly cool cloud base temperature (~ 12 °C), observations by Knight and Knight (1970b, 1979), Knight et al. (1974), and Hubbert et al. (1998) suggest that graupel should be the dominant hail embryo type rather than rain. Of course, the embryos for newly formed hail particles resulting from rain-graupel collisions are certainly graupel particles, though hail formed in this manner accounts for a very small fraction of overall hail production in the simulations (Tables 5.5 and 5.6; Fig. 5.35b,d,f). It should be stressed, however, that hail formed via rain-snow or rain-aggregate interactions does not automatically imply frozen raindrop embryos. It is suggested here that hail resulting from collisions between similar-sized rain and snow/aggregate particles in cases ccn600 and 2Mccn600 could potentially be interpreted as high-density graupel serving as hailstone embryos as in Ziegler (1988). This argument is based on the fact that, for three-component freezing in the 3MHAIL scheme, the coalesced particles are classified as hail if the density associated with the mean mass diameter of these particles is greater than 600 kg m^{-3} (Chapter 3.3.3.1), which is less than the fixed density assigned to hailstones (900 kg m^{-3}). A similar argument could be made regarding hail formation via rain-snow and rain-aggregate collisions for the reg2Mccn600 case in which these collision types always lead to hail. As rain-snow collisions are the dominant mechanism by which hail is generated in all three simulations

(Tables 5.5 and 5.6; Fig. 5.35), it is certainly possible that a significant fraction of these new hailstones have characteristics of high-density graupel rather than frozen raindrops.

The average generation rates of new hail numbers via rain-ice collisions are clearly much larger in cases reg2Mccn600 (Fig. 5.33e) and 2Mccn600 (Fig. 5.33c) relative to the ccn600 case (Fig. 5.33a). Peak average (domain maximum) rates of hail number formation are greater than $75 (2000) \text{ m}^{-3} \Delta t^{-1}$ in reg2Mccn600 and between 5 and 10 (250 and 750) $\text{m}^{-3} \Delta t^{-1}$ in 2Mccn600 compared to peak rates that are generally less than $0.5 (200) \text{ m}^{-3} \Delta t^{-1}$ in ccn600 primarily due to the adjustment of newly formed hailstone numbers in the latter versus the former (domain maximum rates not shown). In addition, smaller average hail number formation rates in 2Mccn600 relative to reg2Mccn600 are mainly due to the fact that not all rain-ice collisions lead to hail formation in the 2Mccn600 case (as in the ccn600 case as well). Average hail mass formation rates from rain-ice collisions for the ccn600 (Fig. 5.34a) and 2Mccn600 (Fig. 5.34c) cases generally exhibit similar vertical structures and magnitudes (rates mostly between 1×10^{-8} and $5 \times 10^{-7} \text{ kg m}^{-3} \Delta t^{-1}$), with slightly higher peak average formation rates in ccn600. This is not surprising given that both the ccn600 and 2Mccn600 cases employ the updated (MY05b) three-component freezing algorithm as well as the rain-pristine ice collection scheme of F94. The larger average hail mass formation rates (1×10^{-7} to $4 \times 10^{-6} \text{ kg m}^{-3} \Delta t^{-1}$) that extend over a greater depth evident in the reg2Mccn600 case (Fig. 5.34e), as well as the significantly larger production in hail numbers (Fig. 5.33e), are indicative of the overproduction of hail via rain-ice collisions in the regular RAMS collection scheme (Chapters 3.3.1 and 4.3).

The average generation rates for hail numbers and mass from rain-ice collisions are greatest between about -15 and -30 °C (~ 5.6 and 7.6 km) in cases ccn600 and 2Mccn600 (Figs. 5.33a,c and 5.34a,c, respectively). These greater hail production rates are mainly attributed to rain-snow

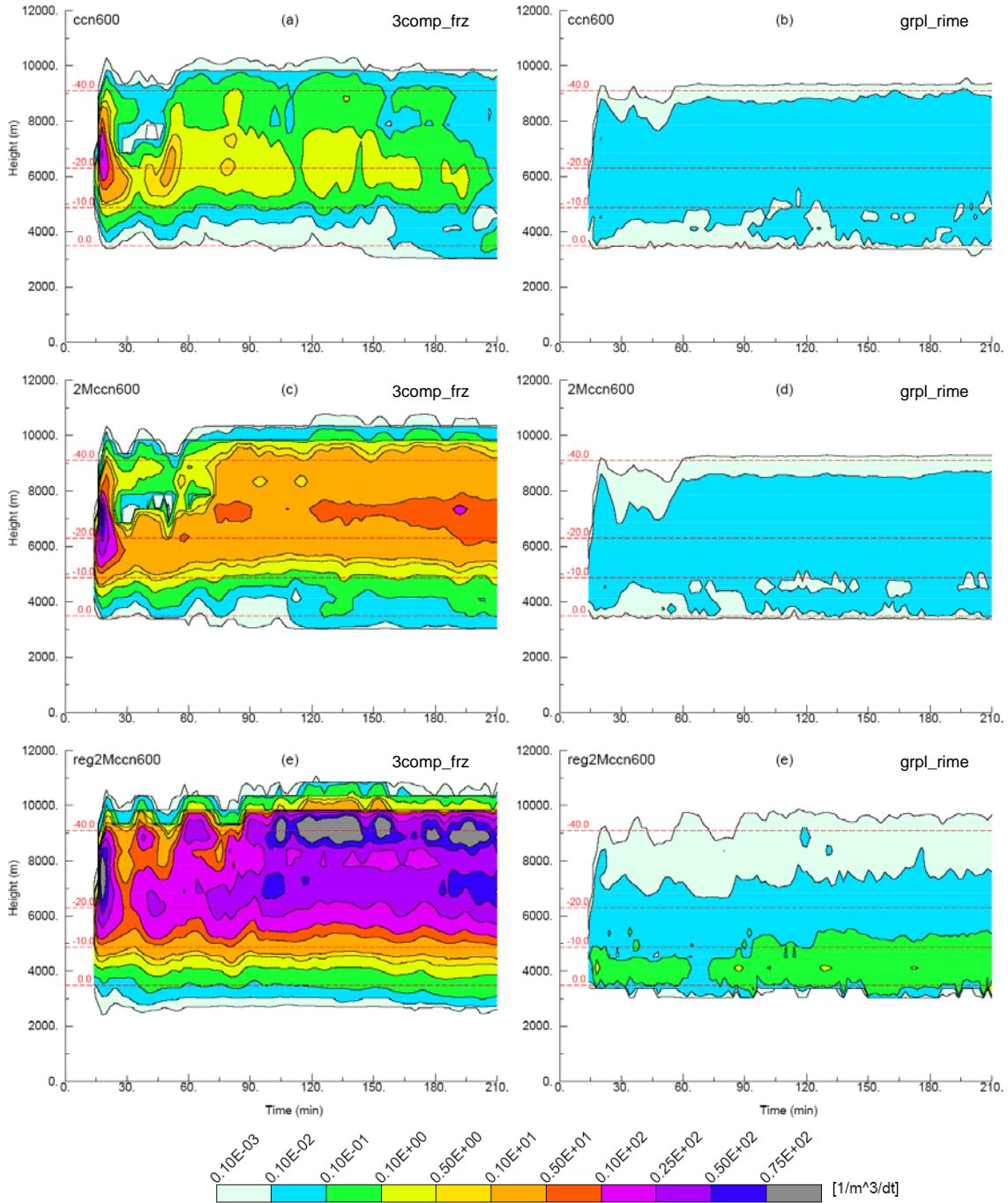


Figure 5.33: Time-height contours of spatially averaged hail number formation rate [$\text{m}^{-3} \Delta t^{-1}$] resulting from three-component freezing (left column) and riming of graupel (right column) for simulations (a,b) ccn600, (c,d) 2Mccn600, and (e,f) reg2Mccn600. Red dashed lines depict approximate heights of 0, -10, -20, and -40 °C isotherms.

collisions (Fig. 5.35a-d), though rain-pristine ice interactions account for a fair amount of the newly generated hail mass as well (Fig. 5.35a,c). Peak average hail formation rates in

Table 5.5: Domain average percentages of newly formed hail mass (values in parentheses) ranked by collision type for simulations prior to right turn ($t < 90$ min) and after right turn ($t \geq 90$ min). r-p denotes rain-pristine ice, r-s is rain-snow, r-a is rain aggregates, r-g is rain graupel, and g-c is riming graupel (both small and large cloud modes). --- signifies less than 0.01 %.

ccn600		2Mccn600		reg2Mccn600	
$t < 90$ min	$t \geq 90$ min	$t < 90$ min	$t \geq 90$ min	$t < 90$ min	$t \geq 90$ min
r-s (52.6)	r-s (47.5)	r-s (53.4)	r-s (49.0)	r-s (64.3)	r-s (57.1)
r-p (36.0)	r-p (40.8)	r-p (34.5)	r-p (41.2)	r-p (23.6)	r-p (31.3)
g-c (11.0)	g-c (11.2)	g-c (11.9)	g-c (9.4)	g-c (5.2)	g-c (4.9)
r-a (0.34)	r-a (0.54)	r-a (0.27)	r-a (0.28)	r-a (3.8)	r-a (3.7)
r-g (---)	r-g (---)	r-g (---)	r-g (---)	r-g (3.0)	r-g (3.0)

Table 5.6: As in Table 5.5 except for newly formed hail numbers.

ccn600		2Mccn600		reg2Mccn600	
$t < 90$ min	$t \geq 90$ min	$t < 90$ min	$t \geq 90$ min	$t < 90$ min	$t \geq 90$ min
r-s (99.3)	r-s (95.4)	r-s (99.6)	r-s (99.76)	r-s (70.2)	r-s (54.5)
r-a (0.57)	r-a (3.03)	r-a (0.3)	r-a (0.21)	r-p (25.5)	r-p (42.5)
g-c (0.06)	g-c (1.4)	g-c (0.01)	g-c (0.01)	r-a (4.3)	r-a (2.9)
r-p (0.03)	r-p (0.1)	r-p (---)	r-p (0.01)	r-g (0.02)	r-g (0.02)
r-g (---)	r-g (0.07)	r-g (---)	r-g (---)	g-c (---)	g-c (---)

reg2Mccn600 are centered around the homogeneous freezing level of -38 °C (~ 8.9 km) for numbers (Fig. 5.33e) and between roughly -10 and -40 °C (~ 4.8 and 9.1 km) for mass (Fig. 5.34e), with new hail mass created primarily by rain-snow collisions (Fig. 5.35e) as in the other two cases. The peak in number production around 9 km results from rain-pristine ice collisions (Fig. 5.35f), which generate significantly more hail particles compared the ccn600 and 2Mccn600 cases (Fig. 5.36a). A lower magnitude peak in average hail number generation is seen between roughly -20 and -30 °C (~ 6.3 and 7.6 km) in reg2Mccn600 as well (Fig. 5.33e) due to rain-snow interactions (Fig. 5.35f). Hail formation via rain-aggregates and rain-graupel collisions in all three simulations is relatively minor compared to hail generated from interactions between rain-snow and rain-pristine ice (Tables 5.5 and 5.6; Fig. 5.35), most likely due to lower number concentrations of aggregates and graupel relative to snow and pristine ice (Fig. 5.30).

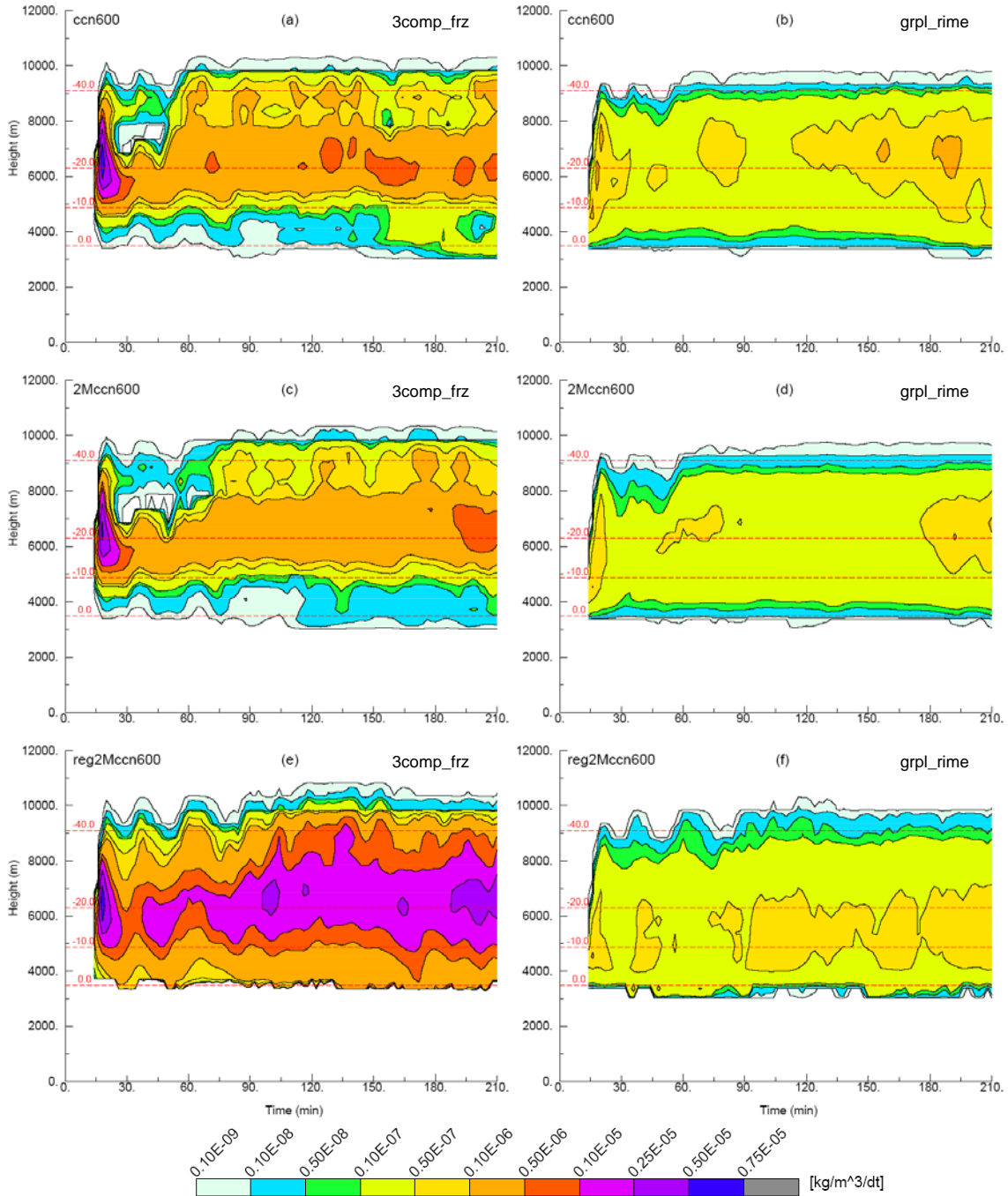


Figure 5.34: As in Figure 5.33 except for spatially averaged hail mass formation rate [$\text{kg m}^{-3} \Delta t^{-1}$].

Average hail formation rates via riming of graupel are relatively similar in all three cases (Figs. 5.33b,d,f and 5.34b,d,f), with slightly greater number generation rates apparent below 5 km in the reg2Mccn600 case compared to the ccn600 and 2Mccn600 cases. It should be

mentioned, however, that significantly fewer grid points contain graupel particles in reg2Mccn600, and the actual hail formation rates from riming of graupel are generally smaller in this case compared to the other cases as evident in the time-averaged vertical profiles of domain total hail formation rates (Figs. 5.36f and 5.37f). Furthermore, riming of graupel accounts for a greater fraction of total hail production in cases ccn600 and 2Mccn600 compared to reg2Mccn600 (Tables 5.5 and 5.6; Fig. 5.35a,c,e), and the domain maximum hail number and mass formation rates from riming of graupel are larger in the former cases than in the latter case (not shown).

Time-averaged profiles of total hailstone number formation show that rain-pristine ice collisions in reg2Mccn600 generate roughly 3 to 5 orders of magnitude more hailstones than in ccn600 or 2Mccn600 (Fig. 5.36a), and hail number production via rain-snow collisions in both 2Mccn600 and reg2Mccn600 is about 1 to 2 orders of magnitude larger than in ccn600 (Fig. 5.36b). The total amounts of hail mass generated from rain-pristine ice collisions are slightly larger in ccn600 and 2Mccn600 relative to reg2Mccn600 (Fig. 5.37a) as raindrops can individually collect more ice crystals (hence more ice mass) in the F94 collection scheme. Total hail masses resulting from rain-snow interactions are mostly similar among the three simulations (Fig. 5.37b) indicating that the MY05b three-component freezing scheme tends to produce hail rather than rimed snow or graupel from these types of collisions. On the other hand, significantly less hail is generated from rain-aggregate and rain-graupel interactions in ccn600 and 2Mccn600 compared to reg2Mccn600 (Figs. 5.36c,d and 5.37c,d) as the MY05b three-component freezing algorithm employed in the former cases allows for alternative outcomes resulting from these collision types whereas hail always results in the reg2Mccn600 case. Overall, total hail numbers generated by rain-ice collisions are greatest in reg2Mccn600 and least numerous in ccn600 (Fig.

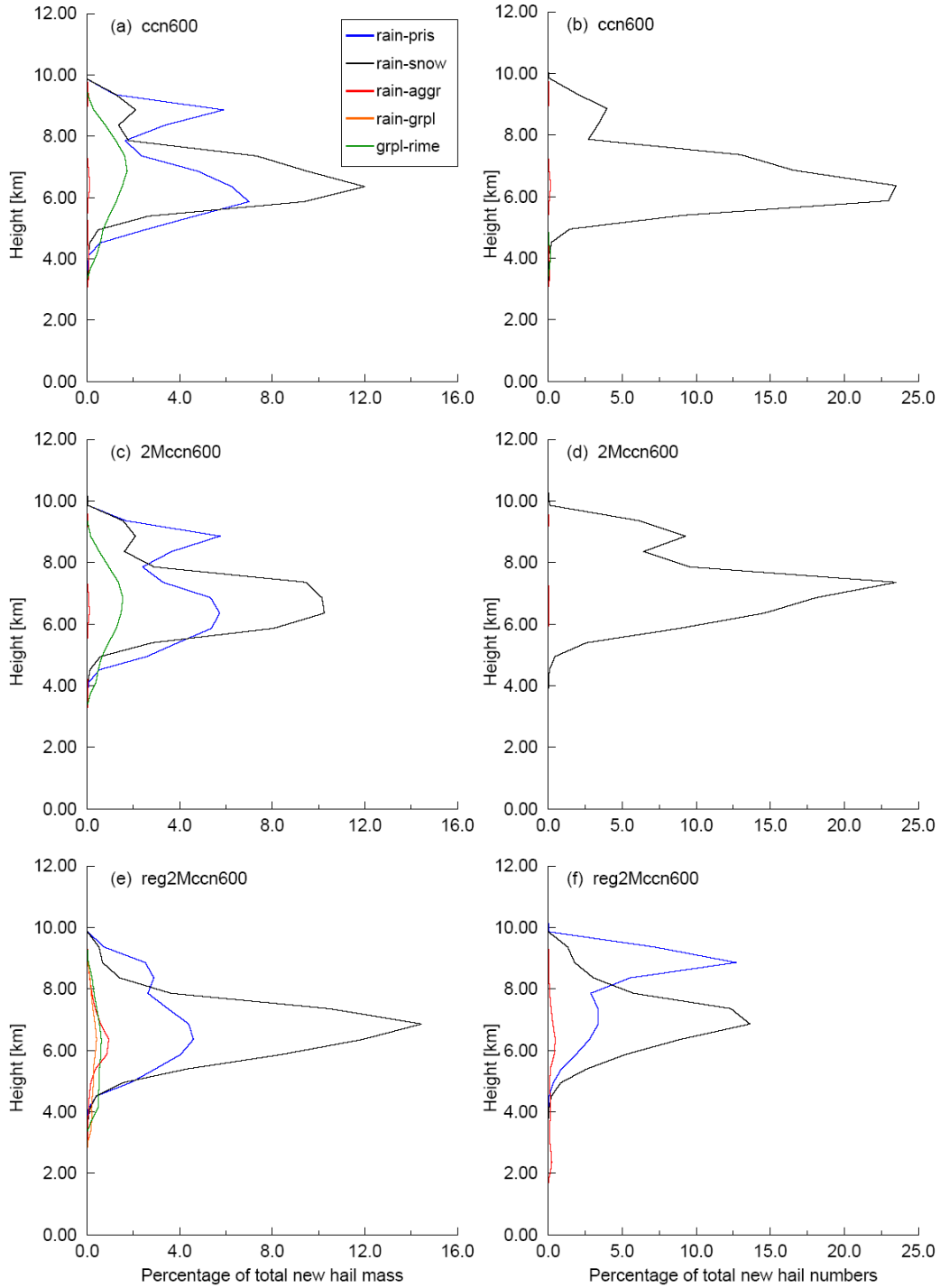


Figure 5.35: Time-averaged percentages of total new hail mass (left column) and numbers (right column) resulting from rain-ice collisions and riming of graupel as a function of height over the entire domain for the simulations listed in Table 5.3. Temporal averaging has a 2 min frequency from $t = 30$ to 210 min.

5.36e), with the 2Mccn600 case in between the other two cases, whereas total amounts of hail mass produced via this mechanism over the depth of the simulated storms are similar in all three

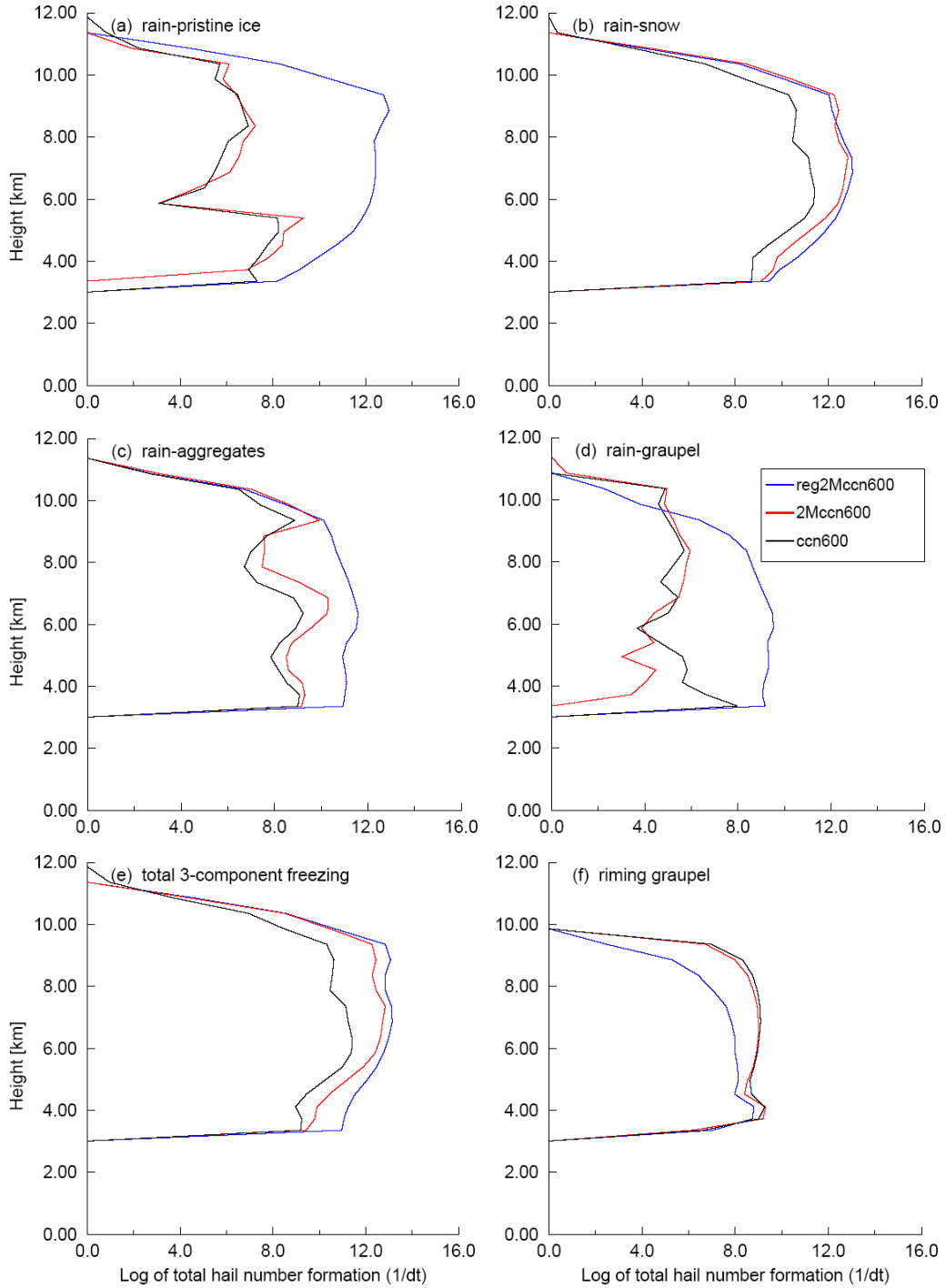


Figure 5.36: Time-averaged vertical profiles of domain total number formation [Δt^{-1}] (on a logarithmic scale) resulting from collisions between (a) rain-pristine ice, (b) rain-snow, (c) rain-aggregates, and (d) rain-graupel, as well as from (e) all three-component freezing and (f) riming of graupel for the three simulations listed in Table 5.3. Time averaging has a 2 minute frequency from $t = 30$ to 210 minutes.

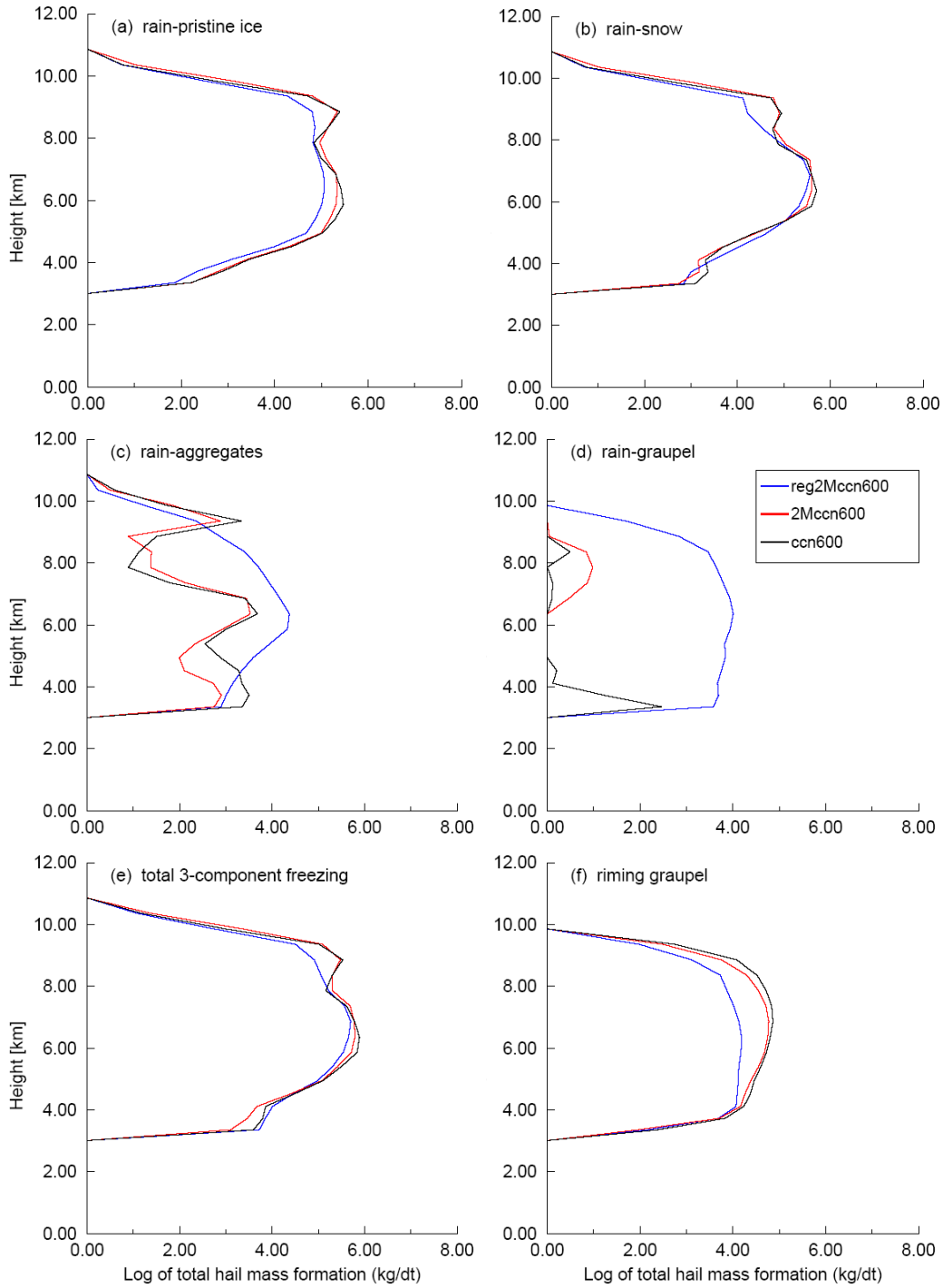


Figure 5.37: As in Figure 5.36 except for domain total mass formation [$\text{kg } \Delta t^{-1}$].

cases (Fig. 5.37e). Correspondingly, the average mean mass diameters of newly formed hail particles from rain-ice collisions are smaller (roughly 1 to 2 mm) in the reg2Mccn600 case and

larger (approximately 1 to 4 mm) in both the 2Mccn600 and ccn600 cases (not shown). The exception is for rain-graupel collisions for which mean mass diameters of new hail particles are considerably larger (about 2 to 8 mm) in the reg2Mccn600 case than in the other cases (about 2 to 4 mm) (not shown). However, as rain-graupel contributions to the net formation of new hail are minor compared to rain-pristine ice and rain-snow collisions, the resulting size distributions of new hail particles in reg2Mccn600 are dominated by the much smaller particles associated with rain-ice and rain-snow interactions. In addition, the greater numbers of small hail particles generated in both 2Mccn600 and reg2Mccn600 in the presence of existing hail cause the higher order moments of the hail distributions to shift towards smaller sizes whereas the higher order moments are largely conserved in ccn600 as demonstrated in Chapter 4.3.2. This ultimately affects the bulk growth characteristics of hail as discussed next.

Time-height contours of spatially averaged hail mass growth rates for the three simulations are displayed in Figures 5.38 and 5.39. It is clearly evident from these figures that hail growth is dominated by riming in all three cases given the similar magnitudes between riming growth (Fig. 5.38b,d,f) and total growth¹ (Fig. 5.38a,c,e), whereas lower growth rates are evident for collection of rain (Fig. 5.39a,c,e) and non-hail ice species (Fig. 5.39b,d,f). Total hail growth in cases ccn600 (Fig. 5.38a) and reg2Mccn600 (Fig. 5.38e) is generally maximized between -10 and -25 °C in agreement with findings by Nelson (1983) and Foote (1984). The same is true for total hail growth in 2Mccn600 prior to about 90 minutes (Fig. 5.38c), though the maximum total hail growth rates shift to a slightly colder temperature range with time in this case. Note that hail growth via collection of all other species occurs below the freezing level in all cases, though when shedding and evaporation/sublimation processes are considered as well, net growth at

¹ Total growth is the sum of all collected mass and net vapor growth minus mass lost due to shedding at each grid point. Net vapor growth is calculated as deposition minus evaporation and sublimation.

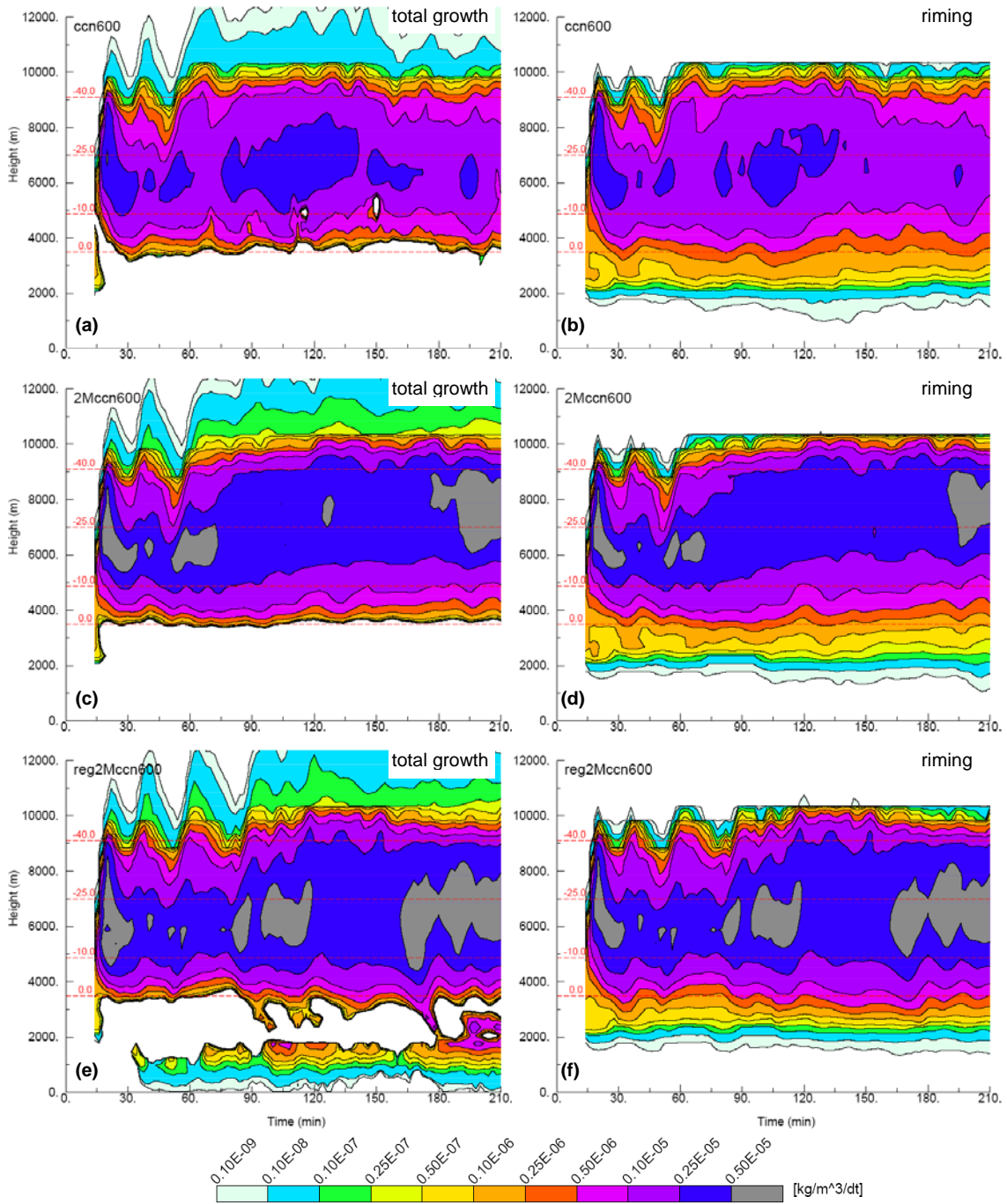


Figure 5.38: Time-height contours of spatially averaged hail mass growth rates [$\text{kg m}^{-3} \Delta t^{-1}$] for total growth (left column) and riming of hail by cloud particles (right column) for (a,b) ccn600, (c,d) 2Mccn600, and (e,f) reg2Mccn600 cases. Red dashed lines depict approximate heights of 0, -10, -25, and -40 °C isotherms.

temperatures greater than 0 °C is zero except in the reg2Mccn600 case (Fig. 5.38e). Average growth rates from net vapor transfers are less than $10^{-9} \text{ kg m}^{-3} \Delta t^{-1}$ in all cases, significantly

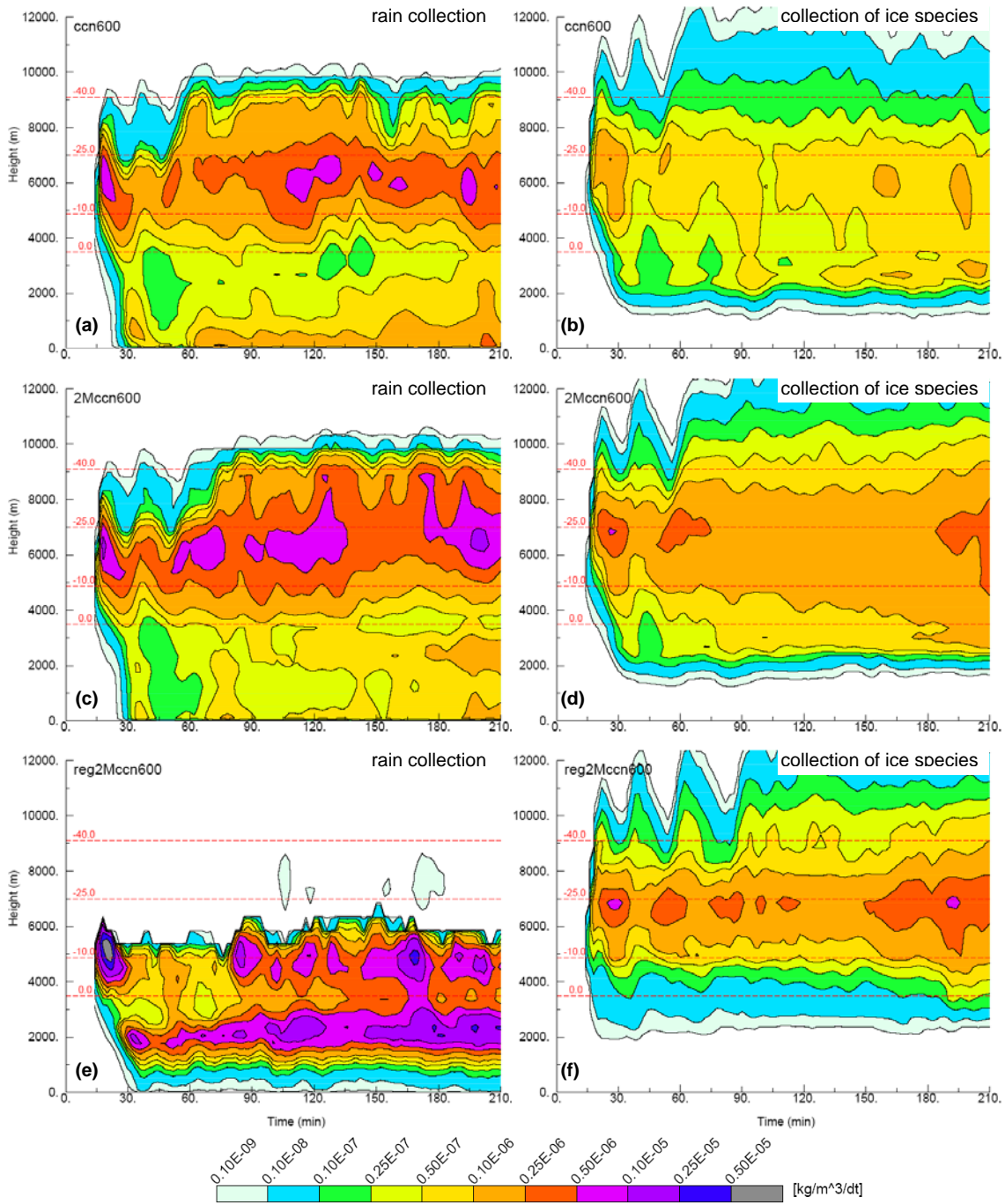


Figure 5.39: As in Figure 5.38 except for hail collecting rain (left column) and hail collecting pristine ice, snow, aggregates, and graupel (right column) for (a,b) ccn600, (c,d) 2Mccn600, and (e,f) reg2Mccn600 cases.

smaller than growth rates by collection in agreement with findings by Iribane and DePena (1962), List (1963), and Heymsfield and Pflaum (1985) and thus are not shown.

Maxima in average growth rates for the various collection processes displayed in Figures 5.38 and 5.39 are smaller in ccn600 compared to the two-moment simulations, however, hail growth in the latter cases occurs over significantly more numerous smaller particles (Fig. 5.40) which present a greater net hail surface area available for collection (Cohen and McCaul 2006). Gilmore et al. (2004) noted a similar increase in growth rates for hail/graupel distributions that contained a much larger fraction of small versus larger particles. In addition, maximum average growth rates aloft from riming and rain collection between approximately 95 and 120 minutes in ccn600 (Figs. 5.38b and 5.39a, respectively) coincide with peak values of N_{2cm} , N_{3cm} , and N_{4cm} during the same time period (Figs. 5.31b and 5.32a,b) and precede the significant precipitation episode of large hail at the surface around 120 minutes (Figs. 5.13b, 5.47 and 5.48). The smaller peak concentrations of large hail seen around 150 and 180 minutes in ccn600 (Figs. 5.31b and 5.32a,b) are better correlated with maxima in rain collection rates (Fig. 5.39a). Similar correlations between local maxima in average riming and rain collection rates and peak magnitudes of N_{1cm} and N_{2cm} are evident for the reg2Mccn600 case (cf. Figs. 5.38f, 5.39f and 5.31e,f) whereas no such correspondence between hail growth rates and hail sizes appear to exist in the 2Mccn600 case.

Hail growth rates due to collection of raindrops are mostly similar between the ccn600 (Fig. 5.39a) and 2Mccn600 (Fig. 5.39c) cases with slightly greater magnitudes in the latter. Peak collection of rain in these two cases occurs around 6 km in accordance with peaks in the time- and spatially averaged rain mass contents located slightly below 6 km (Fig. 5.29c). Greater average growth rates due to rain collection around 5 and 2 km in reg2Mccn600 (Fig. 5.39e) are similarly collocated with peaks in the average rain mass content profile at these heights for this case (Fig. 5.29c). The larger average collection rates of rain at low levels in both ccn600 and

reg2Mccn600 relative to 2Mccn600 result from greater amounts of rain mass produced via shedding in ccn600 (Fig. 5.43b) and melting in reg2Mccn600 (Fig. 5.43e). Collection of rain by hail is insignificant above 6 km in reg2Mccn600 as both hail and rain particles at these heights are very small ($D_{\bar{m}h} < 1$ mm and $D_{\bar{m}r} \leq 0.1$ mm) whereas these particles are generally larger over a deeper portion of the storm in the ccn600 and 2Mccn600 cases. As discussed in Chapter 3.3.1, bulk collection rates for hail collecting other hydrometeors increase as the values of $D_{\bar{m}h}$ and $D_{\bar{m}x}$ increase, all else being equal. Average growth rates for hail via collection of pristine ice, snow, aggregates, and graupel are largest in reg2Mccn600 (Fig. 5.39f) but occur over a greater vertical extent in 2Mccn600 (Fig. 5.39d) most likely due to the greater numbers of larger sized hail particles in this case relative to reg2Mccn600 (Fig. 5.31). In addition, average collection rates of ice particles by hail at temperatures colder than about -30 °C ($z > 7.6$ km) are larger in the two-moment simulations owing to the greater numbers of hail particles at these heights in these cases relative to ccn600 (Figs. 5.30h, 5.40).

Examples of the spatial patterns of hail growth in relation to the spatial distributions of hail and storm-relative flow fields at 116 minutes are shown in Figure 5.40 for the three simulations. Maximum hail growth rates occur within the updrafts in all cases, as expected, with lower growth rates in regions of downward flow to the east of the updrafts. However, only the ccn600 case (Fig. 5.40a) exhibits the juxtaposition of regions of large hail within regions of significant growth along the updraft periphery at this time in agreement with previous observational studies of large hail in supercells (Browning and Foote 1976; Orville 1977; Rasmussen and Heymsfield 1987c). In addition, large hail is partially contained within a region a wet growth² along the updraft edge in this case whereas hail particles undergoing wet growth are generally smaller than

² Wet growth herein refers to grid points for which air temperatures are -1 °C or colder, hail growth rates are equal to or greater than 10^{-6} kg m⁻³ Δt⁻¹ and bulk hail liquid water fractions exceed 0.01.

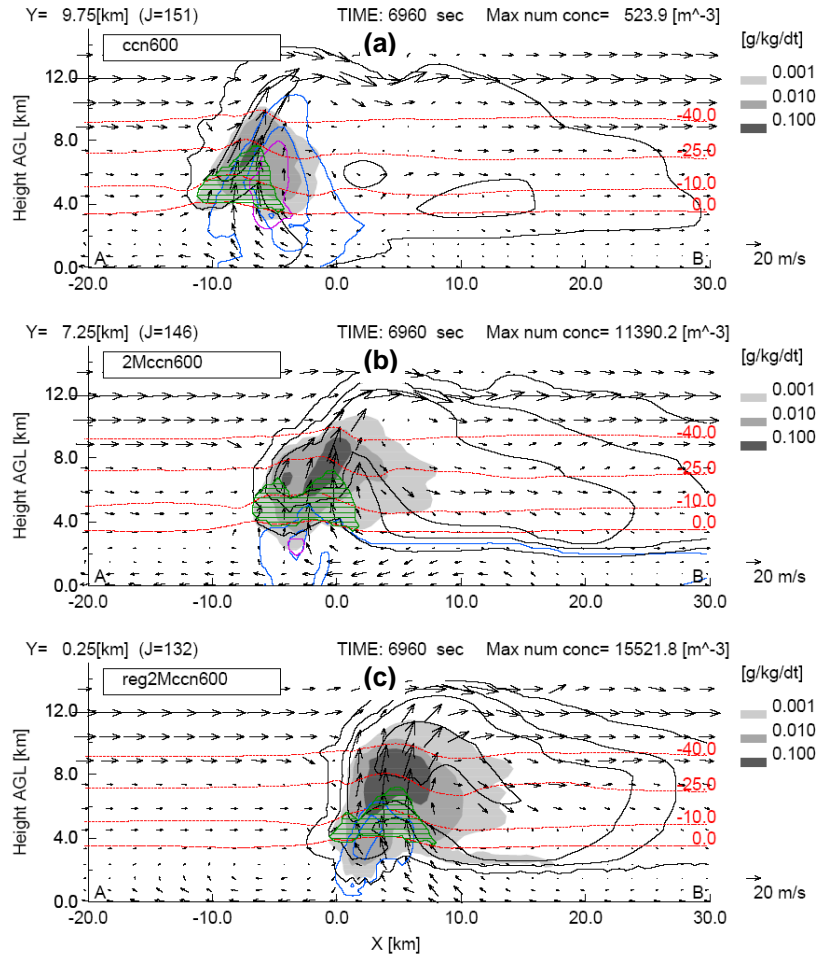


Figure 5.40: East-west cross sections along line AB in Figures 5.24-5.26 at 116 minutes showing hail total growth rates (shaded; 0.001, 0.01, 0.1 $\text{g kg}^{-1} \Delta t^{-1}$), hail number concentration contours [black; 1, 10^2 , 10^3 , 10^4 m^{-3}], and contours of $N_{2\text{cm}}$ (blue) and $N_{4\text{cm}}$ (purple) [10^{-4} , 0.01 m^{-3}] for cases (a) ccn600 and (b) 2Mccn600, whereas blue contours are $N_{1\text{cm}}$ [10^{-4} , 0.01 m^{-3}] for (c) reg2Mccn600. Storm-relative wind vectors are overlaid in each panel, the red dashed lines denote the 0, -10, -25 and -45 $^{\circ}\text{C}$ isotherms, and green hatched areas depict wet hail growth regions.

2 cm in diameter and located within the low-level updraft core in cases 2Mccn600 (Fig. 5.40b) and reg2Mccn600 (Fig. 5.40c). The vertical extent over which wet growth occurs is also greater in the ccn600 case (up to about the -25 $^{\circ}\text{C}$ level) compared to the two-moment cases. Bailey and Macklin (1968) and Rasmussen and Heymsfield (1987c) showed that wet growth at colder temperatures is more likely as liquid water contents and hail sizes increase, both of which are evident in the ccn600 case relative to the two-moment simulations (Figs. 5.29i and 5.40).

The impacts of hail formation and subsequent growth of hail on the heating profiles within the simulated storms are difficult to quantify given that changes in air temperature due to freezing of liquid water are implicitly computed based on net changes in hydrometeor internal energy values as a result of the combined processes of collection, melting, and sedimentation (Tripoli and Cotton 1981; Walko et al. 2000). However, as latent heat released during the freezing of supercooled liquid is proportional to the amount of liquid mass frozen (Cotton and Anthes 1989) and tends to dominate over condensational heating at mid and upper levels in deep convective updrafts (Zeigler 1988; GSR04; Cohen and McCaul 2006), some general relationships between hail processes and heating aloft may be inferred. It is recognized that temperature advection and turbulent mixing also affect heating profiles within updrafts, though no attempt is made here to relate differences in these processes with differences in heating aloft.

Figure 5.41 shows time-height plots of domain maximum potential temperature perturbations (θ'_{max}) along with domain maximum freezing rates of liquid water ($L_{frz,max}$) associated with both the generation of hail and subsequent accretional growth via riming and collection of raindrops for the three simulations. Time series of the maximum θ'_{max} and $L_{frz,max}$ values below 12 km for these simulations are displayed in Figure 5.42. It is evident that the spatiotemporal patterns of θ'_{max} mostly follow those of $L_{frz,max}$ in the two-moment cases (Figs. 5.41c,e and 5.41d,f), and peak θ'_{max} values seem to occur in conjunction with peak $L_{frz,max}$ rates, albeit at slightly higher altitudes (~ 8 km for θ'_{max} versus ~ 7 to 7.5 km for $L_{frz,max}$). The patterns of θ'_{max} and $L_{frz,max}$ in the ccn600 case show a fairly good match prior to about 150 minutes (Fig. 5.41a,b), but are less consistent at later times as evident by the low correlation coefficient between the maximum θ'_{max} and $L_{frz,max}$ values beyond 150 minutes (Fig. 5.42a). The correlations between maximum θ'_{max} and $L_{frz,max}$ values are much better in both of the two-moment case over the duration of the

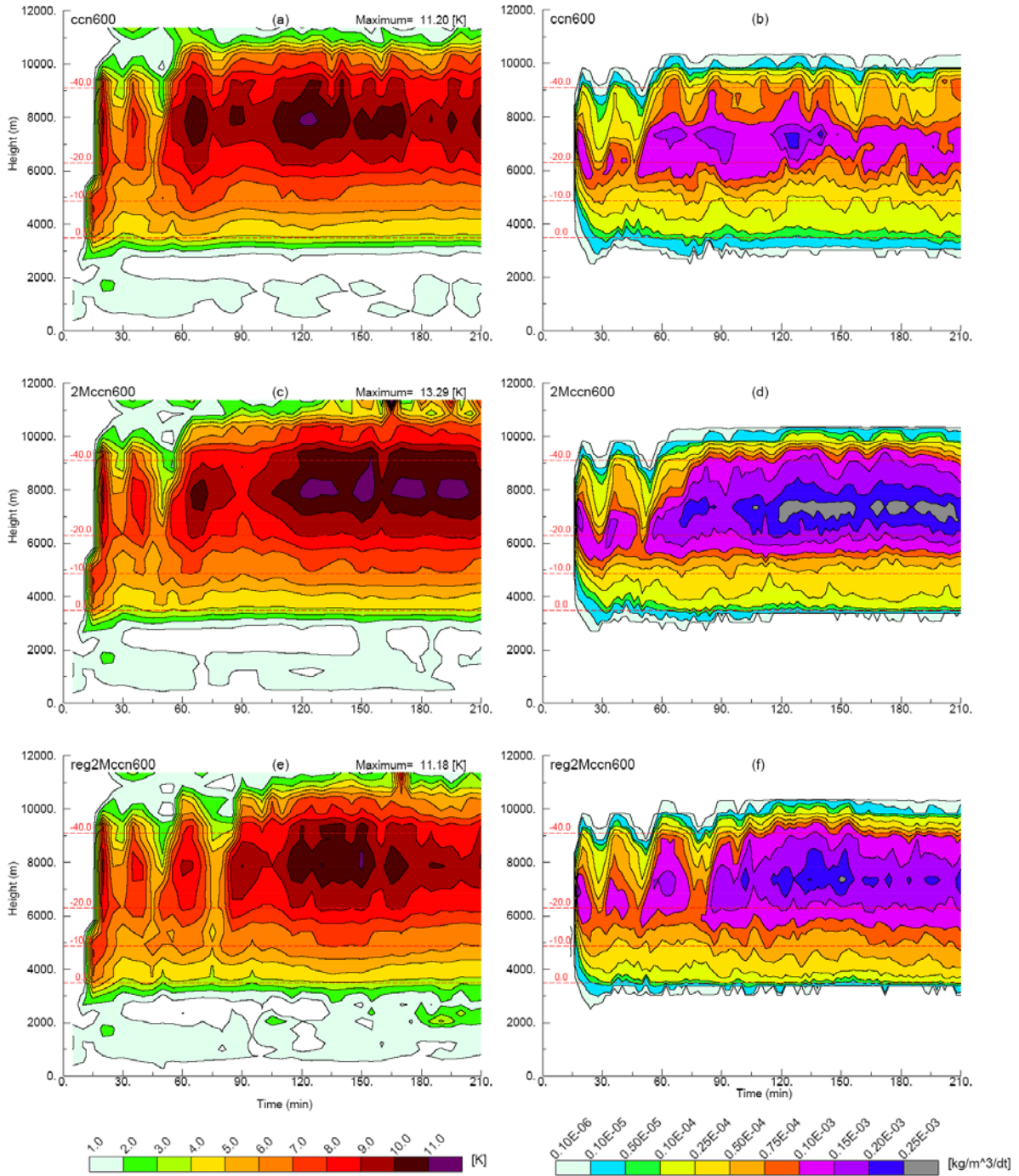


Figure 5.41: Time-height contours of maximum θ' [K] (left column) for cases (a) ccn600, (c) 2Mccn600, and (e) reg2Mccn600, and (right column) time-height contours of maximum liquid freezing rate [kg m⁻³ Δt⁻¹] within updraft ($w \geq 5$ m s⁻¹) associated with hail formation and growth (excluding wet growth regions) for cases (b) ccn600, (d) 2Mccn600, and (f) reg2Mccn600.

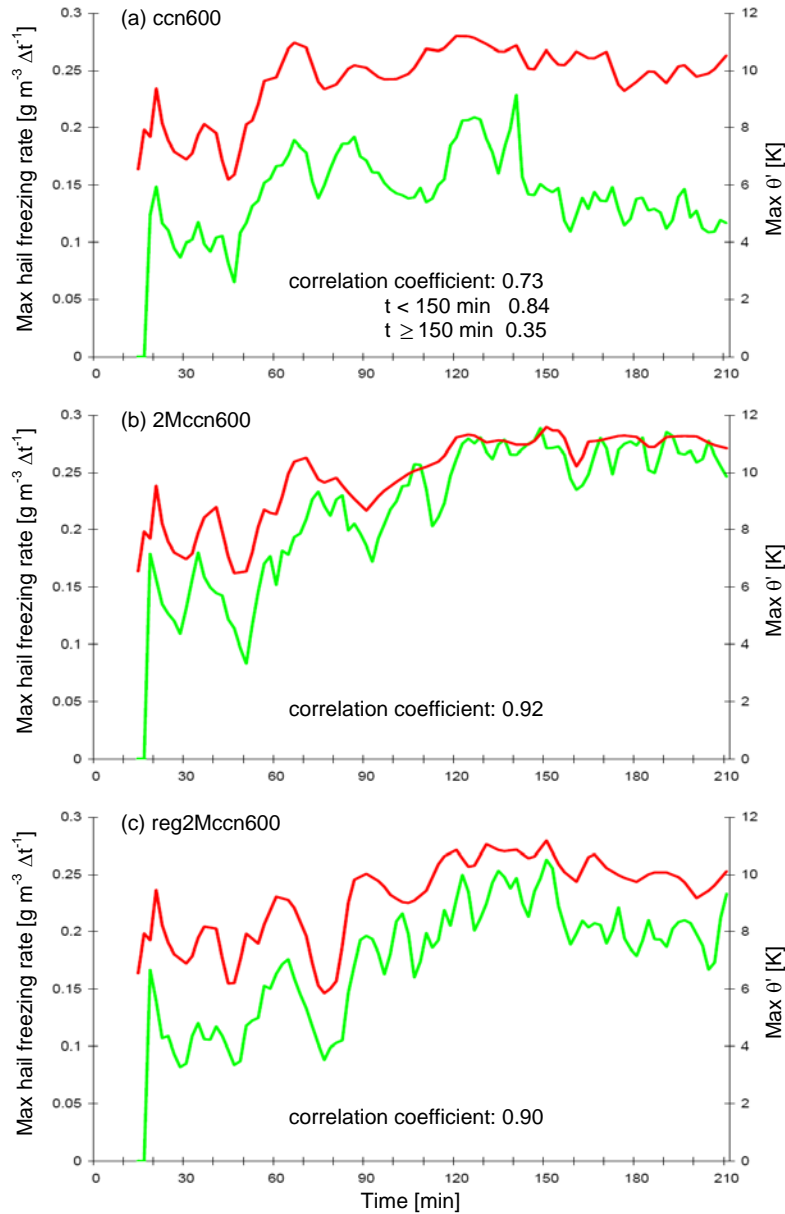


Figure 5.42: Time series of domain maximum freezing rates of liquid water ($L_{frz,max}$, green lines) [$\text{g m}^{-3} \Delta t^{-1}$] and potential temperature perturbation (θ' , red lines) [K] for simulations (a) ccn600, (b) 2Mccn600, and (c) reg2Mccn600. Correlation coefficients for the time series are given for each case, and additional correlation coefficients in (a) are computed for the stated time periods.

simulations (Fig. 5.42b,c). The 2Mccn600 case exhibits the greatest θ'_{max} and $L_{frz,max}$ values (Fig. 5.41c,d), and the θ'_{max} values are generally larger in ccn600 (Fig. 5.41a) relative to reg2Mccn600 (Fig. 5.41e) even though the $L_{frz,max}$ rates tend to be smaller in the former case (Fig. 5.41b) compared to the latter (Fig. 5.41f). Given that cloud water, aggregates and graupel exist in much

greater amounts in ccn600 and 2Mccn600 compared to reg2Mccn600 above 6 km (Figs. 5.29a,f,h and 5.30a,f,h), it is likely that accretional growth of these particles is greater and therefore contributes more to heating aloft in the former relative to the latter as was noted in the sensitivity study of Cohen and McCaul (2006). As accretional growth tends to dominate $L_{frz,max}$, the growth rates associated with the fewer but larger hailstones at mid-and upper levels in ccn600 seem to have less of an impact on heating than the more numerous smaller hail particles in the two-moment cases, which qualitatively agrees with the results of List et al. (1968) and GSR04.

The effects of hail size on the melting process are clearly demonstrated in time-height plots of spatially averaged rates of complete melting (referred to in this discussion simply as melting) and shedding from hail for the three simulations (Fig. 5.43). Melting rates at air temperatures above freezing are inversely proportional to the amount of large hail present and thus are smallest in ccn600 (Fig. 5.43a) and largest in reg2Mccn600 (Fig. 5.43e) in general agreement with the findings of GSR04, VC04, and Cohen and McCaul (2006), with melting rates for the 2Mccn600 case (Fig. 5.43c) in between the other two cases. The more numerous small hailstones that exist at low levels in the two-moment cases, particularly in reg2Mccn600, have a larger surface to volume ratio and experience larger heat transfer rates than the fewer but larger hailstones in the ccn600 case (Pruppacher and Klett 1980; Rasmussen and Heymsfield 1984). The dependence of shedding rates on hail size below the freezing level exhibits an opposite trend, with the largest rates observed for the ccn600 case (Fig. 5.43b) and the smallest rates in the reg2Mccn600 case (Fig. 5.43f) owing to the larger hailstone sizes in the former compared to the latter. These results concur with laboratory and modeling results of Rasmussen and Heymsfield (1984) and RH87b, who found that, under similar environmental conditions, larger

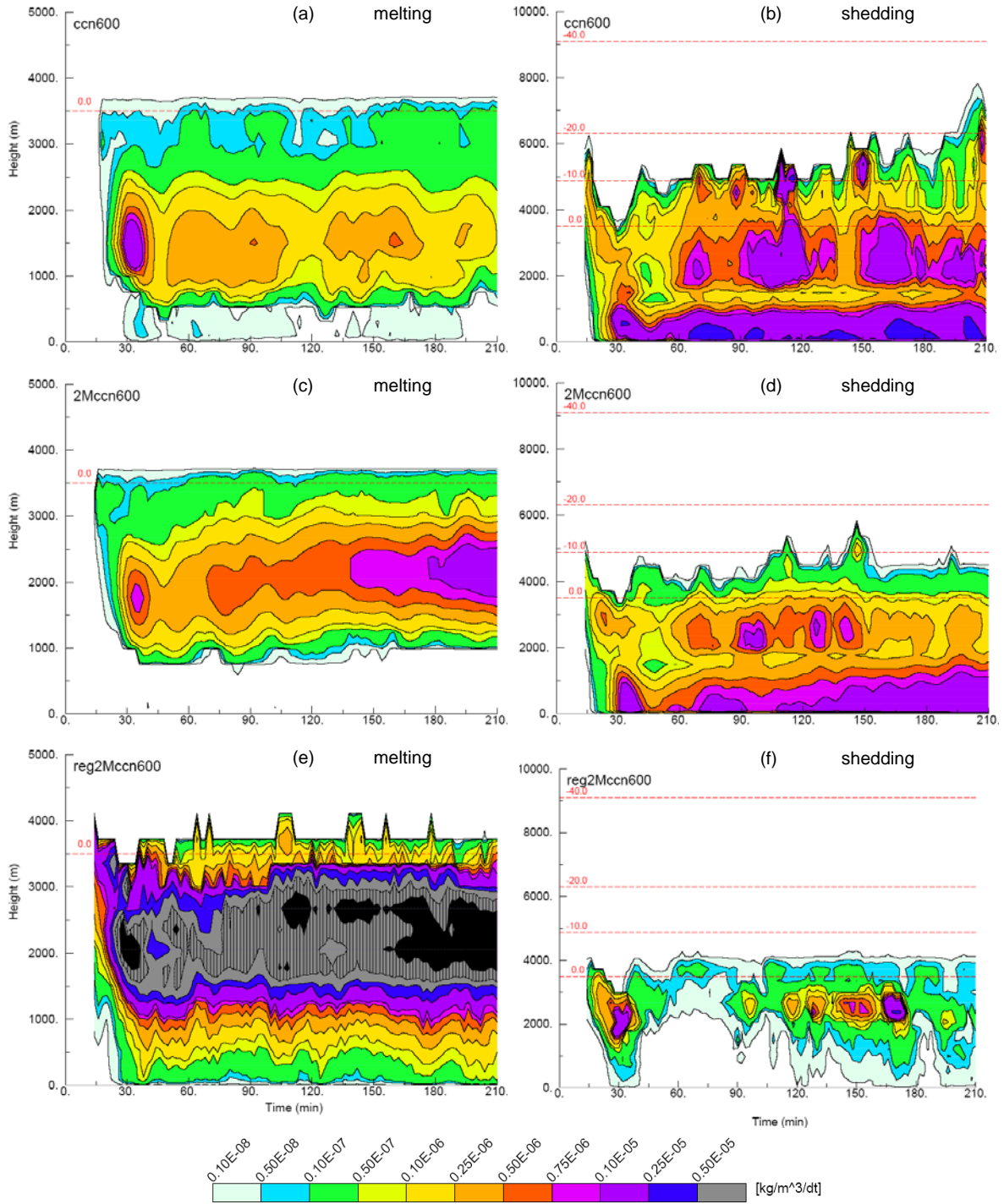


Figure 5.43: Time-height contours of spatially averaged rates [$\text{kg m}^{-3} \Delta t^{-1}$] of complete melting (left column) and shedding rates (right column) for hail for cases (a,d) ccn600, (b,e) 2Mccn600, and (c,f) reg2Mccn600. In panel (c), additional contours are drawn for complete melting rates of 10^{-5} and $2 \times 10^{-5} \text{ kg m}^{-3} \Delta t^{-1}$ (hatched and black regions, respectively). Different vertical scales are used for melting and shedding.

hailstones shed more mass per unit time versus smaller hailstones. Furthermore, the vast majority of hailstones in reg2Mccn600 are smaller than 1 cm, therefore the magnitudes of average shedding rates (Fig. 5.43f) are significantly smaller than those for melting (Fig. 5.43e) given that the minimum diameter threshold for shedding is about 9 mm (Rasmussen and Heymsfield 1984). The opposite is evident for the ccn600 case in which the average rates of shedding (Fig. 5.43b) are mostly larger than for melting (Fig. 5.43a) owing to the dominance of larger hailstones at low levels in this case. The 2Mccn600 case exhibits similar magnitudes for average melting (Fig. 5.43c) and shedding (Fig. 5.43d) rates below the freezing level due to fewer numbers, and hence less mass, of large (small) hailstones relative to the ccn600 (reg2Mccn600). Also of note is that the period of intense hailfall around 120 minutes in the ccn600 case (i.e., Figs. 5.13b and 5.32b,c) is characterized by a decrease in melting and an increase in shedding, both of which are indicative of larger hailstones.

The vertical distributions of average melting and shedding rates below the freezing level reflect the dependence of these rates on hail size, relative humidity and temperature. A comparison of average melting rates (Fig. 5.43) reveals the layer over which melting occurs shifts to increasingly lower altitudes as hail sizes increase (i.e., going from reg2Mccn600 to 2Mccn600 to ccn600) due to the fact that larger hailstones can fall a greater distance before completely melting whereas smaller hailstones melt quickly upon falling into air temperatures above 0 °C. A similar dependence of the melting layer height on mean hail size was reported by GSR04. Melting is seen to extend to much lower altitudes in the reg2Mccn600 case (Fig. 5.43e) in association with locally higher relative humidity values as a result of increased evaporation of the greater amounts of rain mass at these levels compared to the other two cases (Fig. 5.29c). The vertical distributions of average shedding rates are quite different from those for melting, with

two distinct regions of shedding evident in the ccn600 (Fig. 5.43b) and 2Mccn600 (Fig. 5.43d) cases. The first region extends from roughly 2 to 4 km and is associated with collection of liquid water (primarily cloud droplets as the cloud bases are around 2 km), which is shed on subsequent time steps as the melting hailstones can not retain any additional water on their surfaces (RH87b). The second shedding region resides mostly in the lowest kilometer and is due primarily to greatly increased heat transfer to the large hailstones as they fall into much warmer air temperatures, with additional collection of raindrops playing a minor role as well. In contrast, shedding in the reg2Mccn600 case (Fig. 5.43f) is mainly confined to levels between about 2 and 4 km primarily due to the fact that most of the melting hailstones are smaller than the shedding threshold diameter (~ 9 mm) at levels below 2 km. Shedding of liquid drops at subfreezing temperatures corresponds to hail undergoing wet growth (e.g., Fig. 5.40) and is most significant in the ccn600 case (Fig. 5.43b) as previously discussed.

A comparison of the time series of total amounts of rain mass formed from melting and shedding hail with those resulting from cloud droplet collisions and melting of graupel reveals that hail is the primary producer of rain in these simulations (Fig. 5.44). This agrees with findings of RH87b and List (2010) which suggest that melting and shedding hail contributes significantly to rainfall in mid-latitude deep convection. Hjelmfelt et al. (1989) and Straka and Anderson (1993) also noted that primary rain sources were from melting of hail/graupel in simulations of microburst-producing storms. (It should be noted that melting of pristine ice, snow, and aggregates do not contribute to the formation of rain in the model and are instead transferred to the cloud and graupel categories, respectively.) Shedding of liquid water by hail within the lowest kilometer or so is the dominant rain formation mechanism in the ccn600 and 2Mccn600 cases (Figs. 5.44a and 5.44b, respectively), both of which have large hail particles at

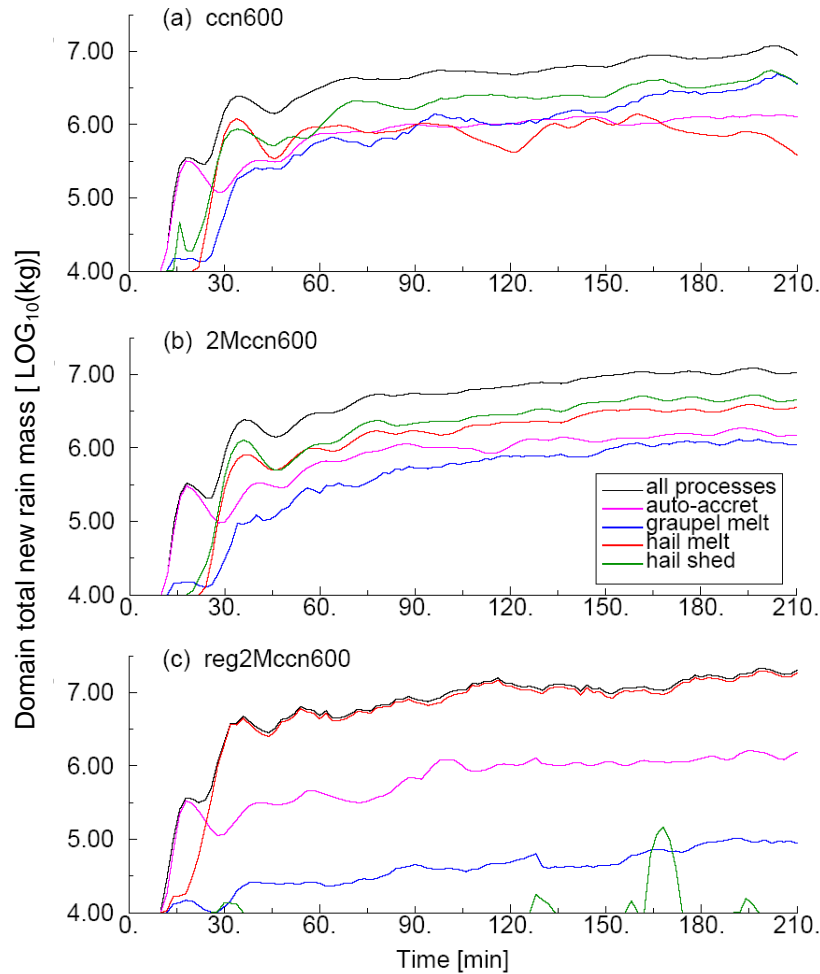


Figure 5.44: Time series of domain total rain mass formation from auto accretion (purple), graupel melt (blue), hail melt (red), shed drops from hail (green) and these processes combined (black) for cases (a) ccn600, (b) 2Mccn600, and (c) reg2Mccn600.

low levels, whereas complete melting of hail between roughly 1 to 3 km AGL dominates total rain production in the reg2Mccn600 case (Fig. 5.44c). Owing to the small hail sizes in reg2Mccn600, shed drops from hail account for less than 0.1% of total new rain mass on average and thus have a negligible impact on total rainfall in this case. Rain formation via cloud droplet collisions is generally similar between the three simulations, and melted graupel appears to contribute the least to total rain mass in the two-moment cases (not considering shed drops in reg2Mccn600). In contrast, melted graupel is initially the smallest contributor to rain production

in the ccn600 case but becomes greater than contributions from melting of hail and cloud droplet collisions following the right turn of the storm ($t > 90$ min) (Fig. 5.44a). *Thus, it is evident that the different methods of representing hail processes in the model affect not only the evolution of hail, but can have a significant impact on the evolution of rain as well.*

5.4.3.2) Surface precipitation and cold-pool evolution

The surface precipitation characteristics and low-level thermodynamic properties of the modeled storms are also affected by the diverse approaches to modeling hail in the simulations. The types and amounts of precipitation arriving at the surface, the amount of cooling at low levels, and the development and evolution of the cold-pool are all strongly influenced by differences in the various hail processes discussed in the previous analyses.

Time series of domain maximum surface precipitation rates for rain ($R_{r,max}$) and hail ($R_{h,max}$) reveal that the highest $R_{r,max}$ values tend to be produced in the reg2Mccn600 case (Fig. 5.45a) whereas the greatest $R_{h,max}$ magnitudes are generated by the ccn600 case (Fig. 5.45b). This result is not surprising given that nearly all of the hail melts to rain prior to reaching the surface in reg2Mccn600 whereas the larger hailstones in the ccn600 case experience much less melting while falling to the surface (Fig. 5.43). The 2Mccn600 case exhibits the smallest $R_{r,max}$ values due in part to the greater areal extent over which hail falls and subsequently melts and sheds in this simulation compared to ccn600 and reg2Mccn600 (Figs. 5.13 and 5.14). Peak $R_{h,max}$ values in 2Mccn600 occur prior to the storm's right turn (~ 90 min) after which time the $R_{h,max}$ magnitudes remain fairly steady whereas peak hailfall in ccn600 occurs after the storm turns right (Fig. 5.45b). Peak $R_{h,max}$ values between 100 to 200 mm hr⁻¹ (liquid equivalent) in the ccn600 case are much larger than those reported by MY06a (~ 50 to 90 mm/hr) for simulations

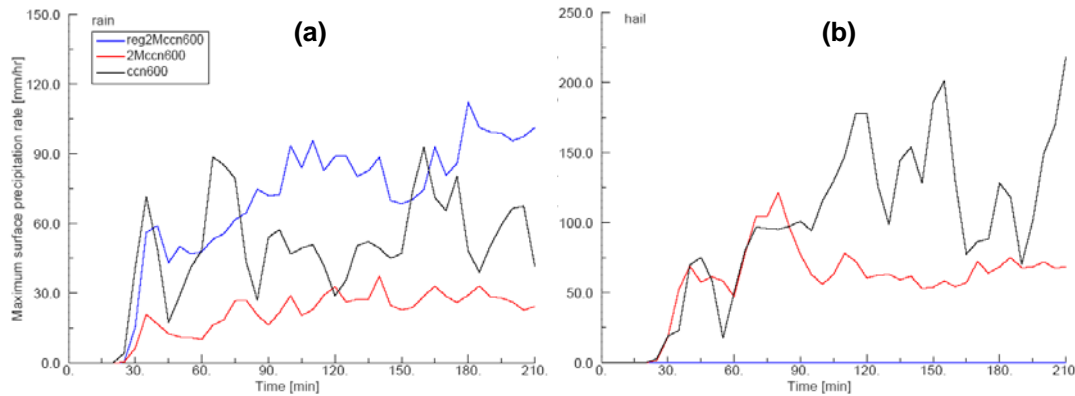


Figure 5.45: Time series of (a) rain maximum surface precipitation rates [mm hr^{-1}] and (b) hail maximum surface precipitation rates [mm hr^{-1} ; liquid equivalent] for the simulations listed in Table 5.3.

of a severe hailstorm in Alberta using triple-moment bulk microphysics. Such large $R_{h,max}$ magnitudes are not unrealistic (computed $R_{h,max}$ values $> 150 \text{ mm hr}^{-1}$ were reported by Federer and Waldvogel 1975) and can be attributed to the fact that much more large hail reaches the surface in ccn600 than in the simulation of MY06a.

The surface distributions of accumulated amounts of hail and rain at the end of the simulation period ($t = 210 \text{ min}$) are displayed in Figure 5.46 for the three experiments. Similar to results for the maximum hail surface precipitation rates, the greatest amounts of accumulated hail at a given surface point are seen in the ccn600 case, with smaller amounts evident for the 2Mccn600 case and negligible hail accumulations in the reg2Mccn600 case. The trend of increased hail accumulations at a surface point with increasing hail size evident in Figure 5.46 (i.e., going from reg2Mccn600 to 2Mccn600 to ccn600) was also observed in the supercell simulations of GSR04 and VC04. Accumulated rain values are greatest in reg2Mccn600 (Fig. 5.46c; Table 5.7) owing to the melting of nearly all hail prior to reaching the surface in this case. This is somewhat contrary to results from GSR04, who found a general increase in accumulated rainfall as hail sizes increased, although rain accumulations in ccn600 are greater than in 2Mccn600 (Fig. 5.46a,b; Table 5.7) due to the greater amounts of liquid water shed from the more numerous

Table 5.7: Total accumulated precipitation mass, maximum accumulated total precipitation (liquid equivalent) at a point, total accumulated hail and rain masses, and percentages of total mass that is hail and rain at the surface at the end of each simulation ($t = 210$ minutes) for the experiments listed in Table 5.3. Total masses are in teragrams [Tg] (trillions of grams) and maximum total precipitation at a point is in mm.

Case	Total [Tg]	Max total [mm]	Total hail [Tg]	Percent hail	Total rain [Tg]	Percent rain
ccn600	19.70	47.63	8.23	41.79	11.46	58.21
2Mccn600	21.40	28.31	12.39	57.92	9.00	42.08
reg2Mccn600	17.87	21.35	0.0013	0.0075	17.87	99.9925

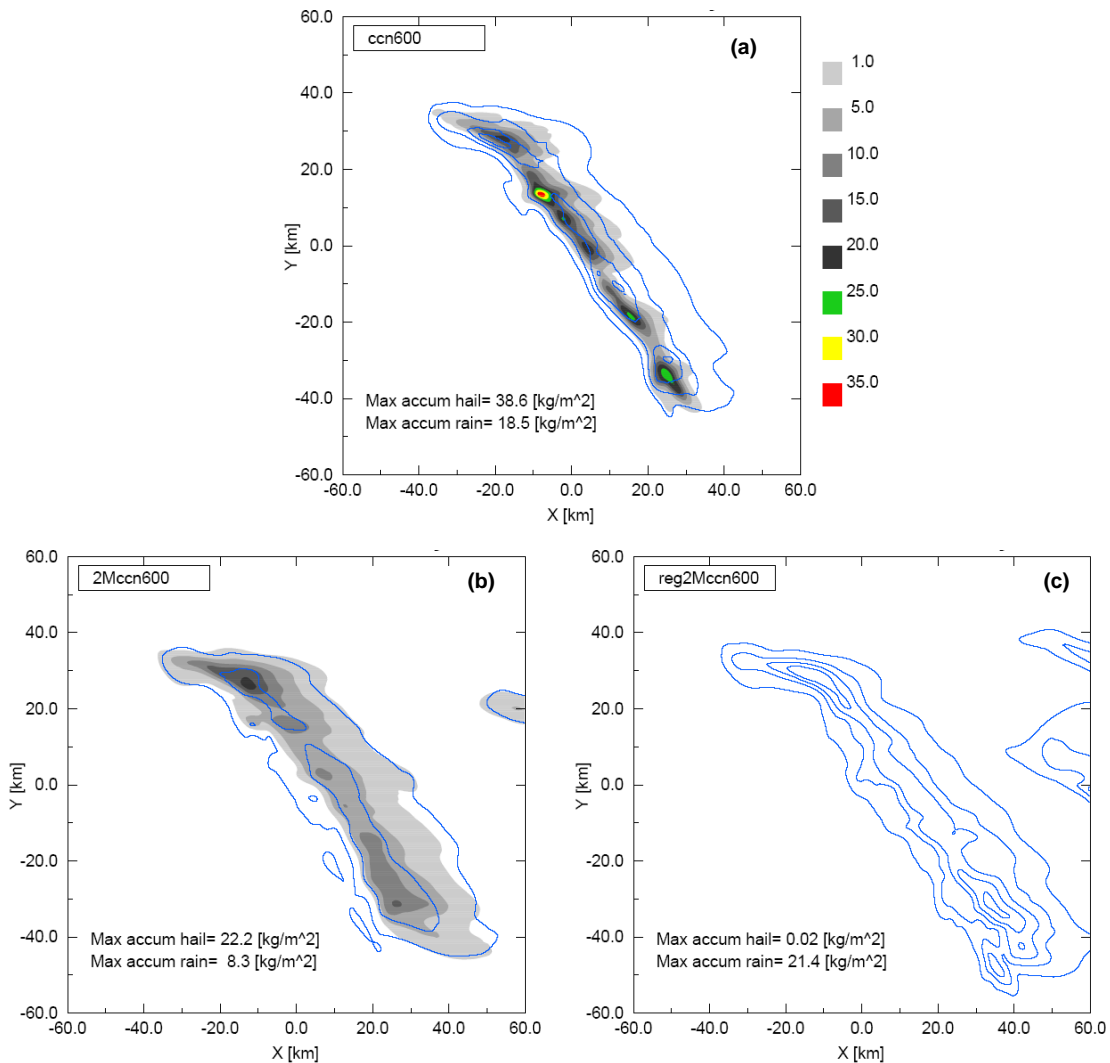


Figure 5.46: Surface accumulated amounts [kg m^{-2}] of hail (shaded contours) and rain (blue contours) at end of simulation (210 minutes) for (a) ccn600, (b) 2Mccn600, and (c) reg2Mccn600 cases. Contour values are 1, 5, 10, 15, 20, 25, 30, and 35 kg m^{-2} .

large hailstones in the former versus the latter (Fig. 5.43). In addition, the horizontal extent of rainfall is larger in the cases with smaller hailstones (2Mccn600 and reg2Mccn600) compared to the ccn600 case (Fig. 5.46). GSR04 and VC04 noted rainfall over larger horizontal areas for hail distributions weighted towards smaller sizes as well due to the fact that smaller hail particles aloft are transported further away from the storm core via horizontal advection before falling into warmer temperatures and melting to form rain. Maximum accumulated precipitation values at a point increase as hail sizes increase in agreement with the findings of VC04, and increases in total accumulated precipitation amounts also generally occur in conjunction with increasing hail sizes as reported by GSR04 (Table 5.7). Total accumulated precipitation and hail mass values at the surface are actually largest in 2Mccn600 (Table 5.7), although the precipitation is spread out over a much larger area in this case relative to ccn600 (Fig. 5.46), and thus the maximum accumulated amounts of precipitation and hail at a point are less in 2Mccn600 relative to ccn600. Lastly, the spatial distributions of surface hail accumulations for the ccn600 case (Fig. 5.46a) reveal localized intense hailfalls within the hail swath that are somewhat consistent with hailstreaks reported in observations (Ludlam and Macklin 1959; Chagnon 1970, 1973; Marwitz 1972b; Parker et al. 2005). Such features are much less distinguishable in the hailswath of the 2Mccn600 case (Fig. 5.46b), which exhibits far less variability in hailfall intensities than in the ccn600 case (Figs. 5.45b and 5.47).

Time-dependent maximum number concentrations at the surface for hail diameters of at least 1, 2, 3, and 4 cm (N_{1cm} , N_{2cm} , N_{3cm} , and N_{4cm}) are displayed in Figure 5.47 for the three simulations. It is clearly evident from this figure that the ccn600 case produces the largest values of maximum N_{1cm} , N_{2cm} , N_{3cm} , and N_{4cm} during the simulated time period compared to the other two cases, with virtually no hail larger than 1 cm evident at the surface in the reg2Mccn600 case.

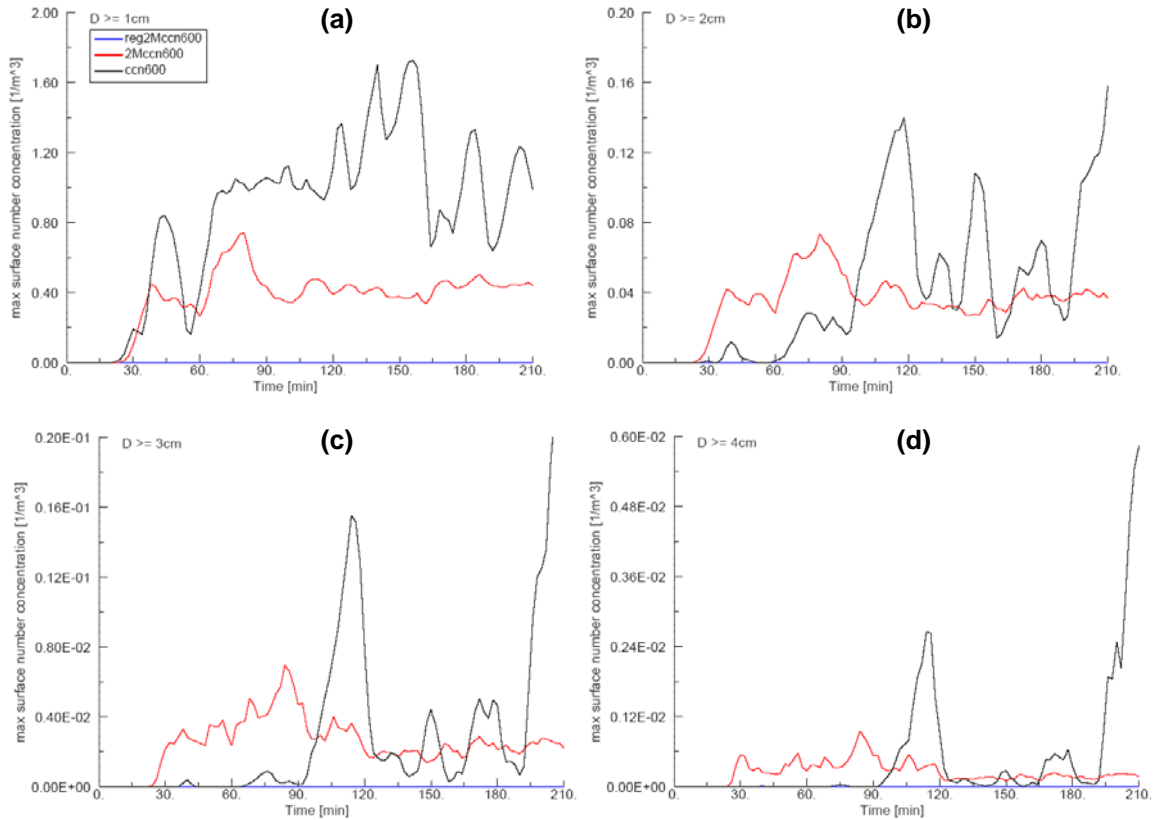


Figure 5.47: Time series of maximum hail number concentrations [m^{-3}] at the surface associated with hailstones having diameters of at least (a) 1 cm, (b) 2 cm, (c) 3 cm and (d) 4 cm for the simulations listed in Table 5.3.

The largest peaks in the time series of maximum N_{2cm} , N_{3cm} , and N_{4cm} for the ccn600 case around 120 minutes denote the occurrence of the most intense hailfall episode, and the smaller peaks evident around 150 and 180 minutes for this case are also associated with significant hailfall events as mentioned in previous analyses. Maximum N_{1cm} , N_{2cm} , N_{3cm} , and N_{4cm} values at the surface for the 2Mccn600 case peak prior to the storm's right turn and remain fairly constant thereafter similar to the time series of $R_{h,max}$ for this case. The approximate ranges of surface maximum N_{1cm} (0.2 to 1.8 m^{-3}), N_{2cm} (0.02 to 0.14 m^{-3}), N_{3cm} (10^{-3} to 0.015 m^{-3}) and N_{4cm} (5×10^{-4} to $2.8 \times 10^{-3} \text{ m}^{-3}$) in the ccn600 case agree well with inferred and computed number concentrations for similarly observed hail sizes at the ground for mid-latitude hailstorms (Ludlam and Macklin 1959; Auer 1972; Hubbert et al. 1998). Smaller yet still reasonable ranges for surface maximum

N_{1cm} , N_{2cm} , N_{3cm} , and N_{4cm} are seen for the 2Mccn600 case, though again, the larger hail sizes in this case are erroneous as evident by the relatively significant concentrations of 3 and 4 cm diameter hail that appear much earlier (around 30 min) in the simulation compared to the ccn600 case.

The low-level cold-pool stems from the conveyance of colder air to the surface by the convective downdrafts, and cooling within these downdrafts results primarily from evaporation of liquid water, melting of ice, and sublimation of ice (Srivastava 1987; Hjelmfelt et al. 1989; Knupp 1988, 1989; Orville et al. 1989; Proctor 1989; Straka and Anderson 1993). The cold-pools at the surface in the simulations are defined by the area enclosed by the -1 K potential temperature perturbation (θ') contour. Time series of surface cold-pool area, minimum θ' (θ'_{min}), average θ' (θ'_{mean}), and maximum downdraft speeds over the lowest 2 km are shown in Figure 5.48 for the three simulations, and the spatiotemporal evolutions of the cold-pools are depicted in Figures 5.49-5.51. Near-surface computed equivalent reflectivity (Z_e) contours of 20, 40 and 60 dBZ are also overlaid in Figures 5.49-5.51 to provide a link between the cold-pool and the precipitation structures of the storms.

The cold-pools in all cases first develop around 30 minutes and steadily increase in size with time (Fig. 5.48a). The cold-pool is largest in the reg2Mccn600 case at all times, whereas the ccn600 and 2Mccn600 cases exhibit similar cold-pool sizes through about 105 minutes after which time the cold-pool in the 2Mccn600 case becomes larger than that in the ccn600 case (Figs. 5.48a, 5.50 and 5.51). The larger cold-pools in the two-moment cases can be partially attributed to the development of secondary convective cells along the leading edge of the outflow beyond 120 minutes in these cases (Fig. 5.50d,f).

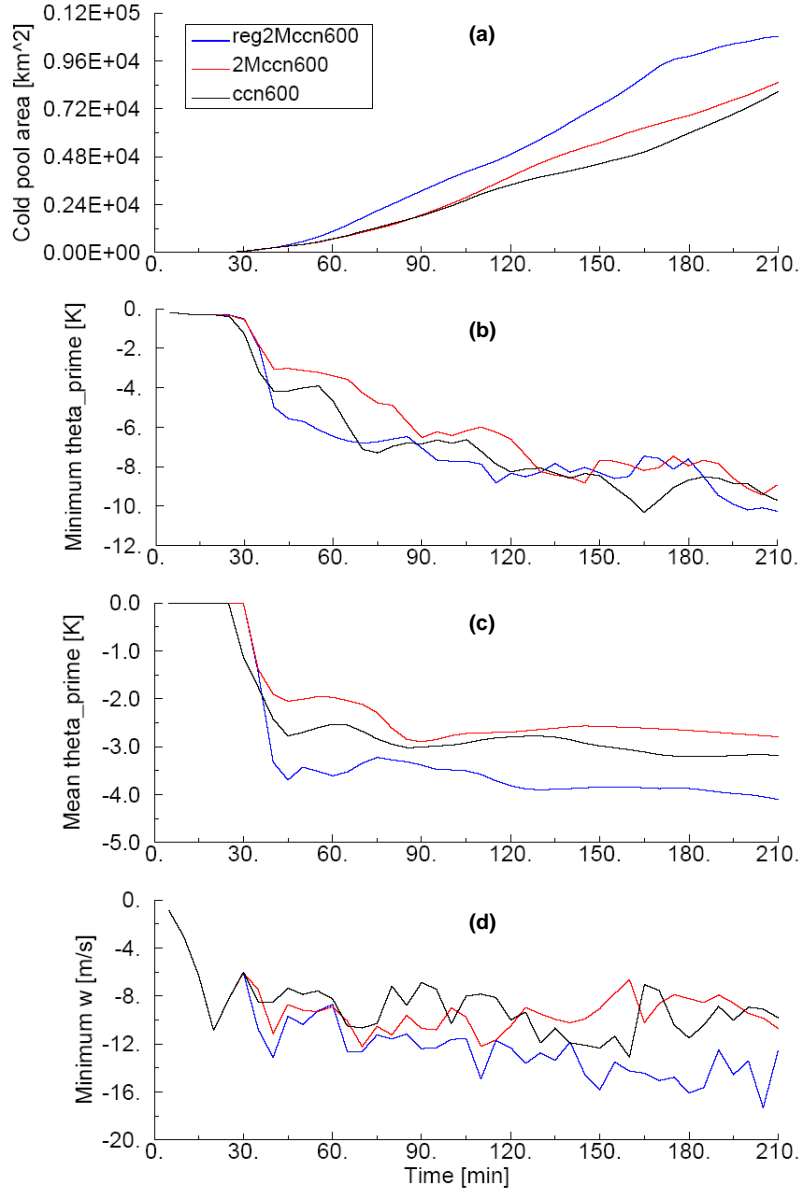


Figure 5.48: Time series of (a) total surface (lowest model level, $z = 98$ m) cold-pool area (defined as the sum of the area of all grid squares with $\theta' < -1$ K), (b) minimum θ' at the surface, (c) mean surface θ' within the cold-pool, and (d) maximum downdraft strengths [m s^{-1}] over lowest 2 km AGL for the simulations listed in Table 5.3.

The coldest θ'_{mean} values are found in the reg2Mccn600 case (Fig. 5.48c), though this case does not necessarily produce the coldest θ'_{min} (Fig. 5.48b), and the cold-pool in the 2Mccn600 case has the least coldest θ'_{mean} and θ'_{min} values. The cold-pool in the ccn600 case exhibits θ'_{mean} values that are slightly cooler than in 2Mccn600 (Fig. 5.48c), but the θ'_{min} values in the former

fluctuate within roughly + or -2 K of θ'_{min} of the other two cases (Fig. 5.48b). GSR04 noted that the coldest time-averaged θ' values in their simulations were associated with the case that produced the most rainfall and warmer cold-pools were observed in cases that were weighted towards larger hail, similar to the results here. Decreases in the mean cold-pool strength and maximum downdraft magnitudes with increasing hail sizes as reported by VC04, Cohen and McCaul (2006), and Snook and Xue (2008) are seen in these experiments as well (Fig. 5.48c,d), although differences in θ'_{min} among the three cases are no more than about 4 K at any given time (Fig. 5.48b). Increased production of rain and associated evaporative cooling in ccn600 (Fig. 5.54) leads to a stronger cold-pool in this case than in 2Mccn600 (Fig. 5.48b,c) even though hail is generally larger in the former compared to the latter. However, in spite of smaller rain evaporative cooling rates in 2Mccn600 relative to ccn600 (Fig. 5.54), maximum downdraft strengths in ccn600 are generally weaker than in 2Mccn600 prior to about 120 minutes (Fig. 5.48d). This is in contrast to findings of GSR04 who noted that increased evaporative cooling and stronger downdrafts in their simulations resulted from increased rainfall, although Srivastava (1987) found that increases in the numbers of small ice particles enhanced cooling and forced stronger downdrafts, similar to what is seen for the 2Mccn600 and reg2Mccn600 cases (Figs. 5.48d and 5.54). Of course, differences in cooling magnitudes and downdrafts between the simulations performed here and those of other studies might also arise due to differences in the environmental soundings and microphysical schemes used.

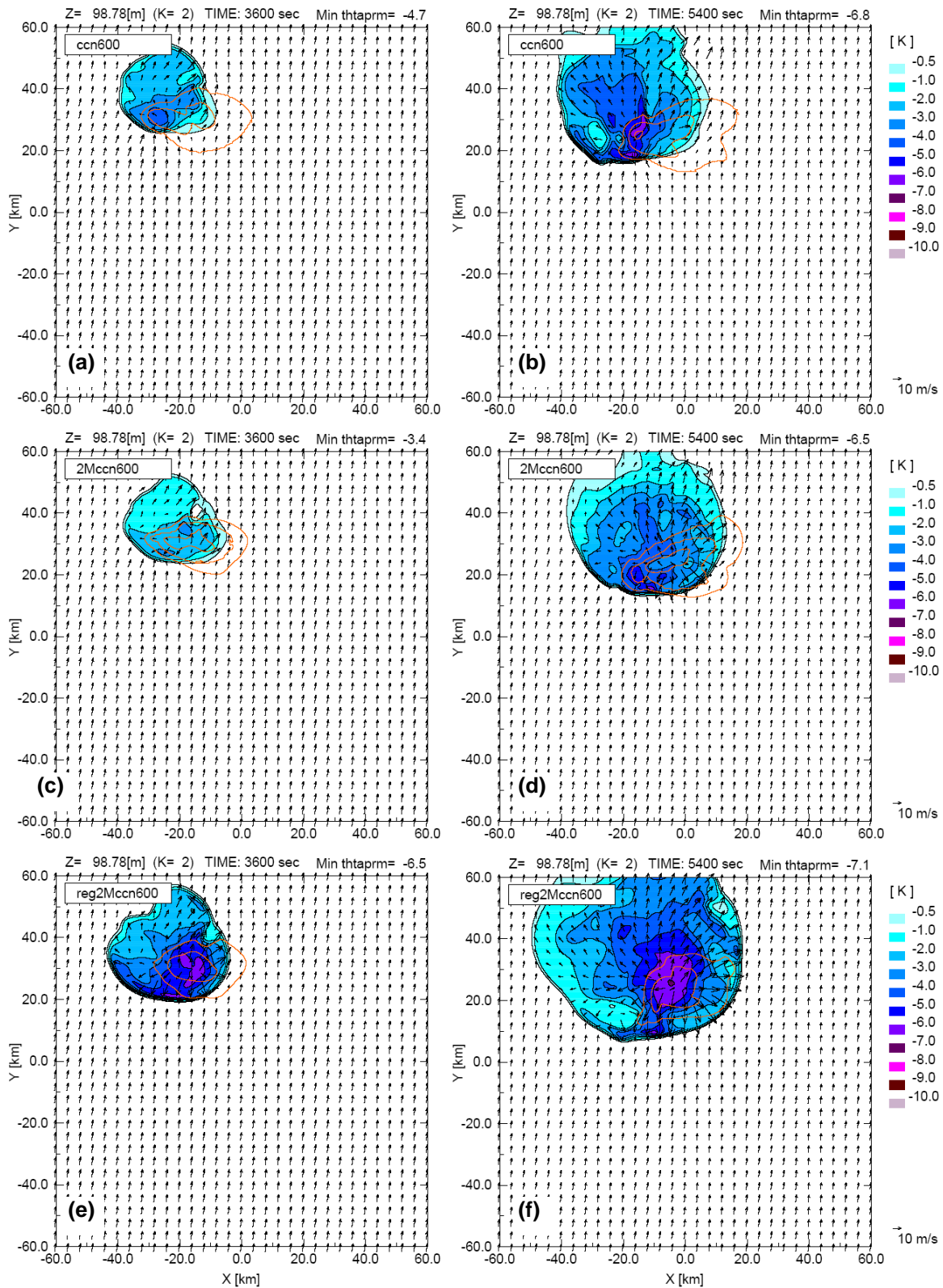


Figure 5.49: Perturbation potential temperature (θ') [shaded, contour intervals of -1 K beginning at -1 K; -0.5 K contour also shown] at lowest model level (98 m AGL) and Z_e contours [orange, contour intervals of 20, 40, and 60 dBZ] at 60 minutes (left column) and 90 minutes (right column) for (a) (b) ccn600, (c) (d) 2Mccn600, and (e) (f) reg2Mccn600. Ground relative wind vectors are also shown.

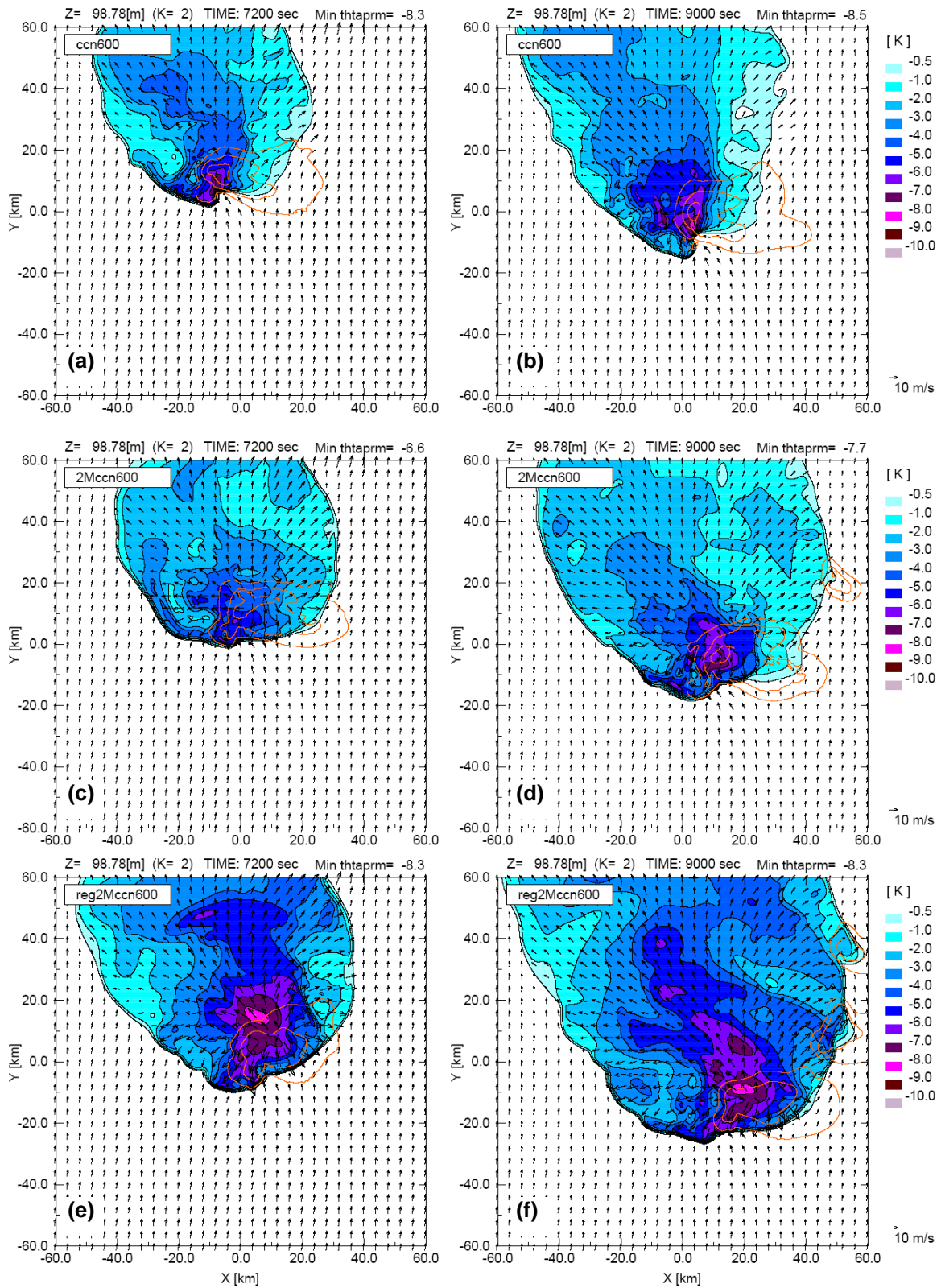


Figure 5.50: As in Figure 5.49 for simulations times 120 minutes (left column) and 150 minutes (right column)

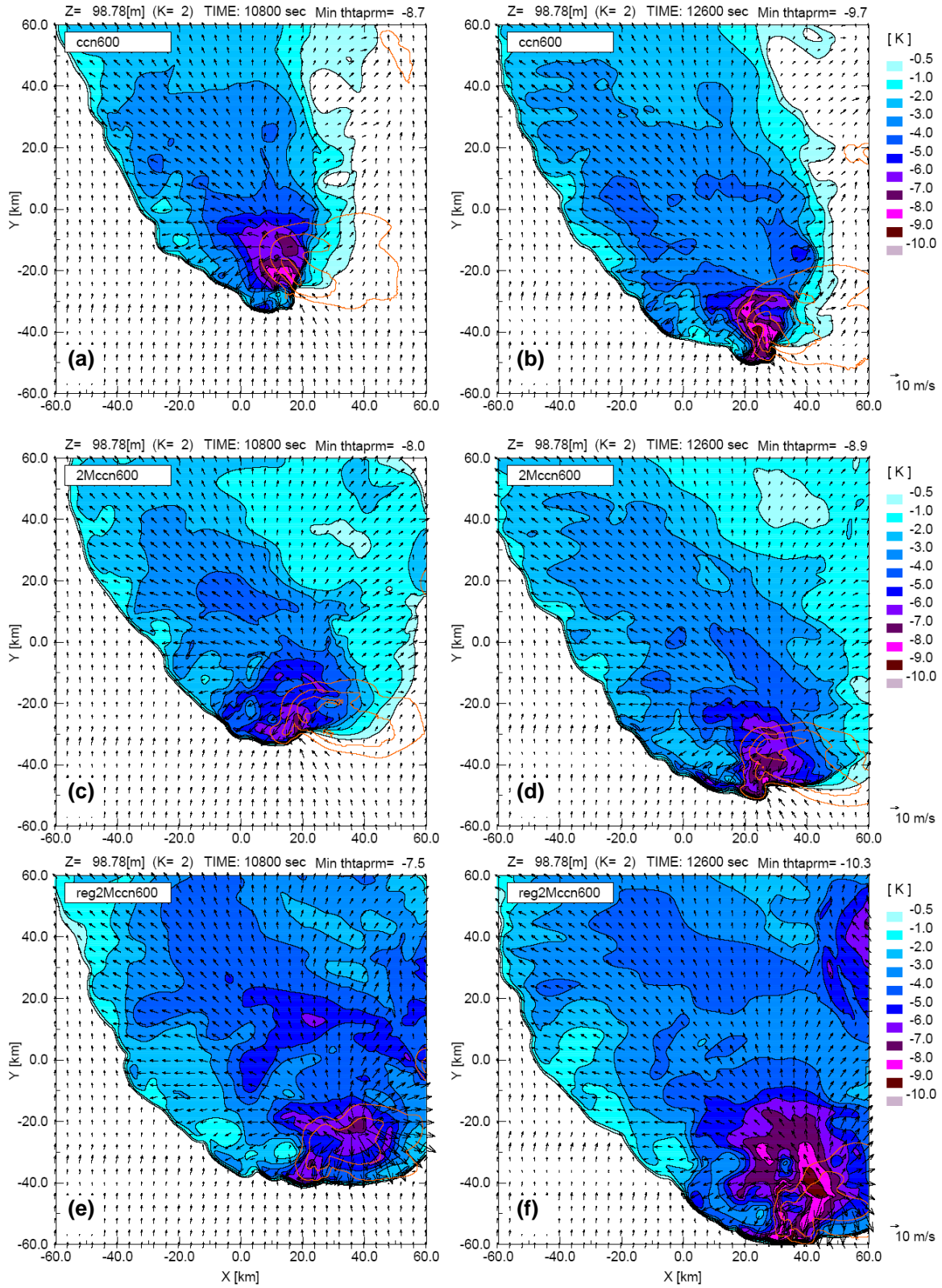


Figure 5.51: As in Figure 5.49 for simulations times 180 minutes (left column) and 210 minutes (right column)

The cold-pools in the two-moment cases, especially reg2Mccn600, are more prominent within the forward-flank downdraft (FFD) regions (to the east and northeast of the high Z_e cores) following the right turn ($t \geq 90$ min) compared to the ccn600 case (Figs. 5.49-5.51). Dawson et al. (2010) noted a similar result regarding colder FFDs in simulations using single-moment microphysics compared to those that used multi-moment microphysics due in part to greater evaporative cooling from rain in the former compared to the latter. θ' values within the rear-flank downdraft (RFD) regions (to the southwest of the high Z_e cores) of the two-moment cases are also colder than in the ccn600 case beyond 150 minutes (Figs. 5.50 and 5.51). Warmer RFDs are considered more supportive of tornadogenesis (Markowski et al. 2002), thus it may be surmised that the larger hail and the associated warmer θ' RFD values in the ccn600 case may increase the probability of a tornado occurring, though this is beyond the scope of this work.

Time-height contours of θ'_{min} for the three simulations performed are shown in Figure 5.52 and depict the time evolution of the cold-pool depth. It is immediately evident that the deepest cold-pool occurs in the reg2Mccn600 case (Fig. 5.52c) based on the deeper layer of colder θ' values, whereas the cold-pools in the ccn600 (Fig. 5.52a) and 2Mccn600 case (Fig. 5.52b) are much shallower. The cold-pool depth appears to be slightly greater in 2Mccn600 compared to ccn600, yet the latter exhibits a deeper layer of colder θ' values near the surface owing to greater evaporative cooling from rain in this case (Fig. 5.54a). The deeper and stronger cold-pool in reg2Mccn600 leads to faster storm propagation that is evident in the greater east- and southward displacements of the low- and mid-level reflectivity fields (Fig. 5.8) and leading cold-pool edge of the storm (Figs. 5.49-5.51) in this case relative to the other two. An increase in cold-pool depth and more rapid storm propagation with decreasing hail sizes was similarly reported by VC04. Additionally, colder θ' values above the cloud base height (~ 2 km) in reg2Mccn600

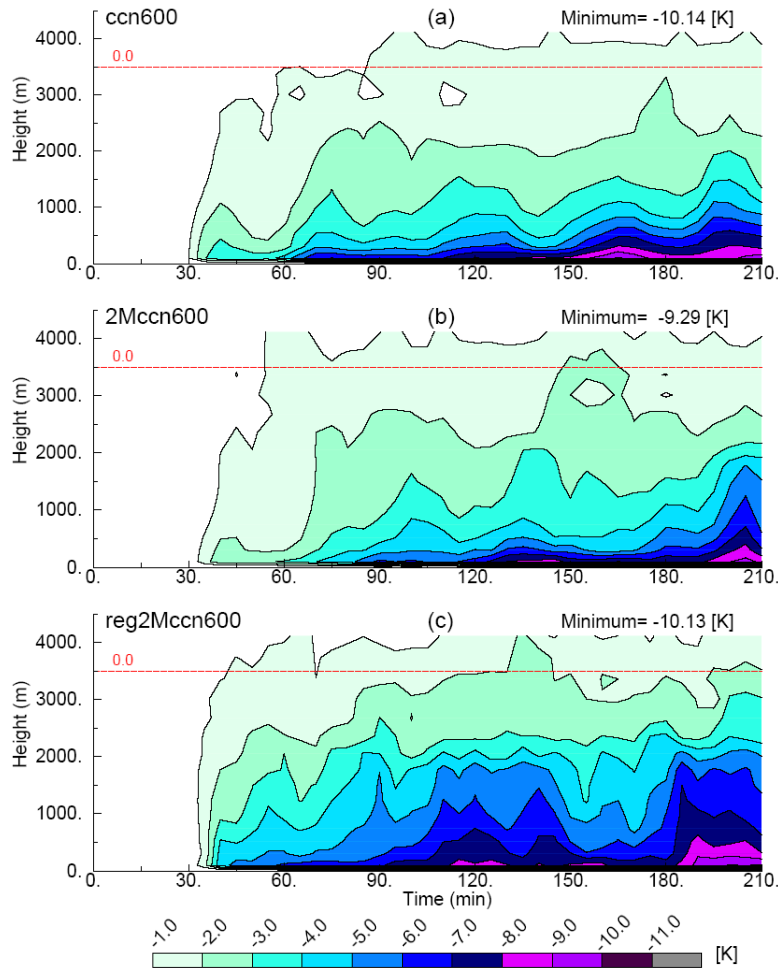


Figure 5.52: Time-height contours of minimum θ' [K] for cases (a) ccn600, (b) 2Mccn600, and (c) reg2Mccn600.

highlight the importance of cooling due to melting of hail in the development of the low-level downdraft and associated cold-pool in this case as cooling from evaporation and sublimation is inhibited within cloud.

In order to understand how differences in the approaches to modeling hail in these simulations lead to differences in the cold-pool characteristics, the relative magnitudes of cooling within low-level downdrafts from melting and evaporation/ sublimation of hail and evaporation of rain are examined via time-height plots of maximum cooling rates for these processes (Figs. 5.53 and 5.54). Changes in air temperature during the melting process are due to sensible heat

transfers from the air to the hailstone surface modulated by latent heating (cooling) of the hailstone surface as a result of vapor transfers to (from) the hailstone surface (Pruppacher and Klett 1980; Rasmussen and Heymsfield 1984; Srivastava 1987). Evaporation from hail refers to evaporation of meltwater as well as previously collected liquid from the hailstone surface, and thus, the resultant cooling from this process is computed separately from cooling due to melting. The equations used to compute the cooling rates from evaporation (sublimation when appropriate) and melting are given by

$$\left(\frac{\partial T_{ac}}{\partial t}\right)_{\text{evap,sublm}} = A \left(\frac{\partial r_x}{\partial t}\right)_{\text{evap,sublm}} \quad (5.3)$$

$$\left(\frac{\partial T_a}{\partial t}\right)_{\text{melt}} = -\frac{r_h}{c_p} \left(\frac{\partial Q_h}{\partial t}\right)_{\text{vapor, heat diffusion}} + \frac{L_v}{c_p} \left(\frac{\partial r_h}{\partial t}\right)_{\text{vapor diffusion}}, \quad (5.4)$$

where $x = r$ or h in Eqn. 5.3 and other variable descriptions are listed in Table 3.6 of Chapter 3.4. Equation 5.4 is more complex than the heating/cooling rate equations of Hjelmfelt et al. (1989) and Straka and Anderson (1993) for which air temperature changes are related solely to changes in hail and/or graupel mixing ratios as a result of melting. The greater degree of complexity is necessitated by the fact that some liquid water is allowed to remain on the hailstone surface during melting, and this retained liquid impacts the calculation of hail internal energy Q_h as well as heat and mass transfers between the hail particle and the environment (Srivastava 1987). Equation 5.4 is derived from the hydrometeor heat budget equation of Walko et al. (2000) which computes changes in Q_h resulting from sensible heat and vapor diffusion as well as from convergence of radiative flux, though the radiation term is neglected here, and is applied only when $Q_h > 0$. The first term on the RHS of 5.4 relates changes in air temperature to net changes in Q_h , and the second RHS term is needed to remove the latent heating (cooling) effects due to vapor transfers, which are considered in Eqn. 5.3, from the net changes in Q_h . Cooling from

evaporation of cloud is not considered here as cloud mixing ratios and number concentrations below the freezing level are similar among the simulations (Figs. 5.29a,b and 5.30a,b) even though this effect may be similar in magnitude to rain evaporative cooling (Dawson et al. 2010).

The larger hail sizes at low-levels in the ccn600 case and the associated reduction in melting rates result in smaller maximum cooling rates from melting and evaporation/ sublimation of hail relative to the 2Mccn600 and reg2Mccn600 cases (Fig. 5.53). Cooling from melting extends from roughly 3 km AGL to the surface in ccn600 (Fig. 5.53a), yet is primarily confined between about 1.4 and 3 km in 2Mccn600 (Fig. 5.53c) owing to a reduction in hail number concentrations from melting and the associated artificial increases in hail sizes within the melting layer in this case. The largest maximum cooling rates from melting hail are seen for reg2Mccn600 (Fig. 5.53e) owing to the significant amounts of small hailstones in this case compared to the other two cases. Larger maximum cooling rates due to hail evaporation/sublimation in the two-moment cases (Fig. 5.53d,f) reflects the greater horizontal transport of smaller hailstones away from the storm core and the subsequent fallout into unsaturated air. In addition, the slower fall speeds and increased melting rates of these small hail particles lead to larger evaporation rates of liquid from the hail surfaces and hence larger hail evaporation cooling rates in the two-moment cases, particularly in reg2Mccn600. The relatively small maximum cooling rates for hail evaporation/sublimation in ccn600 (Fig. 5.53b) are mostly due to the fact that the larger hailstones in this case fallout closer to the updraft in regions that are typically associated with higher relative humidities.

Maximum evaporative cooling rates for rain (Fig. 5.54a,c,e) are directly proportional to the amount of rain at low levels (i.e., Fig. 5.29c), with the largest rates seen for reg2Mccn600, and the smallest rates for 2Mccn600. The heights at which peak evaporative cooling occurs also seem

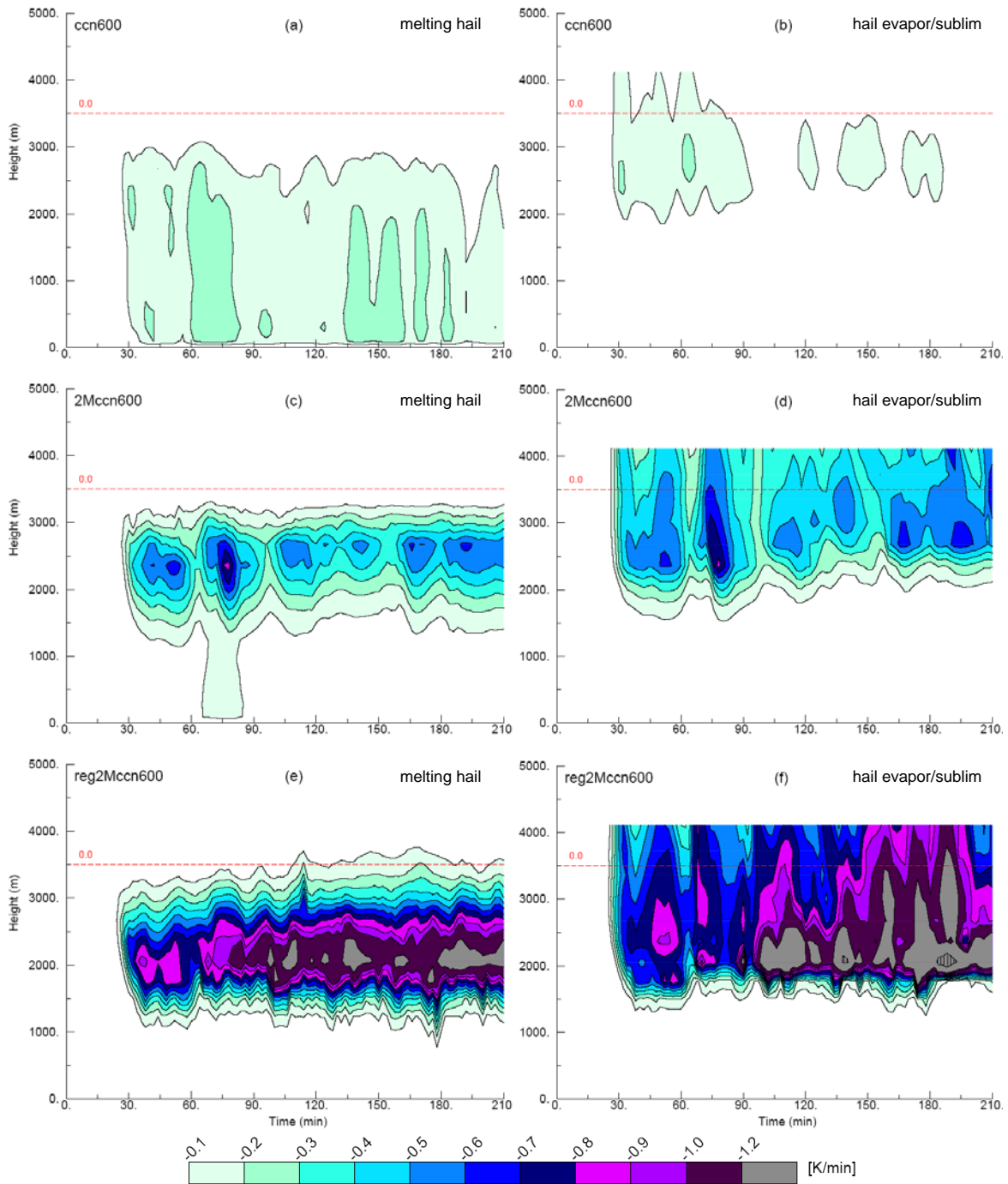


Figure 5.53: Time-height contours of domain maximum cooling rates [K min^{-1}] within downdrafts ($w \leq -0.5 \text{ m s}^{-1}$) from (left column) melting hail and (right column) hail evaporation/sublimation for (a,b) ccn600, (c,d) 2Mccn600, and (e,f) reg2Mccn600. Hatching in panel f denotes cooling rates of at least -2 K min^{-1} .

to be associated with peaks in the vertical distribution of rain mass in each case (i.e., Fig. 5.29c) similar to the results of Hjelmfelt et al. (1989) and Straka and Anderson (1993). Maximum rain

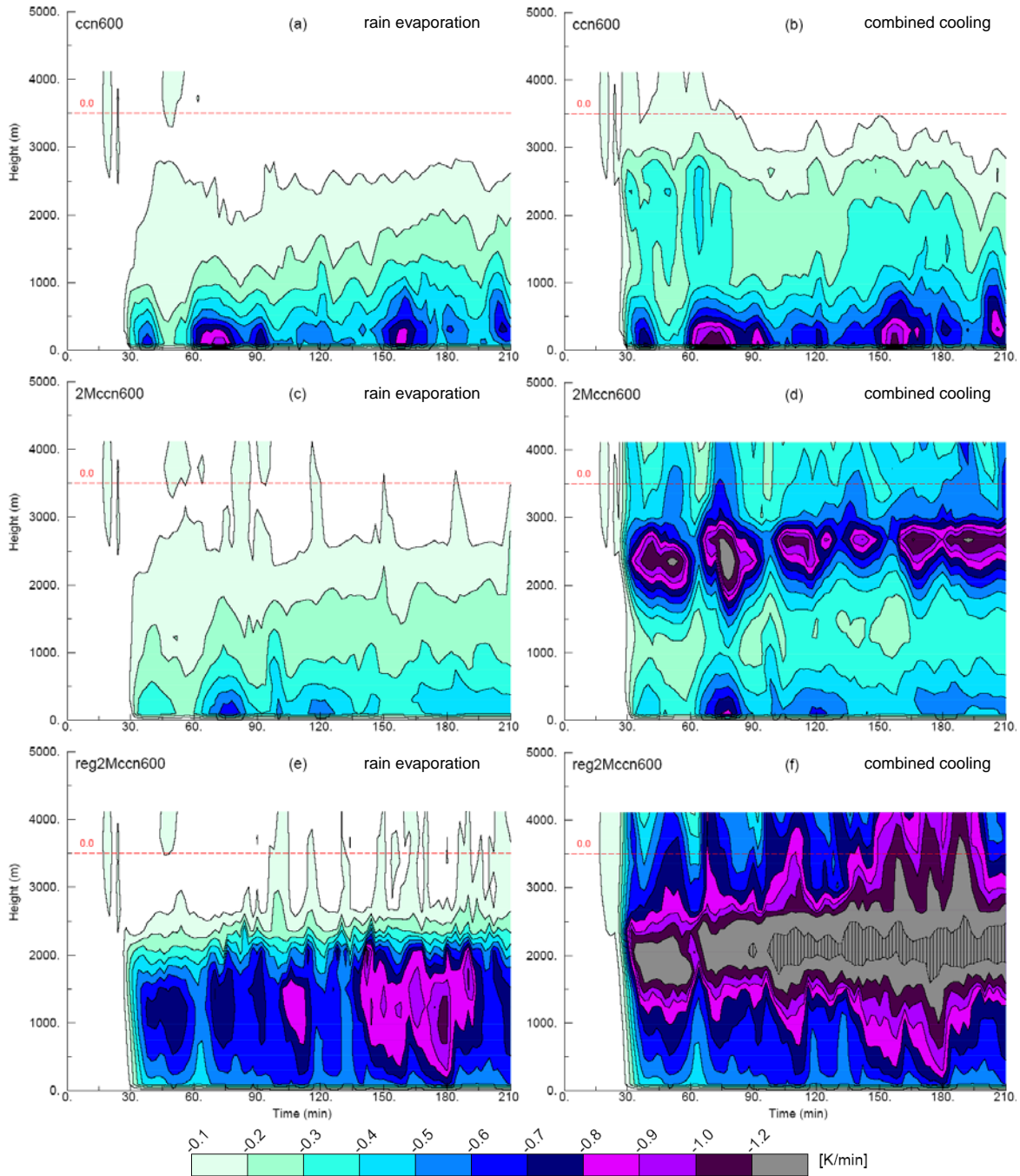


Figure 5.54: As in Figure 5.53 except for (left column) rain evaporation and (right column) combined melting hail, hail evaporation/sublimation and rain evaporation for (a,b) ccn600, (c,d) 2Mccn600, and (e,f) reg2Mccn600. Hatching in panel f denotes cooling rates of at least -2 K min^{-1} .

evaporative cooling rates in ccn600 are larger than in 2Mccn600 as more rain is produced from hail (mainly via shedding) in the former case compared to the latter case. The plots of maximum

cooling rates from the combined processes of melting and evaporation/sublimation (Fig. 5.54b,d,f) reveal rain evaporation within approximately the lowest kilometer dominates total cooling in the ccn600 case whereas melting hail and hail evaporation/ sublimation are the largest contributors to total cooling in the two-moment cases. Interestingly, maximum combined cooling rates in the 2Mccn600 case are larger and occur at a higher altitude than in the ccn600 case, however, the cold-pool produced in the latter is stronger than in the former. Some degree of compressional warming is likely within the downdrafts of the simulated storms, though its effect is probably greatest in 2Mccn600 owing to the generally smaller precipitation-related cooling rates below about 2 km in this case. Maximum total cooling rates are greatest and occur over a much deeper layer in reg2Mccn600 as a direct result of the more numerous smaller hail particles below the melting level in this case compared to the other two cases. *Overall, it is apparent that the magnitudes of low-level cooling increase with decreasing hail sizes in these experiments* as in the sensitivity studies of GSR04, VC04, and Cohen and McCaul (2006).

5.5) *Summary*

The findings presented in this chapter clearly show that predicting an additional third moment of the hail size distribution in the microphysics scheme results in a significant improvement of the simulated storm when compared to the observations for the 29 June 2000 supercell case as well as with previous studies of hail in supercell storms. Additionally, analyses of the different approaches to modeling hail reveal that the impacts of hail on storm structure and evolution are generally represented in a much more realistic manner with the 3MHAIL scheme versus a two-moment scheme. The main findings are now summarized.

- All three simulations with different microphysics are able to reproduce the general evolution and track of the 29 June 2000 supercell storm from an initial multi-cell structure to a right-turning supercell. However, only the simulation with the 3MHAIL microphysics scheme produces a supercell storm that most closely resembles the observed storm on 29 June 2000 in terms of low- and mid-level reflectivity structures, vertical reflectivity structures, generation of large hail and subsequent fallout in qualitative agreement with surface hail reports for this storm. The amounts of large and very large hail both aloft and at the surface in the 3MHAIL simulation are in line with previous observations of hailstorms. In addition, a close match between the propagation speeds of the observed and modeled storms is seen for the case with 3MHAIL microphysics whereas the storms propagate faster in the cases with two-moment microphysics compared to the observations.
- The RAMS regular two-moment microphysics (reg2M) scheme produces only negligible amounts of hail at the surface and no large hail at low-levels in contrast to the observations. This simulation also fails to produce significant amounts of graupel that were found to be present in the actual storm. On the other hand, the new melting algorithm applied in the modified two-moment (mod2M) scheme erroneously produces large hail below the freezing level due to the constraint of a fixed hail distribution shape parameter that results in artificial shifts in the hail size distribution towards larger sizes. Both of the simulations with two-moment microphysics fail to produce large hail aloft indicating that an increase in the allowable maximum mean mass diameter of hail in the RAMS two-moment microphysics scheme does result in the production of large hail.
- In the two-moment cases, the dominance of small hail particles aloft leads to computed reflectivity magnitudes that are much smaller than the observed reflectivity values. In

addition, the lack of hail at low-levels in the case with reg2M microphysics results in reflectivity values that are generally too small whereas the fixed wide spectral widths of the hail distributions artificially weighted towards larger sizes in the simulations with mod2M microphysics lead to unrealistic reflectivity structures at low levels.

- Examinations of the polarimetric signatures related to precipitation processes in supercells reveal that the case with 3MHAIL microphysics exhibits the most realistic patterns in the computed polarimetric variable fields compared to the two-moment cases, particularly for large hail. The production of primarily small hail in the simulation with reg2M microphysics is also depicted rather well in the computed polarimetric variable fields.
- The majority of precipitation mass is contained in the hail category in the simulations with two-moment microphysics whereas precipitation mass is partitioned more realistically among the various hydrometeor categories in the case with 3MHAIL microphysics. In addition, total hail number concentrations are about 5 to 6 times greater in the two-moment simulations than in the case with 3MHAIL microphysics.
- Rain colliding with frozen particles is the dominant hail formation mechanism in all three simulations, although the numbers of newly formed hailstones via this process are larger in the cases with two-moment microphysics compared to the 3MHAIL microphysics case. The newly implemented three-component freezing algorithm in the cases with mod2M and 3MHAIL microphysics results in the production of realistic amounts of graupel from rain-snow and rain-aggregate collisions. Additionally, the algorithm of Ferrier (1994) for rain-pristine ice collisions greatly reduces the numbers of new hailstones formed by this process. In contrast, the collection algorithm in the reg2M microphysics scheme forces all rain-ice collisions to form hail thereby resulting in a plethora of small hailstones.

- Hail growth rates are dominated by the riming process and tend to decrease as hail sizes increase in association with the reduced total surface area of the fewer larger hailstones. Wet growth of hail also becomes more prominent as hail sizes increase.
- The impacts of hail formation and growth on latent heating profiles aloft seem to be greater for distributions containing more numerous smaller hailstones.
- Rain production from melting and shedding of hail below the freezing level tends to be greater than that from conversion of cloud droplets to rain and melting graupel in all three cases. For hail distributions weighted towards smaller sizes, such as in the simulation with reg2M microphysics, complete melting of the small hail particles occurs more rapidly and is the dominant rain formation mechanism. Hail distributions comprised of larger hailstones, as in the cases with the mod2M and 3MHAIL schemes, experience increased shedding rates that account for the majority of the rain production.
- Surface rain rates, accumulated rain mass, and areal coverage of surface rainfall increase with decreasing hail sizes and are largest in the simulation with the regular two-moment microphysics, whereas hail precipitation rates and accumulated hail mass at the surface decrease with decreasing hail sizes. In the large hail cases with the mod2M and 3MHAIL microphysics schemes, the larger hail sizes in the latter case fallout over a much narrower region compared to the wide hailswath produced in the former case.
- The predominantly small hail produced in the simulation with reg2M microphysics results in stronger downdrafts and a deeper, stronger, and more expansive cold-pool due to increased cooling rates from melting hail, evaporation/sublimation of hail, and evaporation of rain. By comparison, the smaller cooling magnitudes associated with the larger hail in the case with 3MHAIL microphysics are associated with weaker downdrafts and a cold-pool that is

shallower, smaller, and generally not as strong as in the simulations with two-moment microphysics.

6. Sensitivity of hail size distributions to CCN experiments

6.1) *Introduction*

In Chapter 5, the impact of the complexity of the microphysical scheme on both the predicted characteristics of hail and overall storm evolution was examined. It was shown that predicting three moments of the hail size distribution with the new 3MHAIL scheme resulted in a simulated storm that was much more representative of the observations compared to two different two-moment microphysics schemes. In this chapter, the 3MHAIL scheme is used to investigate the impact of changing the concentrations of cloud condensation nuclei (CCN) on hail for the 29 June 2000 supercell case. [Note that the term CCN herein refers to CCN concentrations, and the two terms are used interchangeably. In addition, CCN are physically linked to supersaturation values, though the term CCN herein simply refers to aerosols that can be activated under typical atmospheric supersaturation values ($\leq 1\%$).]

Numerous studies have investigated the effects of CCN on the dynamics and precipitation of deep convection in both continental and tropical environments (e.g., Phillips et al. 2002; Andreae et al. 2004; Khain et al. 2004, 2005, 2008; Khain and Pokrovsky 2004; Lynn et al. 2005; Wang 2005; Seifert and Beheng 2006; van den Heever et al. 2006; Fan et al. 2007; Tao et al. 2007; Lee et al. 2008; Lerach et al. 2008; Li et al. 2008; Khain and Lynn 2009; Carrió et al. 2010; Storer et al. 2010; Lim et al. 2011; van den Heever et al. 2011). Most of these studies have found that the convective response to changes in CCN concentrations depend largely on the cloud type (e.g., warm, isolated, multicell) and environmental conditions. To date, however, only two studies that explicitly focus on CCN impacts on hail have been undertaken with conflicting results. Both studies simulated the same severe multicell hailstorm that occurred in southwest Germany on 28

June 2006. Using a two-dimensional cloud model with bin microphysics, Khain et al. (2011) found an increase in hail size and amounts with increasing CCN whereas the study by Noppel et al. (2010) used a three-dimensional cloud model with two-moment bulk microphysics and found a general decrease in hail size and amount at the surface with increasing CCN. The experiments in the current work incorporate features from both of these previous studies, namely a bin-emulating triple-moment bulk scheme for hail within a three-dimensional cloud model, thus the results should be more robust than in the previous studies. The same environmental sounding and model setup as in Chapter 5 (Fig. 5.5 and Table 5.1) are utilized for these experiments, with the exception that these simulations are run out to 180 minutes and the 3MHAIL scheme is applied in all cases.

6.2) *CCN sensitivity experiments*

Five simulations are carried out in which the initial maximum CCN values at the surface vary from 100 to 3000 cc^{-1} (Table 6.1), with these extremes representing conditions typical of clean (maritime) and polluted continental airmasses, respectively. While CCN values less than several hundred cc^{-1} are likely unrepresentative of airmasses over rural areas in the central High Plains of the US (Hobbs et al. 1985; Detwiler et al. 2010), the goal is simply to gauge the response of the model solution to changes in CCN concentrations over a broad range of values. The model is initialized using five different vertical profiles of CCN (Fig. 6.1), four of which have their

Table 6.1: Names of simulations performed for the sensitivity of hail to CCN study.

Experiment Name	Maximum initial CCN [cc^{-1}] at surface
ccn100	100
ccn300	300
ccn600	600
ccn1500	1500
ccn3000	3000

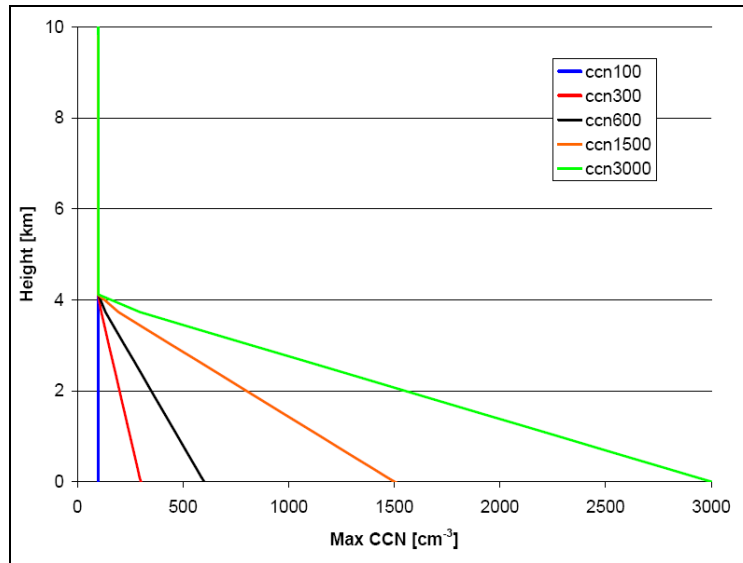


Figure 6.1: Vertical profiles of maximum CCN for aerosol sensitivity tests, decreasing linearly from maximum value at surface to a constant value of 100 cm^{-3} above 4 km.

maximum values at the surface and decrease linearly with height up to 4 km, above which the CCN values are constant at 100 cm^{-3} . van den Heever et al. (2006) used a similar combination of linear profiles at low levels and constant profiles aloft to represent the vertical distribution of observed CCN in their simulations of convection over FL. The concentrations of aerosols (and hence CCN) at cloud base are the primary factor in determining concentrations and size distributions of cloud droplets and ice particles whereas aerosol concentrations aloft do not substantially impact the microphysics of deep convective clouds (Khain and Pokrovsky 2004; van den Heever et al. 2006; Carrió et al. 2007). Based on the environmental sounding used for these simulations (Fig. 5.5), the cloud base is around 2 km. Thus, the prescribed variations in CCN over the lowest 4 km in the current experiments mean that CCN ingested into the storm at cloud base will be different in each case.

6.2.1) *General storm evolution and dynamics*

The general evolutions of the simulated storms in the CCN sensitivity experiments are very similar to that of the ccn600 case presented in Chapter 5 and are thus not repeated here in detail. In all of the sensitivity cases, the simulated storms develop from the initial perturbation into an eastward-moving multicell-type storm up through about 80 minutes, followed by a transition to a right-turning supercell around 90 minutes. The storms continue propagating southeastward and remain in the supercell phase for the remainder of the simulation in all cases. Figure 6.2 shows the evolution of the equivalent reflectivity (Z_e) fields at approximately 1 and 5 km AGL. Similar structures of Z_e are seen in all cases for the selected times shown, though the storms in the ccn300 and ccn600 cases propagate slightly faster beyond 120 minutes as evident by the greater southeastward displacement of the high Z_e cores at low levels compared to the other cases (Fig. 6.2a-e). The largest Z_e magnitudes in all cases are distinctly associated with regions of large hail as was the case in the analyses in the previous chapter. Cases ccn1500 and ccn3000 attain Z_e values greater than 70 dBZ both at low levels and aloft beyond $t = 90$ minutes as a result of greater amounts of large hail produced in these two experiments compared to the other cases as will be detailed in Section 6.2.3.

The time series of maximum updraft speeds (w_{max}) (Fig. 6.3) shows there is generally little difference in updraft strength among the different cases, with nearly identical w_{max} values up through 60 minutes and differences of less than about 3 m s^{-1} between approximately 60 and 110 minutes. Beyond 110 minutes, the differences in w_{max} values among the five experiments increase for a given time, though the values tend to fluctuate between roughly 35 and 45 m s^{-1} in all cases with no systematic increase or decrease as a result of changes in CCN concentrations. This is in contrast to results from previous studies that revealed stronger responses in maximum

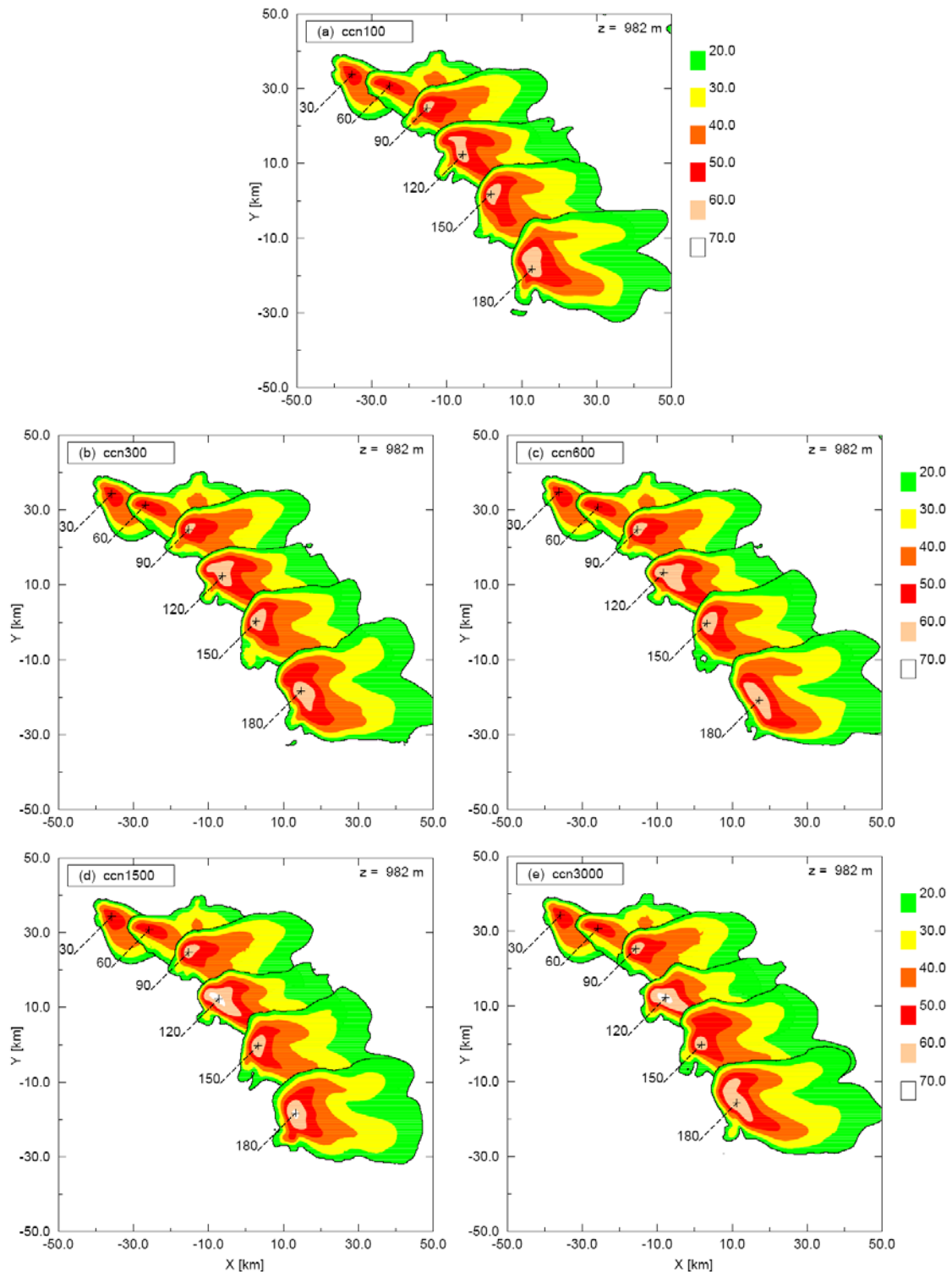
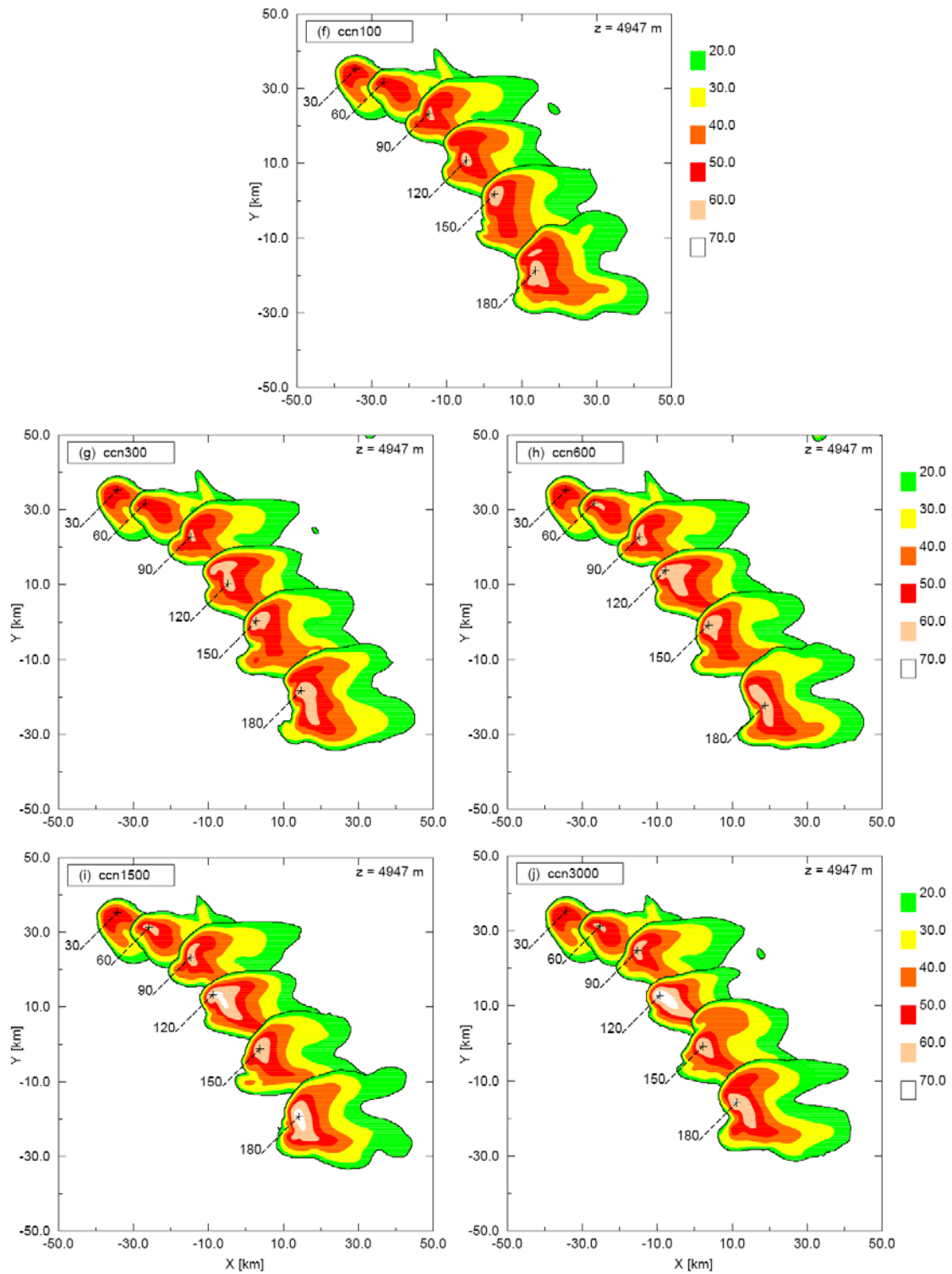


Figure 6.2: Evolution of simulated storm structures depicted by model equivalent reflectivity factor Z_e (dBZ) shown every 30 minutes at $z = 982$ m AGL for (a) ccn100, (b) ccn300, (c) ccn600, (d) ccn1500, and (e) ccn3000, and at $z = 4947$ m AGL for (f) ccn100, (g) ccn300, (h) ccn600, (i) ccn1500, and (j) ccn3000. Locations of maximum computed Z_e at $t = 30, 60, 90, 120, 150,$ and 180 minutes are denoted by the black crosses in each panel. In this and subsequent plan view plots, north is towards the top of the plots. (Figure continues on next page).



(Figure 6.2 continued)

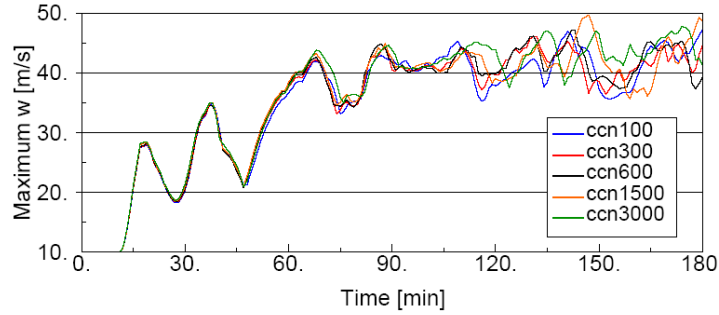


Figure 6.3: Time series of domain maximum updraft speeds for the CCN sensitivity experiments listed in Table 6.1.

updraft speeds of single-cell and organized multicell storms to changes in CCN (Rosenfeld and Woodley 2003; Khain and Pokrovsky 2004; Khain et al. 2005; van den Heever et al 2006, 2011; Seifert and Beheng 2006; Li et al. 2008; Carrió et al. 2010). However, the relative insensitivity of w_{max} in these simulated supercells to changes in CCN concentrations was also reported in previous modeling studies of CCN impacts on supercells (Seifert and Beheng 2006; Lerach et al. 2008; Khain and Lynn 2009; Storer et al. 2010; Lim et al. 2011). The only apparent effect of CCN on w_{max} for these simulations is a slight time delay in maximum updraft peaks with increases in CCN, particularly at times beyond about 75 minutes.

Differences in maximum potential temperature perturbations (θ'_{max}) within updraft among all the cases are generally less than 0.5 K (Fig. 6.4). Thus, changes in CCN in these simulations seem to have only a small impact on the release of latent heat and vertical heating profiles, thereby accounting for the insignificant effect of CCN on w_{max} . This relative insensitivity of heating to changes in CCN agrees with results of Khain (2009) and Khain et al. (2011) for simulations of a multicell hailstorm with a relatively low freezing level (< 3 km AGL), but differs from findings from sensitivity studies by Khain et al. (2005), van den Heever et al. (2006) and Li et al. (2008) for deep convective clouds with relatively high freezing levels (> 4 km AGL). The greatest θ'_{max} values occur in the ccn3000 case and likely result from increased net

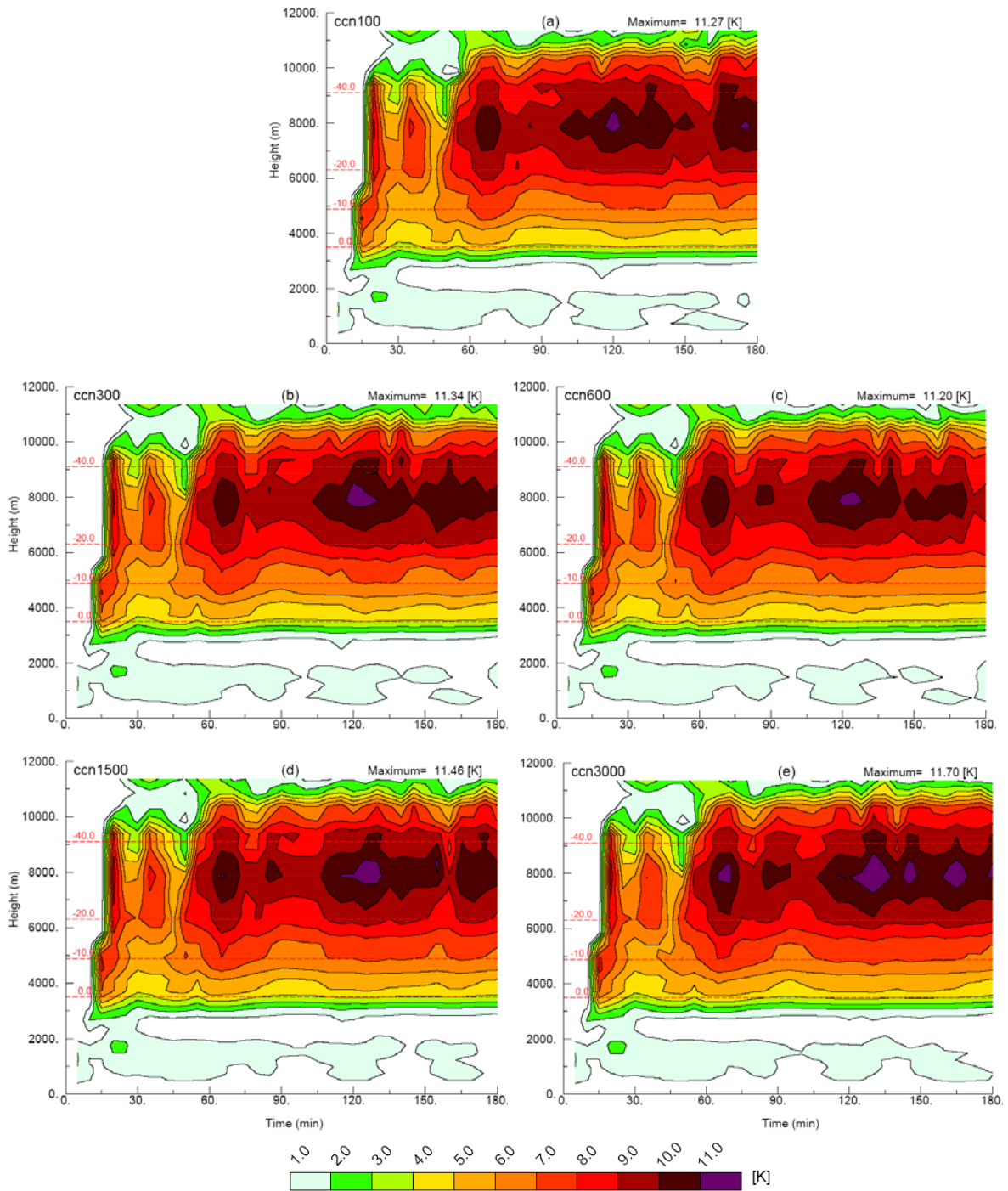


Figure 6.4: Time-height contours of maximum θ' [K] for the CCN sensitivity experiments in Table 6.1.

diffusional growth of the more numerous droplets above the freezing level as in Carrió et al. (2007) and Khain et al. (2011). Larger θ'_{max} values in the ccn100 and ccn300 cases relative to those in the ccn600 case are likely due to increased depositional growth of ice as a result of

increased supersaturations associated with reduced condensational growth of fewer cloud droplets (Tao et al. 2007; Khain et al. 2011). The evolution of the vertical vorticity fields are also mostly similar among the simulated storms as revealed by time-height plots of maximum vertical vorticity (not shown) further suggesting the impact of CCN on the storm dynamics is minimal at best. In addition, changes in CCN do not appear to affect the tracks taken by the simulated storms (Fig. 6.2) in qualitative agreement with Noppel et al. (2010). Thus, it seems the environmental factors responsible for determining the dominant mode of convection, namely CAPE and wind shear (Weisman and Klemp 1982, 1984; Weisman and Rotunno 2000), significantly overwhelm any dynamical effects brought about by changes in CCN in these simulations. However, the results of the sensitivity experiments will show that the impacts of CCN on hydrometeors within supercells can be significant, particularly with respect to hail.

6.2.2) *General CCN effects on hydrometeor fields*

As the formation and growth of hail depends on the characteristics of all of the other hydrometeors, an examination of the general impacts of CCN on all hydrometeor fields is carried out prior to performing a detailed analysis of the effects of CCN on hail. Time-averaged vertical profiles of the horizontally-averaged mass contents (r), total liquid water content (LWC , both cloud modes plus rain), and number concentrations (N_i) for each hydrometeor category are shown in Figures 6.5-6.8 for two time periods. The first time period ($t = 30$ to 90 minutes, defined as P1) corresponds to the developing and transition to supercell phases of the storm, and the second period ($t = 90$ to 150 minutes, defined as P2) refers to the first hour of the supercell phase during which the storm is more or less in a quasi-steady state (Fig 6.3).

To quantitatively assess the response of the simulated hydrometeor fields to changes in CCN, the statistical population mean (p-mean hereafter) of a given variable is used as in Wang (2005) and Li et al. (2008). The p-mean of a variable c is defined by Eqn. 6.1 and gives the average value of the domain mean \bar{C}^D (Eqn. 6.2) over a given length of time, or in this case, number of time steps ΔT . For a given time t , the domain mean is computed over all grid points meeting specified criteria, which for this study are minimum values of mixing ratio ($r_{min} = 10^{-10} \text{ kg kg}^{-1}$) and total number concentration ($N_{tmin} = 10^{-10} \text{ kg}^{-1}$). $N(t)$ is the total number of qualifying grid points at time t . The p-mean values of hydrometeor mean mass diameters (D_m) for the time periods P1 and P2 are listed in Table 6.2 for the five CCN sensitivity simulations.

$$\bar{C}^p = \frac{1}{\Delta T} \sum_{t=1}^{\Delta T} \bar{C}^D(t) \quad (6.1)$$

$$\bar{C}^D(t) = \frac{1}{N(t)} \sum_{r \geq r_{min}, N_t \geq N_{tmin}} c(x, y, z, t) \quad (6.2)$$

In both the pre-supercell and supercell phases, increases in CCN lead to decreases in the sizes and increases in the number concentrations of cloud (first cloud mode, simply cloud hereafter) droplets (Figs. 6.6a and 6.8a; Table 6.2) in agreement with both observational studies (Squires 1956; Warner 1968; Twomey 1977; Albrecht 1989; Rosenfeld and Lensky 1998; Rosenfeld 2000; Andreae et al. 2004) and modeling studies (Khain et al. 1999, 2005; Khain and Pokrovsky 2004; Lynn et al. 2005; van den Heever et al. 2006; Fan et al. 2007) of aerosol effects on clouds. During period P1, the average r (Fig. 6.5) and N_t values (Fig. 6.6) of all hydrometeors in all five simulations are generally less than during period P2 (Figs. 6.7 and 6.8, respectively), with the exception of the graupel and hail mass contents (r_g and r_h , respectively) (Figs. 6.5g,h and 6.7g,h). Greater quantities of hydrometeors during the supercell phase are expected owing to larger mass fluxes into the storm associated with both stronger updrafts (Fig. 6.3) and increased updraft

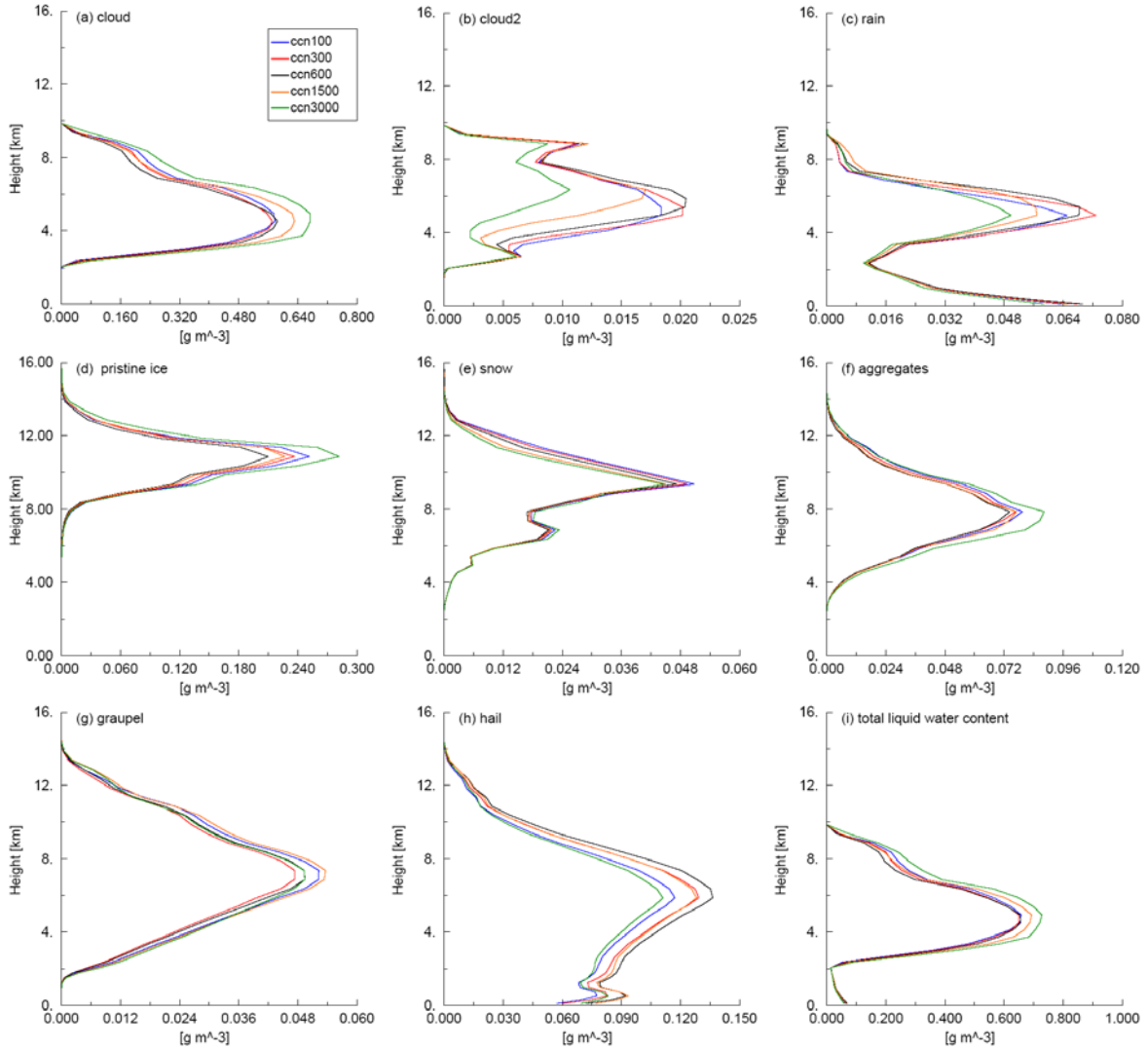


Figure 6.5: Time-averaged vertical profiles of horizontally-averaged water content [g m^{-3}] for (a-h) individual hydrometeor species and (i) total liquid water content prior to supercell phase of simulated storms ($t < 90$ min) for the CCN sensitivity cases listed in Table 6.1. Temporal averaging has a 5 min frequency from $t = 30$ to 90 min and spatial averaging was performed horizontally for all grid points where species mixing ratios were greater than 0 g m^{-3} .

volumes (c.f. Fig. 5.10a,d). The similar average profiles of r_g and r_h for periods P1 and P2 are mainly due to the tendency of the model to rapidly generate large mixing ratios of these quantities with the onset of pristine ice and snow formation during the initial convective pulse associated with the warm bubble. Following this initial pulse, graupel and hail mixing ratios assume more physically realistic values, though the effects of the warm bubble convection linger

slightly beyond 30 minutes until secondary convection forced by low-level convergence begins to dominate.

The average vertical profiles for r and N_i values of cloud2, rain, pristine ice, aggregates, graupel, and hail, as well as the cloud mass and liquid water contents, respond in a non-monotonic manner as increases in CCN from 100 to 3000 cc^{-1} both prior to and during the supercell phase (Figs. 6.5-6.8). This result agrees with recent investigations that find non-monotonic aerosol effects on hydrometeor fields in deep convection over continents (Phillips et al. 2002; Fan et al. 2007; Tao et al. 2007; Li et al. 2008; Khain and Lynn 2009; Noppel et al. 2010; Khain et al. 2011; Lim et al. 2011). However, direct comparisons of the responses of individual hydrometeor species between the current investigation and previous sensitivity studies may not be very meaningful mainly due to the fact that the numbers and types of categories represented vary among the different models (i.e., snow vs. both snow and aggregates, graupel/hail vs. separate graupel and hail species). Nonetheless, most of the studies that reported non-monotonic responses in hydrometeors to increases in CCN noted that a threshold value of CCN (i.e., a tipping point) seems to exist above which the sign of the response changes or the sensitivity to CCN becomes insignificant (Wang 2005; Fan et al. 2007; Li et al. 2008; Carrió et al. 2010; Carrió and Cotton 2011; Khain et al. 2011).

In the current simulations, increases of CCN from 100 to 600 cc^{-1} lead to decreases in the average mass contents of cloud (r_c) and liquid water (panels a and i, respectively, in Figs. 6.5 and 6.7) whereas increases of CCN from 600 to 3000 cc^{-1} result in the opposite response. This result differs from the increases in r_c and LWC with increasing CCN reported for simulations of isolated continental deep convection with bin microphysics (Khain and Pokrovsky 2004) and supercells with two-moment bulk microphysics (Lim et al. 2011). Khain and Lynn (2009), on the

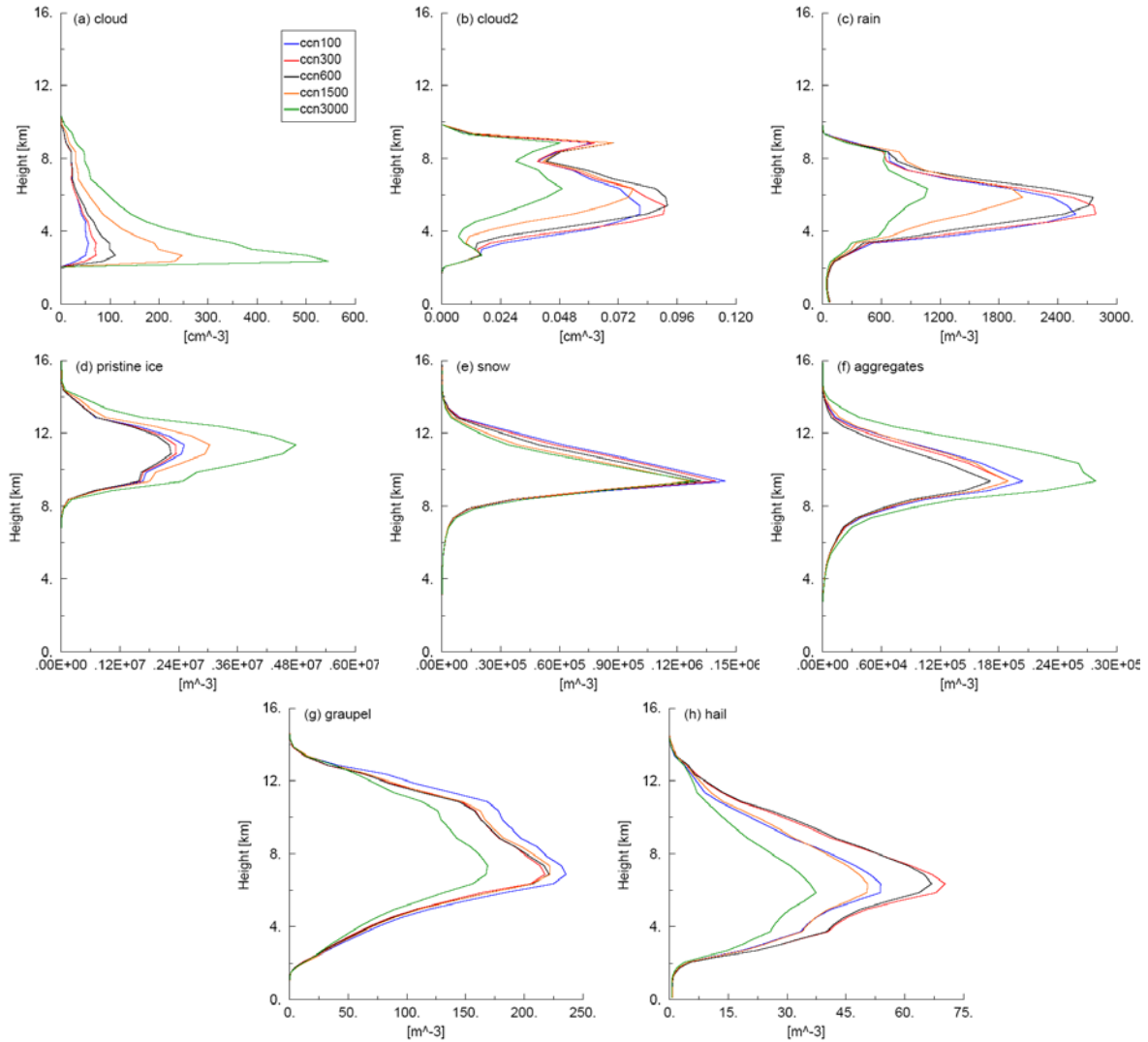


Figure 6.6: Time-averaged vertical profiles of horizontally averaged number concentrations for individual hydrometeor species [cm^{-3} for cloud particles; m^{-3} all other species] prior to supercell phase of simulated storms ($t < 90$ min) for the CCN sensitivity cases listed in Table 6.1. Temporal averaging has a 5 min frequency from $t = 30$ to 90 min and spatial averaging was performed horizontally for all grid points where species number concentrations were greater than 0 m^{-3} .

other hand, noted a non-monotonic response in LWC to increases in CCN for supercell simulations using bin microphysics, although their study also found a general increase in domain-averaged r_c with enhanced values of CCN. The reductions in both r_c and LWC in the ccn600 case relative to all other cases (Figs. 6.5a,i and 6.7a,i) are due primarily to increased conversion of cloud to rain via interactions with the cloud2 mode particles as will be shown in

Section 6.2.3. The profiles of average mass content and number concentrations of cloud2 (r_{c2} and N_{ic2} , respectively) (panels b in Figs 6.5-6.8) reveal a monotonic decrease below about 4 km with increasing CCN, whereas the profile structures above this height show the responses to increases in CCN are mostly opposite to those for cloud and LWC . The average sizes of cloud2 droplets show almost no sensitivity to increases in CCN (Table 6.2). Cloud2 droplets develop from nucleation of GCCN, which are similar in all cases, as well as from self-collection of cloud droplets. The reduction in cloud droplet sizes with increasing CCN results in reduced collection efficiencies between cloud droplets (Pruppacher and Klett 1997; Andreae et al. 2004) and leads to decreases in both r_{c2} and N_{ic2} below roughly 4 km. At greater heights, smaller r_{c2} and N_{ic2} magnitudes in the ccn100 and ccn300 cases relative to ccn600 are largely due to more efficient conversion of cloud2 droplets to rain via collisions with cloud droplets in the former cases. Smaller r_{c2} and N_{ic2} values in the ccn1500 and ccn3000 cases relative to ccn600 can be attributed to reduced production of cloud2 droplets via self-collection of cloud droplets in the higher CCN cases owing to the smaller sizes of cloud particles.

Table 6.2: Population mean (p-mean) values of hydrometeor mean mass diameters [μm for cloud, cloud2 and pristine ice, all others in mm] for simulation time periods of 30 to 90 minutes (P1) and 90 to 150 minutes (P2, bold).

Hydrometeor	ccn100		ccn300		ccn600		ccn1500		ccn3000	
	P1	P2	P1	P2	P1	P2	P1	P2	P1	P2
cloud [μm]	26.1	27.0	25.3	26.5	24.3	25.3	22.0	22.3	19.2	19.3
cloud2 [μm]	80.9	80.4	80.7	80.4	80.6	80.5	79.9	80.0	79.4	79.4
pristine ice [μm]	80.9	78.7	81.2	79.2	80.8	78.4	79.0	77.4	76.4	74.5
rain	0.63	0.62	0.63	0.62	0.63	0.62	0.64	0.63	0.65	0.65
snow	0.3	0.23	0.3	0.22	0.3	0.23	0.3	0.23	0.3	0.22
aggregates	0.5	0.39	0.49	0.38	0.49	0.39	0.49	0.38	0.49	0.35
graupel	1.1	1.03	1.11	1.03	1.13	1.06	1.15	1.1	1.2	1.13
hail	2.57	2.7	2.57	2.65	2.57	2.69	2.62	2.78	2.62	2.84

The average mass contents and number concentrations of pristine ice (r_p and N_{ip} , respectively) (panel d in Figs. 6.5-6.8) and aggregates (r_a and N_{ia} , respectively) (panel f in Figs. 6.5-6.8) respond in a similar manner to r_c and LWC . Greater values of r_p and N_{ip} in the high CCN cases (ccn1500 and ccn3000) relative to the ccn600 case likely result from increased transport of smaller cloud droplets by the updraft to the homogeneous freezing level (around 9 km in these simulations) (Rosenfeld and Woodley 2000; Khain et al. 2004; Carrió et al. 2007, 2010; Fan et al. 2007). At the same time, supersaturation values within the updraft aloft tend to increase as the number concentrations of cloud droplets (N_{ic}) decrease owing to reduced competition among the droplets for the available water vapor (Pinsky and Khain 2002; Fan et al. 2007). Thus at low values of CCN, higher supersaturations associated with the reduction in N_{ic} at sub-freezing temperatures in the ccn100 and ccn300 cases result in the nucleation of greater numbers of ice crystals (Meyers et al. 1992) compared to the ccn600 case. The mean sizes of pristine ice crystals tend to decrease slightly with increasing CCN in qualitative agreement with Khain and Pokrovsky (2004), Lerach et al. (2008), and (Carrió et al. 2010), particularly for CCN values greater than 300 cc^{-1} , owing to decreases in mean cloud droplet sizes (Table 6.2). In the RAMS model, self-collection of pristine ice and collisions between pristine ice and snow are the primary mechanisms leading to aggregate formation. Thus as CCN values increase, the tendencies in the average profiles of r_a and N_{ia} , as well as in the p-mean $D_{\bar{m}a}$ values (Table 6.2), tend to follow those for r_p , N_{ip} , and $D_{\bar{m}p}$, respectively.

The average mass contents and number concentrations of snow (r_s and N_{is} , respectively) generally exhibit a monotonic decrease with increasing CCN (panel e in Figs. 6.5-6.8) whereas mean snow particle sizes seem to be insensitive to changes in CCN (Table 6.2). Decreases in average r_s and N_{is} with increasing CCN seen in the current work are in contrast to results of

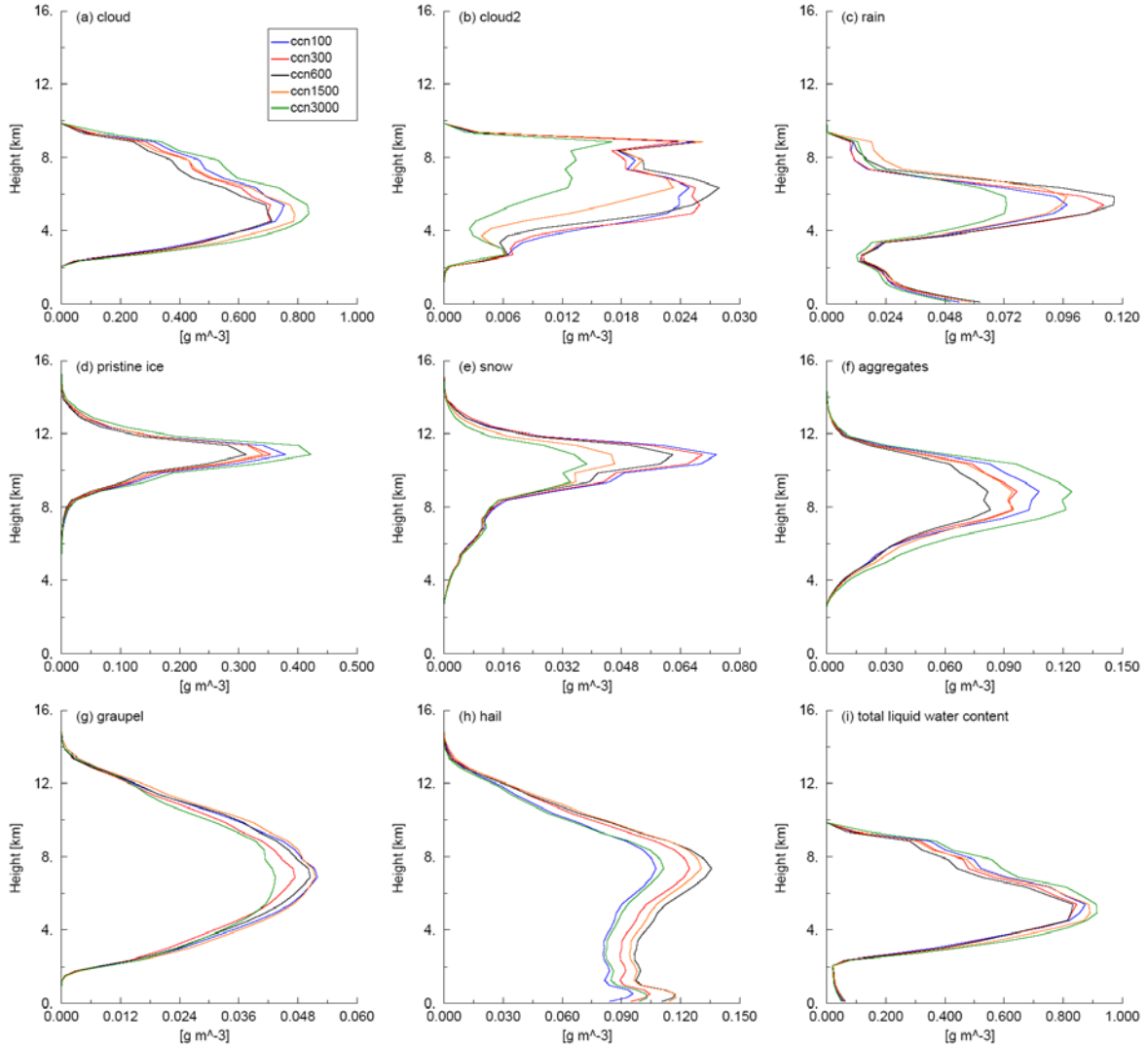


Figure 6.7: As in Fig. 6.5 except for first hour of supercell phase of simulated storms ($t = 90$ to 150 min).

Khain and Lynn (2009) and Lim et al. (2011) who also examined the sensitivity of supercells to changes in CCN, although the microphysics schemes in those studies did not have separate snow and aggregate species. Interestingly, simulations of a multicell hailstorm by Khain et al. 2011 using essentially the same model as in Khain and Lynn (2009) noted a decrease in snow mass content with increasing CCN, similar to the results presented here. Increasingly smaller magnitudes of r_s and N_{ts} , with increasing CCN are related to smaller depositional growth rates of pristine ice to form snow particles at lower supersaturations (Fan et al. 2007; Khain et al. 2011).

Thus, for cases with low (high) CCN, greater (lower) supersaturation values lead to enhanced (reduced) depositional growth of pristine ice to snow as well as enhanced (reduced) depositional growth rates of snow.

Responses in the average mass contents and number concentrations of rain (r_r , N_{rr}) and hail (r_h , N_{rh}) (panels c and h, respectively, in Figs. 6.5-6.8) to increases in CCN are opposite to those for pristine ice and aggregates, showing a general increase with increasing CCN up to 600 cc^{-1} . Further increases in CCN lead to decreases in the quantities of rain and hail, although average hail number concentrations attain maximum values in the ccn300 case. For increases in CCN beyond 600 cc^{-1} , a slight increase in the p-mean values of $D_{\overline{mr}}$ occurs whereas the increase in $D_{\overline{mh}}$ is much more significant (Table 6.2). Increases in raindrop and hail diameters with increasing CCN were also reported in the hailstorm simulations of Khain et al. (2011) and in supercell simulations performed by Storer et al. (2010) and Lim et al. (2011) (raindrops only in the Lim et al. study as hail was not represented) owing to enhanced accretion in the presence of more numerous cloud droplets. In contrast, Noppel et al. (2010) found a general decrease in hail sizes as CCN increased in simulations of the same hailstorm as Khain et al. (2011). The greater average amounts of rain in the ccn300 and ccn600 cases between roughly 4.5 and 6 km result from increased rain production via conversion of cloud and cloud2 droplets in addition to enhanced shedding of liquid drops from hail within the low-level updraft region in these cases as will be shown in Section 6.2.3. The non-monotonic response in average r_h in the current study differs from that of Khain and Lynn (2009) and Khain et al. (2011) in which increases in hail mass with increasing CCN were reported [although Khain et al. (2011) did show a non-monotonic response in surface hail precipitation with increasing CCN]. The impacts of CCN on hail will be discussed in greater detail in Section 6.2.3.

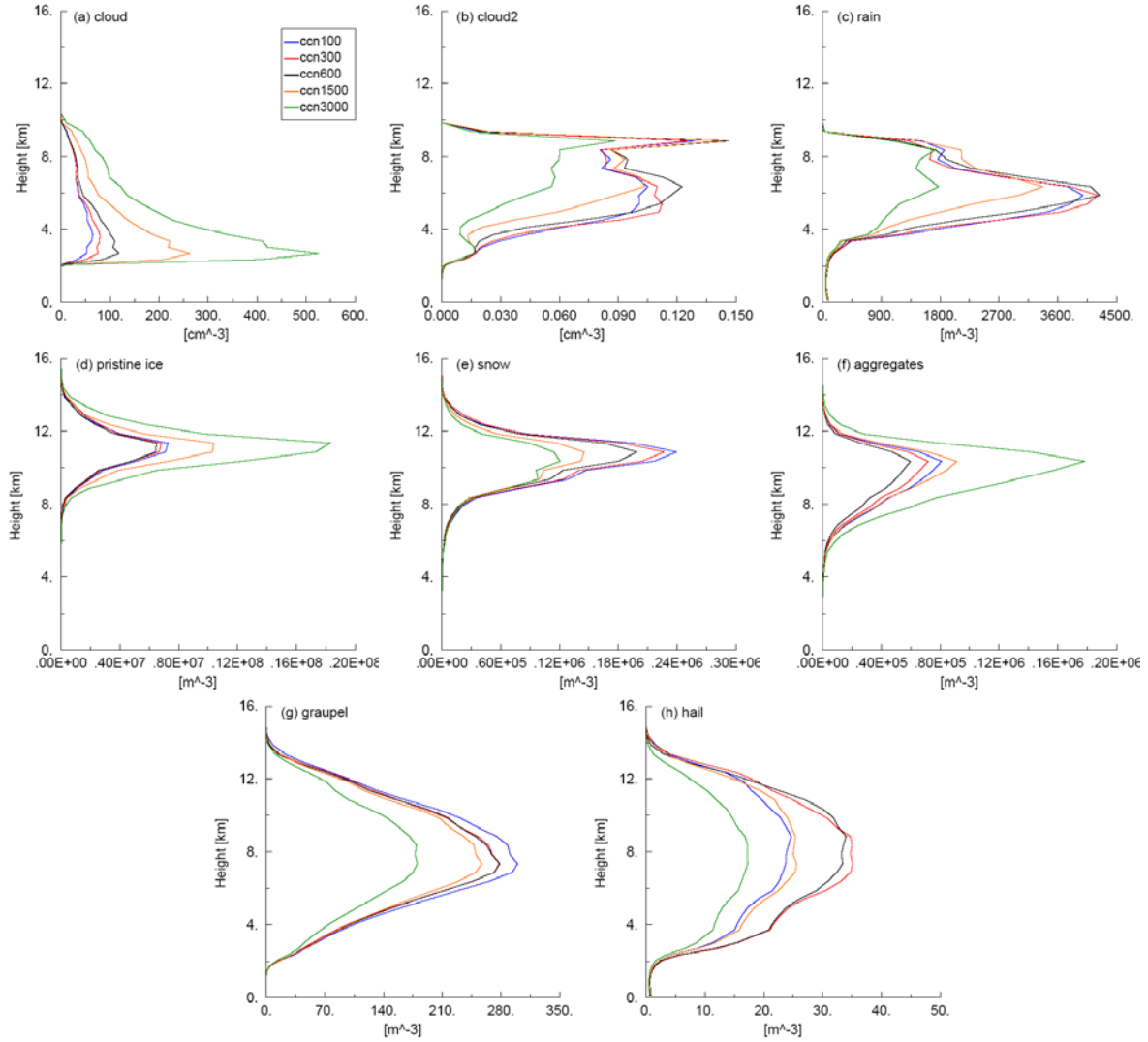


Figure 6.8: As in Fig. 6.6 except for first hour of supercell phase of simulated storms ($t = 90$ to 150 min).

The average graupel mass contents (r_g) are lowest in the ccn3000 case (Figs. 6.5g and 6.7g), however, no clear trend exists in the average profiles of r_g with respect to changes in CCN similar to the results of Khain and Lynn (2009). On the other hand, average graupel number concentrations (N_{tg}) appear to decrease monotonically with increasing CCN (Figs. 6.6g and 6.8g) and the average sizes of graupel tend to increase (Table 6.2) in qualitative agreement with results from sensitivity studies of Phillips et al. (2002), Li et al. (2008) and Lim et al. (2011). Decreases in average r_g with increasing CCN were noted in simulations of multicell convection using the

RAMS model with two-moment microphysics (van den Heever et al. 2006). It was suggested in that study that reductions in graupel were due to increased riming of graupel and subsequent conversion to hail. However, in the current simulations, smaller magnitudes of r_g and N_{ig} in the ccn3000 case are likely due to reduced graupel production resulting from reduced riming efficiencies of snow and aggregates in addition to the fact that rain-ice collisions in the 3MHAIL scheme can result in the return of the coalesced mass to the colliding ice category rather than being sent to the hail category. (Recall that rain-ice collisions ALWAYS result in hail formation in the RAMS two-moment microphysics scheme).

In general, it is clearly evident that even though the storm dynamics are not altered significantly, the impact of changes in CCN on the cloud droplet size distributions (CDS) affects both liquid and ice processes within the simulated supercells. In the next section, the impacts of varying the initial CCN on hail are examined.

6.2.3) *CCN effects on hail*

A hypothesis was recently put forth as part of the European ANTISTORM Project (Anthropogenic Aerosols Triggering and Invigorating Severe Storms) (Rosenfeld and Khain 2008) regarding the effects of aerosols on hail formation and growth. This hypothesis states that increases in aerosol concentrations (such as CCN) in deep convection leads to an increase of both hail mass and size as a result of increased amounts of supercooled water aloft (Khain et al. 2011). The hypothesis is based on the premise that increases in aerosols (CCN) correspond directly to increases in supercooled water content in the upper regions of the storm. For the simulations in the current work, however, the response in the average vertical profile of LWC (supercooled LWC above roughly 4 km) to increases in CCN is non-monotonic (Figs. 6.5i and

6.7i). Furthermore, the ccn3000 case produces the largest average amounts of supercooled water content aloft (Figs. 6.5i and 6.7i), yet this case is associated with smaller average hail mass content values compared to most of the other cases (Figs. 6.5h and 6.7h). This latter point is also evident in time series of the domain total hail mass for the five CCN sensitivity experiments which show that the ccn3000 case generally produces the smallest amount of hail mass throughout the duration of the simulation (Fig. 6.9a). Similar to the vertical profiles of hail mass content, the amounts of total hail mass exhibit a non-monotonic response to increases in CCN, with increases in total hail mass seen for increases in CCN from 100 to 600 cc^{-1} followed by decreases in total hail mass for further increases in CCN prior to 150 minutes. These results differ from those of Khain and Lynn (2009) and Khain et al. (2011) who noted increases in hail mass with increases in aerosol concentrations. *While the goal of the current work is neither to prove nor disprove the ANTISTORM hypothesis, it is noteworthy that the results of the simulations herein do not support the assertion of increased hail mass as a result of increased aerosols (CCN).*

The time series of domain total hail numbers (Fig. 6.9b) reveals a non-monotonic response to increases in CCN much like the average vertical profiles of hail number concentrations (Figs. 6.6h and 6.8h). This differs from the results of Noppel et al. (2010) who noted that the numbers of hailstones increased with increasing CCN in their simulations of a severe hailstorm in Germany. The authors attributed the greater numbers of hailstones in cases with high CCN to increased conversion of graupel to hail, with the graupel particles originating from rimed ice and snow. For the current simulations, it will be shown that the majority of hailstones are formed via rain-snow collisions, and the numbers of new hailstones tend to be limited by the numbers of raindrops. Therefore, the cases with the largest average N_{ir} values (ccn300 and ccn600; Figs. 6.6c

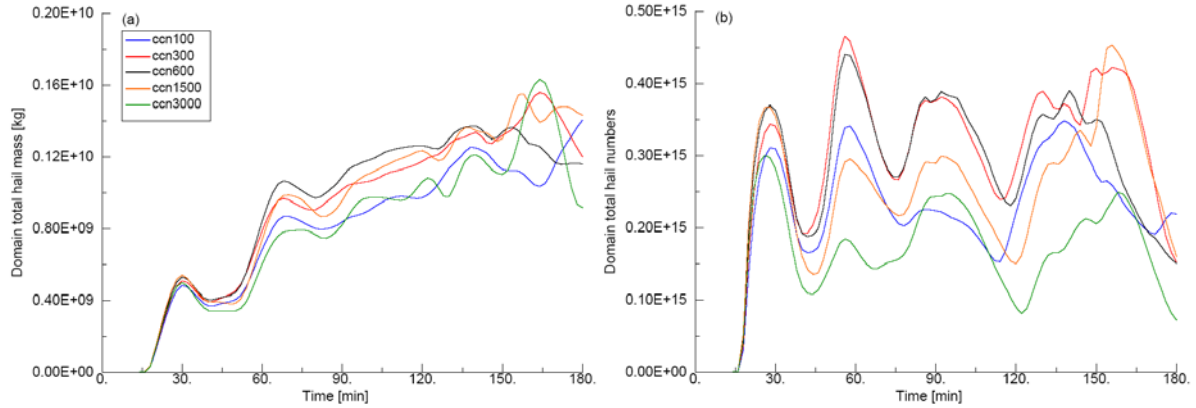


Figure 6.9: Time series of (a) domain total hail mass [kg] and (b) domain total hail numbers for the CCN sensitivity experiments listed in Table 6.1

and 6.8c) tend to produce the greatest numbers of hailstones (Fig. 6.9b), and the ccn3000 case, which is associated with the smallest average N_{lr} values (Figs. 6.6c and 6.8c), generates the fewest numbers of hailstones (Fig. 6.9b).

In contrast to the non-monotonic responses of average and total amounts of hail mass and number to increases in CCN, *increases in hail sizes and the amounts of large ($D \geq 2$ cm) and very large ($D \geq 4$ cm) hail appear to be directly related to increases in CCN*. This is demonstrated in time-height plots of domain maximum N_{1cm} , N_{2cm} , and N_{4cm} , as well as the fractional amounts of total hail mass corresponding to hailstones with diameters of at least 1, 2, and 4 cm for cases ccn100, ccn600, and ccn3000 (Figs. 6.10-6.12). Similar plots for cases ccn300 and ccn1500 reveal a continuum in the fields plotted in Figures 6.10-6.12 as CCN increases from 100 to 3000 cc^{-1} and are thus omitted for brevity. It is evident that large and very large hail is produced in all cases, yet as CCN increases, the maximum amounts of hail having diameters of at least 1, 2, and 4 cm increase accordingly (left columns of Figs. 6.10-6.12). Furthermore, increases in CCN result in a shift of the total hail mass towards larger sizes as apparent in the greater fractional amounts of hail mass associated with 1, 2, and 4 cm diameter hailstones with increasing values of CCN (right columns in Figs. 6.10-6.12). These results agree

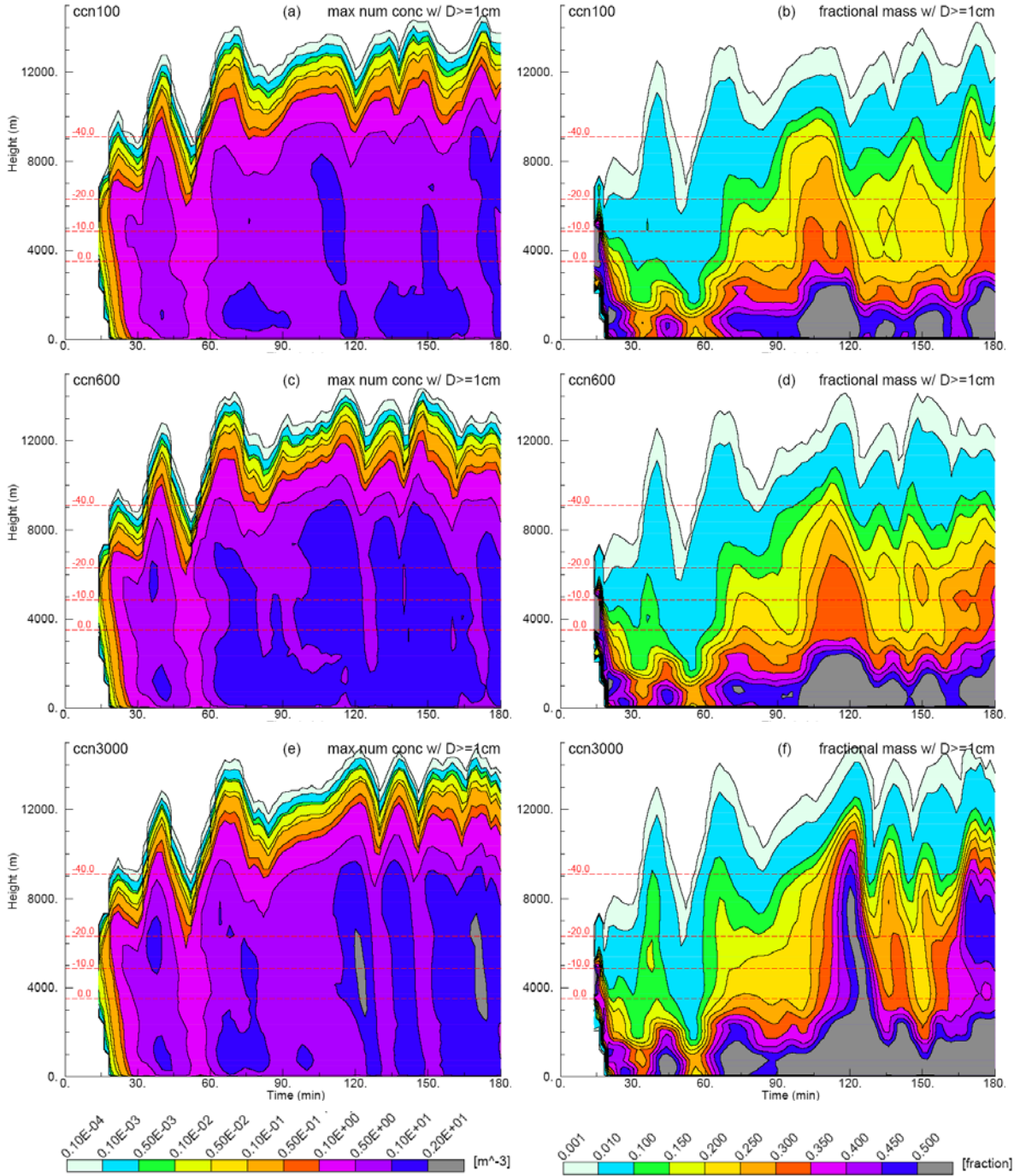


Figure 6.10: Time-height contours of domain maximum N_{1cm} [m^{-3}] (left column) for cases (a) ccn100, (c) ccn600, and (e) ccn3000, and fractional amounts of total hail mass with diameters of at least 1 cm (right column) for cases (b) ccn100, (d) ccn600, and (e) ccn3000. Red dashed lines depict approximate heights of 0, -10, -20, and -40 °C isotherms.

qualitatively with findings by Khain et al. (2011) with respect to increases in hail size for increases in CCN. On the other hand, Noppel et al. (2010) generally observed lower maximum

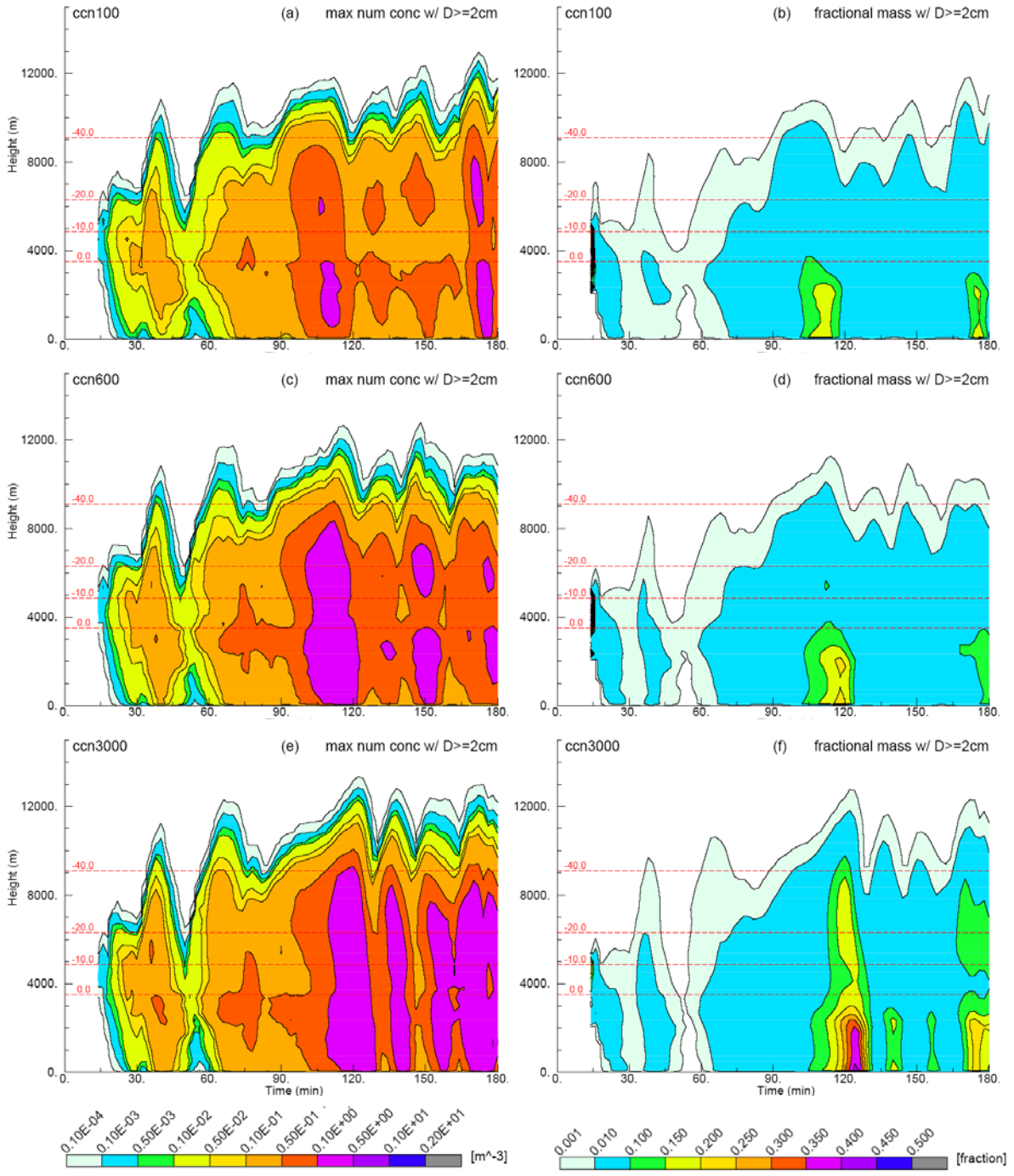


Figure 6.11: As in Fig. 6.10, except for N_{2cm} (left column) and diameters of at least 2 cm (right column).

number concentrations of hailstones with diameters ≥ 2.5 cm at low levels in their simulations with higher values of CCN, thus it is expected that a similar trend of decreasing amounts of large hail with increasing CCN occurred aloft in that study. However, the results of Noppel et al.

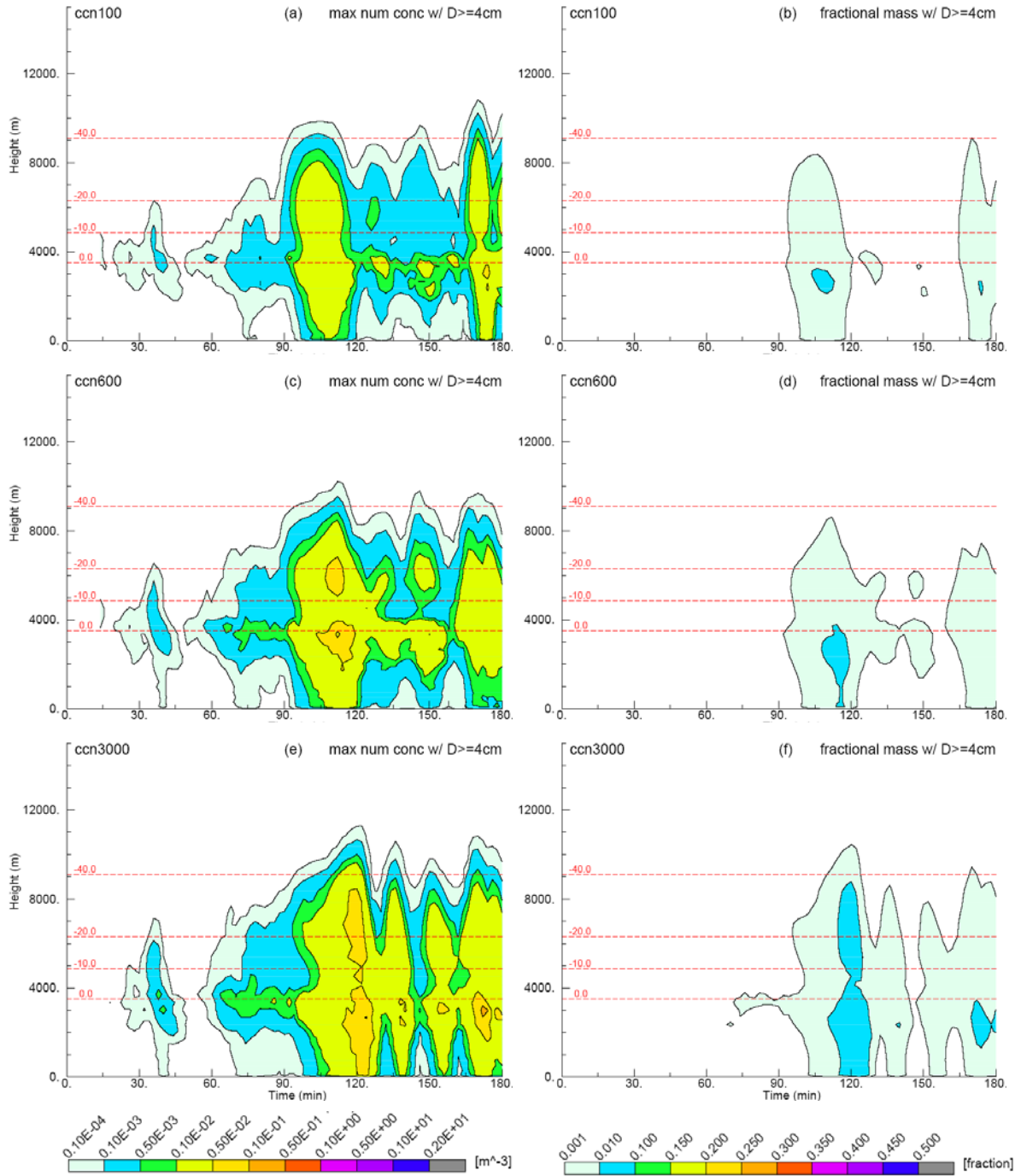


Figure 6.12: As in Fig. 6.10, except for N_{4cm} (left column) and diameters of at least 4 cm (right column).

(2010) also revealed an increase in maximum number concentrations of large hail at low levels for increasing CCN in cases for which the CSDs were narrower and comprised of smaller droplets. The CSDs in the current simulations are also narrow ($\nu_c = 4.0$), and thus, as CCN

increases and the droplets become smaller, the increase in maximum number concentrations of large hail seen at low levels as well as aloft is qualitatively similar to that reported by Noppel et al. (2010).

What causes the increase in hail size and amounts of large hail with increases in CCN? To answer this question, analyses of hail formation and growth processes are performed for the five CCN sensitivity experiments. Figures 6.13 and 6.14 show the time-averaged vertical profiles of the total hail mass and number production rates for the individual and combined processes leading to hail formation during the quasi-steady supercell phase ($t = 90$ to 150 min) of the simulated storms. Plots of these profiles for the time period $t = 30$ to 90 minutes show similar trends to those in Figures 6.13 and 6.14, albeit the magnitudes are generally smaller, and are thus not included here for brevity. In actuality, the model microphysics module is only concerned with the net changes in hail mass and number as a result of the combined hail formation processes, though it is important to understand how the individual formation processes contribute to the net changes.

In all cases, it is apparent that rain-snow ($r-s$) collisions are responsible for the majority of new hail mass production between about 4 and 8 km (Fig. 6.13b) and account for the greatest production of new hail numbers throughout the depth of the storms (6.14b). Collisions between rain and pristine ice ($r-p$) are the second biggest generator of new hail mass between roughly 4 and 8 km and are responsible the greatest production of new hail mass above about 8 km (Fig. 6.13a). The largest producers of new hail numbers behind $r-s$ collisions seem to be rain-aggregate ($r-a$) collisions (Fig. 6.14c) and riming of graupel ($g-c$) (Fig. 6.14e). New hail mass generated by riming of graupel (6.13e) is about an order of magnitude less than that produced by $r-s$ and $r-p$ collisions. On the other hand, the amounts of new hail mass and numbers generated

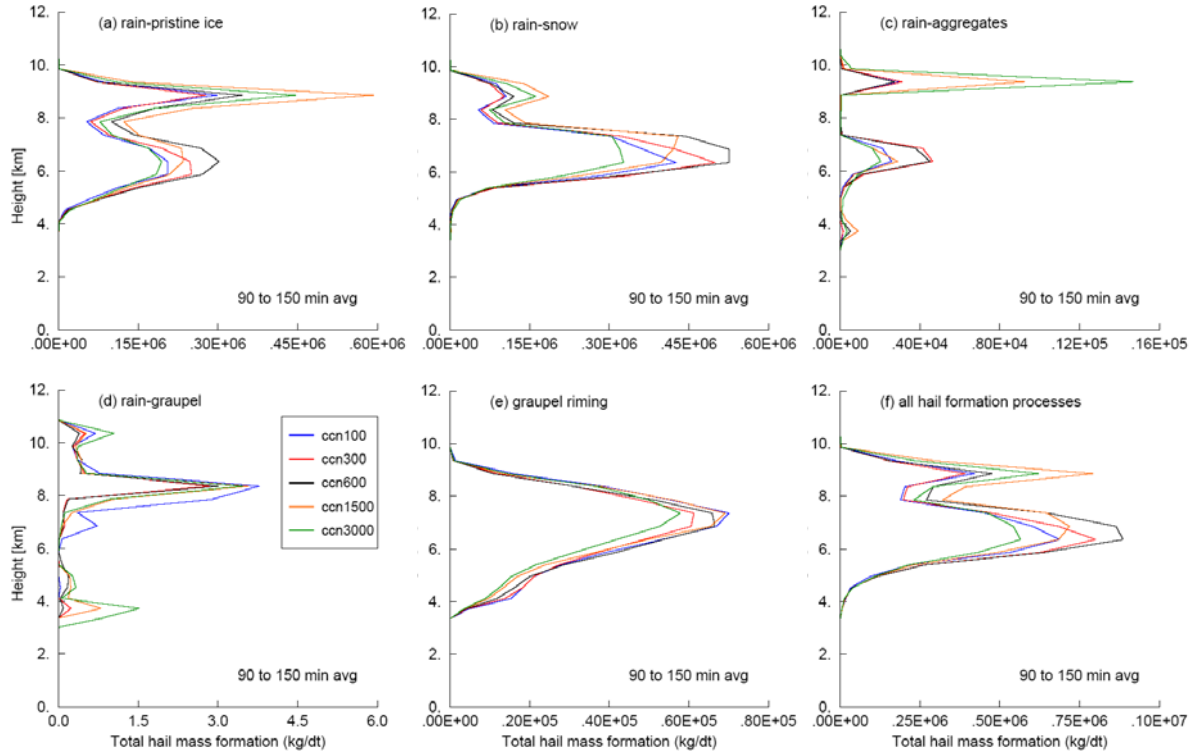


Figure 6.13: Temporally-averaged vertical profiles of domain total hail mass formation [$\text{kg } \Delta t^{-1}$] resulting from collisions between (a) rain-pristine ice, (b) rain-snow, (c) rain-aggregates, and (d) rain-graupel, as well as from (e) riming of graupel, and (f) all hail formation processes combined during first hour of supercell phase of simulated storms ($t = 90$ to 150 min) for the aerosol sensitivity cases listed in Table 6.1. Time averaging has a 2 minute frequency.

by collisions between rain and graupel ($r-g$) (Figs. 6.13d and 6.14d) are very small compared to all other processes leading to new hail generation. The relatively small amounts of new hail mass generated from $r-a$ and $r-g$ collisions are mainly due to the fact that these particles are generally larger than snow particles (Table 6.2) and can thus collect small raindrops without being converted to hail as discussed in Chapter 3.3.3.1. As the number concentrations of aggregates are roughly 3 to 4 orders of magnitude larger than those of graupel (Fig. 6.8), collisions between rain and aggregates lead to significantly greater numbers of new hailstones compared to $r-g$ collisions. It should be noted that hail particles produced at heights greater than about 8 km are generally much smaller than those produced at lower heights and tend to be lofted by the updraft into the anvil region of the storms (e.g., Fig. 6.19). In addition, sharp decreases in LWC with

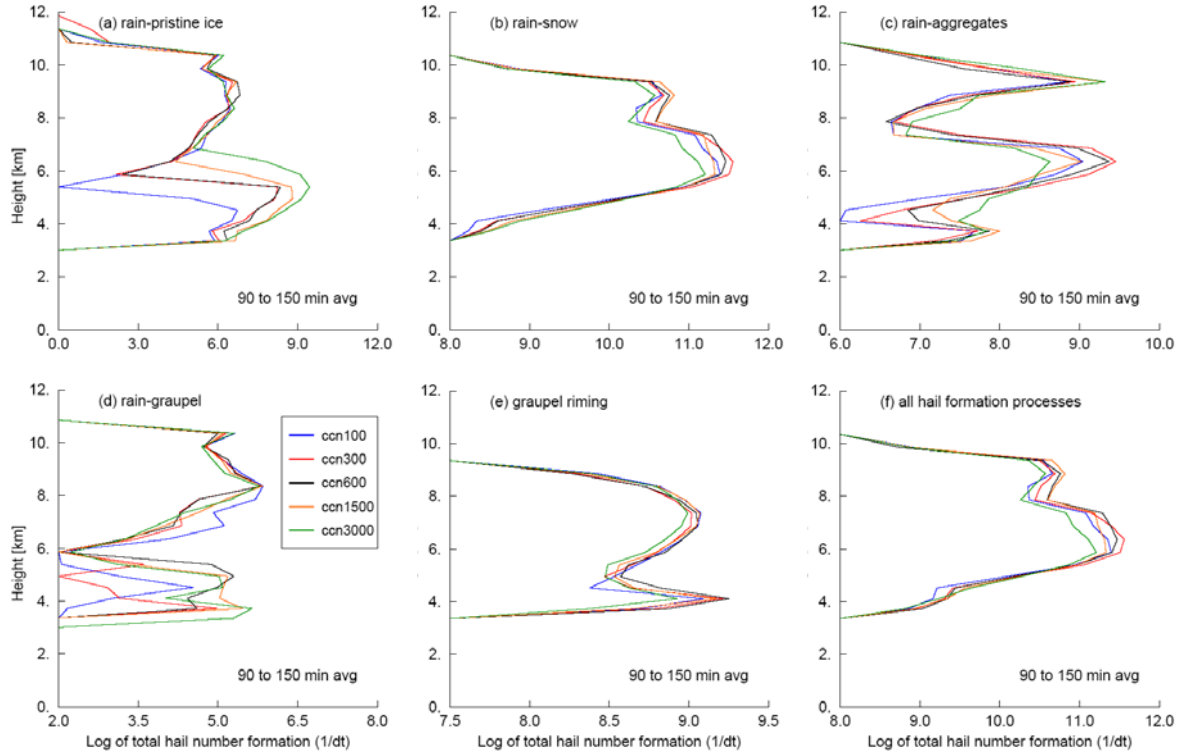


Figure 6.14: As in Fig. 6.13 except for domain total hail number formation $[\Delta t^{-1}]$ on a logarithmic scale.

height above roughly 9 km in all cases (Fig. 6.7i) tend to inhibit substantial hail growth compared to hail forming at lower heights. Thus, the primary hail formation region out of which large hailstones are produced extends from roughly 4 to 8 km and the remainder of this discussion will mainly focus on the generation of hail at heights ≤ 8 km.

As the numbers of snow and aggregate particles tend to be much larger than those of raindrops (Fig. 6.8), the generation of hail via collisions between these ice particles and raindrops is generally limited by the numbers of raindrops in the mixed-phase region of the storm. Thus, when considering the effects of CCN on hail generation, the time-averaged profiles of new hail mass and numbers from $r-s$ and $r-a$ collisions (Figs. 6.13b,c and 6.14b,c) tend to exhibit the same non-monotonic responses as for the time-averaged profiles of r_r and N_{lr} (Figs. 6.7c and 6.8c). In particular, production of new hail mass and numbers from $r-s$ and $r-a$

collisions tend to be maximized (minimized) for CCN values around 300 to 600 cc^{-1} (3000 cc^{-1}) (Figs. 6.13b,c and 6.14b,c). The exception here is the monotonic decrease in the generation of new hail numbers by r - a collisions with decreasing CCN below about 5 km (Fig. 6.14c), though the mass associated with these new hail particles is small compared to that of hail particles forming at higher levels (Fig. 6.13c). The sizes of newly formed hailstones from r - s and r - a collisions tend to increase with increasing CCN as evident from the values of both p-mean $D_{\bar{m}h, new}$ (Table 6.3) and p-mean maximum $D_{\bar{m}h, new}$ (Table 6.4). Thus, while r - s and r - a collisions generate greater numbers of hail particles in ccn600 case compared to ccn100, the newly formed hailstones in the former case are larger on average than in the latter case. The ccn3000 case is associated with the fewest yet largest new hailstones formed from r - s and r - a collisions, whereas the ccn300 case produces the most numerous and smallest hailstones via these interactions (Fig. 6.14b,c; Tables 6.3 and 6.4).

The time-averaged profiles of new hail mass forming via r - p collisions (Fig. 6.13a) tend to exhibit the same non-monotonic responses to increases in CCN as for the time-averaged profiles of r_r (Fig. 6.7c), similar to r - s and r - a collisions. However, the numbers of newly formed

Table 6.3: P-mean values of mean mass diameters of newly formed hail [$D_{\bar{m}h, new}$ mm] resulting from collisions between rain-pristine ice (r-p), rain-snow (r-p), rain-aggregates (r-a), rain-graupel (r-g), riming of graupel (g-c), and all hail formation processes combined (all) for simulation time periods of 30 to 90 minutes (P1) and 90 to 150 minutes (P2, bold).

Experiment	r-p		r-s		r-a		r-g		g-c		all	
	P1	P2										
ccn100	1.22	1.27	1.34	1.7	1.28	1.34	1.78	1.97	3.01	3.56	1.34	1.72
ccn300	1.25	1.21	1.26	1.57	1.27	1.34	1.74	1.95	3.0	3.0	1.26	1.61
ccn600	1.31	1.4	1.3	1.7	1.28	1.42	1.78	2.07	3.14	2.98	1.3	1.72
ccn1500	1.34	1.64	1.35	1.81	1.28	1.51	1.86	2.25	3.51	2.76	1.35	1.83
ccn3000	1.46	1.82	1.38	1.97	1.3	1.59	1.97	2.19	2.71	2.74	1.36	1.95

Table 6.4: As in Table 6.3 except for p-mean values of maximum mean mass diameters of newly formed hail [mm].

Experiment	r-p		r-s		r-a		r-g		g-c		all	
	P1	P2										
ccn100	2.18	2.34	3.97	5.5	2.84	3.0	3.03	3.68	3.77	4.72	3.78	5.14
ccn300	2.19	2.21	3.8	5.29	2.85	3.13	2.9	3.63	4.03	5.05	3.64	4.96
ccn600	2.3	2.46	3.95	5.66	2.93	3.32	2.98	3.82	3.99	5.2	3.78	5.31
ccn1500	2.4	2.87	4.05	6.11	2.95	3.47	3.16	4.34	3.77	4.79	3.87	5.71
ccn3000	2.71	3.3	4.08	6.3	3.1	3.81	3.46	4.33	3.61	4.48	3.92	5.91

hailstones resulting from r - p collisions below about 7 km increase monotonically, and peak values of hail number production are shifted to higher altitudes with increasing CCN, whereas no discernible trend in the profile is evident above 7 km (Fig. 6.14a). Below 7 km, increases in the numbers of new hail particles generated via r - p collisions as CCN increases from 100 to 600 cc^{-1} follow from the fact that the average N_{tr} values below 7 km tend to increase with increasing CCN up to 600 cc^{-1} (Fig. 6.8c). As CCN increases further, the average values of N_{tr} below 7 km decrease (Fig. 6.8c), yet the average values of N_{tp} increase at a much faster rate than the decrease in N_{tr} thereby increasing the probability that raindrops will collide with ice crystals and freeze. It was shown in Chapter 3.3.3.2 that as N_{tp} values increase, the threshold diameter for raindrops that will collect more than one ice crystal per time step decreases, thus greater numbers of raindrops will undergo collisions with ice crystals. In addition, average raindrop sizes increase slightly as CCN increases above 600 cc^{-1} (Table 6.2), and as such, the raindrops are able to coalesce more ice crystal mass during the heterogeneous freezing process. Thus, not only are more hailstones produced for higher CCN values, but the sizes of these newly formed particles are generally larger than those formed under conditions of lower CCN values (Tables 6.3 and 6.4).

The profiles of time-averaged hail mass production rates for riming of graupel (Fig. 6.13e) generally follow the time-averaged profiles of average r_g (Fig. 6.7g) with respect to variations in CCN, and thus, no clear trend exists in the amounts of new hail mass generated as CCN increases. And unlike the monotonic decrease in average N_{tg} values with increasing CCN (Fig. 6.8g), the impact of CCN on the generation of new hail numbers via riming of graupel appears to be minimal at best as evident by the similar structures and magnitudes of the profiles in Figure 6.14e. The numbers of new hailstones from riming of graupel are lowest in the ccn3000 case given that this case produces the fewest numbers of graupel particles (Fig. 6.8g) in addition to a reduction in graupel riming efficiencies as a result of smaller cloud droplet sizes at high CCN (Carrió et al. 2010). Also of note is the spike in hail number formation from riming graupel around 4 km (Fig. 6.14e). This feature is associated primarily with small graupel particles falling within the forward flank region of the storm, and as they approach the melting level, their temperatures warm to near 0 °C such that even minimal riming causes a transfer to the hail category (e.g. Fig. 6.19). Interestingly, as CCN increases, the average sizes of newly formed hailstones from riming of graupel decrease (Table 6.3) even though the average sizes of graupel particles themselves tend to increase (Table 6.2).

The profiles of average hail production via $r-g$ collisions reveal a somewhat chaotic response to changes in CCN (Figs. 6.13d and 6.14d), though there is some evidence that hail production is maximized at mid-levels in the ccn100 case and near the freezing level in cases ccn1500 and ccn3000. Similar to the other rain-ice collisions leading to hail, the values of p-mean $D_{\bar{m}h,new}$ and p-mean maximum $D_{\bar{m}h,new}$ for $r-g$ collisions increase with increasing CCN (Tables 6.3 and 6.4). However, the contribution to net hail generation from $r-g$ collisions is extremely small

(accounting for less than 0.0005% of total hail number and mass production in all cases) and therefore has a negligible impact on new hail formation overall.

An examination of the time-averaged profiles of total hail mass and number generation for the combined formation processes (Figs. 6.13f and 6.14f) clearly points to the fact that r - s collisions dominate hail production within the primary hail formation zone (between roughly 4 and 8 km for these simulations). Trends in the values of p-mean $D_{\bar{m}h,new}$ and p-mean maximum $D_{\bar{m}h,new}$ for the combined hail formation processes are consistent with those for hail generation from r - s collisions, namely that increases in CCN generally lead to newly formed hailstones that are larger (Tables 6.3 and 6.4). *The main results of these analyses are that increases in CCN result in a non-monotonic response in hail formation, with fewer new hailstones generated at both low (100 cc^{-1}) and high (1500 - 3000 cc^{-1}) CCN, and a general increase in the sizes of newly created hailstones.* The relative minimum in the values of p-mean $D_{\bar{m}h,new}$ and p-mean maximum $D_{\bar{m}h,new}$ for the ccn300 case is likely due to the fact that this case produces the greatest numbers of new hailstones ($D_{\bar{m}h,new} \propto 1/N_{th,new}$), although this case ultimately produces greater amounts of large hail at the surface than in ccn100 as will be shown in Section 6.2.4. Having established the general effects of CCN on hail formation, the next step is to examine the impacts of CCN on hail growth.

Time-height plots of the spatially-averaged total hail mass growth rates are displayed in Figure 6.15 for the five CCN sensitivity experiments. Similar plots for cloud droplet riming growth rates and rain collection rates are shown in Figures 6.16 and 6.17, respectively. Average hail growth rates due to collection of other ice particles are similar among all cases and are thus not shown. As was the case in the analyses of hail growth rates for the simulations in Chapter 5, riming by hail is the primary growth mechanism in all of the CCN sensitivity simulations. In

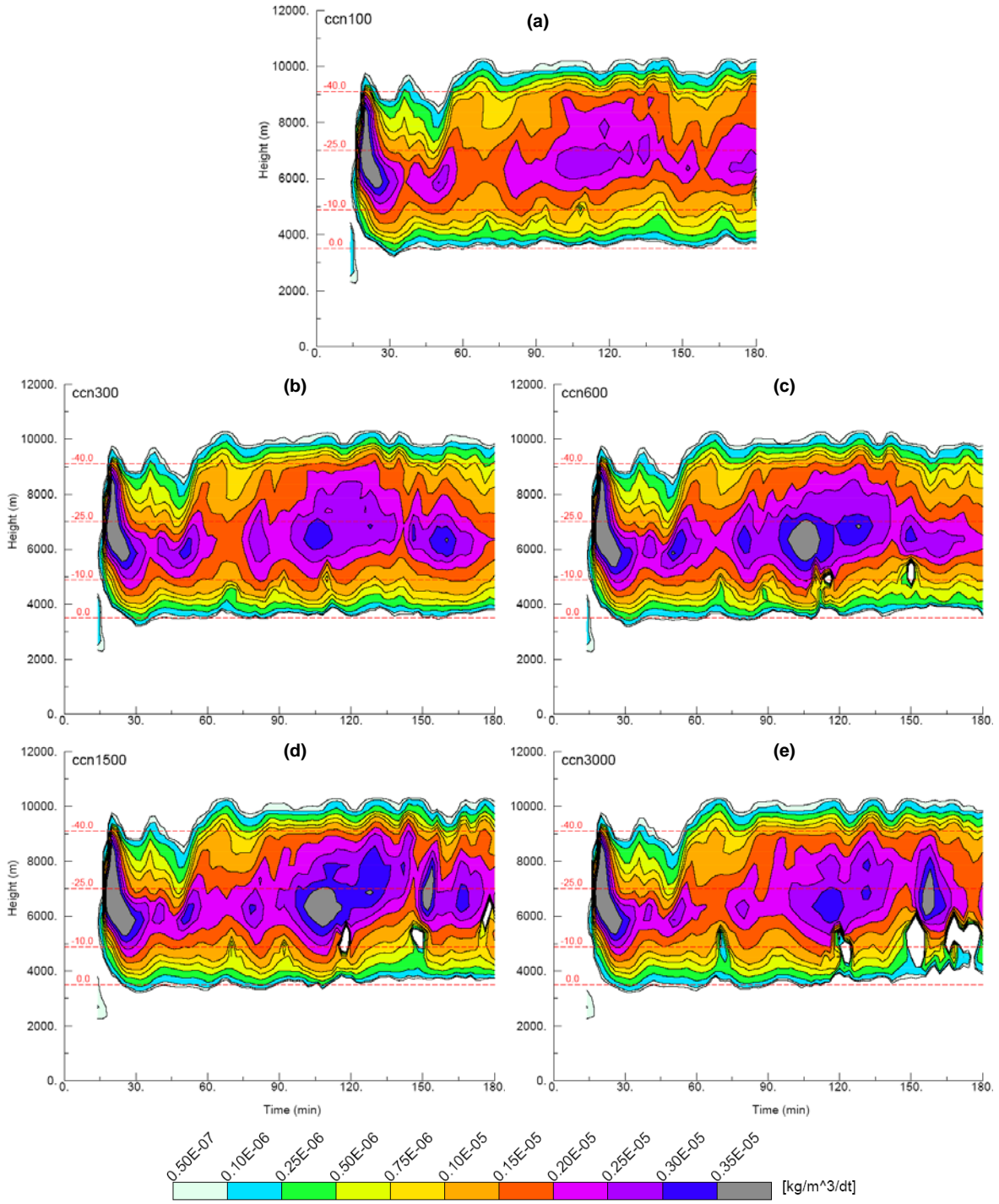


Figure 6.15: Time-height contours of spatially averaged total hail mass growth rates [$\text{kg m}^{-3} \Delta t^{-1}$] for cases (a) ccn100, (b) ccn300, (c) ccn600, (d) ccn1500, and (e) ccn3000. Red dashed lines depict approximate heights of 0, -10, -25, and -40 °C isotherms.

addition, local maxima in average riming rates (Fig. 6.16) generally occur in conjunction with increases in the amounts of large hail aloft (Figs. 6.11 and 6.12) further highlighting the

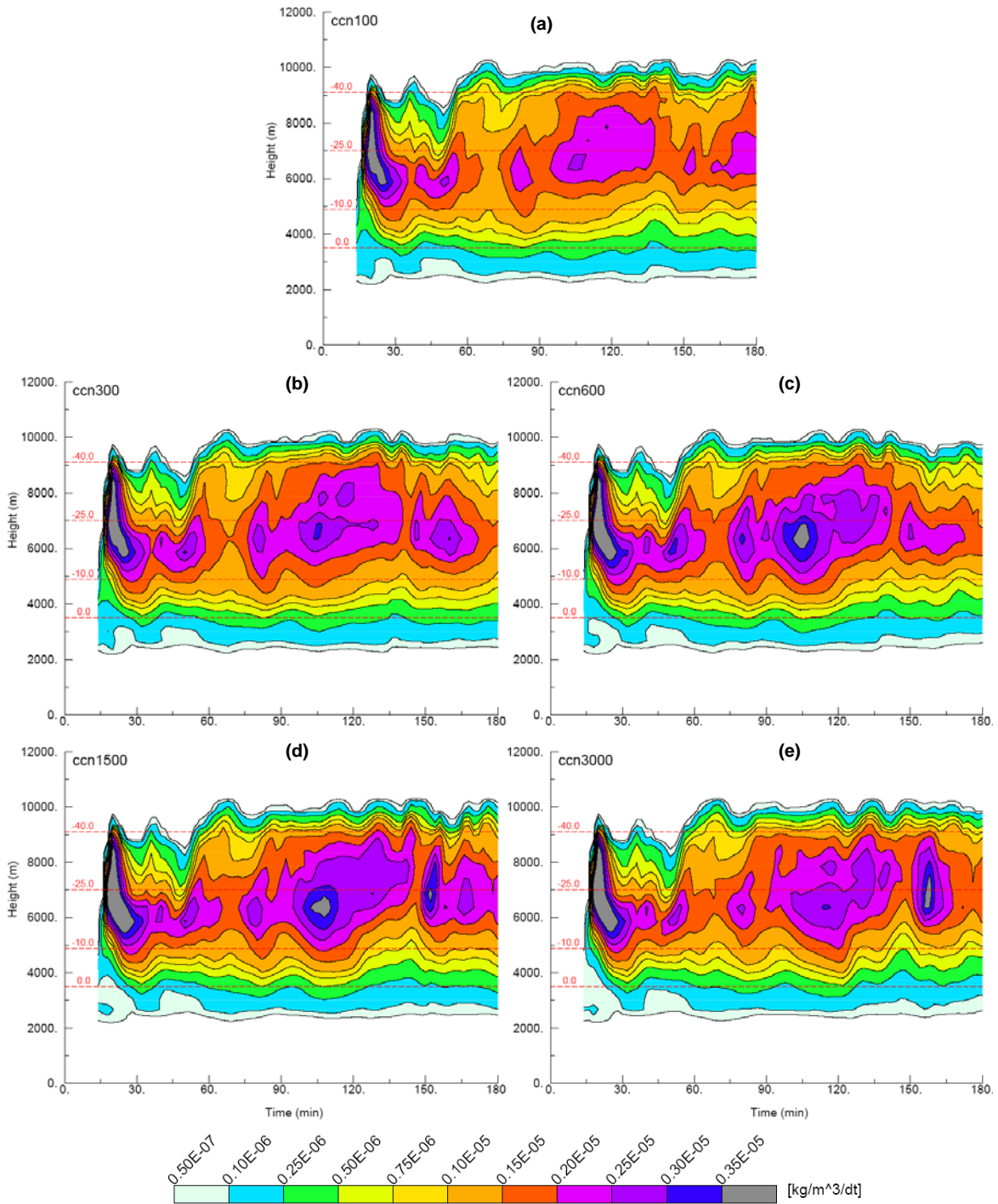


Figure 6.16: As in Fig. 6.15 except for spatially averaged riming hail mass growth rates $[\text{kg m}^{-3} \Delta t^{-1}]$.

importance of riming in the growth of hail to large sizes. As CCN increases from 100 to 1500 cc^{-1} , the maximum magnitudes of total (Fig. 6.15) and riming (Fig. 6.16) growth rates increase whereas a decrease in hail total and riming growth rates is seen as CCN increases from 1500 to

3000 cc⁻¹. A similar trend is seen in the average rain collection rates (Fig. 6.17), although the magnitudes are much smaller than for riming and maximum collection rates peak in the ccn600 case owing to the greater amounts of rain mass in this case compared to the other cases (Fig. 6.7c).

The increase in average riming rates in moving from cases ccn100 to ccn600 (Fig. 6.16a,b,c) is due to both increasing numbers of hailstones (Fig. 6.9b), which provide increased total surface area for collection (Farley and Orville 1986; Cohen and McCaul 2006), as well as to increases in hail sizes. However, it should be stressed that the relationship between larger hailstones and enhanced riming rates is not cause and effect, but rather a feedback process. Even though riming efficiencies decrease as hail sizes increase and cloud droplet sizes decrease (Macklin and Bailey 1966; Levin and Cotton 2009; Carrió et al. 2010), the greater cross-sectional areas and fall speeds of larger hailstones allow for greater collection of mass per unit time (Nelson 1983; Xu 1983; Johnson 1987), thereby further increasing their areas and fall speeds, hence the feedback is positive. The enhanced riming rates in cases ccn300 (Fig. 6.16b) and ccn600 (Fig. 6.16c) associated with the greater numbers of hailstones in these cases (Fig. 6.9b) have minimal impact on the cloud and liquid water contents beyond 90 minutes (not shown), which is somewhat in contrast to results of Farley and Orville (1986). In fact, greater average riming rates in ccn600 occur under conditions of lower average *LWC* relative to the other cases (Fig. 6.7i). This finding disagrees with the results of Noppel et al. (2010) and Khain et al. (2011) who noted a direct correspondence between increased riming by hail and increased amounts of supercooled *LWC*.

Maxima in the average riming rates in the ccn1500 case are smaller compared to those in the ccn600 case prior to about 90 minutes (Fig. 6.16c,d) mostly as a result of fewer hailstones in the former case (Fig. 6.9b) given that average hail sizes are similar between the two simulations

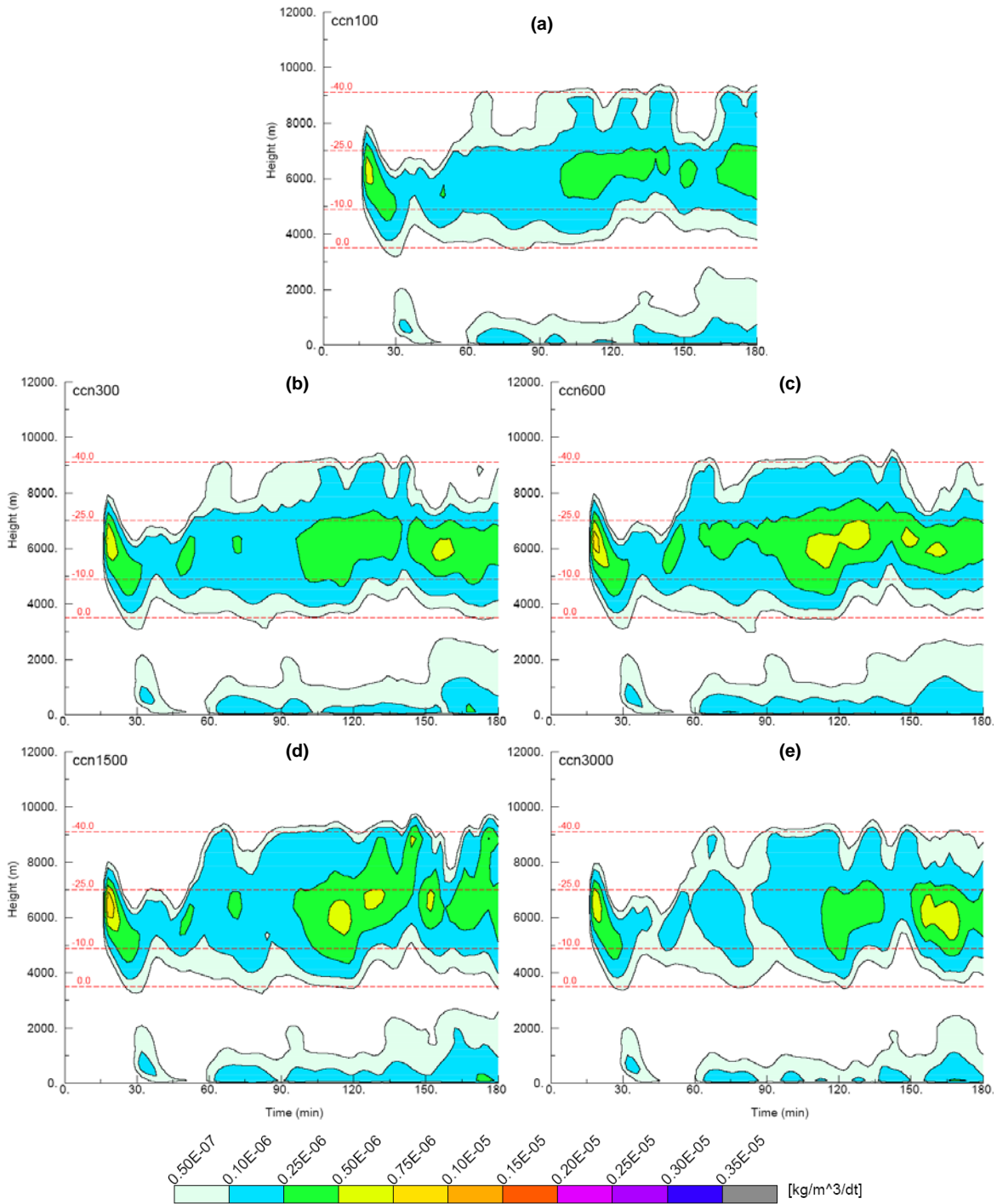


Figure 6.17: As in Fig. 6.15 except for hail mass growth rates [$\text{kg m}^{-3} \Delta t^{-1}$] for hail collecting rain.

during this time (Table 6.2). Beyond 90 minutes, maximum average riming rates in ccn1500 generally exceed those in ccn600 due to the aforementioned positive feedback between fewer but larger-sized hailstones and the amounts of supercooled cloud water collected. The maximum

average riming rates in the ccn3000 case are reduced relative to the ccn600 and ccn1500 cases (Fig. 6.16) as a result of reduced hail riming efficiencies owing to smaller cloud droplets as well as the fact that this case has the fewest hailstones among all the simulations (Fig. 6.9b). Carrió et al. (2010) similarly noted that riming by ice particles was diminished above a certain threshold value of CCN due to increasingly smaller cloud droplet sizes for simulated storms over Houston. Nonetheless, maximum average riming rates in the ccn3000 case are still greater than those of the ccn100 and ccn300 cases as the hailstones tend to be larger in the former versus the latter (Table 6.2), and can therefore collect more supercooled cloud mass per unit time as discussed earlier.

The fact that riming growth of hail does not appear to be related to supercooled LWC amounts in the current study stems from the fact that as cloud droplet sizes decrease with increasing CCN, the riming efficiencies of hail particles decrease. This effect is explicitly represented in the binned riming scheme of Saleeby and Cotton (2004) used for the simulations herein (e.g. Fig. 3.5 in Chapter 3), and is also accounted for in the model employed in the Noppel et al. (2010) study. Larger droplet sizes and greater amounts of supercooled LWC occurred for low values of CCN in the simulations of Noppel et al. (2010), hence the results of greater hail riming efficiency and larger predicted hail sizes at lower versus higher values of CCN in that study. In contrast, Khain et al. (2011) found increases in CCN resulted in larger amounts of supercooled LWC due to the transport of more numerous and smaller cloud droplets to subfreezing levels. The authors also reported that riming by hail became *more efficient*, that is, greater riming growth of hail to larger sizes, with increasing CCN even though the sizes of cloud droplets were reduced. The enhanced riming by hail in the presence of increasingly smaller cloud droplets in the simulations of Khain et al. (2011) can be attributed to the fact that the hail riming

efficiencies were assumed to be equal to 1.0, with only slight deviations from this value for very small cloud droplets ($D_c < 6 \mu\text{m}$) (A. Khain 2012, personal communication).

The relationship between hail growth and hail sizes for increasing CCN is further demonstrated in Figure 6.18, which shows vertical cross-sections of N_{th} , N_{2cm} , N_{4cm} , and total hail growth magnitudes for cases ccn100, ccn600, and ccn3000. The locations and times at which these cross-sections are plotted correspond to the absolute maxima in both N_{2cm} and N_{4cm} during the quasi-steady period of the supercell phase. These maxima occur just prior to the intense hailfall episode that transpires around 120 minutes in each case as depicted in Figures 6.10-612. A time lag and corresponding southeastward displacement of the occurrence of maxima in large hail with increasing CCN account for the different times and locations for the plots shown in Figure 6.18, though the general storm structures and flow fields are similar to each other. In each case, the locations are several km to the north of the updraft maximum.

Figure 6.18 shows that as CCN increases, the region of maximum hail growth (rates $\geq 0.1 \text{ g kg}^{-1} \Delta t^{-1}$) increases in volume and is shifted away from regions containing more numerous and smaller sized hailstones (i.e., maxima in N_{th}) and towards regions containing fewer yet increasingly greater-sized hailstones. The same is generally true for the region of moderate hail growth rates (defined here as rates $\geq 0.05 \text{ g kg}^{-1} \Delta t^{-1}$) as well. Thus, in the ccn100 case (Fig. 6.18a), the more numerous and relatively smaller hailstones within the zone of larger growth rates experience increased competition for the available supercooled water such that growth of individual particles is reduced in a manner consistent with the concept of beneficial competition (Iribarne and DePena 1962; Young 1977; Paluch 1978). On the other hand, larger hail growth rates in the ccn600 (Fig. 6.18b) and ccn3000 (Fig.6.18c) cases are realized by fewer but larger

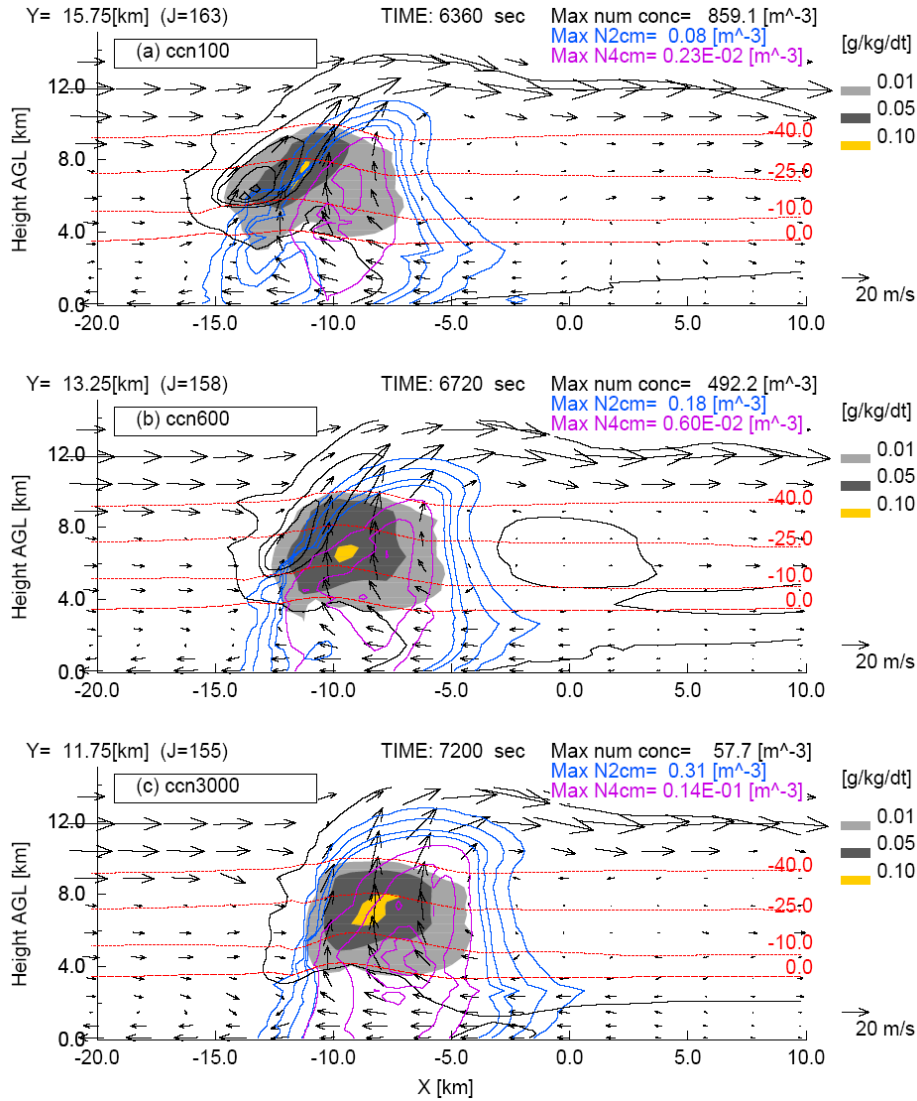


Figure 6.18: East-west cross sections through locations of absolute maximum N_{2cm} and N_{4cm} showing hail total growth rates (shaded; 0.01, 0.05, 0.1 $\text{g kg}^{-1} \Delta t^{-1}$), hail total number concentration contours [black; 1, 100, 250, 500, 750 m^{-3}], and contours of N_{2cm} (blue) and N_{4cm} (purple) [10^{-4} , 10^{-3} , 5×10^{-3} , 10^{-2}m^{-3}] for cases (a) ccn100, (b) ccn600, and (c) ccn3000. In each panel, maximum values of N_{th} , N_{2cm} and N_{4cm} are given in upper-right corner, storm-relative wind vectors are overlaid, and the red dashed lines denote the 0, -10, -25 and -45 $^{\circ}\text{C}$ isotherms.

hailstones thereby allowing these particles to attain even greater sizes much more rapidly than the large hailstones in the ccn100 case (Nelson 1983; Knight and Knight 2001).

The relative locations of new hail formation and hail growth also appear to be impacted by changes in CCN in these simulations. Vertical cross-sections of $D_{\bar{m}h,new}$, number concentrations of newly formed hail particles ($N_{th,new}$), and primary hail growth regions for the ccn100, ccn600,

and ccn3000 cases are displayed in Figure 6.19 for the same times and domain locations as in Figure 6.18. It was shown earlier that increases in $D_{\bar{m}h,new}$ occur with increasing CCN (Tables 6.3 and 6.4), and this is reflected in maximum values of $D_{\bar{m}h,new}$ for the cases shown in Figure 6.19. At these particular times and locations, the numbers of newly generated hail exhibit a decrease with increases in CCN, with the maximum $N_{th,new}$ value in ccn3000 (Fig. 6.19c) nearly an order of magnitude smaller than that in the ccn100 case (Fig. 6.19a). The spatial patterns of $D_{\bar{m}h,new}$ and $N_{th,new}$ are mostly similar among the three cases shown, with the largest new hailstones forming within the eastern flank of the low-level updraft and smaller, more numerous hail particles are generated on the upshear side of the updraft at low and mid levels. A secondary region of hail formation is seen arcing across the updraft between about 8 and 10 km in each case as well. The eastward extensions of these secondary hail generation regions somewhat resemble the embryo curtain of Browning and Foote (1976), although these plots clearly reveal the primary regions of hail embryo formation are near the low-level updraft cores similar to the studies of hail formation and growth in High Plains supercells by Xu (1983) and Miller et al. (1988). The larger newly formed hailstones within the eastern flank of the low-level updraft in the ccn600 (Fig. 6.19b) and ccn3000 cases (Fig. 6.19c) are created within regions of enhanced growth (green hatching) relatively close to the locations of maximum hail growth (red hatching), and the storm-relative flow tends to transport these particles directly into these regions of maximum growth. In the ccn100 case (Fig. 6.19a), the larger newly created hailstones also seem to be transported towards the region of enhanced hail growth, though the distance between the region in which the large hailstones are initiated and the enhanced hail growth region is increased thereby resulting in slower growth of these particles. In addition, numerous newly formed smaller hailstones on the western flank of the low-level updraft are also carried into the

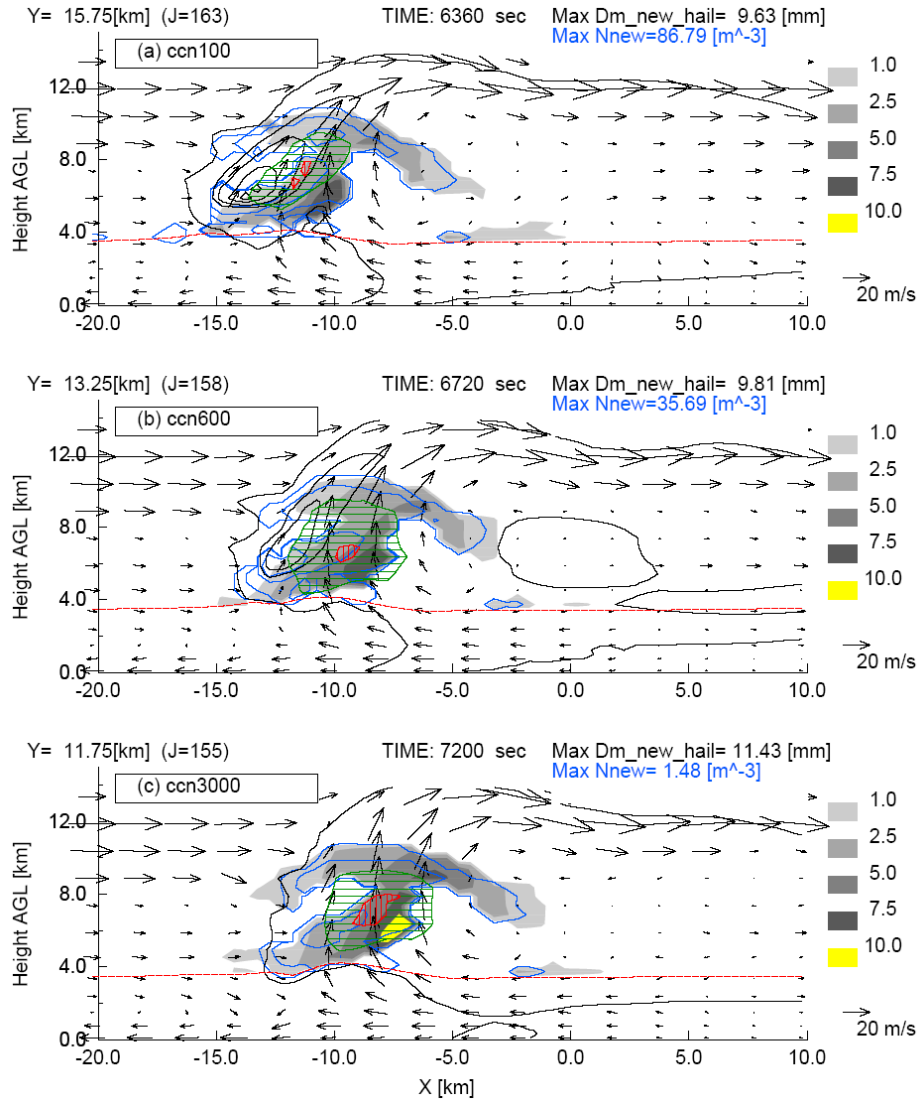


Figure 6.19: As in Fig. 6.18 except shading represents mean mass diameters of newly formed hail [mm] and blue contours depict number concentrations of newly formed hailstones [10^{-4} , 0.01, 1, 10 m^{-3}]. Black contours are total hail number concentration [1, 100, 250, 500, 750 m^{-3}]. In each panel, green and red hatching denote regions of moderate and high total hail growth rates [0.05 and $0.1 \text{ g kg}^{-1} \Delta t^{-1}$, respectively], and the maximum values of mean mass diameters and number concentrations of newly formed hail are displayed in the upper-right corner.

enhanced hail growth region as evident by the greater values of N_{th} that extend from the western-flank hail generation region upwards towards the maximum hail growth location at this time.

Based on these analyses, it is apparent that the larger sizes of newly generated hailstones in the cases with higher values of CCN ($\geq 600 \text{ cc}^{-1}$) (Tables 6.3 and 6.4) tend to experience more rapid riming growth upon formation in agreement with findings by Musil (1970), (Nelson 1983),

Xu (1983), Foote (1984), and Brimelow et al. (2002). Furthermore, the fewer numbers of newly formed hailstones in the cases with high CCN results in reduced competition for the supercooled liquid water available for growth (Charlton and List 1968; Browning 1977). Thus, increasingly larger sizes and localized reductions of numbers of new hailstones associated with increases in CCN tend to promote conditions in which the fewer, relatively larger hail particles undergo rapid growth to larger sizes. In contrast, the more numerous and relatively smaller sizes of newly formed hail particles in cases with lower values of CCN ($< 600 \text{ cc}^{-1}$) result in increased competition for the available supercooled water, and ultimately, in smaller amounts of large hail similar to the beneficial competition concept of Iribane and DePena (1962) and Young (1977).

Overall, these results show that the impacts of CCN on the sizes and numbers of the initial hail particles, as well as the locations of hail generation within the storm, seem to be the decisive factor in determining the amount of large hail that the storm produces. This is different to the results from the studies of Noppel et al. (2010) and Khain et al. (2011) in which the production of large hail or lack thereof was related primarily to the amount of supercooled water content under conditions of varying CCN. For example, the average amounts of supercooled water are less in ccn600 versus ccn100 and ccn300 (Fig. 6.7i), yet the ccn600 case produces greater amounts of larger hail than the cases with lower values of CCN (Figs. 6.11, 6.12, and 6.18). Miller et al. (1988) noted a similar insensitivity of hail sizes to changes in the volume of cloud water in their analyses of hail growth trajectories within a supercell. Of course, the fact that the simulated supercells in all cases produce large hail signifies that the storm dynamics play the dominant role in hail production as suggested by Browning (1977), with the effects of CCN playing a secondary role.

As the melting processes associated with hail play a major role in the production of rain in deep convection (Farley and Orville 1986; Heymsfield and Hjelmfelt 1984; Rasmussen and Heymsfield 1987c, Ziegler 1988; Khain and Pokrovsky 2004; List 2010; Khain et al. 2011), the impacts of CCN on hail should necessarily affect rain formation from hail. Time series of the total domain rain mass generated from conversion of cloud (autoconversion), melting of graupel and hail, and shed liquid water from hail are shown in Figure 6.20 for the five CCN sensitivity experiments. Time-averaged vertical profiles of horizontally-averaged rain production rates corresponding to these processes are shown in Figure 6.21 for the time period from 90 to 150 minutes. It is readily evident from the time series plots that shedding from hail dominates the generation of new rain mass in all cases (Fig. 6.20c) followed by melting graupel (Fig. 6.20b), whereas autoconversion (Fig. 6.20a) and melting of hail (Fig. 6.20d) exhibit similar magnitudes to one another and are the smallest contributors to total new rain mass. Shedding from hail increases in magnitude with decreasing height over approximately the lowest 1.2 km (Fig. 6.21d) and thus contributes significantly to surface rainfall. Melting of hail is maximized around 1 km (Fig. 6.21c), though the smaller average production rates and total rain mass generated via this process (Fig. 6.20d) make hail melt a much smaller contributor to surface rainfall. And while the total amounts of rain generated from melting graupel (Fig. 6.20b) are larger than from hail melt, the majority of graupel particles are advected downwind of the updraft owing to their small sizes and fall over a larger horizontal area in a similar manner as described by GSR04 and Khain and Lynn (2009). Thus, the time- and spatially-averaged graupel melting rates (Fig. 6.21b) are smaller than those for melting hail and are maximized at greater heights, thereby resulting in a minimal contribution to surface rainfall compared to shedding and melting of hail.

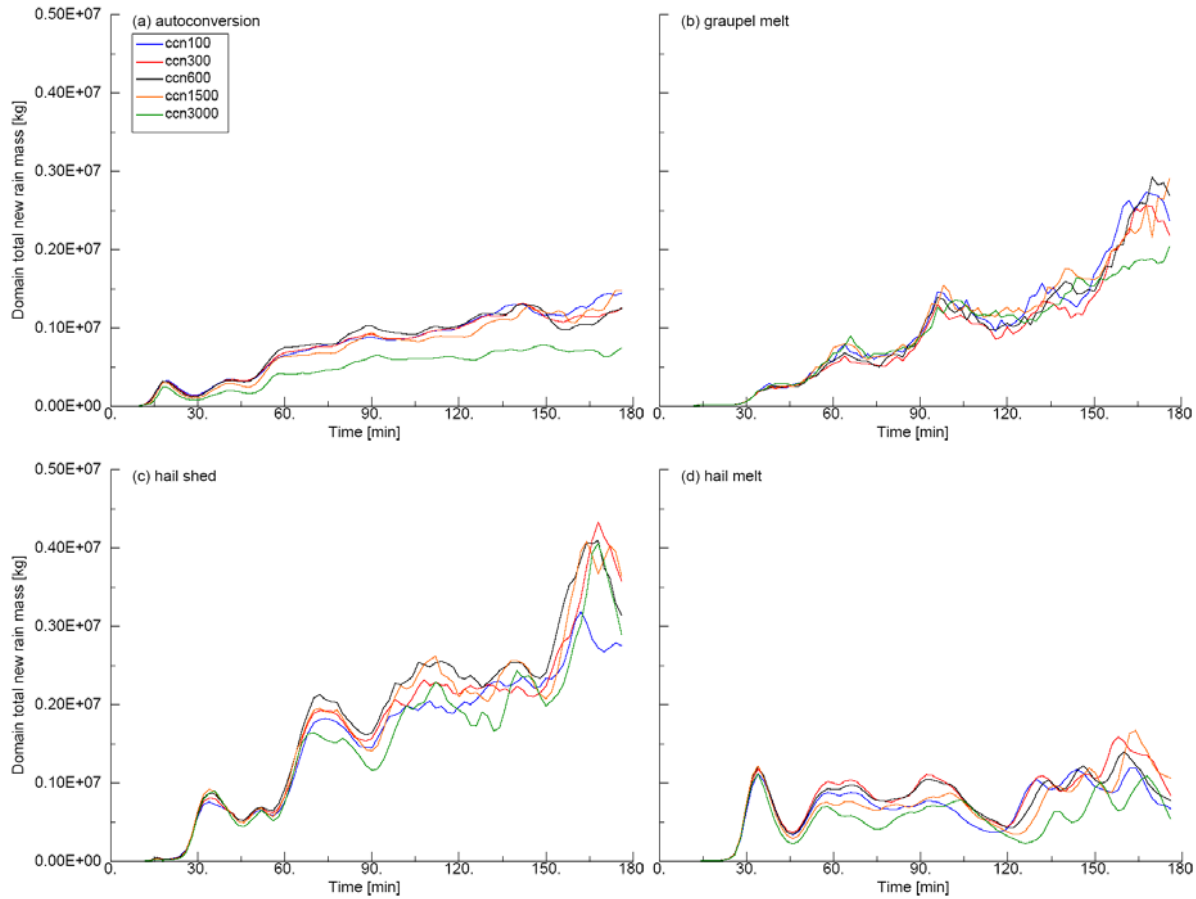


Figure 6.20: Time series of domain total rain mass formation from (a) auto-conversion of cloud droplets, (b) graupel melt, (c) completely melted hail, and (d) shed drops from hail for the CCN sensitivity experiments listed in Table 6.1.

Rain production via the autoconversion process in the current simulations responds in a non-monotonic manner to increases in CCN (Figs. 6.20a and 6.21a), with the largest (smallest) generation rates occurring in the ccn600 (ccn3000) case. This is in contrast to other CCN sensitivity studies in which increased amounts of CCN typically resulted in decreased rates of cloud conversion to rain (Khain et al. 2005; Lee et al. 2008b; Li et al. 2008; Lim et al. 2011). As rain forms by the autoconversion process in the RAMS model owing to self-collection of cloud2 droplets and collisions between cloud and cloud2 droplets (self-collection of cloud droplets results in the formation of cloud2 droplets [Saleeby and Cotton 2004]), the non-monotonic response in rain production arises due to a similar non-monotonic response in the cloud2 mass

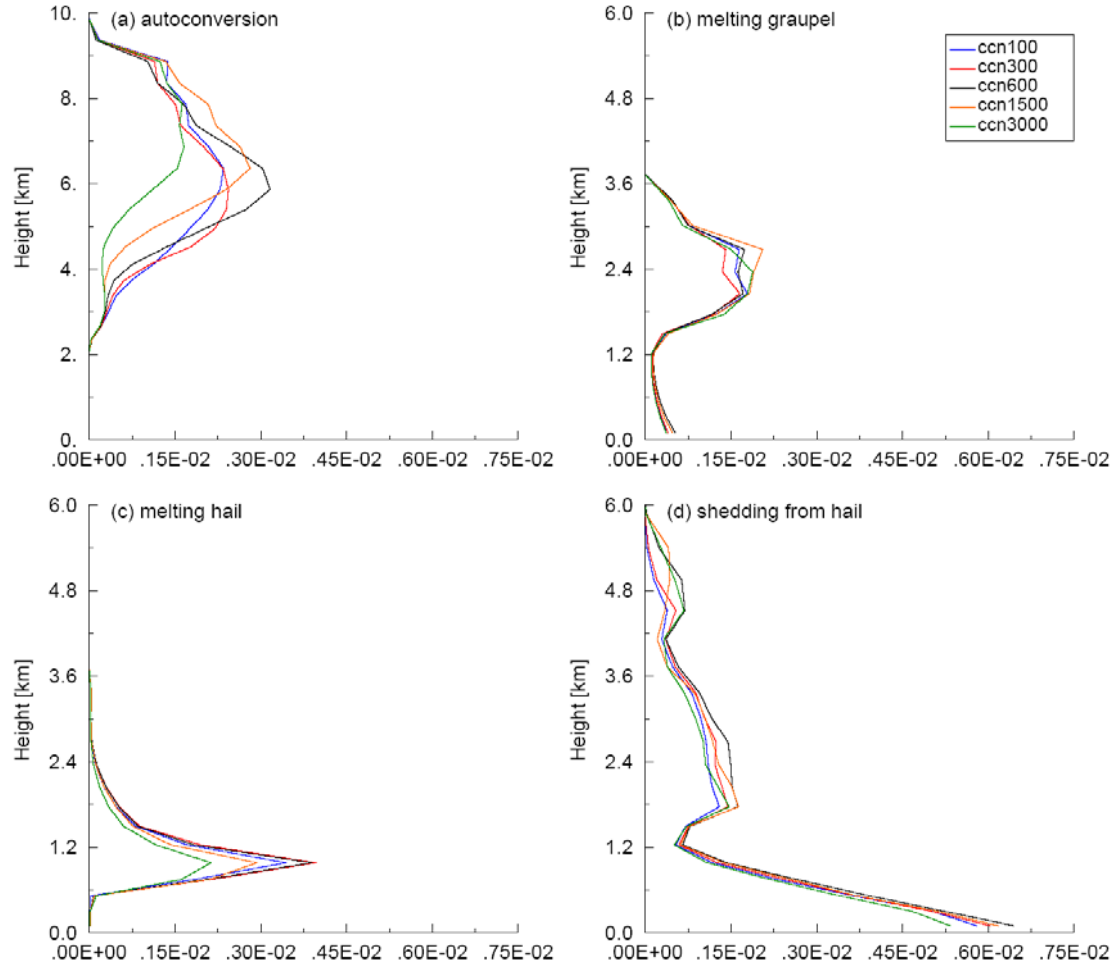


Figure 6.21: Time-averaged vertical profiles of horizontally-averaged rain mass formation rates from (a) autoconversion of cloud and cloud2 droplets, (b) melting graupel, (c) complete melting of hail, and (d) shedding from hail for the CCN sensitivity experiments listed in Table 6.1 for the time period $t = 90$ to 150 minutes.

content field. A comparison of the time-averaged profiles of r_{c2} (Fig. 6.7b) and autoconversion rates (Fig. 6.21a) reveals that the trend in the latter with increasing CCN largely follows the trend in the former.

As all of the simulations produce hailstones that exceed the minimum threshold diameter at which shedding occurs (~ 9 mm), changes in the total amounts of rain produced by shedding from hail with increasing CCN (Fig. 6.20c) generally correspond to the non-monotonic response in total hail mass (Fig. 6.9a). Magnitudes of total shed mass (Fig. 6.20c) and average shedding rates (Fig. 6.21d) are largest in cases ccn600 and ccn1500 due in part to the greater amounts of rimed

mass in these cases compared to the other cases (Fig. 6.16) similar to findings by Lee et al. (2008). The smallest values of total shed mass occur in the ccn3000 simulation (Fig. 6.20c), and this case exhibits the smallest average shedding rates over approximately the lowest 1.2 km (Fig. 6.21d), both of which are attributed to reduced total hail mass and numbers relative to the other cases (Fig. 6.9). Between roughly 4.5 and 6 km, greater amounts of large hail undergoing wet growth in cases with $CCN \geq 600 \text{ cc}^{-1}$ (not shown) result in larger magnitudes of average shedding rates (Fig. 6.21d) given that larger hailstones tend to shed more drops per unit time versus smaller-sized hailstones (RH87b).

The amounts of rain generated from complete melting of hail (Figs 6.20d and 6.21c) are mostly related to the numbers of hailstones in each case (Fig. 6.9b) given that hail size distributions with larger N_{th} values are generally associated with smaller values of D_{mh} , and thus, a greater percentage of small versus large particles. Note that a smaller value of D_{mh} does not automatically imply a reduction in the numbers of large hail as evident in the ccn600 case for which total hail numbers are larger than in the ccn100 case (Fig. 6.9b), yet greater amounts of large hail are produced in the former (Figs. 6.11 and 6.12). The magnitudes of total rain from melted hail (Fig. 6.20d) and average hail melt rates (Fig. 6.21c) are largest in ccn300 and ccn600 as these cases produce the greatest numbers of hailstones (Fig. 6.9b). The ccn3000 case produces the fewest total hailstone numbers (Fig. 6.9b) as well as the greatest amount of large hail (Figs. 6.11 and 6.12), thus the smallest amounts of rain from hail melt are observed in this case (Figs. 6.20d and 6.21c). The total amounts of rain produced by melting graupel generally appear to be insensitive to changes in CCN (Fig. 6.20b), and no discernible trend in the average graupel melt rates is evident within increasing CCN (Fig. 6.21b).

In summary, increases in CCN result in increases in hail size and amounts of large hail even though non-monotonic responses occur in the amounts of hail mass and number produced within the simulated supercells. The increase in large hail with increasing CCN is mainly attributed to increases in the sizes of newly formed hail particles, and more rapid hail growth rates owing to fewer, larger hail particles (reduced competition for the available supercooled water) within the primary hail growth region. This alternate explanation regarding the mechanisms by which increases in CCN lead to large hail differs from previous studies in which changes in supercooled water amounts with changing values of CCN were stated to be the dominant factor in determining the sizes and amounts of large hail (Noppel et al. 2010; Khain et al. 2011). Lastly, the melting processes of hail, especially shedding, contribute significantly to the production of rain at low-levels. Less rain production from hail is evident in cases with very low (100 cc^{-1}) and very high (3000 cc^{-1}) values of CCN owing to lower total amounts of hail whereas enhanced amounts of rain are generated for CCN values between these two extremes. The impacts of CCN on surface hail and rain precipitation, and the associated effects on the characteristics of the low-level cold-pool are examined in the next section.

6.2.4) Effects of CCN on surface precipitation and low-level thermodynamics

Previous investigations concerning the impact of CCN on deep convection have reported changes in surface precipitation as a result of increases in CCN concentrations, with environmental factors playing a key role in determining whether precipitation is suppressed or enhanced (Khain and Pokrovsky 2004; Khain et al. 2004; Wang 2005; Lynn et al. 2005; van den Heever et al. 2006, 2011; Tao et al. 2007; Lee et al. 2008; Khain and Lynn 2009). Only a few studies have examined the response of surface precipitation to increases in CCN in supercell convection, and the results tend to suggest a decrease in precipitation arriving at the ground

(Seifert and Beheng 2006; Lerach et al. 2008; Khain and Lynn 2009; Storer et al. 2010; Lim et al. 2011). In this section, the response of surface precipitation to greater concentrations of CCN for the simulated supercells in the current work are analyzed and compared to previous studies. Analyses of the impacts of increasing CCN on the evolution of low-level cold-pools for supercell convection are also performed as this particular topic has not been thoroughly investigated previously.

Time series of domain maximum surface precipitation rates and total surface accumulated mass for rain and hail are displayed in Figure 6.22 for the CCN sensitivity experiments. It is noted here that surface precipitation for these simulations consists of rain and hail only; all other ice species completely melt prior to reaching surface as evident in the time-averaged profiles of hydrometeor mass contents (Figs. 6.5 and 6.7). The maximum precipitation rates for rain ($R_{r,max}$) and hail ($R_{h,max}$) (Fig. 6.22a,b) reveal that the onset of surface precipitation occurs at nearly the same time in all cases. This result differs from previous studies that noted a delay in the onset of precipitation owing to increases in CCN for both isolated and multicellular deep convection over continents (Khain et al. 2004, 2005; Fan et al. 2007; Tao et al. 2007; Lee et al. 2008b) as well as for an idealized supercell case (Khain and Lynn 2009). Similar precipitation onset times in the current simulations likely result from the rapid generation of large amounts of hail (and graupel) mass during the initial warm bubble convection in all cases (i.e., Figs. 6.9 and 6.10b,d,e). Nonetheless, the time series of $R_{r,max}$ and $R_{h,max}$ do reveal sensitivity to changes in CCN, with lower values of $R_{r,max}$ ($R_{h,max}$) generally observed for cases with $CCN \geq 1500 \text{ cc}^{-1}$ ($\leq 300 \text{ cc}^{-1}$) and higher $R_{r,max}$ ($R_{h,max}$) at $CCN \leq 600 \text{ cc}^{-1}$ ($> 300 \text{ cc}^{-1}$) (Fig. 6.22a,b). Decreases in surface rain rates with increasing CCN were also noted in simulations of isolated deep convection (Khain and Pokrovsky 2004; Khain et al. 2005), squall lines (Tao et al. 2007), and supercells (Lerach et al.

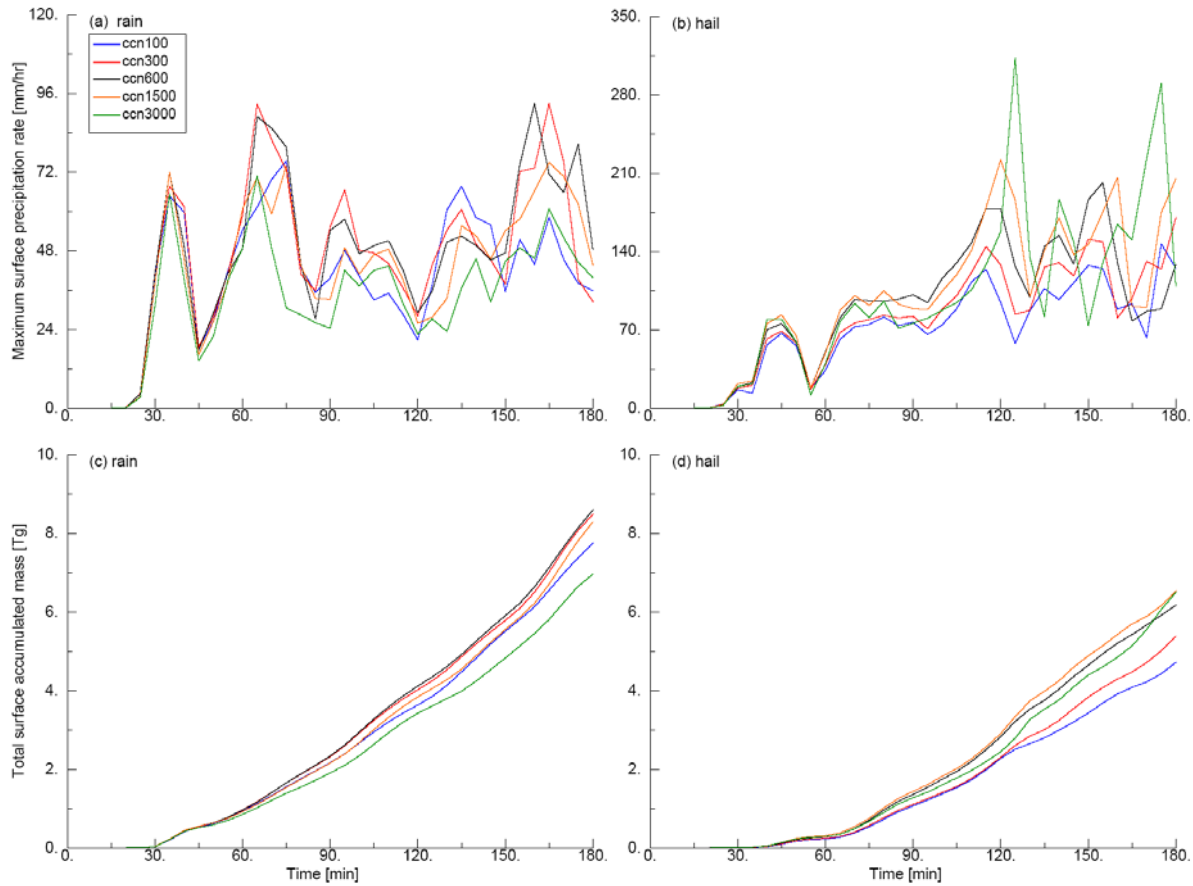


Figure 6.22: Time series of instantaneous maximum surface precipitation rates [mm hr^{-1}] (top row) for (a) rain and (b) hail (liquid equivalent precipitation rate), and total surface accumulated mass [Tg] (bottom row) for (c) rain and (d) hail for the CCN sensitivity simulations listed in Table 6.1.

2008; Khain and Lynn 2009). Despite the fact that the amounts of large hail increase with increasing CCN, $R_{h,max}$ values are non-monotonic with respect to increases in CCN except for the intense hailfall episode that occurs around 120 minutes, as well as the smaller-intensity hailfall event roughly 20 minutes later (Fig. 6.22b). Smaller $R_{h,max}$ values of hail precipitation rates in the cases with low amounts of CCN (ccn100 and ccn300) result from the reduced amounts of large hail produced in these cases compared to those with higher values of CCN (Fig. 6.22b). A slight time lag in the peak $R_{h,max}$ values with increasing CCN is observed for the most intense hail fallout episode (near $t = 120$ min) and is related to the similar time lag in peak updraft velocities with increasing CCN that occurs around the same time (Fig. 6.3).

The total accumulated masses of rain (Fig. 6.22c), and to a lesser extent hail (Fig. 6.22d), at the surface exhibit non-monotonic responses to increases in CCN. The largest values of accumulated rain mass are seen in the ccn600 and ccn300 cases whereas the ccn3000 case produces the lowest amount of total surface rainfall (Fig. 6.22c). Similar non-monotonic responses in accumulated rain with increasing CCN were observed in the simulations of Khain et al. (2011) for a multicell hailstorm as well as by Fan et al. (2007), Li et al. (2008), and Carrió et al. (2010) for simulations of deep convection near the Houston, TX area. On the other hand, the modeling results of Khain and Lynn (2009) and Lim et al. (2011) showed decreases in accumulated rain with increasing CCN in supercells whereas Lee et al. (2008) reported enhanced rain amounts with larger values of CCN for storms developing in environments characterized by high CAPE and strong shear. In the current work, total accumulated hail mass increases as CCN increases from 100 to 1500 cc^{-1} , and further increases in CCN to 3000 cc^{-1} result in a decrease in accumulated hail mass (Fig. 6.22d). This agrees qualitatively with the results of Khain et al. (2011) who reported an increase in average hail precipitation at the surface with increasing CCN up to 3000 cc^{-1} , with decreasing average hail precipitation as CCN increased further. In contrast, Noppel et al. (2010) showed a general decrease in accumulated hail amounts with increasing CCN. The trend in total accumulated hail mass under varying CCN values in the current simulations (Fig. 6.22d) is related to the trend in riming rates (Fig. 6.16); cases with the largest average riming rates (ccn600 and ccn1500) produce the greatest total amounts of hail mass at the surface. Similar relationships between increased (decreased) riming of frozen particles and increased (decreased) surface precipitation amounts with increasing CCN were found by Lee et al. (2008), Khain and Lynn (2009), Carrió et al. (2010), and Khain et al. (2011).

The domain total accumulated mass [Tg] of rain, hail, and total precipitation (rain+hail), as well as the percentages of rain and hail contributing to the total surface precipitation at the end of the simulations ($t = 180$ min) are listed in Table 6.5 for the CCN sensitivity experiments. Maximum liquid-equivalent total precipitation amounts [mm] at a grid point are also shown in this table. The total accumulated precipitation, maximum grid point total precipitation amounts, and total accumulated hail all increase with increasing CCN up to 1500 cc^{-1} and then decrease as CCN increases to 3000 cc^{-1} . A similar trend is observed for total accumulated rain, though the peak in accumulated rain occurs in the ccn600 case. These results are in contrast to results of Seifert and Beheng (2006), Lerach et al. (2008), Khain and Lynn (2009) and Lim et al. (2011), all of which found a decrease in accumulated surface precipitation amounts with increasing CCN in 3D simulations of supercells. However, the simulated storms in these particular studies did not produce precipitation in the form of hail at the surface. The percentage of total surface precipitation comprised of hail is significant in all cases and increases monotonically with increasing CCN from around 38% in ccn100 to nearly 50% in ccn3000. Likewise, a monotonic decrease in the percentage of total precipitation due to rain is seen for increasing CCN. *These results certainly highlight the importance of contributions from hail to the total precipitation in these simulations.*

Table 6.5: Total accumulated precipitation mass, maximum accumulated total precipitation (liquid equivalent) at a point, total accumulated hail and rain masses, and percentages of total mass that is hail and rain at the surface after 180 minutes for the experiments listed in Table 6.1. Total masses are in teragrams [Tg] (trillions of grams) and maximum total precipitation at a point is in mm.

Case	Total [Tg]	Max total [mm]	Total hail [Tg]	Percent hail	Total rain [Tg]	Percent rain
ccn100	12.46	35.36	4.71	37.8	7.75	62.2
ccn300	13.85	39.02	5.37	38.77	8.48	61.22
ccn600	14.75	47.63	6.17	41.83	8.58	58.17
ccn1500	14.82	53.02	6.53	44.06	8.29	55.94
ccn3000	13.45	52.17	6.5	48.33	6.95	51.67

The spatial distributions of accumulated hail and rain at the end of the simulation period ($t = 180$ min) are displayed in Figure 6.23 for the five CCN sensitivity cases. The general patterns of rainfall are similar in all cases, with maximum rainfall occurring prior to the right turn of the storm, though the magnitudes of accumulated rain are largest in cases ccn300 (Fig. 6.23b) and ccn600 (Fig. 6.23c) similar to the time series for total surface rain mass (Fig. 6.22c). The relative insensitivity in the surface rainfall patterns with increasing CCN differs from Khain and Lynn (2009) in which distinct differences in the spatial distributions of surface rainfall were observed for different values of CCN in supercell simulations with bin microphysics. However, simulations of the same storm using single-moment bulk microphysics without hail (Thompson scheme in WRF; Thompson et al. 2004, 2006) showed that the rainfall patterns were largely insensitive to changes in CCN (Khain and Lynn 2009), similar to the simulations in the current work. Increases in CCN result in increased amounts of accumulated hail as well as increased areas over which local maxima in accumulated hail occur within the overall hailswath (Fig. 6.23), both of which are opposite to findings by Noppel et al. (2010).

The amount of damage caused by hail depends not only on the amounts of hail arriving at the ground but also on the sizes of the hailstones, with larger hailstones obviously capable of inflicting greater damage to property and crops (Chagnon 1971, 1999). Table 6.6 reveals that the absolute maximum hail sizes arriving at the surface increase as CCN increases in general agreement with findings by Khain et al. (2011). [Maximum hail size is determined by first partitioning the hail size distributions into discrete size bins at each point within the lowest model level. The diameter of the largest size bin containing a number concentration of at least 10^{-4} m^{-3} , corresponding to an accumulation of 1 per 100 m^{-2} for a layer depth of approximately 100 m, is then taken as the maximum hailstone size at a given point]. Time series plots of the

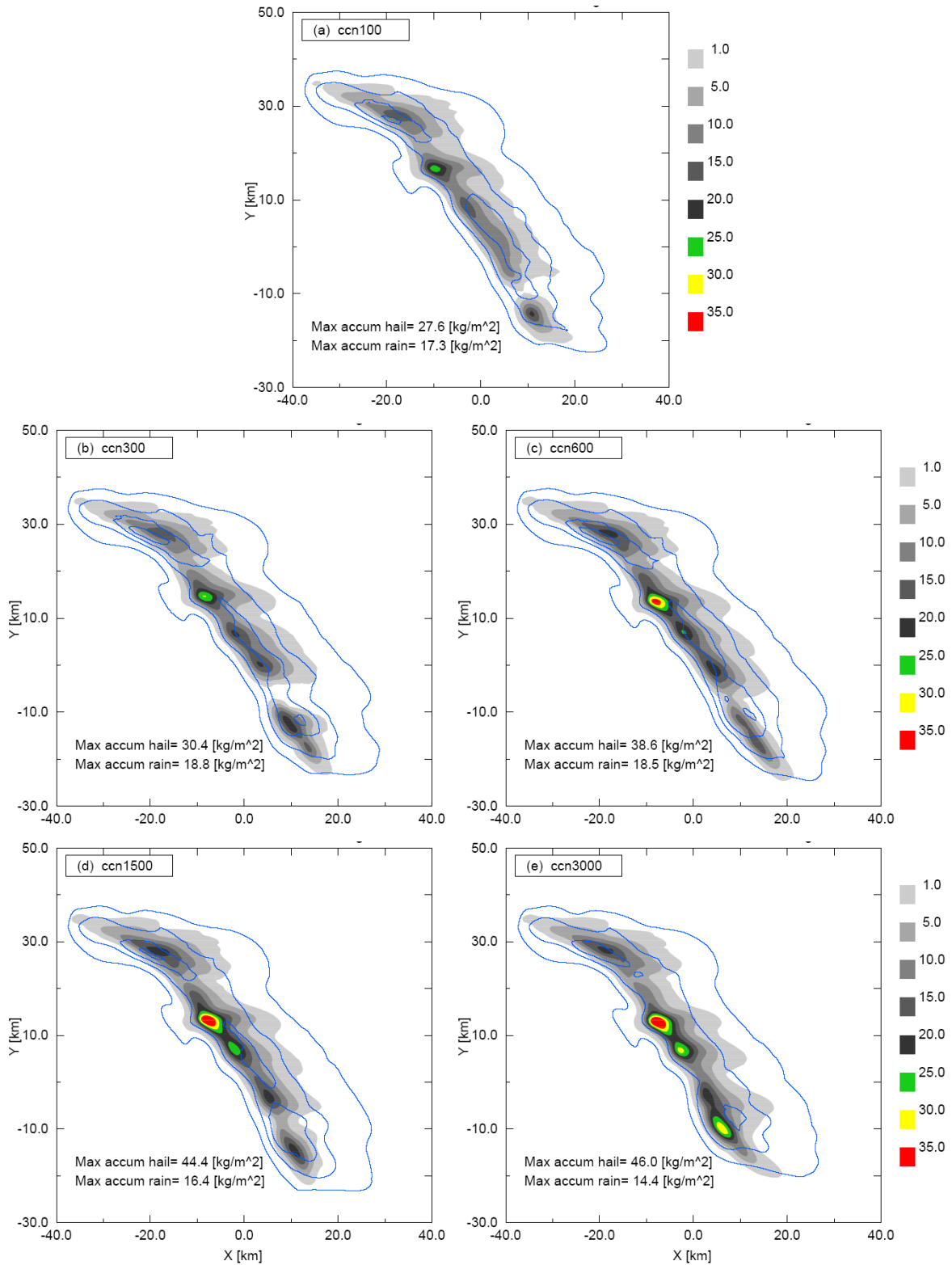


Figure 6.23: Surface accumulated amounts [kg m^{-2}] of hail (shaded contours) and rain (blue contours) at $t = 180$ minutes for (a) ccn100, (b) ccn300, (c) ccn600, (d) ccn1500, and (e) ccn3000 cases. Contour values are 1, 5, 10, 15, 20, 25, 30, and 35 kg m^{-2} .

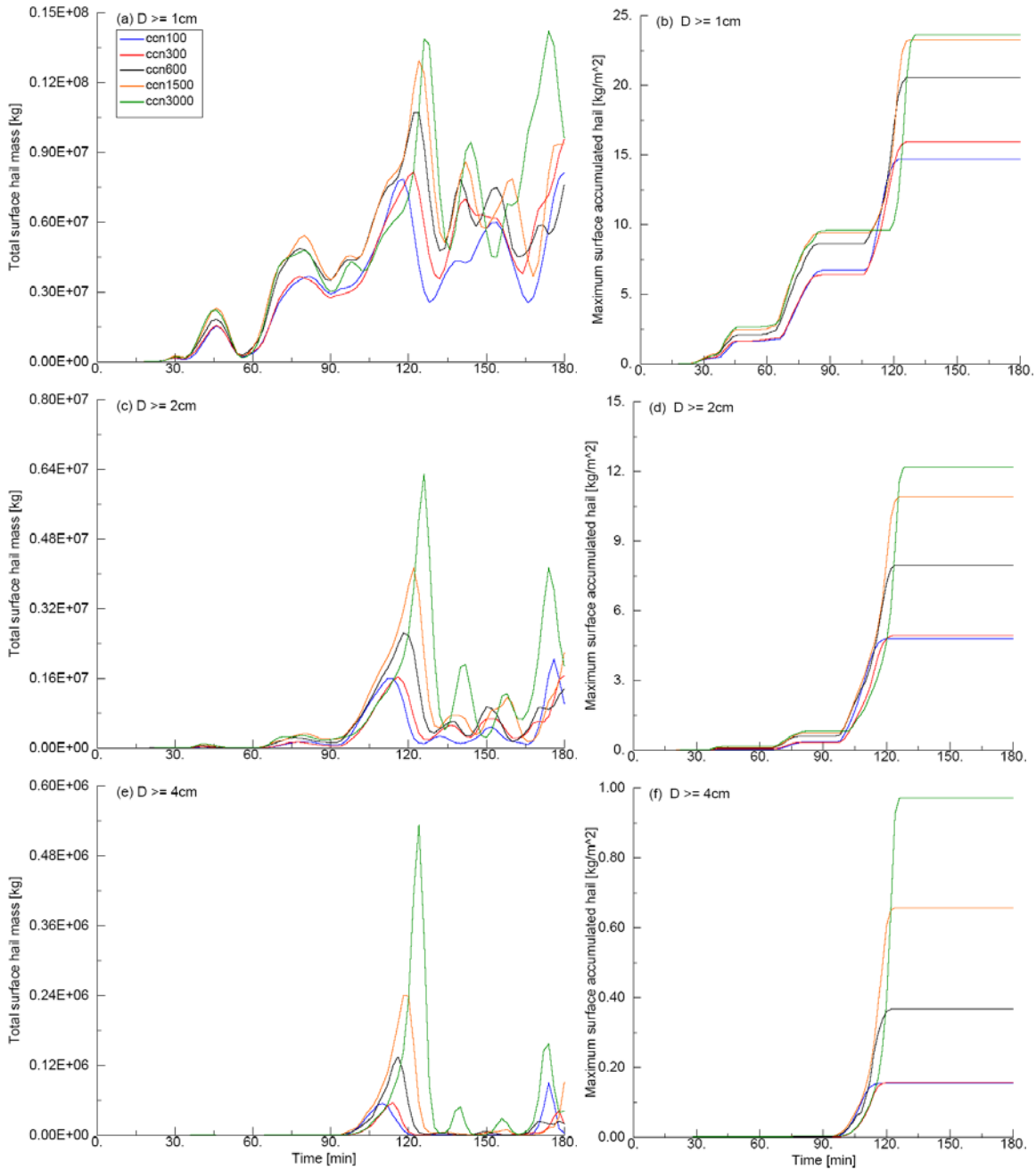


Figure 6.24: Time series of instantaneous total surface hail mass [kg] (left column) and maximum accumulated surface hail mass at a point [kg m^{-2}] (right column) associated with hail diameters of at least (a,b) 1 cm, (c,d) 2 cm, and (e,f) 4 cm for the CCN sensitivity experiments listed in Table 6.1.

total surface hail mass associated with diameters of at least 1, 2, and 4 cm show an increase in the amounts of moderately-sized (1 cm) and large hail arriving at the surface with increasing CCN (Fig. 6.24a,c,e) prior to 165 minutes. Moreover, increases in CCN lead to a monotonic

Table 6.6: Maximum diameters of hail [cm] arriving at the surface during the entire simulation period for the CCN sensitivity experiments. The largest size bin that meets a minimum threshold of at least 1 per 100 m² determines the maximum diameter in each case.

Experiment	Max surface hail size [cm]
ccn100	4.83
ccn300	4.83
ccn600	5.22
ccn1500	5.64
ccn3000	5.86

increase in total hail mass of large and very large hailstones arriving at the surface (Fig. 6.24c,e) in qualitative agreement with the results of Khain et al. (2011). Peak values of the maximum amounts of grid point accumulated hail associated with $D_h \geq 1, 2,$ and 4 cm evident for the hailfall episodes that occur around 120 and 140 minutes (Fig. 6.24a,c,e). It is noted that the peaks in the time series of total surface hail mass for $D_h \geq 1, 2,$ and 4 cm in each case correspond to the respective local maxima in accumulated hail amounts shown in Figure 6.23.

As the generation and evolution of low-level cold-pools are intimately linked with low-level cooling associated with melting and evaporating precipitation particles within downdrafts (Srivastava 1987; Wakimoto and Bringi 1988; Knupp 1988, 1989; Hjelmfelt et al. 1989; Proctor 1989; Straka and Anderson 1993; GSR04; VC04), differences in the precipitation characteristics as a result of changes in CCN should ultimately affect low-level cold-pool development in the simulated supercells. Time series of surface cold-pool area, minimum θ' (θ'_{min}), average θ' (θ'_{mean}), and maximum downdraft speeds over the lowest 2 km are displayed in Figure 6.25 for the CCN sensitivity experiments, and the spatiotemporal evolutions of the cold-pools are shown in Figures 6.26-6.28. A threshold value of $\theta' = -2$ K is used to compute the horizontal areas of the cold-pools in the simulations in order to better highlight differences as a result of changes in CCN.

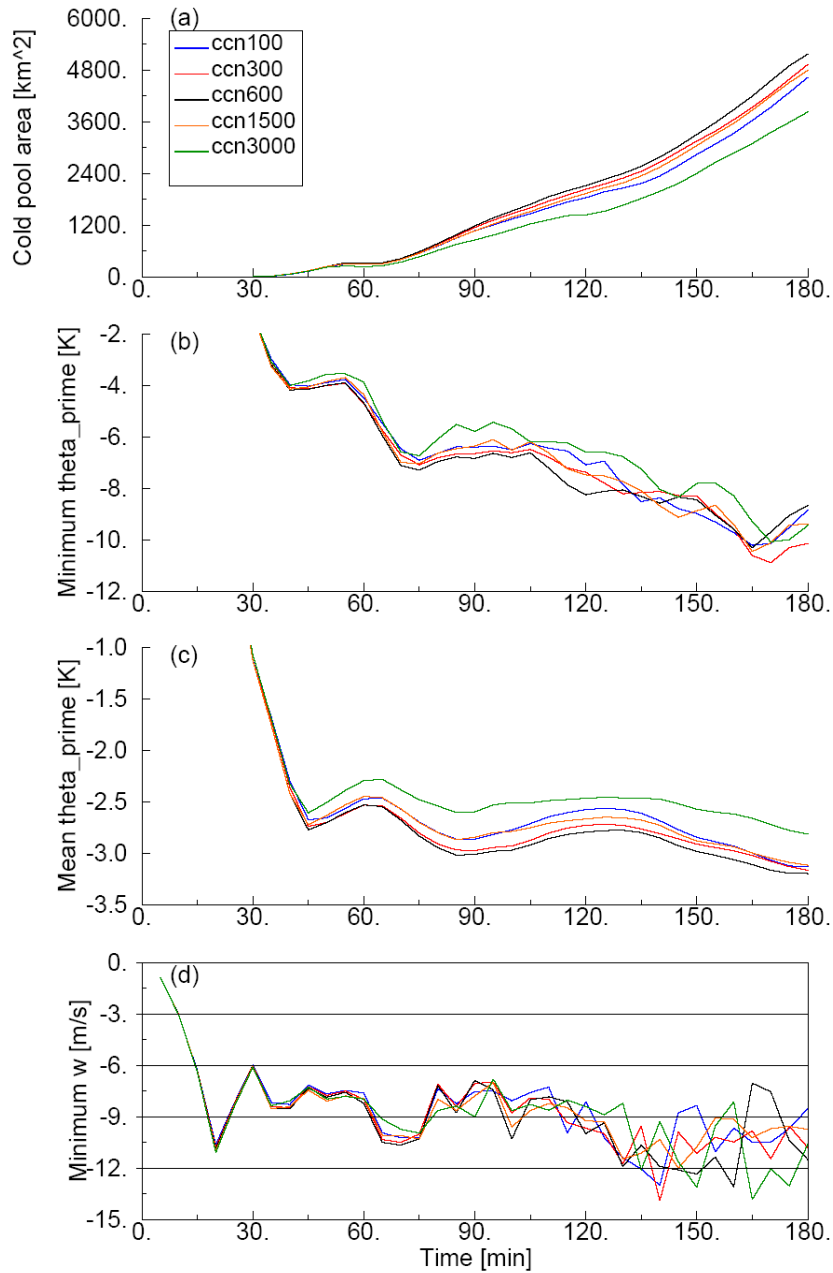


Figure 6.25: Time series of (a) total surface cold-pool area [km²] (defined as the sum of the area of all grid squares with $\theta' \leq -2$ K), (b) minimum θ' at the surface [K], (c) mean surface θ' within the cold-pool, and (d) maximum downdraft speeds [m s⁻¹] over the lowest 2 km for the CCN sensitivity simulations listed in Table 6.1.

Much like the impacts of CCN on surface precipitation, a non-monotonic response in cold-pool size and strength is observed with increasing concentrations of CCN. The largest and strongest (largest negative θ'_{min} values) cold-pools are produced in the ccn300 and ccn600 cases

whereas the supercell in the ccn3000 case creates the smallest and weakest cold-pool (Figs. 6.25a,b,c). Differences in the horizontal structures of the cold-pools are also evident in Figures 6.26-6.28, which show that the areas covered by increasingly colder temperatures within the cold-pools are smaller in ccn3000 (and to a lesser extent in ccn100) compared to the other cases. However, differences in maximum cold-pool strength are generally less than 2 K among the simulations at any time (Figs. 6.25b; 6.26-6.28), and the greatest changes in cold-pool size and strength occur when CCN is increased from 1500 to 3000 cc^{-1} (Fig. 6.25a,b,c). Similarities in the storm-generated cold-pools from simulated supercells under conditions of both low and high concentrations of CCN were also noted by Lerach et al. (2008). In addition, maximum downdraft speeds over the lowest 2 km attain a similar range of magnitudes in all cases and generally do not show a trend towards stronger or weaker downdrafts with increasing CCN (Fig. 6.25d). Similar insensitivities in maximum downdraft speeds to increases in CCN were found in studies by Lim et al. (2011) for supercells and Khain et al. (2011) for a multicellular hailstorm, and the current results provide further evidence of the relatively small impact that changes in CCN have on the overall dynamics of supercell convection.

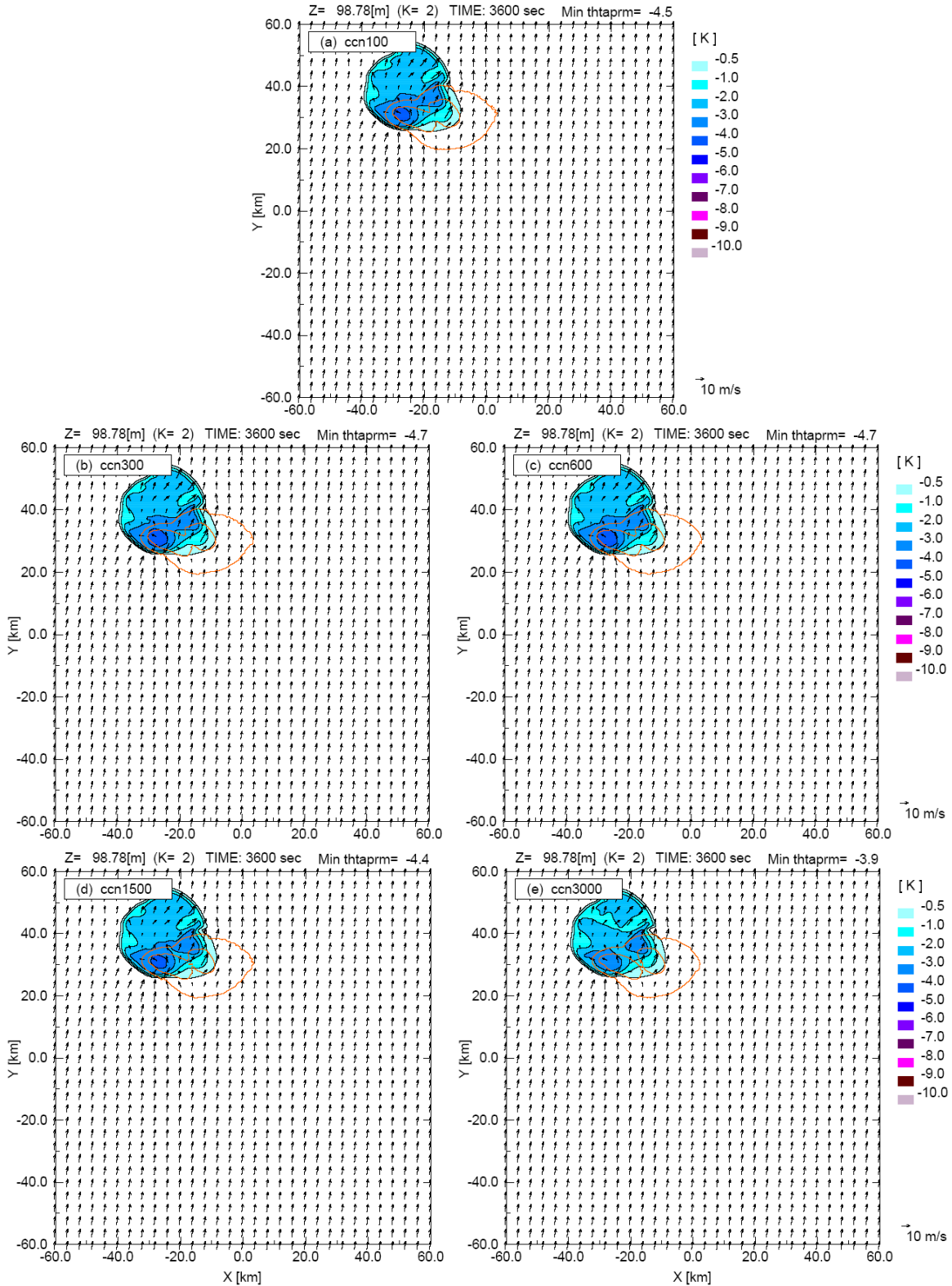


Figure 6.26: Perturbation potential temperature (θ') [shaded, contour intervals of -1 K beginning at -1 K; -0.5 K contour also shown] at lowest model level (98 m AGL) and Z_e contours [orange, contour intervals of 20, 40, and 60 dBZ] at $t = 60$ minutes for (a) ccn100, (b) ccn300, (c) ccn600, (d) ccn1500, and (e) ccn3000. Ground relative wind vectors are also shown.

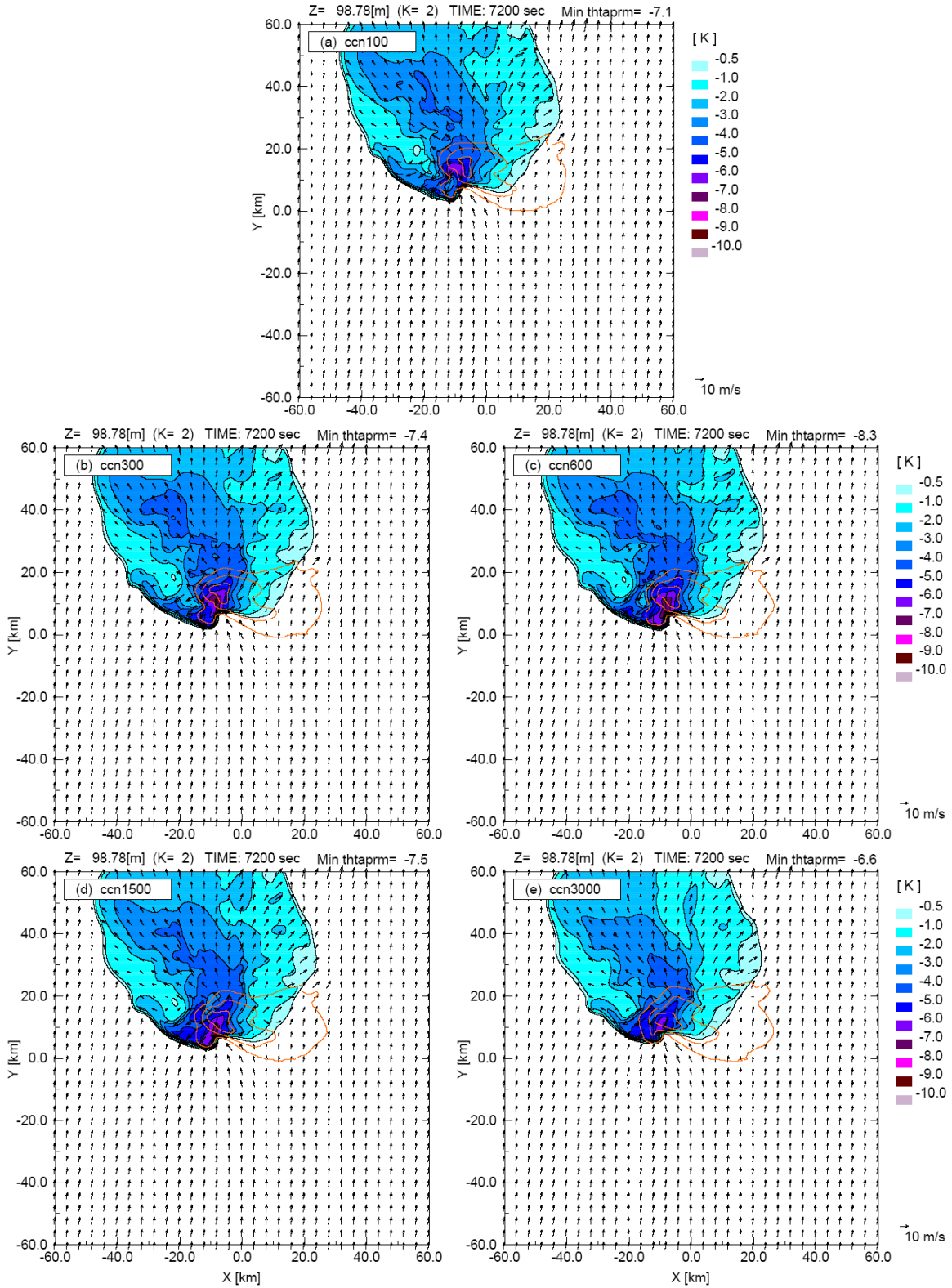


Figure 6.27: As in Figure 6.26 except at $t = 120$ minutes.

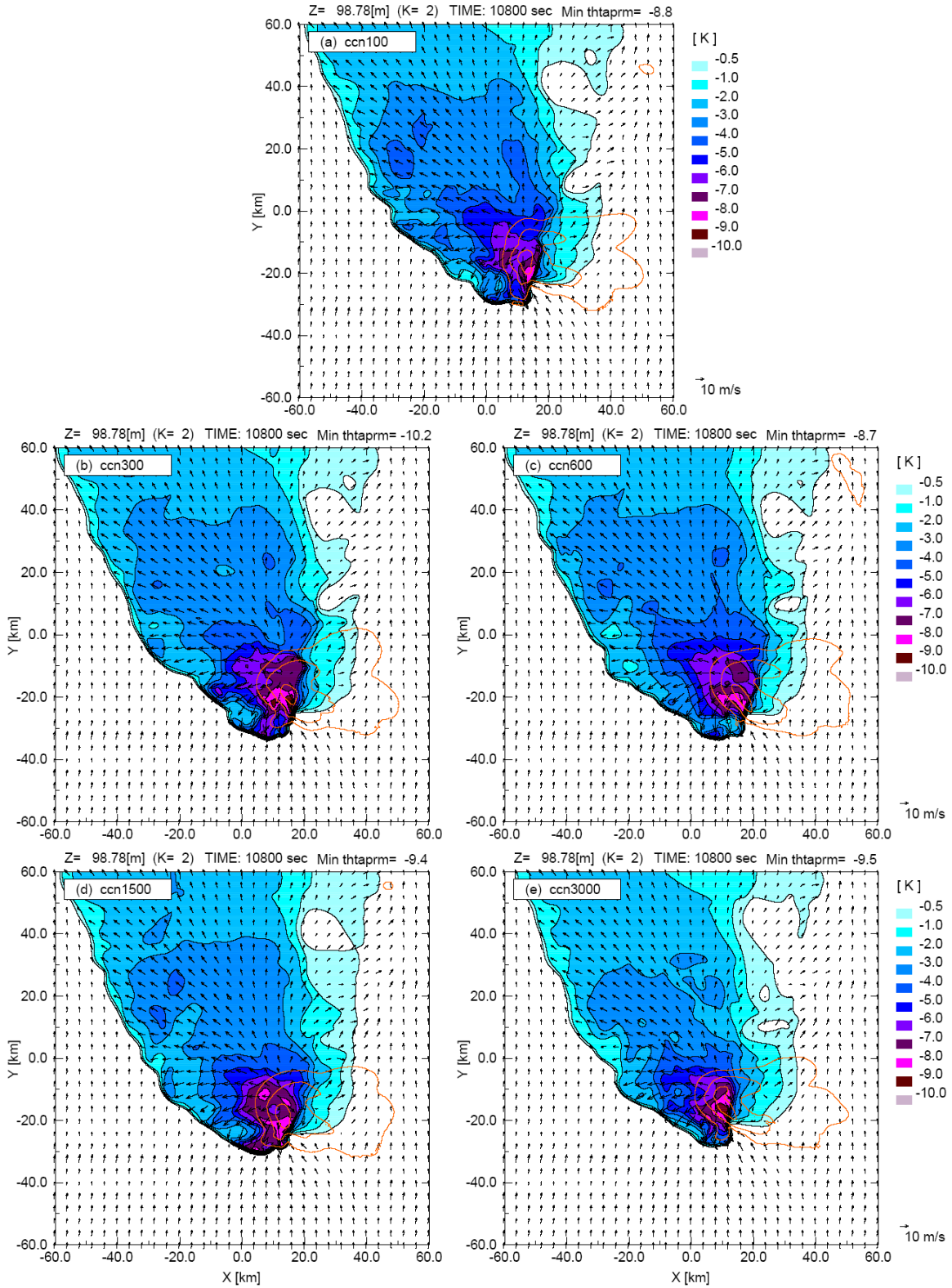


Figure 6.28: As in Fig. 6.26 except at $t = 180$ minutes.

The evolution of the cold-pool vertical structures are largely similar among the five CCN sensitivity simulations as depicted by time-height plots of θ'_{min} (Fig. 6.29). Using the height of the -3 K θ'_{min} contour as a proxy for cold-pool depth (warmer θ'_{min} values could be related to cooling due to adiabatic ascent), it is evident that the ccn3000 case consistently exhibits the shallowest cold-pool depth over time whereas the deepest cold-pools are produced in the ccn100 and ccn300 cases (Fig. 6.29f). However, the differences in cold-pool depth among all cases are generally less than a few hundred meters, thus the effects of increasing CCN on cold-pool depth appear to be minimal for these simulations.

Lastly, an examination of time-height plots of the maximum cooling rates from melting of hail (Fig. 6.30), evaporation of rain (Fig. 6.31), and total cooling (Fig. 6.32) reveals that evaporation of rain dominates cooling at low-levels. Cooling from evaporation/sublimation of hail is generally less than -0.2 K min^{-1} and occurs at heights above roughly 2.5 km, thus its impact on the low-level cold-pool is insignificant. Total cooling rates are largest in ccn300 and ccn600 (Fig. 6.32) owing to larger amounts of rainfall in these cases relative to the other cases (Figs. 6.22c and 6.23). The enhanced cooling as a result of increased rainfall ultimately leads to stronger cold-pools in ccn300 and ccn600 (Fig. 6.25b,c), in qualitative agreement with the

Table 6.7: Linear correlation coefficients between minimum surface θ' and total surface accumulated hail and rain mass, and the total amounts of rain mass produced from complete melting and shedding of hail over the time period $t = 30$ to 180 min for the CCN sensitivity experiments.

Experiment	Total surface hail mass	Total surface rain mass	Total hail melt mass	Total hail shed mass
ccn100	-0.904	-0.921	-0.392	-0.949
ccn300	-0.905	-0.931	-0.456	-0.95
ccn600	-0.857	-0.877	-0.327	-0.936
ccn1500	-0.899	-0.909	-0.511	-0.912
ccn3000	-0.903	-0.927	-0.142	-0.918

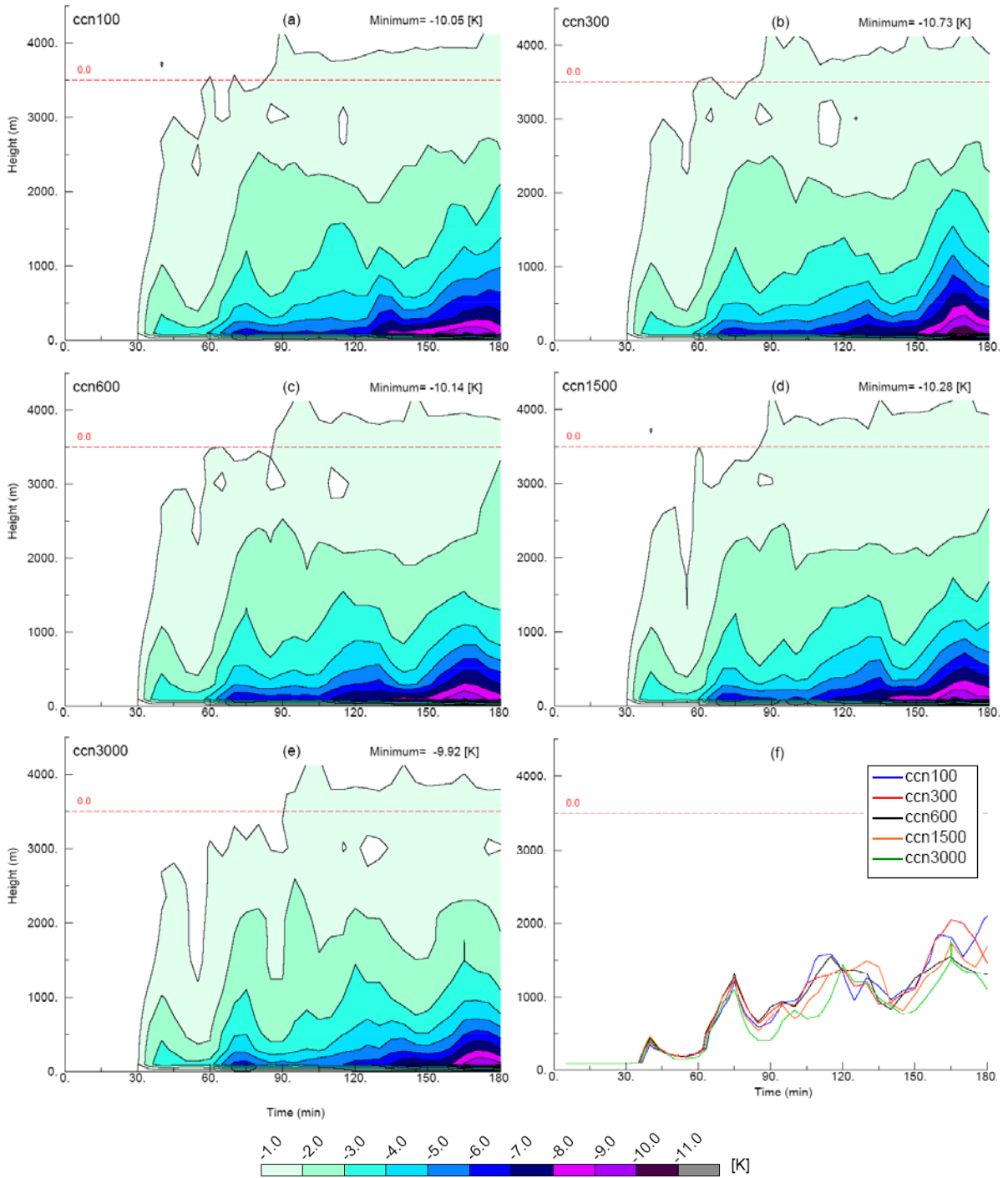


Figure 6.29: Time-height contours of minimum θ [K] for cases (a) ccn100, (b) ccn300, (c) ccn600, (d) ccn1500, and (e) ccn3000. Panel f shows time series of the height of the -3 K θ contour from panels a-e.

findings of GSR04 and Dawson et al. (2010). Furthermore, the amounts of rain at low-levels are strongly influenced by the amounts of liquid water shed from hail (Figs. 6.20c and 6.21d). Thus,

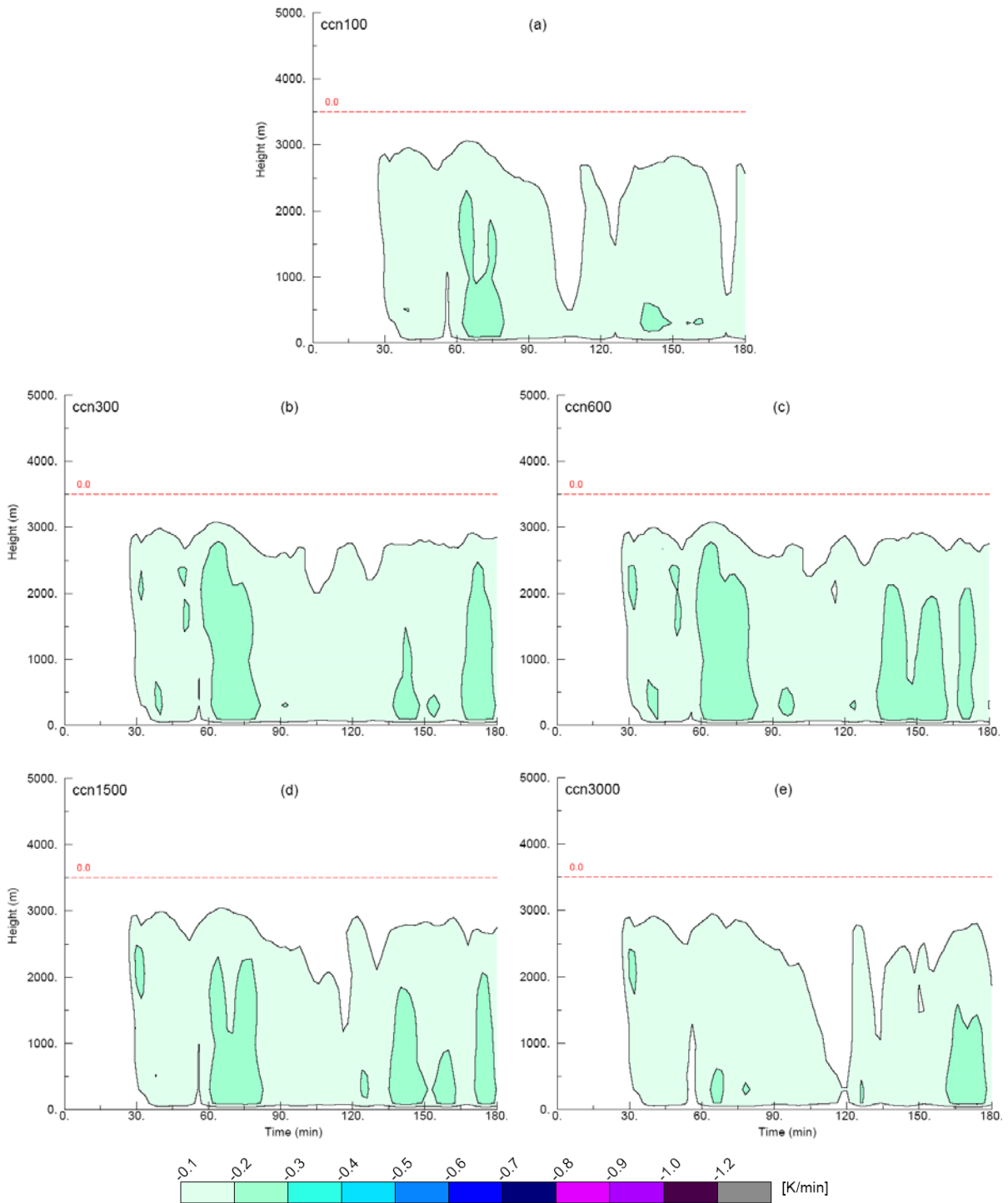


Figure 6.30: Time-height contours of domain maximum cooling rates [K min^{-1}] within downdrafts ($w \leq -0.5 \text{ m s}^{-1}$) from melting hail for cases (a) ccn100, (b) ccn300, (c) ccn600, (d) ccn1500, and (e) ccn3000.

in all cases, maximum cold-pool strength is highly correlated with both total surface rainfall and total mass shed from hail, and to a slightly lesser extent, with total hail mass arriving at the

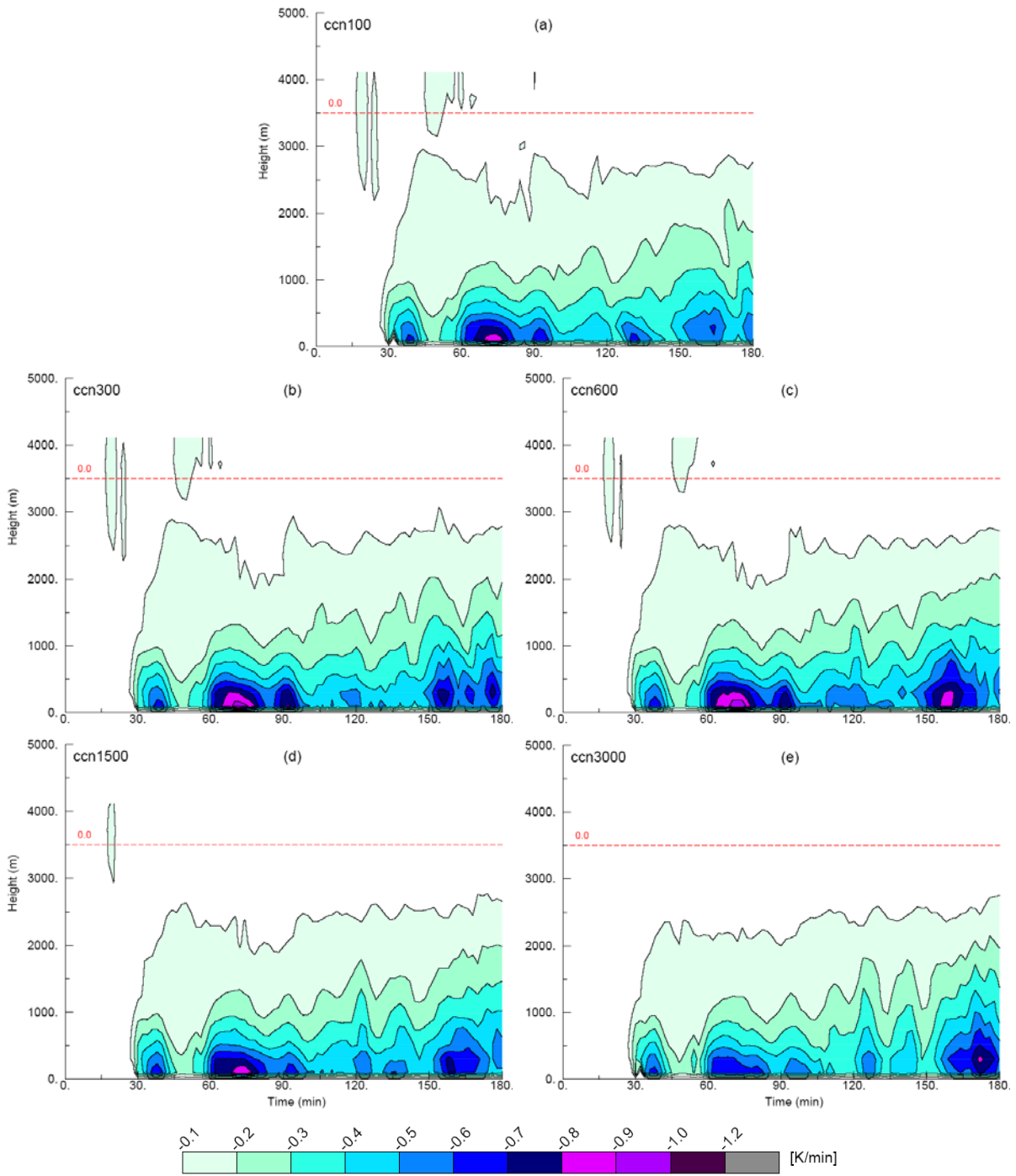


Figure 6.31: As in Fig. 6.30 except for rain evaporation.

surface (Table 6.7). Studies by GSR04, VC04, and Snook and Xue (2008) also showed that the impact of hail on cold-pool strength was largely related to evaporative cooling of rain generated from hail as a result of the melting process. The much smaller correlation between θ'_{min} and

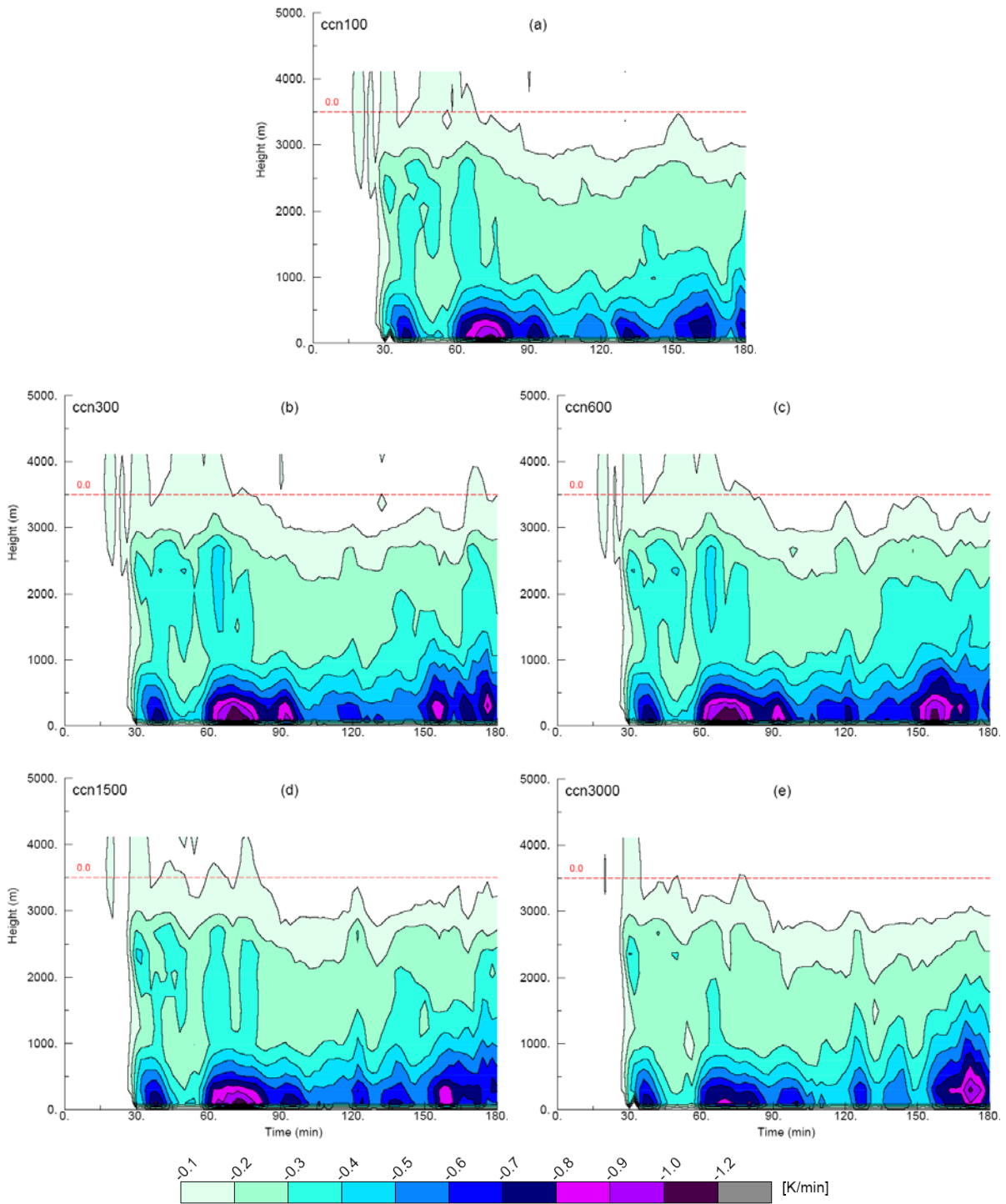


Figure 6.32: As in Fig. 6.30 except for combined cooling from melting and evaporation/sublimation of hail and evaporation of rain.

completely melted hail mass in all cases (Table 6.7) indicates the impact of cooling due to the actual melting of hail is much less than that due to evaporation of rain, as is evident from Figures

6.30 and 6.31. Slightly larger cooling rates for complete melting of hail are seen in the ccn300 and ccn600 cases (Fig. 6.30) as a result of the greater numbers of hailstones (and thus greater numbers of small hail particles) in these cases compared to the others (Fig. 6.9b).

The non-monotonic responses of precipitation and related impacts on the characteristics of the low-level cold-pools to increases in CCN in these simulations can be summarized as follows. *Increases in CCN from 100 to 600 cc^{-1} result not only increased hail sizes and greater amounts of large hail reaching the surface, but also in increased precipitation by both hail and rain, the latter of which is strongly influenced by melting processes of hail. Greater amounts of rainfall lead to enhanced cooling via evaporation at low-levels, and ultimately, to stronger and more expansive cold-pools. Additional increases in CCN to 3000 cc^{-1} result in even greater hail sizes and amounts of large hail, yet rain precipitation amounts are reduced owing to decreases in shedding and complete melting of hail as a result of fewer hailstones. Less total rainfall in the cases with high values of CCN (≥ 1500 cc^{-1}) leads to reduced low-level cooling from rain evaporation, and therefore, a decrease in the size and strength of the cold-pool.*

6.3) Summary

Three-dimensional simulations of the 29 June 2000 supercell storm over northwest Kansas using different initial concentrations of low-level CCN reveal sensitivities in the sub-grid scale microphysical processes, yet the overall storm dynamics are relatively insensitive to changes in CCN. For these particular simulations, an increase in CCN results in larger hail sizes and greater amounts of large diameter (≥ 2 cm) hail both aloft as well as at the surface in qualitative agreement with the results for 2D simulations with bin microphysics of a severe multicell hailstorm (Khain et al. 2011), but in contrast to 3D simulations of the same storm using double-moment bulk microphysics (Noppel et al. 2010). In addition, the physical mechanisms leading to

the production of large hail with increasing CCN for the simulations in the current work are different than those reported in the two aforementioned studies. The main findings from the CCN sensitivity experiments are listed below.

- Increases in CCN result in increased numbers and decreased sizes of cloud droplets in agreement with previous investigations of aerosol-cloud interactions. However, cloud mass contents as well as the mass contents and number concentrations of all other hydrometeor species with the exception of snow respond in a non-monotonic manner to increases in CCN. As in other studies that noted a non-monotonic response in hydrometeor fields to increases in CCN, a threshold value of CCN seems to exist above which the response of hydrometeor mixing ratios and number concentrations to increases in CCN changes sign. For the simulations in the current work, this value is around 600 cc^{-1} . Greater concentrations of CCN also generally result in larger (smaller) sizes of raindrops, graupel particles, and hailstones (pristine ice crystals and aggregates), whereas the sizes of large cloud drops (second cloud mode) and snow particles are relatively unaffected by changes in CCN.
- The formation of hail in all simulations is dominated by collisions between rain and snow particles, and the numbers of newly generated hailstones tend to be limited by the numbers of raindrops available for freezing. Generation of new hail mass and numbers exhibits a non-monotonic response to increasing CCN and is greatest (smallest) for CCN values around 300 to 600 cc^{-1} (3000 cc^{-1}). However, an increase in the average sizes of newly formed hailstones is seen for increasing amounts of CCN.
- Riming of cloud droplets is the dominant hail growth mechanism in all cases, although the non-monotonic responses in supercooled liquid water contents, hail mass, and hail numbers lead to a situation in which average hail growth rates are largest in cases with intermediate

values of CCN (600 to 1500 cc^{-1}) even though the largest hailstones are produced in the case with the highest CCN values (3000 cc^{-1}). The suggestions put forth by Rosenfeld and Khain (2008) and Khain et al. (2011) that increased concentrations of CCN result in increased amounts of supercooled water content, and ultimately to more rapid growth of hail to large sizes is not evident in the current study.

- Regions of maximum hail growth tend to be collocated with regions containing more numerous smaller hailstones in cases with lower CCN thereby increasing competition among the hailstones for the available supercooled water. In cases with higher CCN, maximum hail growth tends to occur over fewer but larger hailstones. Furthermore, larger, newly created hail particles in cases with higher CCN values tend to form in close proximity to regions of maximum hail growth. At lower values of CCN, the generation of relatively large new hail particles also occurs, but these particles undergo slower growth than those in the high CCN cases as they are formed at greater distances from maximum hail growth regions. *The combination of increased sizes of new hail particles, localized reductions in numbers of new hailstones, and increased proximity of hail formation regions to maximum growth regions with increasing CCN tend to promote conditions that lead to increased hail sizes and amounts of large hail in the simulations.* This explanation regarding the impacts of CCN on hail is distinctly different from those of Noppel et al. (2010) and Khain et al. (2011) in which the production of large hail was directly related to changes in supercooled water amounts as a result of changes in the concentrations of CCN.
- Rain production at low-levels from shedding hail is significant in all cases, but is greatest in cases with intermediate values of CCN (600 to 1500 cc^{-1}). These cases exhibit the largest riming rates and produce the greatest amounts of total hail mass, thereby resulting in

increased amounts of shedding relative to the other cases. Rainfall production via complete melting of the smallest hailstones is largest for cases that produce the greatest numbers of hailstones (CCN values of 300 to 600 cc^{-1}), yet complete melting of hail contributes less to total rainfall than does shedding from hail.

- Surface precipitation amounts respond in a non-monotonic manner to increases in CCN, with the greatest amounts produced in cases with intermediate values of CCN (600 to 1500 cc^{-1}). However, the maximum hail sizes and amounts of large hail arriving at the surface, as well as the fraction of surface precipitation comprised of hail all increase with increasing CCN.
- The impacts of increasing CCN on low-level downdrafts is insignificant in these simulations, however, the magnitudes of low-level cooling and the associated effects on cold-pool evolution do exhibit sensitivities to changes in CCN. In all cases, evaporative cooling of rain at low levels has the largest impact on the cold-pools. Cases with lower amounts of CCN (300 to 600 cc^{-1}) produce more rainfall thereby resulting in greater magnitudes of low-level cooling and larger and stronger cold-pools. Low-level cooling due to melting hail has a minimal impact on the cold-pools in all cases, though hail does affect the cold-pool characteristics indirectly through the generation of rain during the melting process.

7. General summary and suggestions for future work

7.1) Summary

The prediction of the 6th moment of the hail size distribution in addition to the 0th and 3rd moments allows for all three parameters of the prescribed gamma distribution function to vary freely, thereby removing the need to 'tune' the hail distribution parameters according to the environment and/or storm type being investigated. The results of the various tests and simulations presented in the previous chapters show that the new 3MHAIL bulk microphysics scheme in RAMS not only leads to improved prediction of hail, but to improved prediction of the structure, evolution, and precipitation processes in simulations of the well-documented supercell of 29 June 2000 that occurred over northwest Kansas.

Idealized tests of the sedimentation, melting, and hail formation components of the 3MHAIL scheme demonstrate a significant improvement in the representation of these processes compared to the existing lower order moment microphysical schemes in RAMS. Simple 1D column sedimentation tests show the 3MHAIL scheme gives results that most closely match those for a true bin sedimentation scheme for a range of initial hail distributions on both stretched and constant spacing vertical grids when compared to sedimentation using the 1M or modified 2M schemes. The ability of the 3MHAIL scheme to predict changes in the spectral width parameter (v_h) owing to both sedimentation and melting also provides much more realism in the evolution of hail spectra, such as broadening aloft and narrowing at low levels, as well as mitigates the artificial shifts in hail size distributions towards larger sizes due to complete melting. The modified 3-component freezing collection algorithm in the 3MHAIL scheme is based on the densities and sizes of the colliding particles and allows for more realistic outcomes as a result of rain-ice collisions, whereas these collisions in the original 2M RAMS collection scheme *always*

result in hail formation. In addition, new hail particles formed in the presence of existing hail do not significantly alter the higher order moments of the existing hail distribution with the 3MHAIL scheme.

Three-dimensional simulations of the 29 June 2000 supercell storm with 3MHAIL and two different 2M microphysics schemes show that the 3MHAIL scheme produces a storm that represents the observed storm characteristics much more accurately than either of the simulations with two-moment microphysics. The locations and timing of fallout episodes of large ($D_h \geq 2$ cm) hail, as well as the predicted sizes of the hailstones in the simulation with 3MHAIL microphysics match well with the observations for this particular storm and show good qualitative agreement with previous observations of hailstorms. The modeled storm using the 2M version (mod2M) of the 3MHAIL scheme, in which the value of v_h is held fixed, artificially produces significant amounts of large hail below the freezing level as a result of unrealistic shifts in the hail size distribution towards larger sizes during the melting process. On the other hand, the simulation with the original RAMS 2M microphysics produces almost no graupel, substantial amounts of small hail, and very little hail at the surface. Analyses of computed polarimetric variables for the simulated storms reveal that the signatures typical of large hail (large values of Z_H , LDR , and HDR in combination with low ZDR and ρ_{vh} values) show good correspondence to regions of large hail predicted in the model and are most realistic in the simulation with 3MHAIL microphysics.

The use of 2M microphysics in the simulations results in the majority of precipitation mass residing in the hail category as well as a five- to six-fold increase in the numbers of hailstones compared to the simulation using 3MHAIL microphysics. Rain-ice collisions are the dominant generator of new hail particles in the 2M and 3MHAIL schemes, yet the newly implemented

three-component freezing algorithms of MY05b and F94, in conjunction with the adjustment of newly formed hailstones to conserve higher order moments, lead to significantly fewer (and more reasonable numbers of) hailstones with the 3MHAIL scheme. In addition, realistic amounts of graupel are produced with the three-component freezing scheme of MY05b compared to the original RAMS binned riming scheme, which produces only tiny amounts of graupel. Rain production at low levels is dominated by melting of the numerous small hailstones in the simulation with the original RAMS 2M microphysics, whereas shedding from larger hailstones accounts for the majority of rain generation in simulations with mod2M and 3MHAIL microphysics. Furthermore, the predominantly small hail produced with the original 2M microphysics results in stronger downdrafts and a deeper, stronger, and more expansive cold pool due to increased cooling rates from melting hail, evaporation/sublimation of hail, and evaporation of rain. By comparison, smaller cooling magnitudes associated with the larger hail in the simulation with 3MHAIL microphysics result in weaker downdrafts and a cold pool that is shallower, smaller, and generally not as strong as in the simulations with 2M microphysics.

The tests examining the sensitivity of hail in simulated supercells to changes in CCN concentrations demonstrate that an increase in CCN leads to an increase in both predicted hail sizes as well as the amounts of large diameter hail, whereas the general storm dynamics are relatively insensitive to changes in CCN. Similar to results from recent studies of CCN effects on deep convection, the majority of the hydrometeor fields respond in a non-monotonic manner to increases in CCN, and the threshold value of CCN at which the response changes sign seems to be around 600 cc^{-1} for the particular environment and storm type examined. A non-monotonic response is also seen in the generation of new hailstones. Fewer numbers and less hail mass are generated in simulations with extremely low (100 cc^{-1}) and very high (3000 cc^{-1}) values of CCN

compared to cases that are initialized with CCN amounts between these two extremes, although the average sizes of newly formed hailstones tend to increase with increases in CCN. Hail growth is dominated by riming of cloud droplets in all simulations, though hail growth rates are maximized in simulations with intermediate values of CCN (600 and 1500 cc^{-1}) that produce greater numbers of large hailstones as opposed to the simulation with very high CCN (3000 cc^{-1}) that produces the largest hailstones owing to fewer hailstones and reduced riming efficiencies in the latter case. In addition, an increase in CCN results in increasingly overlapped regions of maximum hail growth and low concentrations of both large hailstones and newly formed hailstones such that competition for the available supercooled water is reduced. In fact, the combination of increased sizes of new hail particles, localized reductions in numbers of new hailstones, and increased proximity of the hail formation regions to maximum growth regions with increasing CCN tend to promote conditions that lead to increased hail sizes and amounts of large hail in the simulations.

The CCN sensitivity tests also reveal non-monotonic responses in total surface precipitation, magnitudes of low-level cooling, and low-level cold pool characteristics to changes in CCN. Rain production at low-levels via shedding from hail is significant in all cases and is greatest in cases with intermediate values of CCN (600 and 1500 cc^{-1}) that exhibit the largest riming rates, although the largest amounts of surface rainfall occur in cases with lower concentrations of CCN (300 and 600 cc^{-1}) in which the greatest amounts of hail mass and number are produced. Contributions to total rainfall from complete melting of the smallest hailstones are largest in cases that produce the greatest numbers of hailstones (CCN values of 300 and 600 cc^{-1}), though complete melting of hail accounts for much less rain than that from shedding in all simulations. Total surface precipitation amounts increase as CCN increases from 100 to 1500 cc^{-1} , followed

by a decrease in total surface precipitation for CCN values of 3000 cc^{-1} . This non-monotonic response in surface precipitation is in contrast to decreasing precipitation amounts with increasing CCN reported in previous simulations of supercell convection; however, the simulations in these previous studies did not produce hail at the surface. For the simulations in the current study, the maximum hail sizes and amounts of large hail arriving at the surface, as well as the fraction of surface precipitation comprised of hail all increase with increasing CCN. Low-level cooling due to melting hail has a minimal impact on the cold pools in all cases, though hail does affect the cold pool characteristics indirectly through the generation of rain during the melting process. Evaporative cooling of rain at low levels has the largest impact on the cold pools, and cases with lower amounts of CCN (300 to 600 cc^{-1}) produce more rainfall thereby resulting in greater magnitudes of low-level cooling, and hence, larger and stronger cold pools.

The results of this study indicate the new 3MHAIL bulk microphysics scheme will be a valuable tool for future modeling studies of hail-producing storms as well as more general deep moist convection in which ice processes play a major role in precipitation production.

7.2) *Future work*

- As the 3MHAIL scheme was only validated for one storm type in a particular environment in the present study, additional simulations of deep convection occurring in different environments should be performed in order to further validate the 3MHAIL scheme. These tests could include environments characterized by high freezing levels such as summertime convection over FL for which surface hail would not be expected, marginally severe single-cell ordinary thunderstorms such as an event that occurred over central TN on 15 May 2009 in which 2.5 cm diameter hail was reported at the surface, mid-latitude squall lines, and

summertime hailstorms that frequently occur along the Front Range in CO that produce copious amount of small hailstones. Such an undertaking would provide a much better gauge of how hail processes are represented in the 3MHAIL scheme over a wide range of storm types.

- The 3MHAIL scheme could be used to investigate the impacts of CCN in other environments supportive of hail-producing storms as well to determine if the non-monotonic responses in hail and rain precipitation and increases in hail sizes with increasing CCN evident in the current study are observed for different types of hailstorms. One obvious choice would be to simulate the 28 June 2006 severe hailstorm case over Germany investigated by Noppel et al. (2010) and Khain et al. (2011) with the 3MHAIL scheme and compare the results with the aforementioned studies. The 3MHAIL scheme could also be used to investigate the impacts of GCCN and IN on hail processes, with the latter being especially relevant in evaluating the various hail suppression concepts.
- The grid resolution employed for the simulations in the current study are adequate for resolving storm-scale features such as the structure and evolution of updrafts, downdrafts, mesocyclones, and bulk cold-pool characteristics, but simulations using finer grid resolutions would make it possible to determine what, if any, impacts the hail sizes have on tornadogenesis. In addition, as the smallest vertical grid spacing in the current simulations was 200 m, increased vertical resolution, especially over model levels below the freezing level, would likely lead to better representation of precipitation processes associated with hail, particularly melting of hail, as well as the characteristics of the low-level cold-pool.
- The analyses of hail formation conducted herein revealed that the binned riming scheme of Saleeby and Cotton (2008) generates a miniscule amount of graupel, which in the 2M

microphysics scheme, results in rimed graupel accounting for a very small fraction of the total hail formation. The modified three-component freezing algorithm in the 3MHAIL scheme compensates this somewhat by generating graupel from rain-snow and rain-aggregate collisions, thereby leading to a greater proportion of new hail formed via riming of graupel. However, further testing revealed that the sizes of newly formed hail particles from rimed graupel depend only on the amount of rimed cloud mass in the current formulations of both the bulk and binned riming schemes. It is therefore suggested that the parameterization of hail formation from riming of graupel be reformulated following Zeigler (1985) and Milbrandt and Yau (2005b) who compute the graupel diameter threshold above which wet growth occurs. This would permit more accurate conversion rates of riming graupel to hail as well as provide a physical basis for determining the sizes of newly formed hailstones via this process as graupel particles undergoing wet take on the characteristics of hailstones.

- One of the main disadvantages of the 3MHAIL scheme is that the current formulation of the computer code leads to an increase of roughly 25 to 30% in computation time compared to the original 2M RAMS microphysics code. Thus, if the 3MHAIL scheme is to be used in any sort of parameter range study in which many simulations are carried out, the microphysics code should be made more efficient. One of the largest consumers of computational time is the new melting routine in the 3MHAIL scheme. During model runtime, hail distributions at all grid points below the freezing level are partitioned into discrete size bins in order to compute the heat transfer equation for individual hail sizes ≤ 5 mm such that the largest size hailstone to melt completely in one time step can be determined. The fact that hail melting depends on time-dependent characteristics of the hail distributions (i.e., amount of liquid water fraction) as well as on a myriad of environmental conditions largely precludes the use

of look-up tables to perform the melting calculations. Eliminating a portion of the smallest hail size bins and thereby reducing the total number of size bins could be one solution, though further testing would certainly be required to determine what effects this would have on the melting computations as well as other hail processes (i.e., collection, vapor/heat diffusion, and sedimentation).

- Lastly, the additional prediction of the 6th moment could be extended to other hydrometeor categories as well, similar to the triple-moment bulk scheme of Milbrandt and Yau (2005b). Such an endeavor could result in a significantly more accurate representation of hydrometeors and associated microphysical processes. As pointed out by Milbrandt and Yau (2006b), however, not all hydrometeor species may need to be predicted using three moments. It is suggested here that allowing for variable spectral shape parameters for the cloud, graupel, and rain categories (in addition to hail) would likely have the greatest impact in terms of improved representation of precipitation processes in deep convection. In the case of cloud droplets, for example, a narrowing of the spectral width of the cloud droplet size distribution as a result of increased CCN concentrations has been observed, and this effect could be better accounted for by predicting the spectral shape parameter in addition to mixing ratio and number concentration. The current use of two cloud droplet modes in RAMS partially compensates for this by representing the bimodal distribution often observed in clouds. Furthermore, numerous observational, theoretical, and laboratory studies of these hydrometeor types have been performed providing a good physical foundation (i.e., collection efficiencies) from which the necessary formulations for a triple-moment algorithm could be derived. In terms of implementing such a triple-moment scheme into the RAMS model, the parameterization of raindrop breakup would have to be revised such that the

numbers and sizes of drops following the breakup process could be obtained in order to compute changes in the rain reflectivity factor. (Recall that the effects of raindrop breakup are currently parameterized as a modification of the coalescence efficiency for rain-self collection). The prediction of an additional moment for the graupel category could mostly follow the formulations for hail in the 3MHAIL scheme.

REFERENCES

- Albrecht, B. A., 1989: Aerosols, cloud microphysics, and fractional cloudiness. *Science*, **245**, 1227-1230.
- Andreae, M. O., D. Rosenfeld, P. Artaxo, A. A. Costa, G. P. Frank, K. M. Longo, and M. A. F. Silva-Dias, 2004: Smoking rain clouds over the Amazon. *Science*, **303**, 1337-1342.
- Atlas, D., 1966: The balance level in convective storms. *J. Atmos. Sci.*, **23**, 635-651.
- _____, C. W. Ulbrich, and C. R. Williams, 2004: Physical origin of a wet microburst: Observations and theory. *J. Atmos. Sci.*, **61**, 1186-1196.
- Auer, A. H. Jr., 1972: Distribution of graupel and hail with size. *Mon. Wea. Rev.*, **100**, 325-328.
- _____, and J. D. Marwitz, 1972: Hail in the vicinity of organized updrafts. *J. Appl. Meteor.*, **11**, 748-752.
- Aydin, K., T. A. Seliga, and V. Balaji, 1986: Remote sensing of hail with a dual linear polarization radar. *J. Climate Appl. Meteor.*, **25**, 1475-1484.
- _____, and Y. Zhao, 1990: A computational study of polarimetric radar observables in hail. *IEEE Trans. Geosci. Remote Sens.*, **28**, 412-421.
- Bailey, I. H., and W. C. Macklin, 1968: Heat transfer from artificial hailstones. *Quart. J. Roy. Meteor. Soc.*, **94**, 93-98.
- Balakrishnan, N., and D. S. Zrnić, 1990: Use of polarization to characterize precipitation and discriminate large hail. *J. Atmos. Sci.*, **47**, 1525-1540.
- Barber, P., and C. Yeh, 1975: Scattering of electromagnetic waves by arbitrarily shaped dielectric bodies. *Appl. Opt.*, **14**, 2864-2872.
- Bennetts, G. M., and F. Rawlins, 1981: Parameterization of the ice-phase in a model of midlatitude cumulonimbus convection and its influence on the simulation of cloud development. *Quart. J. Roy. Meteor. Soc.*, **107**, 477-502.
- Berry, E. X., and R. L. Reinhardt, 1974: An analysis of cloud drop growth by collection: Part I. Double distributions. *J. Atmos. Sci.*, **31**, 1814-1824.
- Blahak, U., 2008: Towards a better representation of high density ice particles in a state-of-the-art two-moment bulk microphysical scheme. *15th Intl. Conf. on Clouds and Precip.*, July 7-11, 2008, Cancun, México

- Braham, R. R. Jr., 1964: What is the role of ice in summer rain-showers?. *J. Atmos. Sci.*, **21**, 640-645.
- Brimelow, J. C., G. W. Reuter, and E. R. Poolman, 2002: Modeling maximum hail size in Alberta thunderstorms. *Wea. Forecasting*, **17**, 1048-1062.
- Browning, K. A., 1963: The growth of large hail within a steady updraught. *Quart. J. Roy. Meteor. Soc.*, **89**, 491-506.
- _____, 1966: The lobe structure of giant hailstones. *Quart. J. Roy. Meteor. Soc.*, **92**, 1-14.
- _____, and F. H. Ludlam, 1962: Airflow in convective storms. *Quart. J. Roy. Meteor. Soc.*, **88**, 117-135.
- Bringi, V. N., and T. A. Seliga, 1977: Scattering from non-spherical hydrometeors. *Ann. Des. Telecom.*, **32**, (11-12), 392-397.
- _____, J. Vivekanandan, and J. D. Tuttle, 1986: Multiparameter radar measurements in Colorado Convective Storms. Part II: Hail detection studies. *J. Atmos. Sci.*, **43**, 2564-2577.
- _____, K. Knupp, A. Detwiler, L. Liu, I. J. Caylor, and R. A. Black, 1997: Evolution of a Florida thunderstorm during the convection and precipitation/electrification experiment: The case of 9 August 1991. *Mon. Wea. Rev.*, **125**, 2131-2160.
- Bryan, G. H., J. C. Wyngaard, and J. M. Fritsch, 2003: Resolution requirements for the simulation of deep moist convection. *Mon. Wea. Rev.*, **131**, 2394-2416.
- _____, and H. Morrison, 2012: Sensitivity of a simulated squall line to horizontal resolution and parameterization of microphysics. *Mon. Wea. Rev.*, **140**, 202-225.
- Carbone, R. E., and L. D. Nelson, 1978: The evolution of raindrop spectra in warm-based convective storms as observed and numerically modeled. *J. Atmos. Sci.*, **35**, 2302-2314.
- Carey, L. D., and S. A. Rutledge, 1998: Electrical and multiparameter radar observations of a severe hailstorm. *J. Geophys. Res.*, **103**, 13,979-14,000.
- Carras, J. N., and W. C. Macklin, 1973: The shedding of accreted water during hailstone growth. *Quart. J. Roy. Meteor. Soc.*, **99**, 639-648.
- Carrió, G. G., S. C. van den Heever, and W. R. Cotton, 2007: Impacts of nucleating aerosol on anvil-cirrus clouds: A modeling study. *Atmos. Res.*, **84**, 111-131.
- _____, W. R. Cotton, and W. Y. Y. Cheng, 2010: Urban growth and aerosol effects on convection over Houston. Part I: The August 2000 case. *Atmos. Res.*, **96**, 560-574.

- _____, and W. R. Cotton, 2011: Urban growth and aerosol effects on convection over Houston. Part II: Dependence of aerosol effects on instability. *Atmos. Res.*, **102**, 167-174.
- Carte, A. E., 1966: Features of Transvaal hailstorms. *Quart. J. Roy. Meteor. Soc.*, **92**, 290-296.
- _____, and R. E. Kidder, 1966: Transvaal hailstones. *Quart. J. Roy. Meteor. Soc.*, **92**, 382-391.
- Chalon, J. P., J. C. Fankhauser, and P. J. Eccles, 1976: Structure of an evolving hailstorm, Part I: General characteristics and cellular structure. *Mon. Wea. Rev.*, **104**, 564-575.
- Charlton, R. B., and R. List, 1972: Hail size distributions and accumulation zones. *J. Atmos. Sci.*, **29**, 1182-1193.
- Changnon, S. A. Jr., 1971: Hailfall characteristics related to crop damage. *J. Appl. Meteor.*, **16**, 270-274.
- _____, 1977: The climatology of hail in North America. *Hail. A Review of Hail Science and Hail Suppression.*, *Meteor. Monogr.*, No. 38, Amer. Meteor. Soc., 107-128.
- _____, 1999: Data approaches for determining hail risk in the contiguous United States. *J. Appl. Meteor.*, **38**, 1730-1739.
- _____, 2001: *Thunderstorms across the Nation: An Atlas of Storms, Hail, and Their Damages in the 20th Century*, Printec Press, 93 pp.
- Chen, J., and D. Lamb, 1994: Simulation of cloud microphysical and chemical processes using a multicomponent framework. Part I: Description of the microphysical model. *J. Atmos. Sci.*, **51**, 2613-2630.
- Cheng, L., and M. English, 1983: A relationship between hailstone concentration and size. *J. Atmos. Sci.*, **40**, 204-213.
- _____, _____, and R. Wong, 1985: Hailstone size distributions and their relationship to storm thermodynamics. *J. Climate Appl. Meteor.*, **24**, 1059-1067.
- Chisholm, A. J., 1968: Observations by 10-cm radar of an Alberta hailstorm in a sheared environment. Preprints, *13th Radar Meteor. Conf.*, Montreal, Amer. Meteor. Soc., 82-87.
- _____, 1973: *Alberta Hailstorms*. Part I: Radar Case Studies and Airflow Models. *Meteor. Monogr.*, No. 36, Amer. Meteor. Soc., 1-36.
- _____, and J. H. Renick, 1972: The kinematics of multicell and supercell Alberta hailstorms. Alberta Hail Studies, 1972, Research Council of Alberta Hail Studies Report No. 72-2, 24-31.

- Clark, T. L., 1973: Numerical modeling of the dynamics and microphysics of warm cumulus convection. *J. Atmos. Sci.*, **30**, 857-878.
- Cohen, C., and E. W. McCaul Jr., 2006: The sensitivity of simulated convective storms to variations in prescribed single-moment microphysics parameters that describe particle distributions, sizes, and numbers. *Mon. Wea. Rev.*, **134**, 2547-2565.
- Cotton, W. R., M. A. Stephens, T. Nehkorn, and G. J. Tripoli, 1982: The Colorado State University three-dimensional cloud / mesoscale model - 1982 Part II: An ice phase parameterization. *J. Rech. Atmos.*, **16**, 295-320.
- _____, G. J. Tripoli, R. M. Rauber, and E. A. Mulvihill, 1986: Numerical simulation of the effects of varying ice crystal nucleation rates and aggregation processes on orographic snowfall. *J. Climate Appl. Meteor.*, **25**, 1658-1680.
- _____, R. A. Pielke Sr., R. L. Walko, G. E. Liston, C. J. Tremback, H. Jiang, R. L. McAnnelly, J. Y. Harrington, M. E. Nicholls, G. G. Carrio, and J. P. McFadden, 2003: RAMS 2001: Current status and future directions. *Meteor. Atmos. Phys.*, **82**, 5-29.
- _____, and R. A. Anthes, 1989: *Storm and Cloud Dynamics*. Academic Press, 883 pp.
- Danielson, E. F., 1977: Inherent difficulties in hail probability prediction. *Hail: A Review of Hail Science and Hail Suppression*, *Meteor. Monogr.*, No. 38, Amer. Meteor. Soc., 135-143.
- _____, R. Bleck, and D. A. Morris, 1972: Hail growth by stochastic collection in a cumulus model. *J. Atmos. Sci.*, **29**, 135-155.
- Davies-Jones, R. P., D. W. Burgess, and M. Foster, 1990: Test of helicity as a tornado forecast parameter. Preprints, *16th Conf. on Severe Local Storms*, Kananaskis Park, Alberta, Canada, Amer. Meteor. Soc., 588-592.
- Dawson II, D. T., M. Xue, J. A. Milbrandt, and M. K. Yau, 2010: Comparison of evaporation and cold pool development between single-moment and multimoment bulk microphysics schemes in idealized simulations of tornadic thunderstorms. *Mon. Wea. Rev.*, **138**, 1152-1171.
- DeMott, P. J., K. Sassen, M. R. Poellet, D. Baumgardner, D. C. Rogers, S. D. Brooks, A. J. Prenni, and S. M. Kreidenweis, 2003: African dust aerosols as atmospheric ice nuclei. *Geophys. Res. Lett.*, **30**, 1732, doi:10.1029/2003GL017410.
- Depue, T. K., P. C. Kennedy, and S. A. Rutledge, 2007: Performance of the hail differential reflectivity (H_{DR}) polarimetric radar hail indicator. *J. Appl. Meteor. Climatol.*, **46**, 1290-1301.
- Dessens, J., and R. Fraile, 1994: Hailstone size distributions in southwestern France. *Atmos. Res.*, **33**, 57-73.

- Detwiler, A., D. Langerud, and T. Depue, 2010: Investigation of the variability of cloud condensation nuclei concentrations at the surface in western North Dakota. *J. Appl. Meteor. Climatol.*, **49**, 136-145.
- Drake, J. C., and B. J. Mason, 1966: The melting of small ice spheres and cones. *Quart. J. Roy. Meteor. Soc.*, 500-509.
- Dye, J. E., C. A. Knight, V. Toutenhoofd, and T. W. Cannon, 1974: The mechanism of precipitation formation in northeastern Colorado cumulus III. Coordinated microphysical and radar observations and summary. *J. Atmos. Sci.*, **31**, 2152-2159.
- _____, B. E. Martner, and L. J. Miller, 1983: Dynamical-microphysical evolution of a convective storm in a weakly-sheared environment. Part I: Microphysical observations and interpretation. *J. Atmos. Sci.*, **40**, 2083-2096.
- English, M., 1973: Alberta hailstorms. Part II: Growth of large hail in the storm. *Alberta Hailstorms, Meteor. Monogr.*, No. 36, Amer. Meteor. Soc., 37-98.
- Farley, R. D., and H. D. Orville, 1986: Numerical modeling of hailstorms and hailstone growth. Part I: Preliminary model verification and sensitivity tests. *J. Climate Appl. Meteor.*, **25**, 2014-2035.
- _____, 1987a: Numerical modeling of hailstorms and hailstone growth. Part II: The role of low-density riming growth in hail production. *J. Climate Appl. Meteor.*, **26**, 234-254.
- _____, 1987b: Numerical modeling of hailstorms and hailstone growth. Part III: Simulation of an Alberta hailstorm- Natural and seeded cases. *J. Climate Appl. Meteor.*, **26**, 789-812.
- Federer, B., and A. Waldvogel, 1975: Hail and raindrop size distributions from a Swiss multicell storm. *J. Appl. Meteor.*, **14**, 91-97.
- _____, _____, W. Schmid, H. H. Schiesser, F. Hampel, M. Schweingruber, W. Stahel, J. Bader, J. F. Mezeix, N. Doras, G. D'Aubigny, G. DerMegreditchian, and D. Vento, 1986: Main results of Grossversuch IV. *J. Climate Appl. Meteor.*, **25**, 917-957.
- Ferrier, B. S., 1994: A double-moment multiple-phase four-class bulk ice scheme. Part I: Description. *J. Atmos. Sci.*, **51**, 249-280.
- _____, W. Tao, and J. Simpson, 1995: A double-moment multiple-phase four-class bulk ice scheme. Part II: Simulations of convective storms in different large-scale environments and comparisons with other bulk parameterizations. *J. Atmos. Sci.*, **52**, 1001-1033.
- Foote, G. B., 1984: A study of hail growth using observed storm conditions. *J. Climate Appl. Meteor.*, **23**, 84-101.

- _____, 1985: Aspects of cumulonimbus classification relevant to the hail problem. *J. Rech. Atmos.*, **19**, 61-74.
- _____, and C. G. Wade, 1982: Case study of a hailstorm in Colorado. Part I: Radar echo structure and evolution. *J. Atmos. Sci.*, **39**, 2828-2846.
- Fraile, R., A. Castro, L. López, J. L. Sánchez, and C. Palencia, 2003: The influence of melting on hailstone size distribution. *Atmos. Res.*, **67-68**, 203-213.
- García-García, F., and R. List, 1992: Laboratory measurements and parameterizations of supercooled water skin temperatures and bulk properties of gyrating hailstones. *J. Atmos. Sci.*, **49**, 2058-2073.
- Giaiotti, D., E. Ganesini, and F. Stel, 2001: Heuristic considerations pertaining to hailstone size distributions in the plain of Friuli-Venezia Giulia. *Atmos. Res.*, **57**, 269-288.
- Gilmore, M. S., J. M. Straka, and E. N. Rasmussen, 2004: Precipitation uncertainty due to variations in precipitation particle parameters within a simple microphysics scheme. *Mon. Wea. Rev.*, **132**, 2610-2627.
- Greenan, B. J. W., and R. List, 1995: Experimental closure of the heat and mass transfer theory of spheroidal hailstones. *J. Atmos. Sci.*, **52**, 3797-3815.
- Goyer 1977: Response, *Hail. A Review of Hail Science and Hail Suppression.*, Meteor. Monogr., No. 38, Amer. Meteor. Soc.,
- Guyer. J. L., and R. Ewald, 2004: Record hail event- Examination of the Aurora, Nebraska supercell of 22 June 2003. Preprints, *22nd Conf. on Severe Local Storms*, Hyannis, MA, Paper 11B.1.
- Hall, W. D. 1980: A detailed microphysical model within a two-dimensional dynamic framework: Model description and preliminary results. *J. Atmos. Sci.*, **37**, 2486-2507.
- Hallett, J., and S. C. Mossop, 1974: Production of secondary ice particles during the riming process. *Nature*, **249**, 26-28.
- Heymsfield, A. J., and D. J. Musil, 1982: Case study of a hailstorm in Colorado. Part II: Particle growth processes at mid-levels deduced from *in-situ* measurements. *J. Atmos. Sci.*, **39**, 2487-2866.
- _____, and J. C. Pflaum, 1985: A quantitative assessment of the accuracy of techniques for calculating graupel growth. *J. Atmos. Sci.*, **42**, 2264-2274.
- Hill, G. E., 1974: Factors controlling the size and spacing of cumulus clouds as revealed by numerical experiments. *J. Atmos. Sci.*, **31**, 646-673.

- Hitschfeld, W., and R. H. Douglas, 1963: A theory of hail growth based on studies of Alberta storms. *Z. Agnew. Math. Phys.*, **14**, 554-562.
- Hjelmfelt, M. R., H. D. Orville, R. D. Roberts, J. P. Chen, and F. J. Kopp, 1989: Observational and numerical study of a microburst line-producing storm. *J. Atmos. Sci.*, **46**, 2731-2743.
- Hobbs, P. V., M. K. Politovich, and L. F. Radke, 1980: The structures of summer convective clouds in eastern Montana. I: Natural clouds. *J. Appl. Meteor.*, **19**, 645-663.
- _____, D. A. Bowdle, and L. F. Radke, 1985: Particles in the lower troposphere over the High Plains of the United States. Part II: Cloud condensation nuclei. *J. Climate Appl. Meteor.*, **24**, 1358-1369.
- Höller, H., V. N. Bringi, J. Hubbert, M. Hagen, and P. F. Meischner, 1994: Life cycle and precipitation formation in a hybrid-type hailstorm revealed by polarimetric and Doppler radar measurements. *J. Atmos. Sci.*, **51**, 2500-2522.
- Houze, R. A., Jr., 1993: *Cloud Dynamics*. Academic Press, 573 pp.
- Hubbert, J., V. N. Bringi, L. D. Carey, and S. Bolen, 1998: CSU-CHILL polarimetric radar measurements from a sever hail storm in eastern Colorado. *J. Appl. Meteor.*, **37**, 749-775.
- Huschke, R. E., 1959: *Glossary of Meteorology*. Amer. Meteor. Soc., 638 pp.
- Illingworth, A. J., J. W. F. Goddard, and S. M. Cherry, 1987: Polarization radar studies of precipitation development in convective storms. *Quart. J. Roy. Meteor. Soc.*, **113**, 469-489.
- _____, and I. J. Caylor, 1991: Co-polar correlation measurements of precipitation. Preprints, *25th Intl. Conf. on Radar Meteor.*, Paris, France, Amer. Meteor. Soc., 650-657.
- _____, and T. M. Blackman, 2002: The need to represent raindrop size spectra as normalized gamma distributions for the interpretation of polarization radar observations. *J. Appl. Meteor.*, **41**, 286-297.
- Iribarne, J. V., and R. G. De Pena, 1962: The influence of particle concentration on the evolution of hailstones. *Nubila*, **5**, 7-30.
- Jewett, B. F., R. B. Wilhelmson, J. M. Straka, and L. J. Wicker, 1990: Impact of ice parameterization on the low-level structure of modeled supercell thunderstorms. Preprints, *16th Conf. on Severe Local Storms*, Kananaskis Park, Alberta, Amer. Meteor. Soc., 275-280.

- Joe, P. I., R. List, P. R. Kry, M. R. de Quervain, P. Y. K. Liu, P. W. Stagg, J. D. McTaggart-Cowan, E. P. Lozowski, M. C. Steiner, J. Von Niederhäusern, R. E. Stewart, E. Freire, and G. Lesins, 1976: Loss of accreted water from growing hailstones. *Proc. VII Intl. Conf. on Cloud Physics*, Boulder, CO, 264-269.
- _____, _____, and G. B. Lesins, 1980: Ice accretions. Part II: Rain production by cloud water conversion. *J. Rech. Atmos.*, **14**, 357-364.
- Johns, R. H., and C. A. Doswell III, 1992: Severe local storms forecasting. *Wea. Forecasting*, **7**, 588-612.
- Johnson, D. B., 1987: On the relative efficiency of coalescence and riming. *J. Atmos. Sci.*, **44**, 1671-1680.
- Johnson, D. E., P. K. Wang, and J. M. Straka, 1993: Numerical simulations of the 2 August 1981 CCOPE supercell storm with and without ice microphysics. *J. Appl. Meteor.*, **32**, 745-759.
- Jung, Y., M. Xue, and G. Zhang, 2010: Simulations of polarimetric radar signatures of a supercell storm using a two-moment bulk microphysics scheme. *J. Appl. Meteor. Climatol.*, **47**, 146-163.
- Kennedy, P. C., and A. G. Detwiler, 2003: A case study of the origin of hail in a multicell thunderstorm using in situ aircraft and polarimetric radar data. *J. Appl. Meteor.*, **42**, 1679-1690.
- Kessler, E., III, 1969: *On the Distribution and Continuity of Water Substance in Atmospheric Circulation. Meteor. Monogr.*, No. 32, Amer. Meteor. Soc., 84pp.
- Khain, A., A. Pokrovsky, M. Pinsky, A. Seifert, and V. Phillips, 2004: Simulation of effects of atmospheric aerosols on deep turbulent convective clouds using a spectral microphysics mixed-phase cumulus cloud model. Part I: Model description and possible applications. *J. Atmos. Sci.*, **61**, 2963-2982.
- _____, and A. Pokrovsky, 2004: Simulation of effects of atmospheric aerosols on deep turbulent convective clouds using a spectral microphysics mixed-phase cumulus cloud model. Part II: Sensitivity study. *J. Atmos. Sci.*, **61**, 2983-3001.
- _____, D. Rosenfeld, and A. Pokrovsky, 2005: Aerosol impact on the dynamics and microphysics of deep convective clouds. *Quart. J. Roy. Meteor. Soc.*, **131**, 2639-2663.
- _____, and B. Lynn, 2009: Simulation of a supercell storm in clean and dirty atmosphere using weather research and forecast model with spectral bin microphysics. *J. Geophys. Res.*, **114**, D19209, doi:10.1029/2009JD011827.

- _____, D. Rosenfeld, A. Pokrovsky, U. Blahak, and A. Ryzhkov, 2011: The role of CCN in precipitation and hail in a mid-latitude storm as seen in simulations using a spectral (bin) microphysics model in a 2D dynamic frame. *Atmos. Res.*, **99**, 129-146.
- Klemp, J. B., and R. B. Wilhelmson, 1978: The simulation of three-dimensional convective storm dynamics. *J. Atmos. Sci.*, **35**, 1070-1096.
- Knight, C. A., 1968: On the mechanism of spongy hailstone growth. *J. Atmos. Sci.*, **25**, 440-444.
- _____, 1982: The Cooperative Convective Precipitation Experiment (CCOPE), 18 May- 7 August 1981. *Bull. Amer. Meteor. Soc.*, **63**, 386-398.
- _____, 1984: Radar and other observations of two vaulted storms in northeastern Colorado. *J. Atmos. Sci.*, **41**, 258-271.
- _____, and N. C. Knight, 1970a: Lobe structures of hail. *J. Atmos. Sci.*, **27**, 667-671.
- _____, and _____, 1970b: Hailstone embryos. *J. Atmos. Sci.*, **27**, 659-666.
- _____, and _____, 1970c: The falling behavior of hailstones. *J. Atmos. Sci.*, **27**, 672-681.
- _____, and _____, 1973: Quenched, spongy hail. *J. Atmos. Sci.*, **30**, 1665-1671.
- _____, and _____, 1979: Results of a randomized hail suppression experiment in northeast Colorado. Part V. Hailstone embryo types. *J. Appl. Meteor.*, **18**, 1583-1588.
- _____, and _____, 2001: Hailstorms. *Severe Convective Storms, Meteor. Monogr.*, No. 50, Amer. Meteor. Soc., 223-249.
- _____, and _____, 2005: Very large hailstones from Aurora, Nebraska. *Bull. Amer. Meteor. Soc.*, **86**, 1773-1781.
- _____, _____, J. E. Dye, and V. Toutenhood, 1974: The mechanism of precipitation formation in northeastern Colorado cumulus. I. Observations of the precipitation itself. *J. Atmos. Sci.*, **31**, 2142-2147.
- _____, and K. R. Knupp, 1986: Precipitation growth trajectories in a CCOPE storm. *J. Atmos. Sci.*, **43**, 1057-1073.
- _____, P. T. Schlatter, and T. W. Schlatter, 2008: An unusual hailstorm on 24 June 2006 in Boulder, Colorado. Part II: Low-density growth of hail. *Mon. Wea. Rev.*, **136**, 2833-2848.
- Knight, N. C., 1981: The climatology of hailstone embryos. *J. Appl. Meteor.*, **20**, 750-755.
- Knupp, K. R., 1988: Downdrafts within High Plains cumulonimbi. Part II: Dynamics and thermodynamics. *J. Atmos. Sci.*, **45**, 3965-3982.

- _____, 1989: Numerical simulation of low-level downdraft initiation within precipitating cumulonimbi: Some preliminary results. *Mon. Wea. Rev.*, **117**, 1517-1529.
- Koenig, L. R., and F. W. Murray, 1976: Ice-bearing cumulus cloud evolution: Numerical simulation and general comparison against observations. *J. Appl. Meteor.*, **15**, 747-762.
- Kogan, Y., 1991: The simulation of a convective cloud in a 3D model with explicit microphysics. Part I: Model description and sensitivity experiments. *J. Atmos. Sci.*, **48**, 1160-1189.
- Krauss, T. W., and J. D. Marwitz, 1984: Precipitation processes within an Alberta supercell hailstorm. *J. Atmos. Sci.*, **41**, 1025-1034.
- Kuhlman, K. M., C. L. Ziegler, E. R. Mansell, D. R. MacGorman, and J. M. Straka, 2006: Numerically simulated electrification and lightning of the 29 June 2000 STEPS supercell storm. *Mon. Wea. Rev.*, **134**, 2734-2757.
- Lee, S. S., L. J. Donner, V. T. J. Phillips, and Y. Ming, 2008: The dependence of aerosol effects on clouds and precipitation on cloud-system organization, shear and stability. *J. Geophys. Res.*, **113**, D16202, 23 pp. doi:10.1029/2007JD009224.
- _____, _____, _____, and _____, 2008b: Examination of aerosol effects on precipitation in deep convective clouds during the 1997 ARM summer experiment. *Quart. J. Roy. Meteor. Soc.*, **134**, 1201-1220.
- Lew, J. K., D. E. Kingsmill, and D. C. Montague, 1985: A theoretical study of collision efficiency of small planar crystals colliding with large supercooled water drops. *J. Atmos. Sci.*, **42**, 857-862.
- Lesins, G. B., and R. List, 1986: Sponginess and drop shedding of gyrating hailstones in a pressure-controlled icing wind tunnel. *J. Atmos. Sci.*, **43**, 2813-2825.
- Levin, Z., E. Ganor, and V. Gladstein, 1996: The effects of desert particles coated with sulfate on rain formation in the eastern Mediterranean. *J. Appl. Meteor.*, **35**, 1511-1523.
- _____, and W. R. Cotton, Eds., 2009: *Aerosol Pollution Impact on Precipitation. A Scientific Review*. Springer, 386 pp.
- Lilly, D. K., 1962: On the numerical simulation of buoyant convection. *Tellus*, **14**, 148-172.
- List, R., 1963: General heat and mass exchange of spherical hailstones. *J. Atmos. Sci.*, **20**, 189-197.
- _____, 2010: Hailstones, the main source of rain. Preprints, *13th Conf. on Cloud Physics/13th Conf. on Atmospheric Radiation*, Portland, OR, Amer. Meteor. Soc., 12.4.

- _____, R. B. Charlton, and P. I. Buttals, 1968: A numerical experiment on the growth and feedback mechanisms of hailstones in a one-dimensional steady-state model cloud. *J. Atmos. Sci.*, **25**, 1061-1074.
- Loftus, A. M., D. B. Weber, and C. A. Doswell III, 2008: Parameterized mesoscale forcing mechanisms for initiating numerically simulated isolated multicellular convection. *Mon. Wea. Rev.*, **136**, 2408-2421.
- Louis, J. F., M Tiedke, and J. F. Geleyn, 1981: A short history of the PBL parameterization at ECMWF. *Proc. ECMWF Workshop on Planetary Boundary Layer Parameterization*, Reading, Berkshire, United Kingdom, ECMWF, 59-80
- Ludlam, F. H., 1958: The hail problem. *Nubila*, **1**, 12-95.
- _____, 1963: Severe Local Storms: A Review. *Severe Local Storms, Meteor. Monogr.*, No. 27, Amer. Meteor. Soc., 1-30.
- _____, and W. C. Macklin, 1959: Some aspects of a severe storm in S. E. England. *Nubila*, **2**, 38-50.
- Lynn, B. H., A. P. Khain, J. Dudhia, D. Rosenfeld, A. Pokrovsky, and A. Seifert, 2005: Spectral (bin) microphysics coupled with a mesoscale model (MM5). Part I: Model description and first results. *Mon. Wea. Rev.*, **133**, 44-58.
- Macklin, W. C., 1961: Accretion in mixed clouds. *Quart. J. Roy. Meteor. Soc.*, **87**, 413-424.
- _____, and I. H. Bailey, 1966: On the critical liquid water concentrations of large hailstones. *Quart. J. Roy. Meteor. Soc.*, **92**, 297-300.
- Mansell, E. R., 2008: EnKF analysis and forecast predictability of a tornadic supercell storm. Preprints, *24th Conf. on Severe Local Storms*, Savannah, GA, Amer. Meteor. Soc., P5.2.
- _____, 2010: On sedimentation and advection in multimoment bulk microphysics. *J. Atmos. Sci.*, **67**, 3084-3094.
- _____, C. L. Ziegler, and E. C. Bruning, 2010: Simulated electrification of a small thunderstorm with two-moment bulk microphysics. *J. Atmos. Sci.*, **67**, 171-194.
- Markowski, P. M., J. M. Straka, and E. N. Rasmussen, 2002: Direct surface thermodynamic observations within the rear-flank downdrafts of nontornadic and tornadic supercells. *Mon. Wea. Rev.*, **130**, 1692-1721.
- Marshall, J. S., and W. M. Palmer, 1948: The distribution of raindrops with size. *J. Meteor.*, **5**, 165-166.

- Marwitz, J. D., 1972a: The structure and motion of severe hailstorms. Part I: Supercell storms. *J. of Appl. Meteor.*, **11**, 166-179.
- _____, 1972b: The structure and motion of severe hailstorms. Part II: Multi-cell storms. *J. of Appl. Meteor.*, **11**, 180-188.
- _____, 1972c: The structure and motion of severe hailstorms. Part III: Severely sheared storms. *J. of Appl. Meteor.*, **11**, 189-201.
- Mason, B. J., 1971: *The Physics of Clouds*. 2nd ed. Oxford University Press, 671 pp.
- Meyers, M. P., P. J. DeMott, and W. R. Cotton, 1992: New primary ice nucleation parameterizations in an explicit cloud model. *J. Appl. Meteor.*, **31**, 708-721.
- _____, R. L. Walko, J. Y. Harrington, and W. R. Cotton, 1997: New RAMS cloud microphysics parameterization. Part II: The two-moment scheme. *Atmos. Res.*, **45**, 3-39.
- Mesinger, F. and A. Arakawa, 1976: Numerical methods used in atmospheric models. GARP Publication Series, No. 14, WMO/ICSU Joint Organizing Committee, 64 pp.
- Milbrandt, J. A., and M. K. Yau, 2005a: A multimoment bulk microphysics parameterization. Part I: Analysis of the role of the spectral shape parameter. *J. Atmos. Sci.*, **62**, 3051-3064.
- _____, and _____, 2005b: A multimoment bulk microphysics parameterization. Part II: A proposed three-moment closure and scheme description. *J. Atmos. Sci.*, **62**, 3065-3081.
- _____, and _____, 2006a: A multimoment bulk microphysics parameterization. Part III: Control simulation of a hailstorm. *J. Atmos. Sci.*, **63**, 3077-3090.
- _____, and _____, 2006b: A multimoment bulk microphysics parameterization. Part IV: Sensitivity experiments. *J. Atmos. Sci.*, **63**, 3137-3159.
- _____, and R. McTaggart-Cowan, 2010: Sedimentation-induced errors in bulk microphysics schemes. *J. Atmos. Sci.*, **67**, 3931-3948.
- Miller, L. J., J. E. Dye, and B. E. Martner, 1983: Dynamical-microphysical evolution of a convective storm in a weakly-sheared environment. Part II: Airflow and precipitation trajectories from Doppler radar observations. *J. Atmos. Sci.*, **40**, 2097-2109.
- _____, and J. C. Fankhauser, 1983: Radar echo structure, air motion, and hail formation in a large stationary multicellular thunderstorm. *J. Atmos. Sci.*, **40**, 2399-2418.
- _____, J. D. Tuttle, and C. A. Knight, 1988: Airflow and hail growth in a severe northern high plains supercell. *J. Atmos. Sci.*, **45**, 736-762.

- _____, _____, and G. B. Foote, 1990: Precipitation production in a large Montana hailstorm: Airflow and particle growth trajectories. *J. Atmos. Sci.*, **47**, 1619-1646.
- Moller, A. R., C. A. Doswell III, M. P. Foster, and G. R. Woodall, 1994: The operational recognition of supercell thunderstorm environments and storm structures. *Wea. Forecasting*, **9**, 327-347.
- Morrison, H., G. Thompson, and V. Tatarskii, 2009: Impact of cloud microphysics on the development of trailing stratiform precipitation in a simulated squall line: Comparison of one- and two-moment schemes. *Mon. Wea. Rev.*, **137**, 991-1007.
- Mossop, S. C., and R. E. Kidder, 1961: Hailstorm at Johannesburg on 9th November, 1959, II. Structure of hailstones. *Nubila*, **4**, 71-86.
- _____, 1978: The influence of drop size distribution on the production of secondary ice particles during graupel growth. *Quart. J. Roy. Meteor. Soc.*, **104**, 323-330.
- Musil, D. J., 1970: Computer modeling of hailstone growth in feeder clouds. *J. Atmos. Sci.*, **27**, 474-482.
- _____, A. J. Heymsfield, and P. L. Smith, 1986: Microphysical characteristics of a well-developed weak echo region in a High Plains supercell thunderstorm. *J. Climate Appl. Meteor.*, **25**, 1037-1051.
- _____, S. A. Christopher, R. A. Deola, and P. L. Smith, 1991: Some interior observations of southeastern Montana hailstorms. *J. Appl. Meteor.*, **30**, 1596-1612.
- Nelson, S. P., and S. K. Young, 1979: Characteristics of Oklahoma hailfalls and hailstorms. *J. Appl. Meteor.*, **18**, 339-347.
- _____, 1983: The influence of storm flow structure on hail growth. *J. Atmos. Sci.*, **40**, 1965-1983.
- _____, 1987: The hybrid multicellular-supercellular storm- an efficient hail producer. Part II: General characteristics and implications for hail growth. *J. Atmos. Sci.*, **44**, 2060-2073.
- Noppel, H., U. Blahak, A. Seifert, and K. D. Beheng, 2010: Simulations of a hailstorm and the impact of CCN using an advanced two-moment cloud microphysical scheme. *Atmos. Res.*, **96**, 286-301.
- Ntelekos, A. A., J. A. Smith, L. Donner, J. D. Fast, W. I. Gustafson Jr., E. G. Chapman, and W. F. Krajewski, 2009: The effects of aerosols on intense convective precipitation in the northeastern United States. *Quart. J. Roy. Meteor. Soc.*, **135**, 1367-1391.
- Ogura, Y., and T. Takahashi, 1971: Numerical simulation of the life cycle of a thunderstorm cell. *Mon. Wea. Rev.*, **99**, 895-911.

- Orville, H. D., and F. J. Kopp, 1977: Numerical simulation of the life history of a hailstorm. *J. Atmos. Sci.*, **34**, 1596-1618.
- _____, R. D. Farley, Y-C. Chi, and F. J. Kopp, 1989: The primary cloud physics mechanisms of microburst formation. *Atmos. Res.*, **24**, 343-357.
- Ovtchinnikov, M., and Y. L. Kogan, 2000: An investigation of ice production mechanisms using a 3D cloud model with detailed microphysics. Part I: Model description. *J. Atmos. Sci.*, **57**, 2989-3003.
- Paluch, I. R., 1978: Size sorting of hail in a three-dimensional updraft and implications for hail suppression. *J. Appl. Meteor.*, **9**, 763-777.
- Phillips, V. T. J., T. W. Choullarton, A. M. Blyth, and J. Latham, 2002: The influence of aerosol concentrations on the glaciation and precipitation of a cumulus cloud. *Quart. J. Roy. Meteor. Soc.*, **128**, 951-971.
- Pinsky, M., and A. P. Khain, 2002: Effects of in-cloud nucleation and turbulence on droplet spectrum formation in cumulus clouds. *Quart. J. Roy. Meteor. Soc.*, **128**, 1-33.
- Proctor, F. H., 1989: Numerical simulations of an isolated microburst. Part II: Sensitivity experiments. *J. Atmos. Sci.*, **46**, 2143-2165.
- Pruppacher, H. R., and K. V. Beard, 1970: A wind tunnel investigation of the internal circulation and shape of water drops falling at terminal velocity in air. *Quart. J. Roy. Meteor. Soc.*, **96**, 247-256.
- _____, and J. D. Klett, 1980: *Microphysics of Clouds and Precipitation*. D. Reidel, 714 pp.
- Rasmussen, E. N., and D. O. Blanchard, 1998: A baseline climatology of sounding-derived supercell and tornado forecast parameters. *Wea. Forecasting*, **13**, 1148-1164.
- Rasmussen, R. M., V. Levizzani, and H. R. Pruppacher, 1984: A wind tunnel and theoretical study on the melting behavior of atmospheric ice particles: III. Experiment and theory for spherical ice particles of radius $> 500 \mu\text{m}$. *J. Atmos. Sci.*, **41**, 381-388.
- _____, and A. J. Heymsfield, 1987a: Melting and shedding of graupel and hail. Part I: Model Physics. *J. Atmos. Sci.*, **44**, 2754-2763.
- _____, and _____, 1987b: Melting and shedding of graupel and hail. Part II: Sensitivity study. *J. Atmos. Sci.*, **44**, 2764-2782.
- _____, and _____, 1987c: Melting and shedding of graupel and hail. Part III: Investigation of the role of shed drops as hail embryos in the August 1 CCOPE severe storm. *J. Atmos. Sci.*, **44**, 2783-2803.

- Reisin, T., Z. Levin, and S. Tzivion, 1996: Rain production in convective clouds as simulated in an axisymmetric model with detailed microphysics. Part I: Description of the model. *J. Atmos. Sci.*, **53**, 497-519.
- Reisner, J. R. M. Rasmussen, and R. T. Bruintjes, 1998: Explicit forecasting of supercooled liquid water in winter storms using the MM5 mesoscale model. *Quart. J. Roy. Meteor. Soc.*, **124**, 1071-1107.
- Roos, D. v.d. S., 1972: A giant hailstone from Kansas in free fall. *J. Appl. Meteor.*, **11**, 1008-1011.
- Rosenfeld, D., and I. M. Lensky, 1998: Satellite-based insights into precipitation formation processes in continental and maritime convective clouds. *Bull. Amer. Meteor. Soc.*, **79**, 2457-2476.
- _____, 1999: TRMM observed first direct evidence of smoke from forest fires inhibiting rainfall. *Geophys. Res. Lett.*, **26**, 3105-3108.
- _____, 2000: Suppression of rain and snow by urban and industrial air pollution. *Science*, **287**, 1793-1796.
- _____, and W. L. Woodley, 2000: Convective clouds with sustained highly supercooled liquid water down to -37.5°C . *Nature*, **405**, 440-442.
- Rosenthal, A. J. and R. S. Lindzen, 1983: Instabilities in a stratified fluid having one critical level. Part I: Results. *J. Atmos. Sci.*, **40**, 509-520.
- Rosinski, J. and T. C. Kerrigan, 1969: The role of aerosol particles in the formation of raindrops and hailstones in severe thunderstorms. *J. Atmos. Sci.*, **26**, 695-715.
- _____, C. T. Nagamoto, T. C. Kerrigan, and G. Langer, 1973: Freezing nuclei derived from soil particles. *J. Atmos. Sci.*, **30**, 644-652.
- Rutledge, S. A., and P. V. Hobbs, 1984: The mesoscale and microscale structure and organization of clouds and precipitation in midlatitude cyclones. Part XII: A diagnostic modeling study of precipitation development in narrow cold-frontal rainbands. *J. Atmos. Sci.*, **41**, 2949-2972.
- Saleeby, S., and W. R. Cotton, 2004: A large-droplet mode and prognostic number concentration of cloud droplets in the Colorado State University Regional Atmospheric Modeling System (RAMS). Part I: Module descriptions and supercell test simulations. *J. Appl. Meteor.*, **43**, 182-195.
- _____, and _____, 2008: A binned approach to cloud-droplet riming implemented in a bulk microphysics model. *J. Appl. Meteor. Climatol.*, **47**, 694-703.

- Sassen, K., P. J. DeMott, J. M. Prospero, and M. R. Poellet, 2003: Saharan dust storms and indirect aerosol effects on clouds: CRYSTAL-FACE results. *Geophys. Res. Lett.*, **30**, 1633, doi:10.1029/2003GL017371.
- Scharfenberg, K. A., D. J. Miller, T. J. Schuur, P. T. Schlatter, S. E. Giangrande, V. M. Melnikov, D. W. Burgess, D. L. Andra Jr., M. P. Foster, and J. M. Krause, 2005: The joint polarization experiment: Polarimetric radar in forecasting and warning decision making. *Wea. Forecasting*, **20**, 775-788.
- Schumann, T. E. W., 1938: The theory of hailstone formation. *Quart. J. Roy. Meteor. Soc.*, **64**, 3-21.
- Seifert, A., and K. D. Beheng, 2006: A two-moment cloud microphysics parameterization for mixed-phase clouds. Part 2: Maritime vs. continental deep convective storms. *Meteor. and Atmos. Phys.*, **92**, 67-82.
- Smith, P. L., D. J. Musil, A. G. Detwiler, and R. Ramachandran, 1999: Observations of mixed-phase precipitation within a CaPE thunderstorm. *J. Appl. Meteor.*, **38**, 145-155.
- Smagorinsky, J., 1963: General circulation experiments with the primitive equations. I. The basic experiment. *Mon. Wea. Rev.*, **91**, 99-164.
- Squires, P., 1956: The microstructure of cumuli in maritime and continental air. *Tellus*, **8**, 443-444.
- _____, 1958: The microstructure and colloidal stability of warm clouds. *Tellus*, **10**, 256-271.
- _____, and S. Twomey, 1961: The relation between cloud drop numbers and the spectrum of cloud nuclei. *Physics of Precipitation, Geophys. Monogr. No. 5*, Amer. Geophys. Union, 211-219.
- Srivastava, R. C., 1987: A model of intense downdrafts driven by melting and evaporation of precipitation. *J. Atmos. Sci.*, **44**, 1752-1773.
- Storer, R. L., S. C. van den Heever, and G. L. Stephens, 2010: Modeling aerosol impacts on convective storms in different environments. *J. Atmos. Sci.*, **67**, 3904-3915.
- Straka, J. M., and J. R. Anderson, 1993: Numerical simulations of microburst-producing storms: Some results from storms observed during COHMEX. *J. Atmos. Sci.*, **50**, 1329-1348.
- _____, D. S. Zrnić, and A. V. Ryzhkov, 2000: Bulk hydrometeor classification and quantification using polarimetric radar data: Synthesis of relations. *J. Appl. Meteor.*, **39**, 1341-1372.
- _____, and E. R. Mansell, 2005: A bulk microphysics parameterization with multiple ice precipitation categories. *J. Appl. Meteor.*, **44**, 445-466.

- Takahashi, T., 1976: Hail in an axisymmetric cloud model. *J. Atmos. Sci.*, **33**, 1579-1601.
- Tessendorf, S. A., L. J. Miller, K. C. Wiens, and S. A. Rutledge, 2005: The 29 June 2000 supercell observed during STEPS. Part I: Kinematics and microphysics. *J. Atmos. Sci.*, **62**, 4127-4150.
- Thompson, G., R. M. Rasmussen, and K. Manning, 2004: Explicit forecasts of winter precipitation using an improved bulk microphysics scheme. Part I: Description and sensitivity analysis. *Mon. Wea. Rev.*, **132**, 519-542.
- _____, P. R. Field, W. D. Hall, and R. M. Rasmussen, 2006: A new bulk microphysical parameterization for WRF (& MM5). Paper presented at WRF conference, Natl. Cent. for Atmos. Res., Boulder, CO
- Tripoli, G. R., and W. R. Cotton, 1981: The use of ice-liquid water potential temperature as a thermodynamic variable in deep atmospheric models. *Mon. Wea. Rev.*, **109**, 1094-1102.
- Twomey, S., 1977: The influence of pollution on the shortwave albedo of clouds. *J. Atmos. Sci.*, **34**, 1149-1152.
- Tzivion, S., G. Feingold, and Z. Levin, 1987: An efficient numerical solution to the stochastic collection equation. *J. Atmos. Sci.*, **44**, 3139-3149.
- van den Heever, S., 2001: The impact of several hail parameters on simulated supercell storms. Ph.D. dissertation, Department of Atmospheric Science, Colorado State University, 265 pp.
- _____, and W. R. Cotton, 2004: The impact of hail size on simulated storms. *J. Atmos. Sci.*, **61**, 1596-1609.
- _____, G. G. Carrió, W. R. Cotton, P. J. DeMott, and A. J. Prenni, 2006: Impacts of nucleating aerosol on Florida storms. Part I: Mesoscale simulations. *J. Atmos. Sci.*, **63**, 1752-1775.
- _____, G. L. Stephens, and N. B. Wood, 2011: Aerosol indirect effects on tropical convection characteristics under conditions of radiative-convective equilibrium. *J. Atmos. Sci.*, **68**, 699-718.
- Verlinde, J., P. J. Flatau, and W. R. Cotton, 1990: Analytical solutions to the collection growth equation: Comparison with approximate methods and application to cloud microphysics parameterization schemes. *J. Atmos. Sci.*, **47**, 2871-2880.
- Vivekanandan, J., W. M. Adams, and V. N. Bringi, 1991: Rigorous approach to polarimetric radar modeling of hydrometeor orientation distributions. *J. Appl. Meteor.*, **30**, 1053-1063.
- Wacker, U., and A. Seifert, 2001: Evolution of rain water profiles resulting from pure sedimentation: Spectral vs. parameterized description. *Atmos. Res.*, **58**, 19-39.

- _____, and C. Lüpkes, 2009: On the selection of prognostic moments in parameterization schemes for drop sedimentation. *Tellus*, **61A**, 498-511.
- Wakimoto, R. M., and V. N. Bringi, 1988: Dual-polarization observations of microbursts associated with intense convection: The 20 July storm during the MIST Project. *Mon. Wea. Rev.*, **116**, 1521-1539.
- Walko, R., W. R. Cotton, M. P. Meyers, and J. Y. Harrington, 1995: New RAMS cloud microphysics parameterization. Part I: The single-moment scheme. *Atmos. Res.*, **38**, 29-62.
- Wang, C. 2005: A modeling study of the response of tropical deep convection to the increase of cloud condensation nuclei concentration: 1. Dynamics and microphysics. *J. Geophys. Res.*, **110**, D21211, 16 pp. doi:10.1029/2004JD005720.
- Wang, P. K., T. J. Greenwald, and J. Wang, 1987: A three parameter representation of the shape and size distributions of hailstones- A case study. *J. Atmos. Sci.*, **44**, 1062-1070.
- Warner, J., 1968: A reduction in rainfall associated with smoke from sugarcane fires: An inadvertent weather modification? *J. Appl. Meteor.*, **7**, 247-251.
- _____, and S. Twomey, 1967: The production of cloud nuclei by cane fires and the effects on cloud droplet concentration. *J. Atmos. Sci.*, **24**, 704-706.
- Waterman, P. C., 1965: Matrix formulation of electromagnetic scattering. *Proc. IEEE*, **53**, 805-812.
- Weisman, M. L., and J. B. Klemp, 1982: The dependence of numerically simulated convective storms on vertical shear and buoyancy. *Mon. Wea. Rev.*, **110**, 504-520.
- _____, and _____, 1984: The structure and classification of numerically simulated convective storms in directionally varying wind shears. *Mon. Wea. Rev.*, **112**, 2479-2498.
- _____, and R. Rotunno, 2000: The use of vertical shear versus helicity in interpreting supercell dynamics. *J. Atmos. Sci.*, **57**, 1452-1472.
- Wicker, L. J., and R. B. Wilhelmson, 1995: Simulation and analysis of tornado development and decay within a three-dimensional supercell thunderstorm. *J. Atmos. Sci.*, **52**, 2675-2703.
- Wisner, C., H. D. Orville, and C. Meyers, 1972: A numerical model of a hail-bearing cloud. *J. Atmos. Sci.*, **29**, 1160-1181.
- Wong, R. K. W., N. Chidambaram, L. Cheng, and M. English, 1988: The sampling variations of hail size distributions. *J. Appl. Meteor.*, **27**, 254-260.

- Xue, M., K. K. Droegemeier, and V. Wong, 2000: The Advanced Regional Prediction Systems (ARPS)—A multiscale nonhydrostatic atmospheric simulation and prediction tool. Part I: Model dynamics and verification. *Meteor. Atmos. Phys.*, **75**, 161-193.
- _____, D.-H. Wang, J.-D. Gao, K. Brewster, and K. K. Droegemeier, 2003: The Advanced Regional Prediction System (ARPS), storm-scale numerical weather prediction, and data assimilation. *Meteor. Atmos. Phys.*, **82**, 139-170.
- Yin, Y., Z. Levin, T. Reisin, and S. Tzivion, 2000: The effects of giant cloud condensational nuclei on the development of precipitation in convective clouds: A numerical study. *Atmos. Res.*, **53**, 91-116.
- Young, K. C., 1977: A numerical examination of some hail suppression concepts. *Hail: A Review of Hail Science and Hail Suppression*, *Meteor. Monogr.*, No. 38, Amer. Meteor. Soc., 195-214.
- _____, 1993: *Microphysical Processes in Clouds*. Oxford Press. 427 pp.
- Ziegler, C. L., P. S. Ray, and N. C. Knight, 1983: Hail growth in an Oklahoma multicell storm. *J. Atmos. Sci.*, **40**, 1768-1791.
- _____, 1988: Retrieval of thermal and microphysical variables in observed convective storms. Part II: Sensitivity of cloud processes to variations in microphysical parameterization. *J. Atmos. Sci.*, **45**, 1072-1090.
- Zrnić, D. S., V. N. Bringi, N. Balakrishnan, K. Aydin, V. Chandrasekar, and J. Hubbert, 1993: Polarimetric measurements in a severe hailstorm. *Mon. Wea. Rev.*, **121**, 2223-2238.

APPENDIX A

A.1) Construction of melting and shedding look-up tables for 3MHAIL scheme

This section describes the methodology for constructing the look-up tables used in the 3MHAIL microphysics scheme. The general algorithm for making these look-up tables was already contained within the RAMS microphysics and was not designed by the author of the current work. The variable subscripts denoting the hail category have been omitted in the following equations.

The ratios of the mean mass diameter $D_{\bar{m}}$ to the characteristic diameter D_n are determined for each ν value [1.0, 1.5, 2.0, ... 9.5, 10.0] by

$$\frac{D_{\bar{m}}}{D_n} = \left[\frac{\Gamma(\nu + \beta_m)}{\Gamma(\nu)} \right]^{1/\beta_m}, \quad (\text{A.1})$$

which depends only on the value of ν . For each ν value, hail mean masses \bar{m} are divided into 40 incremental bins increasing exponentially from \bar{m}_{\min} to \bar{m}_{\max} , where the mean mass of bin j is given by

$$\bar{m}_j = \bar{m}_{\min} \left(\frac{\bar{m}_{\max}}{\bar{m}_{\min}} \right)^{\frac{j-1}{39}}, \quad (\text{A.2})$$

and the mean mass diameter $D_{\bar{m}_j}$ of bin j is computed using

$$D_{\bar{m}_j} = \left(\frac{\bar{m}_j}{\alpha_m} \right)^{1/3}. \quad (\text{A.3})$$

The characteristic diameter D_n is then determined from (A.1) and (A.3) for the current values of ν and \bar{m}_j

$$D_n = D_{\bar{m}_j} \left[\frac{\Gamma(\nu + \beta_m)}{\Gamma(\nu)} \right]^{-1/\beta_m} \quad (\text{A.4})$$

The hail distribution is then divided into discrete size bins spanning the range 0.2 to 150 mm, with mass doubling every 6 bins, and bin integral values of the 0th moment ($M_i 0$) of the distribution are computed using Eqn. A.5 (a discrete version of Eqn (3.3)) incorporating the value of D_n from (A.4) for the current (\bar{m}_j, ν) pair

$$M_i P \approx \frac{[f_{gam}(D_{i-1/2}) + f_{gam}(D_{i+1/2})]}{2} [D_i]^P (D_{i+1/2} - D_{i-1/2}), \quad (\text{A.5})$$

where $D_i = 0.5[D_{i-1/2} + D_{i+1/2}]$ is the average diameter for bin i and P is an integer representing the moment of the distribution ($P = 0$ in this case). The integral amounts of mass (m_i^*), as well as the terminal velocity, ventilation coefficient (f_{REi}) for heat and vapor transfer, and energy transfer factor (q_i') for each size bin i are calculated using Eqns (A.6), (3.5), (A.7), and (A.8), respectively.

$$m_i^* = \alpha_m D_i^{\beta_m} \times M_i 0 \quad (\text{A.6})$$

$$f_{REi} = (1.0 + 0.229[V_u D_i / \nu_k]^{0.5}) \quad (\text{A.7})$$

$$q_i' = D_i^{1-\beta_m} \times f_{REi} \quad (\text{A.8})$$

The bracketed term in (A.7) is the Reynolds number (N_{RE}), where ν_k is the kinematic viscosity of air, and q_i' has units of energy/(mass*time). Note that the same ventilation coefficient is used for both heat and vapor transfer. The total 'mass' M^* of the representative distribution is computed by summing the individual bin 'masses' m_i^* , and the total amount of energy Q^* required to melt the entire distribution is obtained by multiplying M^* by the latent heat of fusion L_f ($L_f = 80 \text{ cal g}^{-1}$).

Next, bulk LWF values are assigned to the hail distribution in increasing increments l of 0.005 in order to obtain the fractional amounts of Q^* (A.9) required to melt a certain amount of hail mass such that the specified LWF value is attained. These fractional amounts of energy Q_i^* are applied to the distribution at the proper relative rates (i.e., $m_i^* q_i$) for each size bin in order to obtain a 'psuedo'³ time step' (dt^*), which is defined as a relative time step required to melt 1/2% more of the total (liquid + ice) hail mass over all bin sizes (Walko, personal communication). Based on the computed value for dt^* for the current value of LWF , the internal energies q_i of each size bin are computed and stored in the Q_{tab} table. The M_i0 values of bins that are completely melted ($q_i = L_f$) are stored in the M_{tab} table, whereas the amount of liquid mass ($m_{i\ liq}^*$) above a critical value ($m_{i\ crit}^*$) (A.10) for partially melted bins ($q_i < L_f$) is added to the S_{tab} table, where $m_{i\ ice}^*$ is the ice mass in grams as in Rasmussen and Heymsfield (1987a). Eqn. (A.10) is based on laboratory studies on melting hail particles by Rasmussen et al. (1984), who showed that shedding occurs only for hailstones having diameters of about 9 mm or greater, and allows for some liquid to be retained on the hailstone surface similar to spongy growth (List 1963). The smallest size bins are the first to completely melt, and as the bulk LWF values increase, larger size bins contain increasingly more liquid water and eventually become completely melted as well. A flowchart detailing the construction of the tables for the current (\bar{m}_j, ν) pair is presented in Figure A.1.

$$Q_i^* = Q^* \times l \quad l = [0.005, 0.01, 0.015, \dots, 0.990, 0.995] \quad (A.9)$$

$$m_{i\ crit}^* = 0.268 + 0.1389m_{i\ ice}^* \quad (A.10)$$

³ The amount of physical time required for hail in a given size bin to completely melt does not explicitly appear in the computations of the melt/shed table factors. Physical time is considered during model runtime when the meteorological conditions, and hence the actual energy transfer rates, are known.

The construction of these look-up tables considers the shedding and melting processes simultaneously such that the amount of hail mass lost via these processes can not be greater than the total amount of hail mass present. In addition, as the values contained in these tables are based on the amount of heat energy applied to the hail distribution without consideration of where the energy came from, the Q_{tab} table is used to compute complete melting of the smallest hail particles owing to heat and vapor diffusion as described in Chapter 3.5.2.

The M_{tab} table is used to determine $D_{\text{max,melt}}$ based on the grid point values of LWF , \bar{m} , and ν_h . The bulk LWF values computed using (3.56) for the shedding scheme are used here as well, and the melting algorithm is only applied if $0.3 < LWF < 0.95$. Starting with the smallest size bin

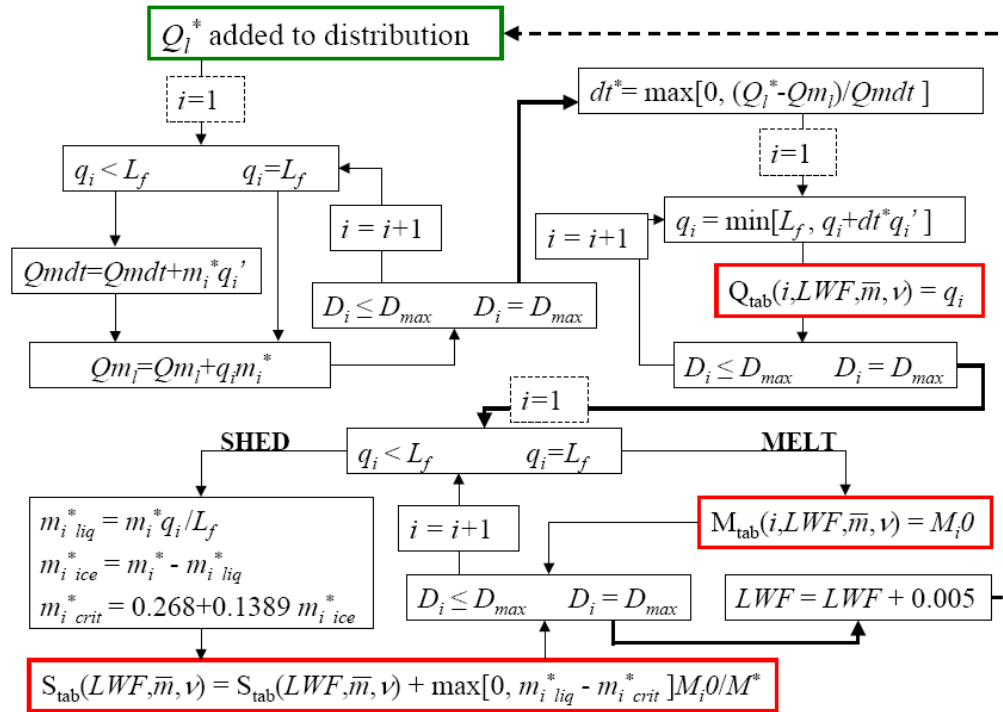


Figure A.1: Flowchart showing the calculations involved in the construction of the melt and shed tables. Dashed boxes containing $i = 1$ denote beginning of loop over size bins i , solid bold arrows signify exit from loop over size bins (i.e., $D_i = D_{\text{max}}$), and dashed bold arrow depicts incremental increase in fractional amount of energy Q_i^* applied to entire distribution. Q_{mdt} is the energy transfer rate [cal/s] summed over partially melted bins and Q_{m_i} is the total internal energy [cal] of the representative distribution for the current LWF value. Bold red boxes denote assignment of values to look-up tables.

(D_{min}) for fixed LWF , \bar{m} , and v_h values, the M_{tab} values are summed over increasingly larger size bins until a size bin containing a value of zero is reached. Because partially melted size bins have table values of zero, the diameter associated with largest size bin containing a non-zero value is taken as $D_{max,melt}$. The fractional amounts of each moment P [$P = 0, 3, 6$] associated with the completely melted hailstones are then determined using Eqn. (A.11), the ratio of the moment integrated over the melted portion of the size distribution (D_{min} to $D_{max,melt}$) to the moment integrated over the entire size distribution, where the integrals in (A.11) are solved numerically using (A.5). These fractional moment amounts are then multiplied by their respective physical quantities (N_{th} , r_h , and Z_h) to obtain the amounts lost ($N_{th,melt}$, $r_{h,melt}$, and $Z_{h,melt}$) due to complete melting of hail particles. $N_{th,melt}$ and $r_{h,melt}$ are subtracted from the hail category and added to the rain category, and $Z_{h,melt}$ is subtracted from Z_h .

$$\frac{M(P)|_{melted}}{M(P)} = \frac{\int_{D_{min}}^{D_{max,melt}} D^P f_{gam}(D) dD}{\int_{D_{min}}^{D_{max}} D^P f_{gam}(D) dD} \quad (A.11)$$

A.2) Original 3MHAIL method for melting of smallest hailstones

The problem of using the M_{tab} values to determine $D_{max,melt}$ is illustrated in Figure A.2, which shows that for a specified combination of LWF and $D_{\bar{m}h}$, $D_{max,melt}$ can be much too large given that the model has a time step on the order of seconds. For example, for a mean mass diameter of 2 cm with bulk LWF of 0.4, the largest hail diameter to completely melt in one $\Delta t = 4$ s is computed to be around 1 cm, and at a bulk LWF of 0.6, the largest diameter to melt is near 1.6 cm! Furthermore, as mentioned in footnote 1, the time it takes for a hailstone in a given size bin to completely melt does not explicitly appear in the construction of the melt tables. Thus for a given combination of v_h , $D_{\bar{m}h}$, and LWF , the same value of $D_{max,melt}$ can be computed whether Δt

= 1 sec or 10 sec. Because $D_{max,melt}$ is used as an upper limit in the integration of the moments over the melted portion of the distribution (Eqn. A.11), this can lead to errors in the calculations of the fractional amounts of the moments lost due to complete melting. This is clearly evident in the erroneously large values for the computed fractional amounts of $M0$ to completely melt in one Δt , particularly for spectrally wide distributions (i.e., $\nu_h = 2$) at lower LWF values (i.e., $0.3 < LWF < 0.5$). This effect on the fractional amounts of $M3$ and $M6$ lost due to complete melting

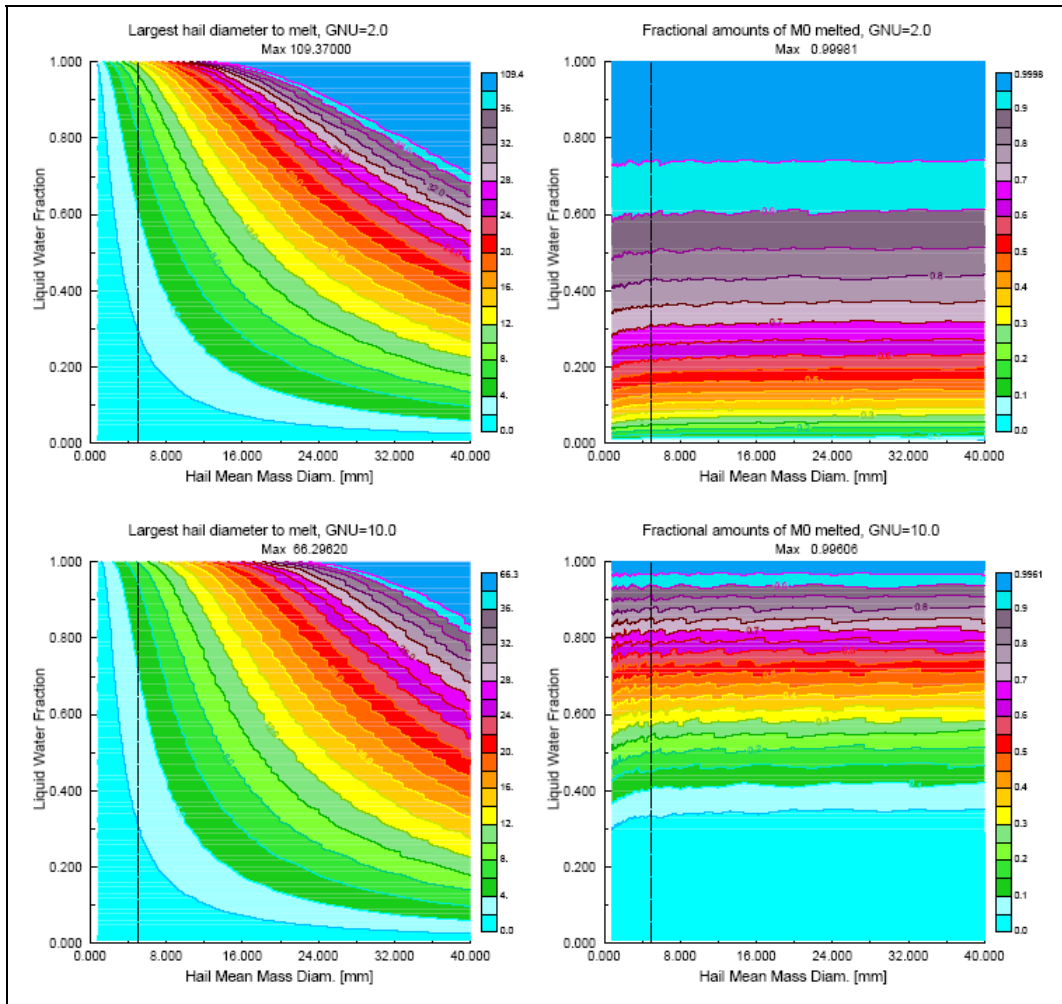


Figure A.2: Contours of $D_{max,melt}$ [mm] (left) and fractional amounts of $M0$ to completely melt (right) (M_{tab} values summed from D_{min} to $D_{max,melt}$) as a function of hail mean mass diameter and LWF for $\nu_h = 2$ (top) and $\nu_h = 10$ (bottom).

(Figs. A.3 and A.4) doesn't appear to be as great, although it introduces some uncertainty into the original 3MHAIL melting algorithm.

Examples of the fractional amounts of $M3$ and $M6$ lost due to the individual and combined processes of shedding and melting as computed from the look-up tables are displayed in Figures A.3 and A.4. Shed fractional amounts of $M3$ are simply the S_{tab} table values, whereas shed fractional amounts of $M6$ are computed using Eqn. 3.59. The fractional amounts of $M3$ and $M6$ lost due to complete melting are computed using Eqn. A.11. Losses of $M3$ and $M6$ due to shedding have peak values for LWF between 0.6 and 0.8 for $D_{\bar{m}h}$ greater than about 10 mm, whereas losses of $M3$ and $M6$ due to complete melting increase monotonically with increasing LWF and are independent of $D_{\bar{m}h}$. Virtually no losses to $M3$ and $M6$ due to shedding occur for $D_{\bar{m}h} < 8$ mm. The fractional amounts of $M6$ lost due to shedding exhibit a similar pattern to those of $M3$, although the magnitudes are larger and the contour gradients are steeper for $M6$ owing to the dependence on the 6th power of diameter. It is also evident that for a fixed LWF value, complete melting has a much greater impact on $M3$ than on $M6$ due to the fact that the smallest particles are the first to melt completely, and thus, changes in D^3 versus D^6 are more pronounced.

The combined melting and shedding values show that as LWF increases from zero, shedding of liquid water is the first process to reduce $M3$ and $M6$. Once LWF attains a value of about 0.5 for $\nu_h = 2.0$ (0.6 for $\nu_h = 10.0$), complete melting begins to have an appreciable impact on the reduction of $M3$, whereas an appreciable impact on $M6$ due to melting doesn't occur until LWF reaches values around 0.85 for $\nu_h = 2.0$ (0.8 for $\nu_h = 10.0$). As LWF increases further, the relative amounts of $M3$ lost due to complete melting outweigh those due to shedding since the smallest hailstones have completely melted to rain leaving only the relatively few largest particles

available to shed. The scenario for $M6$ is a bit different as LWF is increased further, with combined fractional amounts decreasing to a local minimum before increasing again, and this behavior is more pronounced for smaller values of ν_h .

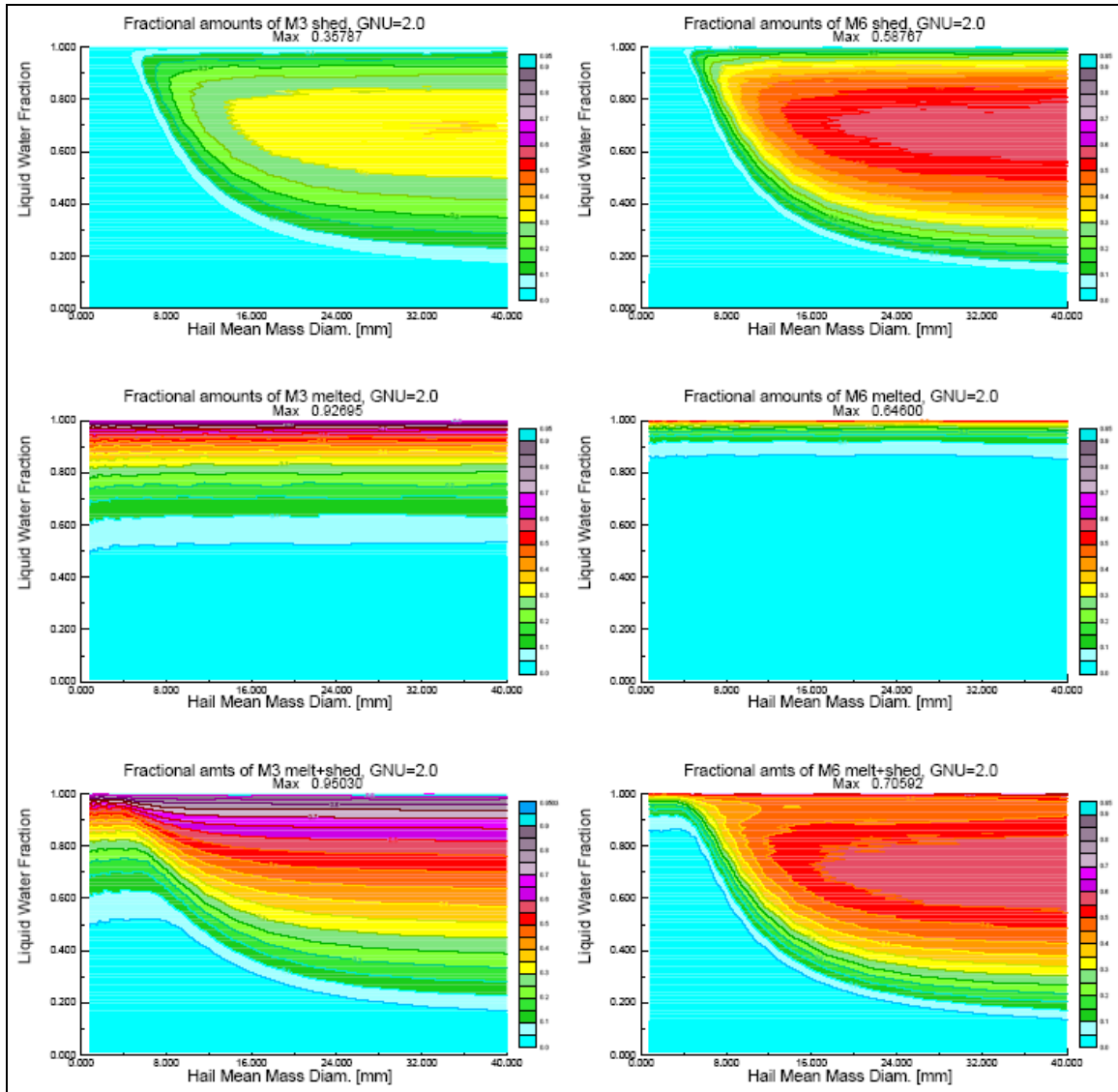


Figure A.3: Contours of fractional amounts of $M3$ (left column) and $M6$ (right column) lost due to shedding (top), complete melting of the smallest hail particles (middle) and combined melting and shedding (bottom) as a function of D_{mh} and LWF for $\nu_h=2$. Shed fractional amounts of $M3$ are simply the S_{tab} table values, whereas shed fractional amounts of $M6$ are computed using Eqn. 3.59. The fractional amounts of $M3$ and $M6$ lost due to complete melting are computed using Eqn. A.11.

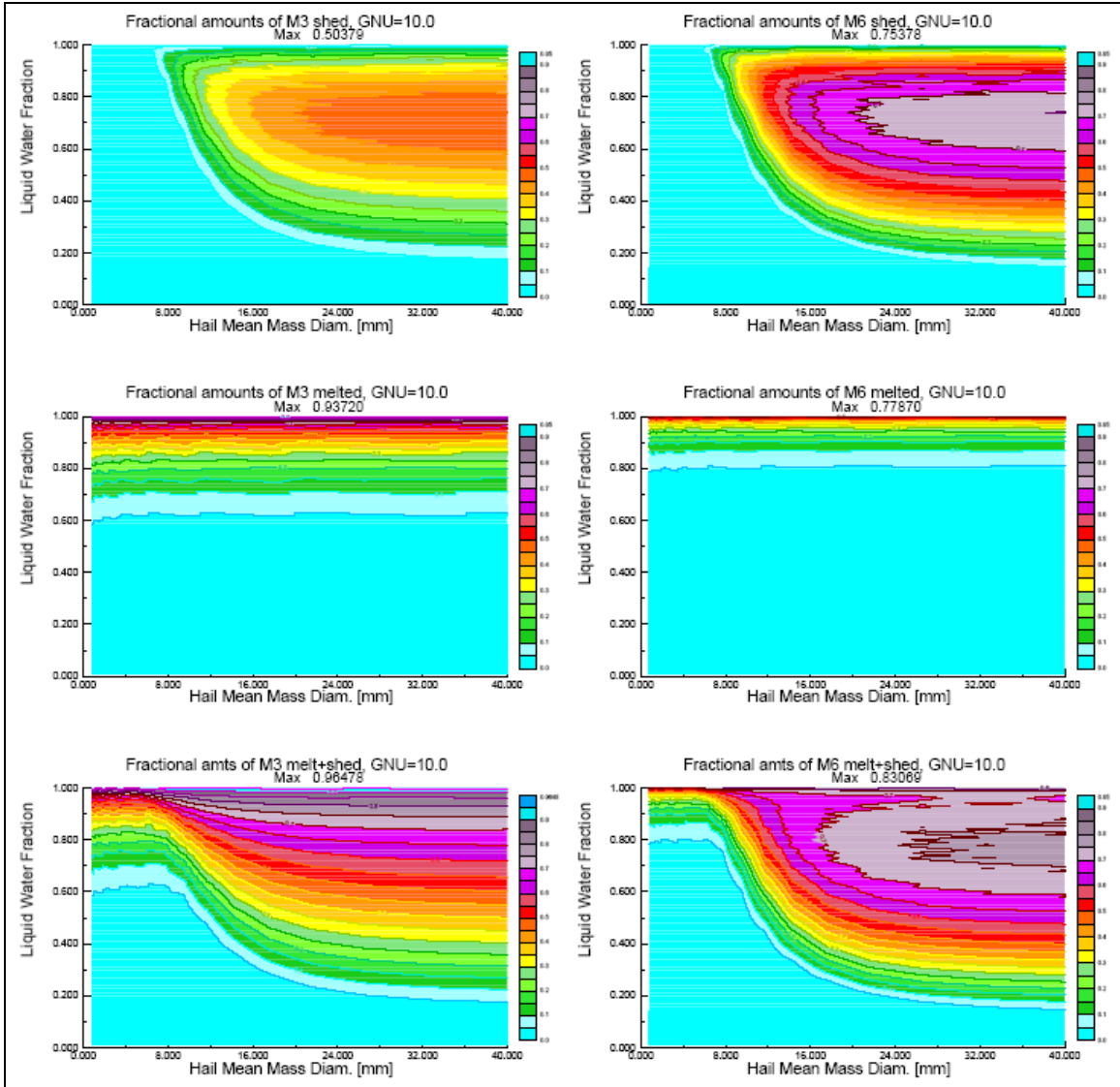


Figure A.4: As in Figure A.3, but for $\nu_i=10$.

APPENDIX B

B.1) Bulk sedimentation table construction for 3MHAIL

The construction of the sedimentation look-up tables (SED_{Φ}) is similar to that for the melting/shedding tables with Eqns. A.1-A.5 used to assign and discretize representative distributions, except that the absolute range of hail diameters is from 0.2 to 150 mm and $P = 0, 3,$ and 6 so that the individual bin values of these moments ($M_i0, M_i3,$ and $M_i6,$ respectively) can be found. The bin values of the moments are then normalized (Eqn. B.1), and the terminal velocity (V_{ti}) of each size bin is determined from Eqn. (3.5).

$$M_i^*P = M_iP / \left(\sum_{r=1}^N M_rP \right) \quad (B.1)$$

At each vertical grid level (k), the distance fallen (' $disp$ ') in one time step Δt is computed for each size bin, taking into account the effect of air density on terminal velocity,

$$disp = F_{\rho} V_{ti} \Delta t \quad (B.2)$$

At level $z(k)$, the new top and bottom of the 'bin layer' are computed as

$$z_{topnew} = z(k) - disp \quad (B.3)$$

$$z_{botnew} = z(k-1) - disp \quad (B.4)$$

that is, the layer between levels $z(k-1)$ and $z(k)$ is displaced by an amount ' $disp$ ' as shown schematically in Figure B.1. The 'bin layer' may be displaced over several vertical levels and is limited by the maximum displacement of the largest hail size allowed. The fractional amounts of the displaced 'bin layer' overlapping the current and lower grid layers are then computed (see figure B.1) and multiplied by the normalized bin moment values (M_i^*0, M_i^*3, M_i^*6) to obtain sedimentation table factors for number, mass, and reflectivity. Since portions of other size bin

layers may also occupy the same level, say $z(k-2)$, either by remaining at that level or by falling into the level from different layers (e.g., from $z(k+1)$, $z(k)$ or $z(k-1)$ to $z(k-2)$), the table factors are the sum of all possible fractional amounts of all bins that may 'fall into' (or remain in) a given level for given values of v_h and \bar{m}_h . The maximum number of levels ($kfall_{max}$) over which the hail particles can be displaced in one Δt is determined by the displacement of $D_{h,max}$. For the lowest model levels, a surface precipitation table (SFC) is constructed in a similar manner by summing the fractional amounts of mass bins displaced below the surface ($z = 0$).

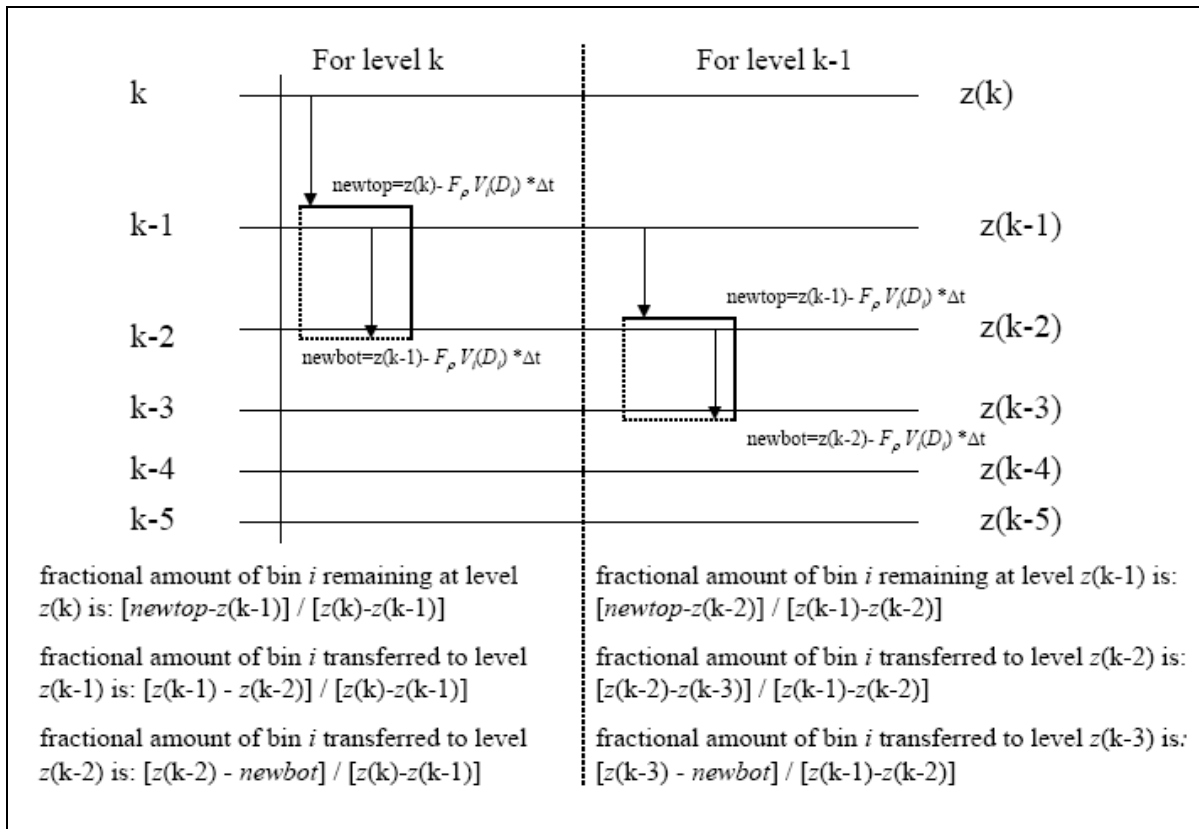


Figure B.1: Schematic of fractional amount computations of 'bin layers' transferred to lower grid levels for sedimentation table factors using stretched grid spacing. Calculation of these table factors for constant grid spacing follows the identical procedure.

B.2) *Bin sedimentation model* (for 1D sedimentation tests; section 4.1)

For the bin scheme, the initial distribution at each level is partitioned into 172 size bins spanning the range $D_{min} = 0.2$ mm to $D_{max} = 150$ mm, with mass doubling every 6 bins, and the bin values of number concentration, mass mixing ratio, and reflectivity are computed using Eqns. (B.5), (B.6), and (B.7), respectively, where M_i0 is calculated from (A.5). The terminal velocities (V_i) for each size bin are computed from Eqn. (3.5) taking into account density effects. The particles in each size bin are assumed to be distributed uniformly over a layer equal in depth to the vertical grid spacing (Δz); particles in the i th bin at level $z(k)$ are actually located between levels $z(k)$ and $z(k-1)$. Thus, the vertical displacement of a size bin after a given time $n\Delta t$ is equivalent to the vertical displacement of the layer over which a particular size bin previously resided. For each time step n , the new heights of the top and bottom of each bin 'layer' are computed (Eqns B.8 and B.9) relative to their initial locations ($z_{t0,i}$ and $z_{b0,i}$, respectively) to determine the fractional amount of each bin to be transferred to subsequently lower levels (Figure B.2). At any time, the total amounts of N_{lh} , r_h , and Z_h at level k are computed by summing the bin values of these quantities at that level (layer).

$$n_{hi}(D_i) = N_{th} M_i0 \quad \text{units are } [\# / \text{m}^3] \quad (\text{B.5})$$

$$r_{hi}(D_i) = \alpha_{mh} D_i^{\beta_{mh}} n_{hi}(D_i) \quad \text{units are } [\text{kg} / \text{m}^3] \quad (\text{B.6})$$

$$Z_{hi}(D_i) = D_i^6 n_{hi}(D_i) \times 10^{18} \quad \text{units are } [\text{mm}^6 / \text{m}^3] \quad (\text{B.7})$$

$$newtop(D_i) = z_{t0,i} - F_\rho V_i n\Delta t \quad (\text{B.8})$$

$$newbot(D_i) = z_{b0,i} - F_\rho V_i n\Delta t . \quad (\text{B.9})$$

The 'mean mass diameter' at level k is computed using (B.10) as in Milbrandt and McTaggart-Cowan (2010), where the moments M_j are computed from (B.11).

$$D_m = (M3/M0)^{(1/3)} \quad (B.10)$$

$$M_j = \sum_i D_i^j N_i(D_i) \Delta D. \quad (B.11)$$

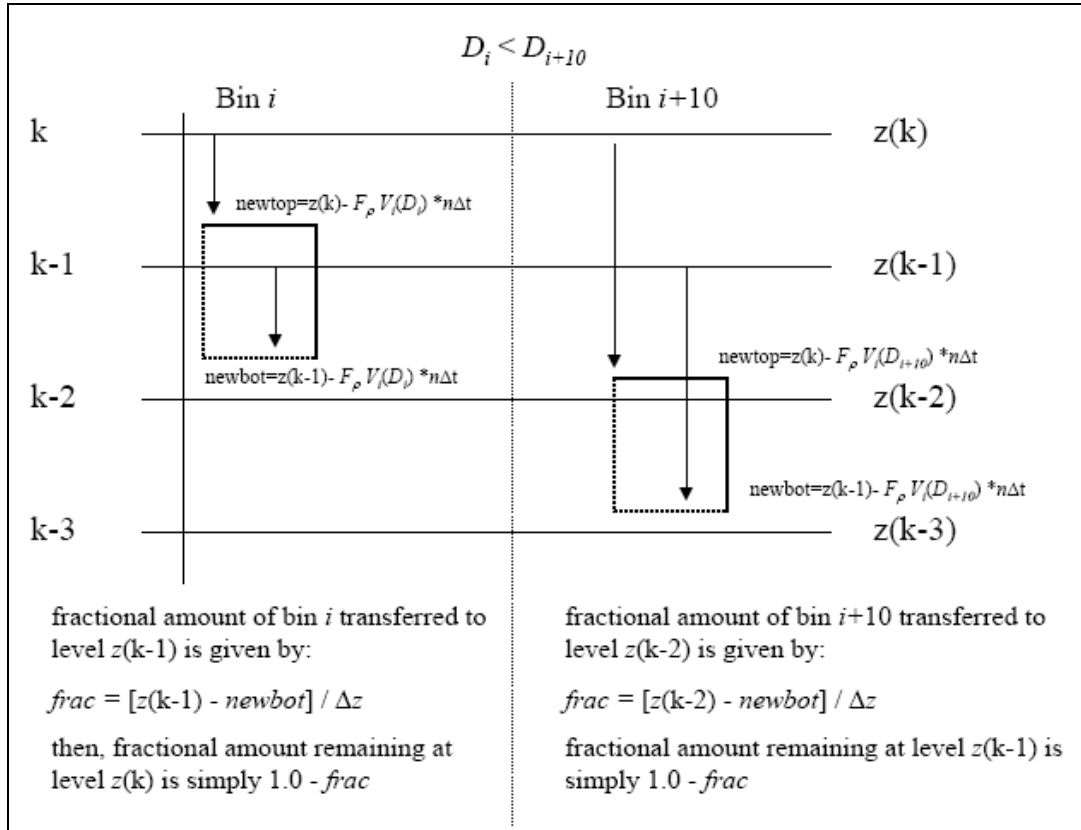


Figure B.2: Schematic of fractional amount computations of initial 'bin layers' transferred to lower grid levels for constant grid spacing

B.3) 1D sedimentation tests for 3MHAIL vs original RAMS 1M & 2M sedimentation

Extensive testing of the bin-emulating 3MHAIL sedimentation scheme was performed by applying the scheme to an initial hail distribution within a 1D column model separate from the main RAMS model. The RAMS original bin-emulating 1M and 2M sedimentation schemes were also modeled, and the results from all three sedimentation schemes were compared to those from

a true bin sedimentation scheme. Examples of time-height profiles of the predicted N_{th} , r_h , and, Z_h values using the different sedimentation schemes are displayed in Figures B.3 through B.9 for hail distributions initialized with various values for r_h , N_{th} , and v_h (Table B.1). The ranges for these variables were chosen such that distributions spanning the ranges of $D_{\bar{m}h}$ and v_h associated with the 3MHAIL scheme were represented. For the 1M scheme, r_h is predicted and N_{th} is diagnosed from the fixed $D_{\bar{m}h}$ value, whereas for the 2M scheme, both r_h and N_{th} are predicted. Z_h is diagnosed from r_h , N_{th} , and the fixed v_h value for both the 1M and 2M sedimentation schemes. A vertically stretched grid is used for sedimentation tests SR1, SR2, SR3, and SR4 (Figures B.3 to B.6), with spacing of 200 m at the lowest model level and a stretch ratio of 1.05 up through 6.1 km, above which the grid spacing is constant at 500 m. Constant vertical grid spacing of 153 m is employed for tests CN1, CN2 and CN3 (Figures B.7 to B.9). Different combinations of minimum grid spacing values (25, 50, 100, and 250 m) and stretch ratios (1.01, 1.025 and 1.1), as well as various constant grid spacing values (50, 100, 200, and 250 m) were also tested and generally gave results similar to those presented in Figures B.3 through B.9.

The initial hail distribution is defined by specifying r_h to vary sinusoidally over a layer between heights of 6.6 and 8.6 km (8.1 to 9.3 km for constant grid spacing cases), with a

TABLE B.1: Names of 1D sedimentation test cases, time step lengths and initial hail distribution parameters for the time-height profiles displayed in Figures B.3 through B.9.

Figure	Case	Δt [s]	N_{th} [m^{-3}]	r_h [g m^{-3}]	v_h	$D_{\bar{m},\text{min}}$ [cm]	$D_{\bar{m},\text{max}}$ [cm]	$D_{\bar{m},\text{fixed}}$ [cm]
B.3	SR1	4	250.4	0.551	2	0.098	0.121	0.1
B.4	SR2	4	1.5	1.5	5	0.86	1.08	1.0
B.5	SR3	4	0.025	1.008	7	3.07	3.87	3.5
B.6	SR4	4	0.0501	2.504	8	3.36	4.23	3.75
B.7	CN1	3	48.912	0.498	1	0.126	0.164	0.15
B.8	CN2	3	0.498	1.467	5	1.05	1.56	1.3
B.9	CN3	3	0.122	2.445	8	2.47	3.1	2.8

maximum value for r_h at 7.6 km (8.7 km for constant grid spacing cases). N_{th} is specified as a constant multiplied by air density $\rho_a(z)$, v_h is initially constant over the layer, and Z_h is computed based on the values of r_h , N_{th} , and v_h .

The time-height profiles displayed in Figures B.3 through B.9 show that the 3MHAIL sedimentation scheme (bottom rows) produces far superior results than either the 1M (top rows) or 2M (middle rows) schemes when compared to the true bin sedimentation scheme (solid curves in all panels) for the various initial distribution parameters shown. Gravitational size sorting is clearly evident in the bin sedimentation profiles as exhibited by the progressive downward shift in the profiles for increasing moment order (N_{th} to r_h to Z_h) at a given time beyond $t = 0$. Due to the fact that N_{th} and Z_h are diagnosed directly from r_h in the 1M sedimentation cases, the profiles of N_{th} and Z_h are largely similar to those for r_h with the maxima of N_{th} and Z_h following the maxima in r_h . These results demonstrate the inability of the 1M sedimentation scheme to represent size sorting and agree qualitatively with results from similar investigations of different 1D sedimentation models by MY05a, Wacker and Lüpkes (2009), and Milbrandt and McTaggart-Cowan (2010). Beyond $t = 0$, the Z_h profiles for the 1M and 2M schemes maintain their respective general vertical structures and maximum magnitudes (except in cases SR1 and CN1 for 2M), and the 1M N_{th} profiles exhibit values that are larger than those for the bin scheme owing to the restriction that $D_{\bar{m}h}$ be constant. The maxima in the diagnosed Z_h profiles for the 1M scheme cases are generally less than those for all other schemes due to N_{th} values that are consistently greater in the 1M sedimentation cases. In general, the 3MHAIL sedimentation scheme tends to underpredict the maxima in the predicted quantities in all cases, though these profiles still show the closest match to the bin scheme.

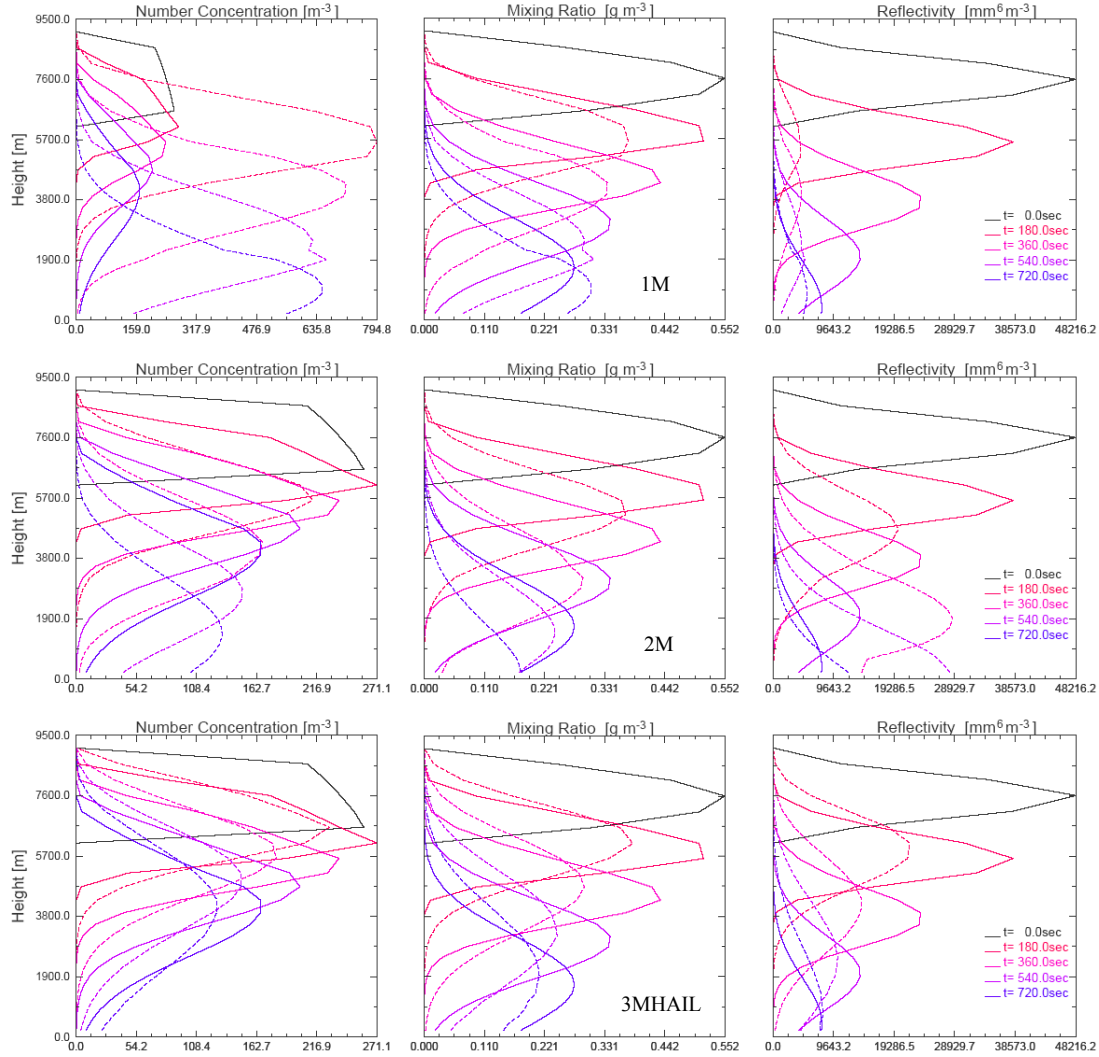


Figure B.3: Time-height profiles of hail number concentration [m^{-3}] (left column), hail mixing ratio [g m^{-3}] (middle column), and hail reflectivity [$\text{mm}^6 \text{m}^{-3}$] (right column) for a bin sedimentation scheme (solid curves) and for bulk (dashed curves) 1M (top row), 2M (middle row), and 3MHAIL (bottom row) sedimentation schemes for case SR1. Distribution is initialized with parameters that resemble a wide size distribution ($\nu_h = 2$) weighted towards smaller hail sizes, with mean mass diameters ranging from 0.98 to 1.21 mm. Note that in this and subsequent figures, the abscissa for the top left panel has different scale than the other two panels in the left column.

For initial distributions weighted towards small and moderate hail sizes (SR1, SR2, CN1, and CN2), the N_{th} , r_h , and Z_h profiles for the 1M and 2M schemes are shifted downwards with respect to the profiles for the bin scheme, signifying that sedimentation of these distributions is occurring too rapidly in these cases. This leads to an overestimation in the predicted and diagnosed quantities at low levels with these schemes similar to results for 1D sedimentation

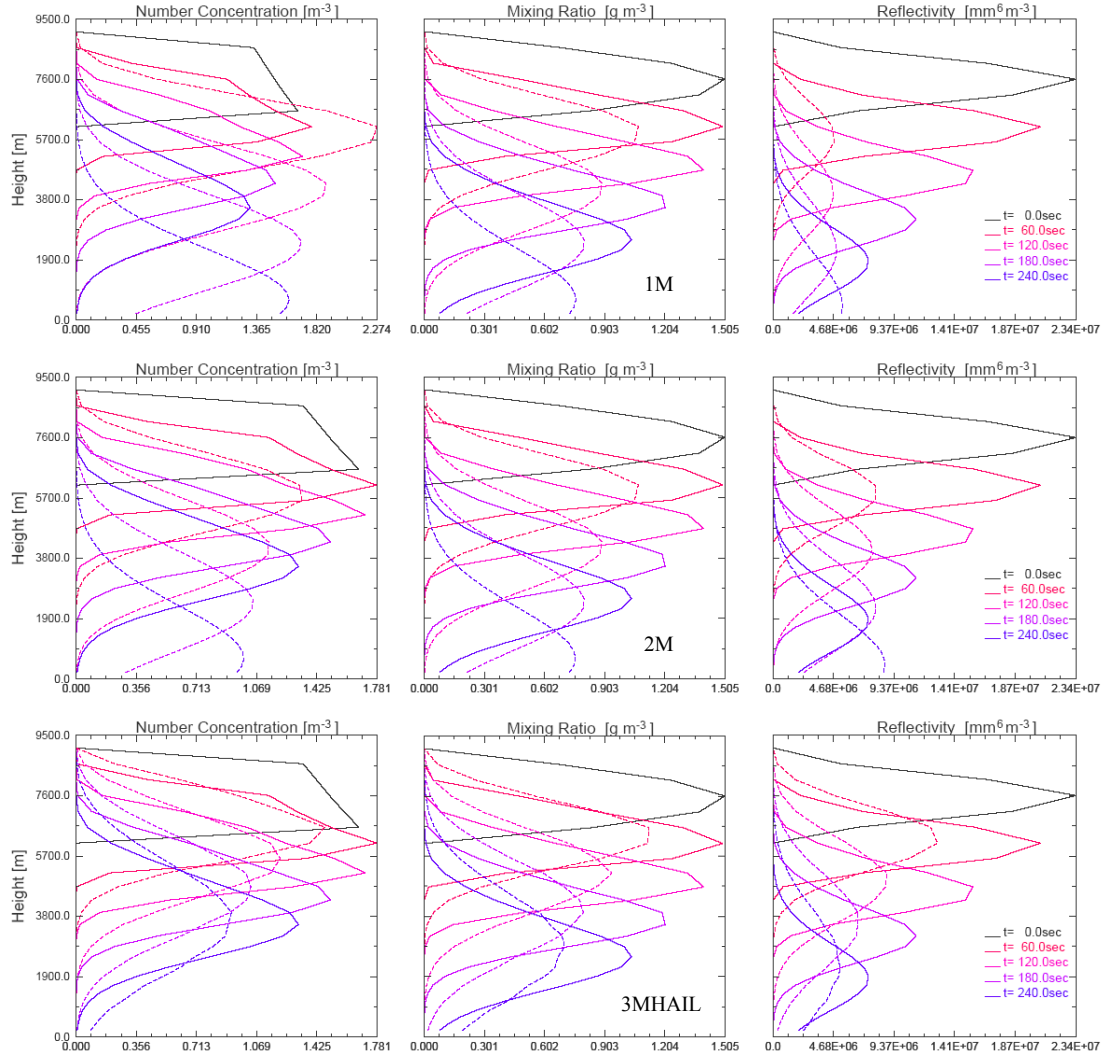


Figure B.4: As in Figure B.3, except for case SR2 in which distribution is initialized with parameters that resemble a narrower size distribution ($\nu_h = 5$) weighted towards moderate sizes, with mean mass diameters ranging from 0.86 to 1.08 cm.

with a 2M scheme reported by Wacker and Seifert (2001). The exceptions are the 1M profiles for case CN1, for which the predicted r_h and diagnosed Z_h values fall slower than in the bin scheme, whereas the diagnosed N_{th} values fall much more quickly than the corresponding bin scheme values.

Also evident is that in cases with low ν_h values (SR1 and CN1), the diagnosed Z_h values for the 2M scheme are seen to increase well beyond the bin scheme Z_h values. These artificial

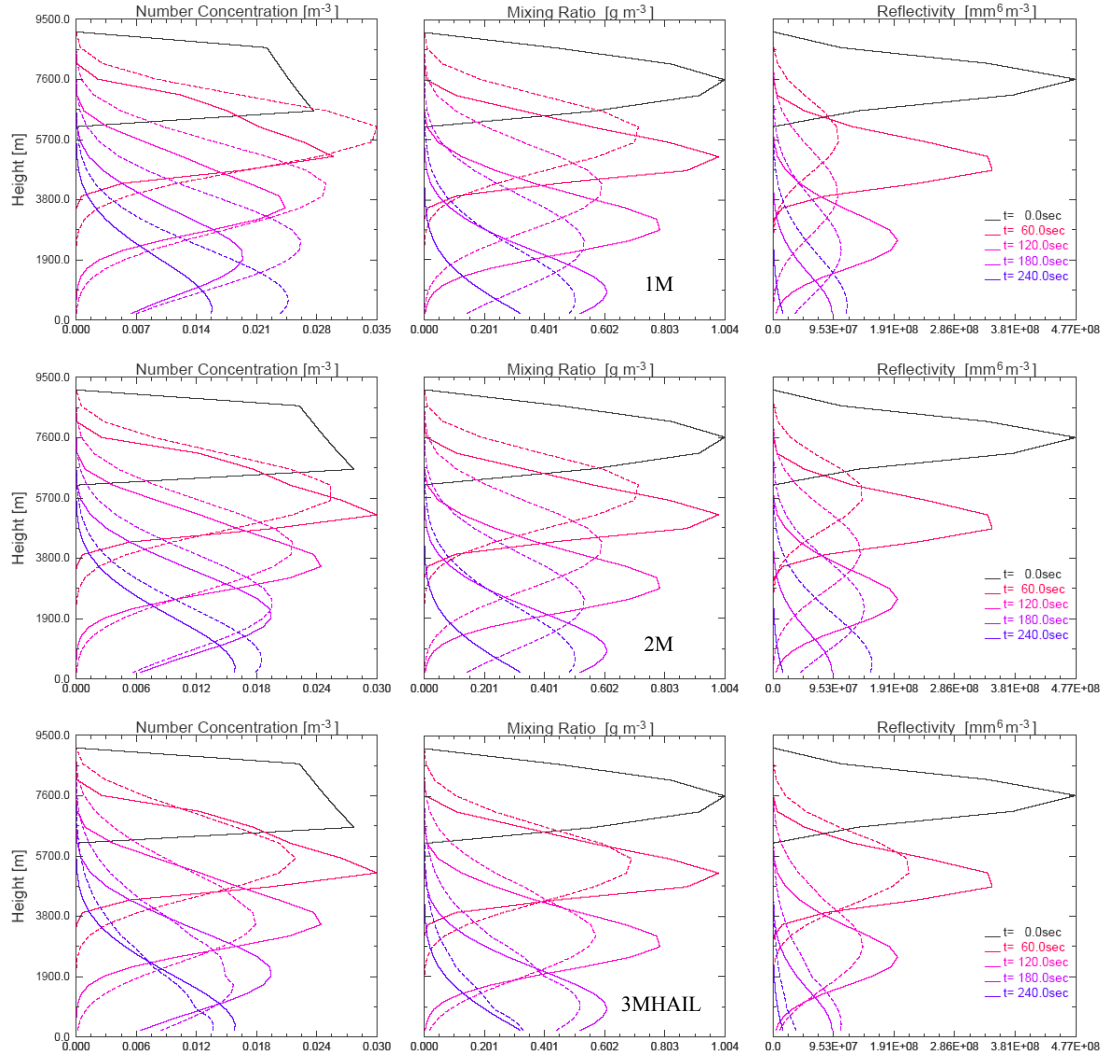


Figure B.5: As in Figure B.3, except for case SR3 in which distribution is initialized with parameters that resemble a narrow size distribution ($\nu_h = 7$) weighted towards large sizes, with mean mass diameters ranging from 3.07 to 3.87 cm.

increases in Z_h are partly attributed to exacerbated size sorting in the 2M sedimentation scheme due to the greater number of larger particles in the tail of the distribution when ν_h is small (MY05a, Mansell 2010). The diagnosis of the 6th moment (Z_h) from predicted lower order moments M0 and M3 (N_{th} and r_h) in the 2M scheme can cause the maxima in Z_h to overshoot the initial maximum value (Wacker and Lüpkes 2009; Milbrandt and McTaggart-Cowan 2010), as clearly evident in case CN1 (Figure B.7), though this does not occur in any other of the 2M cases

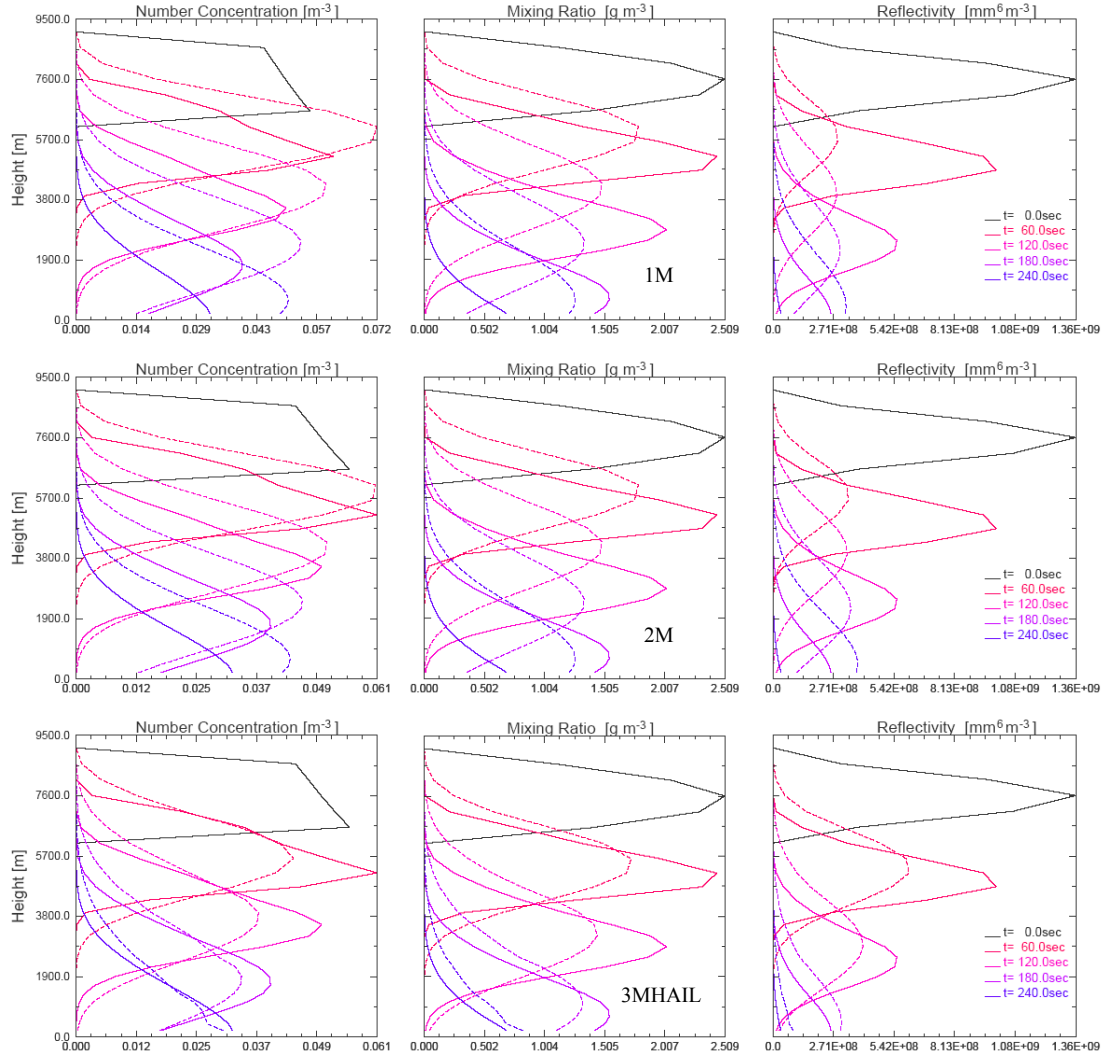


Figure B.6: As in Figure B.3, except for case SR4 in which distribution is initialized with parameters that resemble a narrow size distribution ($\nu_h = 8$) weighted towards large sizes, with mean mass diameters ranging from 3.36 to 4.23 cm.

examined. The maxima of the predicted quantities for the 1M and 2M sedimentation schemes tend to be underpredicted in cases SR1 and SR2, yet the maxima in r_h tend to be overpredicted in cases CN1 and CN2 for the 1M scheme and both r_h and N_{th} maxima are overpredicted in the CN2 case for the 2M scheme. On the other hand, the r_h and N_{th} profiles for the 2M scheme in the CN1 case show fairly good agreement with the bin scheme profiles, albeit a slight downward shift with respect to the bin scheme profiles is evident. The 3MHAIL profiles in the SR1 and

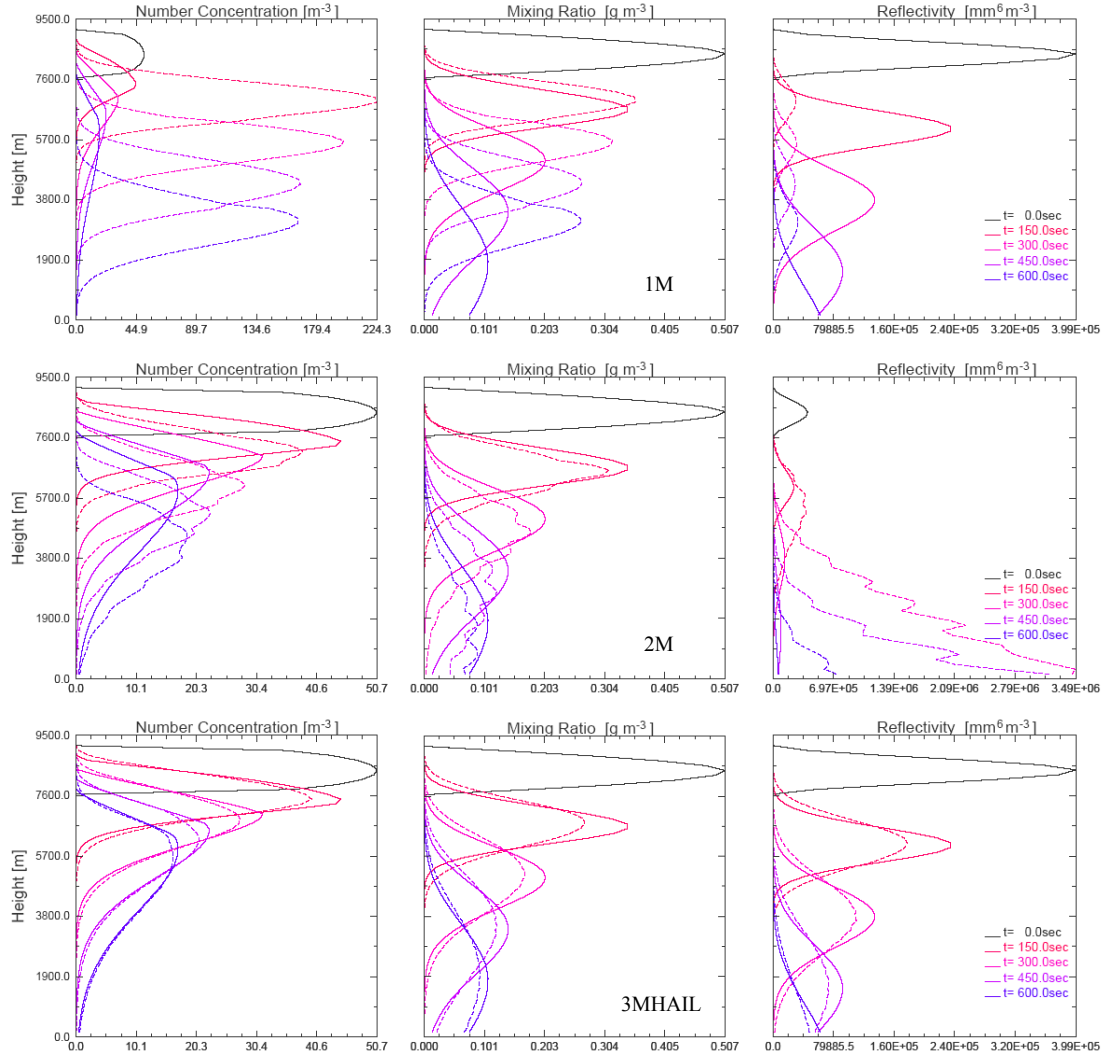


Figure B.7: As in Figure B.3, except for case CN1 in which distribution is initialized with parameters resembling an exponential distribution as in MY05a ($\nu_h = 1$). Mean mass diameters range from 1.26 to 1.64 mm. Note the abscissa for the middle right panel also has a different scale than the other two panels in the right column.

SR2 cases also exhibit overestimation (underestimation) of sedimentation of the predicted quantities in the lower (upper) portions of each profile, yet these profiles still most closely resemble those produced by the bin scheme compared to either the 1M or 2M schemes. For the CN1 and CN2 cases, all of the 3MHAIL profiles display excellent agreement with the bin scheme profiles, with the exception of the 3MHAIL Z_h profile for the CN2 case in which the lower regions of the Z_h profile are overestimated, particularly at later times.

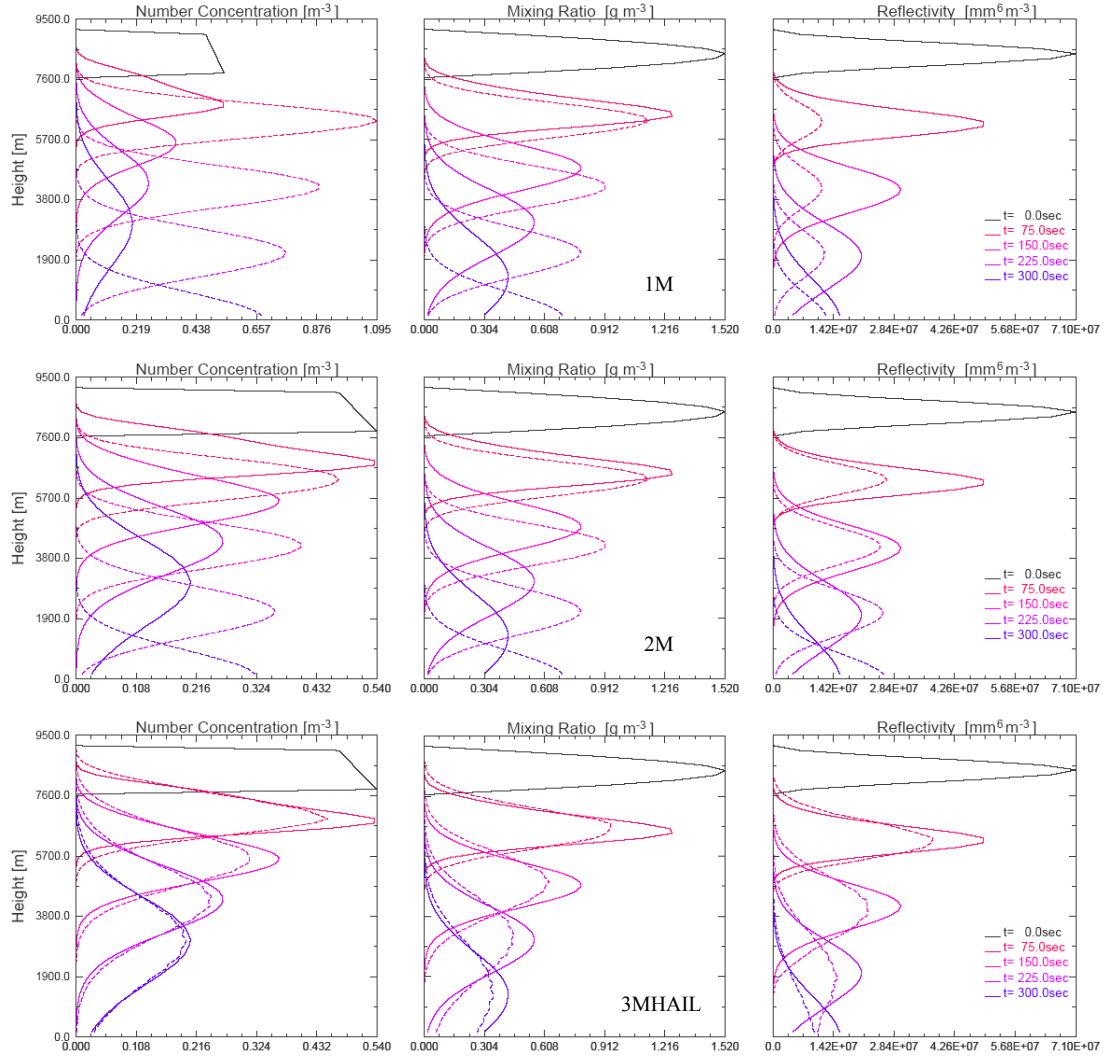


Figure B.8: As in Figure B.7, except for case CN2 in which distribution is initialized with parameters that resemble a narrow size distribution ($\nu_h = 8$) weighted towards moderate sizes, with maximum mean mass diameters ranging from 1.05 to 1.56 cm.

Cases for which the initial hail distributions are narrow and weighted towards large mean mass diameters (SR3, SR4, and CN3) reveal that sedimentation occurs too slowly with the 1M and 2M schemes as evident by the N_{th} , r_h , and Z_h profiles that are generally shifted upwards with respect to the bin solution profiles. Furthermore, unlike in cases SR1, SR2, CN1, and CN2, the predicted r_h profiles for the 1M and 2M schemes are indistinguishable from one another, and only slight differences in the maximum values of the N_{th} and Z_h profiles exist between the 1M and 2M

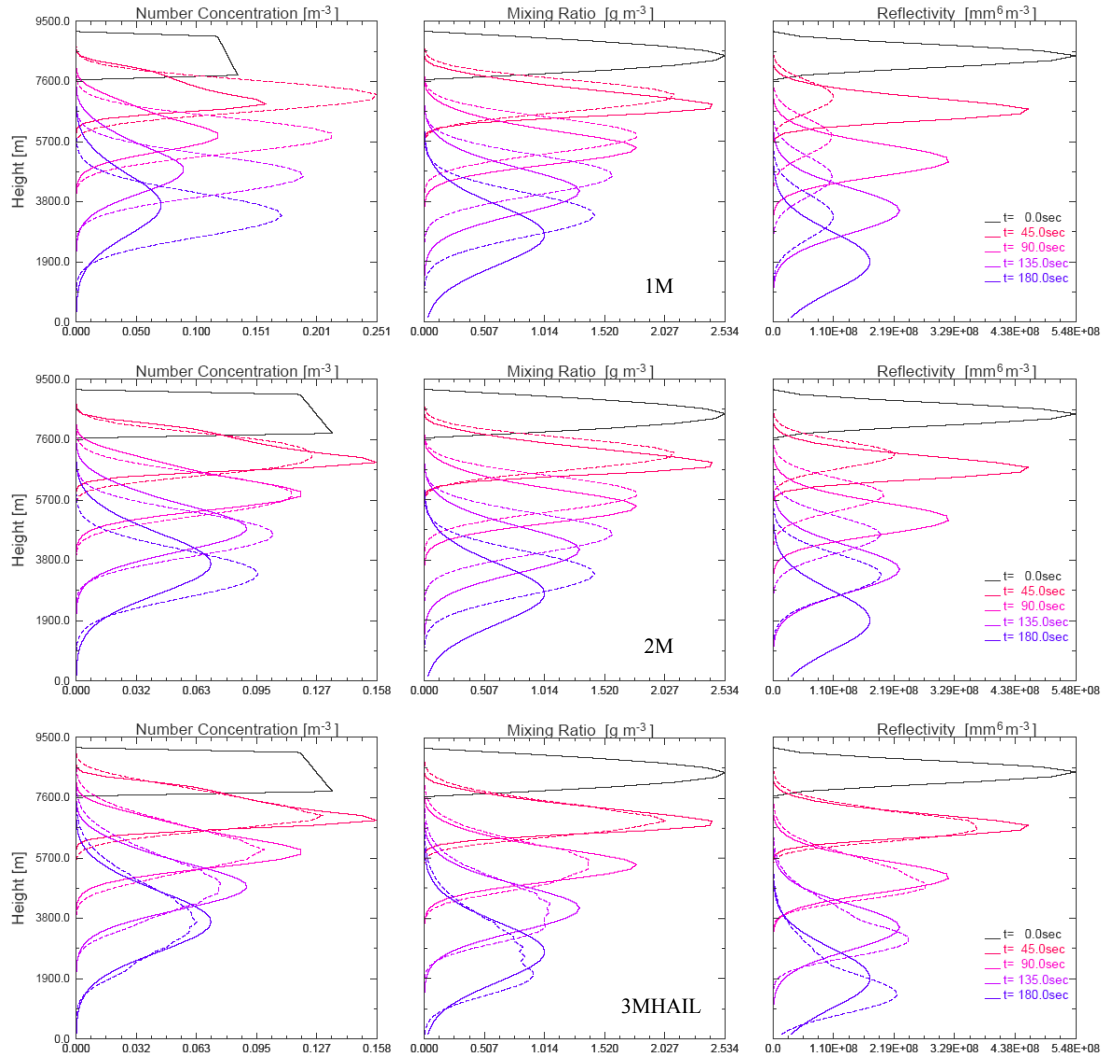


Figure B.9: As in Figure B.7, except for case CN3 in which distribution is initialized with parameters that resemble a narrow size distribution ($\nu_h = 8$) weighted towards large sizes, with maximum mean mass diameters ranging from 2.1 to 3.1 cm.

solutions. Thus, it appears that for these distribution types, little to no improvement is obtained in the solutions for sedimentation when predicting two moments versus only one. This is in contrast to the general conclusions for similar 1D sedimentation tests reached by MY05a, Wacker and Lüpkes (2009), and Mansell (2010), namely that the prediction of two moments produces superior results than the prediction of a single moment. However, these studies examined distributions for only a single initial mixing ratio value weighted towards small particle sizes,

and sedimentation was carried out using moment-weighted bulk fall velocities on constant vertical grid spacing. Once again, the N_{th} , r_h , and Z_h profiles produced by the 3MHAIL sedimentation scheme for cases SR3, SR4, and CN3 are clearly more accurate than either the 1M or 2M schemes when compared to the bin profile solutions.

APPENDIX C

Computation of radar reflectivity from model hydrometeor fields using T-matrix / Mueller matrix method

The T-matrix method is used to compute the complex scattering amplitudes of nonspherical dielectric bodies (Waterman 1965; Barber and Yeh 1975) and is especially suited for particles that are Mie scatterers (i.e., large hailstones) for which the oscillatory nature of the scattering behavior must be considered. The T-matrix only calculates the scattering behavior of a single particle with arbitrary orientation, thus in order to compute the scattering of a radar volume containing particles of different sizes, shapes, phase, and orientation, the Mueller-matrix method is used (Vivekanandan et al. 1991). In the current study, a two-layer T-matrix code (courtesy of Patrick Kennedy at CSU-CHILL) is used for the hail distributions to account for liquid-coated hailstones undergoing wet growth or melting (Bringi and Seliga 1977). All other precipitating hydrometeors (rain, snow, aggregates, and graupel) use a single layer T-matrix code. As the sizes of cloud droplets and pristine ice particles are very small compared to the S-band radar wavelength used in this study (11 cm), reflectivity from these particles is assumed to be negligible.

C.1) Construction of T-matrix look-up tables

In order to ease the computational burden of calculating the scattering behaviors for all types of particles, a large number of look-up tables are generated with the T-matrix codes over a range of representative hydrometeor distributions for hail, rain, snow, aggregates, and graupel. All hydrometeor distributions conform to a three-parameter gamma type distribution (Chapter 3.1),

and all hydrometeors are assumed to be oblate spheroids falling with the major axis aligned horizontally. The axis ratios of snow, aggregates, and graupel are fixed at 0.75 similar to Jung et al. (2010), whereas the axis ratios of raindrops depend on size and are determined using the formula of Pruppacher and Beard (1970). The axis ratios of hailstones also depend on size and are determined empirically based on observations of Oklahoma hailstones by Knight (1986) (Fig. C.1). To further reduce both the computational and storage demands of the look-up tables, the temperature of hail is fixed at 0 °C, and the temperatures of snow and aggregate particles are fixed at -15 °C. The look-up tables for raindrops (graupel) are constructed for a temperature range of -20 to 30 °C (-40 to 0 °C) at uniform temperature intervals of 5 °C.

For each hydrometeor type considered, representative size distributions are computed over a range of mean mass diameters (D_m) specified in Table 3.1 (Chapter 3.1) using the method described in Appendix A.1, with the exception that only 20 mean mass (\bar{m}) increments and

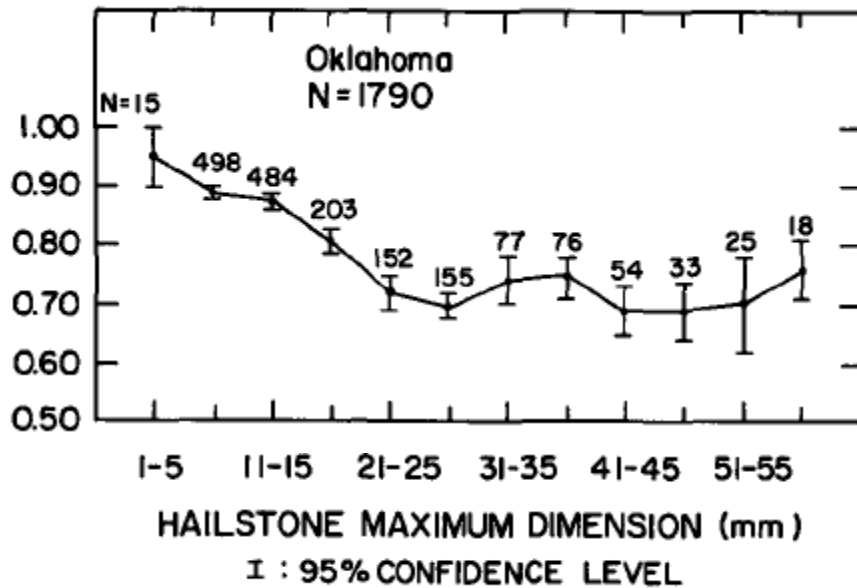


Figure C.1: Average shape factors (axis ratios, a/b) for Oklahoma hailstones as a function of longest hailstone axes (b). Bars indicate 95% confidence level for average axis ratio from the t distribution. [From Knight 1986].

fixed shape parameters of $\nu=2$ are used for rain, snow, aggregates, and graupel. For each \bar{m} increment, the representative distribution is partitioned into discrete size bins according to the specified ranges and size increments listed in Table C.1, and the gamma distribution (Eqn. 3.1) values for each size bin are computed. Hydrometeor size distributions are truncated at particle sizes for which the bin gamma distribution values are below a threshold of 10^{-35} in order to omit unnecessary T-matrix computations. For example, the representative size distribution for rain with $D_{\bar{m}r} = 0.015$ cm includes only 12 size bins ranging from 0.01 to 0.45 cm, thereby reducing the total number of calculations performed during execution of the T-matrix program. This process is repeated for rain and graupel distributions for the specified temperature ranges. Thus, snow and aggregates each have 20 T-matrix look-up tables, whereas the number of look-up tables for rain and graupel are 220 and 180, respectively.

Construction of the T-matrix look-up tables for hail follows the same process as for the other hydrometeors, although a much greater number of look-up tables are generated given that the representative distributions are a function of \bar{m} , ν , (Appendix A.1) and hail liquid water fraction (LWF , values range from 0.0 to 0.95 in increments of 0.05). For each combination of (\bar{m} , ν , LWF), the size distribution is partitioned into discrete size bins as before, but now the hail

Table C.1: Particle diameter ranges, size increments, and maximum number of size bins for partitioning of hydrometeor distributions into discrete size bins for T-matrix computations.

Hydrometeor type	Diameter range (cm)	Diameter increment (cm)	Max number of increments
rain	0.01 to 1.65	0.04	42
snow	0.001 to 3.001	0.05	61
aggregates	0.001 to 3.001	0.05	61
graupel	0.01 to 1.65	0.04	42
hail	0.1 to 10.1	0.2	51

internal energies of each size bin are determined via interpolation of the values stored in the pre-computed Q_{tab} look-up table (Appendix A.1). The bin internal energies are then used to compute the individual bin LWF values from which the ice core diameters of the hailstones can be computed using Eqn. 3.83 (Chapter 3.5.2). Hail size bins that have LWF values greater than 0.95 are considered completely melted and are thus not included in the T-matrix scattering calculations for the representative hail size distributions. For example, for $D_{\bar{m}h} = 1.08$ cm ($\bar{m} = 6.03 \times 10^{-4}$ kg), $\nu=4.0$, and $LWF = 0.5$, the two-layer T-matrix program computes the scattering amplitudes for liquid-coated hailstones within the diameter range from 0.9 to 10.1 cm, with the corresponding ice core diameters ranging from 0.6 to 10.0 cm. The total number of T-matrix look-up tables for the 3MHAIL scheme is 31160 and requires about 215 GB of storage, hence the reason for using only a single temperature for hail. Fortunately, all of the look-up tables only need to be computed once and can be used to compute reflectivity and polarimetric variables for any simulation using the Mueller matrix program.

C.2) *Mueller-matrix calculations*

The Mueller-matrix (Vivekanandan et al. 1991) program incorporates the characteristics of individual hydrometeor distributions contained within a single model grid point and calculates the total reflectivity volume (Z_H) as well as the polarimetric radar quantities (ZDR , LDR , r_{hv} , k_{dp} , and reflectivity difference) utilizing the scattering properties of individual particles stored in the T-matrix look-up tables. The Mueller-matrix method also considers the orientations of falling hydrometeors (canting angles) and radar elevation angles in computing the reflectivities and associated polarimetric variables. A Gaussian distribution type for the canting angles is assumed for all hydrometeors, with a mean canting angle of 0° . The standard deviation of the canting

angle is assumed to be 30° for raindrops, 60° for hail, 20° for both snow and aggregates, and 0.5° for graupel (B. Dolan, personal communication). Hydrometeor distributions are described by a gamma-type distribution function (C.1) similar to that for RAMS

$$N(D) = N_o D^m e^{\left[-(3.67+m)\frac{D}{D_o}\right]}, \quad (C.1)$$

where N_o is the intercept parameter, D_o is the median volume diameter (for $D_{max} = \text{infinity}$), and $m = \nu - 1$ is the spectral shape parameter (Illingworth and Caylor 1991; Illingworth and Blackman 2002). In terms of RAMS variables, N_o and D_o are given by Eqns. (C.2) and (C.3), respectively.

$$N_o = \frac{N_t}{\Gamma(\nu)} \left(\frac{1}{D_n} \right)^\nu \quad (C.2)$$

$$D_o = (2.67 + \nu) D_n. \quad (C.3)$$

At each grid point containing hail, rain, snow, aggregates, and/or graupel, the N_o and D_o terms for each hydrometeor type are computed from the grid point values of total number concentration (N_t) and mean mass diameter (D_m), as well as ν_h for hail in the case of simulations using the 3MHAIL scheme, where D_n is calculated from D_m using Eqn. (A.1) from Appendix A.1. The radar elevation angles θ (C.6) are computed by first determining the horizontal distance s from the specified radar location (x_{radar}, y_{radar}) to the the grid point of interest (x, y, z)

$$s = \frac{y - y_{radar}}{\sin(\alpha)}, \quad (C.4)$$

where

$$\alpha = \tan^{-1} \left(\frac{y - y_{radar}}{x - x_{radar}} \right). \quad (C.5)$$

The radar elevation angle is computed as

$$\theta = \tan^{-1}\left(\frac{h}{s}\right), \quad (\text{C.6})$$

where h is the height from the surface ($z = 0$) to the center of the grid point of interest.